DOE/NASA/0167-12
NASA CR-180891
GARRETT NO. 31-3725(12)

ADVANCED GAS TURBINE (AGT) TECHNOLOGY DEVELOPMENT PROJECT

FINAL REPORT

Engineering Staff of
Garrett Auxiliary Power Division
A Unit of Allied-Signal Aerospace Company

March 1988

Prepared for
NATIONAL AERONAUTICS AND SPACE ADMINISTRATION
Lewis Research Center
Cleveland, Ohio 44135
Under Contract DEN3-167

for
U.S. DEPARTMENT OF ENERGY
Office of Transportation Systems
Heat Engine Propulsion Division
Washington D.C. 20585

TABLE OF CONTENTS

		Page
1.0	SUMMARY	1
1.1	Powertrain Development	1
1.2	Power Section Development	1
1.3	Component/Subsystem Development	2
1.4	Ceramic Materials and Component Development	3
2.0	INTRODUCTION	6
3.0	REFERENCE POWERTRAIN DESIGN	8
4.0	POWER SECTION DEVELOPMENT	13
4.1	Engine Mechanical Development	13
4.1.1	Foil Bearing	13
4.1.2	Thrust Bearing Development	19
4.1.3	Ball Bearing and Compressor Seal Design	22
4.1.4	Rotor Clearance Evaluation	23
4.1.5	Metallic Structure Design	25
4.2	Engine Rotor Dynamic Development	26
4.2.1	AGT101 Rotor Dynamic History	26
4.2.2	Current Rotor System Configuration	31
4.2.3	Rotor System Test Results	31
4.2.4	Rotor Static Modal Determination Testing	32
4.2.5	Rotor System Analysis	32
4.2.6	Rotor Stability Analysis	33
4.3	Engine Development Evaluations	34
4.3.1	Metallic Engine Testing	36
4.3.2	Ceramic Structure/Metallic Turbine Engine Development	39
4.3.3	Ceramic Engine Development	42
4.3.4	Engine Performance Testing	45
4.3.5	Ceramic Engine Seal Development	45
5.0	COMPONENT/SUBSYSTEM DEVELOPMENT	47
5.1	Compressor Development	47
5.1.1	Compressor System Requirements	47
5.1.2	Aerodynamic Development	47
5.1.3	VIGV Design and Testing	56
5.1.4	Impeller Mechanic Design	57
5.1.5	Compressor Design for Improved Producibility	61

TABLE OF CONTENTS (Contd)

		Page
5.2	Turbine Development	65
5.2.1	Aerodynamic Design	65
5.2.2	Turbine Aerodynamic Performance Testing	73
5.2.3	Metallic Dual Alloy Rotor	79
5.2.4	Ceramic Turbine Rotor Design	84
5.3	Combustor Development	88
5.3.1	Combustor Design	88
5.3.2	Combustor Development	90
5.4	Regenerator System	93
5.4.1	Ford Regenerator Development	94
5.4.2	Garrett Regenerator Development	124
5.5	Gearbox/Transmission	139
5.6	Controls and Accessories	141
5.6.1	Engine Electronic Control Unit	142
5.6.2	Engine Fuel Control	144
5.6.3	Variable Inlet Guide Vane Actuator	144
5.6.4	Electrical Accessories	144
6.0	CERAMIC MATERIALS AND COMPONENT DEVELOPMENT	147
6.1	Ceramic Materials Testing	147
6.1.1	Fast Fracture and Stress Rupture	147
6.1.2	Ceramic Compatibility Testing	149
6.1.3	Ceramic Interface Evaluation	170
6.1.4	RBSN Spalling Study	177
6.1.5	Laser Marking of Ceramic Materials	177
6.1.6	Slip Casting Rheology Studies	178
6.1.7	Turbine Diffuser Insulation Evaluation	179
6.2	Ceramic Turbine Rotor	182
6.2.1	Initial Evaluations	182
6.2.2	Bladed Rotor Fabrication	183
6.2.3	Hot Turbine Rig	187
6.2.4	Turbine Rotor Attachment	188
6.2.5	Cold Spin Testing	190
6.2.6	Rotor Blade Vibration	190
6.2.7	Rotor Stress Analysis	199
6.2.8	Rotor Life Prediction	200

TABLE OF CONTENTS (Contd)

		Page
6.3	Ceramic Structures	207
6.3.1	Component Design/Analysis	208
6.3.2	Rig Design/Development	255
6.3.3	Component Rig Testing	268

APPENDIX A AIRESEARCH CASTING COMPANY ADVANCED GAS TURBINE (AGT) TECHNOLOGY DEVELOPMENT PROJECT FINAL REPORT

APPENDIX B FORD MOTOR COMPANY ADVANCED GAS TURBINE (AGT) TECHNOLOGY DEVELOPMENT PROJECT FINAL REPORT

APPENDIX C PURE CARBON COMPANY ADVANCED GAS TURBINE (AGT) TECHNOLOGY DEVELOPMENT PROJECT FINAL REPORT

APPENDIX D LIST OF SYMBOLS, ABBREVIATIONS, AND ACRONYMS

APPENDIX E REFERENCES

NASA C-168 FORM

LIST OF FIGURES

Figure	Title	Page
1	AGT101 Program Schedule	7
2	AGT101 RPD Powertrain	8
3	AGT101 Power Section	9
4	AGT101 Drive System Schematic	10
5	AGT101 Installation - Side View	11
6	AGT101 Installation - Front View	11
7	AGT101 Estimated Performance Curves	12
8	AGT101 Specific Fuel Consumption	12
9	Basic Bearing Configuration	14
10	Foil Bearing Deflected State at 100,000 RPM Operating Speed	14
11	Film Pressure Distribution at Operating Speed	15
12	Foil Bearing Designs Compared	16
13	Foil Bearing Surface Coating Development	17
14	Foil Bearing Dynamic Properties Wear Rig	17
15	TiN Coated Ring (Top) Versus Au Coated Disk (Bottom) After 591 Starts at Ambient Temperature and 4.3 psid Load	19
16	Typical Results of Dynamic Friction Test	20
17	AGT101 Hydrodynamic Thrust Bearing Configuration	21
18	Thrust Bearing Design Detail	21
19	Thrust Bearing/Ball Bearing Load Share Characteristic	22
20	Total Analytical Heat Generation for AGT101 Fluid Film Thrust Bearing Cavity	22
21	AGT101 S/N 001 Build 21 Fluid Film Thrust Bearing (Test 4-19-84)	23
22	Thrust Bearing Power Consumption Decrease with Oil Flow	23

LIST OF FIGURES (Contd)

Figure	Title	Page
23	Floating Ring Seal	23
24	Typical Turbine Axial Clearance Transient for Cold Start	24
25	Compressor and Turbine Clearance Loss Due to Thermal Growths	25
26	AGT101 Metal Structured Power Section	27
27	AGT101 Engine Rotor System Configurations	28
28	AGT101 Engine Initial Rotor System Configuration Response	29
29	AGT101 Engine Motoring Rotating Group Configurations Tested	30
30	AGT101 Engine Aerodynamic Components Excite Subsynchronous Motion	30
31	AGT101 Rotor Dynamics Rig Impact Test Configuration	30
32	AGT101 Engine Operational Rotor System Configuration	31
33	AGT101 Engine Current Rotor System Configuration	32
34	AGT101 Engine Rotor Mass and Stiffness Model	33
35	AGT101 Engine Rotor Support Schematic	34
36	AGT101 Engine Critical Speed Mode Shapes	35
37	AGT101 Engine Unbalance Response/Support Displacements	36
38	AGT101 Engine Unbalance Response/Support Forces	37
39	AGT101 Engine Whirl Speed Map	38
40	AGT101 Engine Forward Mode Log Decrements	39
41	The AGT101 Evolves to Ceramics	40
42	Ceramic Turbine Rotor Failed at 62,000 rpm	40
43	Strain Gaged Ceramic Turbine Rotor	41
44	S/N 002C - T4 Schedule Tested on February 16, 1984	42
45	Ceramic Structures Used in the 1149C (2200F) Test	43

LIST OF FIGURES (Contd)

Figure	Title	Page
46	Ceramic Components Following the 100-Hour Endurance Run at 1149C (2100F)	43
47	Dual Alloy Rotor Showing Cooling Air Path	43
48	Engine Test Data Setup Model	45
49	Single Separator Seal Configurations	46
50	Flow Separator Seal Configuration	46
51	AGT101 Impeller Design Exit Loss Function Distribution	48
52	AGT101 Impeller Design Exit Deviation Angle	49
53	Compressor Inducer Leading Edge Blade, Air Angle Distributions	49
54	Compressor Impeller Relative Air Angle Distribution	49
55	Compressor Impeller Blade Surface Mach No. Distribution - Shroud	49
56	Compressor Impeller Blade Surface Mach No. Distribution - Mean	50
57	Compressor Impeller Blade Surface Mach No. Distribution - Hub	50
58	AGT101 Impeller Design Minimum a/a*geom.	50
59	Impeller Normal Thickness Distribution	50
60	AGT101 Impeller Design Vector Diagrams	50
61	Splitter Blade Hub Leading Edge Movement	51
62	Splitter Leading Edge Tangential Position	51
63	Diffuser Deswirl Vane Analysis	51
64	AGT101 Diffuser and Deswirl Vane Assembly Axial View	52
65	AGT101 Diffuser Meriodional Flowpath	52
66	AGT101 Diffuser Vector Diagrams	53
67	AGT101 Modified Impeller Blade Loadings--Tip	53
68	AGT101 Modified Impeller Blade Loadings--Hub	53

LIST OF FIGURES (Contd)

Figure	Title	Page
69	AGT101 Modified Impeller Geometry	54
70	Compressor Rig	54
71	Full Stage Compressor Data, IGVs Open	55
72	Full Stage Compressor Data, IGVs = 40 Degrees	55
73	Full Stage Compressor Data, IGVs = 70 Degrees	55
74	AGT101 Inlet Guide Vane	56
75	AGT101 Compressor Inlet Guide Vane Test Rig	56
76	Inlet Guide Vane Flow Tabs	57
77	Inlet Guide Vane Test Results	57
78	AGT101 3-D Airfoil Elastic Stress at 100,000 rpm	58
79	AGT101 Impeller Airfoil Campbell Diagram	59
80	AGT101 Impeller Blade Vibratory Modes	59
81	AGT101 3-D Splitter Elastic Stress at 100,000 rpm	59
82	AGT101 Impeller Splitter Campbell Diagram	60
83	AGT101 Impeller Stress at 100 Percent Speed	60
84	AGT101 Impeller Isotherms - 29.4C (85F) Inlet Temperature	60
85	AGT101 Impeller Deformation at 100 Percent Speed	61
86	AGT101 Impeller Blade Vibratory Mode 1	62
87	AGT101 Impeller Blade Vibratory Mode 2	62
88	AGT101 Impeller Blade Vibratory Mode 3	63
89	AGT101 Titanium Impeller Campbell Diagram	63
90	Strain Gaged Impeller, Front View	63
91	Strain Gaged Impeller Blade	64

LIST OF FIGURES (Contd)

Figure	Title	Page
92	Strain Gaged Impeller, Backface	64
93	Compressor Test Rig with Slip Ring Assembly Installed in Test Cell	64
94	AGT101 Titanium Impeller Campbell Diagram Excitation Source	65
95	Strain Gage Test Results	65
96	Tensile Properties of Forged ALCOA PM A1-Fe-Ce	65
97	ALCOA A1-Fe-Ce Forged Properties (1000-Hour Temperature Exposure)	66
98	Tensile Properties of Aluminum Alloys	66
99	Stress Rupture Properties of Aluminum Alloys	66
100	HCF Properties of ALCOA A1-Fe-Ce	67
101	Impeller Blade Loading-Hub	67
102	Blade Loading-Mid-Passage	67
103	Impeller Blade Loading - Shroud	67
104	Off-Design Performance Characteristics as a Function of Design-Point Exit Swirl for NASA-DOE Advanced Gas Turbine Powertrain System Development Program	68
105	Turbine One-Dimensional Vector Diagrams	69
106	Turbine Design Summary	70
107	Baseline Turbine Inlet Duct Configuration	71
108	Turbine Inlet Strut Sections [Modified NACA 16-201 (t/c = 0.30)]	71
109	Turbine Inlet Hub and Tip Velocity Distribution for Baseline Configuration	71
110	Ceramic Turbine Stator Profile Design	72
111	Ceramic Turbine Stator Velocity Distribution (Base, 19 Vanes)	72
112	Ceramic Turbine Stator Profile Design	72

LIST OF FIGURES (Contd)

Figure	Title	Page
113	Ceramic Turbine Stator Velocity Distribution (Linear Pressure Surface, 19 Vanes)	72
114	Ceramic and Metal Turbine Flow Paths	73
115	Turbine Rotor Blade Angle Distribution	74
116	AGT101 Rotor Radial Loss Distribution	74
117	Turbine Rotor Velocity Distribution	74
118	Exhaust Diffuser Velocity Distribution	75
119	Cold Turbine Test Rig	76
120	AGT101 Test Rig Installed in Test Cell	78
121	Baseline Ceramic Cold Turbine Rig Test Results, System Efficiency Versus Pressure Ratio	78
122	Baseline Ceramic Cold Turbine Rig Test Results, System Efficiency Versus Engine Speed	78
123	AGT101 Exhaust System Loss Characteristics	79
124	AGT101 Metal Dual Alloy Wheel - 13 Blades, Conical Astroloy Hub	79
125	AGT101 Dual Alloy Steady-State Temperature Distribution	79
126	Stress Distribution for Dual Alloy Turbine Wheel	80
127	AGT101 Dual Alloy Steady-State Equivalent Stresses	80
128	AGT101 Metal Dual Alloy Wheel	80
129	Turbine Vibration Modes at Maximum Power	81
130	Dual Alloy Hub/Bladed Ring Assembly Cross Section	82
131	As-Cast AGT101 Bladed Rings and Machined Dual Alloy Wheel Assemblies	83
132	Machined AGT101 Dual Alloy Wheel Assembly--PM LC Astroloy Hub and MAR-M 247 Blade Ring	84
133	Microetched Cross Section of AGT101 Dual Alloy Wheel Test Specimen	84

LIST OF FIGURES (Contd)

Figure	Title	Page
134	Braze Closure After HIP Diffusion Bonding (Sample was Subjected to Yo-Yo Heat Treatment)	85
135	Radial Turbine Design Flow	86
136	AGT101 Ceramic Rotor Z-Section	86
137	Turbine Rotor Blade Angle Distribution	86
138	AGT101 Rotor Surface Velocity Distribution (Shroud)	86
139	AGT101 Rotor Surface Velocity Distribution (Mean)	87
140	AGT101 Rotor Surface Velocity Distribution (Hub)	87
141	Piloted Premixed/Prevaporizing Variable Geometry Combustor	88
142	Combustor Configurations Investigated In Emissions Testing	89
143	Element Test Rig Emission Test Results	89
144	Current Configuration Ceramic Combustor	89
145	Duplex Airblast Fuel Nozzle	90
146	Simplex Fuel Nozzle	90
147	Delavan Nozzle Configuration	91
148	Pilot Combustor Proof-of-Concept (Metal Configuration)	91
149	Enlarged Pilot Zone Combustor	93
150	AGT101 "Regenerator System" Components	93
151	AGT101 Regenerator System Components	95
152	Typical Regenerator Seal Schematic	97
153	Regenerator Seal Design Phase Comparison	98
154	Static Seal Leakage Comparison for Seal Design Phases	100
155	Inboard (Hot) Seal Crossarm Diagram Cooling Schematic	101
156	Middle (Support) Crossarm Diagram Temperature Distribution	102

LIST OF FIGURES (Contd)

Figure	Title	Page
157	Regenerator Seal Coating Wear Test Rig	103
158	3-D Thermal Stress Analysis	107
159	Regenerator Support Roller Locations	109
160	Regenerator Drive and Support System Bearing Designs	109
161	Diagonal Bond Configurations	110
162	Leak Paths and Pressure Notations	111
163	Analytical Model for Dynamic Rig Leakage	113
164	Seal Diaphragm Temperatures at 0.4 Percent Cooling Flow	114
165	Seal Coating Delamination from Crossarm Shoe	115
166	Seal Systems Comparison	116
167	Analytical Model Evaluating Non-Diaphragm Leak Paths as a Function of Component Distortions	117
168	Regenerator Core Axial Distortion Effects	118
169	Non-Diaphragm Seal Leakage Versus Uniform Clearance	119
170	Non-Diaphragm Seal Leakage Versus Uniform Clearance	120
171	Effect of Temperature on Seal Leakage	121
172	Regenerator LP Cold Rig	125
173	3-D Hot Wire Calibration Tunnel	126
174	Regnerator LP Cold Rig Preswirl and Screen Assemblies	126
175	Measured LP ΔP Data From Regenerator Cold Rig	127
176	LP Regenerator Cold Rig Upstream Diverter	127
177	LP Regeneration Cold Rig, Effects of Upstream Diverter	127
178	Regenerator HP Cold Rig	128
179	HP Regenerator Cold-Rig Flow Effects of Bonnet	129

LIST OF FIGURES (Contd)

Figure	Title	Page
180	Measured HP ΔP Data From Regenerator Cold Rig with Bonnet	129
181	Measured Analytical Flow Distortion Model	130
182	Measured HP ΔP Data From Regenerator Cold Rig	131
183	Measured LP ΔP Data From Regenerator Cold Rig	131
184	Capacity Rate Ratio and Integrated Mass Flux Versus Radial Position	132
185	Predicted AGT101 Regenerator Discharge Gas Isotherms for the Cruise Condition Based on Cold Rig Pressure Distortion Patterns	132
186	Predicted AGT101 Regenerator Local Core Mass Velocities for the Cruise Condition Based on Cold Rig Pressure Distortions	133
187	Effect of Linear Radial Distortion on Regenerator HP Effectiveness	134
188	Effect of Measured HP and LP Distortion on Effectiveness and Fuel Flow	134
189	Hot Regenerator Rig Schematic	135
190	Schematic of Helium Seeding Technique for Measuring Regenerator Leakage	136
191	Steady State Regenerator Discharge Temperature Distributions	137
192	Regenerator Seal Leakage	138
193	Regenerator Drive Torque	138
194	Phase V Regenerator Seal Drive Torque Versus Seal Pressure	139
195	Phase V Regenerator Seals Clearance Test	139
196	AGT101 Regenerator Seal Leakage	140
197	AGT101 Regenerator Core Torque	140
198	AGT101 Drive System,	141
199	AGT101 Transmission System	142
200	VSTC Test Results	143

LIST OF FIGURES (Contd)

Figure	Title	Page
201	Engine Electronic Control Unit (ECU)	143
202	ECU Logic Diagram	145
203	Fuel Control Test Setup (P/N 3601500)	146
204	View A. Four-Point Flexure Strength of ASEA Si_3N_4-2 1/2 Percent Y_2O_3	150
204 (Contd)	View B. Four-Point Flexure Strength of Ford RM-20, Hipped by ASEA, Cut From Rotor S/N 96	151
204 (Contd)	View C. Four-Point Flexure Strength of Kyocera SN 220M Sintered Silicon Nitride	152
204 (Contd)	View D. Kyocera SN 220M Flexural Stress Rupture	153
204 (Contd)	View E. Four-Point Flexure Strength of Kyocera SN 250M Sintered Silicon Nitride	154
204 (Contd)	View F. Kyocera SN 250M, Flexural Stress Rupture	155
204 (Contd)	View G. Four-Point Flexure Strength Comparison of Kyocera 250M SN 250M Cut From Rotors and Fabricated as Test Bar Specimens	156
204 (Contd)	View H. Stress Rupture Lives of Kyocera SN 250M From Rotors is Considerably Less Than That Fabricated as Test Bars	157
204 (Contd)	View I. Four Point Flexure Strength of Kyocera SN 270M Sintered Silicon Nitride	158
204 (Contd)	View J. Kyocera SN-270M, Flexural Stress Rupture	159
204 (Contd)	View K. Four-Point Flexure Strength of NGK SN-73 Sintered Silicon Nitride	160
204 (Contd)	View L. Four-Point Flexure Strength of NGK SN-81 Sintered Silicon Nitride	161
204 (Contd)	View M. NGK SN-81, Flexural Stress Rupture	162

LIST OF FIGURES (Contd)

Figure	Title	Page
204 (Contd)	View N. Four-Point Flexure Strength of NGK SN-82 Sintered Silicon Nitride	163
204 (Contd)	View O. NGK SN-82, Flexural Stress Rupture	164
204 (Contd)	View P. Four-Point Flexure Strength of NGK SN-84 HiPped Silicon Nitride	165
204 (Contd)	View Q. Four-Point Flexure Strength of NGK SN-84 HIPped Silicon Nitride Cut From Rotors S/N 135 and S/N 136	166
204 (Contd)	View R. NGK SN-84, Flexural Stress Rupture of Test Specimens and Rotors	167
204 (Contd)	View S. Four-Point Flexure Strength of Kyocera SC201 SSC	168
204 (Contd)	View T. Four-Point Flexure Strength of Standard Oil SASC	169
205	Interface Conditions for 871, 1149, 1371C (1600, 2100, 2500F) TIT Engines	170
206	Compatibility Test Condition III, Interface Material Combinations	172
207	Interface Test Apparatus	172
208	Static Coefficients of Friction Versus a Normal Load for RBSN and SASC at Room Temperature	173
209	Friction Versus Relative Motion for Bare SASC and RBSN Under the Point Contact Condition With a Normal Load of 25 Pounds	173
210	Coefficients of Friction for Oxidized RBSN Point Contact	174
211	Coefficients of Friction for Oxidized SASC Point Contact	174
212	Friction Versus Relative Motion for Bare SASC and RBSN Under the Line Contact Condition With a Normal Load of 25 Pounds	175
213	Room Temperature Strength RBSN and SASC After Line and Point Contact Tests	175
214	Calculated Peak Tensile Stresses for 1100C Contact Tests of RBSN and SASC	177

LIST OF FIGURES (Contd)

Figure	Title	Page
215	RCG Coated and Machined HTP Insulation from Lockheed	180
216	AGT101 Insulation Test Rig	180
217	Maximum Power and Idle Condition of Lockheed HTP-16 Insulation	181
218	Lockheed HTP-16 Cylinders After Cyclical Flow Testing	181
219	Simulated Rotors Were Used to Demonstrate Thick Section Fabrication Capability	182
220	Hollow Shaft Design Improves Fabricability	183
221	Example of Incomplete Blade Fill	184
222	Rotor S/N 256 Failed During Spin Test in Mode Similar to Previous Engine Failure	186
223	Increasing Consistency Evident in Cold Spin Test	187
224	IN907 Ceramic Test Sleeves	188
225	Initial Attachment Method Involved Solid Stub Shaft Rotor	189
226	Installation Difficulties with Initial Attachment Method	189
227	Installation Difficulties Solved with New Method	190
228	Internal Collet Attachment Method	190
229	Typical 3-D Views of the Finite Element Blade Vibration Model	191
230	Comparison of Inspected Z Sections (heavy lines) to TLs at 2.54 mm (0.10 inch) From Inducer Backface	192
231	Comparison of Inspected Z Sections (heavy lines) to TLs at 3.68 cm (2.45 inch) From Inducer Backface	193
232	Campbell Diagram for SN 250M Rotors Showing 19/Rev Stator Excitation Line	194
233	Consistency of Blade Frequency Response	195
234	Comparison of Holography Results with Predicted First Exducer Mode	196

LIST OF FIGURES (Contd)

Figure	Title	Page
235	Comparison of Holography Results with Prediced First Inducer Mode	196
236	Comparison of Holography Results with Prediced Second Exducer Mode	197
237	Initial Rotor Orientation Excited Exducer Tips (Bullen Test)	197
238	Rotor Re-oriented to Excite Inducer Tips (Bullen Test)	198
239	Cold Motoring Test Analysis Results	198
240	AGT101 Rotor Finite Element Stress Models	199
241	Maximum Power Thermal Distributions, T_4 = 1371C (2500F)	200
242	Partial Power Thermal Distributions, T_4 = 1227C (2240F)	201
243	Principal Stresses for Room Temperature 115,000 RPM Proof Test Predicted from No-Fillet Model	202
244	Principal Stresses for Maximum Power, Predicted from No-Fillet Model	203
245	Comparison of Concurrent and Independent Surface and Internal Failure Distributions	204
246	Effect of Biaxial Tension on Fracture Risk According to Batdorf's Criteria	204
247	Rotor Failure Probability for Partial Power Operating Conditions	205
248	Rotor Failure Probability for Maximum Power Operating Condition	205
249	Rotor Failure Probability for Partial Power Conditions Based on Properties of SN 250M Rotors	206
250	AGT101 Ceramic Components	207
251	Worst Case Light-Off Cycle (1282C)	209
252	Rig Cycle 871C (1600F) Static Structures	210
253	Effect of Scalloping Outer Diffuser	210
254	Outer Diffuser B1 and B2 Configurations	211

LIST OF FIGURES (Contd)

Figure	Title	Page
255	Inner Diffuser Initial Configuration Stress Analysis Results	211
256	Inner Diffuser Scalloped Configuration Stress Analysis Results	211
257	Turbine Shroud/Outer Diffuser Critical Stress Areas (Static Structures Rig Model)	212
258	Phase B Turbine Shroud Configurations	213
259	Static Structure Rig Light-Off Cycle	214
260	Static Structure Rig Operating Cycle	215
261	Turbine Shroud Critical Stress Areas (Shroud Screening Rig Model)	217
262	Screening Rig Cycle 13	218
263	Second Model Refinement to Shroud Fillet Radius	219
264	Normal Engine Light-Off, (Cycle 8)	222
265	Ramp Type Engine Cycle 11	222
266	Turbine Shroud/Outer Diffuser Critical Stress Areas (Engine Model)	223
267	Turbine Shroud Stress Response for Ramp Type Cycle (Engine Cycle 11)	223
268	Engine Heat Transfer Coefficients on Turbine Shroud/Outer Diffuser Model	224
269	Design Change From Type B2 to Type A3 Outer Diffuser	224
270	Shroud Cone to Insulation Radiation	224
271	Shroud Configurations Investigated in Phase C Study	225
272	Development Engine Lightoff (Cycle 17)	228
273	RBSN Shroud Stress for Various Stages of Development	229
274	Transition Duct/Combustor Baffle/Turbine Backshroud Critical Stress Areas	229
275	Static Structure Rig Light-Off Cycle 9	230

LIST OF FIGURES (Contd)

Figure	Title	Page
276	Static Structure Rig Cool-down Cycle 10	230
277	A1 and A2 Configurations Combustor Baffle	232
278	Engine Cycle 15 (Light-Off to 1149C Max Power)	234
279	Alternate Configurations of the Turbine Backshroud	237
280	Flow Separator Housing Strain Gage Test Correlation	237
281	The Original and Strutted RBSN Flow Separator Housing FEMS	238
282	Flangeless Flow Separator Housing Outer Cone and Attachment Configuration (Type X1)	238
283	Flow Separator Housing Critical Stress Areas	239
284	Pressure Deflections at the Regenerator Seal for Types B1 and B2 RBSN Flow Separator Housings	240
285	Pressure Deflections at the Regenerator Seal for Types B1 and B2 LAS Flow Separator Housings	240
286	Pressure Deflections at the Regenerator Seal for Type X1 RBSN Flow Separator Housings	240
287	Steady-State Cruise Radial Temperature Distribution Along the Flow Separator Housing Crossarm	241
288	Steady-State Cruise Thermal Deflections at the Regenerator Seal for Type B1 RBSN and LAS Flow Separator Housing	242
289	Steady-State Cruise Thermal Deflections at the Regenerator Seal for the RBSN Type B2 Flow Separator Housing	242
290	Type B1 Flow Separator Housing Thermal Stress Response During Lightoff	242
291	Turbine Stator Cutback Vane Trailing Edge Redesign	244
292	Turbine Stator Finite Element Stress Models	245
293	Turbine Stator Finite Element Thermal Model	245
294	Metallic Stator Assembly Thermocouple Locations	245

LIST OF FIGURES (Contd)

Figure	Title	Page
295	Typical Correlation Between Test and Analytical Turbine Stator Thermal Response	246
296	Turbine Stator Temperature Distribution 20 Seconds After Light-Off	246
297	Turbine Stators Maximum Temperature and MPS Response (at Mid-Span Trailing Edge)	247
298	Original Turbine Stator MPS Distribution 20 Seconds After Light-Off	247
299	Cutback Turbine Stator MPS Distribution 20 Seconds After Light-Off	247
300	Combustor Assembly Design	248
301	Combustor Assembly Finite Element Model	248
302	Combustor Assembly Steady-State 1371C (2500F) Max Power Temperatures	249
303	Combustor Assembly Steady-State 1371C (2500F) Max Power MPS	249
304	Engine Start to Cruise (Cycle 22)	250
305	Spacer Sleeve (RBSN) Start Transient MPS	250
306	Nozzle Support (RBSN) Start Transient MPS	250
307	Combustor Support (RBSN) Start Transient MPS	251
308	Combustor Liner (SASC) Start Transient MPS	251
309	Ceramic Components Stackup Load Paths	251
310	First and Second Generation Diffuser Support System	252
311	Inner Ceramic Support Rocker Assembly	253
312	First and Second Generation Rocker/Eccentric Design Comparison	253
313	Slotted Versus Slotless Turbine Shroud Configuration	254
314	High Temperature Ceramic Seal Areas	254
315	Dual Piston Ring Seal Performance Benefit	256
316	Combustor Baffle/Backshroud Wave Spring Location	256

LIST OF FIGURES (Contd)

Figure	Title	Page
317	Ceramic Component Qualification Sequence	257
318	Strain Gaged Regenerator Shield and Mechanical Screening Rig	259
319	Flow Separator Housing Mechanical Screening Rig	259
320	Turbine Shroud/Rocker Assembly Mechanical Screening Test Setup	260
321	Standard Oil SASC Stator Vanes in the Thermal Shock Test Rig	261
322	Inner and Outer Diffuser Screening Rig	262
323	Transition Duct and Baffle Screening Rig with Original (top) and Final (bottom) Configurations	262
324	Turbine Shroud Screening Rig Original (top) and Final (bottom) Configuration	263
325	Static Structure Rig Original (top) and Final (bottom) Configurations	265
326	1371C (2500F) Static Turbine Rig Original (top) and Final (bottom)	267
327	Mechanical Screening Component Test Results	269
328	Outer Diffuser Housing Design Evolution	270
329	Inner Diffuser Housing Design Evolution	271
330	Turbine Shroud Design Evolution	272
331	Thermal Screening Component Test Results	273
332	Turbine Shroud Piston Ring Seals	279
333	Turbine Shroud Piston Rig Seals	280
334	Single LAS Flow Separator Seal Configuration	281
335	Dual LAS Flow Separator Seal Configuration	281
336	Single vs. Dual Piston Ring Seals	282
337	Increased Loading Effect on Single LAS Seal - 5-28-86	282
338	Regenerator Shield Piston Ring Seal Configuration	283

LIST OF FIGURES (Contd)

Figure	Title	Page
339	Regenerator Shield Seal Leakage over Operating Pressure Range	284
340	Cracked Dome On a Bladeless Rotor Casting After Drying	287
341	Part After Sintering Cracked Into Several Pieces Due to Incomplete Drying	287
342	Green Vane Tip Showing Discolored Area	292
343	Flow Chart Showing Slip Casting Procedure	296
344	Plaster Base and Mylar Ring for Casting Solid Ingot	297
345	Ingot After Casting	297
346	Ford SRBSN Process	300
347	Oxidation Kinetics in RM-20	302
348	Strength After Oxidation of RM-1	302
349	Microstructure of RM-2	303
350	Oxidation Kinetics in RM-2	303
351	Strength at Temperature Data for RM-1, 2 and 3	304
352	Oxidation Kinetics in RM-3	304
353	Sintered Silicon Nitride Process for Fabrication of Advanced Gas Turbine Rotors	306
354	Relationship of Viscosity Vs. Spindle Speed for Various Concentrations of Dispex A-40 Deflocculant	307
355	Single Dip Wax, Plaster Base and Steel Retaining Ring	309
356	Rotor Pore Size Versus Spin Test Rotor Speed	317
357	Static Oxidation Test	323
358	Cornell Melt Front Advance	325
359	Stator Tool	326

LIST OF FIGURES (Contd)

Figure	Title	Page
360	Fill Pattern With 0.010 Inch Eccentric, 0.006-0.014-inch Diaphragm Gate Short Shorts (a) and (b), and Full Shot (c)	327
361	Vane Trailing Edges Typically Formed With Eccentric Gate Good Fill (a), Knot Line (b) and Cold Packing (c)	327
362	Effect of Material Temperature on Vane Trailing Edge Knit Line Flaws	328
363	Effect of Tool Temperature on Vane Trailing Edge Cold Packing Flaws	328
364	Changing Fill Pattern With Material Temperature Concentric Diaphragm Gate (0.015 in) Material Temperatures of 200F (a) and 275F (b)	329
365	Relative Frequency of Vane Cracks as a Function of Material and Tool Temperature	329
366	Short Hot Fill Pattern When Using Single Point Gate	331
367	Full Shots Using Point Gate Material Pull-Out in Gate Area (a) and Solid Shroud Cracks (b)	331
368	Effect of Injection Sequence Timing on Material Pull-Out and Shroud Cracks - Tool Temperature, 70F	332
369	Effect of Injection Sequence Timing on Material Pull-Out and Shroud Cracks - Tool Temperature 90F	332
370	Frequency of Cracks Relative to Vane Numbers (Leading Edge)	334
371	Frequency of Cracks Relative to Vane Number (Trailing Edge)	334
372	Plot of Leading Edge Cracks Vs. Injection Time	335
373	Plot of Trailing Edge Cracks Vs. Injection Time	335
374	Strength and Thermal Expansion of Corning Code 9458 Lithium Aluminum Silicate	339
375	Thermal Conductivity of Corning Code 9458 Lithium Aluminum Silicate	339
376	Modulus of Elasticity of Corning Code 9458 LAS	340

LIST OF FIGURES (Contd)

Figure	Title	Page
377	Dimensional Stability of Corning 9458 LAS Material at Various Times and Temperatures	341
378	Flow Separator Housing Pressure Test Fixture Shown Assembled to Wooden Model of the Housing	341
379	Ceramic Flow Separator Housing Showing Strain Gages in Place	343
380	Ceramic Flow Separator Housing Mounted to Mechanical Test Fixture	344
381	Ceramic Flow Separator Housing with Double Wall Bulkhead	345

LIST OF TABLES

Table	Title	Page
1	Comparison of Foil Bearing Designs	16
2	Dynamic Properties Rig Test Results	18
3	Single Bearing Rig Evaluation of High Temperature Bearing Coatings	20
4	Steady State Ceramic Turbine Clearance Corrections	25
5	Ceramic Engine Turbine Axial Build Clearance	26
6	Operating Clearance For Ceramic Engine	26
7	AGT101 Impeller Design Aerodynamic Design Summary	47
8	AGT101 Impeller Design Geometric Design Summary	48
9	Impeller Properties	57
10	AGT101 Impeller Life Summary (-3σ Material Properties)	61
11	Summary of Vibratory Blade Modes (ℓ, 0 RPM, 70F)	61
12	Turbine Design Point Cycle Conditions Sea Level, 29C (85F) Day, Maximum Power	70
13	AGT101 Cold Turbine Rig Operating Conditions	77
14	AGT101 Turbine Development Test Summary	78
15	Dual Alloy Turbine Wheel Design Parameters	82
16	Combustor Data	92
17	Test Sample Temperature Limit	104
18	Regenerator Core Performance	106
19	Regenerator Matrix Thermal Properties	108
20	Calculated Elastomer Temperature	110
21	Leakage Air Flow Conditions	118
22	Flow Separator Housing Axial Distortion	122

LIST OF TABLES (Contd)

Table	Title	Page
23	Non-Diaphragm Seal Leakage Analysis	123
24	Regenerator Analysis Summary	134
25	Regenerator Rig Test Results	137
26	AGT101 Component and Material Summary	148
27	Fast Fracture and Stress Rupture Data was Measured for Many Advanced Si_3N_4 and SiC Materials	149
28	Ceramic Interface Test Summary	171
29	Predicted Contact Tensile Stresses For Point- and Line-Contact Conditions	176
30	Flexure Strength and Fracture Origins of Laser Marked Test Bars	178
31	ACC Bladed Rotor Test Results	185
32	Analytical Results	194
33	Acoustic Blade Ring Results	195
34	Predicted Ceramic Blade Stresses	198
35	Rotor Fast Fracture Predictions	204
36	Phase B Shroud Configuration Study	214
37	Static Structure Shroud Cycle Study	216
38	Turbine Shroud Seal Radius Study	218
39	Material Sensitivity in Screening Rig	220
40	Engine Shroud Cycle Study	221
41	Phase C Shroud Configuration Study	226
42	Shroud Material Sensitivity in Engine	227
43	Transition Duct/Combustor Baffle Analyses in Static Structure Rig Configuration	231

LIST OF TABLES (Contd)

Table	Title	Page
44	Transition Duct/Combustor Baffle/Turbine Backshroud Analyses with Rotor Effect	233
45	Transition Duct/Combustor Baffle/Turbine Backshroud Model Material Study	235
46	Turbine Backshroud Alternate Configuration Study	236
47	Flow Separator Housing Pressure Stresses	239
48	Flow Separator Housing Steady-State Thermal Stresses	241
49	Flow Separator Housing Transient Thermal Strsses	243
50	Ceramic Component Rig Tests	258
51	AGT101 Static Components Proof Test Cycles	264
52	Test Cycle for Initial 1371C (2500F) Testing in the Stator/Shroud Screening Rig	276
53	Yield Point of Slip and Quality of Casting	286
54	AGT101 Rotor Discoloration Analysis	292
55	Discoloration Analysis of a Green Rotor	293
56	Particle Size Variation Within a Green Rotor	294
57	Slip Cast SRBSN Material Properties	301
58	Physical Properties RM-20 Material	305
59	Improved RM-20 Slip Preparation Procedure	307
60	Summary of Heat Treat Cycles and X-Ray Diffraction Results	312
61	Mean MOR Results for Heat-Treated Rotors	312
62	Life Improvements Resulting from Furnace Redesign	314
63	AGT RM-20 Rotor Spin Test Results	315
64	Flexural Strength Of Pressureless Sintered and HIPped RM-20 Rotor Material	317

LIST OF TABLES (Contd)

Table	Title	Page
65	The Effect of Heat Treatment On Flexural Strength and Secondary Phases In RM-20 Rotor Material	318
66	Stress Rupture Test Results RM-20 Rotor Material	320
67	The Effect of PSZ Addition to RM-20 Si_3N_4 Material	322
68	Fillet Crack Inspection Results	333
69	Fillet Crack Inspection Results - Variables	336
70	Variable Investigation using 0.015 X 3.0 Gate	337
71	Material Temperature Investigation 0.065 X 3.0 Gate	338
72	Stators Delivered to Garrett	338
73	Physical Properties of Corning 9458 LAS	339
74	AGT Flow Separator Housing Quality (Period 1980 - 1985)	345

This Page Intentionally Left Blank

1.0 SUMMARY

1.1 Powertrain Development

The powertrain of the AGT101 is comprised of the AGT101 power section, a split path Variable Stator Torque Converter (VSTC), and a Ford-built four-speed Automatic Overdrive (AOD) Transmission. The AGT101 is intended for use in a 1364 kg (3000 pound) vehicle, and is capable of a nominal 74.5 kw (100 hp) and a specific fuel consumption of 0.18 kg/kw-hr (0.3 lb/hp-hr). It employs a radial turbine wheel and a centrifugal compressor, mounted on a single shaft and supported by an air foil bearing and a high speed ball bearing. Maximum rotational speed is 100 krpm, and idle speed is approximately 50 krpm.

The design of the AGT101 is based upon the use of high technology structural ceramics in the hot gas flowpath. Symmetry of the ceramic structures was a primary design consideration, as it provided more uniform stresses throughout each part and eased the fabrication of components. It also made analysis by finite element methods a much simpler task, as most work could be done using two-dimensional models.

A continously variable transmission (CVT) with high reduction was required for use with a single shaft turbine engine in an automotive application. Power transmission is through a VSTC coupled with a high reduction planetary gearbox. This assembly is bolted direct to a Ford four-speed AOD transmission. Offsetting speed changes in the transmission and the planetary gearbox produce a continuously variable drive. The VSTC was tested early in the program to generate a performance map, and gearbox differential ratios were selected to operate the VSTC in the most efficient areas. Activities related to the development of the power transmission portion of the powertrain were deferred for industry sponsorship when project funding levels were reduced and the project was redirected. Note that the components of the system were all of a proven technology.

The Reference Powertrain Design (RPD) utilized the standard rear wheel drive layout common to the automotive industry. A front-wheel drive configuration was also shown as feasible.

Performance of the RPD was projected based on tested component performance and as-designed leakage flows, heat losses, and pressure losses. CFDC mileage was projected at 5.5L/100 km (42.5 mpg), and a 49 krpm idle speed satisfies the driveability criterion of 2.62 m (8 feet) displacement in 2 seconds' time.

1.2 Power Section Development

Engine Mechanical Development

The gas lubricated foil bearing is located at the hot end of the turbine rotor, between the compressor and the turbine wheel. The self-generated gas film requires no external pressurization, and the bearing is tolerant of high temperatures as well as a degree of rotor misalignment and distortion. Once developed for stability and load capacity, foil bearing temperature capability and material compatibilty were developed. The bearing configuration in use at the end of the AGT101 program employed gold coated foils running against a sintered silicon nitride (SSN) journal (the rotor shaft). This configuration offers excellent load capacity (24 lb at 75,000 rpm) as well as a low wear rate.

The rotating group support system also employs a circular thrust runner, added to the engine configuration to increase damping and control subsynchronous rotor whirl. This thrust runner is part of a pressurized oil-lubricated thrust bearing. The compressor end of the rotating group is supported by a high speed ball bearing, and sealed by floating ring seals.

Operational clearances were measured during metallic engine operation, and then corrected to determine ceramic engine clearances.

Engine Rotor Dynamic Development

During the course of the engine development, dynamic instabilities in the rotating group were addressed by isolating the rotor from gearbox excitations, inserting an oil film thrust bearing into the design, and by making the tieshaft integral with the gearbox input quill shaft. These modifications allowed consistent operation to full speed of 100 krpm.

Engine Development Evaluations

The AGT101 test bed was developed in three consecutive configurations. The first was metallic, with only the regenerator core and regenerator seals employing ceramics. This configuration was used early in the program for system development to 1600F Turbine Inlet Temperature (TIT), and for rotor dynamics, controls development, heat transfer coefficient determinations, rotor system evaluations, and regenerator development. This configuration was also used to test a ceramic turbine wheel to 97 krpm, and was employed as a proof test of ceramic turbine wheels prior to their installation in the all-ceramic engine.

An intermediate configuration incorporated ceramic structures in the hot gas flowpath, but retained the metal turbine wheel and used a metal combustor with a thermal barrier coating. This configuration was used to verify the design of the ceramic structures, and to obtain performance data at 2100F. A successful 100-hour endurance test was also run with this configuration.

The third major iteration featured a ceramic combustor and turbine rotor as well as ceramic structures. Operation during the AGT101 program was limited to 1204C (2200F), due to material limitations of the turbine rotor. Long term steady-state operation at 2200F was demonstrated, although further development was indicated in the areas of combustor performance, flowpath leakage, and regenerator durability.

While some performance data was obtained at 1149C (2100F) using the metallic (dual alloy) turbine rotor, performance testing of the all-ceramic configuration was limited by the material properties of the rotor. The performance data taken was used primarily to assist in seals development.

One seal area recognized as critical was that between the turbine shroud, flow separator housing, and transition duct. The high temperatures in this area dictate the use of a ceramic sealing element. The initial concept for this area, which employed two seals separated by a ceramic wave spring, was eventually modified to three sealing elements with an increased axial load.

1.3 Component/Subsystem Development

Activities centered around the development of the following major components and subsystems: compressor, turbine, combustor, and regenerator.

The compressor system consists of a single stage backward swept wheel with 12 full and 12 splitter blades, a three stage radial diffuser, and a set of 17 variable inlet guide vanes (VIGVs). One design iteration from the original design yielded a compressor with the required ratio and flow, diffuser performance close to predictions, and a desirable efficiency envelope for the automotive application. Although considerable work was done with Alcoa on the development of a forged powder metal aluminum compressor wheel, the backup titanium impeller was used for engine testing, due primarily to time constraints.

The AGT101 turbine wheel is a single stage radial inflow design, specifically for ceramic materials. The turbine wheels used inthe 871C (1600F) and 1149C (2100F) configurations utilized the ceramic design, but these metals wheels were cut back at the inducer tips to reduce stress. Turbine stators were made in two basic configurations, with an integral ring

fabricated of metal used successfully in the lower temperature 871C (1600F) configuration, while 19 individual segments were required to make the higher temperture ceramic stators survive.

For the 1149C (2100F) design, a dual alloy turbine wheel of MAR-M 247 and Astroloy was employed, although its use was discontinued after a reliability proglem with the bond joint between hub and blade ring was identified.

The ceramic rotor was redesigned during the course of the project to improve fabricability. The changes made to the blade shape did not significantly affect the efficiency of the design.

Combustor development looked at both variable and fixed geometries as a means of achieving the requirements of low emissions, multi-fuel capability, and good fuel economy. The fixed geometry was determined to be more feasible, for its lack of moving parts, and at program's end, a redesign incorporation a larger primary burn zone was favorably evaluated. Nozzle development emphasized good atomization and reduced heat load, with a simplex design incorporating air cooling, air assist, and a center-body ignitor as the favored arrangement at the close of the project.

Regenerator development was carried out at Ford motor Company and at Garrett. The regenerator cores, supplied by Corning and by NGK-Locke, exhibited performance approaching RPD goals. Critical to the successful development of the regenerator system is the design of regenerator seals. The performance of these seals has been improved on a static basis over the course of the program, approaching AGT goals, but performance and durability have been hampered by distortions at engine operating temperatures. Further development of these seals if required before RPD goals can be successfully met.

Activities at Garrett included studies to determine the pressure profiles of the system, evaluate means of controlling flow, and predict effectiveness.

Testing was also done in a hot rig to measure leakages in the regenerator system, determine matrix effectiveness, measure core drive torques, and measure the cavity pressure at the core ID to determine the bleed orifice size. It was seen during this testing that while the effect of core clearance on leakage at low pressures was small, at higher pressures the leakage was very sensitive to clearance.

1.4 Ceramic Materials and Component Development

Ceramic Materials Testing - In the last two years of the AGT program, significant testing was done to characterize the advanced sintered silicon nitride and silicon carbide materials. The high temperature properties of several candidate rotor materials were determined to be inadequate to meet the rotor requirements. Data from as-fabricated test bars showed adequate properties in four materials: SN-82 and SN-84 from NGK-Locke, and SN 250M and SN 270M from Kyocera. The SN-82 and SN 270M materials could not be formed into the complex rotor shape, and testing of the material properties of the SN 250M rotors revealed significantly lower material properties than indicated by the initial test bar data. Similar testing of SN-84 rotors also showed lower properties than test bars, but the reduction in properties was not as significant, and so the SN-84 material appears to be suitable for 1371C (2500F) engine testing.

Although large improvements have been made during the AGT program, additional work needs to be done to achieve better elevated temperature properties, fracture toughness, and shape capability.

Ceramic Compatibility Testing -Stress and temperature conditions at various engine interfaces were identified, and a series of tests was performed using test bars to evaluate the sticking characteristic at these interfaces. In those cases where sticking was observed, retest showed that no sticking occurred when flame-sprayed mullite coating was used at the interface.

Other testing was performed to investigate the effects of line contact and point contact at component interfaces and to evaluate coefficients of friction for reaction bonded silicon nitride (RBSN) and sintered alpha silicon carbide (SASC). Also, a study was performed to determine causes for spalling in RBSN, and fabrication techniques were successfully modified to reduce the occurrence of spalling.

Identification of components by laser marking of serial numbers was introduced following a study which showed little or no strength degradation in most materials. Only lithium-aluminum-silicate (LAS) was unsuited due to excessive damage to a legibly marked surface.

Ceramic Structures

Initial design criteria for AGT101 components were established empirically, with component testing providing feedback to the analytical process and material selection. Component symmetry was pursued in the basic design to eliminate circumferential element analysis. This reduced cost, and allowed for rapid analysis and extensive design iterations. The only exception is the flow separator housing, whose function required an asymmetrical design.

To eliminate extensive design optimization on each material/component combination an evaluation was performed on the preliminary configuration for each component to identify primary and alternate materials. Subsequently, design optimization was performed using a prime material candidate for each component. After design optimization was achieved, alternate candidate materials again were evaluated.

Because of the lack of ductility in ceramics, localized stress concentrations cannot plastically redistribute stresses. Consequently, known stress concentrations must be reduced or eliminated from the design wherever possible. When component analysis revealed significant tensile stresses near known stress concentrations, additional analyses using a finer substructure model mesh were performed.

Stresses were analyzed for 3 modes of loading encountered during normal engine operation; one pressure (full power) and 2 thermal (steady-state and lightoff transient). Shutdown transient conditions were initially considered but were insignificant due to core thermal inertia.

Rig Design/Development

Major structural components, such as regenerator shield, flow separator housing, turbine shroud and rocker assembly components, are first tested in mechanical rigs to simulate the pressure and contact loading encountered in engine operation. These tests then are followed by a proof test in thermal screening rigs to simulate the maximum principal stresses encountered in engine operation. The thermal cycles for the screening rigs are defined so as to simulate stresses which exceed predicted engine stresses under normal start by 25 percent.

Screening tests are intended to eliminate components with gross internal defects and/or smaller defects located in regions of high stress. Lower quality components will fracture during screening, allowing only the highest quality parts to continue through qualification and engine test. Results of these tests can also feed back into the empirical design loop. Significant examples of this are: the inner diffuser housing, which was redesigned from a shape similar to a birdbath to a shape more like a dinner plate following failures in the screening rigs; the elimination of slots from the turbine shroud flange following mechanical screening tests in which failures of RBSN shrouds initiated at those slots; and the redesign of the turbine shroud to reduce a stress concentration in the seal fillet radius following repeated thermal screening failures with origins in that radius.

The static structures rig test utilizes all of the ceramic components in an assembly of the engine structure, without the rotor, and

checks the mechanical functioning of the assembly. Further, the static structures rig evaluates the sealing capability, component capability, axial and radial pilots, contact loading, and stresses at elevated temperatures. The maximum operating condition for this rig was set at 1093C (2000F), which corresponds to the maximum operating temperature of the turbine exhaust. Sufficient confidence was eventually gained in the thermal and mechanical screening rigs that use of the static structures rig was discontinued as a qualification rig.

To evaluate ceramic components upstream of the turbine exhaust, another rig, capable of operation of 1371C (2500F), was required. The initial 1371C (2500F) milestone was achieved twice in the stator/shroud screening rig in the spring of 1984, for short durations. A separate rig, the 1371C (2500F) static rig, was later developed and used for long-term at 1371C (2500F) to investigate high temperature effects on ceramics. To date, limited sticking at 1371C (2500F) has been seen, and no failure has occurred due to sticking. Some interfacial distress was seen between the transition duct and combustor baffle, but this can be eliminated by using an alternating material stack in this area.

A cold seal leakage rig was also developed in which the performance of three ceramic sealing areas could be evauated: turbine shroud/flow separator (piston rings), regenerator shield/flow separator (butt joint), and regenerator shield/exhaust housing (piston rings). The cold leakage data allowed a comparison of seal concepts, and measured the effects of load, concentricity, and pressure distortion on these sealing interfaces.

2.0 INTRODUCTION

This report is the final in a series of Technical Summary Reports for the Advanced Gas Turbine (AGT) Technology Development Project, authorized under NASA Contract DEN3-167 and sponsored by the DOE. This report has been prepared by the Garrett Turbine Engine Company (hereinafter referred to as Garrett), and includes information provided by the Ford Motor Company hereinafter referred to as Ford), Standard Oil Engineered Materials Company (Standard Oil), and AiResearch Casting Company (ACC). The project was administered by Mr. Thomas Strom, Project Manager, NASA-Lewis Research Center, Cleveland, Ohio. This report summarizes plans and progress from October 1979 through June 1987.

Project effort conducted under this contract is part of the DOE Gas Turbine Highway Vehicle System Program. This program is oriented at providing the United States automotive industry the high-risk, long-range technology necessary to produce gas turbine engines for automobiles that will have reduced fuel consumption and reduced environmental impact. The intent is that technology resulting from this program be capable of reaching the marketplace by the 1990s.

The advanced gas turbine, when installed in a Ford vehicle with a 1364 kg (3000 lbs) inertia weight would provide:

- o A combined federal driving cycle (CFDC) fuel economy of 5.5 L/100 km (42.8 miles per gallon) based on Environmental Protection Agency (EPA) test procedures using DF-2. The AGT-powered vehicle shall give substantially the same overall vehicle driveability and performance as a comparable production vehicle powered by a conventional spark-ignition powertrain system
- o Emissions less than federal standards
- o Ability to use a variety of fuels

The Garrett/Ford automotive Advanced Gas Turbine has been designated the AGT101. The AGT101 nominally is a 74.5 kw (100 shp) engine, capable of speeds to 100,000 rpm and operating at turbine inlet temperatures (TIT) to 1370C (2500F) with a specific fuel consumption level of 0.18 kg/kw-hr (0.3 pounds/horsepower-hour) over most of the operating range.

The program was initiated in October 1979 and was to entail 68 months. Two phases were planned; Phase I was 45 months long and involved most of the component/ceramic technology effort and the early engine and vehicle testing. The 23-month Phase II was scheduled to include completion of the all-ceramic engine effort plus the vehicle deliveries and evaluation.

Budget reductions in mid-FY81 resulted in a re-orientation of the program. The vehicle, transmission and engine gearbox/transmission efforts were deleted. The program was then oriented toward developing the long-range high-risk technology of the AGT101 gas turbine such that the auto industry can carry that technology forward to production in the 1990's. Emphasis was placed on ceramics, gas bearings, low emission combustion and improved component performance. The AGT101 gas turbine was envisioned as a test bed in which to develop these technologies.

The program schedule with milestones is shown in Figure 1. Key milestones accomplished include completion of the design review in January 1980, the first set of ceramic structures passing rig test to 1093C (2000F) in August 1983, ceramic structures engine test to 1149C (2100F) in February 1984, first ceramic structure rig test to 1370C (2500F) in May 1984, first all ceramic engine

test in January 1986, and completion of an 85-hour all ceramic engine test to 1204C (2200F) in October 1986. While the feasibility of applying ceramics to a gas turbine was demonstrated, further improvements in the ceramic turbine rotor material properties were needed for further testing.

This final report summarizes the power-train design, power section development, and component/ceramic technology development. Appendices include reports of progress from Ford, ACC, and Pure Carbon. Work performed by Standard Oil is published in NASA topical report CR-180871.

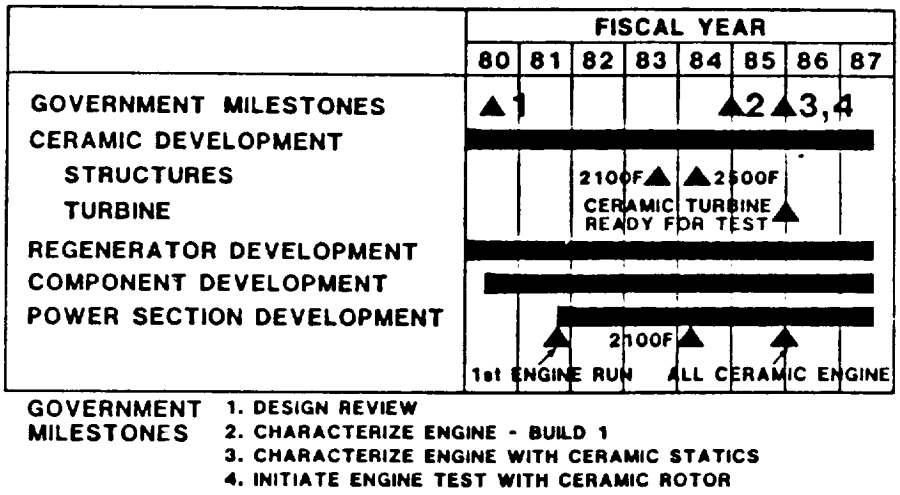

Figure 1. AGT101 Program Schedule.

3.0 REFERENCE POWERTRAIN DESIGN

This reference powertrain design (RPD) is comprised of the AGT101 power section, split-path variable stator torque converter (VSTC) gearbox and Ford automatic overdrive (AOD) transmission as depicted in Figure 2. The RPD is to be installed in a 1364 kg (3,000 lbs) inertia weight vehicle.

The AGT101 engine, shown in Figure 3 is flat rated at 74.57 kw (100 hp) with a minimum SFC of 0.18 kg/kw-hr (0.3 lb/hp-hr). The single-shaft rotating group is composed of a radial turbine, centrifugal compressor, and output gear supported by an air-lubricated foil-journal bearing and an oil lubricated ball bearing. The maximum (steady state) engine speed is 100,000 rpm, and idle speed is approximately 50,000 rpm.

Ambient air enters the engine through variable inlet guide vanes and passes through the single-stage compressor. The compressed air, at approximately 185C (365F), is routed around the full engine perimeter to the high pressure side of the ceramic rotary regenerator. This feature provides increased thermal efficiency by minimizing heat loss. The partially heated air passes through the regenerator core where it is further heated to approximately 1060C (1940F) temperature (at idle), and then to the combustor.

The combustion system features a fixed geometry, lean-burn, low-emission combustor. Combustor air temperature increases to a maximum of 1370C (2500F) with the addition of fuel, is ducted to the ceramic stator, and then expanded across the radial turbine rotor. Turbine exhaust gases 1093C (2000F) maximum temperature at idle) are ducted through the low pressure side of the rotary regenerator and out the engine exhaust at a maximum temperature of 266C (510F) at maximum power.

All ceramic hot section structural components are symmetrical except for one housing

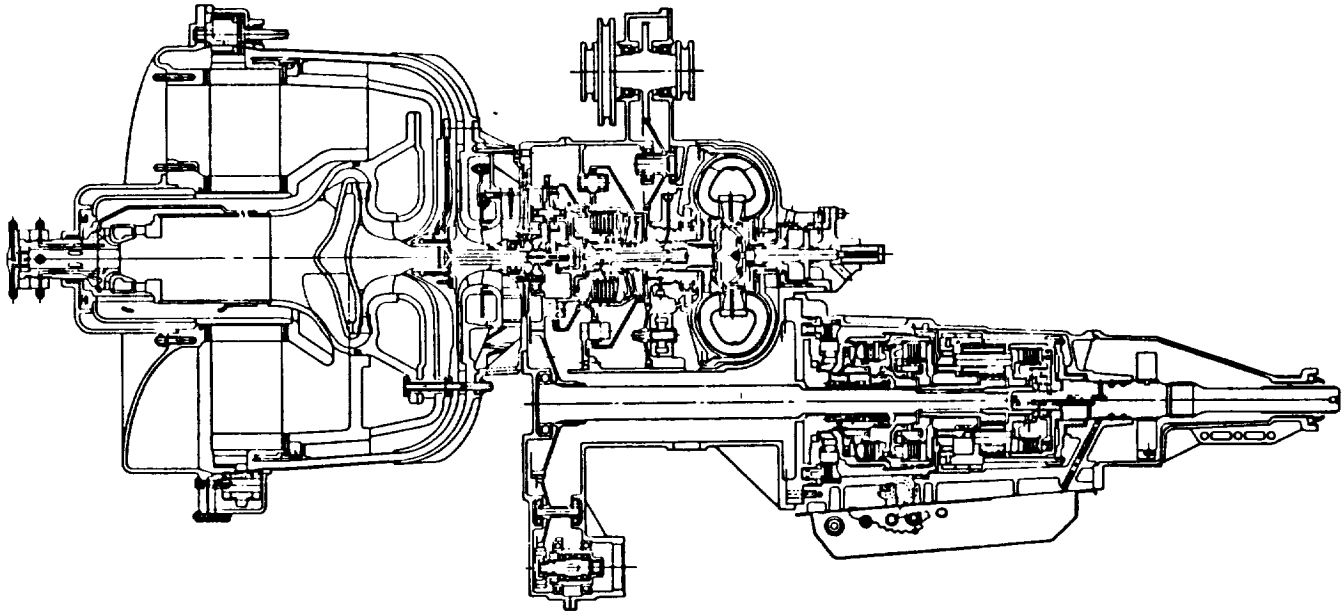

687-078-158

Figure 2. AGT101 RPD Powertrain.

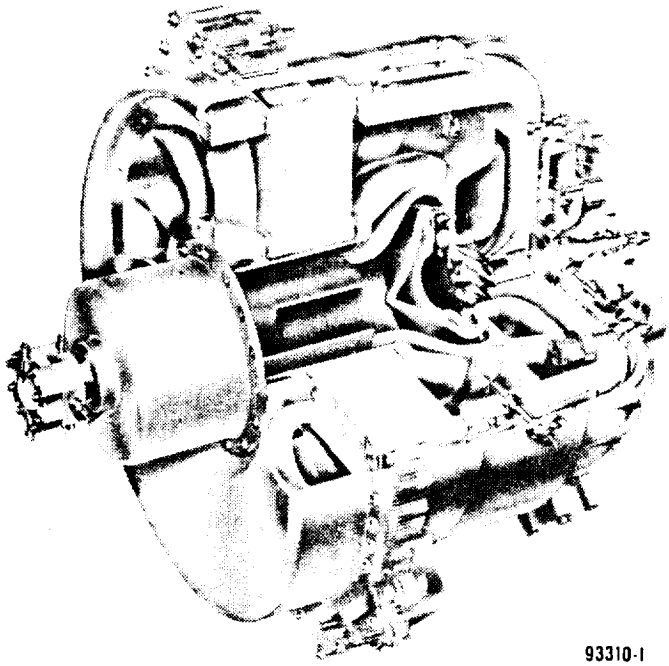

GB7-078-157

Figure 3. AGT101 Power Section.

that separates high and low pressure regenerator flow. The symmetrical design provides a more uniform stress distribution and eases manufacturing of the components.

Output power from the gas turbine is delivered to the vehicle via a variable high speed single-stage differential planetary gearbox in conjunction with a modified four-speed Ford AOD transmission. This combination results in a continuously variable speed transmission required for the optimization of a single-shaft gas turbine vehicle system.

The planetary gearbox (schematically shown in Figure 4) incorporates a differential in which power is split into two paths. Gas turbine power is input at the planetary sun gear and extracted from the planetary carrier. One power path extends directly to the carrier while the second path passes through the planetary ring gear to a VSTC utilized as a speed changing device. The variable output speed of the VSTC is connected to the carrier via a clutch that is open during vehicle idle and closed during normal driving modes. Speed ratio modulation across the VSTC results in a variable output speed of the planetary carrier, which in turn is geared directly to the AOD transmission. Step ratio changes in the AOD are phased with offsetting speed ratio changes in the variable speed gearbox. This produces a continuously variable drive line system which allows the engine to operate at optimum speeds to deliver high efficiency cruise power, acceleration power, or engine braking power.

Preliminary packaging studies were completed for incorporating the RPD in Ford rear-wheel and front-wheel drive configurations. The rear-wheel drive configuration is the reference powertrain design (Figures 5 and 6) and can be installed in a 1364 kg (3,000 lb) inertia weight vehicle without modifications to the engine compartment structure. The same confuguration with a modified gearbox and transmission was repackaged and shown to fit a front-wheel drive vehicle.

Performance of the RPD is based on tested component performances and as designed leakage flows, heat losses and pressure losses. Using this data and analytical modeling this engine/gearbox-transmission and vehicular characteristics the projected combined federal driving cycle (CFDC) mileage and 2-second distance traveled versus idle speed is shown in Figure 7. As shown, an idle speed of 49,800 rpm satisfied the 2.44 m (8 feet) in-2 seconds distance criteria for acceptable driveability. The resulting fuel consumption is 5.5 L/100 km (42 mpg). The engine performance characteristics are shown in Figure 8 and depict the outstanding specific fuel consumption (SFC).

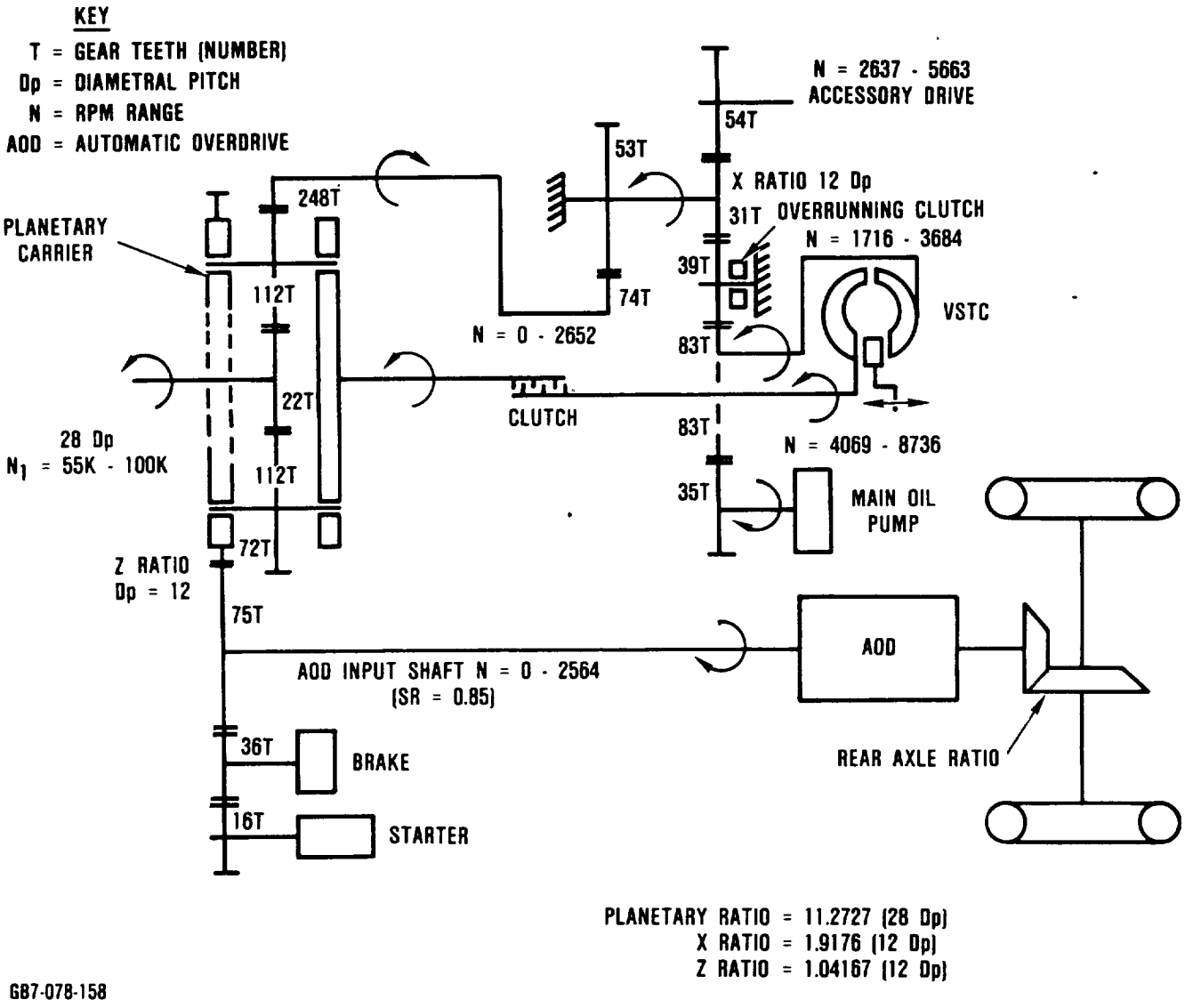

Figure 4. AGT101 Drive System Schematic.

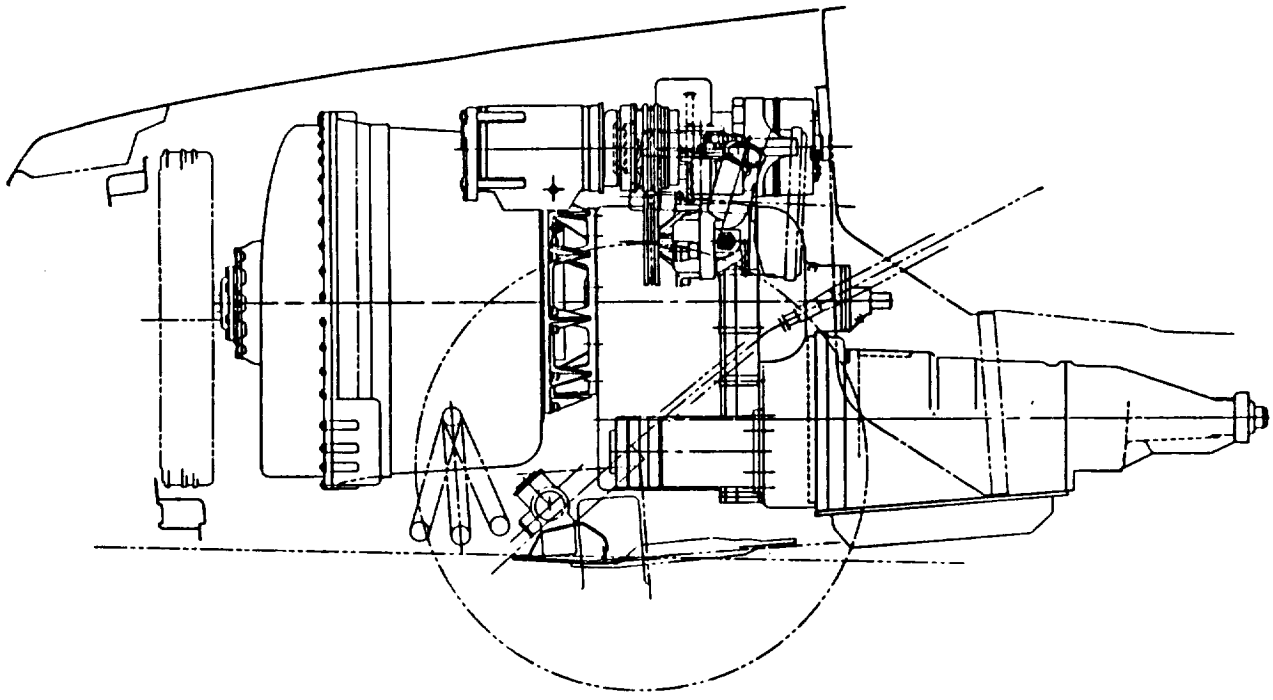

GB7-078-159

Figure 5. AGT101 Installation - Side View.

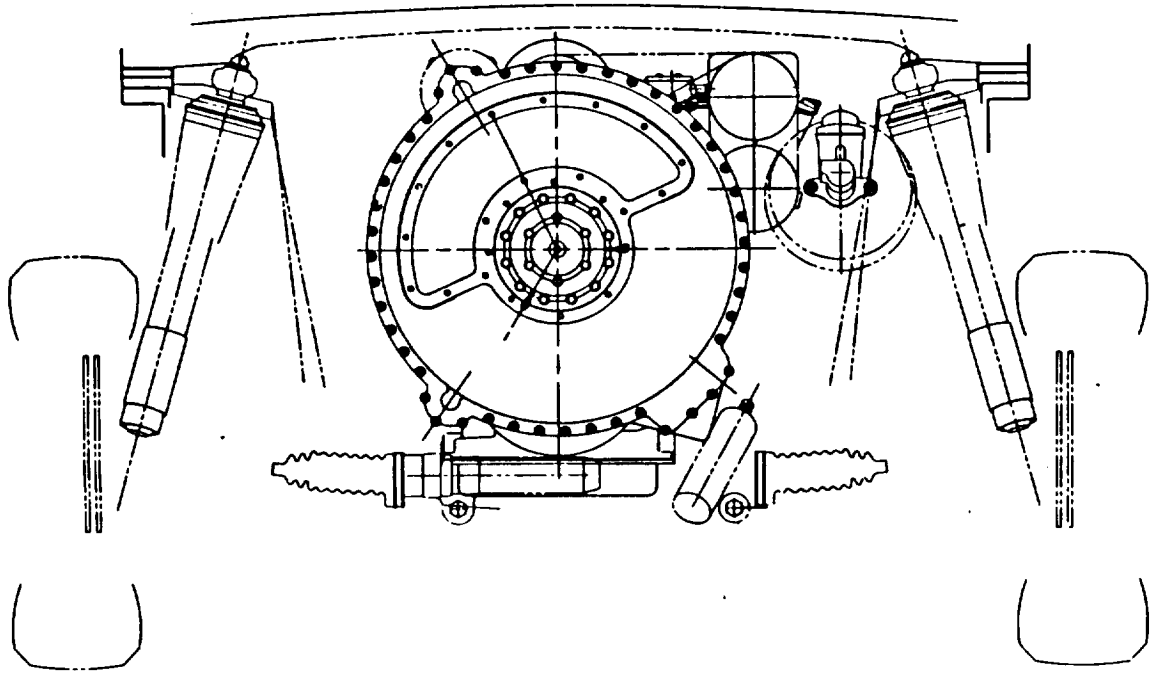

GB7-078-160

Figure 6. AGT101 Installation - Front View.

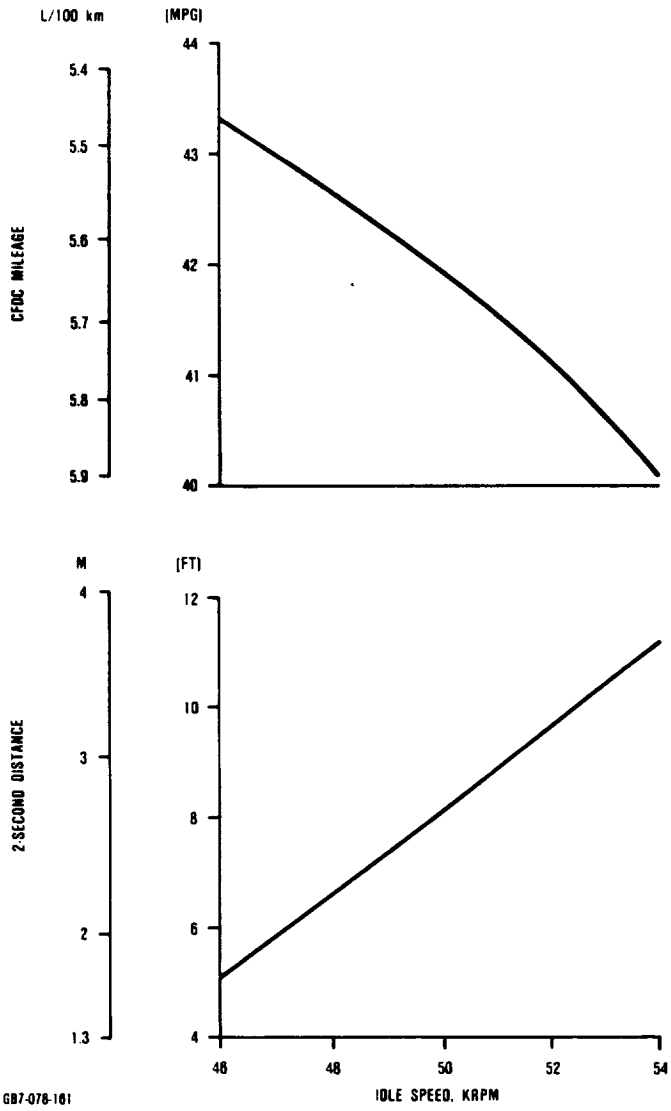

Figure 7. AGT101 Estimated Performance Curves.

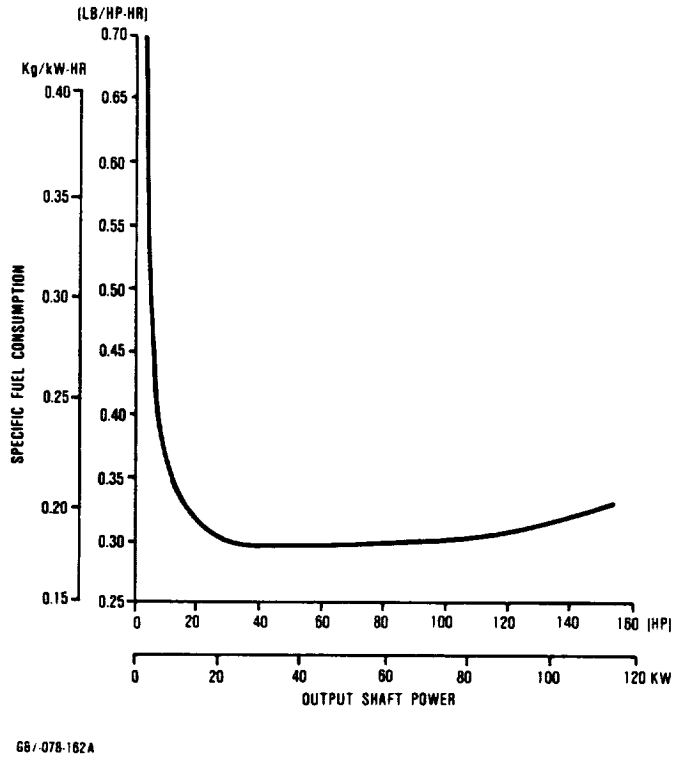

Figure 8. AGT101 Specific Fuel Consumption.

4.0 POWER SECTION DEVELOPMENT

Power section development on the AGT101 concentrated on several key areas: gas foil bearing development, engine rotor dynamic development, and engine development evaluations. Development of the major components of the power section is discussed in Section 5.0 - Component and Subsystem Development.

Experimentation with several different foil, coating, and backing spring materials and configurations eventually yielded a successful, robust design in which gold coated foils run directly against a sintered silicon nitride journal (the rotor shaft).

Dynamic instabilities in the rotating group also required considerable effort to overcome. In order to dampen the system and help to control subsynchronous rotor whirl, the system as finally developed employs a circular thrust runner as part of a pressurized oil-lubricated thrust bearing. This and other modifications, including the integration of the rotor tieshaft and the gearbox input quill shaft, finally allowed consistent operation to full speed of 100 krpm.

The AGT101 test bed was developed in three consecutive configurations. The first was metallic, with only the regenerator core and regenerator seals employing ceramics. This configuration was used early in program for system development to 871C (1600F) turbine inlet temperature (TIT), and for rotor dynamics, controls development, heat transfer coefficient determinations, rotor system evaluations, and regenerator development. this configuration was also used to test a ceramic turbine wheel to 97 krpm, and was employed as a proof test of ceramic turbine wheels prior to their installation in the all-ceramic engine.

An intermediate configuration incorporated ceramic structures in the hot gas flowpath, but retained the metal turbine wheel and used a metal combustor with a thermal barrier coating. This configuration was used to verify the design of the ceramic structures, and to obtain performance data at 1149C (2100F). A successful 100-hour endurance test was also run with this configuration.

4.1 Engine Mechanical Development

4.1.1 Foil Bearing

The AGT101 foil bearing design was required to meet the following operating conditions:

Operating speed	50,000 to 100,000 rpm
Maximum load	6 g for 0.2 seconds
Maximum temperature	649C (1200F)

The operating range shown above represents the actual engine operating range, however during engine starts and stops, the engine must operate at speeds of less than 50,000 rpm and pass through 2 rigid body rotor critical speeds. Additionally, the bearing breakaway torque must be below the engine starter stall torque.

In addition to the above, this application has imposed additional requirements on the foil bearing which are unique relative to other foil bearing applications developed at Garrett:

- o High unit loading at 1-g load. This bearing has a 30 kPa (4.3 psi) unit loading with a ceramic turbine rotor or 39 kPa (5.6 psi) with metal rotor. Previous high temperature foil bearings were subjected to unit loads in the 7.5 to 14.5 kPa (1.1 to 2.1 psi) range.

- o Rotor excursions can exceed the calculated bearing sway space. The bearing may not be hydrodynamic when the first critical rotor speed occurs.

The AGT101 foil bearing was first developed for stability and load capacity. This work was performed through a combination of

analysis and testing in the single bearing rig. Bearing stiffness and damping were evaluated during rotor dynamic development when minor changes in the bearing geometry were effected to optimize these characteristics. Temperature capability and material compatibility were developed once the basic geometry was established. This work utilized the foil coating wear rig as well as the single bearing rig to evaluate potential foil coatings.

The resulting foil bearing configuration is shown in Figure 9 and described in the table below:

Number of foils	7
Foil thickness	0.15 mm (0.006 inch)
Foil arc length	29.2 mm (1.150 inch)
Foil axial length	26.5 mm (1.045 inch)
Foil preform radius	29.2 mm (1.150 inch)
Foil material	Inco X750
Backing spring web thickness	0.14 mm (0.0055 inch)
Backing spring arc length	13.3 mm (0.525 inch)
Backing spring preform radius	27.9 mm (1.100 inch)
Backing spring material	Inco X750
Bearing sway space	0.15 - 0.25 mm 0.006-0.010* inch
Foil coating	Au-Ni or Au-Co
Journal surface	Sintered Silicon Nitride
Journal diameter	34.3 mm (1.350 inch)

*Diametral clearance between the journal and foils with the foils and springs making all contacts in the carrier.

4.1.1.1 Foil Bearing Geometry Development

Initial design of the foil bearing was conducted analytically using a computer program that was developed by Garrett using IR&D funding. This parametric model was used to study the influence of changing various bearing geometric parameters. This analysis provides the simultaneous elasto-hydrodynamic solution for an operating foil bearing. The profile of the deflected foil is determined using the strain energy approach. The gas film pressure distribution is then calculated based on the deflected profile of the foils and shaft speed. Convergence is achieved when the gas film thickness matches the deflected foil profile for the same pressure distribution.

Figure 10 shows the model output for the deflected height for the baseline bearing lightly loaded at 100,000 rpm. Take note that

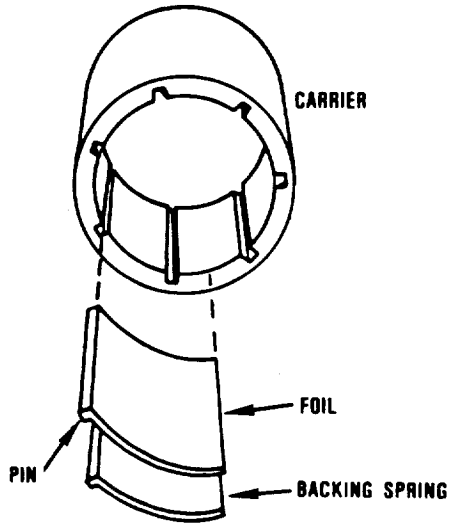

Figure 9. Basic Bearing Configuration.

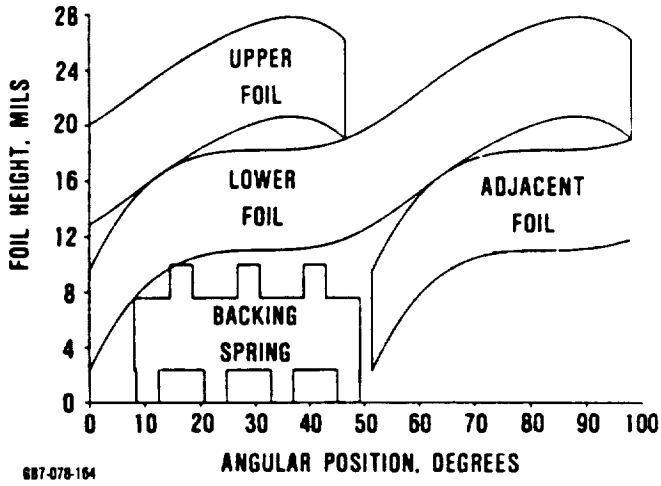

Figure 10. Foil Bearing Deflected State at 100,000 RPM Operating Speed.

most of the bearing deflection is taken in the curvature of the foils and not in the backing spring. This is because the backing spring is used to help the bearing sustain high loads and the model only simulates a lightly loaded condition. Figure 11 shows the pressure distribution for that bearing at operating speed. This model proved useful for establishing an initial bearing configuration and for screening proposed bearing geometries before fabrication and testing.

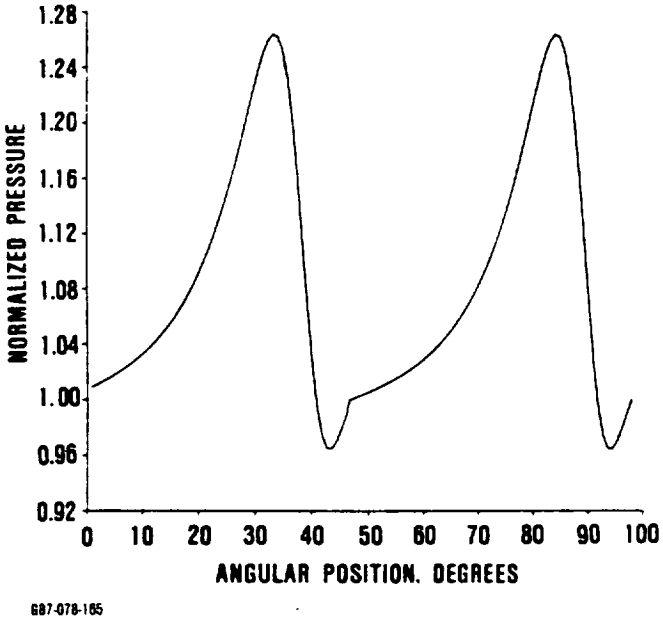

Figure 11. Film Pressure Distribution at Operating Speed.

During geometry development of the foil bearing there were two types of testing, static spring rate testing and dynamic testing for stability and load capacity. Static spring rate testing was utilized to characterize the load/deflection of a stationary foil bearing assembly. The static spring rate, while not precisely duplicating the dynamic spring rate, is the benchmark parameter used in predicting bearing behavior.

The Single Bearing Rig is propelled by a small air turbine motor. This rig can spin the test shaft up to 110,000 rpm and impose static radial loads up to 222.4 N (50 lbs) on the test bearing at ambient temperatures. Test bearing torque is measured via a torque arm and load cell attached to the test bearing housing.

Compatibility of the foil bearing with the rest of the rotor system was evaluated in the rotor dynamics rig and in the engine test beds. This work is discussed in the rotor dynamics discussion in Section 4.2.1.

Table 1 shows the progressive development of the foil bearing geometry through the present.

The "P" type foil is compared with the reference bearing in Figure 12. This bearing featured a redesigned backing spring and foil. The polyimide foil coating on the P type bearing provided temperature capability up to 343C (650F), which was a 38C (100F) improvement over the temperature capability of the Teflon S coating used in the reference foil.

4.1.1.2 High Temperature Foil Bearing Development

High temperature foil bearing development built on the basic "P" type bearing design. Several different foil/journal coating systems were researched and evaluated to develop the bearing soakback capability to 649C (1200F) and maintain the stability and load capacity goals. This effort resulted in a hardened gold alloy foil coating that was compatible with either a bare silicon nitride ceramic shaft or a metallic shaft sputter coated with titanium nitride.

Foil bearing surface coating development was conducted according to the diagram in Figure 13. During this process, a candidate coating/journal combination was evaluated in the dynamic properties test rig. The dynamic properties test rig, also called the foil bearing wear rig is shown schematically in Figure 14. This rig tested the dynamic wear and friction of the candidate surfaces at 427, 538, and 649C (800, 1000, and 1200F). After eliminating combinations with unacceptable wear or friction, the single bearing rig was then used to evaluate surviving candidate systems for load capacity, power consumption, and

Table 1. Comparison of Foil Bearing Designs.

Bearing Parameter	Reference Bearing	Increase Web Thick	Increase Foil Thick	"P" Type Bearing Design	Current Bearing
Foil Coating	Teflon S	Teflon S	Teflon S	Polyimide	Au/Ni
Foil Material	302 CRES	302 CRES	302 CRES	IN 718	IN X750
Foil Thick, mm (inch)	0.15 (0.006)	0.15 (0.006)	0.178 (0.007)	0.178 (0.007)	0.15 (0.006)
Foil Length, mm (inch)	30.2 (1.19)	30.2 (1.19)	30.2 (1.19)	30.2 (1.19)	26.4 (1.040)
Foil Radius, mm (inch)	21.6 (0.85)	21.6 (0.85)	21.6 (0.85)	27.9 (1.100)	29.2 (1.150)
Spring Web, mm (inch)	0.127 (0.005)	0.15 (0.006)	0.15 (0.006)	0.15 (0.006)	0.14 (0.0055)
Spring Radius, mm (inch)	17.78 (0.70)	20.3 (0.80)	20.3 (0.80)	22.9 (0.90)	27.9 (1.10)
Spring Material	302 CRES	302 CRES	302 CRES	IN 718	IN X750
Journal Coating	METCO 443	METCO 443	METCO 443	METCO 443	TiN or SSN
Sway Space, mm (inch)	0.279 (0.011)	0.259 (0.0102)	0.259 (0.0102)	0.203 (0.008)	0.203 (0.008)
Static Spring Rate, Nm (lb/in)	1000	1887	2358	2400	2400
Load Capacity, N (lb)	53.4 (12) at 100,000 rpm	88.9 (20) at 100,000 rpm	88.9 (20) at 100,000 rpm	88.9 (20) at 100,000 rpm	106.7 (24) at 75,000 rpm
Turbine Vibration, mm (mil)	0.076 (3) at 100,000 rpm	0.038 (1.5) at 100,000 rpm	0.02 (0.8) at 100,000 rpm	0.02 (0.8) at 100,000 rpm	0.013 (0.5) at 100,000 rpm

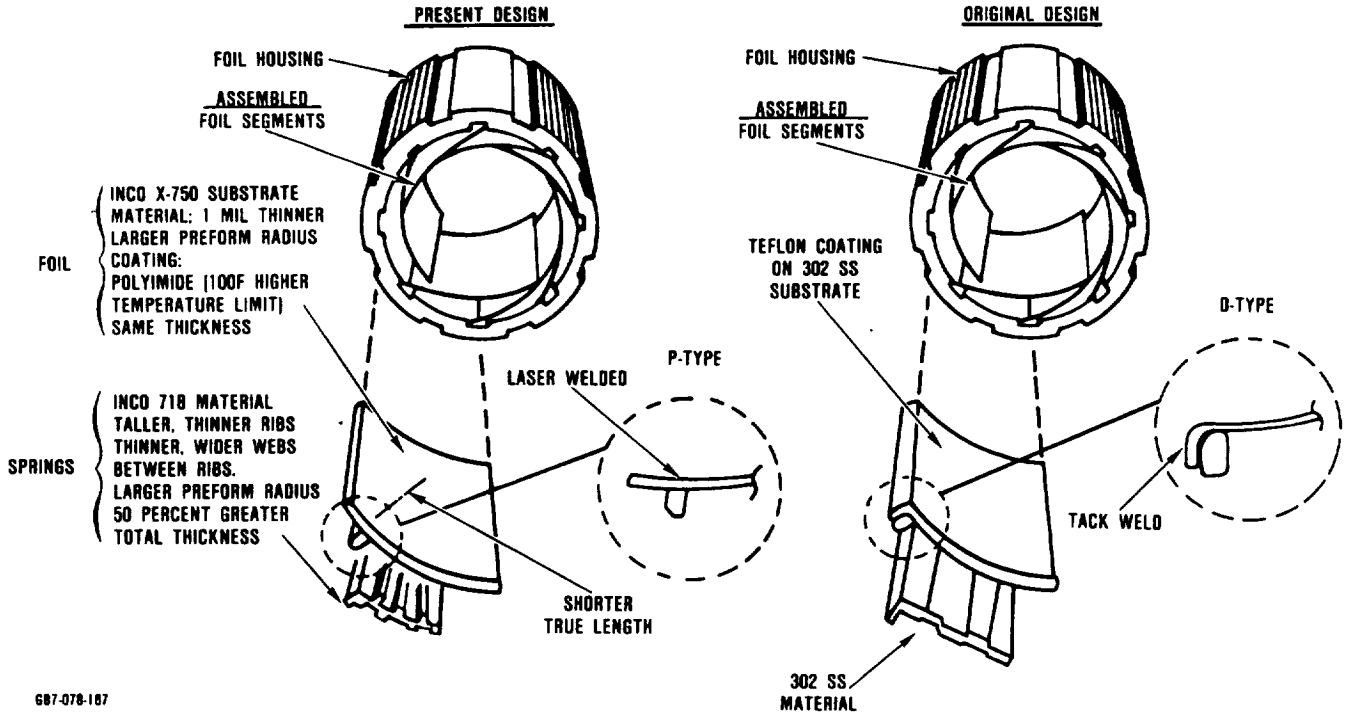

Figure 12. Foil Bearing Designs Compared.

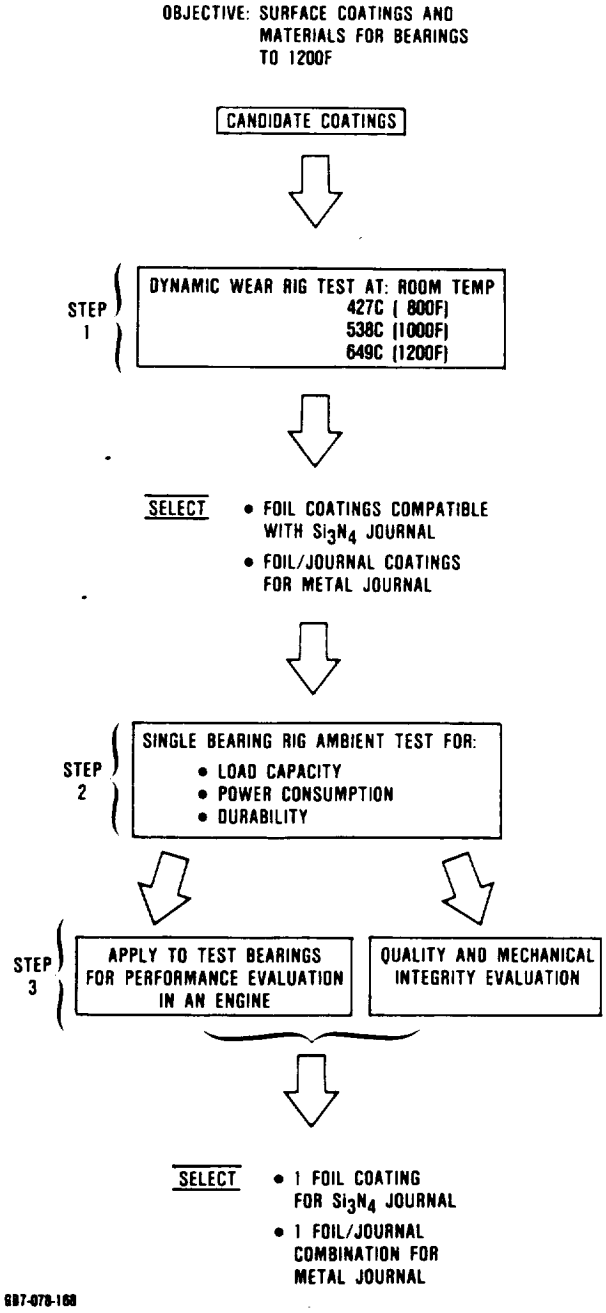

Figure 13. Foil Bearing Surface Coating Development.

start/stop durability. Once coating systems passed the single bearing rig evaluation, they were evaluated in an actual rotor system, either in the rotor dynamics rig or in an engine. The dynamic properties wear rig tests simulate the non-hydrodynamic operation of a foil bearing during starts and stops with cold

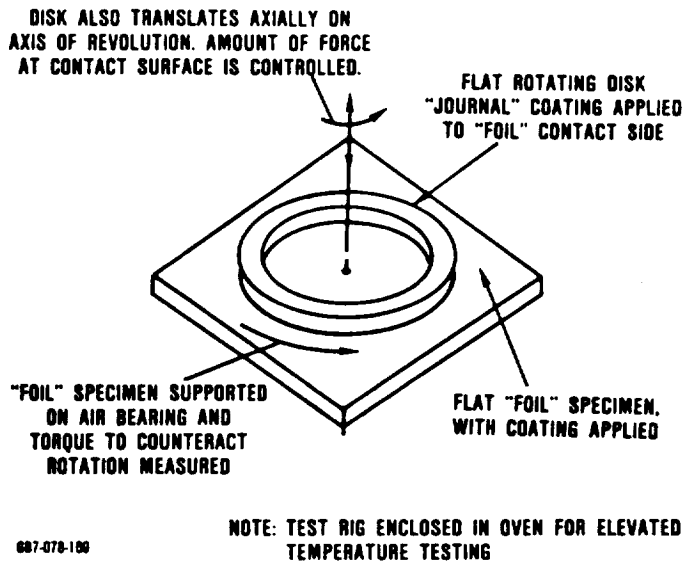

Figure 14. Foil Bearing Dynamic Properties Wear Rig.

and hot engine environments. Specimens were examined for coating wearthrough, excessive abrasion, and material transfer. Testing was automatically stopped on a coating system when the dynamic friction increased dramatically, evidence of surface breakdown. The matrix of coating systems evaluated are shown in Table 2.

Only three of the systems evaluated in the dynamic wear rig showed acceptable wear and friction. These systems were Au/SSN, Au/TiN, and TiC/SCA systems. The photograph in Figure 15 shows the Au/TiN test specimens after completion of the test series. The strip chart in Figure 16 shows the speed and friction traces for a typical cycle for this material combination. The TiC/SCA coating system, initially developed for other Garrett high temperature applications, was used as the baseline of comparison for all coating systems evaluated.

The test procedure for single bearing rig evaluation of the candidate foil bearing systems was as follows:

- o Ten no load starts to 50,000 rpm. Measure bearing static friction before and after starts

Table 2. Dynamic Properties Rig Test Results.

	Foil Coatings				
Journal Coatings	Gold (Au)	IN718 Boronized	Yttria Stabilized Zirconia (YSZ)	Titanium Carbide (TiC)	Chromium Oxide
Sintered Silicon Nitride (SSN)	Good at all temperature	Not tested	Excessive abrasion at ambient	Not tested	Not tested
Titanium Nitride (TiN)	Good at all temperatures	Not tested	Not tested	Not tested	Not tested
1090 Chrome	Coating failure at 1000F	Not tested	Not tested	Not tested	Not tested
Karamite	Good at all temperatures	Not tested	Not tested	Not tested	Not tested
Yttria Stabilized Zirconia (YSZ)	Not tested	Excessive abrasion at ambient	Not tested	Not tested	Not tested
Kaman SCA	Not tested	Not tested	Not tested	Good at all temperatures	Coating failure

- o Ten 1-g load starts to 50,000 rpm. Measure bearing static friction before and after starts
- o Remove bearing and visually examine for damage. If there is no damage, reinstall the bearing and measure static friction
- o Measure power consumption at loads from 1-g to the maximum load attainable for 2 seconds or more
- o Remove bearing and examine
- o Replace bearing foils and shaft if necessary. Measure static friction. Run 1000 1-g load starts. Measure static friction, then examine bearing.

Single bearing rig testing was used to evaluate surviving candidates from dynamic properties rig testing. Table 3 summarizes the results of this testing.

The initial testing with the METCO 105 (plasma sprayed Alumina) and METCO 202 (plasma sprayed Yttria Stabilized Zirconia) coated shafts with the soft and then with the hard gold coatings gave a lead that the hardened gold foil coating might be compatible with the high density silicon nitride ceramic shaft. Subsequent testing in the dynamic properties rig and then in the single bearing rig proved this combination to be the optimum system.

The rig testing of the SCA/TiC coating system required some manipulation of the foil bearing geometry to achieve the 85.3N (19.2 lb) load capacity. Initial bearing geometry was the same as the "P" type bearing described in Table 1, however the load capacity

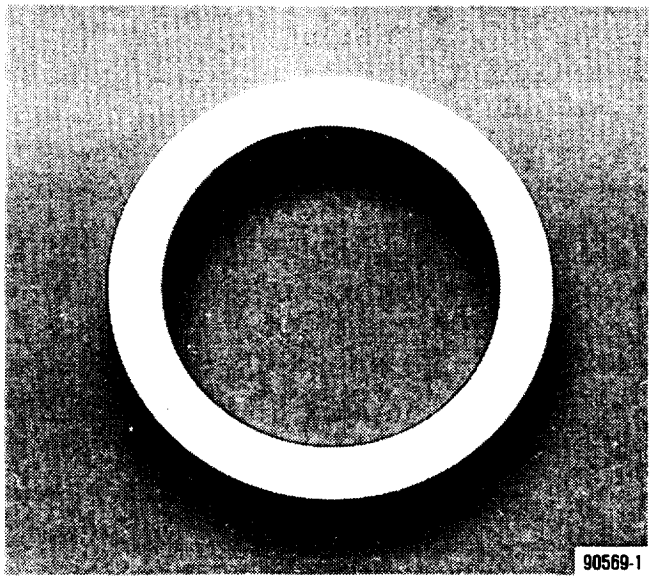

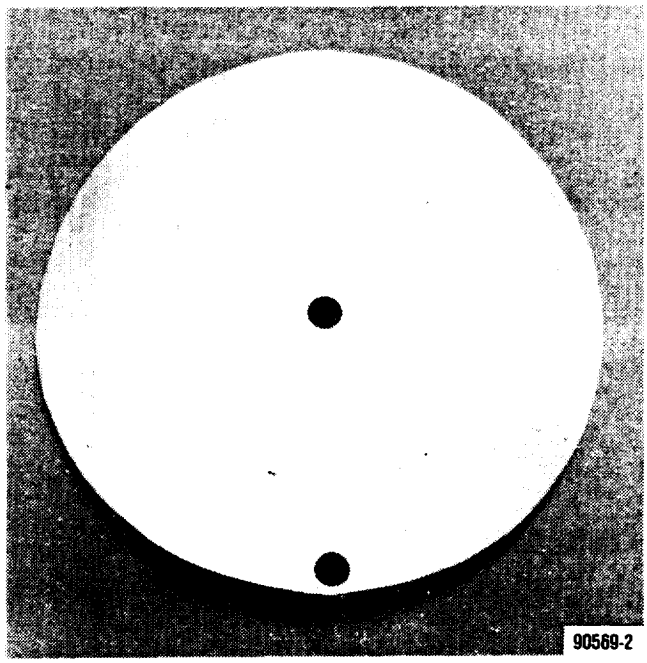

GB7-078-170

Figure 15. TiN Coated Ring (Top) Versus Au Coated Disk (Bottom) After 591 Starts at Ambient Temperature and 4.3 psid Load.

with the geometry and the SCA/TiC coatings system was only 58.2 N (13.1 lbs). Bearing foil thickness had to be decreased to 0.127 mm (0.005 inch) to provide compliancy to attain the desired load capacity. This geometry change was carried over to the Au/SSN bearing configuration.

The successful development of the Au/SSN high temperature bearing system demonstrated that bearing load capacity could not only be maintained in making the transition from low to high temperature foil coatings, but also increased. This improvement was the result of the use of a "thick" coating with a relatively "soft", more compliant material such as gold.

4.1.2 Thrust Bearing Development

The AGT101 hydrodynamic (oil film) thrust bearing was added to the engine configuration to increase the available damping in the rotor system and control subsynchronous rotor whirl. A similar system was used successfully in Garrett's CCGT25-1, which was a closed cycle gas turbine engine with a straddle mounted foil bearing rotor support similar to the AGT101.

The drawing in Figure 17 shows the bearing crossection used in the AGT101 engine. A circular thrust runner on the engine shaft inboard of the existing ball bearing. The engine rotor thrust loads are transferred from the runner to an oil pressure lubricated thrust washer that is fixed to the housing. A splash lubricated reverse thrust washer supports the runner in the event of reverse thrust caused by compressor surge or engine failure.

The ball bearing outer race is retained in a hydraulic mount and is restrained axially by two springs, fore and aft. These springs pinch the outer race with a 89N (20 lb) load to prevent spinning. During engine operation, an additional 178N (40 lbs) of axial load is transmitted through the ball bearing as rotor thrust compresses the forward bearing spring to prevent bearing skidding. The amount of this preload is controlled by the axial thrust bearing clearance.

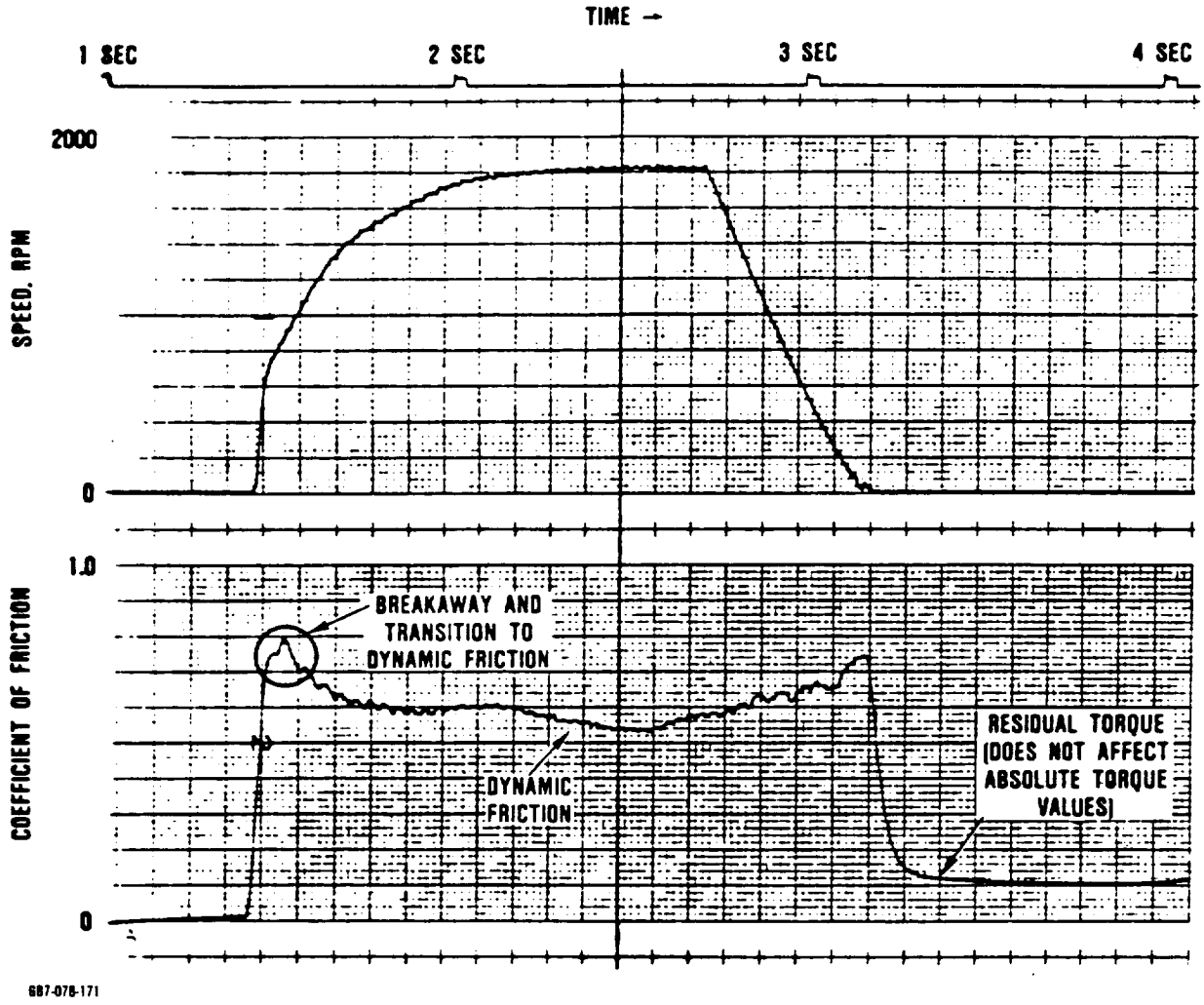

Figure 16. Typical Results of Dynamic Friction Test.

Table 3. Single Bearing Rig Evaluation of High Temperature Bearing Coatings

Foil/Journal System	Durability Test	Load Test
SCA coated shaft, TiC sputter coated foils	Heavy wear and high friction after 263 starts	85N (19.2) lbs for 2 sec at 75,000 rpm
Sintered silicon nitride shaft, >200 KNOOP gold coated foils	Unmeasurable wear after 1000 starts, rig failed after 2934 starts due to shaft failure	107N (24) lbs for 30 sec at 75,000 rpm
PVD TiC on shaft, >200 KNOOP gold coated foils	Applied to dual alloy turbine rotor and run on rotor dynamic rig. Despite high synchronous motion due to bladed component, bearing showed minimal wear	

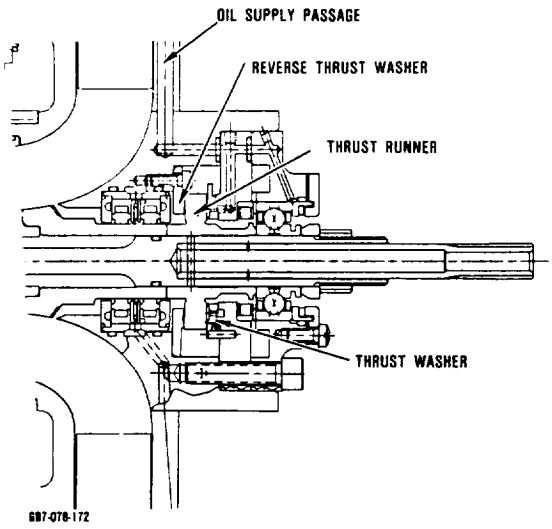

Figure 17. AGT101 Hydrodynamic Thrust Bearing Configuration.

4.1.2.1 Tapered Pad Thrust Bearing Design

The oil film thrust bearing is a 6 pad, tapered step design. Design details are shown in Figure 18. The design thrust load is 20 percent higher than that determined in the thrust analysis to provide a reasonable margin of safety.

To assure proper alignment, the interface seat surfaces of the washer and the thrust plate assembly are made spherical. This configuration will permit the thrust washer to align exactly flush with the mating thrust surface of the thrust rotor. This arrangement also will sustain the alignment through small displacements of the housing or the shaft during thermal excursions in engine operation.

The thrust bearing is designed to utilize ATF-Dextron II lubricant which conforms to SAE Specification SAE-J-311B. The oil supply is fed through the same drilled passages used in the original AGT101 configuration. From the main supply duct, oil is metered through a 2 mm (0.080 inch) orifice to the bearing through six holes in the thrust washer. The hydraulic mount is also fed from the main supply duct in parallel to the thrust bearing. Oil supply parameters are shown below:

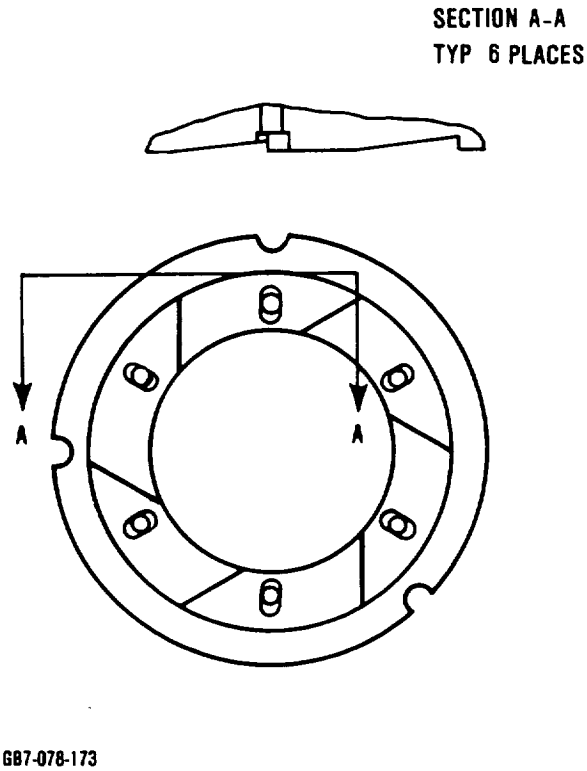

Figure 18. Thrust Bearing Design Detail.

Inlet housing supply pressure	551.6 to 1241 kPa (80 to 180 psig) temperature dependent
Metering orifice design pressure	448 kPa (65 psig)
Design inlet temperature	82 C (180F)
Maximum oil discharge temperature	121C (250F)
Oil flow (Thrust bearing only)	4.16 L/min (1.1 gpm)
Total oil flow (Thrust bearing plus hydraulic mount)	5.3 L/min (1.4 gpm)

In the static condition the thrust runner is set up with axial clearance between both forward and reverse thrust washers. As the engine accelerates during a start and forward thrust builds, the rotor assembly moves forward, compressing the spring which preloads the ball bearing. The oil film thrust bearing is not

actually loaded until forward rotor movement decreases the forward bearing clearance sufficiently to develop the supporting oil film. The curve in Figure 19 shows the rotor thrust curve and the ball bearing/thrust bearing load share as a function of rotor speed.

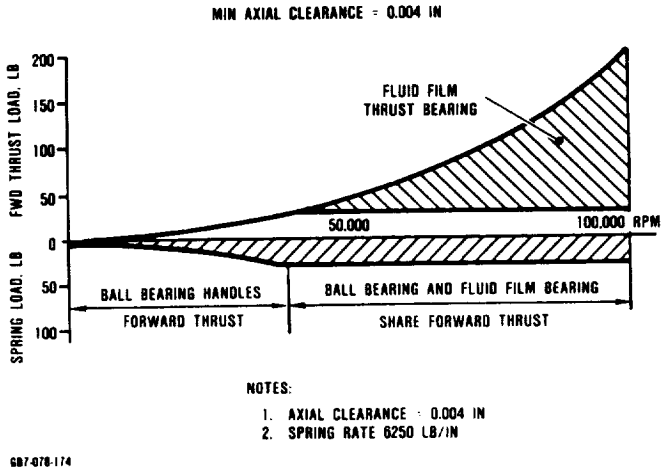

Figure 19. Thrust Bearing/Ball Bearing Load Share Characteristic.

4.1.2.2 Thrust Bearing Power Consumption Evaluation

Theoretical bearing power consumption is shown in Figure 20. An engine test was performed to evaluate this power consumption and determine whether bearing scavenging was sufficient. These test results, shown in Figure 21 indicate that the apparent penalty due to the thrust bearing is much higher than predicted. It is believed that the higher test results are an indication of insufficient scavenging and the resulting churning that is taking place.

Another test was performed to evaluate the effect of reduced oil flow on thrust bearing power consumption. This test was conducted at 70,000 rpm and the oil supply to the thrust bearing was separated from the hydraulic mount so that reduced thrust bearing supply pressures would not affect the hydraulic mount damping or stiffness. The results of this test, shown in Figure 22, indicated that at partial speed, the power consumption reduced substantially with reduced oil flow. This was

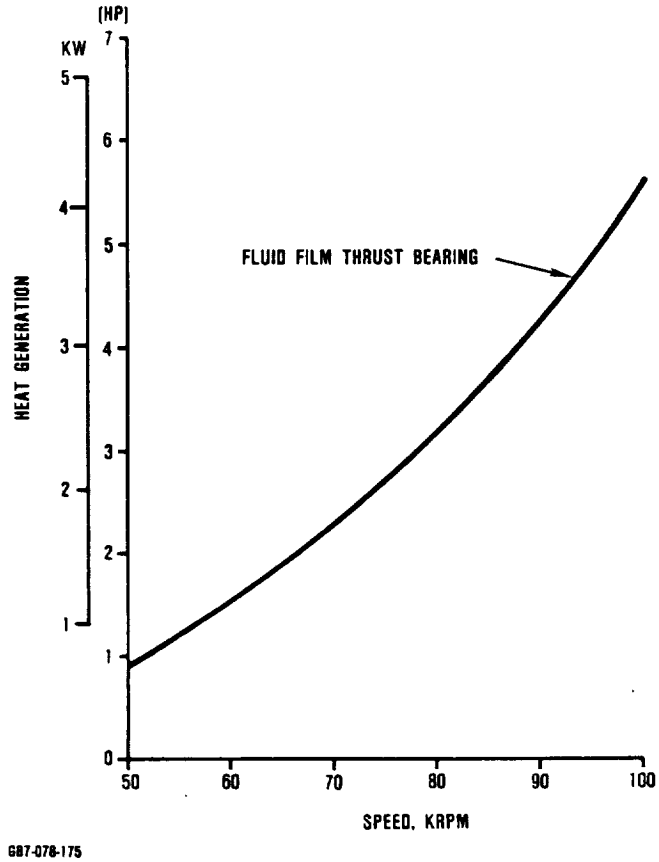

Figure 20. Total Analytical Heat Generation for AGT101 Fluid Film Thrust Bearing Cavity.

supporting evidence for the theory that excessive oil in the bearing cavity produced insufficient scavenging and caused oil churning.

4.1.3 Ball Bearing and Compressor Seal Design

4.1.3.1 High Speed Ball Bearing Design

The AGT101 ball bearing is a 15 mm 202 series ball bearing designed to carry a maximum predicted radial load of 182N (41 lbs) and a thrust load of approximately 1335N (300 lbs) at 100,000 rpm.

The bearing was designed to meet the following conditions:

Speed	55,000 to 100,000 rpm
Radial loads	42.3 to 182 N (9.5 to 41 lbs)

Thrust loads	311 to 1335N (70 to 300 lbs)
Life	CFDC 3900 hours at variable speed and load. 100 hours at 100,000 rpm and 1.335 kN (300 lbs)
Lubricant	Automotive transmission fluid
Lubricant temperature	38 to 166C (100 to 300F)

When the hydrodynamic thrust bearing was added to the system midway through the program, the ball bearing axial load was limited to 178N (40 lbs). This reduction in bearing load significantly increased bearing life beyond the design goal of 3900 hours.

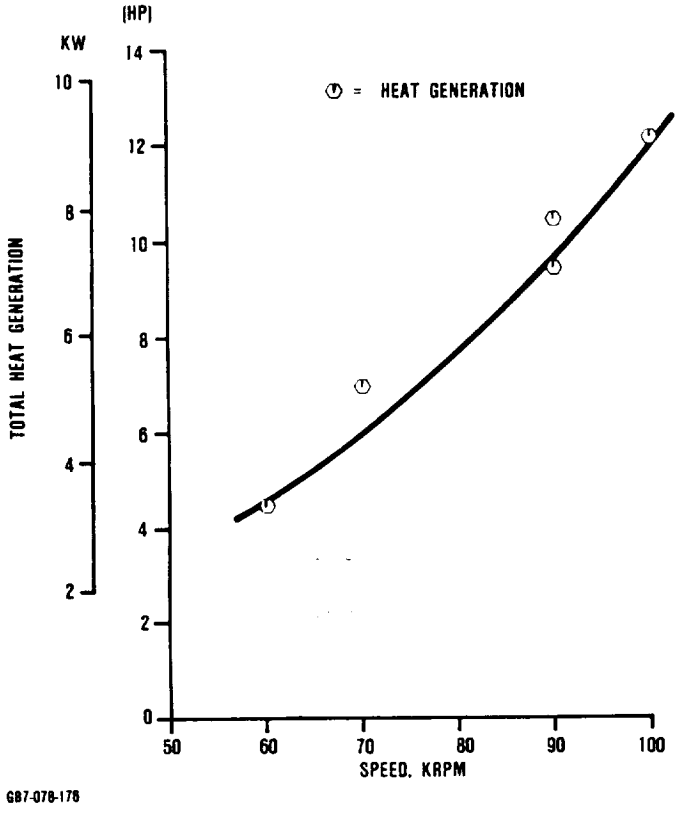

Figure 21. AGT101 S/N 001 Build 21 Fluid Film Thrust Bearing (Test 4-19-84).

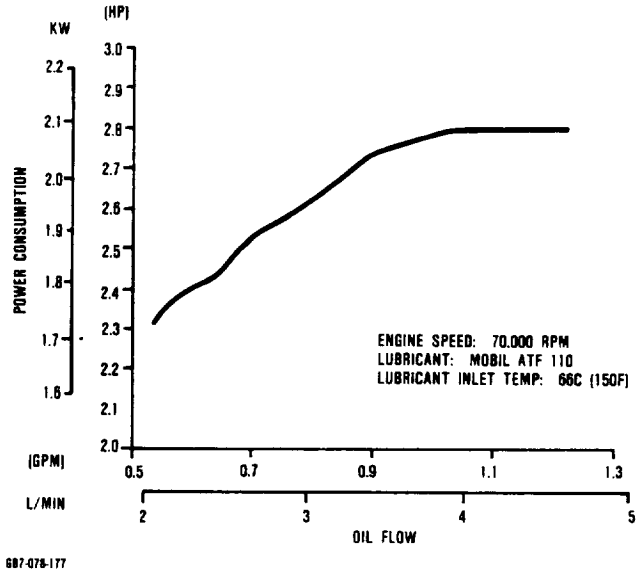

Figure 22. Thrust Bearing Power Consumption Decreases with Oil Flow.

4.1.3.2 High Speed Ring Seal Design

The high speed ring seal for the AGT101 is shown in Figure 23. The seal has a double floating carbon ring design with provisions for buffer air between the elements. Initial shaft clearance was designed at 0.013 mm (0.0005 inch) diametral, however after testing the carbon consistently wore to 0.038 to 0.064 mm (0.0015 to 0.0025 inch) diametral clearance. Testing in the rotor dynamics rig and in the engine revealed no significant leakage despite this wear.

4.1.4 Rotor Clearance Evaluation

The rotor axial clearances in the AGT101 are critical from both a performance and

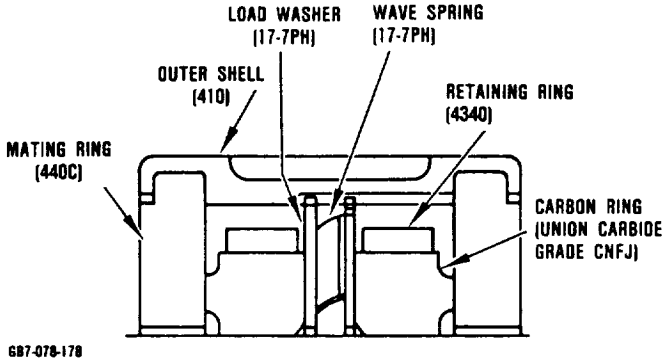

Figure 23. Floating Ring Seal.

durability standpoint. Rotor clearances assembled into the engine will vary depending on the effects of thermal and pressure distortion on the rotor support structure and on the rotor shrouds. These effects were measured during actual engine testing in the metal engine test bed using capacitance probes mounted in the rotor shrouds with metallic rotors.

4.1.4.1 Metallic Engine Clearance Testing

Running clearances were measured on the compressor and turbine rotor during metallic engine operation. These data included clearance changes during low speed operation due to light-off thermals and clearance changes as a function of engine speed under essentially isothermal operation at 871C (1600F). The engine build clearance is established when the engine centerline is vertical and the support bearings have no radial static load. When the engine running clearances are measured the engine centerline is oriented horizontally, and the rotor supports are radially loaded by the weight of the rotor assembly.

The metal turbine clearance was strongly affected by the start from a cold initial state. The curve in Figure 24 shows how the turbine clearance changed as a function of time after the initial engine start. This change is a function of the rotor droop effect in combination with thermal effects on the rotor blades, hub, and static structures. At a constant idle speed where pressure effects are minimal, the turbine clearance decreased by as much as 0.46 mm (0.018 inch).

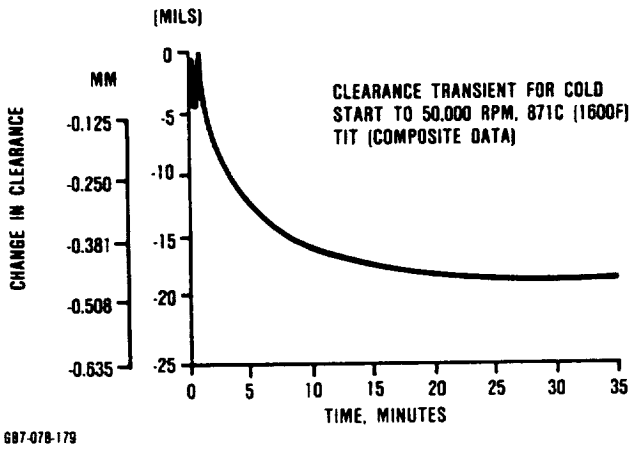

Figure 24. Typical Turbine Axial Clearance Transient for Cold Start.

Once thermally stabilized, the turbine clearance changed very little as a function of speed. The curve in Figure 25 shows the variation of axial turbine and compressor clearance as a function of speed. The compressor axial clearance decreased by 0.30 mm (0.012 inch) as a function of engine speed. Half of this change was attributed to "flowering" of the compressor rotor due to centrifugal effects and the other half was due to pressure/thermal distortion of the adjacent structures.

Based on these test results, the build clearances for the compressor on the metal and ceramic engines was established on a go forward basis. The rationale for establishing the compressor clearance is shown below:

Compressor Axial Clearance

	mm (inch)
Thermal/Centrifugal	**0.30 (0.012)**
Rotor Droop Allowance	**0.025 (0.001)**
Worst Transient	**0.051 (0.002)**
Worst Excursion	**0.038 (0.0015)**
Build Tolerance	**0.025 (0.001)**
Minimum Running Clearance	**0.076 (0.003)**
Minimum Axial Build Dimension	**0.52 (0.0205)**

4.1.4.2 Ceramic Turbine Clearance Analysis

The measured turbine running clearance values from the metallic engine test noted above were corrected by comparing the calculated thermal growth of the metallic structures under the engine test conditions to the ceramic structure thermal growth at the

desired operating condition. Further corrections were made for pressure induced structural deflections resulting from differing speed conditions. Table 4 shows these corrections.

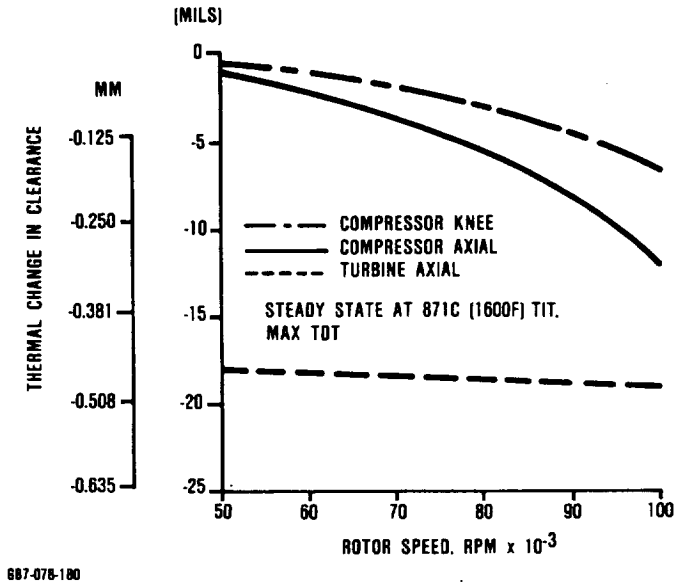

Figure 25. Compressor and Turbine Clearance Loss Due to Thermal Growths.

The ceramic turbine build clearance was calculated based on the start effect noted during metallic turbine testing, plus similar allowances used for establishing compressor build clearance. This information is summarized in Table 5.

After the turbine build clearance was established, corrections for running clearances in normal engine operation were calculated. On the basis of these corrections, the axial operating clearances of the ceramic engine were predicted. These values are shown in Table 6.

The analysis summarized above is conservative since it does not reduce rotor droop allowance to compensate for the reduced mass of the ceramic turbine rotor.

4.1.5 Metallic Structure Design

The initial design of the AGT101 metallic structures was consistent with the standards and practices of the automotive industry. The design emphasis was on simplicity for enhanced producibility and cost effectiveness.

Table 4. Steady State Ceramic Turbine Clearance Corrections.

Parameter Evaluated	TIT = 1174C (2146F) Idle 50 krpm	TIT = 1281C (2337F) Cruise 65 krpm	TIT = 1371C (2500F) Maximum Power 100 krpm
Pressure deflection	--	+0.0076 mm (+0.3 Mils)	+0.043 mm (+1.7 Mils)
Thermal growth of turbine shroud and rocker assembly	+0.033 mm (+1.28 Mils)	+0.274 mm (+10.8 Mils)	+0.323 mm (+12.7 Mils)
Thermal growth of compressor backshroud	--	-0.023 mm (-0.9 Mils)	-0.099 mm (-3.9 Mils)
Thermal and centrifugal growth of turbine rotor	-0.038 mm (-1.5 Mils)	-0.036 mm (-1.4 Mils)	-0.053 mm (-2.1 Mils)
Thermal growth of compressor	+0.0127 mm (+0.5 Mils)	+0.0127 mm (+0.5 Mils)	+0.0076 mm (+0.3 Mils)
Net axial clearance change	+0.299 mm (+11.8 Mils)	+0.236 mm (+9.3 Mils)	+0.213 mm (+8.4 Mils)

Symmetrical design philosophy was used throughout the engine, and low cost, highly producible materials were used for the metallic components where possible.

The engine cross section in Figure 26 indicates the metallic engine components in the engine structural assembly. The other components, the compressor housing, exhaust housing and inlet housing, are the main structures in the engine. These structures contain the pressurized gases within the engine, provide burst containment for the rotating components, support the engine at the mounting interfaces and provide a reacting load path for the pressure loads generated within the engine.

The design of the compressor housing and exhaust housing was augmented by finite element analysis to provide a stable support for the engine ceramic and rotating components. Section stiffeners and gussets were designed into these components to minimize pressure induced deflections.

Table 5. Ceramic Engine Turbine Axial Build Clearance.

	mm	(inch)
Thermal/Centrifugal/ Rotor Droop	0.036	(0.015)
Worst Speed Transient	0.0762	(0.003)
Worst Excursion	0.127	(0.005)
Build Tolerance	0.051	(0.002)
Minimum Running Clearance	0.127	(0.005)
Minimum Axial Turbine Clearance	0.762	(0.030)

4.2 Engine Rotor Dynamic Development

4.2.1 AGT101 Rotor Dynamic History

The initial AGT101 rotor system was supported by an oil mounted ball bearing and a foil bearing. This initial rotor system configuration, which includes a metal turbine for

Table 6. Operating Clearances For Ceramic Engine.

Engine Operating Condition	Reference Metal Engine Axial Clearance		Ceramic Shroud Axial Clearance		Ceramic Backshroud Clearance	
	mm	(inch)	mm	(inch)	mm	(inch)
Build	0.762	(0.030)	0.762	(0.030)	0.508	(0.020)
Transient after light-off to idle	0.381	(0.015)	0.381	(0.015)	0.584	(0.023)
649C (1200F) steady state idle	0.3048	(0.012	—	—	—	—
871C (1600F) steady state idle	—	—	0.645	(0.0254)	0.320	(0.0126)
1174C (2146F) steady state idle	—	—	0.605	(0.0238)	0.361	(0.0142)
1280C (2337F) steady state high cruise	—	—	0.541	(0.0213)	0.424	(0.0167)
1371C (2500F) steady state	—	—	0.518	(0.0204)	0.447	(0.0176)

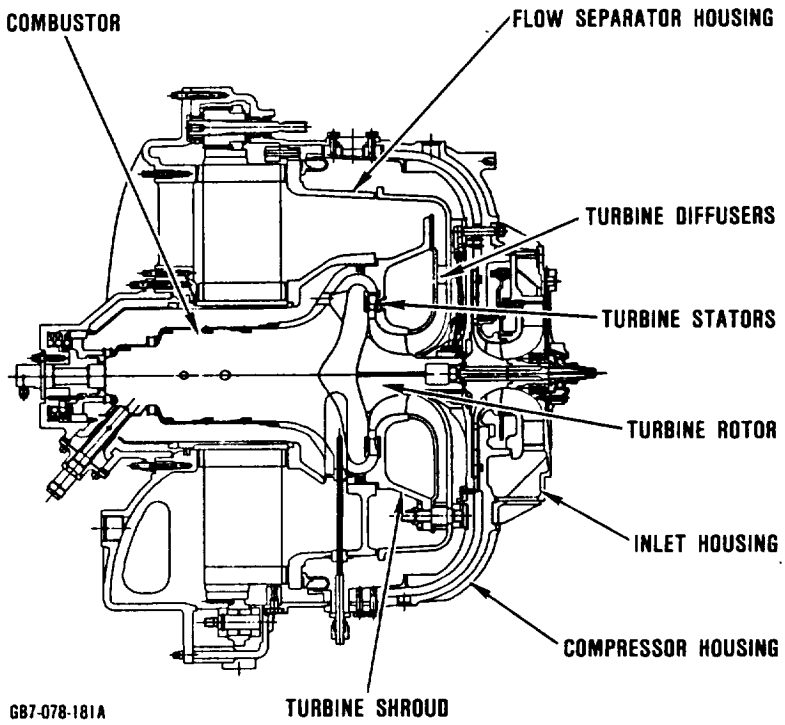

Figure 26. AGT101 Metal Structured Power Section.

development purposes, is shown in View A of Figure 27. The operational rotor system configurations with metal and ceramic turbines are respectively shown in Views B and C of Figure 27.

Rotor thrust loads were transmitted to the support structure through the oil mounted ball bearing. Rotor torque was transmitted to the drive train through a sun gear mounted on the rotor shaft. The sun gear meshes with 3 planet gears on a compound planetary gearbox to provide a speed reduction of 37.143 to 1.

Alignment and timing of the rotor mounted sun gear to the gearbox planet gears was found to be important. Misalignment and mistiming contributed to the inability to repeat early successful engine testing.

Engine testing of the initial AGT101 rotor system showed that full speed operation could not be achieved because of high amplitude motion at the foil bearing that caused the rotor system to go unstable. This high amplitude motion was subsynchronous in nature (meaning that its frequency was lower than the frequency caused by rotor unbalance) and increased as the engine was loaded.

A waterfall plot of engine vibration during acceleration, shown in Figure 28 clearly shows the existence of gearbox excitation frequencies.

A design was then introduced to isolate the gearbox from the AGT101 rotor in order to eliminate gearbox excitation frequencies that may be causing rotor instability. To accomplish this, the gearbox was separated from the rotor by a splined quillshaft with the sun gear mounted on its own bearings.

Subsequent testing showed the near elimination of gearbox excitation frequencies. However, a subsynchronous frequency of large, pulsating amplitude was present. As the rotor system speed increased, the amplitude of this subsysnchronous frequency increased, causing foil bearing failure consistently between 75,000 and 85,000 rpm.

The cause of the detrimental subsynchronous rotor system excitation was identified

through a series of engine motoring tests. The engine was powered externally using a high speed air turbine starter so that the engine bladed aerodynamic components could be replaced by dummy components systematically. Figure 29 shows the sequence of rotor systems evaluated. As each of the aerodynamic components were replaced, the rotor instability

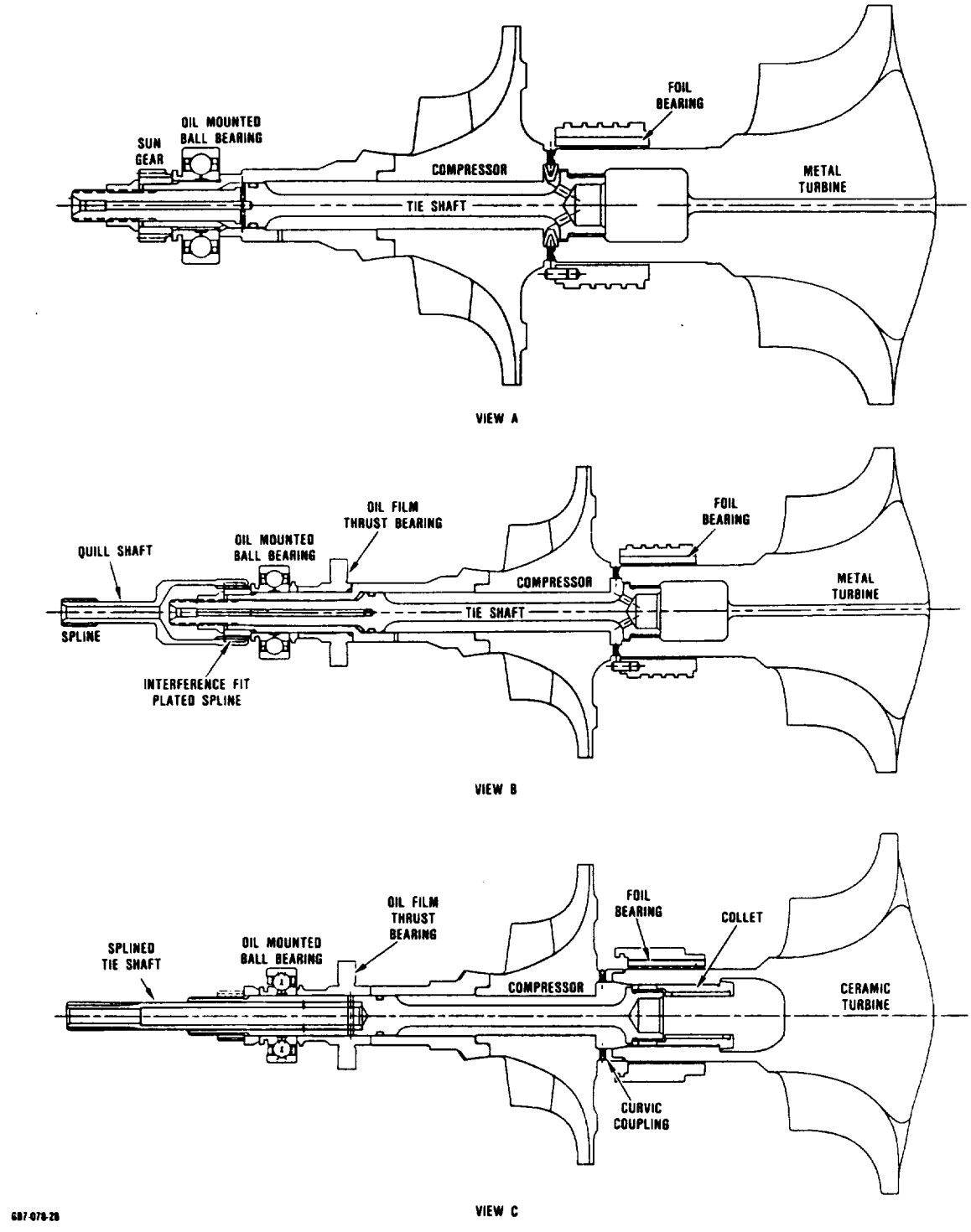

Figure 27. AGT101 Engine Rotor System Configurations.

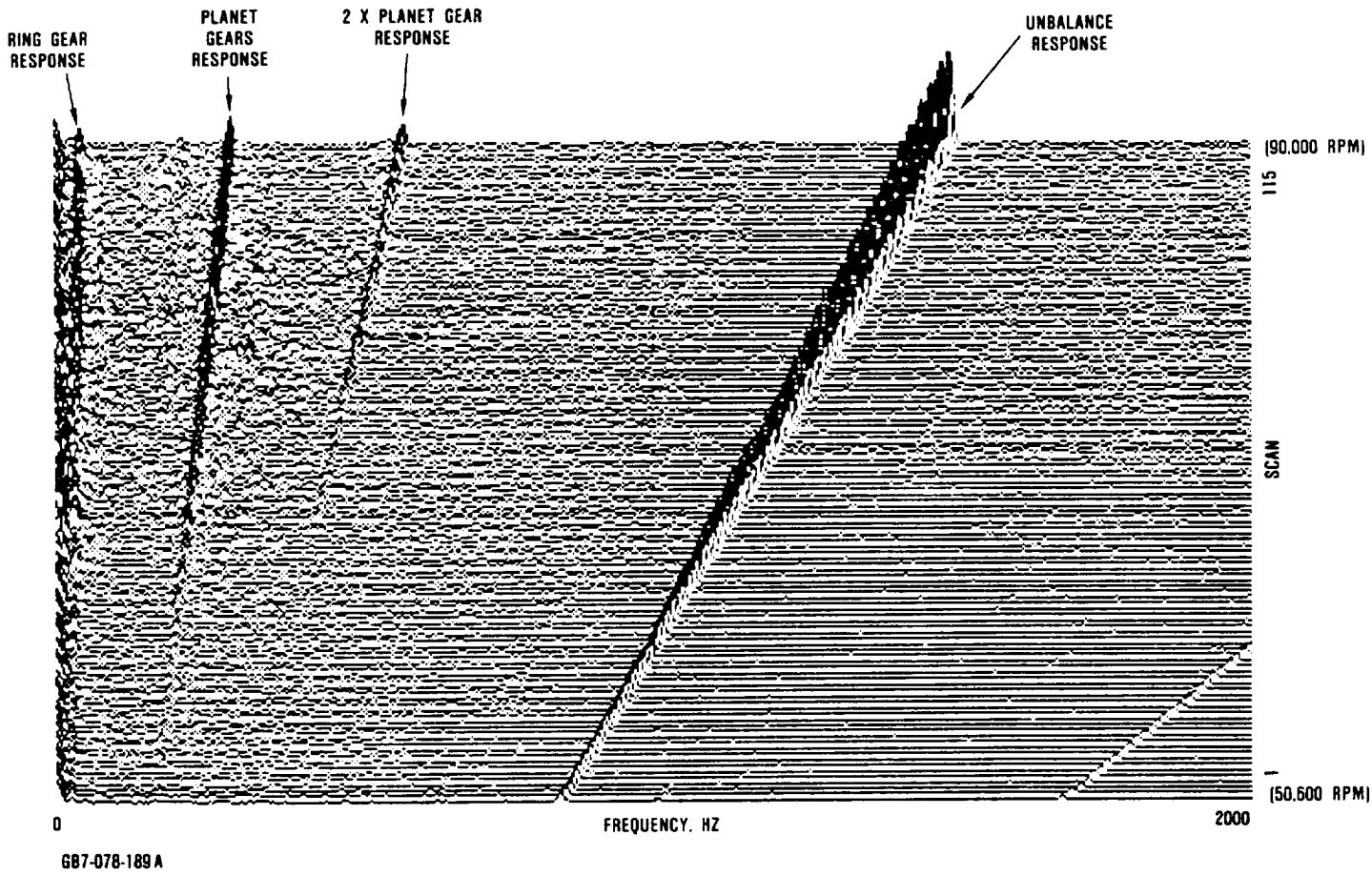

Figure 28. AGT101 Engine Initial Rotor System Configuration Response.

threshold speed increased. This trend is shown in the curve in Figure 30. The conclusion drawn from these engine motoring tests is that detrimental rotor system excitation was aerodynamically induced.

Since aerodynamic excitation will always be present, an investigation was made of ways to improve the stability of the rotor system.

Testing indicated that rotor system motion during unstable operation was conical whirl with motion at the foil bearing. A detailed investigation of the foil bearing was undertaken to determine if the stiffness and the damping of the foil bearing, which affect rotor stability, could be significantly improved.

Tests were conducted in which foil bearing length, foil thickness, backing spring stiffness, foil sway space, foil materials and foil coatings were varied. Impact testing was also conducted to determine the foil bearing damping at operating speed.

Impact testing consists of striking the rotor system in the radial direction while it is rotating, as shown in Figure 31. The rotor responds primarily in free vibration of the first mode. The decay rate of rotor subsynchronous whirl is an indication of the damping in the rotor supports. The results of the impact testing showed that the foil bearing has a relatively low viscous damping coefficient of approximately 2.0 lbf-sec/in.

By extending the length of the foil bearing and reducing the sway space, the instability threshold speed was increased by 10 percent. However, foil bearing stiffness and damping

could not be significantly improved while maintaining an acceptable foil bearing thermal environment. Therefore, a more stable rotor system would have to be obtained by improvements in other areas.

The stability of the rotor system was improved by changing the rotor support configuration. The ball bearing was moved forward (toward the gearbox) and an oil film thrust bearing inserted to provide additional rotational stiffness and damping to the rotor system. In addition, interference fit plating was added to the quill shaft spline closest to the oil mounted ball bearing to cause the splined connection at the sun gear to act as an additional rotor support.

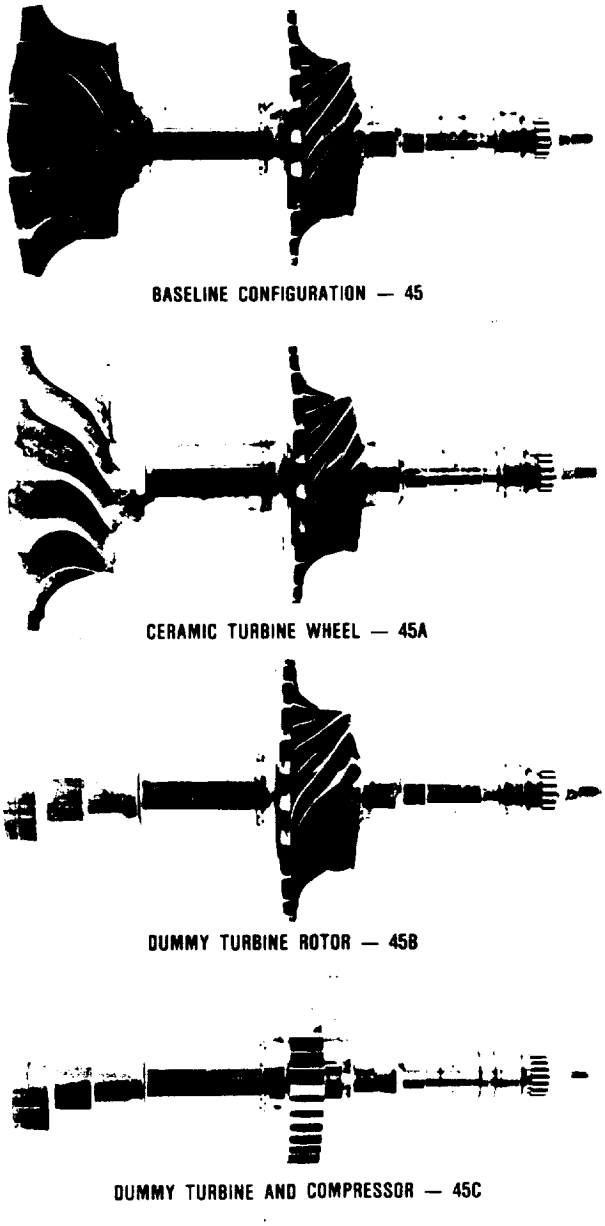

Figure 29. AGT101 Engine Motoring Rotating Group Configurations Tested.

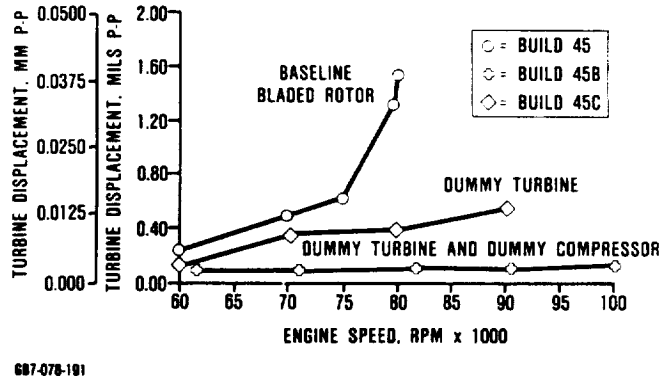

Figure 30. AGT101 Engine Aerodynamic Components Excite Subsynchronous Motion.

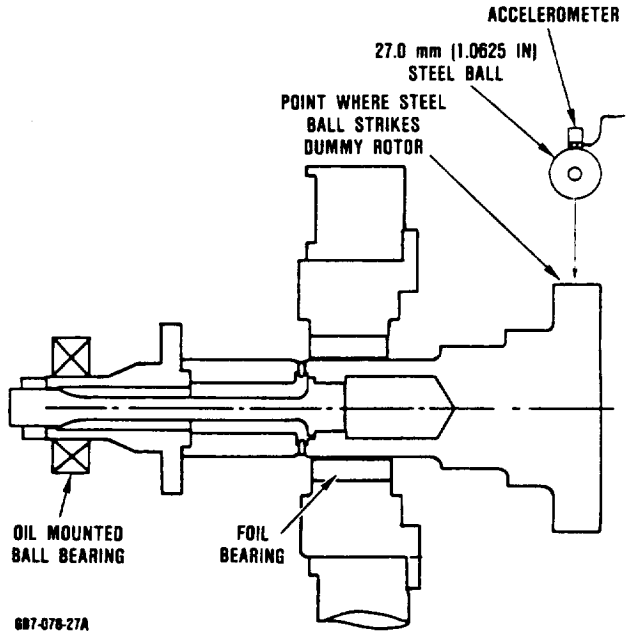

Figure 31. AGT101 Rotor Dynamics Rig Impact Test Configuration.

Testing showed that this new configuration was sensitive to gearbox-to-engine alignment,

but that careful assembly yielded consistent, stable operation. The resulting operational rotor system configuration is shown in Figure 32.

4.2.2 Current Rotor System Configuration

The current rotor system configuration is similar to the operational rotor system configuration with the metal turbine except that it has a ceramic turbine with a collet attachment. To simplify assembly, the plated splined quillshaft was removed and the tieshaft extended into the gearbox as shown in Figure 33. The extended tieshaft has the same stabilizing effect as did the plated splined quillshaft.

4.2.3 Rotor System Test Results

The current rotor system configuration with the ceramic turbine has been tested through the entire operating speed range and its rotor dynamic behavior recorded.

The 1st critical speed occurs at approximately 12,000 rpm and the 2nd critical speed is not seen because it is highly damped. A 3rd critical speed exists at approximately 82,000 rpm. This 3rd critical was seen in the test data between 70,000 and 90,000 rpm. Testing has demonstrated that these critical speeds are of no concern to the operation of the AGT101 current rotor system configuration. The 3rd mode in the current rotor system

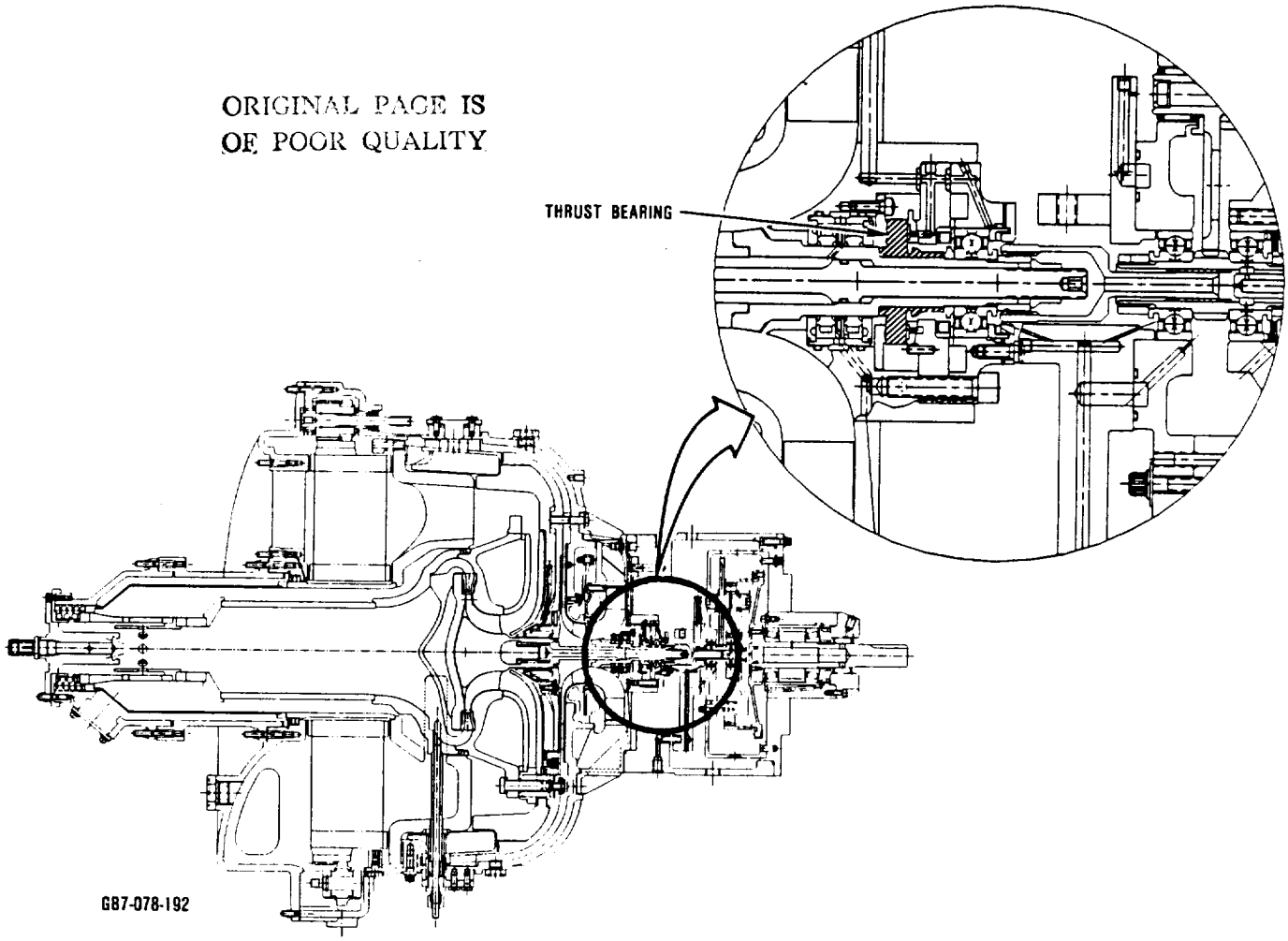

Figure 32. AGT101 Engine Operational Rotor System Configuration.

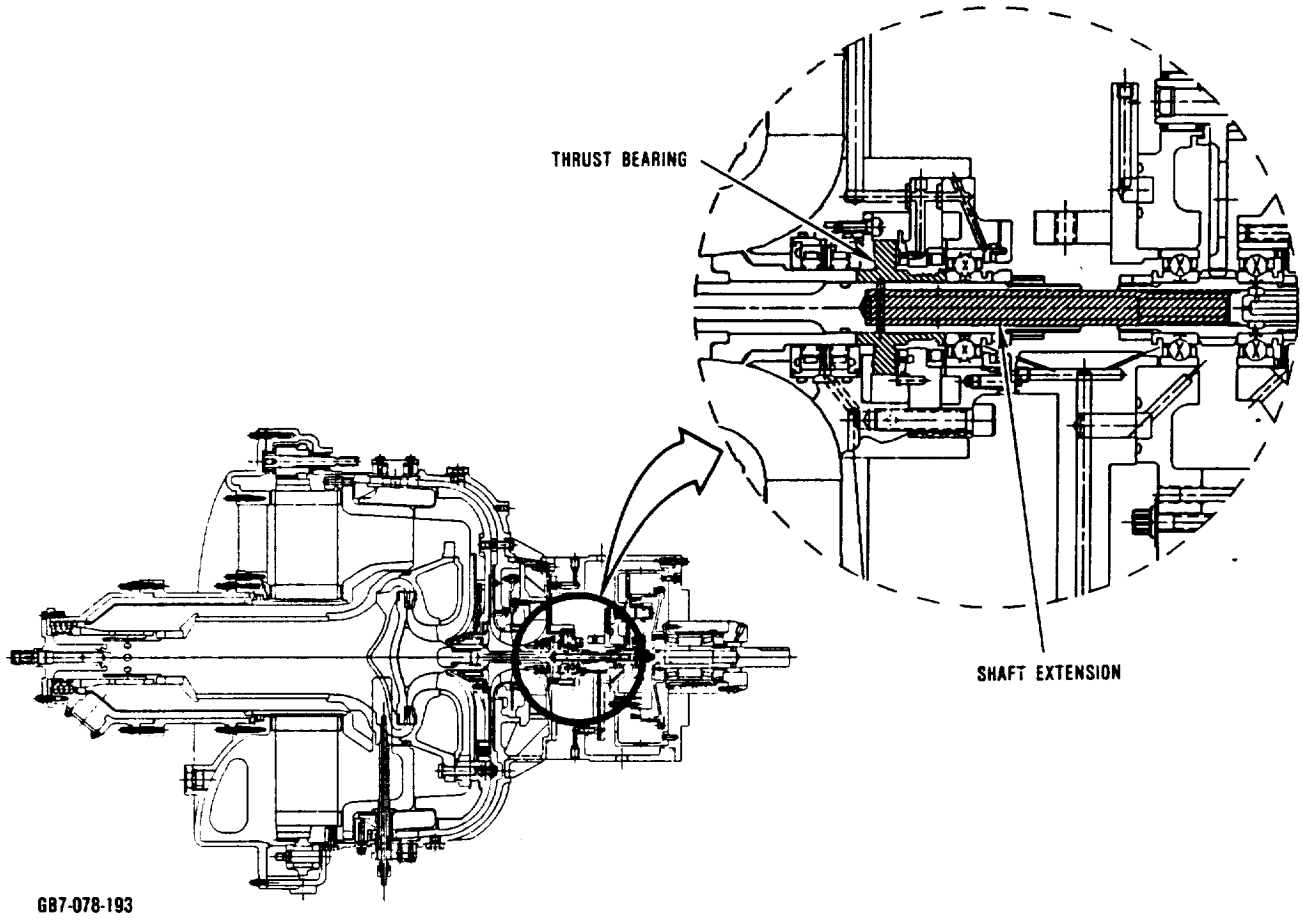

Figure 33. AGT101 Engine Current Rotor System Configuration.

configuration is caused by the relatively low rotational stiffness of the collet which has axial slots cut in it for assembly. Also, the 3rd mode rotor response at the foil bearing is different in the horizontal and vertical directions indicating that the rotor system is whirling in an elliptical orbit.

4.2.4 Rotor Static Modal Determination Testing

Static modal tests were performed on the current rotor system configuration to verify analytical prediction and to correlate with engine test results.

Static modal testing showed that a bending critical speed does exist in the operating speed range. If gyroscopic stiffening were added, the bending critical speed would occur near 82,000 rpm, which is the bending critical speed seen in current engine testing.

4.2.5 Rotor System Analysis

A rotor dynamic analysis was performed in order to analyze the rotor system critical speeds and the response of the rotor system to unbalance.

The rotor dynamics model used in analyzing the current rotor system is shown in Figures 34 and 35. The relatively low rotational stiffness of the collet is due to the axial slots in this part and was calculated from simple beam bending theory. The rotational stiffness near the curvic coupling was specifically chosen such that the predicted bending

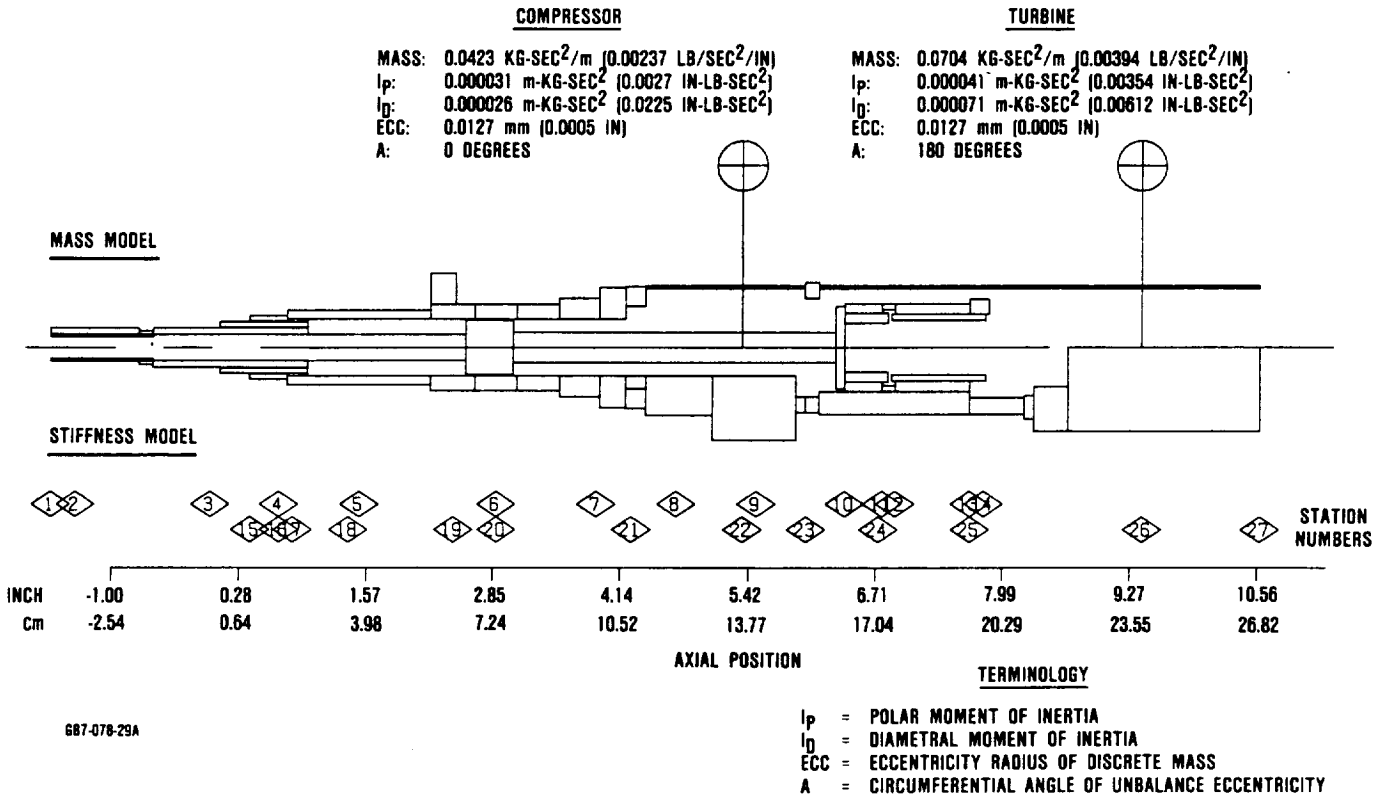

Figure 34. AGT101 Engine Rotor Mass and Stiffness Model.

critical speed matched the observed bending critical speed of 82,000 rpm.

The rotor system mode shapes were determined by an undamped critical speed analysis and can been seen in Figure 36. The 1st mode is conical whirl at the foil bearing and the 2nd mode is whirl with more motion at the oil film thrust bearing than at the foil bearing. The 3rd mode shows the rotor flexing near the curvic coupling because of a relatively soft collet rotational stiffness.

Unbalance response plots of rotor deflection and bearing loads are shown in Figures 37 and 38 and a whirl speed map is shown in Figure 39 for reference purposes. Predicted rotor displacements at the first and third critical speeds are similar to measured rotor displacements. Although relatively large displacements were predicted at the 2nd critical speed, engine tests did not show large displacements because the engine accelerated rapidly through this critical and this mode was highly damped.

4.2.6 Rotor Stability Analysis

The dynamic characteristic of a stable rotor is to have low amplitude subsynchronous motion and the rotor supports are able to positively dampen subsynchronous motion. Improved stability usually occurs when there is an increase in the forward mode log decrement, which is a calculated value from the rotor dynamic analysis. In the case of the AGT101 with a ceramic turbine and collet attachment, the 1st and 3rd forward mode log decrements are important.

The stability analysis of the rotor system shows that the difference between a stable and unstable AGT101 rotor system configuration is predicted by a relatively small log decrement.

Log decrement values for the 1st and 3rd forward whirl modes have been plotted and are shown in Figure 40. Damping is present when the log decrement is greater than zero. The

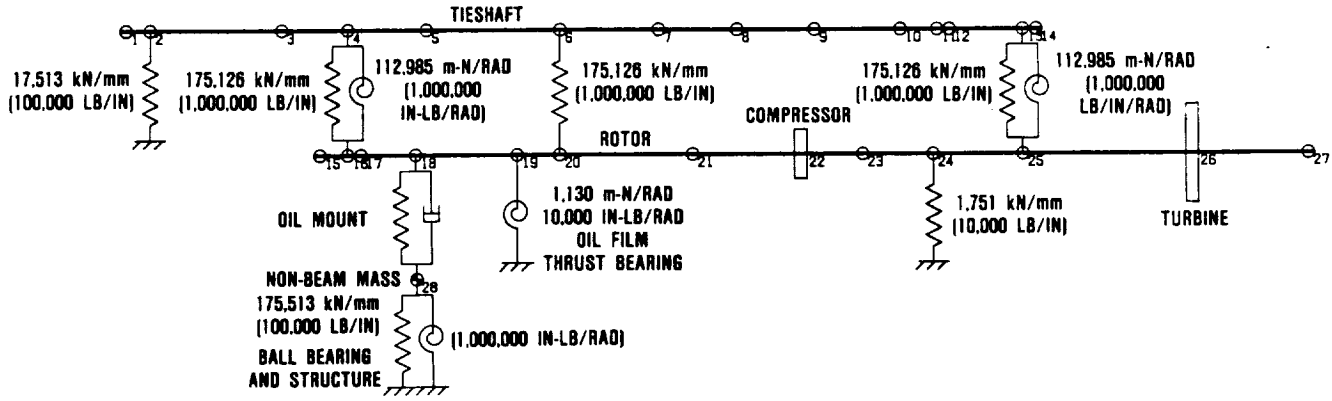

STATION	LOCATION	SHEAR STIFFNESS	ROTATIONAL STIFFNESS
11	COLLET	1,751,268 kN/mm (100,000,000 LB/IN)	6553 m-N/RAD (58,000 IN-LB/RAD)
12	COLLET	1,751,268 kN/mm (100,000,000 LB/IN)	59,430 m-N/RAD (526,000 IN-LB/RAD)
23	CURVIC COUPLING	1,751,268 kN/mm (100,000,000 LB/IN)	16,948 m-N/RAD (150,000 IN-LB/RAD)

GB7-078-308

OIL MOUNT PARAMETERS

MOUNT LENGTH: (0.3 INCH) 7.62 mm
JOURNAL OUTER RADIUS: (0.685 INCH) 1740 mm
RADIAL CLEARANCE: (0.00235 INCH) 0.0597 mm
OIL VISCOSITY: 0.000001 REYNS, 93C (200F)

Figure 35. AGT101 Engine Rotor Support Schematic.

current AGT101 rotor system configuration has demonstrated consistent stable operation to 100,000 rpm.

4.3 Engine Development Evaluations

AGT101 engine development testing augmented the engine design effort through verification of engine design. This program utilized three basic test bed configurations shown in Figure 41, each representing different stages of ceramic engine development. These test beds were used toward the development of a high temperature engine configuration capable of achieving the reference powertrain design goals.

All three engine test bed configurations were similar in design and function, and all required the same facilities and energies for testing. These test beds shared the same rotor bearing system and regenerator system. The gas flow paths, structural support systems, and rotor configurations were also similar, though differing according to the specific requirements of ceramic and metallic components.

The metallic configuration engine was the first operational AGT engine. Featuring all metal structural and rotating components, this engine was limited to 871C (1600F) maximum turbine inlet temperature. The metallic engine was used principally for system development prior to ceramic engine testing. This engine was used for rotor dynamic development, engine controls development, heat transfer coefficient determination, rotor system evaluation, and low temperature regenerator development.

The ceramic/metallic engine was a hybrid engine with a combination of ceramic and metallic components in the hot power section. This engine, was an intermediate step in the

ceramic engine evolution, featuring ceramic engine structures, metallic combustor and a metallic dual alloy turbine rotor. The development of ceramic structures as part of the engine system was performed in this engine.

The all ceramic engine featured ceramic structures, ceramic combustor, and ceramic turbine rotor. The operating temperature of this engine was limited by the stress-rupture properties of the turbine rotor material.

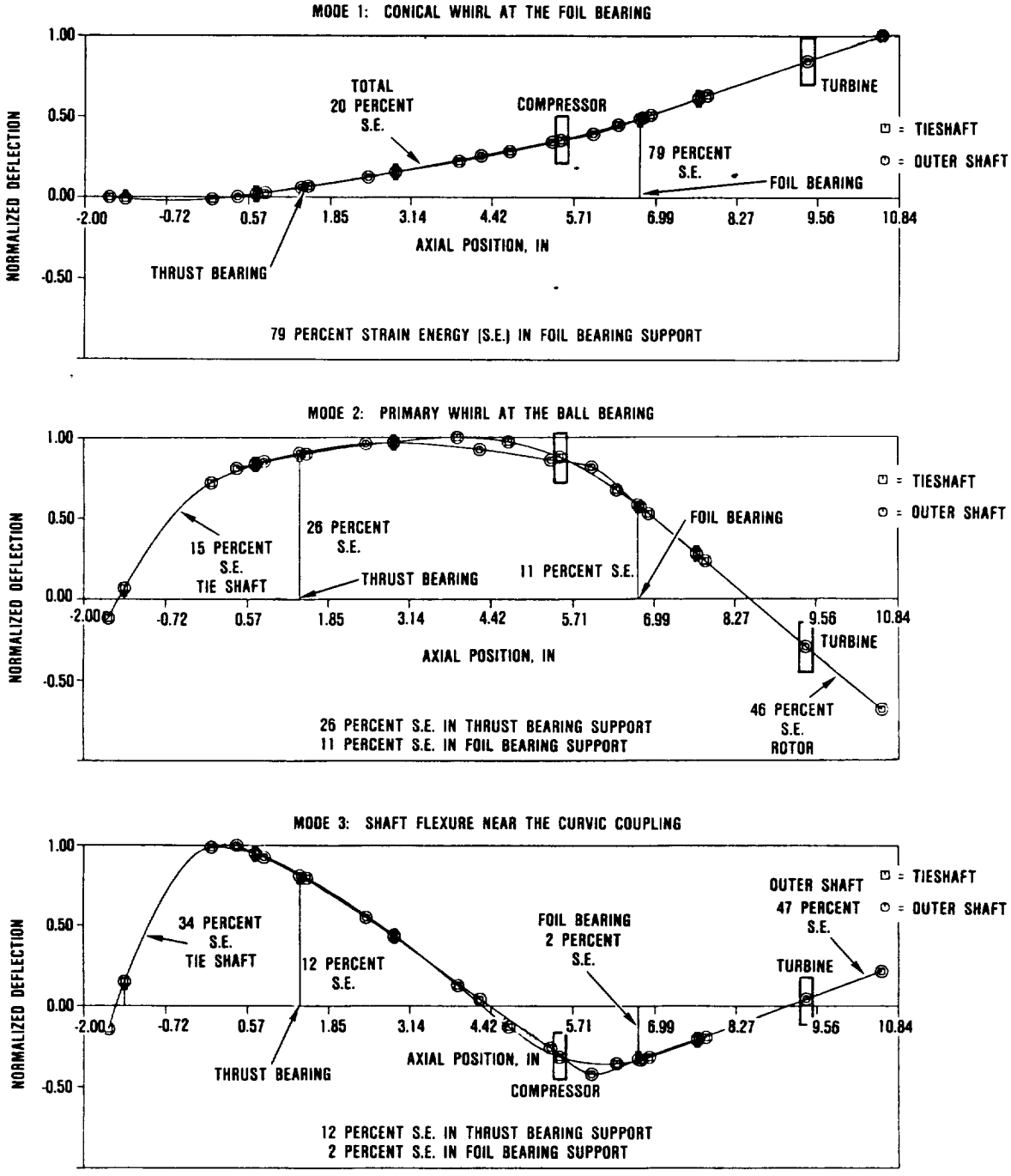

Figure 36. AGT101 Engine Critical Speed Mode Shapes.

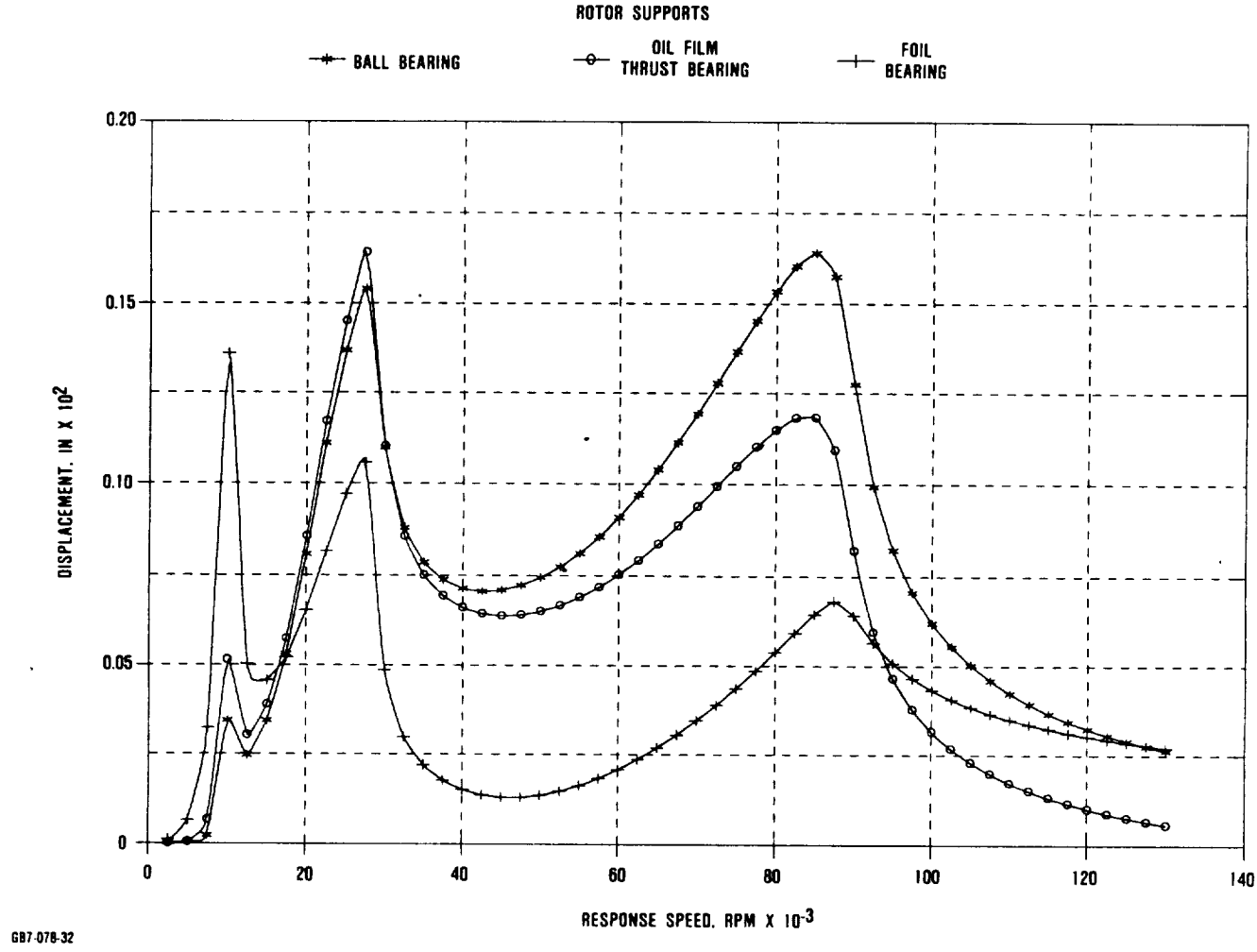

Figure 37. AGT101 Engine Unbalance Response/Support Displacements.

Turbine inlet temperatures of 1204C (2200F) were achieved. This engine was used to evaluate the characteristics of all ceramic engine operation.

4.3.1 Metallic Engine Testing

The AGT101 metallic engine saw extensive use during the first five years of the program. these engines compiled a total of 270 hours and 720 starts. This experience was accumulated during two types of evaluations, for engine mechanical development, and for ceramic engine development. Basic mechanical system development include the following activities, engine operating procedure development, engine control unit (ECU) operation, foil bearing operation, regenerator drive system operation, fuel control operation, and rotor dynamic development.

Because the ceramic and metallic engines shared similar operating systems, the metallic engines provided a low risk test bed to evaluate new design features before they were used in the ceramic engine. Examples of this work were the testing of new ECU software, light-off evaluations of new combustor configurations, the evaluation of a new regenerator drive control, and evaluations of a new engine air starter system.

Because the metallic and ceramic gas flow paths were similar, metallic engine testing was used to improve the analytical methods

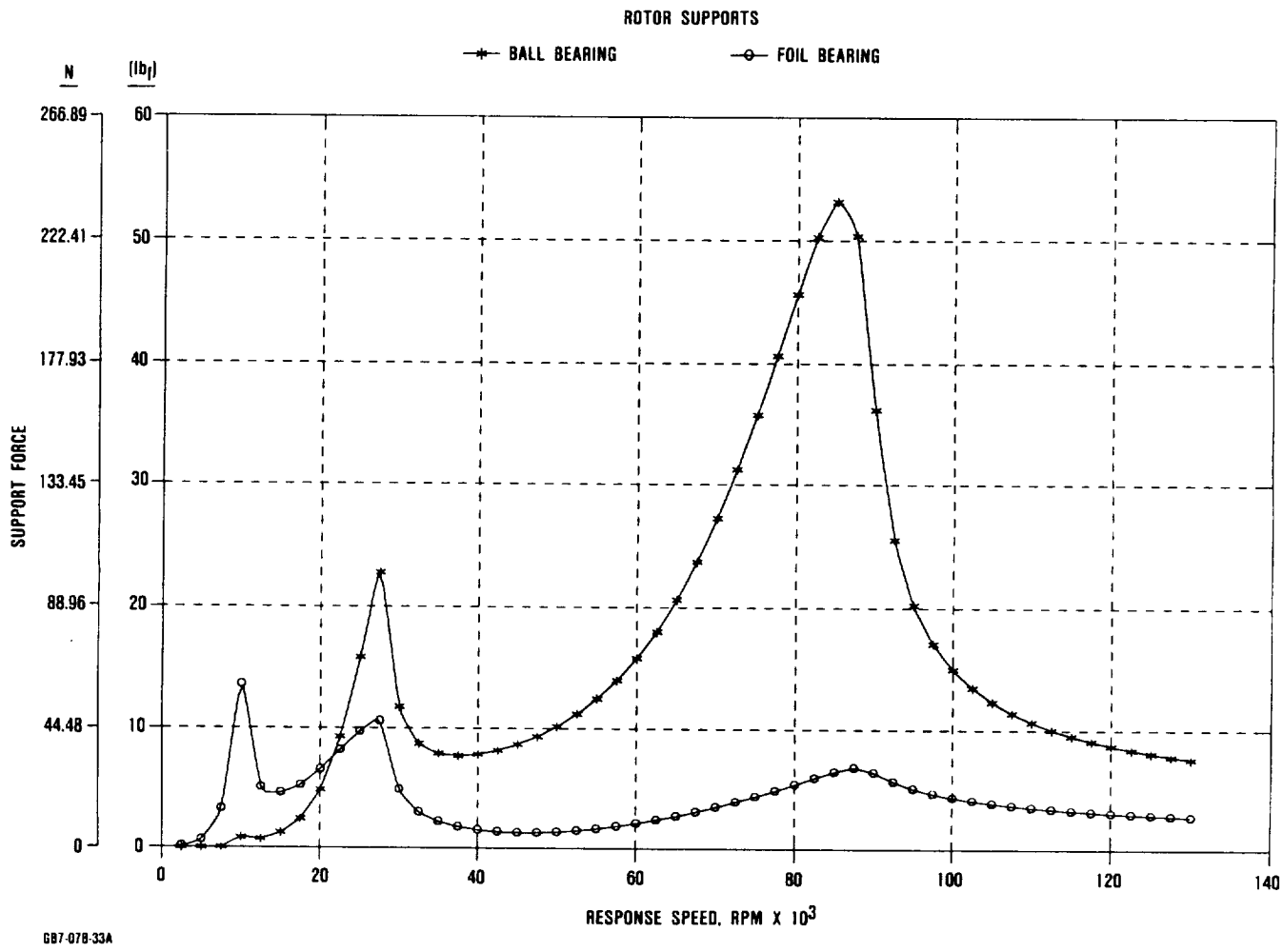

Figure 38. AGT101 Engine Unbalance Response/Support Forces.

employed in the design of ceramic components. Thermocouples were installed in the metallic engine flow path to collect data on the heat transfer characteristics of the engine flow path. This information was used to calculate heat transfer coefficients along the flow path. Extrapolations were made based on these data to simulate the ceramic engine condition for improved analysis of ceramic components.

Ceramic turbine rotors were evaluated in the metallic structured engine. Ceramic turbine blade vibration was noted as a potential problem when a ceramic rotor failed during testing in a metallic engine. Turbine blade variation was evaluated by testing an instrumented rotor in a metallic engine. Ceramic rotors have been pretested to high speeds and 871C (1600F) in a metallic engine before testing in a ceramic structured engine.

Significant in the development work performed in the metallic engine were rotor dynamic engine testing and ceramic turbine blade vibration evaluations. Engine rotor dynamic development was discussed in Section 4.2.1, ceramic turbine blade vibration evaluations are discussed below.

Turbine Blade Vibration

As a result of early ceramic turbine rotor tests performed in a metallic structured engine, turbine blade vibration was identified as a potential rotor failure mode.

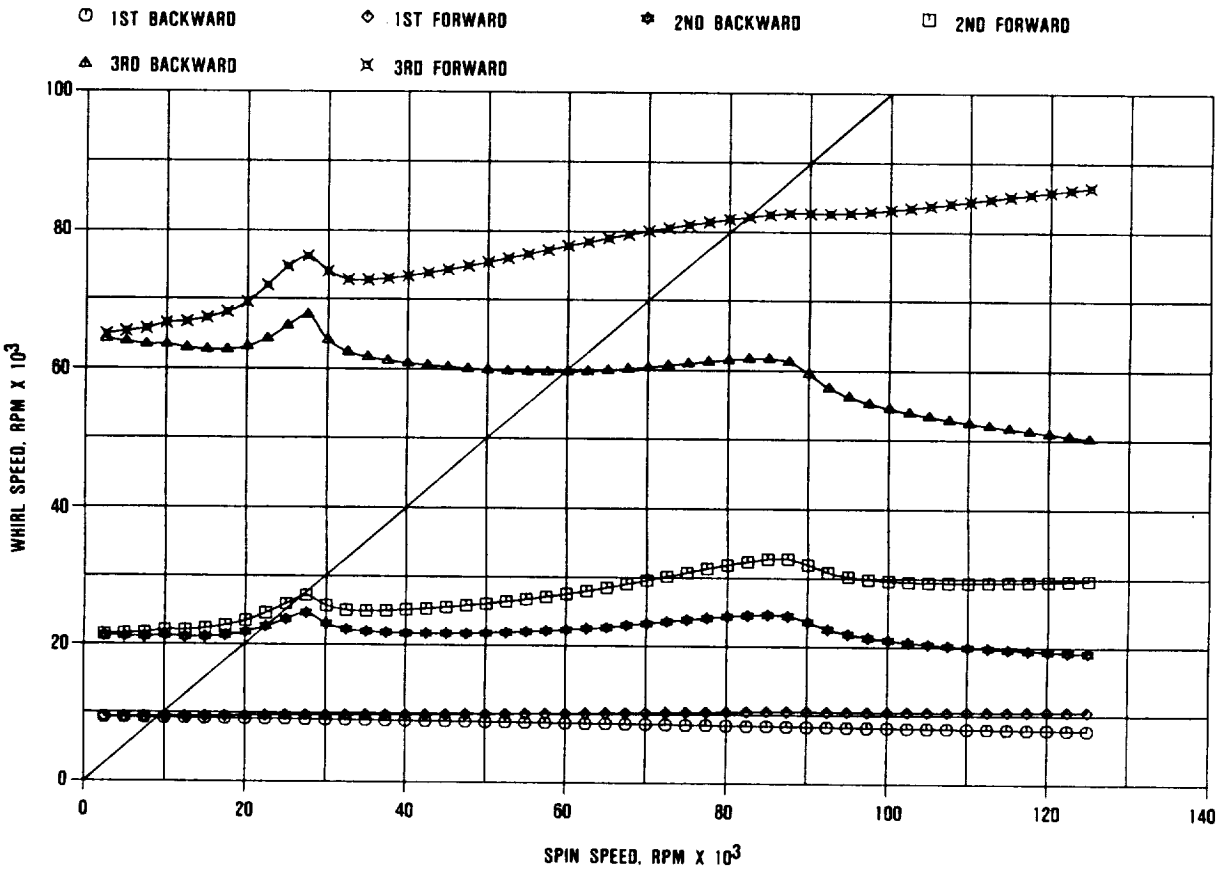

Figure 39. AGT101 Engine Whirl Speed Map.

In those tests of S/N 001 engine, early generation sintered silicon nitride ceramic turbine rotors were evaluated. These rotors contained several defects which were removed through extensive blade shroudline and backface recontouring, and hand finishing. Consequently, the rotors did not conform to print dimensions. The first rotor was installed in S/N 001 engine and operated to 97,300 rpm at 871C (1600F) turbine inlet temperature before a failure occurred. The second rotor, shown in Figure 42, failed at 62,000 rpm. Analysis of the rotor excursions during the failures indicated that a sudden imbalance was imposed on the turbine rotors which caused them to depart from a previously stable orbit. in the second test the rotor failed at a speed known to excite blade resonance.

A test plan was developed to evaluate the blade vibration problem. Two different blade vibration tests were conducted. In the first test, cold strain gages were located at the point of peak stress for the fundamental vibration modes, on the inducer and exducer portions of the ceramic blades as shown on Figure 43. Then the rotor was installed on a magnetostrictive shaker and vibrated at the blade natural frequencies to determine strain-to-failure.

Following this test, a similar strain-gaged rotor was installed in a metallic structured engine. This engine was then motored, forcing ambient temperature air through the turbine section, powering the engine through the blade resonant speed range.

The results of this test, reported more fully in Section 6.2, indicate that these newer generation turbine rotors have the room temperature strength and toughness to withstand

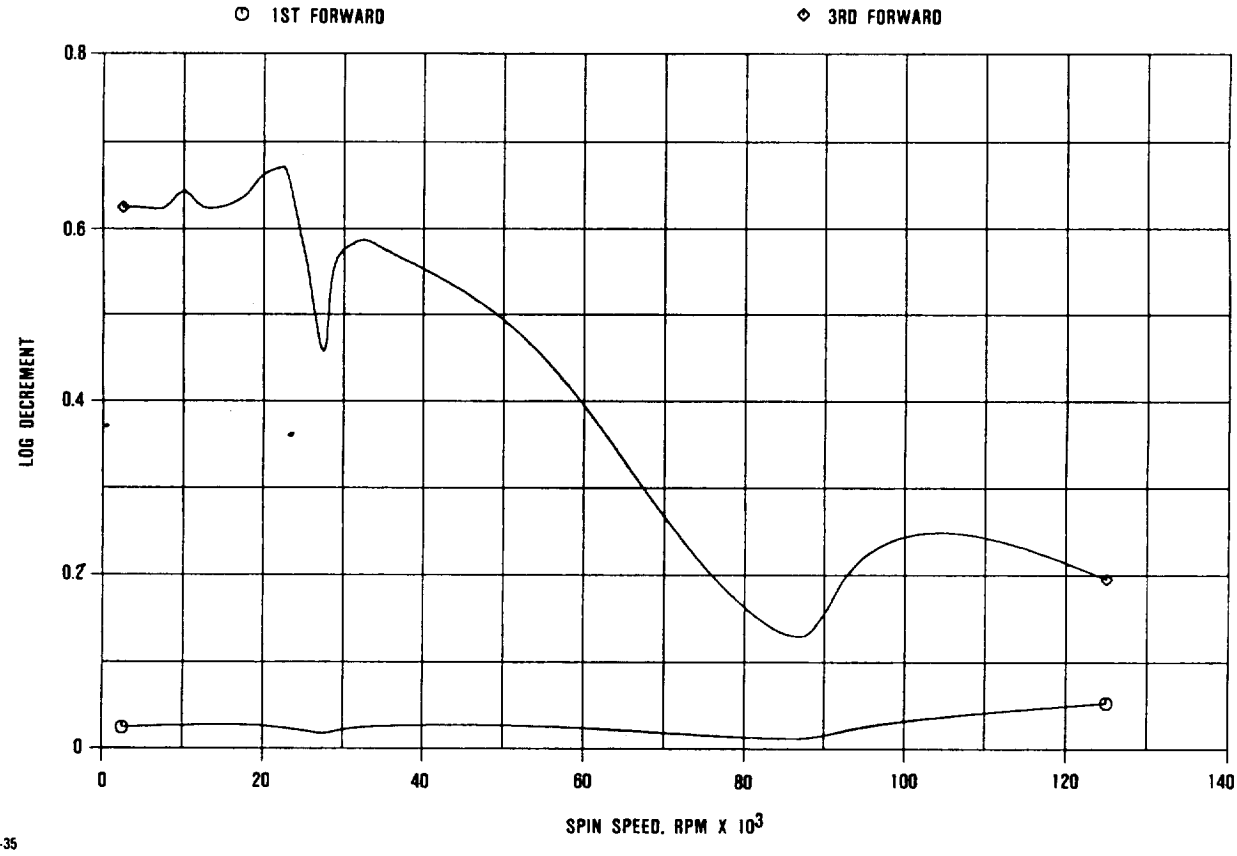

Figure 40. AGT101 Engine Forward Mode Log Decrements.

blade vibration induced by the passing of the blades through the stator wake. Analysis indicates that the cold condition is much more severe with larger driving forces; however this can be avoided in engine testing by limiting the speed of the engine without a flame in the combustor.

4.3.2 Ceramic Structure/Metallic Turbine Engine Development

The ceramic structure/metallic turbine engine configuration was an intermediate step in the evolution of the AGT101 engine. All of the ceramic structures had been developed to the engine test stage in the ceramic structures rig, however the ceramic turbine and ceramic combustor were not yet ready for engine testing. A dual alloy turbine rotor and the metallic diffusion flame combustor, slightly modified and incorporating a thermal barrier coating, were used on an interim basis to achieve operation with 1149C (2100F) turbine inlet temperatures.

Principal evaluations with this engine addressed the design verification of the ceramic structures, and for transient thermal strength during starting. In addition, this engine was used to induce the maximum pressure loads on the ceramic structures through operation at maximum speed and the collection of 1149C (2100F) engine performance data.

Analysis indicated that the highest stresses occurred in the ceramic structural components during the few minutes immediately following engine start. During early testing, precise control was exercised over the engine thermal conditions and extended thermal transient schedules were used during the start to minimize the thermal shock to the ceramic components. The start transient for the first 1149C (2100F) engine test took 52 minutes to

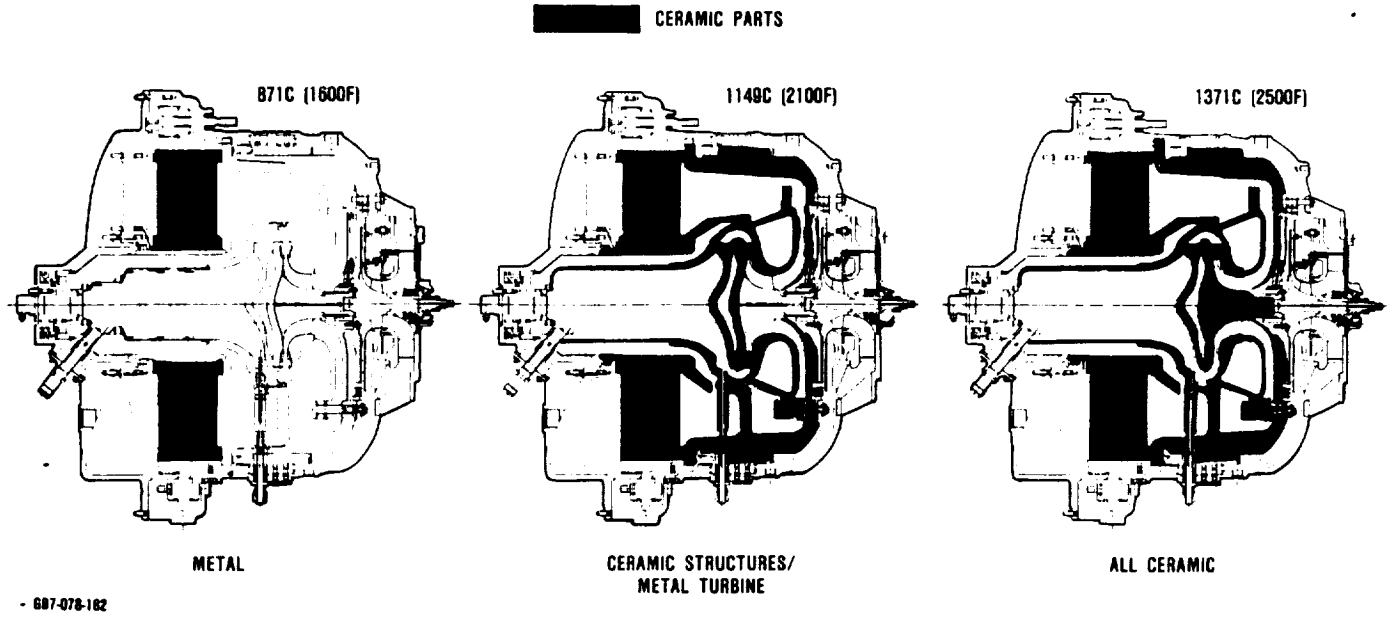

Figure 41. The AGT101 Evolves to Ceramics.

Figure 42. Ceramic Turbine Rotor Failed at 62,000 rpm.

reach 1149C (2100F) as shown in Figure 44. Confidence increased as better ceramic materials were available and component designs improved to reduce thermal stresses. By the end of the 1149C (2100F) configuration testing, the start transients were shortened to 15 seconds to reach 982C (1800F) with a 6-minute hold before increasing the turbine inlet temperature to 1149C (2100F)

4.3.2.1 Endurance Testing

Significant testing of the 1149C (2100F) engine configuration was conducted to evaluate the long term durability of the engine ceramic structures at 1149C (2100F) turbine inlet temperature. The ceramic components used in this engine came from a variety of manufacturers using several ceramic materials. The cross section in Figure 45 shows the origin of these components.

The purpose of the endurance test was to evaluate the durability of the ceramic components in the engine environment under long term steady state conditions. This engine was operated in the test facility for 100 hours at a simulated cruise condition in two cycles. The first cycle was 80 hours long and was terminated when an oil line in the test facility burst. A precautionary teardown revealed some fractured turbine stators and local coating delaminations of the regenerator seals. These components were replaced and the engine was reinstalled in the test facility and

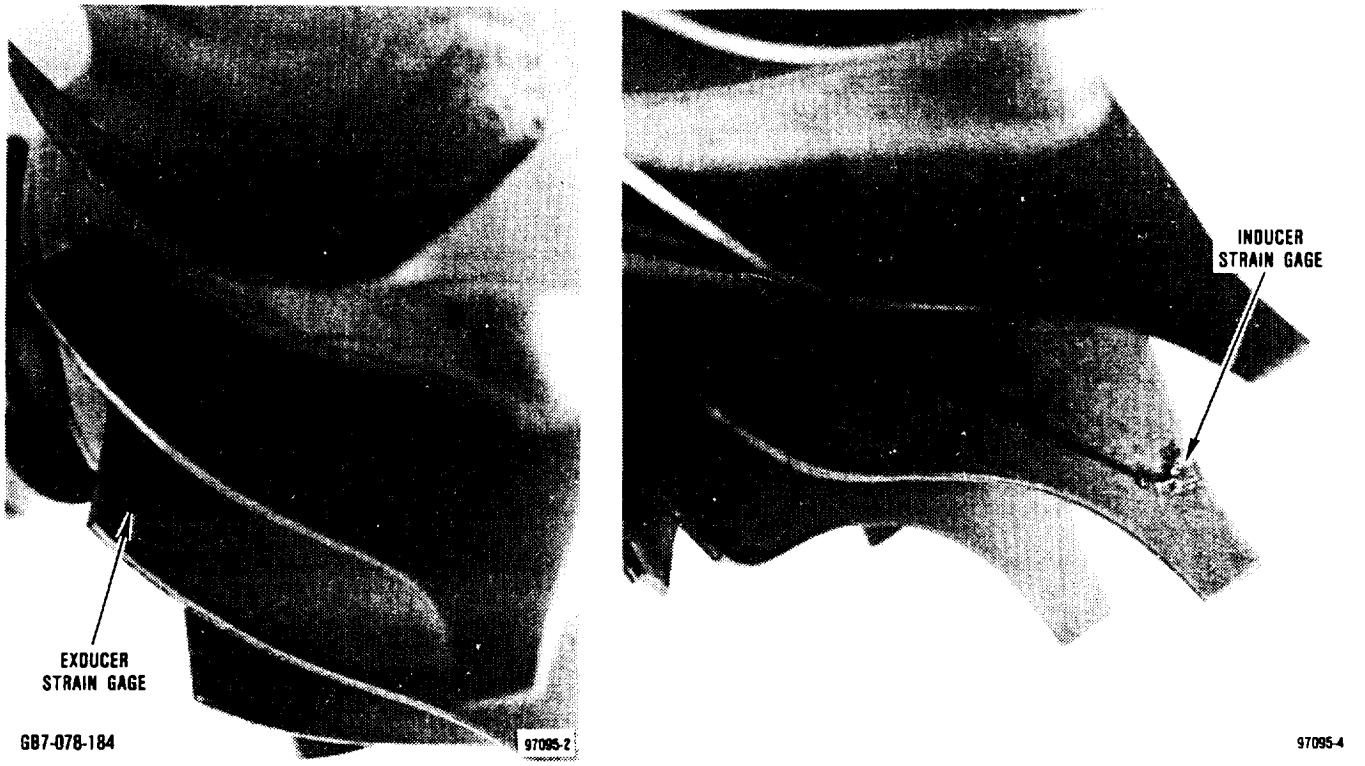

Figure 43. Strain Gaged Ceramic Turbine Rotor.

the remaining 20 hours of testing was performed on the engine.

The ceramic engine components were in very good condition after the completion of the test. These parts are shown in the photograph in Figure 46. Neither excessive oxidation nor sticking at the ceramic component interfaces were noted. The regenerator seals did show significant distress though the core and drive components were in good condition.

The successful completion of this test indicated that the ceramic structural engine assembly could endure the rigors of engine operating conditions for extended periods. Confidence was gained to proceed with engine testing to high speeds where component pressure loading and interface stresses were at their maximum level.

Several full and near full speed tests were conducted in the 1149C (2100F) engine. During this series of tests, improvements in internal engine and regenerator seals were also evaluated. The ceramic components endured the full pressure conditions without failure. Problems were encountered concerning the durability of the metallic components operating at the elevated temperature and high speeds.

4.3.2.2 Dual Alloy Rotor Integrity

The dual alloy turbine rotor was designed for short term operation at 1149C (2100F) turbine inlet temperature and was utilized to enable ceramic engine development on an interim basis until a ceramic turbine rotor was available. The rotor was designed with a forged powder metal Astroloy hub hot-isostatic-press (HIP) bonded to a directionally solidified cast MAR-M 247 blade ring. Shown in Figure 47, this rotor had provisions to cool the bore of the rotor with air bled from the compressor seal, enabling operation at 1149C (2100F).

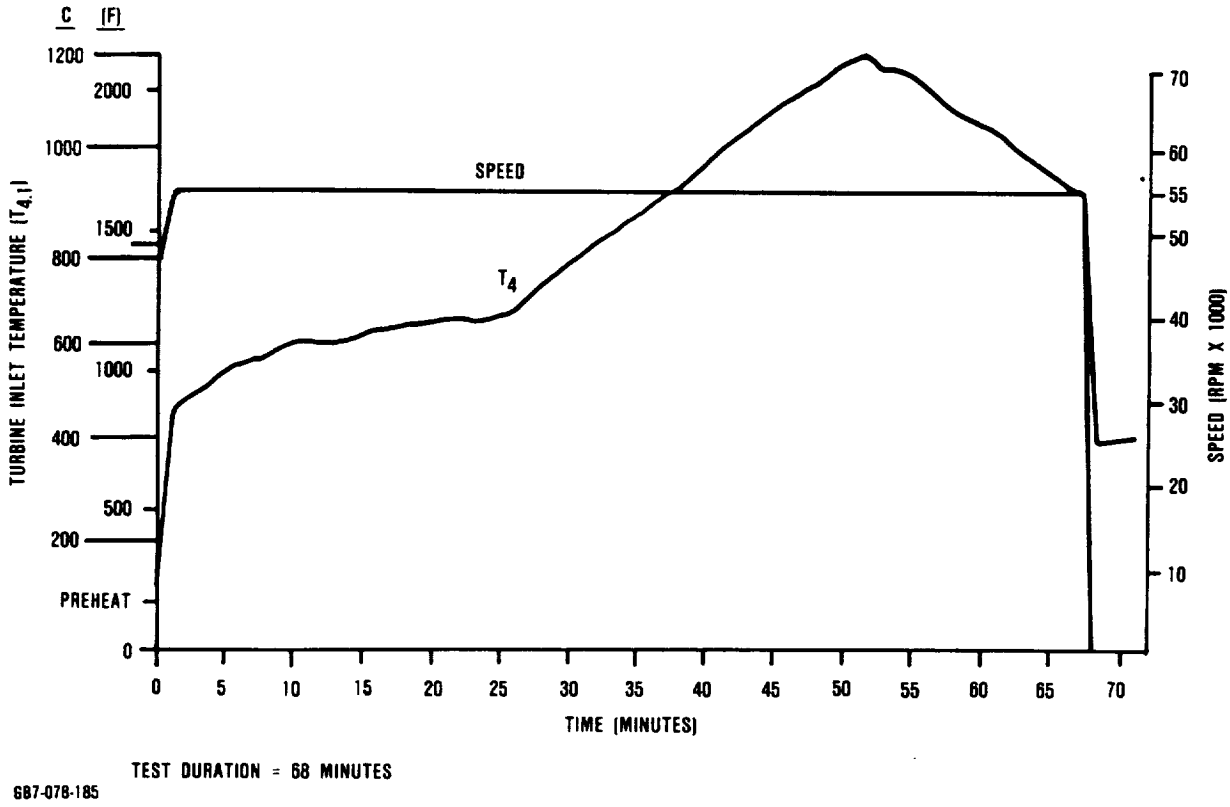

Figure 44. S/N 002C - T4 Schedule for the First Ceramic Engine Test.

These rotors were used in all 1149C (2100F) engine testing, including the 100-hour endurance test and the various runs to maximum speed. During the course of this testing, two dual alloy rotors failed. These rotors had a predicted stress rupture life of 500 hours at 100,000 rpm with 1149C (2100F) turbine inlet temperature. The first rotor failed due to stress rupture of the cast blade ring after 100 hours of testing at 67,000 rpm, and a short time at 95,000 rpm. This failure was an indication that the blade crystal geometry was less than optimum, resulting in a less than predicted stress rupture life. The second dual alloy rotor failure occurred during engine testing at 68,000 rpm and 982C (1800F). This rotor experienced a separation of the blade ring from the hub. An examination of the rotor remnants revealed that the HIP bond joint was discontinuous in several areas.

This experience caused a review of the other dual alloy rotors in the AGT inventory. Both ultrasonic inspection techniques and visual methods were used to examine the rotor bond joints. These inspections indicated that most of the rotors had detectable bond joint defects, though whether these defects could cause a rotor failure was not known. Moreover, the review disclosed that there was no effective proof test or NDE technique that could positively weed out defective rotors from the good rotors. As a result, the use of dual alloy rotors was discontinued in future engine testing due to the uncertainty of their integrity.

4.3.3 Ceramic Engine Development

The ceramic engine configuration incorporated an entirely ceramic hot power section, including ceramic engine structures, ceramic combustor, and ceramic turbine rotor. The evolution of this engine was the progression from the ceramic structure/metallic turbine configuration as the ceramic turbine rotor and

KEY	MATERIAL	SOURCE
1	MAS — MAGNESIUM ALUMIMUM SILICATE	NGK-LOCKEE
2	LAS — LITHIUM ALUMIMUM SILICATE	CORNING GLASS WORKS
3	RBSN — REACTION BONDED SILICON NITRIDE	AIRESEARCH CASTING CO
4	SAME AS 3 ABOVE	
5	SN-50 SILICON NITRIDE	NGK-LOCKE
6	SASC — SINTERED ALPHA SILICON CARBIDE	CARBORUNDUM (STD OIL)

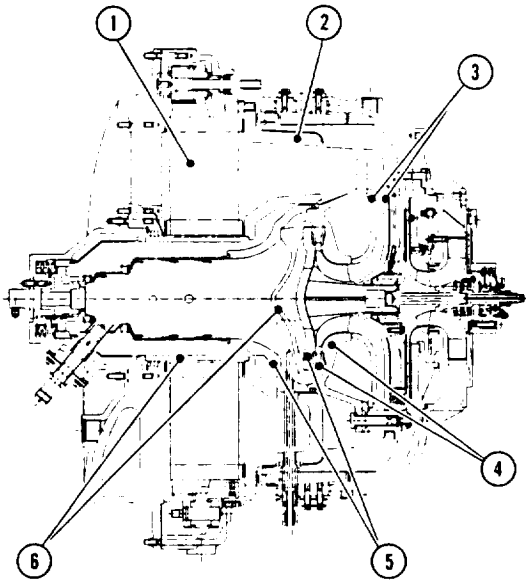

687-078-186A

Figure 45. Ceramic Structures Used in the 1149C (2200F) Test.

ceramic combustor were developed to the engine testing phase.

Significant testing of the ceramic engine configuration included the activities noted below:

- o Long term steady state testing at 1204C (2200F)
- o Combustor performance and carbon forming tendencies
- o Interpath gas leakage
- o Regenerator durability

Evaluation of the ceramic engine configuration was initially approached from a durability standpoint. Engine performance was regarded as secondary to insuring that the ceramic structures were sound, that the ceramic turbine had sufficient life at temperature, and that this system would operate as a

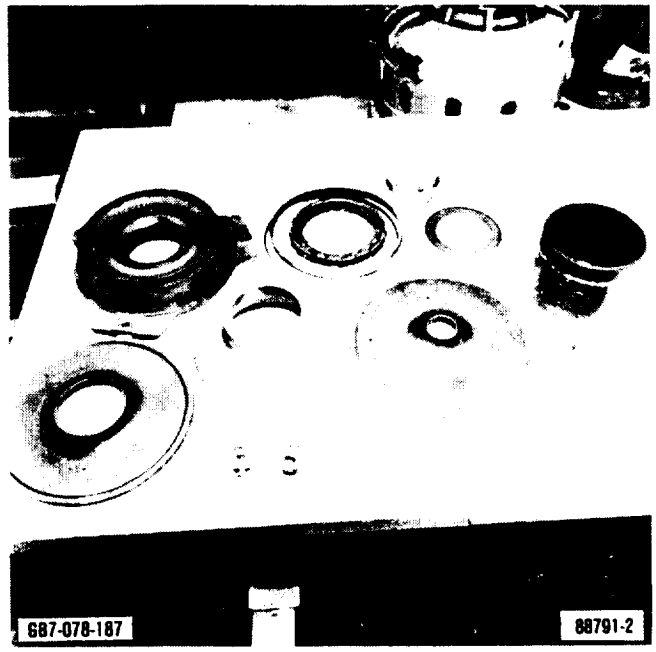

Figure 46. Ceramic Components Following the 100-Hour Endurance Run at 1149C (2100F).

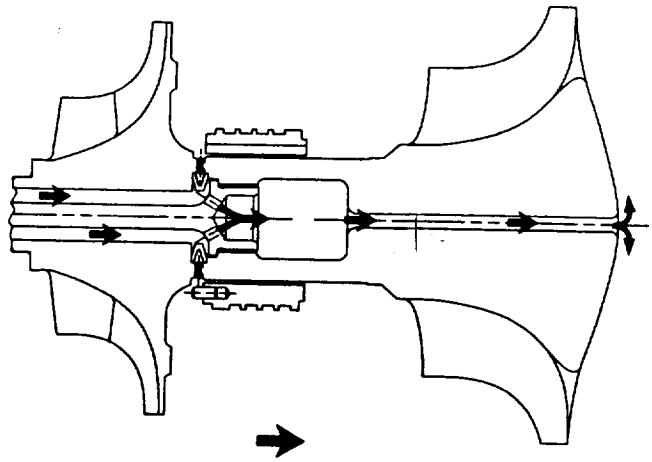

687-078-188

Figure 47. Dual Alloy Rotor Showing Cooling Air Path.

unit. The development of performance enhancing components such as interpath seals and the regenerator system, was performed in their individual rigs until basic engine durability was established.

Ceramic engine durability testing was performed to identify the weak areas in ceramic engine design and to demonstrate the capability of the ceramic engine system. To this end, the ceramic engine was tested steady state at 1204C (2200F) and 60,000 rpm for 85 hours until a failure of the ceramic turbine rotor stopped the test. The results of this test provided much valuable information on the durability of the ceramic components used in the engine.

The cause of the engine failure was traced to partial plugging of the air assist ports in the fuel nozzle. The plugged ports allowed two unatomized fuel streams to impinge with the wall of the pilot combustor, forming deposits of hard carbon. When the carbon deposits broke loose from the combustor wall, they traveled down the gas path and impacted the turbine rotor inducer blade tips causing damage to the turbine and subsequent engine failure.

The engine regenerator system showed severe thermal distress. The magnesium aluminum silicate (MAS) regenerator core had indications of high thermal stress with thermal cracks emanating from the outer rim toward the center. The regenerator seal wearface coating on the hot side seal had delaminated about the inner periphery and the shape of the seal crossarm was significantly distorted. This damage occurred during the course of the test and was not a result of the failure.

Follow-up testing in the combustor rig had indicated that the key to preventing fuel nozzle fouling was to maintain proper nozzle face temperatures. Indications were that excessive temperatures in the air-assist passages of the nozzle caused fuel in those passages to coke and plug the passage.

The ceramic structures survived the test intact. Oxidation was minimal and sticking at the ceramic component interfaces was not a problem. These structural components were reused on a subsequent test.

This engine was rebuilt incorporating several improvements in the combustor fuel nozzle and regenerator system. The combustor fuel nozzle was thoroughly flow checked and tested in the combustor rig for carbon forming tendencies. The regenerator core was fabricated from an improved MAS material with reduced thermal expansion. In addition the inner regenerator seal was modified to relieve potential thermal interference at the crossarm to outer peripheral interface. The test cycle was similar to the 85-hour test except that a periodic shut down would be made to pull and inspect the fuel nozzle for plugging.

After 12 hours of testing, another failure occurred. This time the turbine rotor experienced a hub burst, most probably as a result of premature stress rupture. The stress rupture properties of specimens cut from similar rotors were inconsistent and lower by orders of magnitude than the stress rupture properties of test bars of the same material. Further rotor material development is required to resolve this problem.

The regenerator system fared much better during the 12-hour test. The regenerator core showed minimal distress and thermal stress cracking was not significant. The regenerator seals, however were again distorted. Follow-up work at Ford was performed to resolve the seal distortion problem. This subject is discussed more thoroughly in Section 5.4.1.

Ceramic combustor light-off performance has been marginal. During steady state operation at high temperatures, this combustor has provided consistent, reliable, stable operation. However further development is required to improve the combustor system start and low temperature performance.

The design deficiencies of this combustor have been identified and design improvements have been made. This modified combustor design, reported in Section 5.3, has been fabricated in metal, tested in the combustor rig,

and tested in the metallic structured engine. Engine testing of the enlarged bore combustor has shown dramatic improvements in start and low temperature performance.

4.3.4 Engine Performance Testing

Engine performance testing was limited during the AGT101 project due to limitations in the capabilities of the ceramic materials and design development of the engine internal seals. What testing was performed was done at development conditions, that is, at conditions less severe than the RPD, for the purpose of seal development.

Performance testing was performed at various engine operating conditions for use in determining the leakage levels of the engine cycle. This data was used in conjunction with the engine performance model to establish the overall leakage of the engine and determine the equivalent engine performance at sea level standard conditions. Using the measured data as a starting point in the engine performance model, the internal leakages are varied until the best data match is obtained. During this iterative modeling exercise, energy and mass balance is maintained.

Performance data was obtained at 1149C (2100F) turbine inlet temperature in a ceramic structured engine with a dual alloy turbine rotor over a range of speeds from 60,000 to 100,000 rpm. Limited component instrumentation downstream of the compressor could be accommodated due to the ceramic structures. Based on this approach, the internal leakage was 21 percent. The 21 percent leakage level is consistent with a standard seal level performance of 32.2 kw (43.2 shp). The engine configuration was far from optimum, but the test represents the baseline performance from which efforts can be addressed and comparisons made. This model and the data match is summarized in Figure 48.

4.3.5 Ceramic Engine Seal Development

The interface between the turbine shroud, the flow separator housing, and the transition

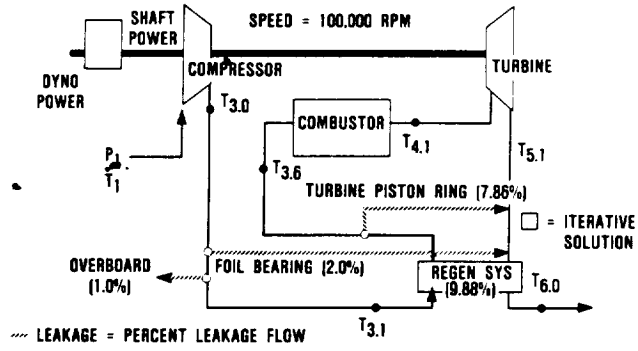

	TEST DATA	CALCULATED VALUES
DYNO POWER	22.42 kW (30.07 HP)	22.43 kW (30.08 HP)
SHAFT POWER	—	32.4 kW (43.4 HP)
P_1	97.188 kPa (14.096 PSI)	97.188 kPa (14.096 PSI)
T_1	29C (85F)	29C (85F)
$T_{3.0}$	229C (445F)	241C (466F)
$T_{3.1}$	261C (502F)	260C (501F)
$T_{3.6}$	750C (1383F)	762C (1404F)
$T_{4.1}$	1170C (2139F)	1170C (2139F)
$T_{5.1}$	—	869C (1597F)
$T_{6.0}$	360C (680F)	347C (658F)

GB7-078-194

Figure 48. Engine Test Data Setup Model.

duct is recognized as critical to the overall leakage performance of the AGT101 engine. Because temperatures in the region will approach the 1371C (2500F) TIT at full power, use of ceramic sealing elements is required.

The concept employed for the first ceramic engines involved two sealing elements separated by a ceramic wave spring, as shown in Figure 49. The wave spring concept was originally the result of observed distortion of RBSN rings during nitriding. The wave pattern generated as the rings drooped over the furniture in the furnace was recognized as having potential application as a spring.

This design was found to have shortcomings in terms of sealing capacity and especially repeatability. The effectiveness of the seals depended greatly on their ability to seat themselves under a pressure load, with the wave spring serving little purpose other than to

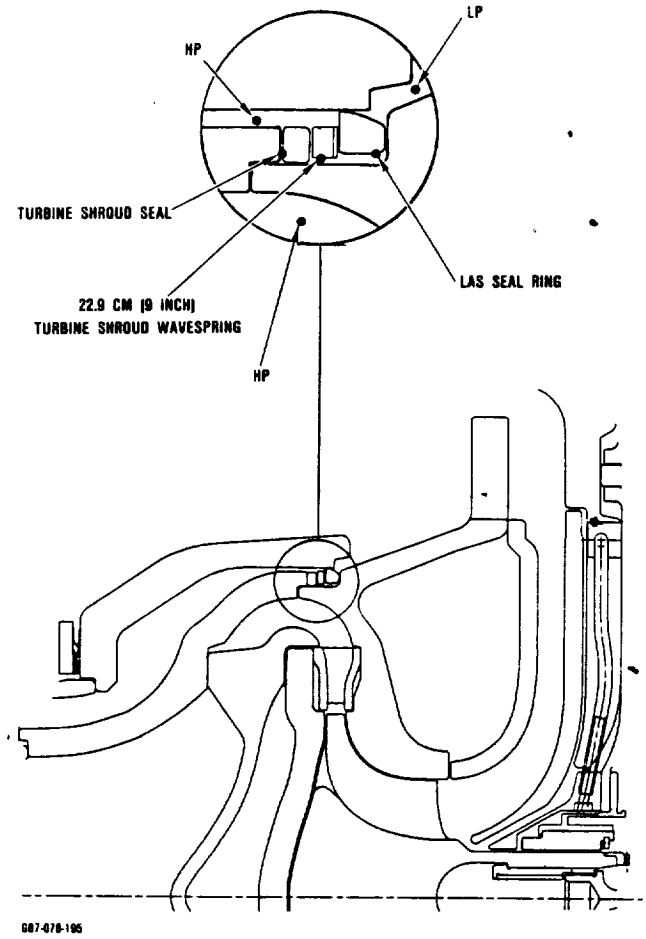

Figure 49. Single Separator Seal Configuration.

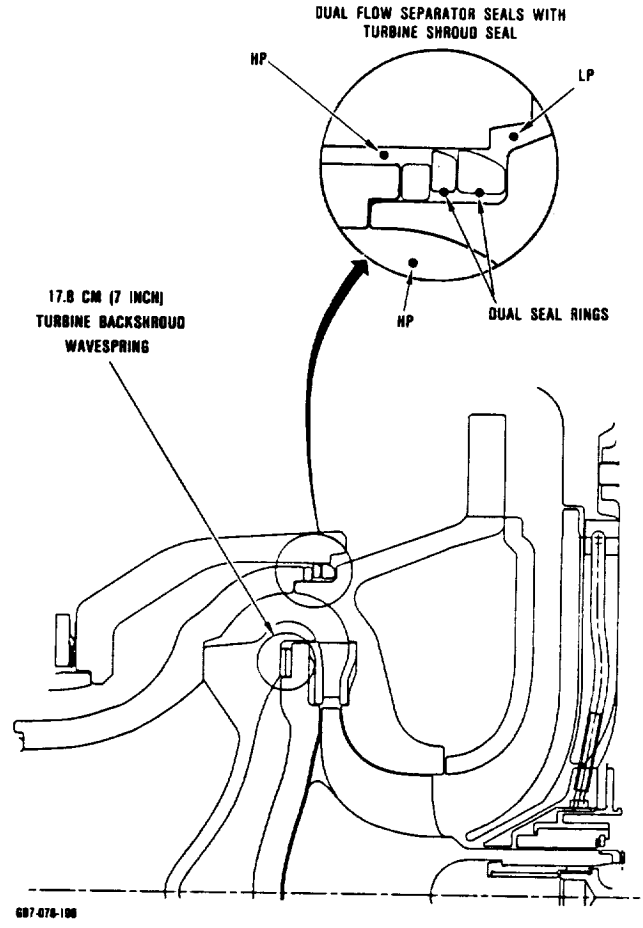

Figure 50. Flow Separator Seal Configuration.

position the seals during startup. Sealing capability was often improved by physically jarring the engine external housing. This is an indication that the ability of the wave spring to reliabily seat the sealing elements is marginal at best.

To improve the sealing capacity and reliability of this system, modifications were made to ceramic hardware as shown in Figure 50. Specifically, the wave spring (now made of sintered silicon nitride) was made smaller and installed between the turbine backshroud and the combustor baffle. The seal pocket was now able to accommodate two sealing elements between the turbine shroud OD and the flow separator ID (a large pressure drop area where leakage represents a direct loss to the power cycle). As in the previous configuration, tight-fitting custom-ground LAS seals, with no end gap, could be used for engine operation up to 1204C (2200F) TIT. Higher operating temperatures required the use of a sintered silicon nitride or RBSN rings, with an overlapping and gap to accommodate the different thermal growth rates of the rings and the flow separator.

Testing was performed to evaluate the improvement which the updated design afforded. This is discussed in detail in section 6.3.2.6.

5.0 COMPONENT/SUBSYSTEM DEVELOPMENT

Activities centered around the development of the following major components and subsystems: compressor, turbine, combustor, and regenerator.

5.1 Compressor Development

5.1.1 Compressor System Requirements

The AGT101 compressor system is comprised of a single-stage backward swept centrifugal impeller having 12 full blades and 12 splitter blades, a three stage radial diffuser with one stage of diffusion vanes and two stages of deswirl vanes, and an upstream set of seventeen variable inlet guide vanes (VIGV). Performance predictions for this compressor system at maximum power operating condition are as follows:

- Mass Flow at 29C (85F) sea level — 0.388 kg/sec (0.8542 lb/sec)
- Stage Pressure Ratio — 5
- Stage Efficiency, Total-to-Total — 0.805
- Rotational Speed — 100,000 rpm

These performance goals are quoted at maximum power; however, as previously stated, the AGT101 was designed using a "systems design" philosophy wherein a distinct recognition of CFDC duty cycle has been considered. Therefore, since a significant portion of operation is at low power levels, during the course of development, maximum power performance goals were compromised with more important program goals, i.e., fuel economy over the duty cycle.

5.1.2 Aerodynamic Development

5.1.2.1 Compressor Aerodynamic Design

The aerodynamic and geometric impeller design summary is shown in Tables 7 and 8.

Table 7. AGT101 Impeller Design Aerodynamic Design Summary.

Inlet Total Temperature	302.6C	(544.7R)
Inlet Total Pressure	99.5 kPA	(14.431 psia)
Speed		100,000 rpm
Flow Rate	0.387 kg/sec	(0.8542 lb/sec)
Tip Speed	570 m/sec	(1872 fps)
Impeller Efficiency, Total/Total, No Dump Loss		89.67 percent
Specific Speed		57.2
Shroud Inlet Relative Mach Number		1.125
Shroud Relative Velocity Ratio (PD Analysis)		0.600 (0.529 Caps)
Shroud/Mean Meridional Velocity Ratio (PD Analysis)		1.25
Average Exit Blade Deviation		3.27
Inlet Aerodynamic Blockage		0.98
Exit Aerodynamic Blockage		0.90
Average Slip Factor		0.9488

Table 8. AGT101 Impeller Design Geometric Design Summary.

Inlet Hub/Tip Ratio		0.464
Inlet Hub Radius	1.52 cm	(0.600 in)
Inlet Sweep Angle (Meridional Projection)		7.47 Deg.
Exit Radius	4.45 cm	(2.146 in)
Exit B-Width	0.39 cm	(0.154 in)
Blade Number		12/24
Average Exit Blade Angle		49 Deg.
Exit Rake Angle		0
Axial and Radial Clearance	0.076 mm	(0.003 in)
Inlet Shroud Normal Thickness	0.381 mm	(0.015 in)
Inlet Hub Normal Thickness	0.635 mm	(0.025 in)
Exit Shroud Normal Thickness	0.381 mm	(0.015 in)
Exit Hub Normal Thickness	1.32 mm	(0.052 in)

Aerodynamic boundary conditions used in the detailed blade shape design are shown in Figures 51 and 52. These conditions include impeller exit crosspassage distributions of the entropy function, which relates total pressure to total temperature and blade deviation angle. The entropy function (Q) and aerodynamic blockage (A_{eff}/A_{geo}) were distributed linearly through the impeller along each streamline from the leading to trailing edge. Deviation was distributed parabolically from the point of inception to the exit according to an established method.

The blade/air angle relationship at the inducer leading edge is shown in Figure 53. For completely subsonic flow conditions, the impact-free incidence relationship, corrected for compressibility, is normally used. However, proceeding outward to the inducer tip, mach number exceeds 1. For this region, blade incidence was modified (from impact free) according to transonic axial compressor blade design rules (toward 0-degree meanline incidence). Higher blade angles resulting from this correction will be advantageous for part-speed operation.

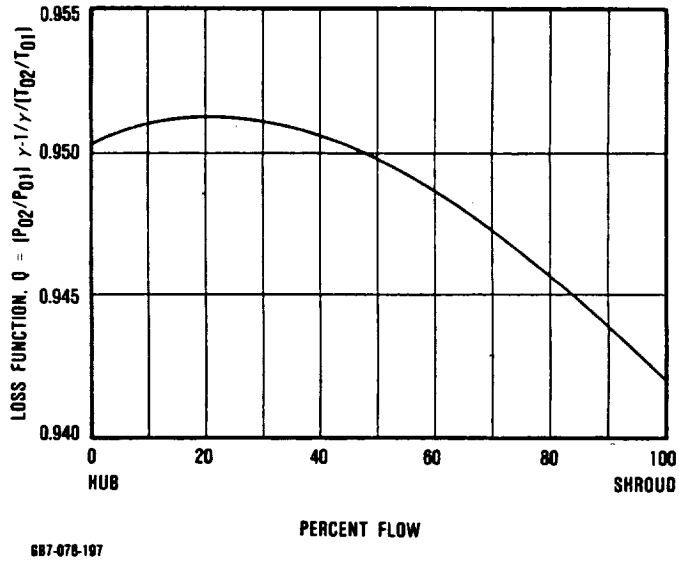

Figure 51. AGT101 Impeller Design Exit Loss Function Distribution.

Final air/blade angle distributions are shown for shroud, mean, and hub streamlines in Figure 54. Resulting blade suction and pressure surface velocities are shown in Figures 55 through 57 for the shroud, mean (50-

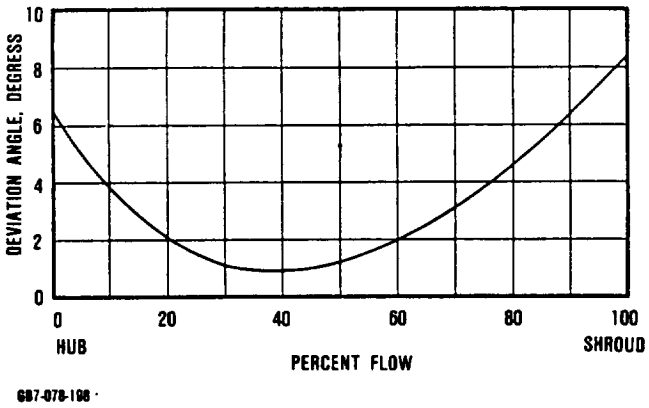

Figure 52. AGT101 Impeller Design Exit Deviation Angle.

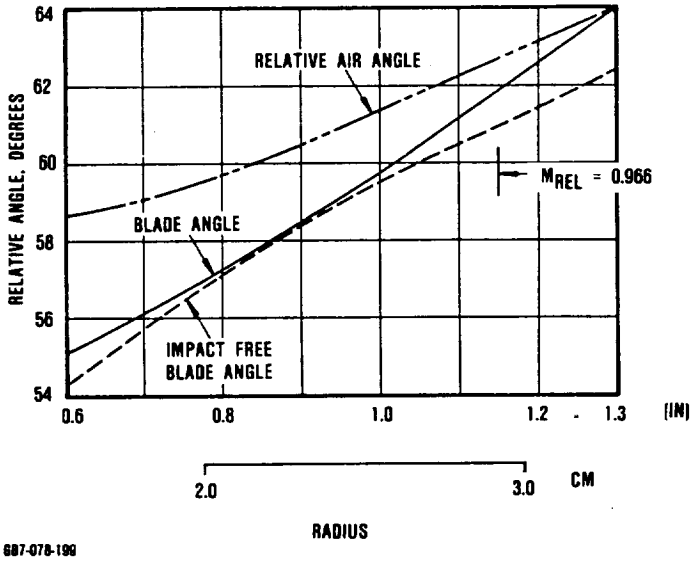

Figure 53. Compressor Inducer Leading Edge Blade, Air Angle Distributions.

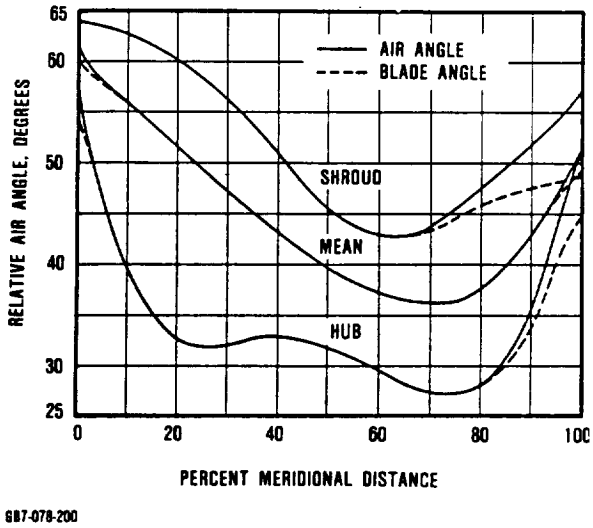

Figure 54. Compressor Impeller Relative Air Angle Distribution.

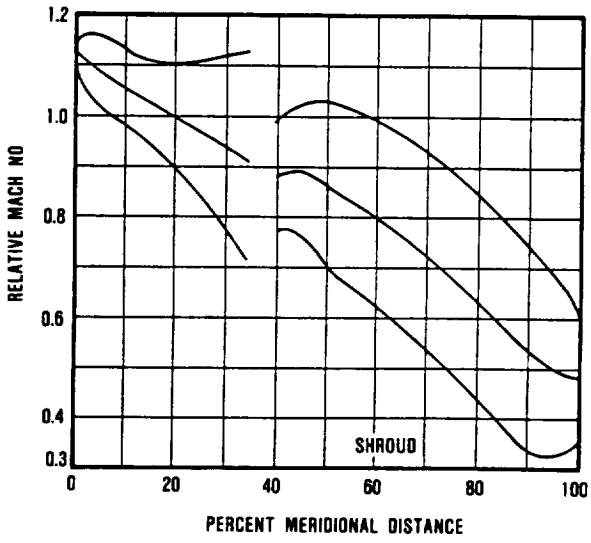

Figure 55. Compressor Impeller Blade Surface Mach No. Distribution - Shroud.

percent flow), and hub streamlines. These velocity distributions compare favorably with previously designed, successful compressors of similar pressure ratios.

To assure adequate impeller flow area at design point conditions, a check of available inducer throat area was made using a ratio of local geometric (blade-to-blade) area to the area required for sonic flow conditions at leading edge stagnation conditions. A minimum value curve of this parameter across the inducer is shown in Figure 58. Current design procedure requires that the local value not be less than 1.04, a condition met for all streamlines.

The final main blade normal thickness distribution is shown in Figure 59. This distribution was required to satisfy blade stress and vibration criteria.

Impeller vector diagrams are shown in Figure 60.

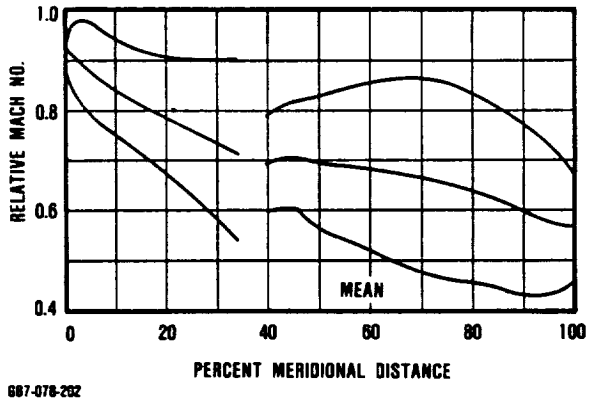

Figure 56. Compressor Impeller Blade Surface Mach No. Distribution - Mean.

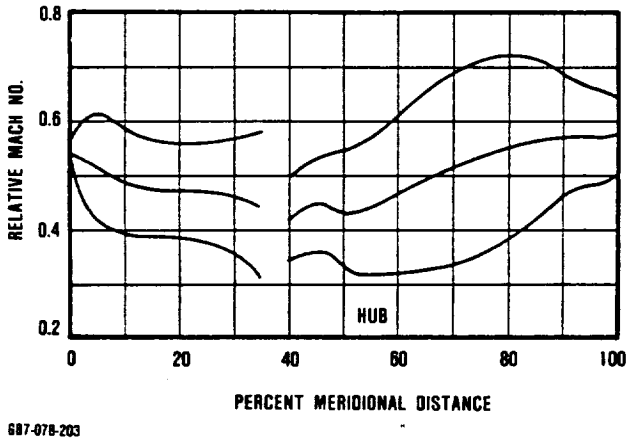

Figure 57. Compressor Impeller Blade Surface Mach No. Distribution - Hub.

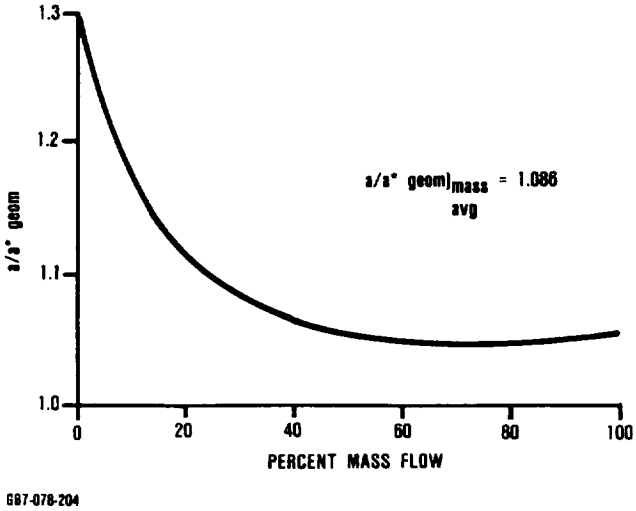

Figure 58. AGT101 Impeller Design Minimum a/a*geom.

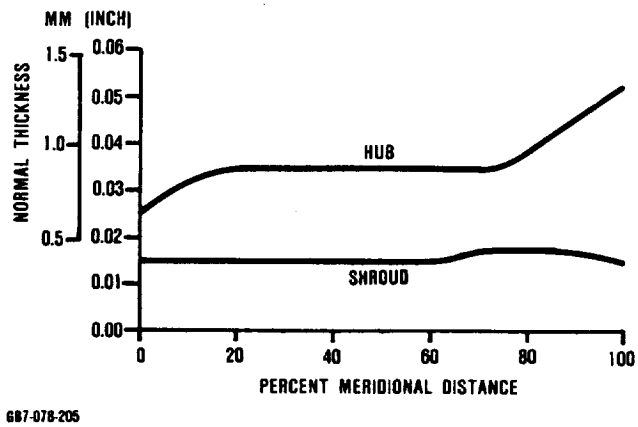

Figure 59. Impeller Normal Thickness Distribution.

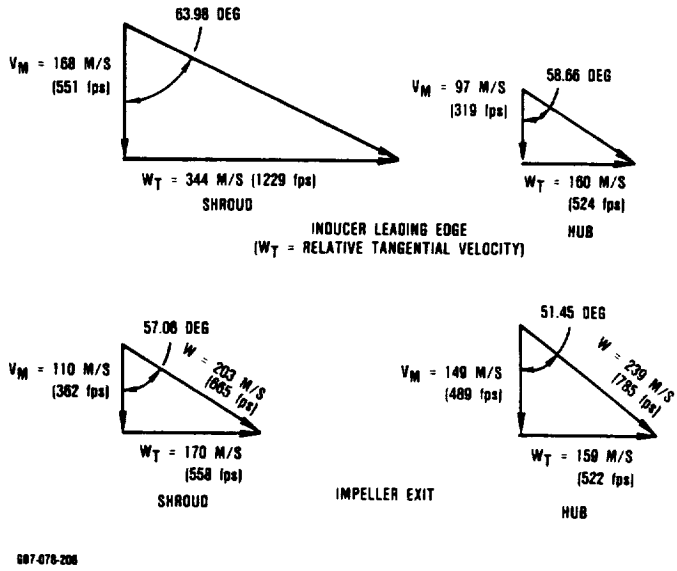

Figure 60. AGT101 Impeller Design Vector Diagrams.

Impeller splitter aerodynamic and stress analyses were completed. To reduce a locally high splitter leading edge stress, the hub leading edge was moved axially forward from the original position to make the edge more radial (Figure 61). The circumferential position of the splitter leading edge then was shifted to match the 50-percent mass flow streamline across the entire blade height. This meanline shift was accomplished as shown in Figure 62 for each streamline calculation. The repositioning was performed to eliminate a potential loss penalty associated with a non-uniform

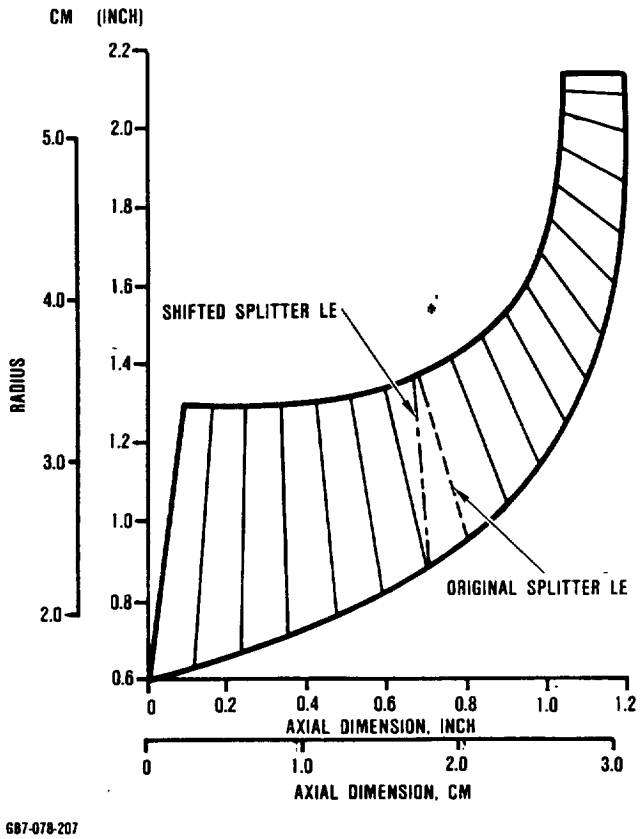

Figure 61. Splitter Blade Hub Leading Edge Movement.

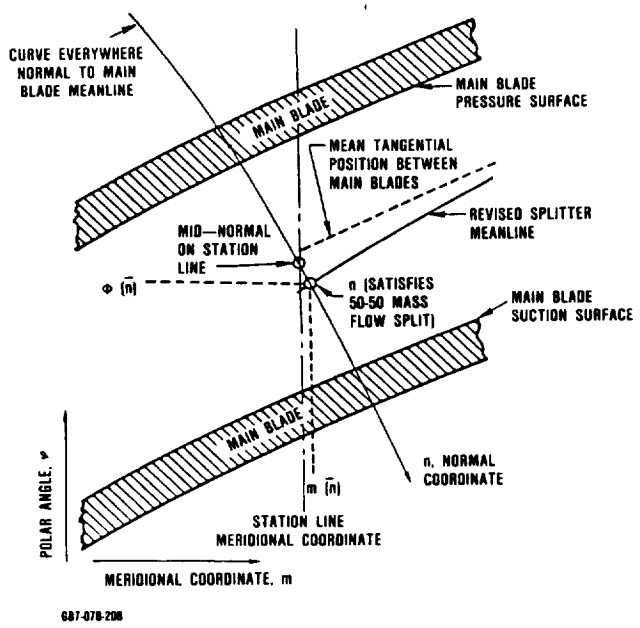

Figure 62. Splitter Leading Edge Tangential Position.

flow split which might result if the splitter blades were left at the mean tangential position between main blades. This technique has been successfully used on previous Garrett high pressure ratio compressor designs.

Diffuser Design

Based on the reference study and subsequent design analyses, the radial diffuser design consists of three vane rows. The first row is a standard 2-D vane island diffuser with a converging end wall followed by a cascade of two deswirl vane rows. During the analysis, a tradeoff was made between the first stage (vane island) diffuser area ratio and the tandem deswirl vane diffusion factors. The effect of varying the first deswirl vane exit angle on the diffusion factor of each row is shown in Figure 63. The first deswirl vane row

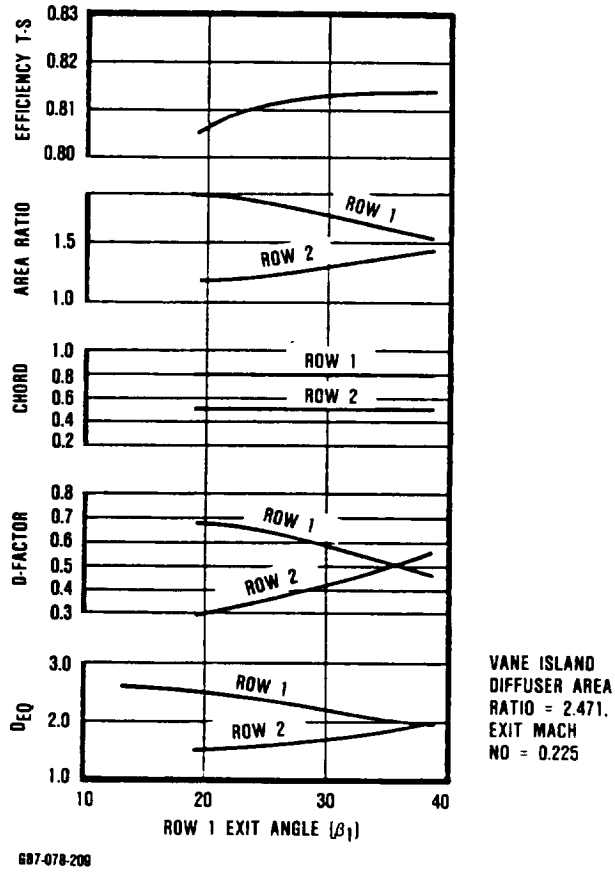

Figure 63. Diffuser Deswirl Vane Analysis.

inlet Mach Number was 0.225, a value providing the vane island diffuser with an area ratio of 2.59 which is consistent with Garrett experience.

Further design iterations resulted in a diffusion system having a convergence over the radial vane island of 0.05 cm (0.020 inch) from the leading to trailing edge, and a trailing edge thickness of the vane island of 0.178 cm (0.070 inch) and 34 vanes. An axial projection of the diffuser-system is shown in Figure 64 and meridional flowpath in Figure 65. Diffuser vector diagrams are shown in Figure 66.

5.1.2.2 High Flow Modification

Based on initial test data, the impeller was found to be low on work input and flow capacity. To restore these deficiencies back to

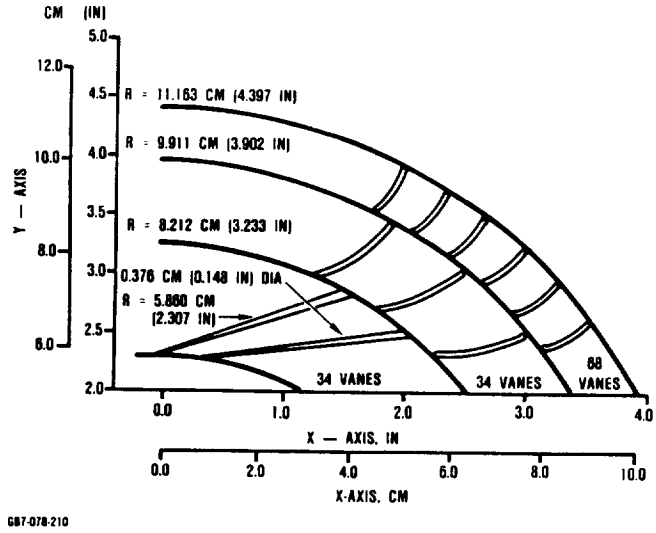

Figure 64. AGT101 Diffuser and Deswirl Vane Assembly Axial View.

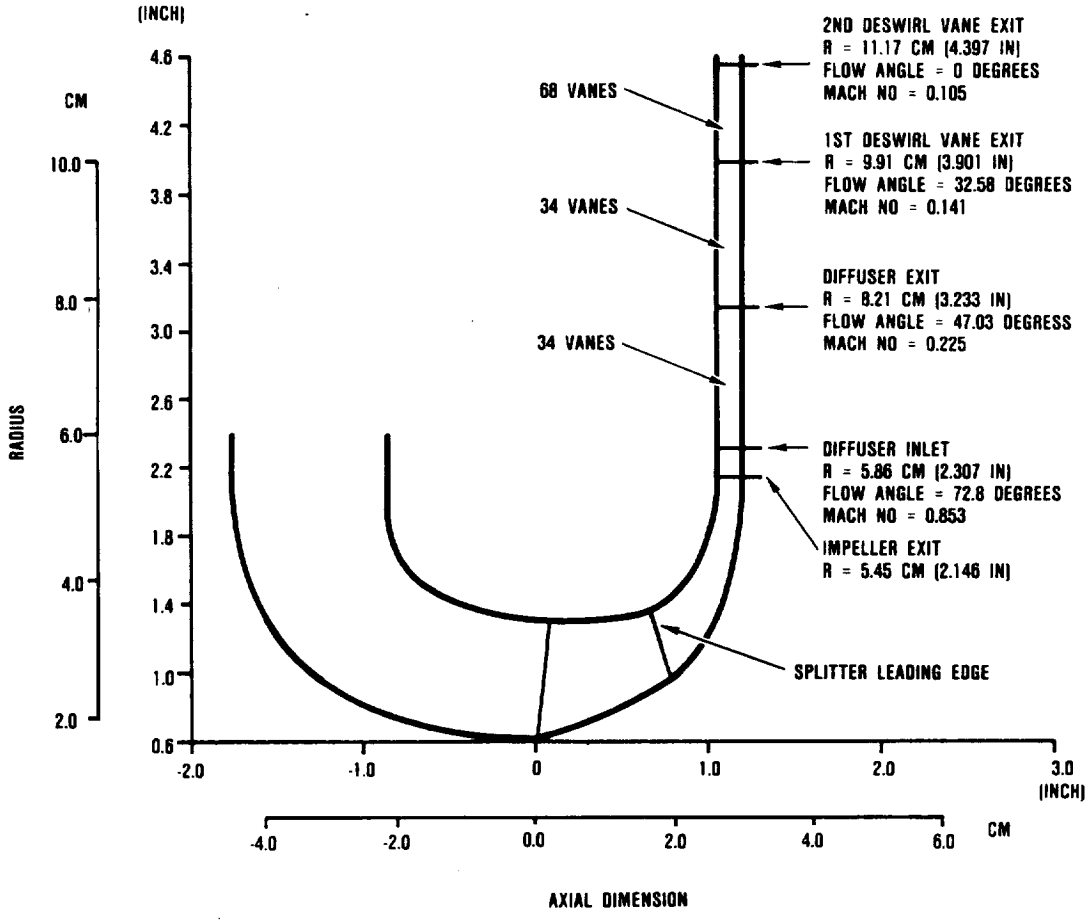

Figure 65. AGT101 Diffuser Meridional Flowpath.

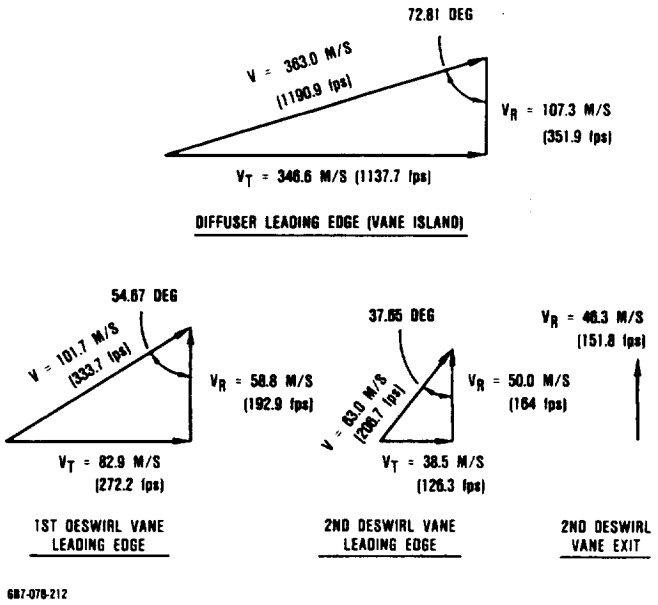

Figure 66. AGT101 Diffuser Vector Diagrams.

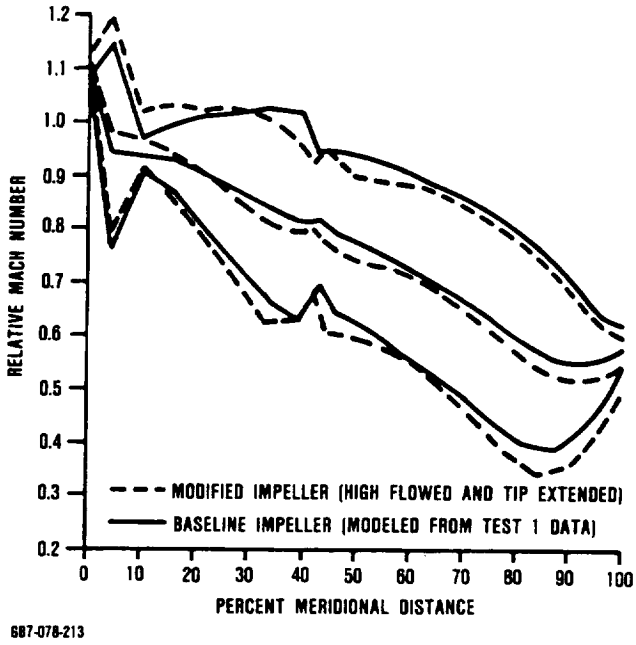

Figure 67. AGT101 Modified Impeller Blade Loadings—Tip.

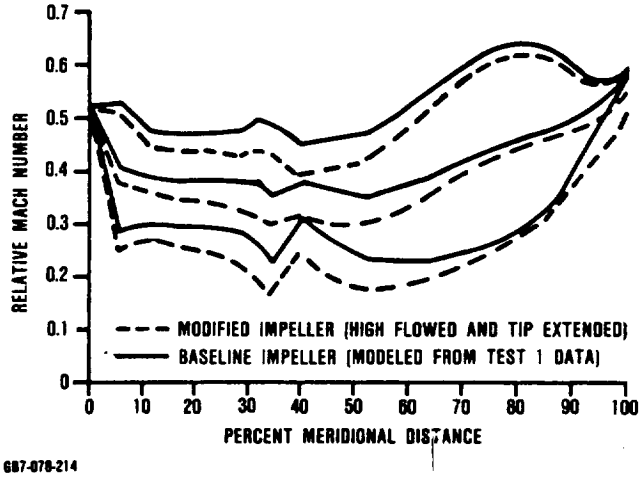

Figure 68. AGT101 Modified Impeller Blade Loadings—Hub.

design levels, an analysis was conducted to evaluate several exclusive and related modifications. Working within available hardware constraints, modifications that added 0.02 cm (0.052 inch) to the impeller tip radius, 0.019 cm (0.048 inch) to the inducer shroud line and 0.007 cm (0.018 inch) to the exit blade height were analyzed to increase flow capacity and work. A comparison of the modified impeller blade loadings and loadings based on Test 1 (reference paragraph 5.1.2.3) data is shown in Figures 67 and 68 for the shroud and hub respectively. The loadings shown for this Test 1 impeller were modeled using tested losses and deviation. Figure 69 shows the modified impeller geometry.

Based on the modified impeller geometries, the stationary shroud and diffuser also were modified. Since Test 1 data indicated that the diffuser minimum loss occurred at design incidence, the original diffuser design criteria was retained. In addition, since the match obtained between vane rows 1, 2, and 3 showed good performance, a decision was made to modify only the 1st vane row to accommodate the larger impeller and retain the 2nd and 3rd vane geometries as designed and tested. To accomplish this, vane row 1 was increased in height, and the vane height was linearly converged to match vane row 2.

5.1.2.3 Aerodynamic Testing

Compressor development testing was conducted on test rigs suitable to aerodynamically and mechanically evaluate the impeller, diffuser, VIGVs, inlet plenum and compressor discharge airflow path.

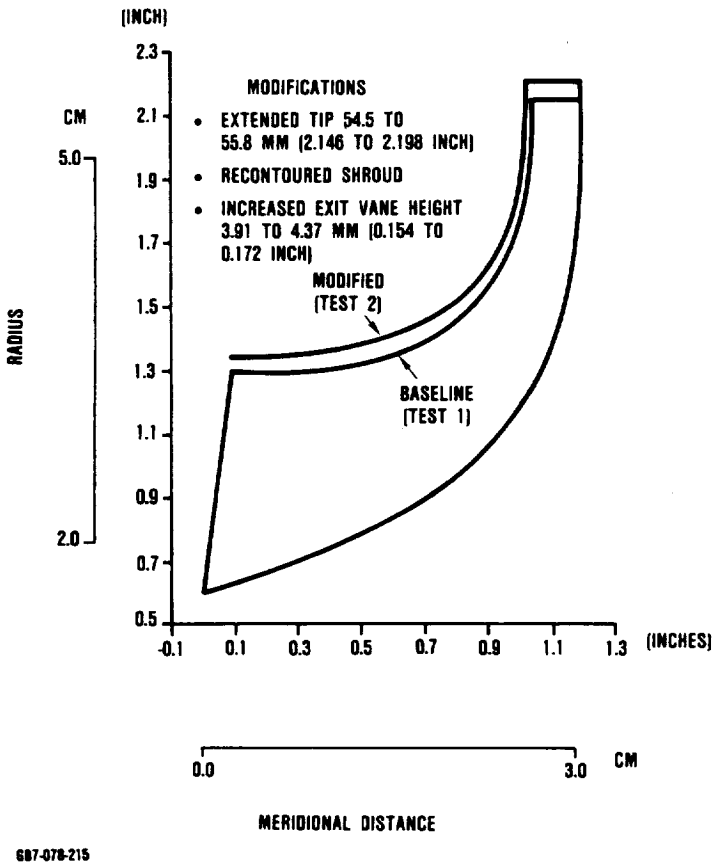

Figure 69. AGT101 Modified Impeller Geometry.

As discussed in paragraph 5.1.5 powder metal aluminum materials were evaluated during this program. However, due to timing constraints titanium was used during this test program.

Compressor Test Rig

The compressor test rig, is a straddle-mounted bearing configuration utilizing the AGT101 engine ball bearings. Power is derived from a drive turbine system composed primarily of the Garrett Model TV81 turbocharger hot flowpath components. Actual AGT compressor stage hardware (VIGVs, impeller and diffuser) is utilized in the rig to permit detailed compressor design performance mapping. As shown in Figure 70, power section ducting has been incorporated to establish any flow phenomena effects resulting

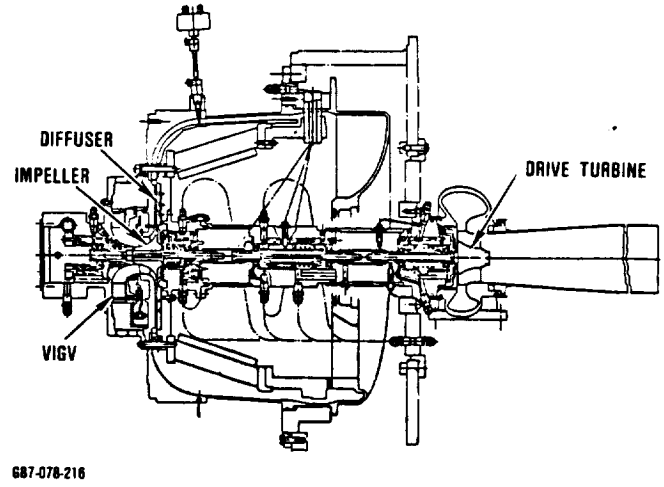

Figure 70. Compressor Rig.

from transitioning compressor discharge flow to regenerator high pressure inlet. In addition, the inlet air filter and associated ducting (not shown) can be accommodated to verify aerodynamic design intent and again establish any detrimental flow effects resulting from the installation.

The rig incorporates the capability for controlling and evaluating critical compressor impeller running clearances based on capacitance probe measurements at selected stations along the impeller meridional flowpath. The clearance control mechanism is based on a design concept successfully demonstrated on other Garrett programs. This mechanism features an Acme thread, used to axially adjust the position of the impeller under dynamic operation. This is accomplished by fixing the internal thread and turning the external thread, thus forcing the externally threaded members (impeller shafting) to move axially. Clearance control capability allows thermal stabilization of the test rig and dynamic stabilization of the impeller prior to recording data such that desired clearances can be evaluated. In addition, this mechanism will allow performance evaluation of larger than desired clearances and/or duplication of engine conditions for performance comparisons.

Compressor test rig instrumentation was identified such that detailed evaluation of individual and system compressor components

can be achieved. Instrumentation is of a size consistent with the small stage dimensions and of sufficient number and spacing to provide realistic average values for all parameters measured.

Two compressor stage tests were conducted on the AGT101 compressor. During Test 1, compressor flow and pressure ratio were below design intent. Based on Test 1 results and subsequent analysis of test data, a modification to the impeller was accomplished. Test 1 data showed that diffuser performance was essentially as predicted, thus modification to the diffuser was accomplished only as required to accommodate the impeller modification. Figures 71 through 73 show the comparative results of Test 1 and Test 2A. Performance mapping was completed at speeds from 40 to 100 percent of design corrected speed and IGV settings of 0, +20, +40, +60, and +70 degrees. Axial clearance for Test 2 was controlled to within 0.076 to

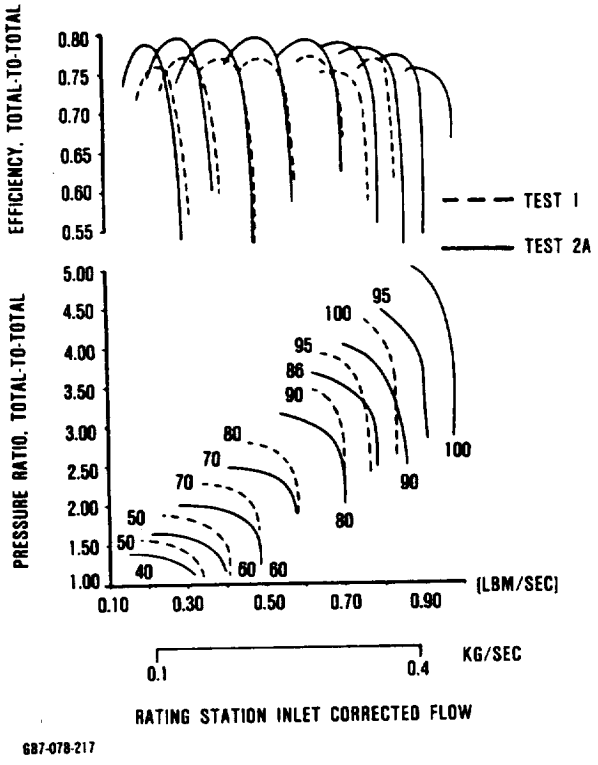

Figure 71. Full Stage Compressor Data, IGVs Open.

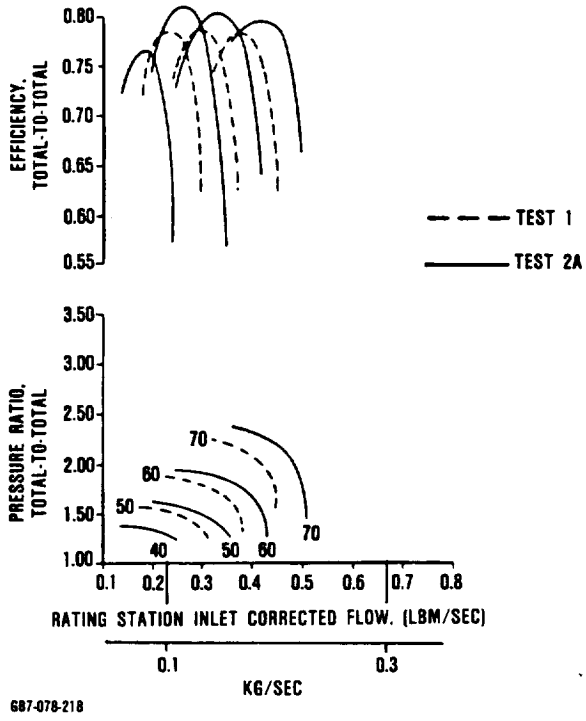

Figure 72. Full Stage Compressor Data, IGVs = 40 Degrees.

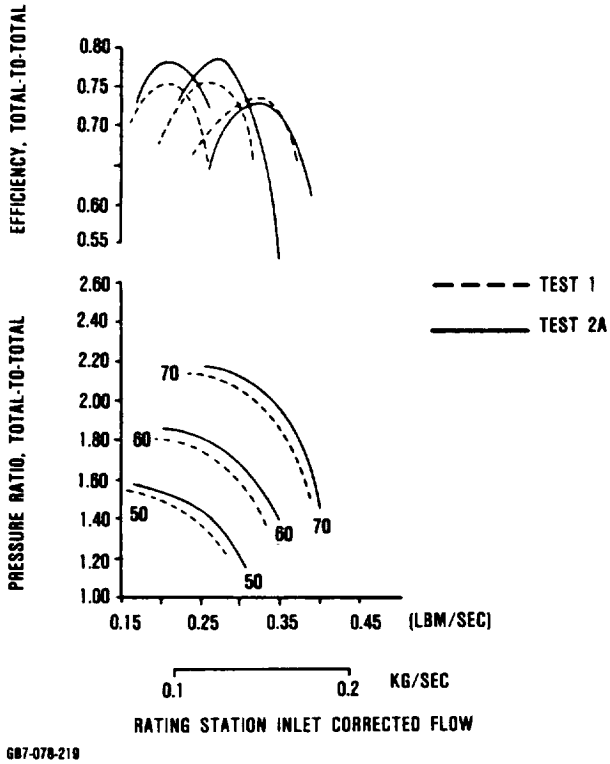

Figure 73. Full Stage Compressor Data, IGVs = 70 Degrees.

0.102 mm (0.003 to 0.004 inch) as designed. Test data indicates the following:

- o Design pressure ratio and flow were achieved
- o Diffuser performance was very close to predicted levels
- o A highly desirable efficiency envelope has been achieved, which has the peak stage efficiencies occurring at the lower end of the speed range

Compressor performance characteristics demonstrated during Tests 1 and 2 indicate that the compressor was performing as desired when considering an automotive duty cycle application, i.e., low power/high efficiency. This results from the fact that the vast majority of driving time occurred over the CFDC between 48- and 70-percent engine speed.

5.1.3 VIGV Design and Testing

5.1.3.1 Variable Inlet Guide Vane Design Analysis

The VIGV is an articulated design (fixed leading edge, movable trailing edge) using a NASA 63-0012 series thickness distribution modified to a maximum thickness of 13.5 percent of chord for the articulated portion of the vane. The fixed leading edge uses 26 percent of a NASA 63-0010 modified for a maximum thickness of 13 percent of chord. This design (Figure 74) is based on a similar articulated guide vane successfully being used on several engine compressors under development at Garrett. Results of tests conducted on these similar designs have been used in the off-design compressor performance for AGT101 cycle calculations.

5.1.3.2 Inlet Guide Vane Testing

Development testing on compressor stage hardware encompassed inlet guide vane (IGV) acoustic evaluation. The IGV test rig is shown in Figure 75.

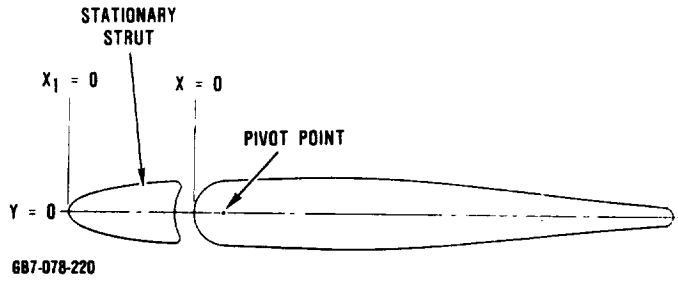

Figure 74. AGT101 Inlet Guide Vane.

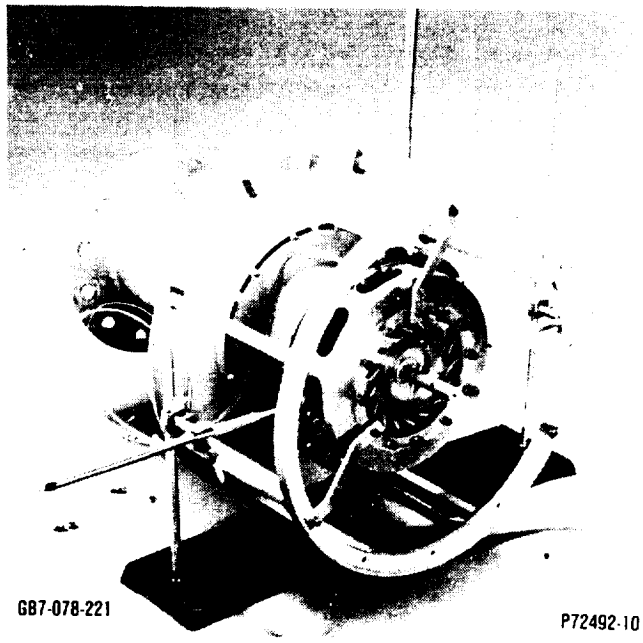

Figure 75. AGT101 Compressor Inlet Guide Vane Test Rig.

Initial testing identified objectionable acoustic noise levels (in the audible range) in excess of 130 dB when the IGVs were closed to 50 degrees or higher. This phenomena was similar in nature to previous Garrett experience on another articulated radial IGV system. Although the exact mechanism generating the tones is not well understood, it is believed that the IGV-induced swirl transfers flow energy to acoustic energy.

This problem was resolved, based on prior Garrett experience, by introducing a minimal disturbance in the flow field. Flow tabs, as shown in Figure 76, were installed on the fixed

Figure 76. Inlet Guide Vane Flow Tabs.

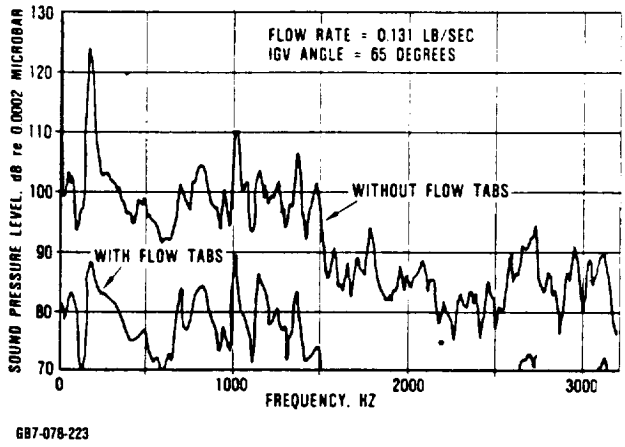

Figure 77. Inlet Guide Vane Test Results.

leading edge of two IGVs. These flow tabs dramatically reduced the tone amplitude. Figure 77 presents the results of IGV testing with and without flow tabs.

5.1.4 Impeller Mechanical Design

5.1.4.1 Stress Analysis

The selected long term impeller material is a powder metal aluminum (section 5.1.5). Due to the availability of property data for the PM alloy, forged 2219 T6 Al material characteristics were initially used for stress and life analyses (titanium material was used for engine test). Impeller properties are provided in Table 9.

Elastic three-dimensional stress and frequency analysis was performed on the final blade configuration. The blade was optimized to provide good aerodynamic performance while maintaining stress levels necessary to assure mechanical integrity. Blade vibrations primarily are confined to the inducer region of low specific speed impellers. The short exducer blade height makes this blade region insensitive to aerodynamic excitations. To assure an inducer region vibratory margin, stress levels were limited to 137.9 MPa (20 ksi), thereby permitting vibratory stress levels of 34.5 MPa (5 ksi) with 2219 T6 Al. Plots showing stress results from a three-dimensional finite element analysis are presented in Figure 78. This analysis was performed with zero displacement boundary conditions at the

Table 9. Impeller Properties.

Total Weight, kg (lbs)	0.249	(0.549)
Blade Weight, kg (lbs)	0.015	(0.034)
I_p kg-m-sec^2 (lb-in-sec^2)	1.61 x 10^{-5}	(0.0014)
I_d kg-m-sec^2(lb-in-sec^2)	1.15 x 10^{-5}	(0.0001)
Hub Area, cm^2 (in^2)	7.645	(1.185)
CG cm (in) (Forward of Blade Root Exit)	0.704	(0.277)
Kinetic Energy kg-m (in-lb)	907.0	(78700)
Density g/cm^3 (lb/in^3)	2.80	(0.101)

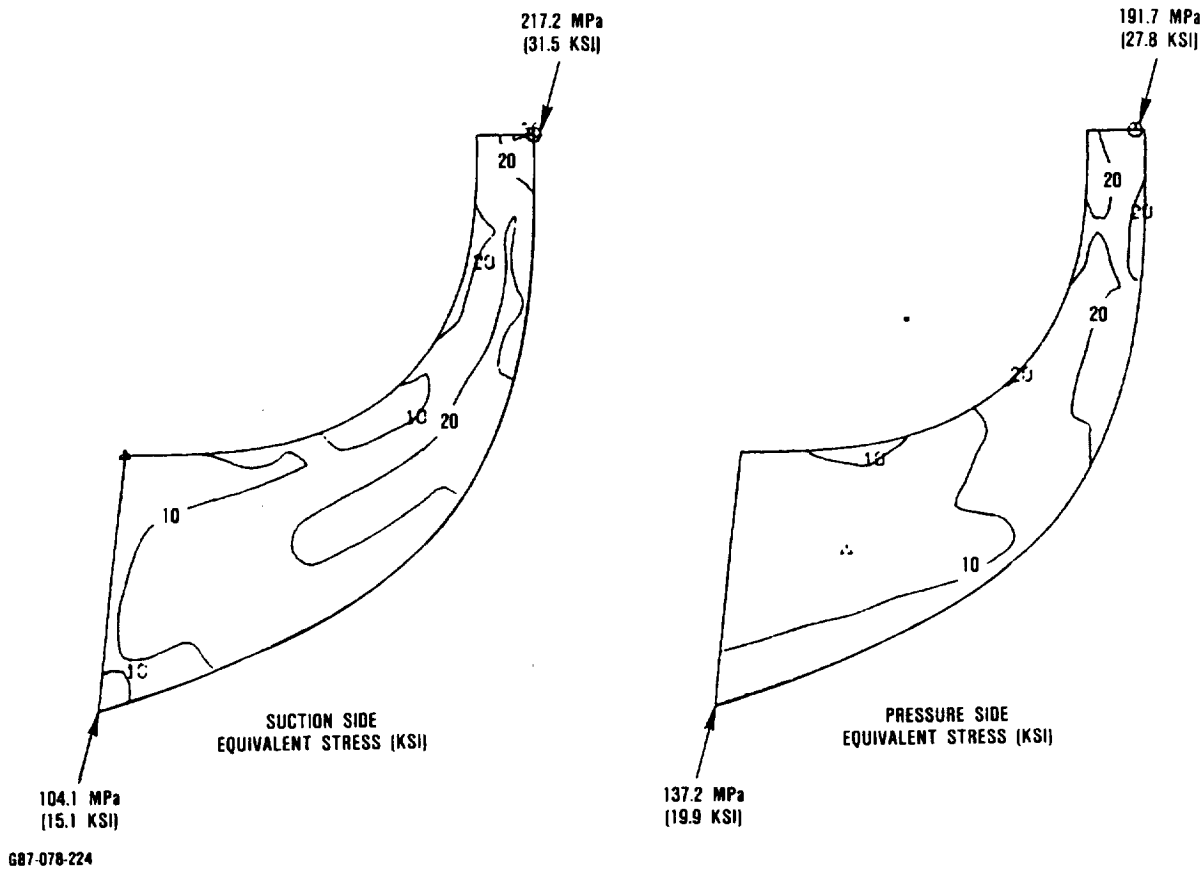

Figure 78. AGT101 3-D Airfoil Elastic Stress at 100,000 rpm.

blade/hub interface. Calculated blade frequencies are shown in Figure 79 and the first four mode shapes in Figure 80. The first vibratory mode is at 3.5E (where E represents the rotational speed) at 100-percent speed. Experience has shown that impeller blades are relatively insensitive to distortion related excitations when the first mode frequency is above 3E. The first three blade modes will not have interferences with 17E IGV wakes in the operating range. With the relatively long flow space between the IGVs and blades, higher mode excitation is not expected.

Exducer region stress levels have to be controlled to provide adequate rupture life. The combination of 614 m/sec (1872 ft/sec) tip speed and 50-degree backward curvature results in a maximum elastic stress at the exit of 214 MPa (31 ksi) and an adiabatic wall temperature of 190C (374F).

A 3-D elastic stress and vibration analysis was performed on the final splitter configuration. Results are provided in Figures 81 and 82. The splitter stress levels are similar to the levels in the main blade. Frequency analysis of the impeller splitter blades shows potential interferences of the first and second vibratory modes with the IGV excitation. This analysis also shows physical location on the airfoil where the maximum vibratory strain would occur for each of these modes. Since these modes occur at part speed, the blade steady-stress level and metal temperatures will be significantly lower than the levels that exist at the 100-percent speed mechanical design point. Using the stress and temperature values that exist at the peak vibratory strain location for the predicted speeds of the interferences, the analysis shows that the allowable vibratory stresses of the first and second modes respectively are 51.7 and 69.0

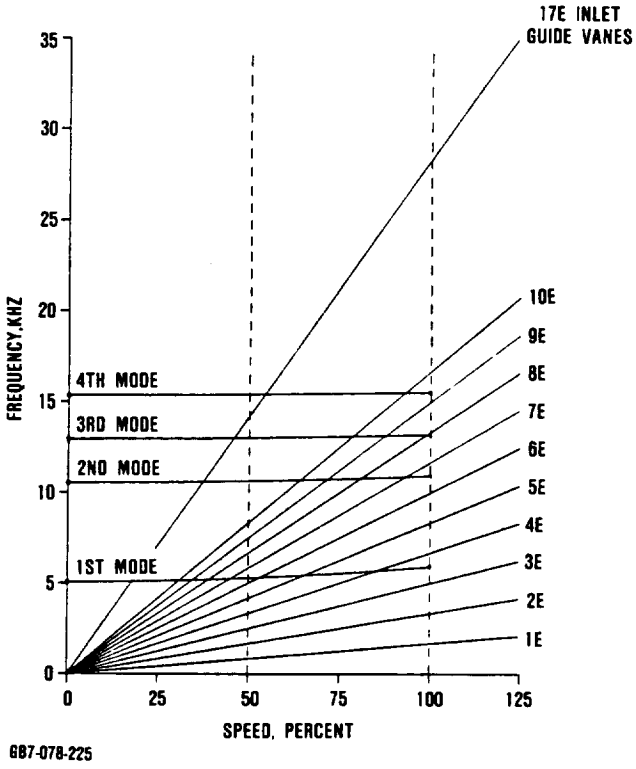

Figure 79. AGT101 Impeller Airfoil Campbell Diagram.

MPa (7.5 and 10 ksi). This allowable vibratory stress should provide adequate fatigue margin, particularly since the vane to rotor spacing is more than 1.5 times the chord length of the IGVs.

Elastic stress analysis was completed for the impeller hub. Results of this analysis are shown on Figures 83 and 84 along with the isotherms for the 29.4C (85F) day design point. These stress levels are consistent with Garrett experience on similar aluminum impeller designs. A life summary is presented in Table 10.

The axial and radial displacements of the blade, taking into account maximum temperature 100-percent operating speed and centrifugal stiffening is shown in Figure 85.

5.1.4.2 Impeller Holography Tests Results

An aluminum (2219-T6) and titanium (Ti-6-4) impeller were mechanically evaluated to

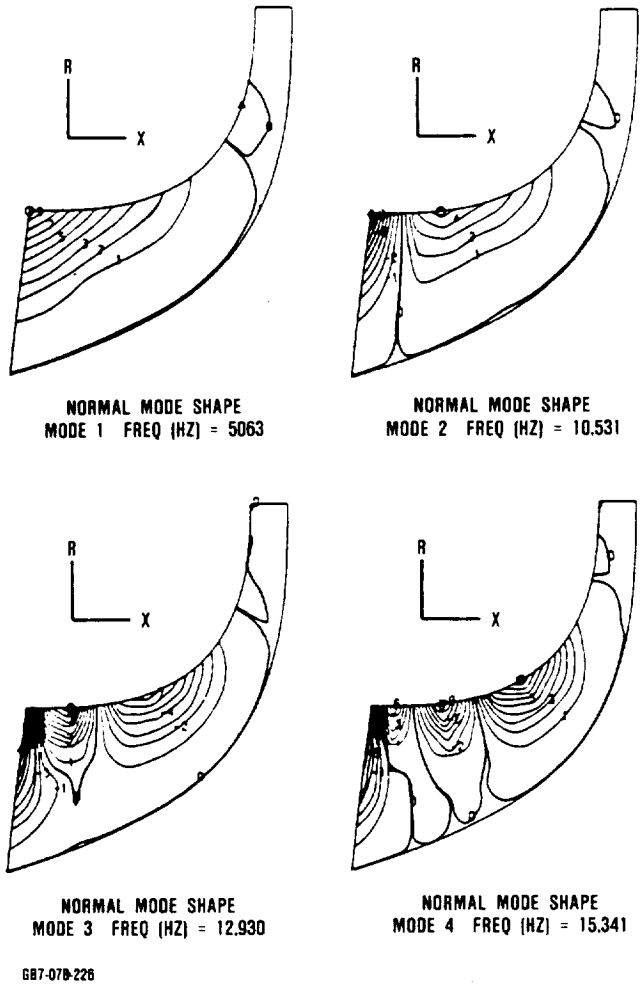

Figure 80. AGT101 Impeller Blade Vibratory Modes.

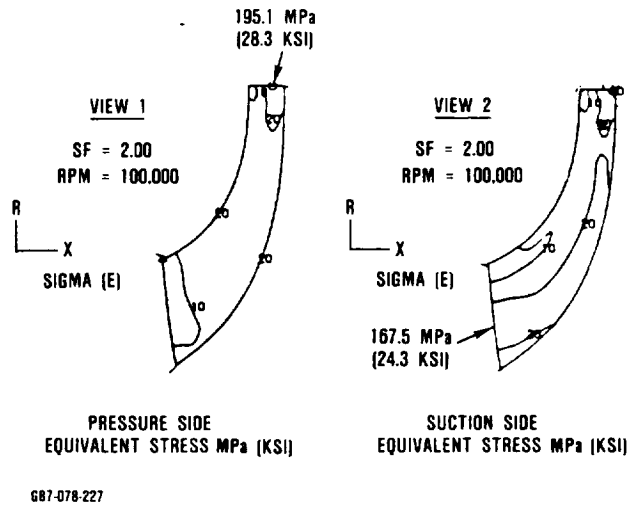

Figure 81. AGT101 3-D Splitter Elastic Stress at 100,000 rpm.

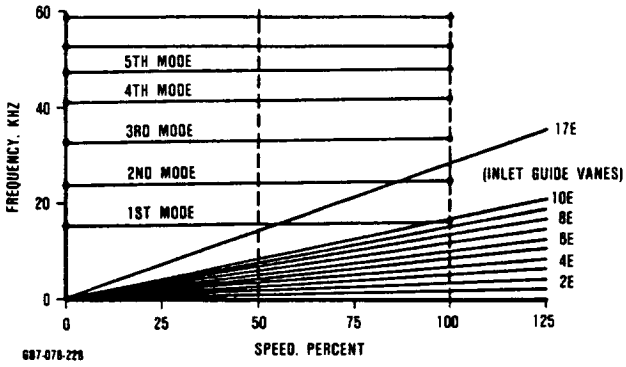

Figure 82. AGT101 Impeller Splitter Campbell Diagram.

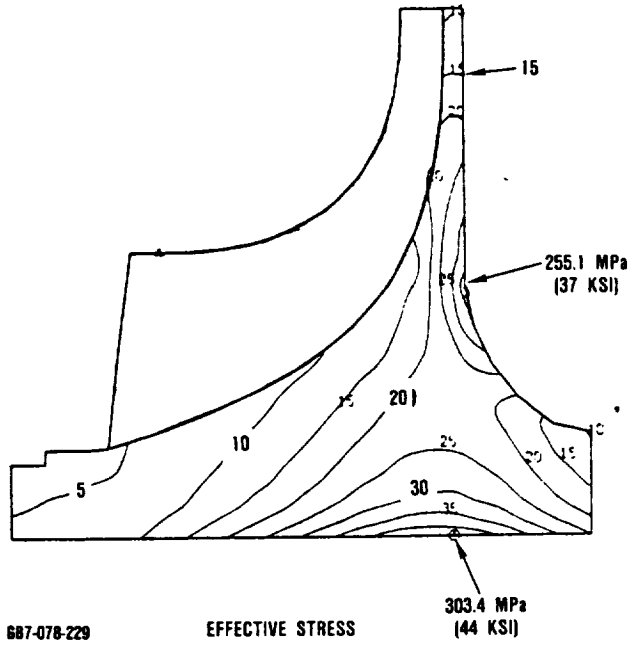

Figure 83. AGT101 Impeller Stress at 100 Percent Speed.

determine vibratory blade and disk characteristics. Holography and acoustic testing was conducted, and these results then were compared with previously predicted analytical results. Table 11 summarizes these efforts. Figure 86 through 88 show the predicted vibratory mode shapes and the holography results for selected frequencies. Figure 89 presents a Campbell diagram for the titanium impeller. In general, test values agree closely with analytical predictions.

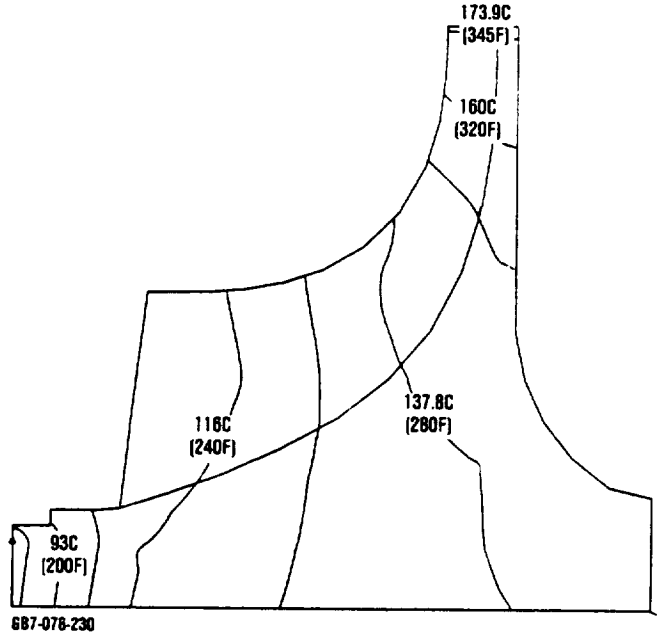

Figure 84. AGT101 Impeller Isotherms - 29.4C (85F) Inlet Temperature.

5.1.4.3 Impeller Strain Gage Test Results

The titanium impeller was instrumented with 10 strain gages. Placement was based on holographic and acoustic test results. Gages were placed on full and splitter blades with two gages on the impeller backface. Figures 90 through 92 show the strain-gaged impeller prior to test. Figure 93 shows the compressor rig in the test facility with the slip ring assembly installed.

Data obtained during strain gage testing, showed an excitation at 73,000 rpm (Figure 94) induced by a 4 per rev source (inlet distortion). The vibration was noted on five full blades at two different occasions (Figure 95). The maximum strain level measured was less than 500$\mu\varepsilon$. This correlates to a maximum blade stress level of 181.3 MPa (26.3 ksi) for the titanium impeller and 113.1 MPa (16.4 ksi) for the aluminum impeller. Stress values for the aluminum impeller were ratioed by the modulus of elasticity for the two materials. These values compare reasonably well with the predicted stress values. Maximum strain levels measured on the splitter blades were less than 150$\mu\varepsilon$.

Table 10. AGT101 Impeller Life Summary (-3σ Material Properties).

o Material - A2219-T6 Al Development Impellers	
o Burst Ratio $BR = \frac{0.85\ (UTS-3\sigma)}{\sigma Ave\ Tan}$	1.50
o Bore LCF Life (Starts to 100% speed W/O Transient Thermal Stress)	>10,000 cycles
o Stress Rupture Life Based on Estimates from Elastic Stress levels (3-D Creep Analysis Has Been Initiated)	>100 hours
o Airfoil Allowable Vibratory Stress (Inducer Region)	34.5 MPa (5 ksi)

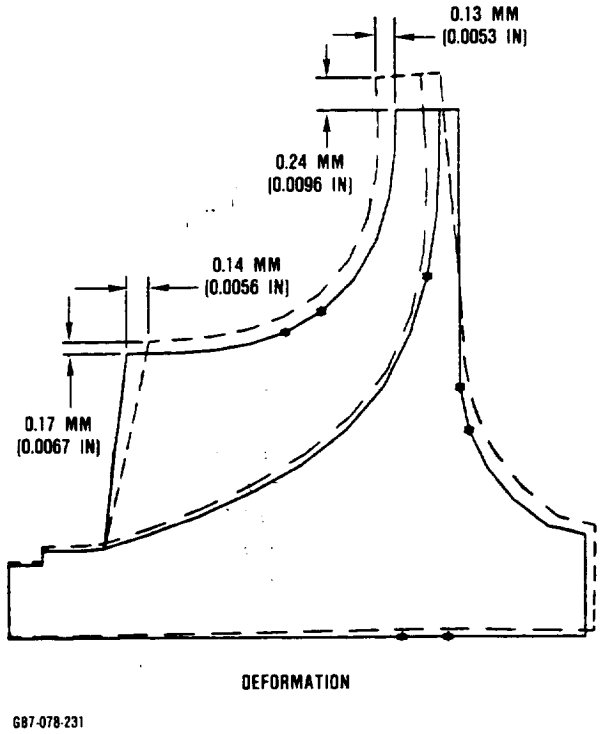

Figure 85. AGT101 Impeller Deformation at 100 Percent Speed.

Table 11. Summary of Vibratory Blade Modes (Aℓ, 0 RPM, 70F).

Blade Mode	Predicted ISOVIB	Acoustic (Average)	Holography (Average)
1	22,174	24,877	25,277
2	10,340	10,427	10,411
3	12,341	13,108	13,138
4	15,172	16,858	17,127
5	17,194	18,467	18,681
6	18,201		22,256
7	22,174	24,877	25,277

5.1.5 Compressor Design for Improved Producibility

To improve the long term producibility of the impeller two items were considered, material and blade design. Early producibility studies indicated emerging aluminum materials could be considered for the impeller, however due to availability, titanium was recommended for testing. Following test, a

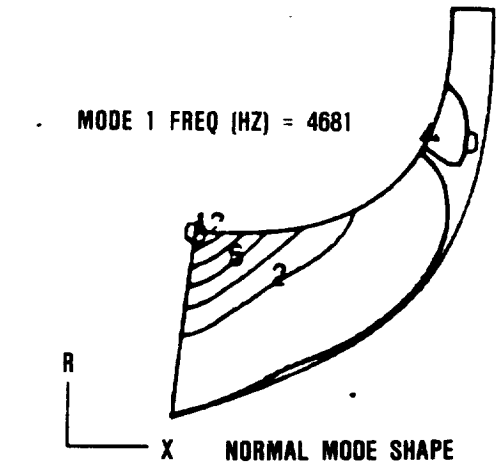

Figure 86. AGT101 Impeller Blade Vibratory Mode 1.

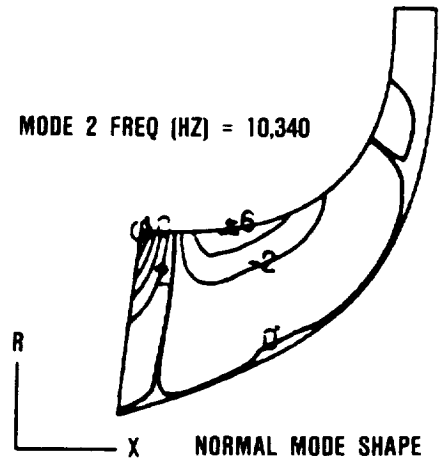

Figure 87. AGT101 Impeller Blade Vibratory Mode 2.

redesign of the impeller was initiated to improve producibility. The efforts regarding these studies are discussed in the following paragraphs.

5.1.5.1 Material Evaluation - Powder Metal Aluminum

Material characterization and evaluation of the ALCOA Al-Fe-Ce powder metal (PM) aluminum continued. Baseline screening tests on sub-size pancake forgings indicated the material had the capability to exceed the design goals (Figure 96). Based on these early evaluations, component size pancake forgings were procured 11.4 cm (4.5-inches) diameter by 7.6 cm (3 inches) thick. These forgings were thermomechanically processed (TMP) specifically to improve alloy ductility.

Results show (Figure 97) that the ductility improvement goal was successfully met. Tensile strengths, as predicted, are lower than the baseline data but continue to exceed AGT101 design goals. Properties at elevated temperatures, particularly above 288C (550F), were observed as less sensitive to TMP variables, as evidenced by the convergence of property levels at 343C (650F). Comparing the tensile strength of PM Al-Fe-Ce with two of the high-strength aluminum alloys commercially available (A2219-T6 and A201-T7), shows it to be superior even after the 1000-hour exposed condition (Figure 98). Stress rupture capability of the alloy also is significantly better than the two commercial high strength alloys (Figure 99).

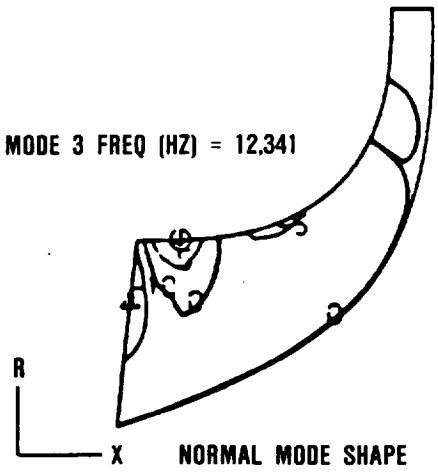

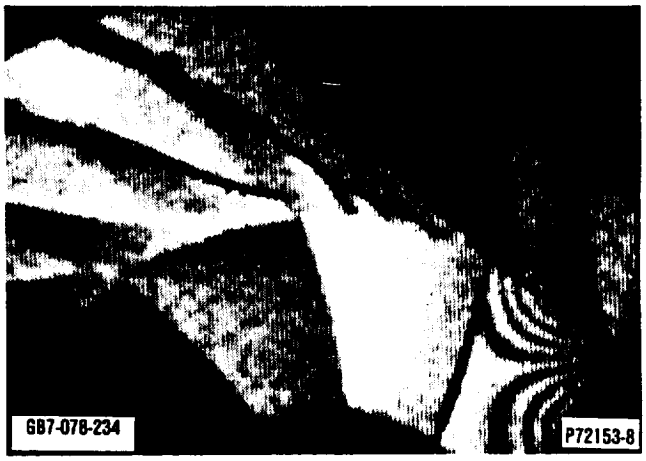

Figure 88. AGT101 Impeller Blade Vibratory Mode 3.

High cycle fatigue (HCF) properties of the Al-Fe-Ce alloy at room temperature and 232C (450F), shown in Figure 100, tend to indicate good HCF life capability. Stress levels of 207 MPa (30 ksi) at room temperature resulted in runout at 10^8 cycles while cycles exceeding 10^7 were obtained at stress levels of 172 MPa (25 ksi) at 232C (450F).

5.1.5.2 Straight Line Element Design

Impeller redesign activities were done on the straight line element (SLE) blade definition to address near-net-shape powder metal die forging. The basis of the redesign was to maintain the performance levels demonstrated

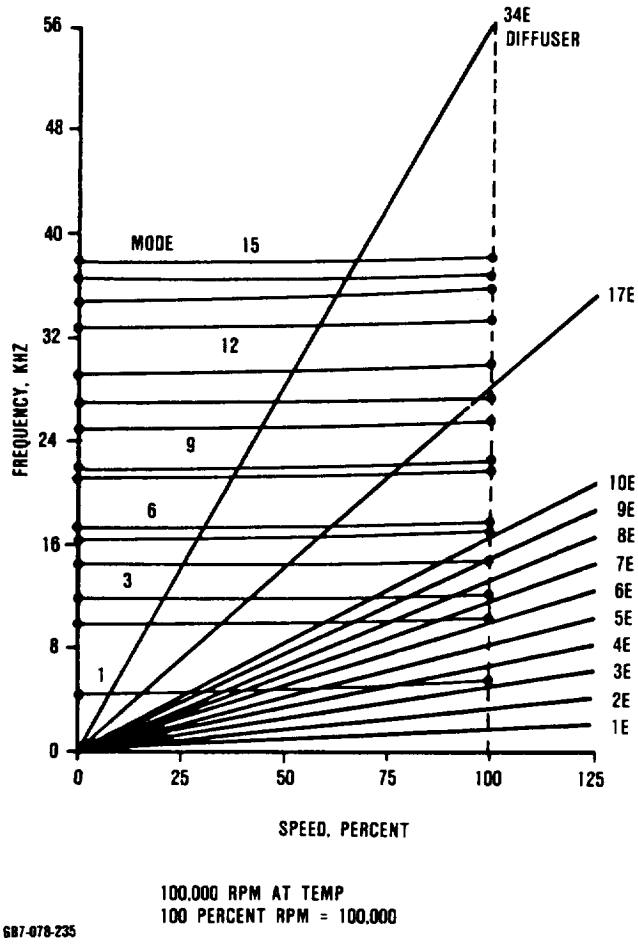

Figure 89. AGT101 Titanium Impeller Campbell Diagram.

Figure 90. Strain Gaged Impeller, Front View.

Figure 91. Strain Gaged Impeller Blade.

Figure 92. Strain Gaged Impeller, Backface.

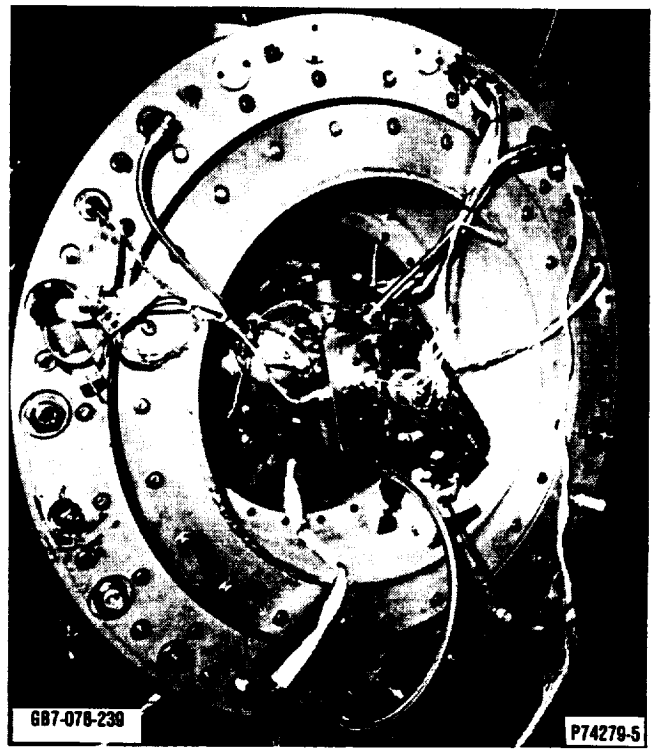

Figure 93. Compressor Test Rig with Slip Ring Assembly Installed in Test Cell.

during Test 2A (Reference paragraph 5.1.2.3), while approximating the arbitrary blade shape using straight line elements. Duplication of the Test 2A impeller exit blade angle distribution could not be fully accommodated using SLE methodology. For example, to keep the same hub and shroud blade angles in the exit region resulted in an average exit blade angle less than Test 2A impeller. This lower exit blade angle gives rise to a lower slip factor and higher work for the same tip diameter. Therefore, the tip radius was reduced from 2.198 to 2.182 inches to compensate for the reduction in average exit blade angle from 50.71 to 47.97 degrees. Blade loadings are shown in Figures 101 through 103. All other salient design features were satisfactorily preserved using the SLE technique.

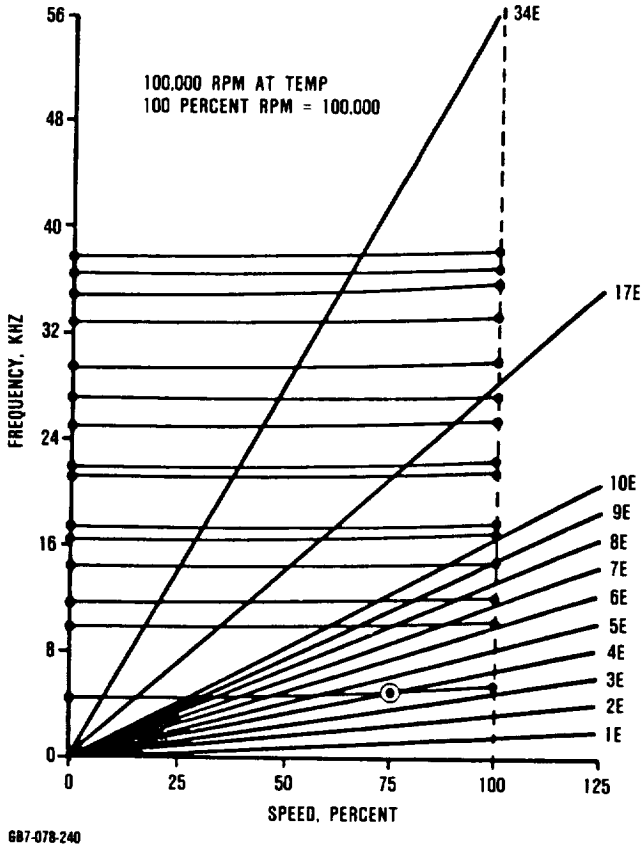

Figure 94. AGT101 Titanium Impeller Campbell Diagram Excitation Source.

LOCATION	BLADE	MEASURED STRAIN (με)
1	2	311
1	6	229
1	8	493
2	3	224
2	9	291

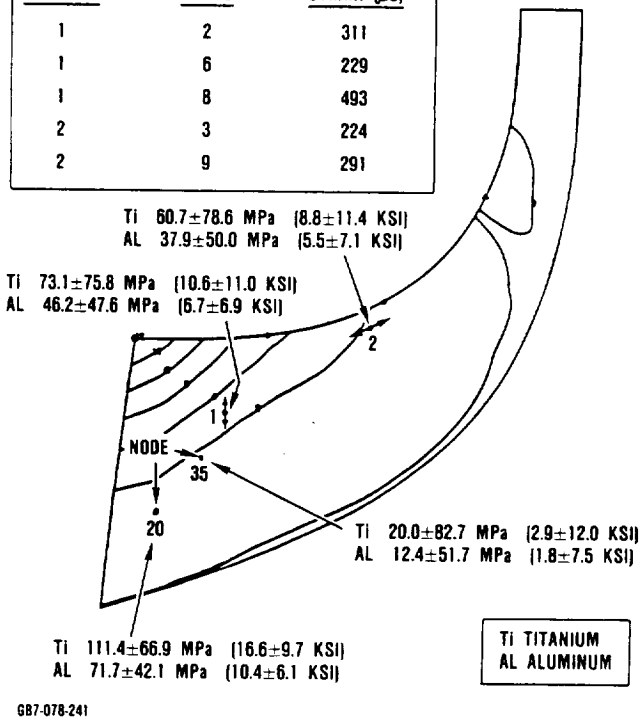

Figure 95. Strain Gage Test Results.

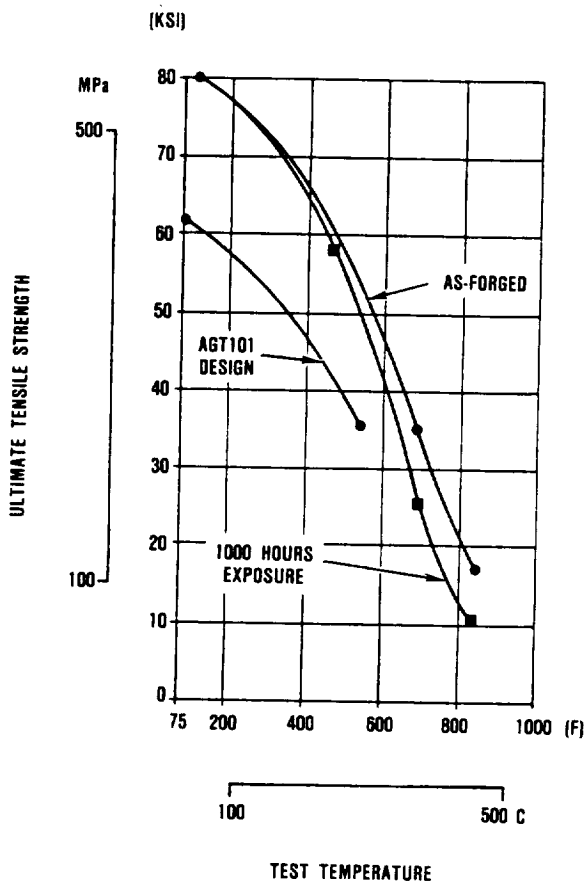

Figure 96. Tensile Properties of Forged ALCOA PM Al-Fe-Ce.

5.2 Turbine Development

The AGT101 turbine is a single stage radial inflow design. It included a ceramic stage and a metallic stage. The metallic stage was a duplication of the ceramic design but fabricated in metal. To achieve operating temperatures, a dual alloy fabrication technique was employed. The following sections discuss the design and development of the turbine components. Details of the ceramic turbine mechanical analyses are given in paragraph 6.2.7.

5.2.1 Aerodynamic Design

Three maximum power design point vector diagrams were evaluated with the engine driving cycle. The three turbine designs were

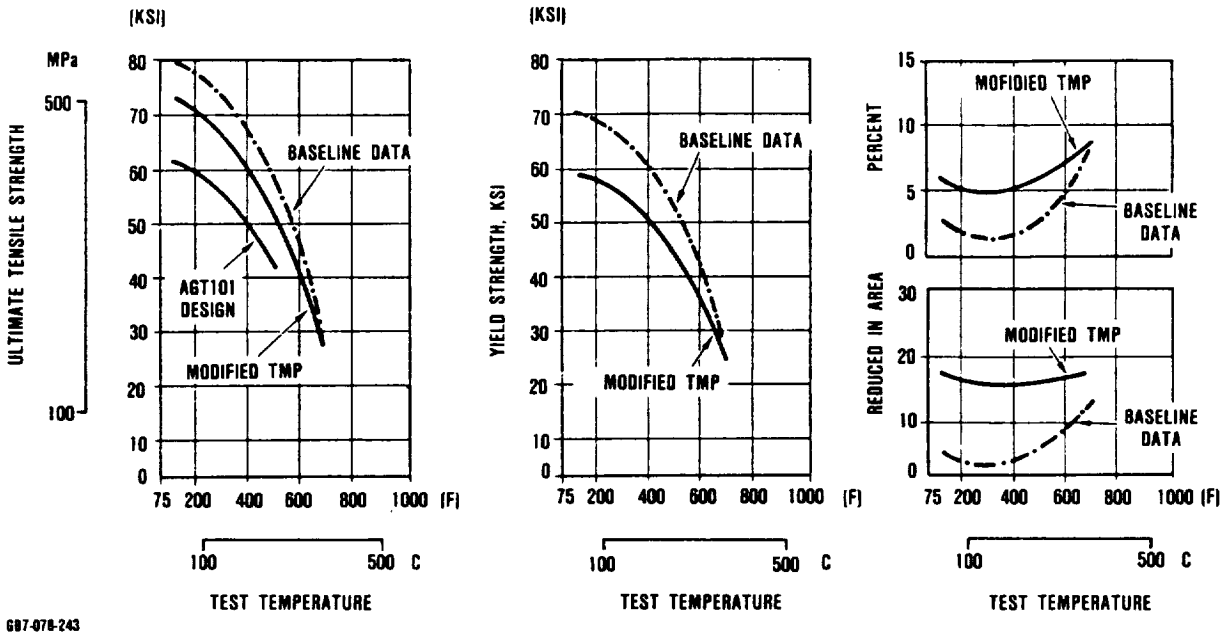

Figure 97. ALCOA Al-Fe-Ce Forged Properties (1000-Hour Temperature Exposure).

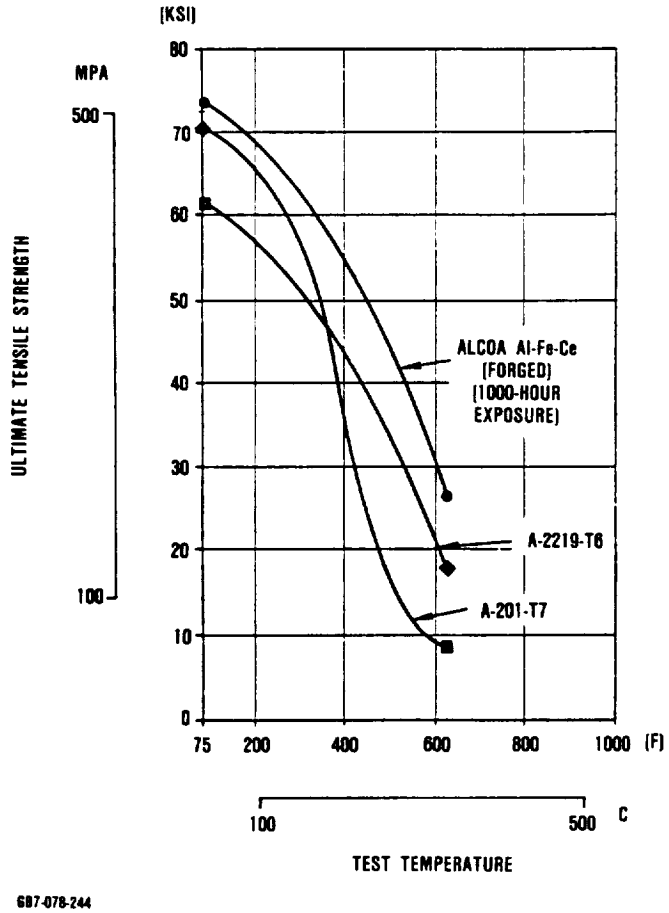

Figure 98. Tensile Properties of Aluminum Alloys.

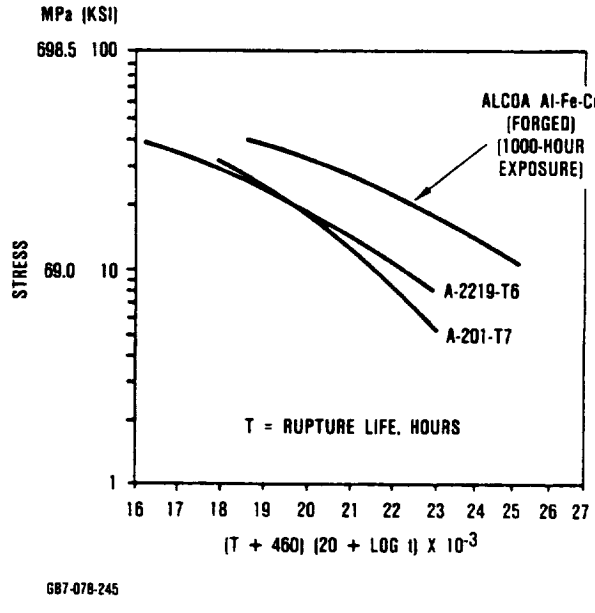

Figure 99. Stress Rupture Properties of Aluminum Alloys.

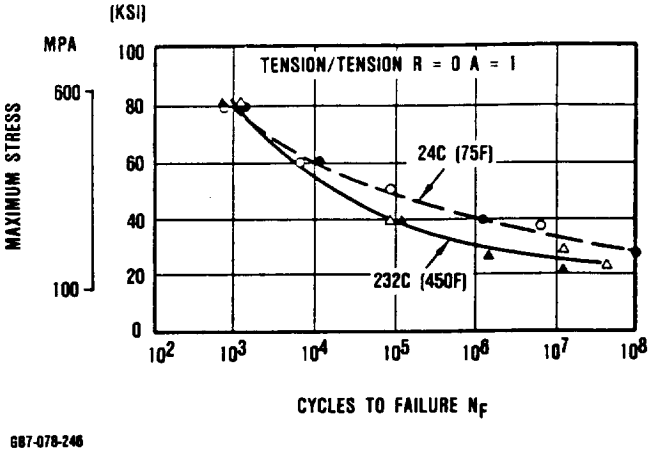

Figure 100. HCF Properties of ALCOA Al-Fe-Ce.

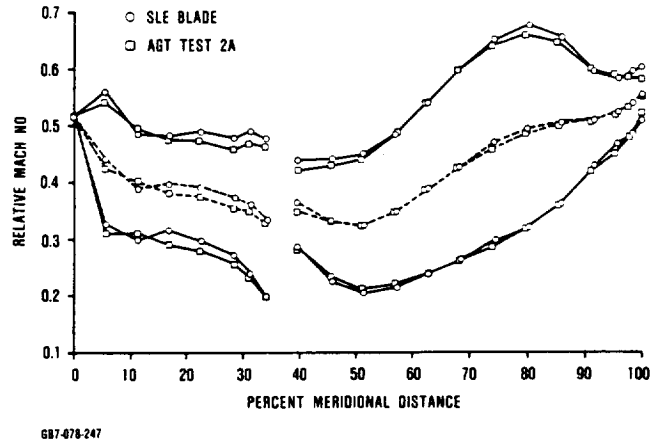

Figure 101. Impeller Blade Loading-Hub.

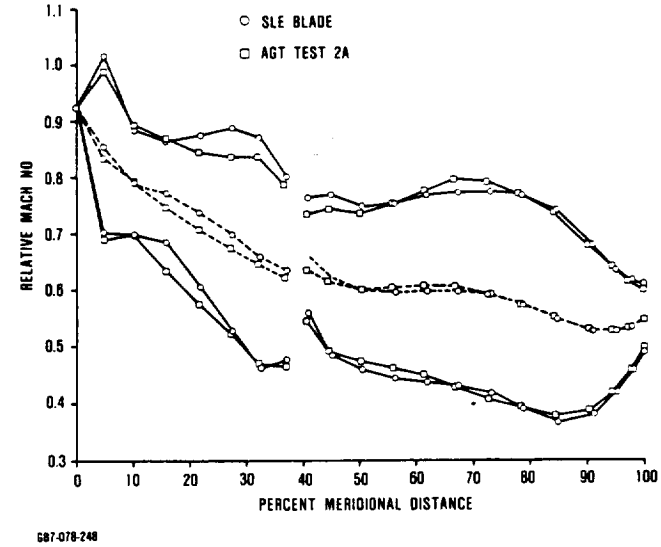

Figure 102. Blade Loading-Mid-Passage.

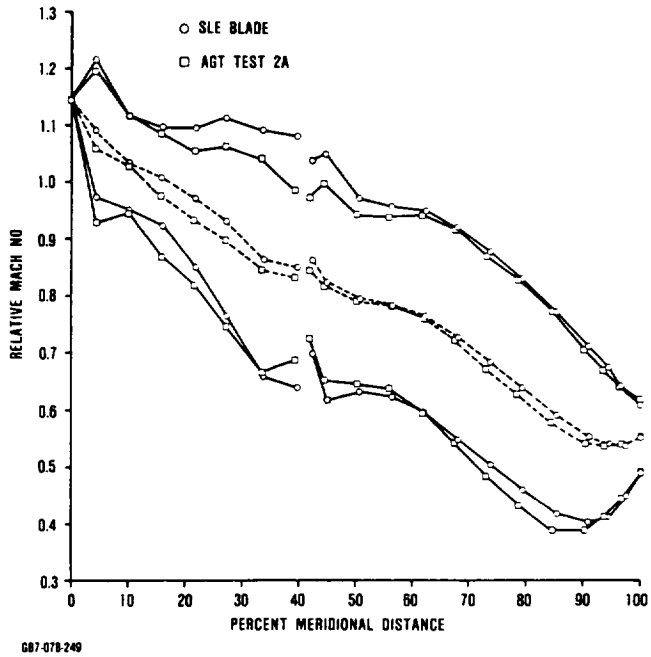

Figure 103. Impeller Blade Loading - Shroud.

identified as -9.8 (low), -27 (high) and -37 degree (maximum) rotor exit swirl angle designs. As shown in Figure 104, examination of the original optimized -9.8 degree case showed significant performance decrement at engine idle, and since "system design" objectives are to maximize engine performance at low power while maintaining acceptable vehicle acceleration capabilities, the -27 degree exit swirl design was selected for the baseline ceramic turbine. Vector diagrams for maximum power and idle are presented in Figure 105 (-27 degree exit swirl design). Also shown is the maximum power vector diagram for the 1149C (2100F) AGT101 metallic rotor configuration.

The maximum power design point cycle conditions for the selected -27 degree rotor exit swirl design are presented in Table 12. The turbine system station designations are shown in Figure 106.

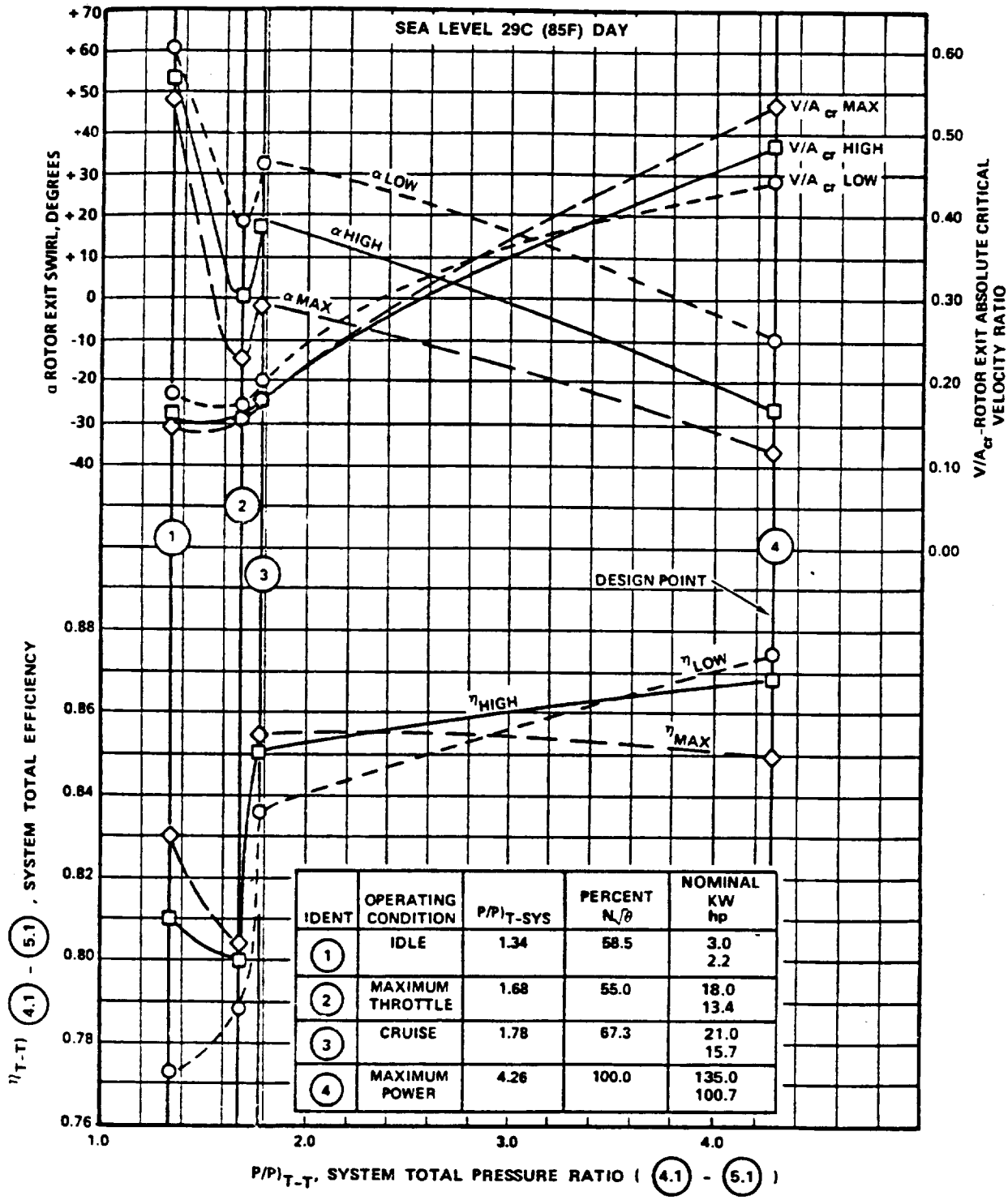

IDENT	OPERATING CONDITION	P/P T-SYS	PERCENT N/√θ	NOMINAL KW hp
1	IDLE	1.34	58.5	3.0 2.2
2	MAXIMUM THROTTLE	1.68	55.0	18.0 13.4
3	CRUISE	1.78	67.3	21.0 15.7
4	MAXIMUM POWER	4.26	100.0	135.0 100.7

Figure 104. Off-Design Performance Characteristics as a Function of Design-Point Exit Swirl for NASA-DOE Advanced Gas Turbine Powertrain System Development Program.

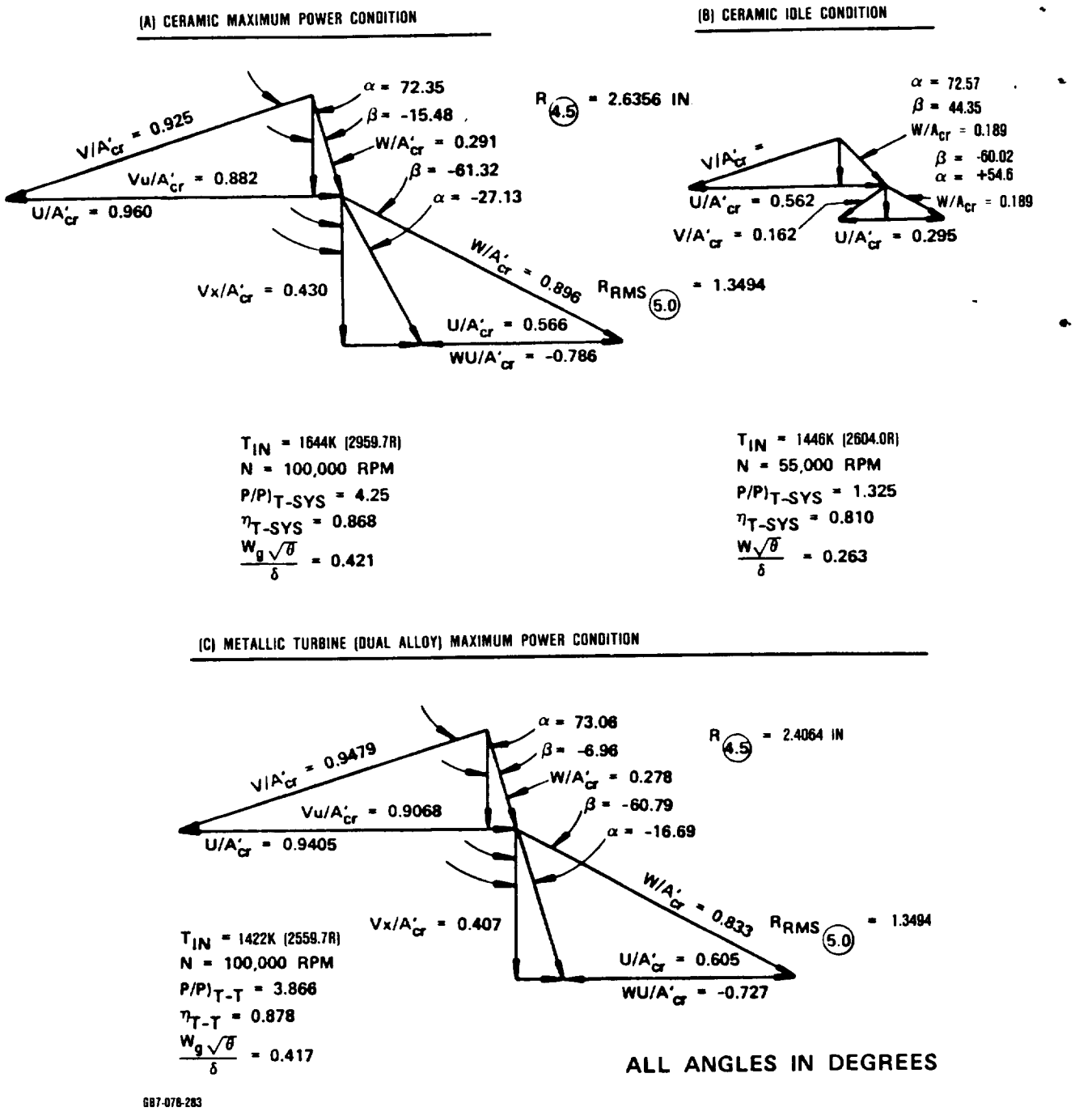

Figure 105. Turbine One-Dimensional Vector Diagrams.

Table 12. Turbine Design Point Cycle Conditions Sea Level, 29C (85F) Day, Maximum Power.

	Ceramic	Dual Alloy Metallic
T_{IN}, Turbine Inlet Total Temperature K (R)	1644.3 (2959.7)	1422.1 (2559.7)
$(P/P)_{T-T}$, Stage Total-to-Total Pressure Ratio	4.000	3.866
$W_g\sqrt{\theta}/\delta$, Stage Inlet Corrected Flow, kg/sec (lbm/sec)	0.191 (0.421)	0.189 (0.417)
W_g, Mass Flow, kg/sec (lbm/sec)	0.373 (0.8231)	0.378 (0.8325)
ΔH, Stage Specific work kJ/kg (Btu/lbm)	88.318 (37.970)	85.292 (36.669)
$P_{T_{IN}}$, Stage Inlet Total Pressure, kPa (psia)	473.235 (68.637)	449.380 (65.177)
η_{t-t}, Stage Total-to-Total Efficiency	0.901	0.892
N. Rotational Speed, rpm	100,000	100,000
$N/\sqrt{\theta}$, Corrected Speed, rpm	41863.3	45015.6
U_t, Rotor Inducer Tip Speed, m/s (ft/sec)	701.04 (2300.0)	640.08 (2100.0)
$\Delta P_T/P_T)_{Exhaust}$, Total Pressure Loss From Rotor Exit-to-Regenerator Inlet	0.0607	0.0312
$\Delta P_T/P_T)_{Inlet}$, Total Pressure Loss From Turbine Duct Inlet-to-Stator Inlet	0.010	0.010
αExit, Exit Swirl, Degree	-27.0	-16.7

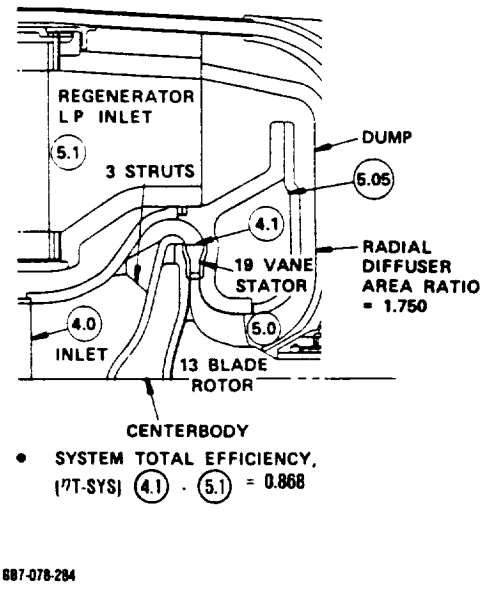

Figure 106. Turbine Design Summary

5.2.1.1 Stator Inlet Flowpath

The turbine inlet duct design was completed as shown in Figure 107. Three modified NACA 16-021 airfoil design struts have been selected to reduce strut tip blockage and thus decrease tip loading (Figure 108). The resulting inlet duct velocity distribution is shown in Figure 109. A 2-D boundary layer analysis, which verifies that flow through the inlet duct is stable, was performed.

5.2.1.2 Stator

The stator vane profile design objective was to maximize stator inlet loading (which is then relieved with end-wall contouring) and minimize exit loading from the throat region to the trailing edge. This approach minimizes total vane loading and, therefore, secondary flow losses. Nineteen vanes were selected based on turbine rotor blade vibration analyses.

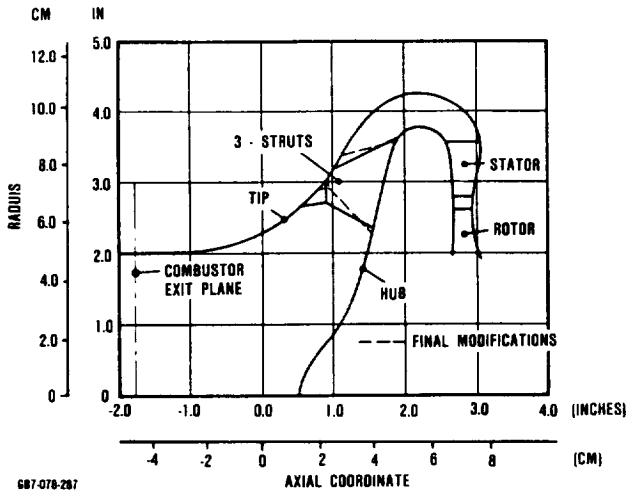

Figure 107. Baseline Turbine Inlet Duct Configuration.

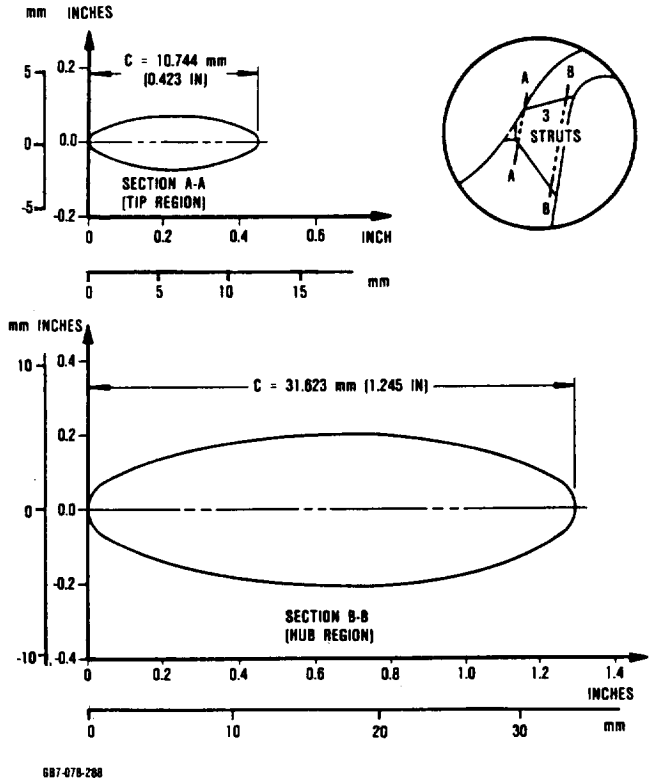

Figure 108. Turbine Inlet Strut Sections [Modified NACA 16-201 (t/c = 0.30)].

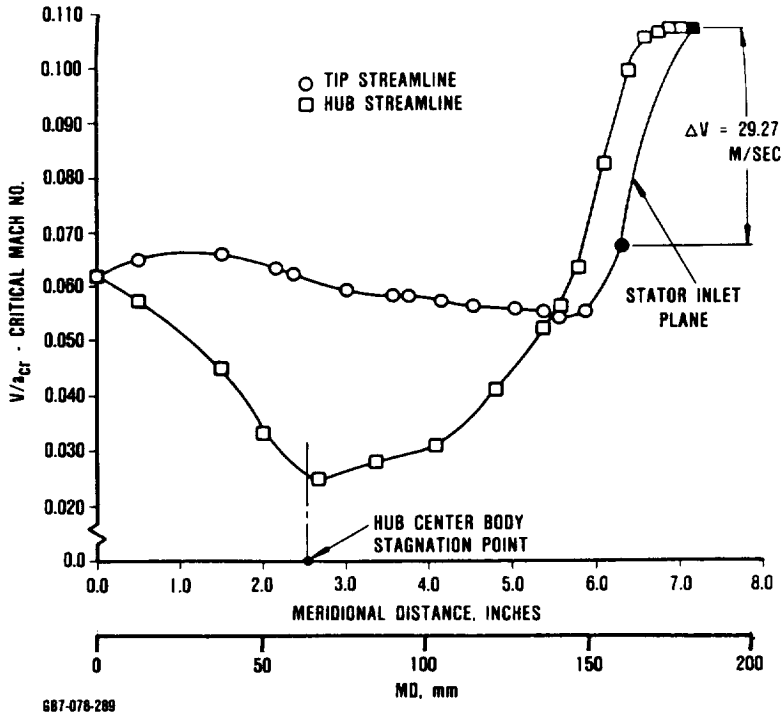

Figure 109. Turbine Inlet Hub and Tip Velocity Distribution for Baseline Configuration.

Two stator vane profile designs were completed. The baseline design is based on a trailing edge thickness (normal) of 0.508 mm (0.020 in) and a fillet radius of 0.762 mm (0.030 in). The design is consistent with previous turbine designs used for the specific speed correlation (i.e., no additional aerodynamic performance penalty is required). This profile, presented in Figure 110, was based on the selected vane number of 19. Vane suction and pressure surface velocity distribution is presented in Figure 111 with the end-wall contour established from the inlet duct optimization. The second vane profile was designed to facilitate tooling for an injection molded integral vane ring. Trailing edge thickness was increased to 0.762 mm (0.030 in) and the fillet to 1.220 mm (0.050 in). In addition, the entire pressure surface and a portion of the suction surface were modified to straight lines, as shown in Figure 112. The effect of a linear pressure surface on the vane velocity distribution is presented in Figure 113.

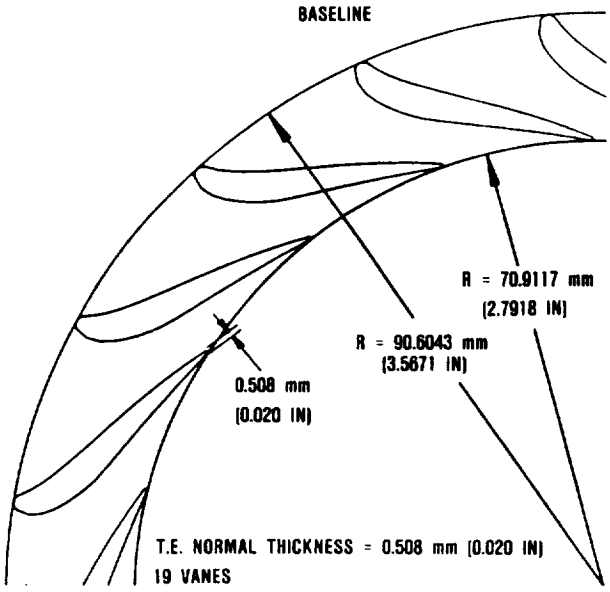

Figure 110. Ceramic Turbine Stator Profile Design.

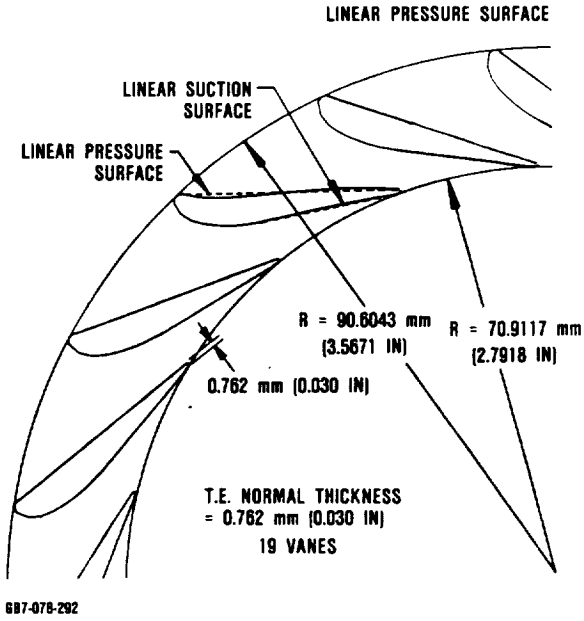

Figure 112. Ceramic Turbine Stator Profile Design.

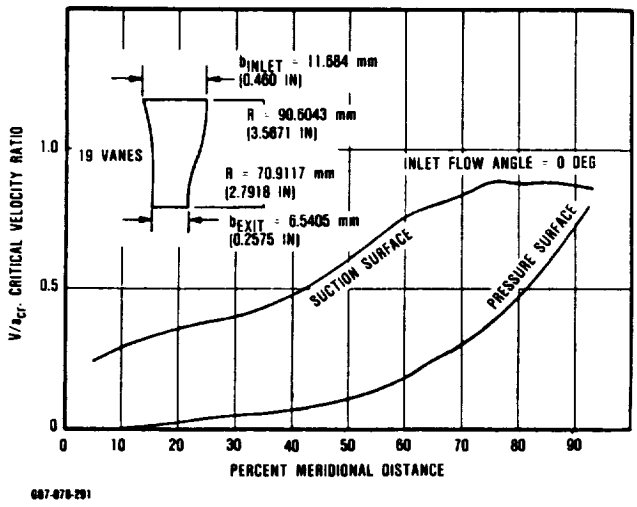

Figure 111. Ceramic Turbine Stator Velocity Distribution (Baseline, 19 Vanes).

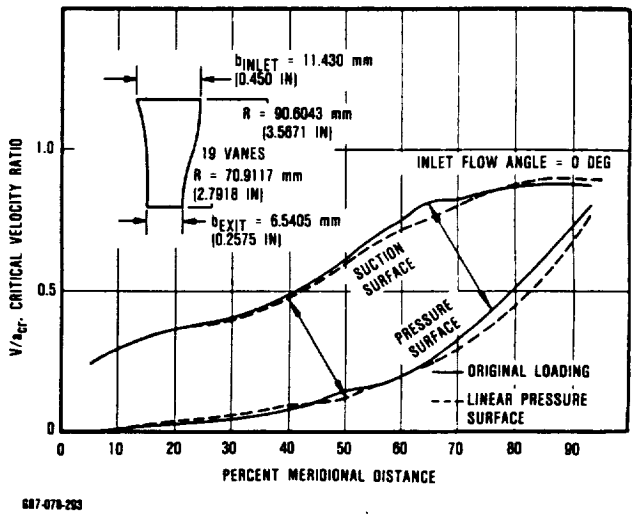

Figure 113. Ceramic Turbine Stator Velocity Distribution (Linear Pressure Surface, 19 Vanes).

5.2.1.3 Rotor

Figure 114 shows the meridional view of the ceramic and metallic rotor design. Since the metallic rotor blading geometry is identical to the ceramic, the metallic rotor is achieved by a simple tip cutback to reduce stresses in the rotor.

The turbine rotor blade angle distribution for the hub, mean, and shroud streamlines are shown in Figure 115. Calculated radial rotor loss distribution as a function of blade height is shown in Figure 116. These calculations are consistent with past design and Garrett empirical experience wherein rotor exit survey data shows that the radial loss characteristics for

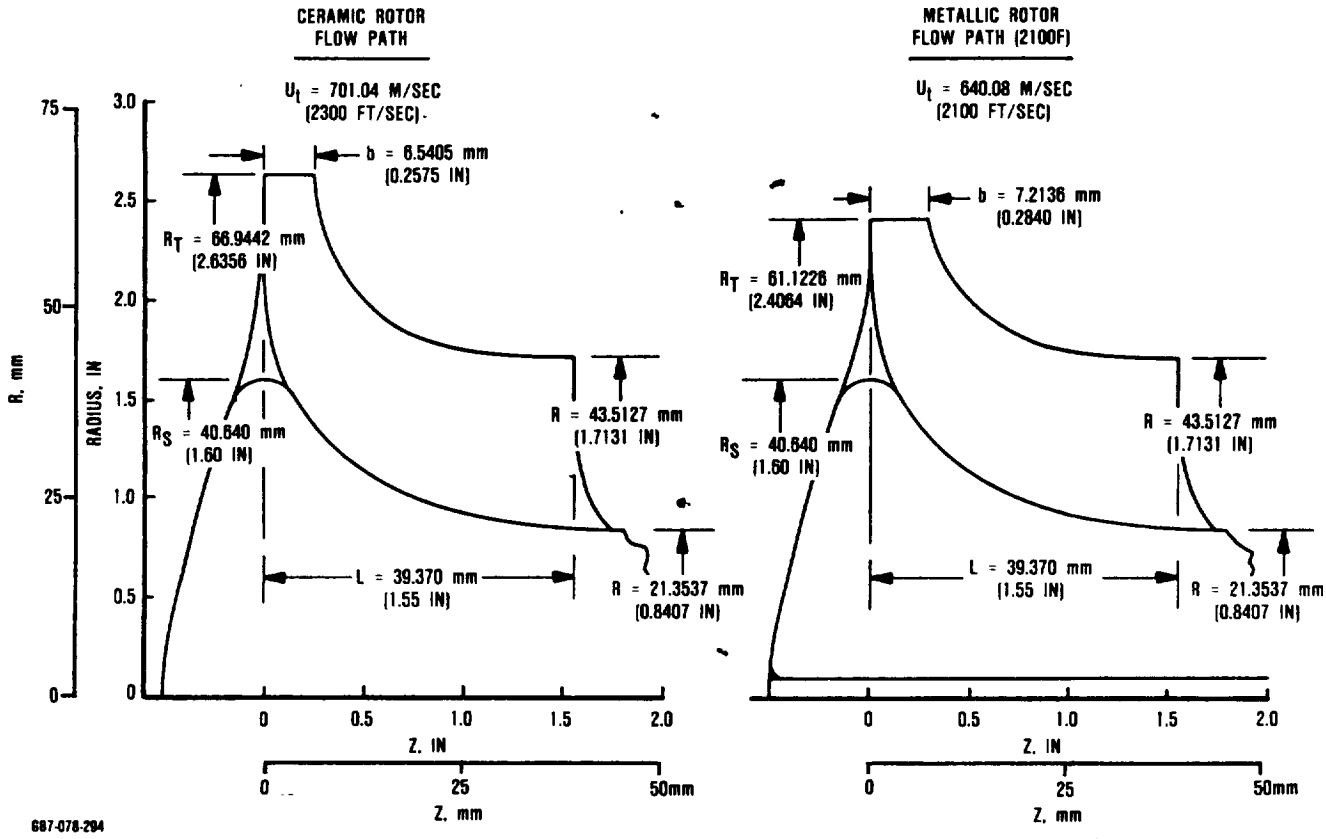

Figure 114. Ceramic and Metal Turbine Flow Paths.

radial turbines are similar. That is, in the hub region the losses are low (due to lower loading) and progressively increase to about 80-percent blade height, and then are fairly uniform to the tip. Velocity distributions for the rotor are shown in Figure 117. The velocity distribution for the ceramic and metallic rotors are similar at shroud, mean, and hub streamlines except in the inducer area where the higher inducer loading of the metallic rotor is evident.

5.2.1.4 Exhaust Diffuser

For the exhaust diffuser, additional calculation stations were added to the rotor flow solution, since the velocity distribution into the exhaust diffuser is strongly dependent on the rotor exit radial swirl and associated loss distribution. Both uniform and non-uniform inlet conditions were evaluated. The current configuration is shown in Figure 118 for an area ratio of 1.75.

5.2.2 Turbine Aerodynamic Performance Testing

The test rig, shown in Figure 119, is a double overhung assembly supported by two angular contact ball bearings. During the turbine and rig design effort, an investigation was conducted concerning off-design performance mapping, particularly accurate performance measurement at the idle-cruise regime of the CFDC. A summary of the investigation and subsequent impact on the cold turbine test rig design is outlined below.

- The aerodynamic analysis has shown cold turbine rig power requirements at maximum power of 19.3 to 20.1 kw (26 to 27 hp) with a temperature differential across the rig of 98-107C (208-224F). The power level drops to 0.56-2.38 kw (0.75-3.2 hp) at idle-cruise and the temperature differential decreases to 3-19C (37-67F) for these conditions. The kw/rpm ratio (hp/rpm)

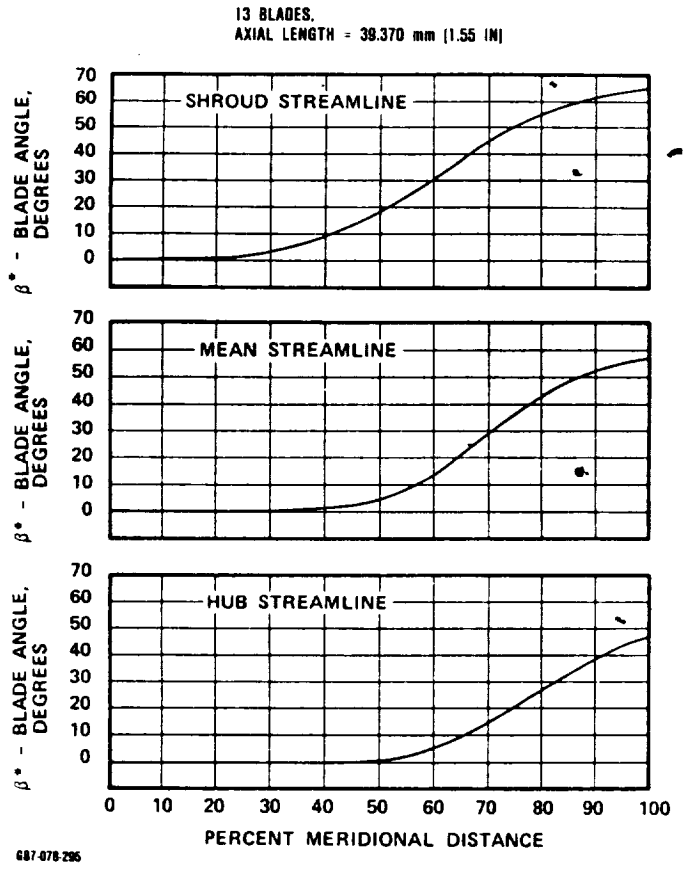

Figure 115. Turbine Rotor Blade Angle Distribution.

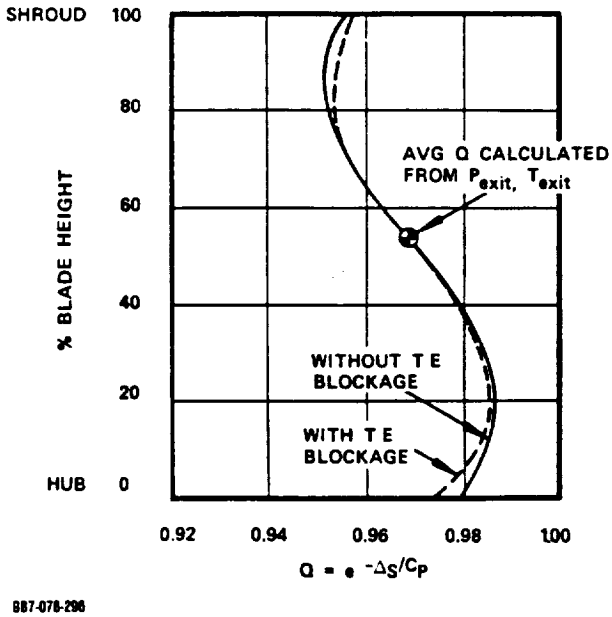

Figure 116. AGT101 Rotor Radial Loss Distribution.

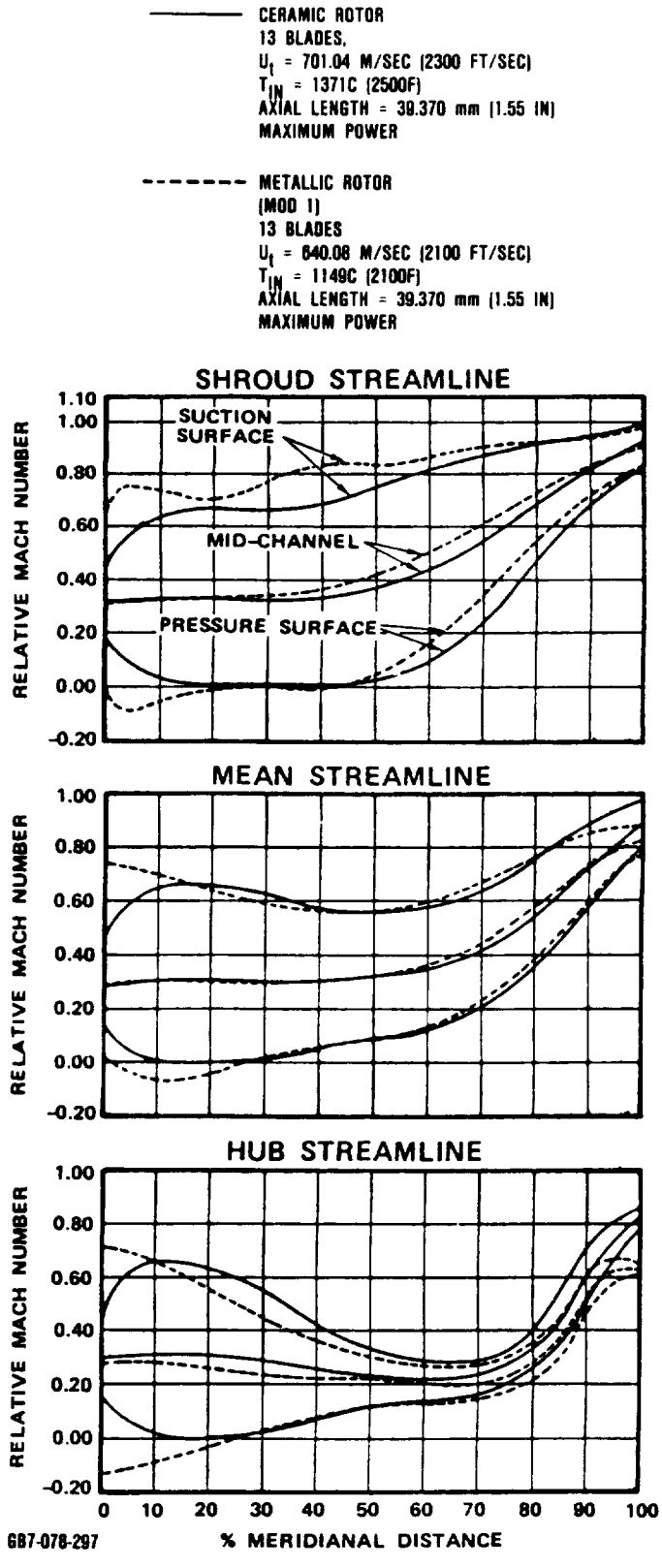

Figure 117. Turbine Rotor Velocity Distribution.

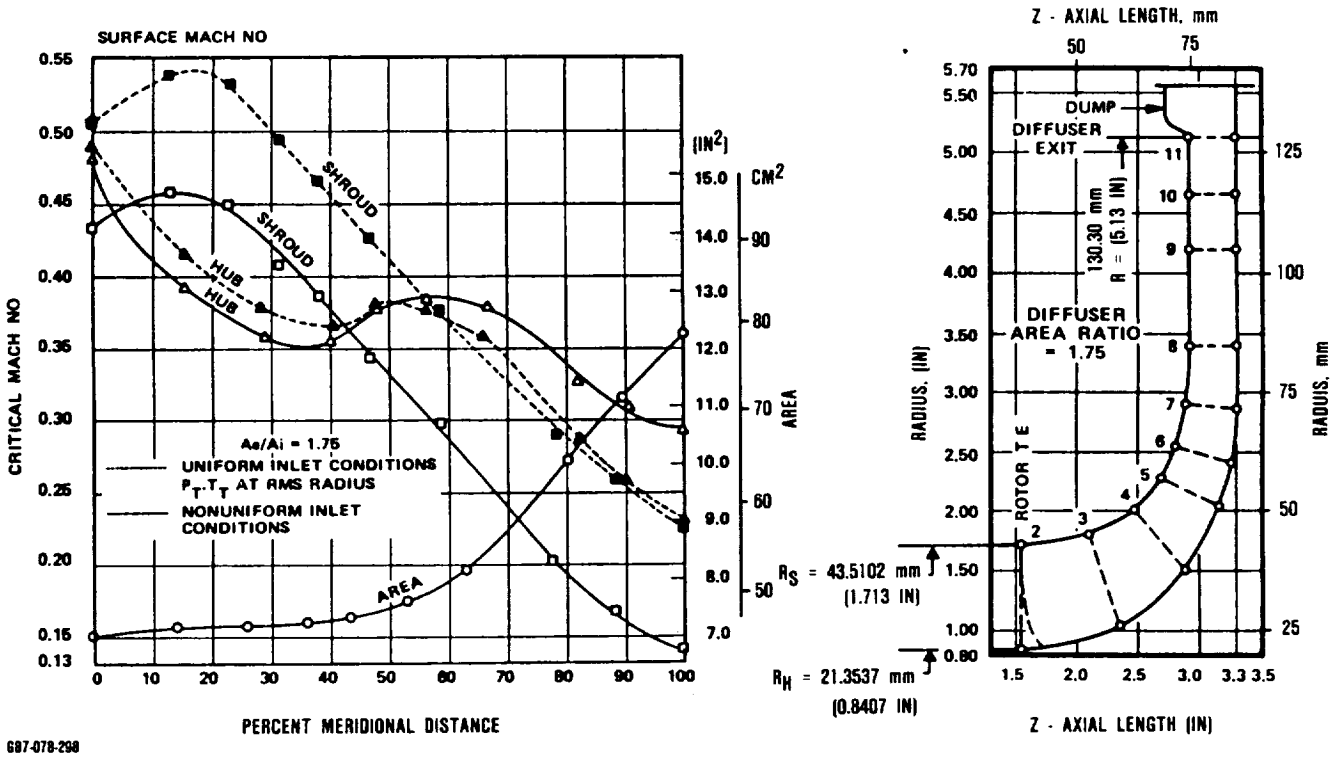

Figure 118. Exhaust Diffuser Velocity Distribution.

ratio varies from 3.728×10^{-4} (5×10^{-4}) at maximum power to a low of 2.237×10^{-5} (3×10^{-5}) at the idle condition (see Table 13)

- o Preliminary results of the heat transfer analysis of the cold turbine test rig indicates heat transfer losses could introduce significant errors. Revisions were introduced to the test rig design to provide insulation both internal and external to the rig, and to introduce conduction heat transfer barriers where possible

- o The survey of the industry for precision instrumentation confirmed the availability of platinum resistive temperature sensors and direct-coupled, high speed electronic torque meters with the desired accuracy
  - The high speed, direct-coupled, torque meter represents the instrumentation with accuracy both for high and low power mapping (mfgr., Torque Meters Ltd., Northhamption, England)
  - The platinum resistive temperature sensors provide secondary or backup measurement of performance and provide an important reference for the temperature surveys at various points in the turbine system.

- o The combination of direct coupled torque meter and platinum resistive temperature sensors as backup provided a desirable performance measurement system to assure design goals and to properly assess CFDC mileage estimates during the cold turbine mapping program.

COMBUSTOR EXIT (4.0)	T_T - 6 THERMOCOUPLES - 3 ROSEMONT PROBES P_S - 8 KIEL PROBES
TRANSITION DUCT (4.0) TO (4.1)	P_S - HUB SHROUD
ROTOR SHROUD (4.5) TO (5.0)	P_S - HUB
ROTOR EXIT (5.0)	P_S - 8 KIEL PROBES
EXHAUST DIFFUSER (5.0) TO (5.05)	P_S - HUB SHROUD
DIFFUSER EXIT BEND (5.05) TO (5.07)	P_S - HUB SHROUD
REGENERATOR INET (5.1)	T_T - 9 THERMOCOUPLES - 3 ROSEMONT PROBES P_S - SHROUD
ROTOR CLEARANCE PROBES	4 RADIAL PROBES 4 AXIAL PROBES
MECHANICAL INSTRUMENTATION (A)	BEARING TEMPERATURE. VIBRATION. OIL FLOW. OIL TEMPERATURE
TORQUEMETER (B)	TORQUE
MASS FLOW (C)	SONIC NOZZLE

GB7-078-299

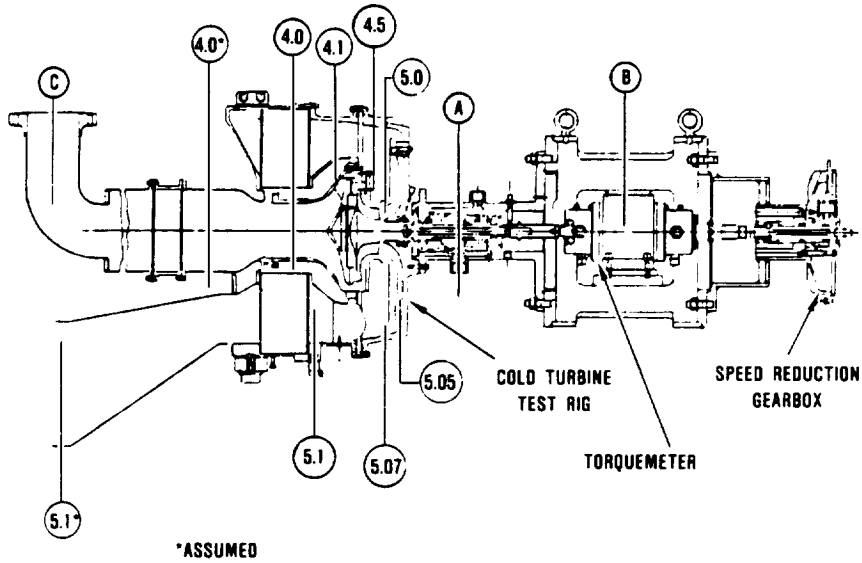

Figure 119. Cold Turbine Test Rig.

5.2.2.1 Test Procedure

During mechanical checkout tests, the rig was configured with a "dummy" rotor for tare loss calibration tests. The dummy bladeless rotor was designed with identical mass and inertia characteristics of the bladed rotor. Test rig operation was accomplished to full speed using the dynamometers in the driving mode and under full vacuum to eliminate dummy rotor disk friction characteristics.

The test rig then was assembled with the AGT101 871C, (1600F) machined Astroloy turbine rotor. Capacitance probes were used in all planes (radial, axial and backface) to assess rotor running clearances during aerodynamic mapping.

The torquemeter was configured with the appropriate shaft depending on the selected mapping range. Prior to each data run, a dead weight calibration was performed. Data records were obtained following an iterative procedure wherein inlet temperature at a desired pressure ratio was adjusted to obtain a rig discharge temperature within several degrees of cell ambient, thereby minimizing heat

Table 13. AGT101 Cold Turbine Rig Operating Conditions.

Parameter	Maximum Power	Cruise No. 1	Cruise No. 2	Maximum Throttle	Idle
$P/P_{T\text{-System}}$	4.263	1.787	1.639	1.676	1.341
T_{IN}, C (F)	151.3 (304.3)	70.8 (159.5)	63.6 (146.5)	63.1 (145.5)	47.4 (117.4)
T_{OUT}, C (F) (Assumed)	26.7 (80.0)	26.7 (80.0)	26.7 (80.0)	26.7 (80.0)	26.7 (80.0)
N, rpm	52,000	30,804	28,379	24,870	25,849
$N/\sqrt{\theta}$, rpm	41,863	28,194	26,251	23,025	24,507
$W\sqrt{\theta}/\delta$, Corrected flow, kg/sec (lb/sec)	0.192 0.423	0.171 0.377	0.164 0.362	0.171 0.376	0.117 0.259
W, Physical Flow, kg/sec (lb/sec)	0.1594 (0.35141)	0.0524 (0.11556)	0.04590 (0.10120)	0.04459 (0.0983)	0.02667 (0.0588)
Reynolds Number, $R_e = W/R_t\mu$	1.0×10^5	38,128	34,130	33,150	20,600
$P_{T_{IN}}$, kPa (psia)	102.153 (14.816)	33.92 (4.92)	30.61 (4.44)	28.61 (4.15)	(3.52)
$P_{T_{EXIT}}$, kPa (psia)	24.13 (3.50)	20.00 (2.75)	18.68 (2.71)	17.07 (2.476)	18.098 (2.625)
kw (hp)	19.95 (26.76)	23.26 (3.119)	1.70 (2.28)	1.630 (2.186)	0.5569 (0.7468)
kw/rpm (hp/rpm)	0.00037 (0.0005)	0.000075 (0.00010)	0.000060 (0.000081)	0.000067 (0.00009)	0.000022 (0.00003)

Note: Gamma effects not included will alter results by few percent.

transfer effects. Speed then was set based on inlet temperature, and inlet pressure (for a given pressure ratio) was adjusted to obtain the desired turbine Reynolds number. This procedure was followed for all performance tests and data records obtained after system stabilization for approximately 10 minutes.

Figure 120 shows the unit installed in the test facility.

A series of cold rig tests were conducted to aerodynamically evaluate the baseline ceramic configuration (as represented by the Astrology rotor). Baseline ceramic cold rig

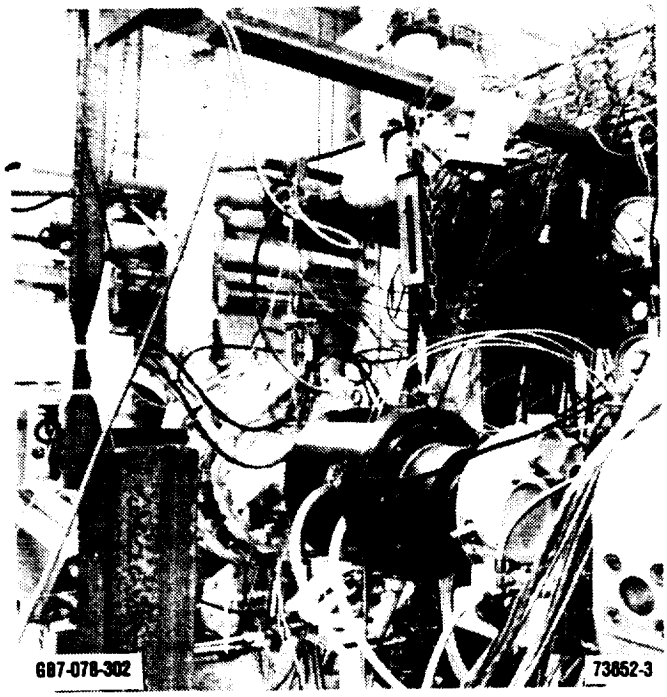

Figure 120. AGT101 Test Rig Installed in Test Cell.

test results are directly applicable to the 1371C (2500F) AGT101 design.

Figure 121 shows turbine system efficiency characteristics as a function of system pressure ratio over the operating conditions. The system is rated, for cycle analyses purposes, from the combustor exit-to-regenerator LP inlet. The overall system efficiencies at the cycle operating rpm and pressure ratios are cross plotted in Figure 122. Table 14 presents a summary of the AGT101 turbine development.

At idle, an 84-percent efficiency was achieved compared with the 79 percent program goal. Cruise performance was 84.5 percent versus 84.3 percent predicted. At maximum power, an initial design efficiency goal of 83.7 percent was projected; test results show that 85.2 percent was achieved, slightly below the program goal of 86.5 percent.

An exhaust system loss coefficient is presented versus diffuser inlet (rotor exit) swirl

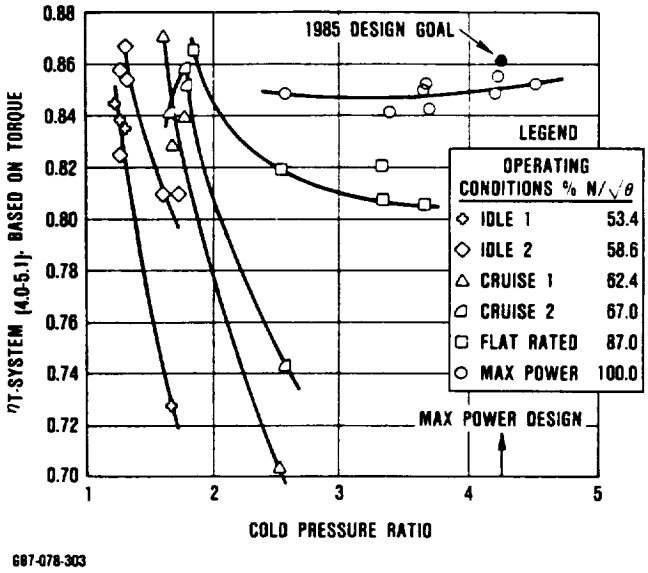

Figure 121. Baseline Ceramic Cold Turbine Rig Test Results, System Efficiency Versus Pressure Ratio.

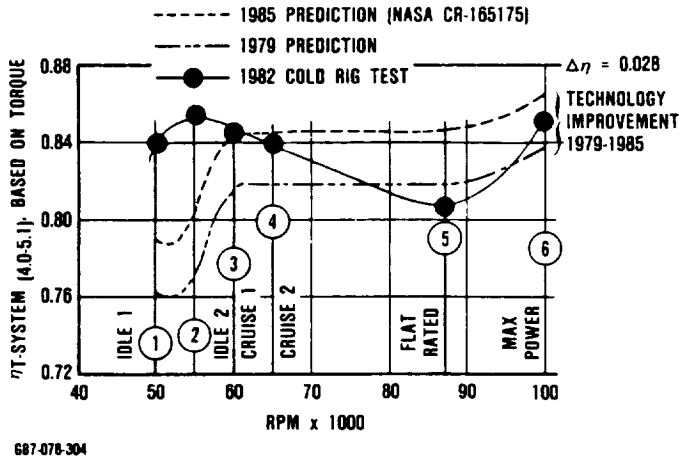

Figure 122. Baseline Ceramic Cold Turbine Rig Test Results, System Efficiency Versus Engine Speed.

Table 14. AGT101 Turbine Development Test Summary.

	Efficiency 1371C (2500F)	
	Program Test (1982)	Goal (1985)
Idle	0.840	0.790
Cruise	0.845	0.843
Maximum Power	0.852	0.865

angle in Figure 123. Results of baseline ceramic tests (indicated by square symbols) are compared with metallic turbine test data (circles) and an average curve. The additional data confirms that the exhaust system loss characteristics are low and decrease with increasing swirl. This significantly increases the turbine system performance at the engine idle and cruise conditions where swirl angles are 55 degrees and 40 degrees, respectively.

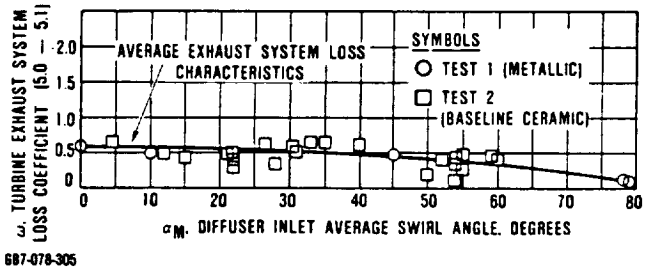

Figure 123. AGT101 Exhaust System Loss Characteristics.

It should be noted that the original off design predictions were based on increasing diffuser losses with increasing swirl angle and thus yielded a low value of turbine system efficiency (0.762 percent) at idle. The marked decrease in exhaust system loss contributes significantly to the baseline ceramic turbine system efficiency (0.840).

5.2.3 Metallic Dual Alloy Rotor

5.2.3.1 Dual Alloy Mechanical Analyses

Thermal and stress analyses were conducted for the AGT101 (1149C, 2100F) dual-alloy turbine rotor at maximum power (100,000 rpm) and idle power (55,000 rpm). Turbine inlet temperature is limited to 1059C (1930F) relative blade temperature to maximize life. The rotor is comprised of a MAR-M 247 cast blade ring and a powder metal astroloy hub HIP bonded as shown in Figure 124. The rotor is bore cooled using one percent of total mass flow.

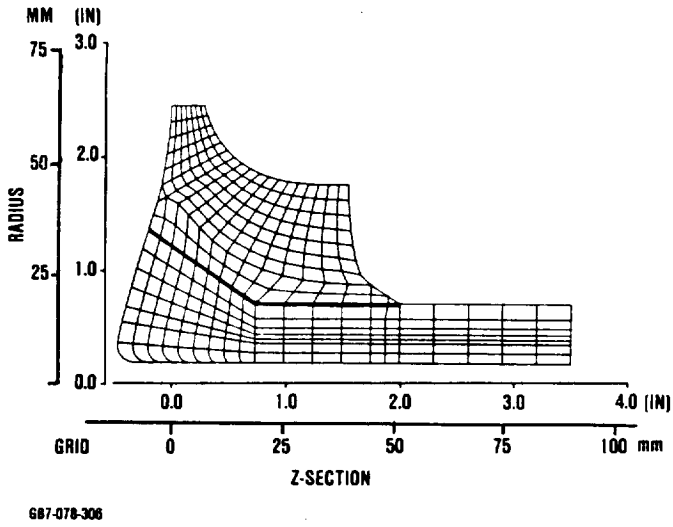

Figure 124. AGT101 Metal Dual Alloy Wheel - 13 Blades, Conical Astroloy Hub.

The predicted temperature distribution at maximum power is shown in Figure 125. Idle and maximum power equivalent stress distributions are shown in Figures 126 and 127 respectively. Blade vibration analysis results are shown in Figures 128 and 129. Table 15 summarizes the dual alloy rotor mechanical properties.

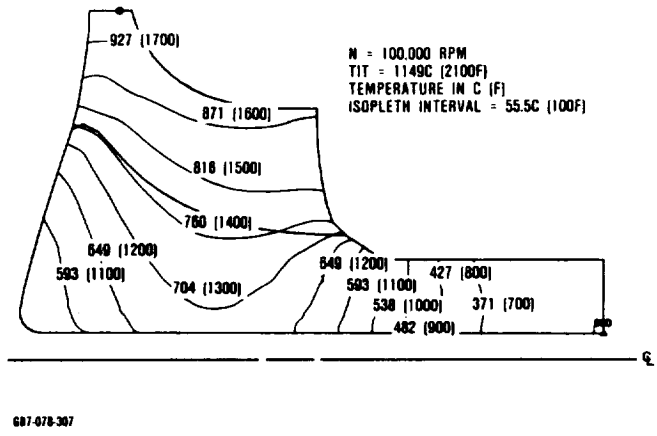

Figure 125. AGT101 Dual Alloy Steady-State Temperature Distribution.

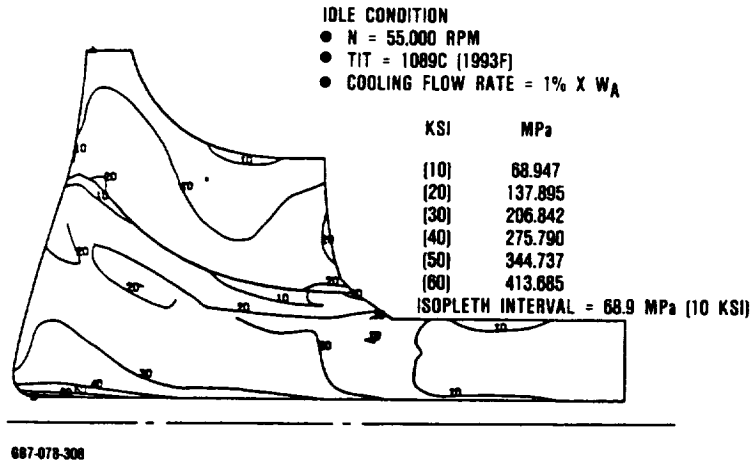

Figure 126. Stress Distribution for Dual Alloy Turbine Wheel.

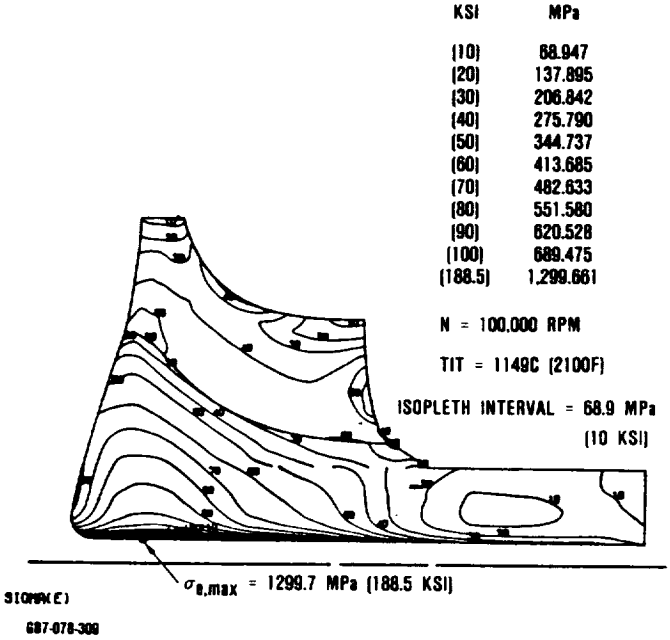

Figure 127. AGT101 Dual Alloy Steady-State Equivalent Stresses.

Use of the dual alloy rotors was discontinued following a rotor failure. Subsequent careful inspections of the bond joint between blade ring and hub led to the conclusion that the bond joint was not sufficiently reliable to continue the test program with the dual alloy rotor.

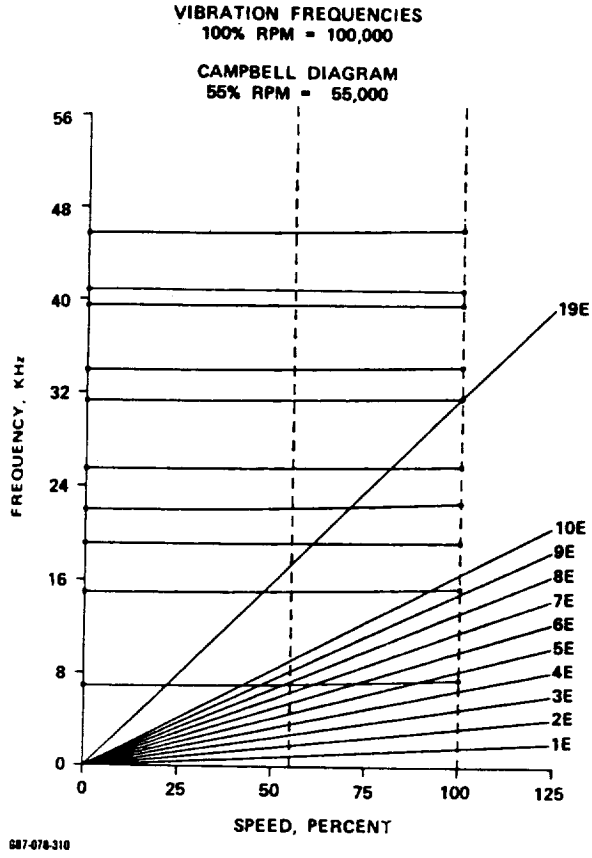

Figure 128. AGT101 Metal Dual Alloy Wheel.

5.2.3.2 AGT101 (1149C, 2100F) Dual Alloy Turbine Rotor Fabrication

The turbine inlet temperature for AGT101 (1149C, 2100F) engine development imposes unique materials requirements for the turbine rotor fabrication. One material cannot satisfy all mechanical properties requirements. The limiting conditions for airfoils are stress rupture and creep, and tensile strength and hub low cycle fatigue.

Rather than compromise the turbine temperature capability and performance, a materials mix or dual alloy fabrication concept for the radial turbine wheel was preferred. Materials selected for the dual alloy wheel fabrication are a cast MAR-M 247 bladed ring with directionally solidified (DS) inducer blade

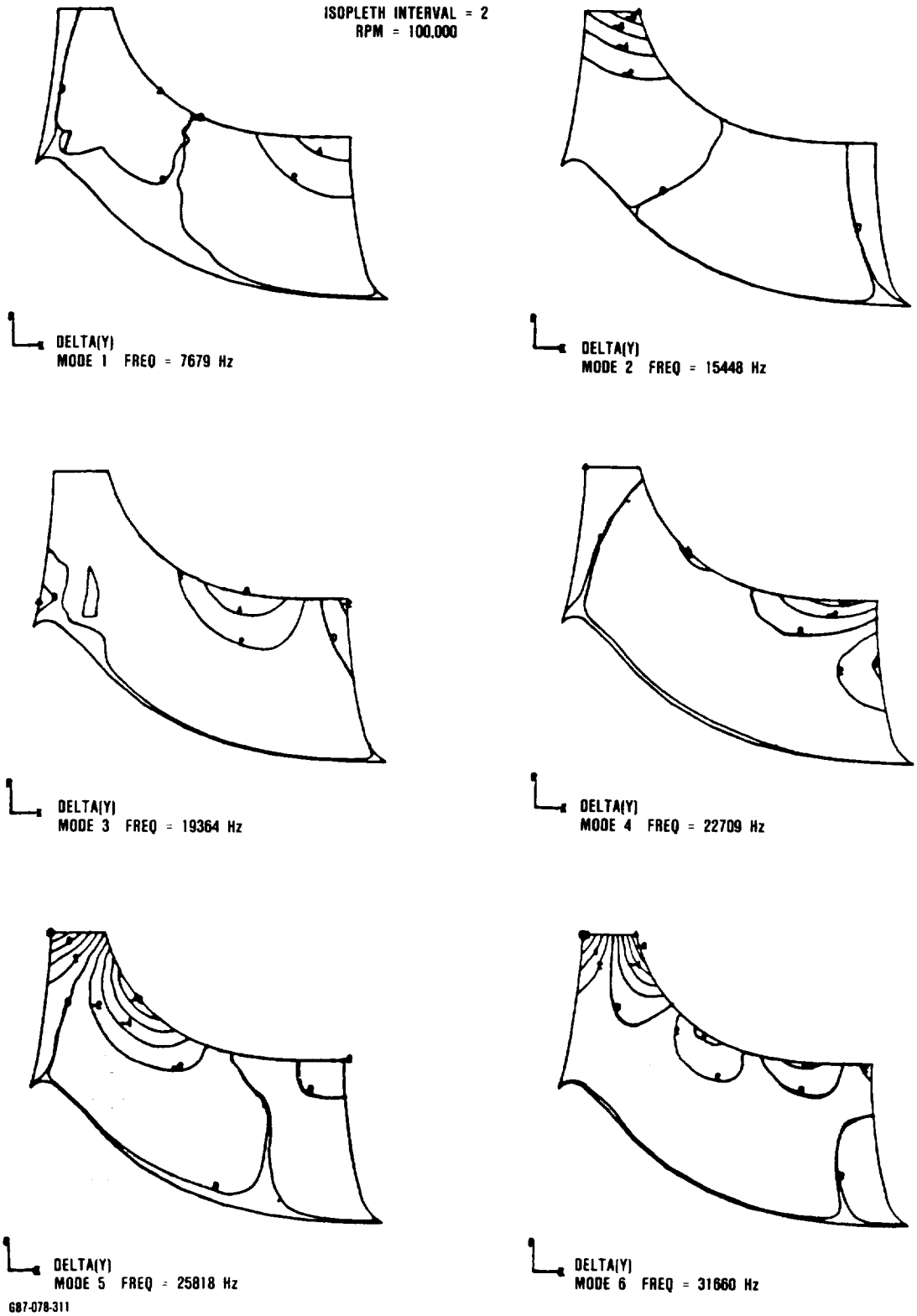

Figure 129. Turbine Vibration Modes at Maximum Power.

Table 15. Dual Alloy Turbine Wheel Design Parameters.

Inlet temperature C (F)	1149 (2100)
Number of Blades	13
Material (Blade Ring/Hub)	MAR-M 247 (DS)/Astroloy
Weight kg (lb)	1.73 (3.82)
Ip kg-in^2 (lb-in-sec^2)	0.001024 (0.0092)
Characteristics at Max Power (100,000 Rpm)	
Tip Speed m/sec (ft/sec)	640.08 (2100)
Avg. Tangential Stress MPa (ksi)	441.264 (64)
Burst Margin	1.49
Energy Joule (lb-in)	56876.6 (503,400)
S-R Life (Hrs) at R = 49.784 mm (1.96 in)	103

tips for higher temperature capability and powder metallurgy (PM) Astroloy for hub construction. The mated hub blade ring geometry in shown in Figure 130.

Dual Alloy Wheel Assembly

The Astroloy was purchased as HIP powder consolidated logs. The TRW Prototype Foundry developed the DS blade casting technique.

The hubs and bladed rings were machined as mated pairs to a 5-degree tapered fit (Figure 130). Borazon (cubic BN) grinding wheels were used to arrive at a surface finish typically about RMS 62 (Figures 131 and 132). Past experience at Garrett shows that the use of other grinding wheel compositions (ie, Al_2O_3 or SiC) results in foreign particles becoming imbedded in the work surfaces.

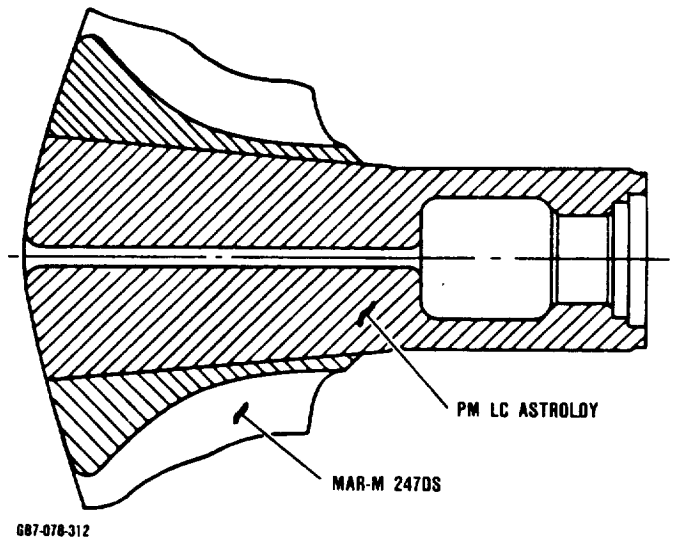

Figure 130. Dual Alloy Hub/Bladed Ring Assembly Cross Section.

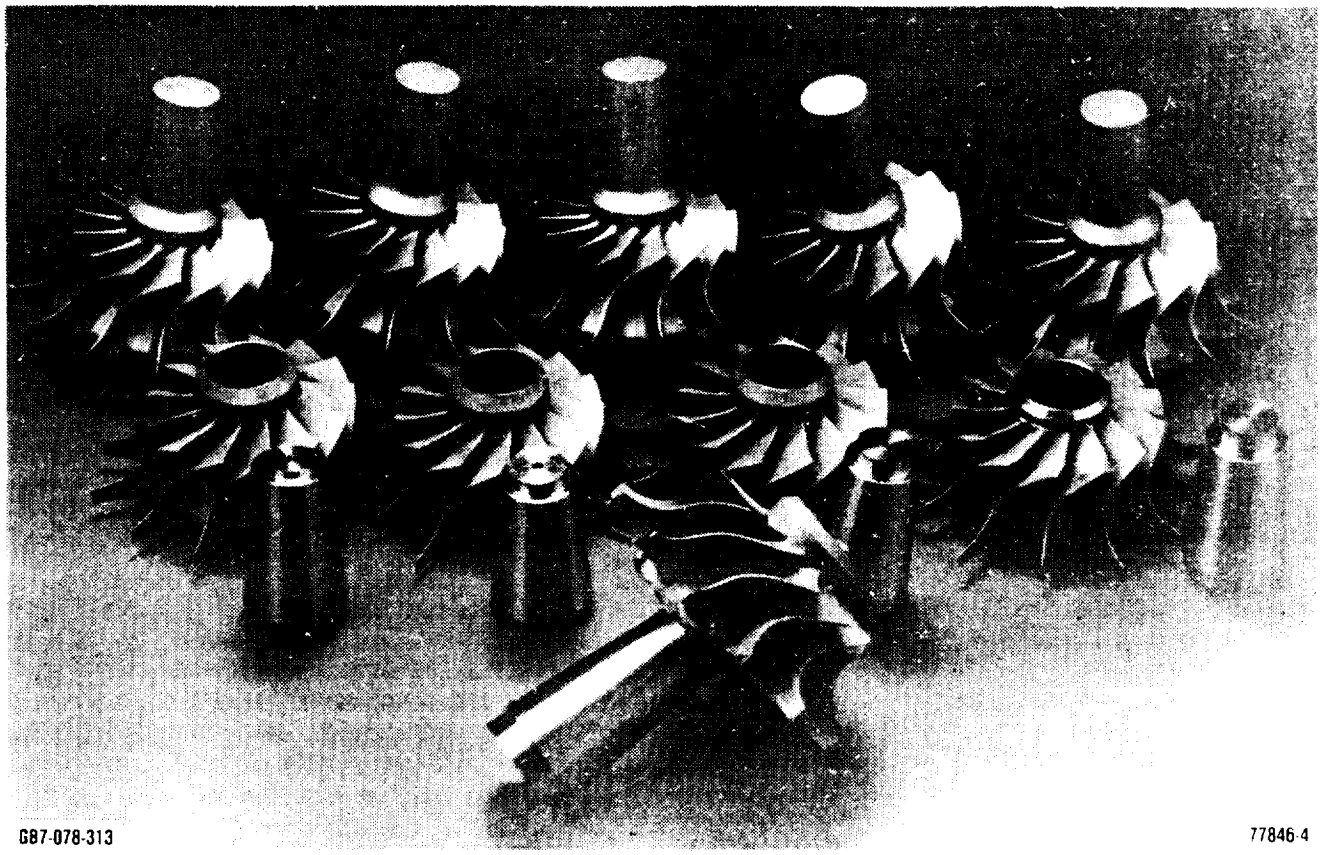

Figure 131. As-Cast AGT101 Bladed Rings and Machined Dual Alloy Wheel Assemblies.

Exposed edges of mated assemblies were brush nickel 0.005-0.010 mm (0.0002-0.0004 inch) plated and all parts were then cleaned using Garrett developed procedures. These include a sequence of steps starting with vapor degreasing followed by MEK solvent, HCl solution, distilled water, and Freon rinses. The mated assemblies were hermetically sealed using a vacuum brazing technique.

The first batch of five dual alloy assemblies were diffusion bonded during exposure to a HIP cycle consisting of 1204 ±14C for four hours at 103.42 MPa (2200 ±25F/4 hrs/15 ksi) at the Howmet Turbine Components Corporation facilities. After bonding, all five assemblies were heat treated using the following standard Yo-Yo procedure developed for LC Astroloy:

Solution	1079C (1975F)/4 hrs/rapid argon cool
plus	871C (1600F)/8 hrs/AC
	972C (1800F)/4 hrs/AC
	649C (1200F)/24 hrs/AC
	760C (1400F)/8 hrs/AC

Bond Zone Evaluation

A representative macroetched cross-section of an AGT101 dual alloy wheel, shown in Figure 133, indicates the presence of a continuous bond. Some braze alloy penetration is detected and a view of an unetched section of the bond zone shows the absence of porosity due to the Kirkendall effect or other causes (Figure 134). The area of braze penetration will be removed during final machining.

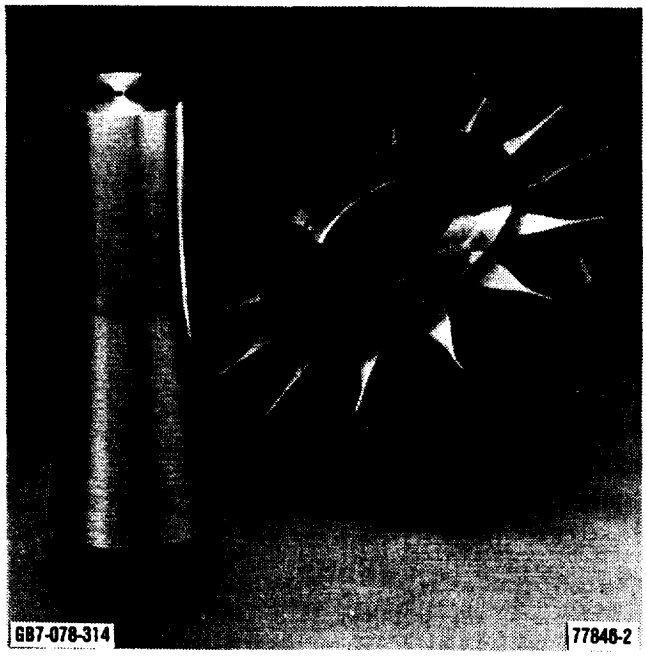

Figure 132. Machined AGT101 Dual Alloy Wheel Assembly—PM LC Astroloy Hub and MAR-M 247 Blade Ring.

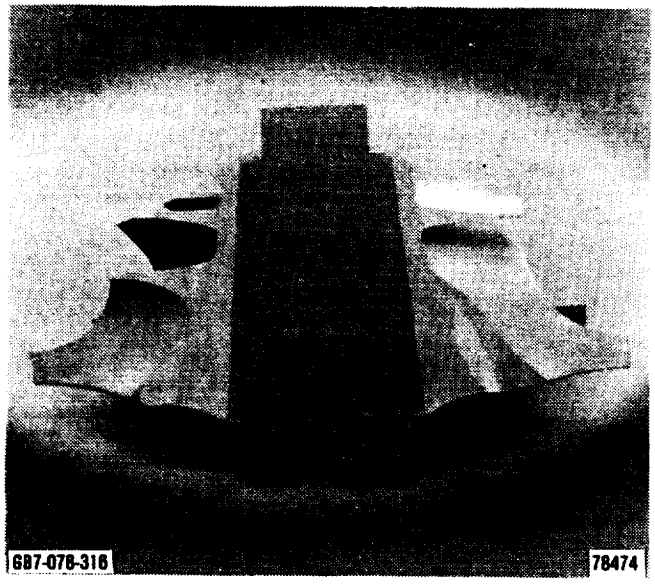

Figure 133. Microetched Cross Section of AGT101 Dual Alloy Wheel Test Specimen.

5.2.4 Ceramic Turbine Rotor Redesign

The rotor aerodynamic design is the determination of the blade geometry at hub, mean, and shroud (and other streamline locations as required), which satisfies the optimum velocity diagram and distribution consistent with the work output requirement. The radial rotor is designed through a number of steps, which are given in the flow chart in Figure 135.

To improve ceramic manufacturing capabilities, the baseline rotor was redesigned with increased blade thickness and modified blade shapes, as shown in Figure 136. The redesigned rotor preserved the original blade angle distribution to match the baseline velocity diagram. The rotor blade angle distribution for the hub, mean, and shroud streamlines are shown in Figure 137.

Blade surface velocity distributions, calculated from the axisymmetric flow solution at the shroud, mean, and hub streamlines are shown in Figures 138 through 140 and compare baseline design rotor loadings. The figures illustrate the hub-to-shroud variations in the surface velocities and the blade loadings, as well as the variations along the flowpath. The blade is more heavily loaded along the shroud than elsewhere because of lower solidity. Loading near the rotor inlet where the flow is nearly radial, is considerably higher than the loading near the rotor exit where the flow is nearly axial. A comparison of blade loadings between the redesigned and baseline rotor shows that the redesigned rotor loading at the exit converges to a single value (which was lacking in the baseline design). Theoretically, this means higher work extraction in the redesigned rotor. However, the redesigned rotor loading indicates some diffusion downstream of the throat when compared with baseline rotor design. The performance penalty due to the surface diffusion probably offsets any benefit that could be claimed due to loading closure. Thus, no efficiency changes in the redesigned rotor are expected.

Detailed stress analysis of the ceramic turbine rotor is discussed in paragraph 6.2.7.

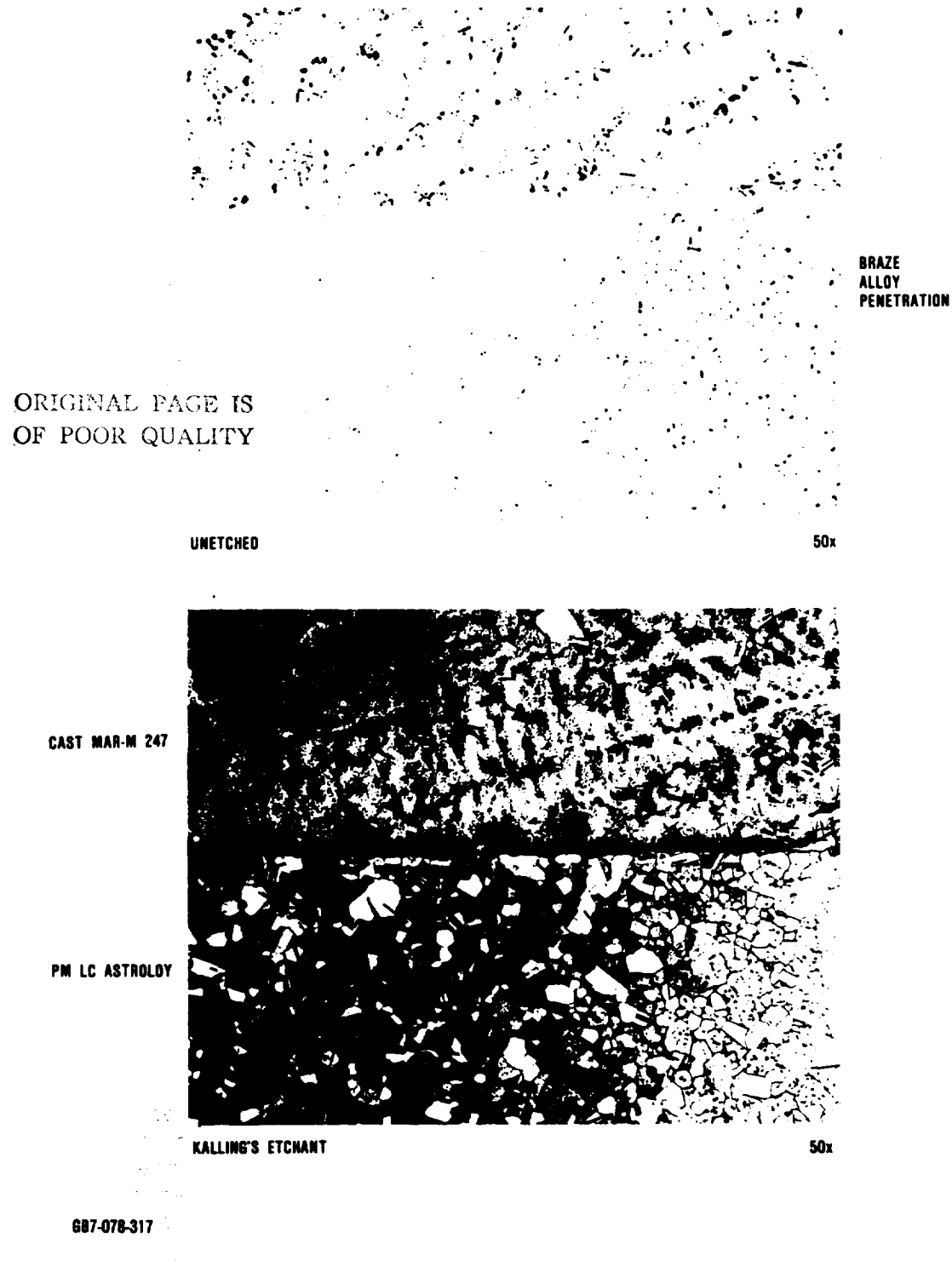

Figure 134. Braze Closure After HIP Diffusion Bonding (Sample was Subjected To Yo-Yo Heat Treatment).

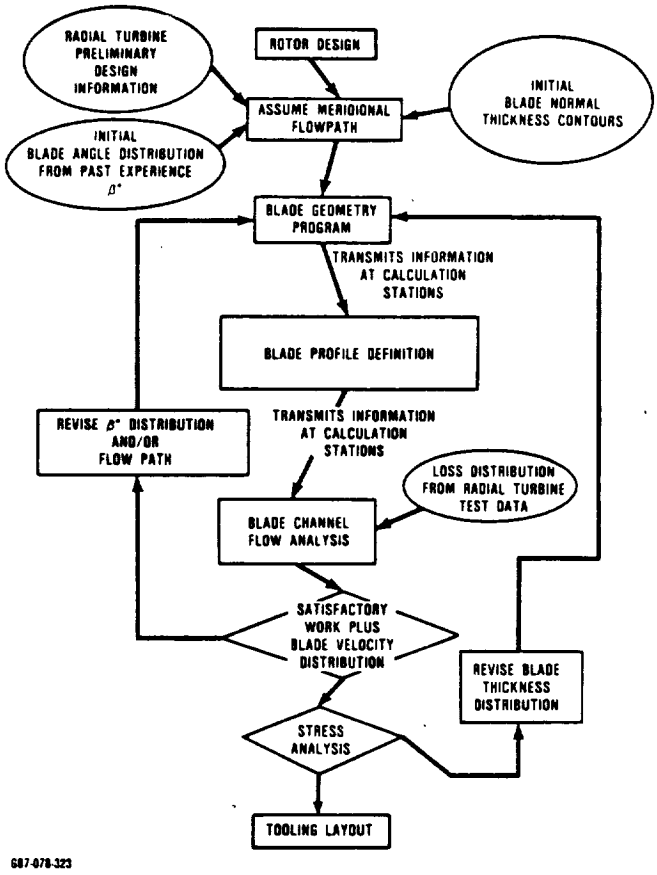

Figure 135. Radial Turbine Design Flow.

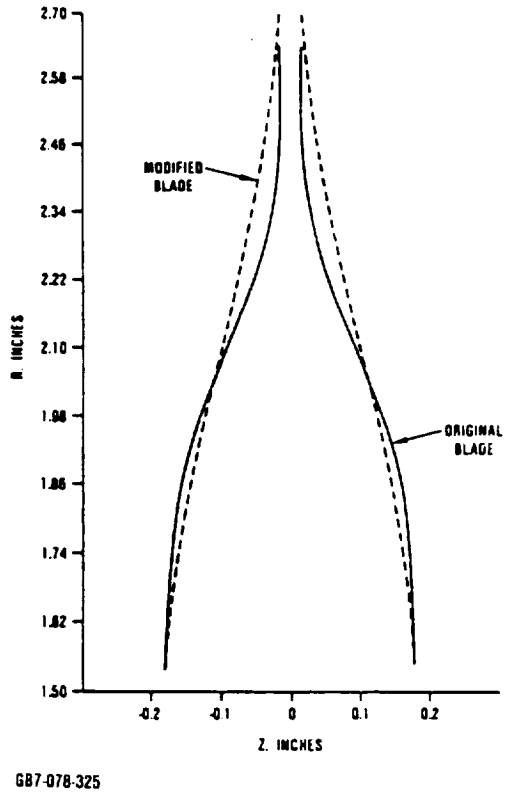

Figure 136. AGT101 Ceramic Rotor Z-Section.

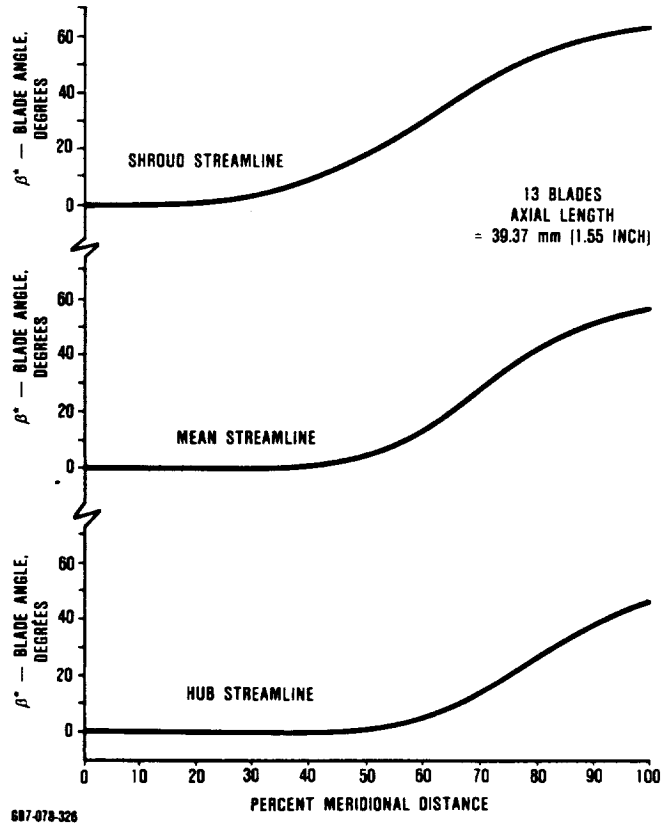

Figure 137. Turbine Rotor Blade Angle Distribution.

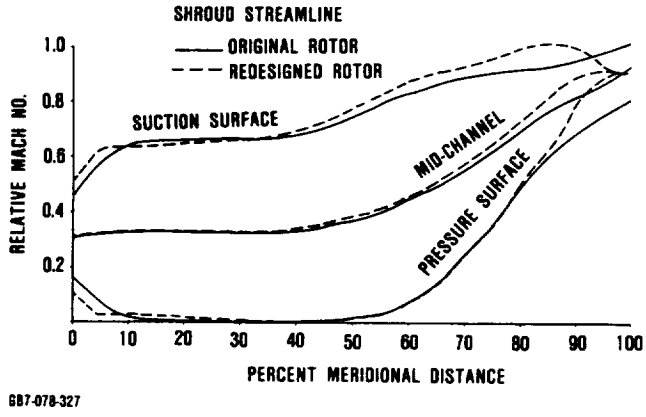

Figure 138. AGT101 Rotor Surface Velocity Distribution (Shroud).

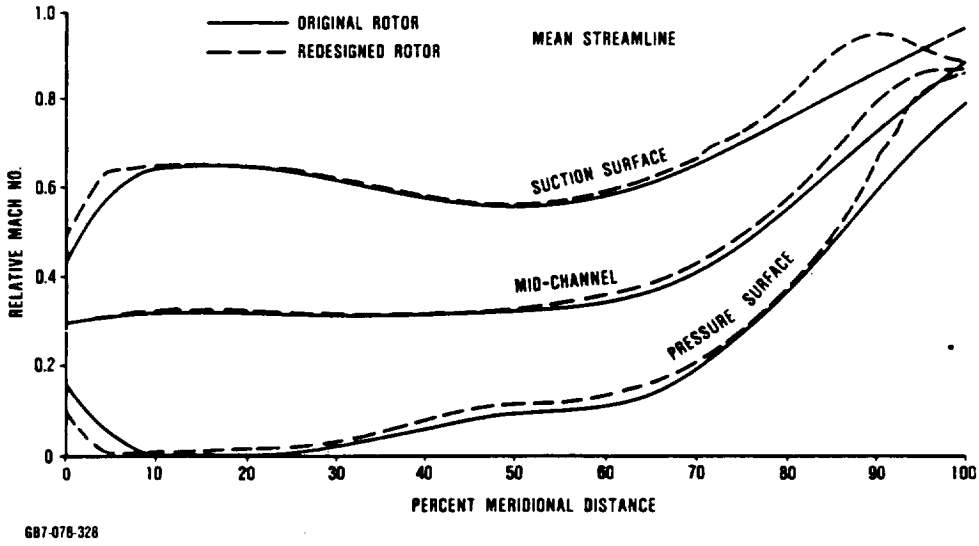

Figure 139. AGT101 Rotor Surface Velocity Distribution (Mean).

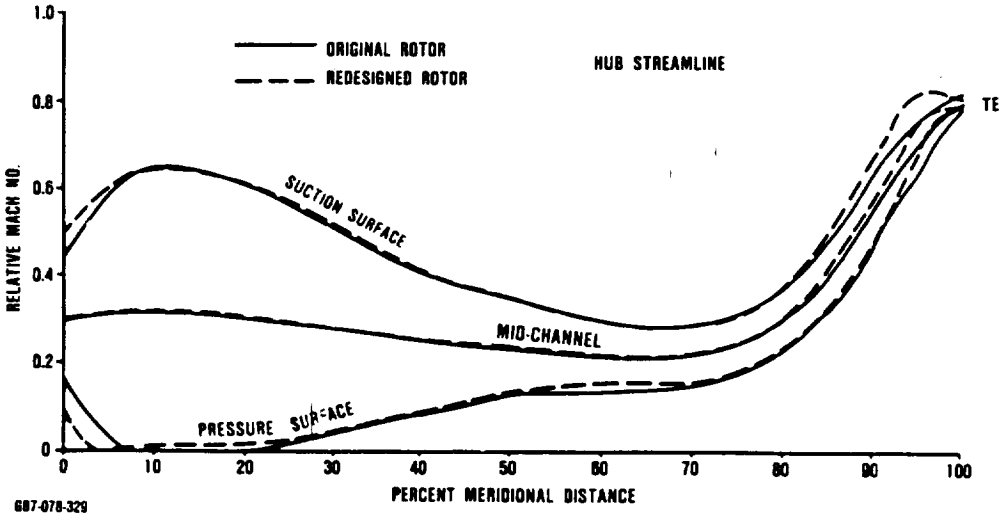

Figure 140. AGT101 Rotor Surface Velocity Distribution (Hub).

5.3 Combustor Development

5.3.1 Combustor Design

5.3.1.1 Variable Geometry

Emphasis on gaseous emissions, multifuel capability, and fuel economy in an automotive duty cycle created unique requirements for the AGT101 combustor. The combustor problem statement included the requirement to operate on gasoline and diesel fuel, with alternate fuels designated by the NASA project manager. Emissions goals were set as follows:

Oxides of Nitrogen, NOx	0.24 gm/km (0.40 gm/mile)
Total Unburned Hydrocarbons, HC	0.25 gm/km (0.41 gm/mile)
Carbon Monoxide, CO	2.1 gm/km (3.40 gm/mile)
Total particulates	0.12 gm/km (0.20 gm/mile)

The ceramic rotary regenerator, designed to recover waste heat, creates combustor inlet temperatures up to 1093C (2000F), which make it necessary that ceramic combustor components be capable of withstanding the extreme inlet and discharge temperatures.

In response to these requirements, and based on experience with a 46-month Variable-Geometry Combustor Development Program jointly sponsored by the U.S. Air Force Propulsion Laboratory and the U.S. Naval Air Propulsion Center, a variable geometry concept was examined for the AGT combustor. The initial variable geometry design included an axial pilot combustor in-line with the main combustor to assist in cold starting. Figure 141 shows the piloted premixed/prevaporizing variable geometry design with its performance specifications for idle and maximum power conditions.

Concurrent with the variable geometry effort, a fixed geometry design was evaluated empirically and analytically to determine the possibility of meeting emissions goals without the associated complexities of variable geometry. One of the tests conducted in this

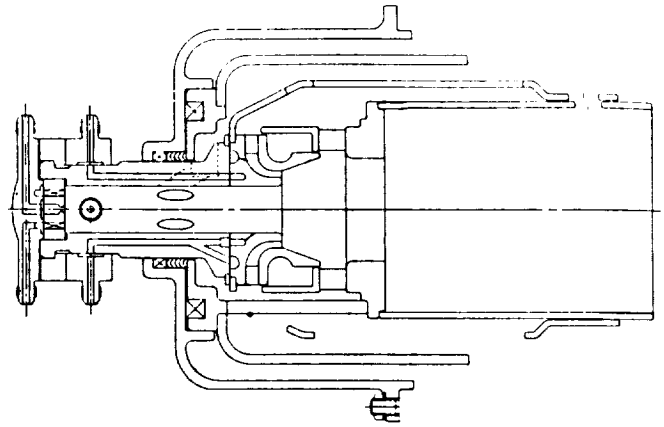

	MAX POWER	IDLE
PM/PV LENGTH, CM (IN)	1.1-5.1 (0.44-2.0)	0.36-1.7 (0.14-0.68)
REFERENCE VELOCITY, M/S (FPS)	76.2 (250)	17.2 (56.5)
PM/PV RESIDENCE TIME, MS	0.15-0.7	0.2-1.0
PM/PV AIR, PERCENT W_a	59.1	17.1
NOZZLE A/F	20.0	35.4
PM/PV F/A	0.0234	0.0183
PRIMARY ZONE τ, MS	1.33	5.9
LOADING PARAMETER, KG/M^3-KPA-SEC (LBM/FT^3-ATM-SEC)	0.003 (0.0197)	0.00098 (0.0062)

GB7 078-250

Figure 141. Piloted Premixed/Prevaporizing Variable Geometry Combustor.

evaluation utilized an element test rig with CO_2 injection to determine the fuel/air mixing performance of various combustor configurations. A number of different combustor geometries were evaluated for fuel-air mixing with the best configuration being a radial/axial swirler combination. Analytical modeling of this configuration showed streamlines and temperature fields to be very uniform. The element test rig was then used to test concentrations of CO, CO_2, NO, and HC emissions. Four different radial/axial swirler combinations were evaluated and are depicted schematically with airflow splits in Figure 142. Configuration No. 1, with a full radial and no axial swirler was the best all-around performer in emissions testing. Correcting the data to engine temperatures and airflow rate based on published lean-burn flame tube data revealed that CO and NO_x were below design levels (Figure 143). Based on these results, the lean-burn combustion concept was deemed capable of meeting emissions requirements and was

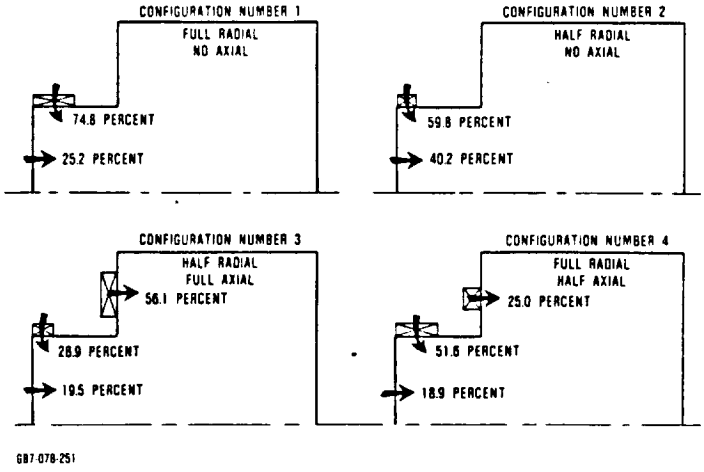

Figure 142. Combustor Configurations Investigated In Emissions Testing.

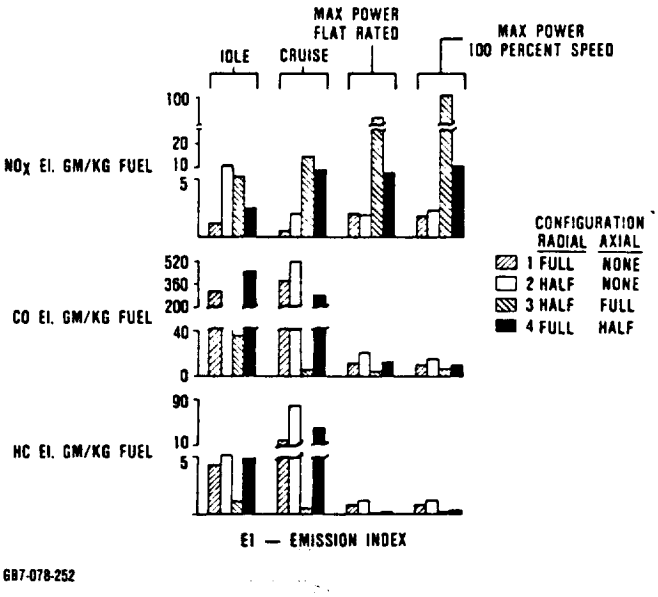

Figure 143. Element Test Rig Emission Test Results.

chosen for development using ceramic components. The design objective was to create a uniform, lean fuel-air ratio that minimized NO_X and oxidized CO and HC with high combustor inlet temperatures.

As seen in Figure 144, the all ceramic lean burn combustor is a simple, multiple piece

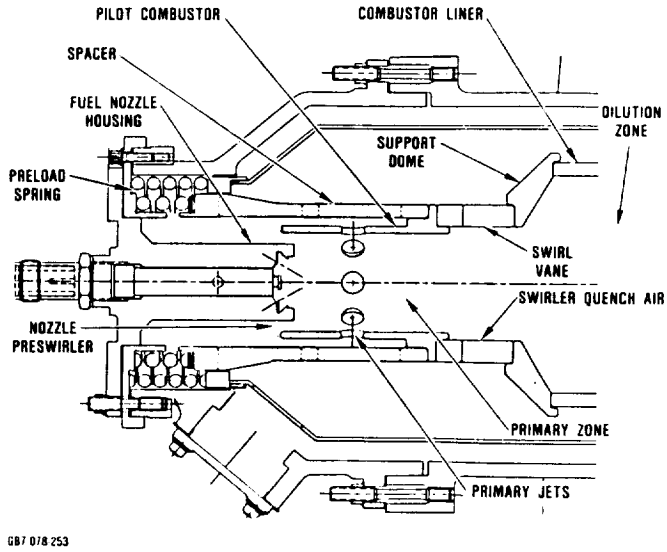

Figure 144. Current Configuration Ceramic Combustor.

construction which helps minimize thermal stresses. The actuators and sliding fits required with variable geometry are eliminated with fixed geometry, creating an inherently more reliable design. The ignitor is mounted on the centerline of the fuel nozzle, providing reliable start capability with cooler operating temperatures to prolong ignitor life. The combustor is composed of a primary burning zone immediately followed by a dilution/quenching zone. The primary zone is activated by 8 primary jets which carry 22 percent of the total airflow. A small axial swirler mounted on the O.D. of the fuel nozzle adds a 45-degree swirl to 14 percent of the total flow. The quench air enters approximately 2.54 cm (1 inch) downstream of the primary zone through a 30 degree radial swirler. The swirler carries 64 percent of the total airflow and is designed to penetrate and mix the products of combustion with relatively cool quench air. This minimizes the dwell time at high temperature when NO_X is produced and lowers the pattern factor at the turbine inlet. All of the combustor components are made of sintered silicon nitride (SSN) except for the combustor liner which is sintered alpha silicon carbide (SASC) and the fuel nozzle, which is made of Hastelloy X.

5.3.2 Combustor Development

5.3.2.1 Fuel Nozzle Development

Throughout the design evaluation of variable and fixed geometry combustor configurations, fuel nozzle development proceeded with emphasis on improved atomization and reduced heat-load. A duplex-type nozzle from The Delavan Corporation was initially selected for use in the variable geometry combustor. The 50-mm (2-inch) diameter duplex nozzle is shown in Figure 145. As depicted in the figure, three flow swirlers were incorporated; an outer swirler, inner swirler, and central swirler. Airflow entered through the outer swirler to atomize the secondary fuel while air through the inner swirler atomized the primary fuel. Central swirler air flow helped enhance the radial fuel-air mixing intensity in an effort to produce a more uniform fuel-air distribution. The nozzle was fabricated using a modular construction so that various swirler angles could be investigated. Although the duplex nozzle performed acceptably in rig testing, a simplex design, shown in Figure 146, matched its performance and offered the advantages of lower production cost along with

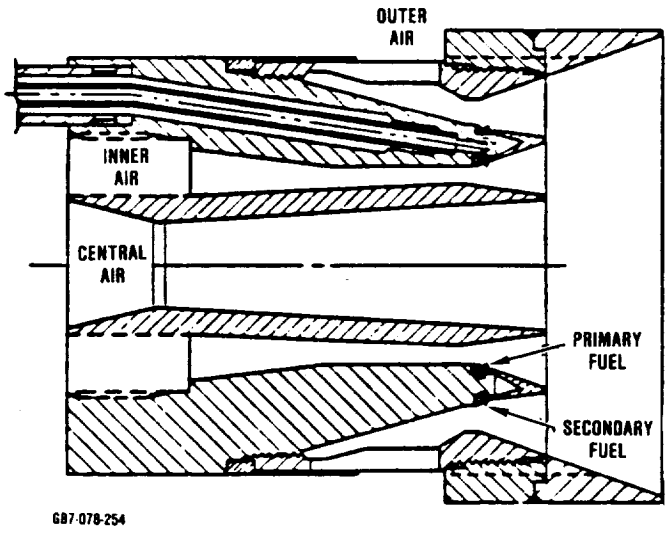

Figure 145. Duplex Airblast Fuel Nozzle.

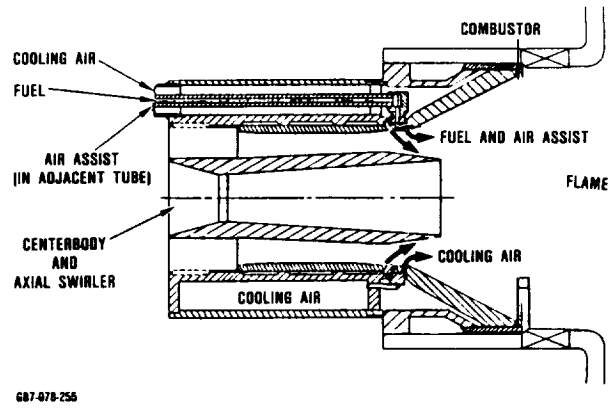

Figure 146. Simplex Fuel Nozzle.

adaptability to ceramic fabrication. Unfortunately, both exhibited fuel coking problems during rig testing. In order to solve the problem, air cooling was incorporated into the simplex design, along with air assist for enhanced fuel atomization. Fuel injection orifice diameters were also increased from 0.3 to 0.46 mm (0.012 to 0.018 inch) for greater particle tolerance. Additional development relocated the ignitor to the axial center line of the nozzle. This configuration produced good light-off results and lowered the ignitor operating temperature, however, coking was still occurring during rig testing at high combustor inlet temperature.

Garrett continued to address the coking problem by developing a modular fuel nozzle ignitor assembly as a replacement for the simplex. The modular construction was designed to allow installation of extensive instrumentation used to gather temperature and pressure data inside the nozzle. Like the simplex, the modular Garrett nozzle contained air assisted fuel injection and air cooling systems. Fuel injection was concentrated at the nozzle ID, near the ignitor, and fuel was directed toward the centerline of the combustor, creating a locally rich zone for ignition. After initial rig testing of the Garrett prototype demonstrated good light off and steady state performance, the Delavan Corporation was asked to design and fabricate a fuel

nozzle based on this design which would also be easy to manufacture. One of three nozzles delivered by Delavan was heavily instrumented with thermocouples and pressure probes to assess the potential of coking and fouling problems. Testing at most severe conditions showed the nozzle was sufficiently cooled to prevent coking and led to the selection of the Delavan nozzle for all subsequent engine and rig testing. The current configuration Delavan nozzle, shown in Figure 147, has been used successfullly in light-offs with JP-4 and gasohol and with some success using DF-2. Future effort will be directed at improving the nozzle's ability to atomize DF-2.

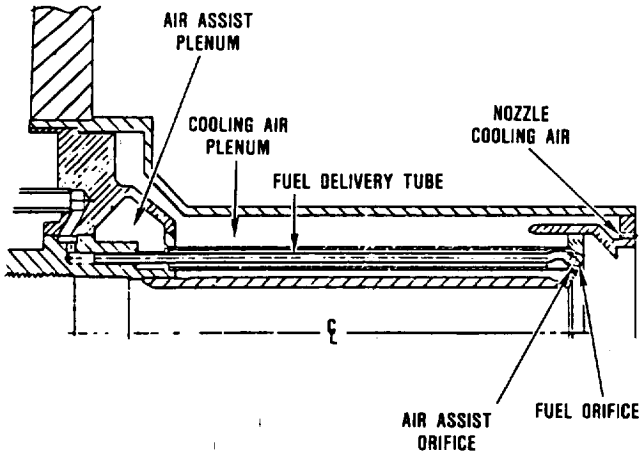

Figure 147. Delavan Nozzle Configuration.

5.3.2.2 Ceramic Combustor Development

After selection of the lean-burn, center body ignition combustor concept, hardware was produced in the configuration shown in Figure 148. The arrangement included a metal pilot combustor welded onto the fuel nozzle which proved the viability of the design through testing, but was not capable of 1371C (2500F) discharge temperatures due to material property limitations. After successful completion of 1149C (2100F) rig testing, the metal pilot combustor was replaced with a sintered silicon nitride pilot combustor which became a part of the spring-loaded stack of

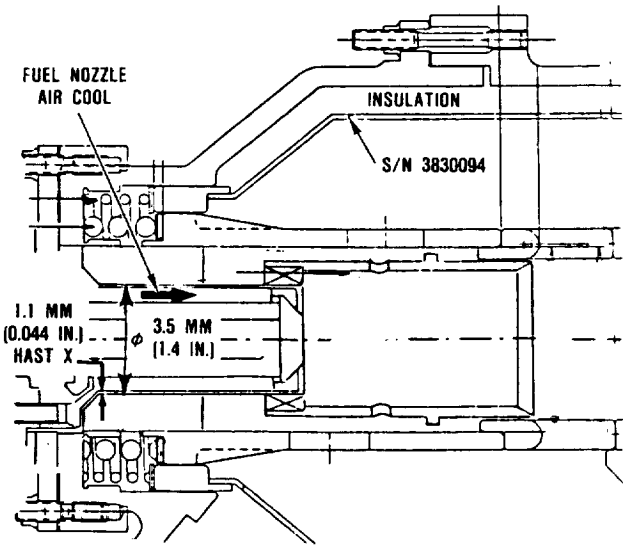

Figure 148. Pilot Combustor Proof-of-Concept (Metal Configuration).

ceramic components shown in Figure 144. This represents the latest configuration combustor for the all-ceramic engine. Data which defines combustor geometry and performance are listed in Table 16. The configuration has been used successfully in hundreds of hours of rig and engine operation. Testing has demonstrated its capability to operate on DF-2, JP-4, and gasohol. CO and HC emissions are well within program goals and the ceramic hardware has demonstrated excellent reliability in rig and engine operation. Further improvements are required in reducing No_x emissions and DF-2 cold start performance. These improvements are being pursued through an analytical/empirical approach involving 3-D combustion flow analysis, nozzle testing, and continued combustor rig and engine testing. This approach has resulted in a combustor iteration which contains an enlarged primary zone developed to improve DF-2 combustion and cold start performance. The configuration, shown in Figure 149, is currently fabricated in metal to facilitate instrumentation and geometry changes, and is also designed to be easily produced with ceramic materials. In a metal engine test, the combustor demonstrated light-offs with perfect consistency

Table 16. Combustor Data.

Parameter	Units	AGT101
Configuration		Can
Combustor Length	cm (In)	30.5 (12.0)
Diameter at Primary Zone	cm (In)	4.8 (1.9)
Length/P.2. Diameter		2.8 (6.3)
Combustor Airflow	kg/s (lbm/s)	0.729
Combustion Efficiency at Design Point	Percent	99.9
Airflow Split		
Primary Zone	Percent	22.18
Dilution Zone	Percent	63.41
Swirler/Injector	Percent	14.38
Inlet Static Pressure	kPa (psia)	394 (57.1)
Combustor Total Pressure Loss	Percent	3.6
Inlet Total Temperature	C (F)	975 (1787)
Average Total Exit Temperature	C (F)	1371 (2500)
Pattern Factor		<0.09
Combustor Surface Area	cm^2 (in^2)	897 (139.1)
Combustor Volume	cm^3 (in^3)	1627 (99.3)
Liner Wall Material		Sintered Silicon Nitride
Overall F/A Ratio		
Rich Blowout		7.100
Design Point Steady State		0.0118
Lean Blowout at Design Point		0.001
Primary Zone F/A Ratio of Design Point		0.0569
Fuel Injector Type		Air Assist
No. Fuel Injectors		1
Design Point Fuel Flow	g/s (lbm/hr)	3.9 (31.1)
Minimum Fuel Flow for Lightoff at Start Limit	g/s (lbm/hr)	0.34 (3.0)
Maximum Viscosity for L/O at Start Limit	centistoke	12
Turndown Ratio		21
Tolerance to Diffuser Exit Swirl Angle	±degrees	12
Types of Fuel Used		DF-2 JP-4 Gasohol
Heat Release Rate at Cruise	j/hr-kPA-m^3 (Btu/hr-atm-ft^3)	9.6×10^8 (2.61×10^6)
Aerodynamic Loading at Cruise	kg/m^3-kPA-sec (lb/ft^3-sec-atm)	7.5×10^{-5} (0.015)
Reference Flow Area	cm^2 (in^2)	67.1 (10.40)
Inlet Mach No.		0.06
Primary Zone Reference Velocity	m/s (ft/sec)	43.2 (141.6)
Residence Time at Cruise	ms	5.4
Emissions at Cruise		
NO_x	gm/kg fuel	13.5
CO	gm/kg fuel	2.4
HC	gm/kg fuel	0.21
Number of Ignitors		1

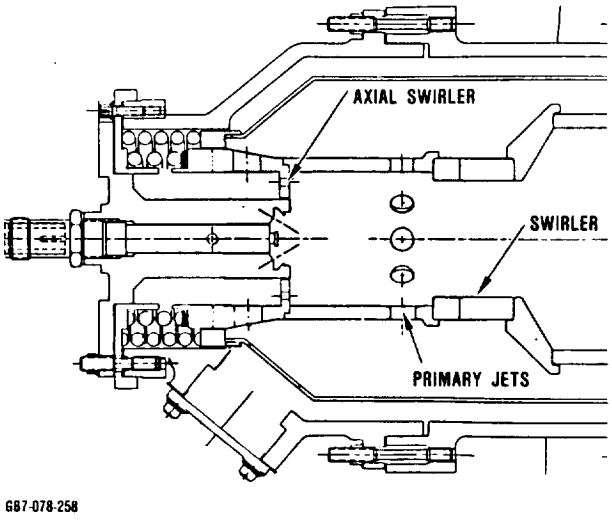

Figure 149. Enlarged Pilot Zone Combustor.

using both JP-4 and DF-2. It also demonstrated excellent temperature ramping characteristics which easily meet performance goals. Testing of the metal and ceramic versions of this configuration will continue to characterize its performance.

5.4 Regenerator System

The term "Regenerator System" involves the iterative design/analysis/test/evaluation of the following components as defined below and as shown in Figure 150:

- o Regenerator Core Matrix - The circular ceramic honeycomb waste heat transfer matrix.
- o Ring Gear Elastomer - The silicone based polymer used to bond the metallic drive/support ring gear to the ceramic core matrix.
- o Ring Gear - The cast iron ring gear used to drive and support the ceramic matrix in a rotary motion.
- o Drive Pinion and Support Rollers - The pinion gear designed to mesh with the ring gear while support rollers circumferentially support the ring gear and ceramic matrix assembly. These drive and support components, radially position the ceramic matrix and drive it in a rotary motion.

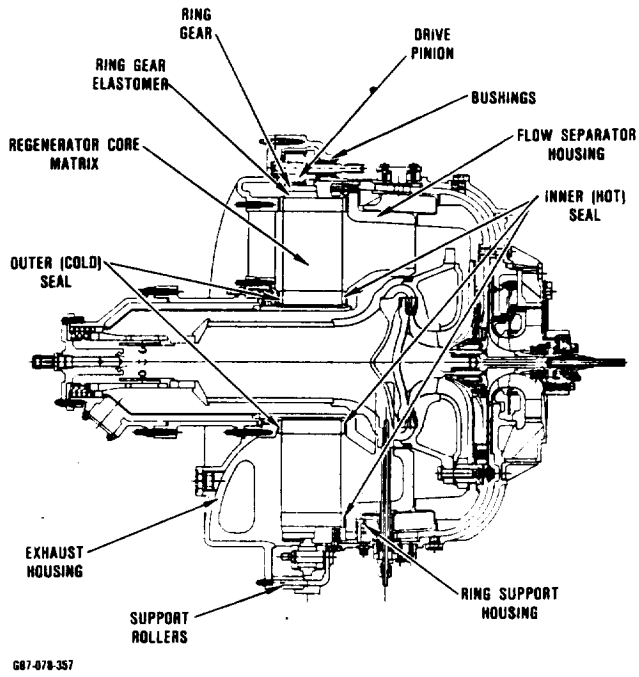

Figure 150. AGT101 "Regenerator System" Components.

- o Regenerator Drive and Support system Bushings - The bearing material developed for the drive pinion and support rollers.
- o Regenerator Seals - The combination of static metallic diaphragm seals and ceramic coated dynamic seals.
  - Hot Side Seal - Inner regenerator seal composed of two peripheral "C" shoes and a crossarm
  - Cold Side Seal - Outer regenerator seal composed of a single peripheral "C" shoe and a crossarm
- o Regenerator Seal Coatings - The ceramic rub coating applied to the metallic regenerator seal shoe substrate that provides high temperature dynamic sealing against the ceramic core matrix.

- o Flow Separator Housing - A ceramic housing that divides engine compressed air from turbine discharge exhaust gas and provides the platform for the inner regenerator seal.

- o Exhaust Housing - The metallic housing that divides engine compressed air from turbine discharge exhaust gas and provides the platform for the outer regenerator seal.

- o Ring Support Housing - The metallic housing that provides the platform for the flow separator housing.

Regenerator system development activities were conducted at Ford and at Garrett Turbine Engine Company (Garrett). Specific component development activities to each company are listed below and are discussed in detail in paragraphs 5.4.1 for Ford Regenerator Development, and 5.4.2 for Garrett Regenerator Development, respectively.

Ford Development Activities:

- o Regenerator matrix performance evaluation

- o Drive and support system design

- o Ring gear elastomer configuration design

- o Regenerator seal design

- o Regenerator system durability testing

Garrett Development Activities:

- o High pressure (HP) and low pressure (LP) gas regenerator flowpath design

  - Regenerator matrix flow pattern matching between HP and LP regenerator matrix inlets

    - o Flow separator housing
    - o Exhaust housing

- o Regenerator Seal Platform Design for minimum distortion/co-planar engine operation

- o Hot regenerator rig design/testing/evaluation-seal leakage evaluation with helium injection

- o Exhaust housing distortion analysis/test evaluation

- o Drive and support roller bearing/material tests

5.4.1 Ford Regenerator Development

The primary AGT101 program objectives for the regenerator system were to obtain an effectiveness of 92.9 percent, a total pressure loss of less than 7.5 percent at the maximum power operating condition, and a seal system capable of operation at 1090C maximum temperature with 3.6 percent leakage. In addition, the design and development of a durable drive and support system was required. This report summarizes the design and development efforts from October 1979 through June 1987 toward achieving the program objectives.

By using the extensive operating experience in the Ford 707 gas turbine engine, the initial regenerator system for the AGT101 program was designed to be capable of operating at a maximum system temperature of 980C (1800F). The system temperature requirement was subsequently increased to 1090C (2000F). Utilizing a regenerator matrix core with a wrapped, thin-wall, corrugated, sinusoidal fin from Corning Glass Works, the regenerator effectiveness was projected to be 90 percent at the maximum power operating condition. Therefore, an increase of 2.9 percent in effectiveness was required. In addition, regenerator seal system leakage at this condition was estimated at 7.2 percent based on comparable seals in the Ford 707 engine. A significant reduction in leakage was required to meet the AGT objective of 3.6 percent.

The AGT101 regenerator system components are shown in the photograph in Figure 151. This system consists of the regenerator seals, which sandwich the regenerator core. The core in turn is supported radially and rotated by the regenerator drive system components; a pinion roller, a fixed roller, and a

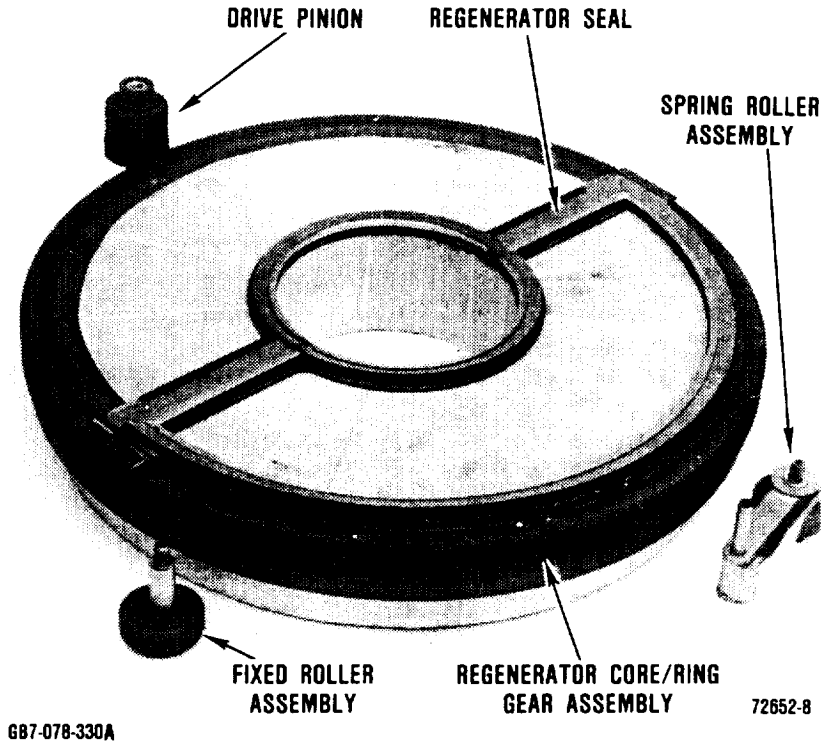

Figure 151. AGT101 Regenerator System Components.

spring roller. The development of these components are described in the following paragraphs.

5.4.1.1 Regenerator Seals

The primary purpose of this task was to develop new seal designs to achieve the program leakage objective of 3.6 percent of total engine airflow at the maximum power operating conditions. Six distinct phases of seal design were investigated analytically and experimentally to develop the final design.

Design criteria for the initial AGT seal (Phase I) were derived principally from seven years of experience in developing the Ford 707 seal, which involved thousands of hours of engine testing in various performance and durability cycles. This development was followed by an additional 218,000 regenerator-hours of engine tests in a joint Ford and DOE/NASA program to develop ceramic regenerators, which demonstrated over 4,000 hours of seal system durability. These design criteria were applied to the following areas of the new AGT seal system:

1) Weldless diaphragm system
2) Rubbing shoe size
3) Diaphragm fabrication technique

The "weldless" designation refers primarily to the fact that the diaphragm system is independent of the rubbing shoe system. This design demonstrated a proven record of reliability and performance in the programs mentioned above, and had demonstrated uniform seal loading and coating wear characteristics. With the additional surface contact of the diaphragm on the rubbing shoe, the weldless seal provided the additional benefit of friction damping which is essential for maintaining shoe contract on the regenerator in the dynamic operating modes.

The relationships of width and thickness in both the crossarm and peripheral shoes were

also derived from the 707 seal. The inboard (hot) seal assembly is positioned vertically to the flow separator housing by means of a retaining rig. Peripheral seal component stiffness had to exceed the critical buckling stresses to prevent radial distortion when the limits of constraint (due to thermal growth) were reached, but also must have sufficient flexibility to conform to the profile of the regenerator core. Wider shoes tend to reduce leakage by creating a better labyrinth effect. Since low leakage was a prime objective for the AGT regenerator system, the peripheral shoe width (190 mm) is equivalent to the 707 system. The crossarm shoe width is 38.0 mm compared to 41.1 mm for the 707.

The diaphragm system, which is the compliant member between the shoe and engine structure, was also based on 707 technology. The diaphragms were formed from foil material 0.0762 to 0.203 mm thick. The material that had proven durability, Inconel X750, was selected for the initial fabrication.

In order to design a low leakage regenerator seal system, the following design considerations required investigation:

1) Control of engine structures that affect seal operating clearance.

2) Diaphragm design to optimize seal load for minimal leakage without excessive coating wear and drive torque requirements.

To assist in the development of a low leakage seal system, the following test rigs were utilized:

1) Static seal leakage rig to monitor design changes.

2) Test fixtures to establish seal assembly mechanical load characteristics.

3) Hot test rig to evaluate system leakage and coating wear characteristics.

Seal Leakage Development

Starting with the Ford regenerator seal technology as a baseline, further reduction of seal leakage was a development process in which seal systems were initially analyzed via computer programs for shoe loadings and diaphragm clearance throughout their operating range. Seals were then fabricated for evaluation in the static seal leakage fixture at room temperature. Concepts that demonstrated leakage reduction in the static seal rig were then tested under hot operating conditions in the regenerator test rig and engine. The rig and engine results were used to update the computer analysis and refine the design of the next generation of seals. Such an approach was successful in the development of seal systems for other engines at Ford.

A typical regenerator seal cross-section is illustrated in Figure 152. The seal working height (SWH) represents the total clearance for the seal assembly resulting from the installed clearance minus the axial movement of the adjacent engine structures and regenerator core at specific engine conditions. The diaphragm clearance (C) represents the amount of clearance from the sloid height of the assembly. Regenerator system build clearance is defined as the total diaphragm clearance (2C) that exists for both seals at engine assembly. The total above shoe force (F_T) imposed on the rubbing shoe, consists of the mechanical loads from the deflection of the diaphragm elements in addition to the air pressure force. The combined forces acting above the shoe can be represented equivalently as a force (F_T) acting at a specified distance (D_U) from the inner edge of the rubbing shoe, as illustrated on Figure 152.

The primary engine structures that control regenerator seal working height are the flow separator housing and exhaust housing. Axial thermal growth and distortion of these components directly affect the SWH.

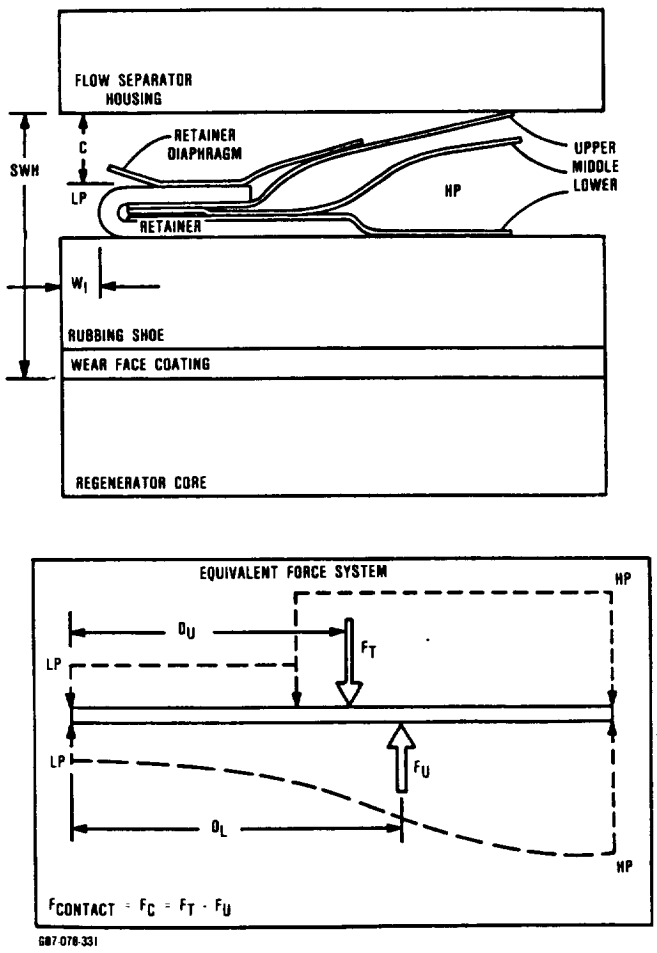

Figure 152. Typical Regenerator Seal Schematic.

To minimize this problem, the flow separator housing was redesigned to be positioned and supported off the outer casing. This change resulted in acceptable variations in SWH for both the metallic AGT and ceramic AGT engines and allowed the same diaphragm system to be used on both engines.

The AGT101 seal design evolved through a series of configurations, or phases, shown in Figure 153. The initial design, Phase I, was based on prior Ford experience combined with extensive analysis. Subsequent designs were generated as a result of static leakage testing, hot regenerator rig testing, and AGT101 engine testing, supported by additional loading and thermal analysis.

Analytical Regenerator Design Methodology

In order to analytically determine the diaphragm load and stress as a function of clearance, the diaphragm load characteristics were required input to the "core position" analysis computer program, which performed a summation of forces and moments imposed on the regenerator. Once the operating plane was determined, the variation in force and stress distribution for each component of the regenerator seal system was defined.

The main objective for the regenerator seal system design was to achieve sufficient contact force (F_C) with minimal variance at each seal component location to provide effective sealing with coating wear at a uniform and an acceptable rate. Contact force (F_C) is defined as the net load resulting from the above shoe diaphragm mechanical and pressure forces (F_T) that are partially offset by the undershoe pressure force distribution (F_U) that exists between the seal wear face coating and the regenerator matrix face (Figure 152). The undershoe pressure distribution is a function of the labyrinth effect due to leakage characteristics between the shoe and regenerator core.

In order to minimize contact force on the LP carry-over portion of the crossarms while ensuring contact on the HP carryover portion, optimization of the location of the retainer with respect to the LP edge of the rubbing shoe (W_I) was required. For the initial AGT regenerator seal system, the crossarm retainer was positioned 17.8 mm for the LP carryover portion and 2.54 cm for the HP carry-over position. The significance of the estimated contact force levels for the reference seal system was established by the coating wear pattern of the actual seal hardware after rig and engine testing. Seal design changes were suggested by the leakage test data and visual examination of the coating contact pattern. Input data to the core position analysis was modified to simulate the proposed design

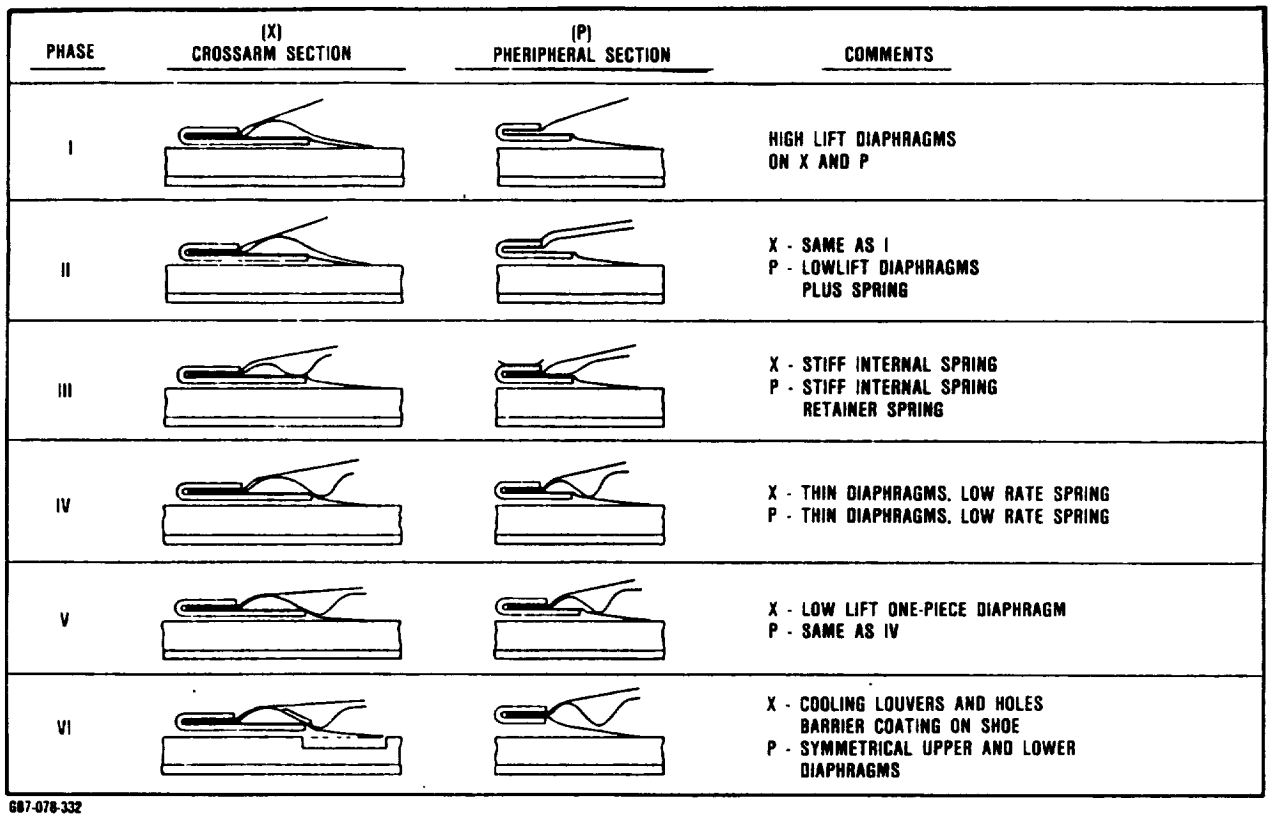

Figure 153. Regenerator Seal Design Phase Comparison.

changes and the results were compared on a relative basis to the baseline regenerator seal system. In this manner, the comparative results served as a guideline to provide direction to additional design changes. This procedure was used in previous engines for optimizing the regenerator seal system design.

The initial Phase I seals evaluated in the static seal rig at the design clearance exhibited leakage slightly above the initial objective of 7.2 percent of total engine airflow at the maximum power operating condition. Subsequent testing at Garrett indicated marginal seal loading and subsequent high leakage at part power engine conditions.

The Phase II seal configuration featured a spring diaphragm inserted between the two sealing diaphragms, and provide the seal loading required to reduce seal leakage. Parametric studies in the static leakage rig indicated the need for increased loading of the lower sealing diaphragm against the metal seal shoe in order to reduce leakage at low pressure levels.

The Phase III regenerator seal diaphragm design evolved from parametric studies in the static seal leakage rig to minimize leakage at low pressures.

The most significant change was the addition of a supplementary spring mounted on the retainer. Engine and rig testing indicated substantially improved leakage over Phase I and II, though seal loading was excessive.

A parametric test series was conducted on the Phase III configuration in parallel with a parametric analysis. This work evaluated the effect of seal loading on seal leakage.

Through optimization of load distribution, it was found that seal loading could be substantially reduced without sacrifice of leakage.

The main objective for the Phase IV seal system were to preserve the leakage characteristics associated with the Phase III design with a further reduction in mechanical load characteristics to reduce drive torque requirements. Additionally, the Phase IV seal incorporated cooling passages which used a controlled amount of leakage to maintain the diaphragm temperatures within the limits of diaphragm material capabilities.

Through another series of parametric tests and analysis, further improvements in leakage and mechanical loading were attained.

The mechanical load characteristics for each of these seals were measured. The load characteristics indicated the Phase IV design was an effective compromise between the Phase I and Phase III designs. Consequently, the actual hardware substantiated the analytical predictions.

Rig and engine testing indicated that in the dynamic thermal environment of a regenerator system, drive loads for the regenerator were higher than the Phase III designs. Leakage was equivalent to the Phase III configuration, though the allowable SWH tolerance was much more broad with the Phase IV seal.

Based on the test results for the Phase IV seal design, a new design iteration (Phase V) was initiated. The design objectives for the Phase V seal (Figure 153) configuration were to further decrease the leakage and drive torque requirements. In order to accomplish these objectives, the Phase V design featured an integrated crossarm diaphragm which eliminated the inner secondary diaphragm that was used in previous designs. Tests in the static seal rig indicated a significant portion of the total leakage occurred at the inside and outside corners. In addition, the integrated crossarm diaphragm had a reduced lift angle, which would reduce the mechanical load characteristics and drive torque requirements.

In addition to these design improvements, the quality of the prototype hardware was improved through the procurement of new tooling and improved processes.

An interim quality control standard was established at that time for the static seal leakage rig to ensure that low leakage seals would be sent to Garrett for engine and test rig evaluation. A 0.006 m^3/s static leak test requirement per seal (inboard or outboard) at a 7.0 mm seal working height (SWH), was established. This represented the state-of-the-art at this time for the Phase V seals. Hot and cold seals that totaled 0.011 m^3/s leakage at 7.0 mm SWH in the Ford static test rig were evaluated in the hot regenerator rig at Garrett using the helium tracer technique and indicated a leakage of about 5.5 percent.

Additional testing in the static seal rig with symmetrical upper and lower outer peripheral diaphragms and equal length retainer legs demonstrated a potential 20 percent reduction in static leakage. This concept was adopted as the basis for the next generation seal design, which was designated as Phase VI, as illustrated on Figure 153. In addition, the Phase VI design can accommodate more cooling air for the inboard (hot) crossarm seal compared to Phase V.

Additional features of the Phase VI seal configuration included a crossarm thermal barrier coating for improved seal diaphragm cooling and bore pressure relief slots in the cold seal inner periphery.

Phase VI seals qualified with less than 0.011 m^3/s leakage at 7.0 mm seal working height. These hot seals were also made with reprocessed, used shoes. Based on engine exhaust flow at full power conditions and corrected for ambient temperature, a static seal rig leakage of 0.004 m^3/s per seal was estimated to be adequate to meet the program objective of 3.6 percent for the regenerator system. Therefore, the combination of the low leakage Phase VIB cold seal (0.004 m^3/s) with one of the Phase VIB hot seals (0.005 m^3/s should nearly meet the program objective in an engine.

Seal Design Summary

The initial AGT101 regenerator seal system was based on prior experience with the Ford 707 gas turbine engine combined with extensive analysis. The systematic reduction of seal system leakage toward achieving the program objectives was described. Design methodology was based on a development approach consisting of six unique phases. Design changes were incorporated based on static and dynamic test rig evaluations supplemented by analysis that provided guidance for each design iteration. The initial design, which was very sensitive to operating clearance, was capable of achieving the original leakage level of 7.2 percent at design clearance. Subsequent designs systematically reduced leakage to 50 percent of the initial level. In addition, sensitivity to operating clearance was practically eliminated for clearance variations within 0.63 mm of design. The curves in Figure 154 illustrate these trends during the AGT101 regenerator seal development effort. Seal wear-face coatings were changed where necessary in the final design to accommodate the design temperature levels.

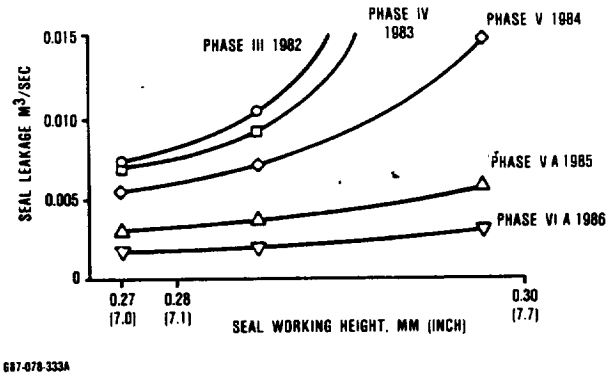

Figure 154. Static Seal Leakage Comparison for Seal Design Phases.

Seal Diaphragm Cooling

To help establish the environment for the hot side seal diaphragms a detailed finite element model of the AGT flow separator housing was generated and a heat transfer analysis was performed. Based on this analysis, the temperature level at the inner circular portion of the RBSN or LAS FSH will be 1040 to 1065C for a gas inlet temperature of 1090C. The linear segments that connect the inner and outer circular sections of the FSH were estimated to operate at 930C.

In order to accommodate the 1090C regenerator system operating temperature associated with the all ceramic engine, the regenerator inboard (hot) seal crossarm required diaphragm cooling to keep the metal diaphragm temperatures below 930C. This design (Figure 155) had a funnel incorporated into the crossarm end diaphragm, which allowed cooling air to flow between the upper and lower diaphragms. A transfer tube at the corner allowed the air to continue through the high pressure side of the inner periphery. The amount of cooling air flow is dependent on the pressure differential that exists in the channel. For discharge holes in the middle diaphragm at the center of the HP periphery, the pressure differential (less than 1.7 kPa) establishes the minimum rate of cooling air flow. For maximum cooling, holes in the retainer (Figure 155) allow the air to discharge into the center hole cavity, which is vented to the exhaust duct. Use of this discharge location would require the incorporation of a restriction at the opening of the funnel on the crossarm end diaphragm to throttle the cooling flow required.

A three-dimensional heat transfer analysis program was modified to analyze the seal cooling system (Figure 155). To minimize the number of nodes and elements, three axial locations were selected (X=O, 130, 254 mm), which corresponds to cooling flow inlet at the end of the crossarm, transfer location from linear to peripheral, and cooling flow exit location, respectively. Convection coefficients were estimated based on cooling air flow rate and cross-sectional area of the channel. Since the cooling flow exists on both sides of the main support leg of the middle diaphragm, the heat transfer coefficient can be maximized. By incorporating an appropriate number of openings (slots or louvers) in the

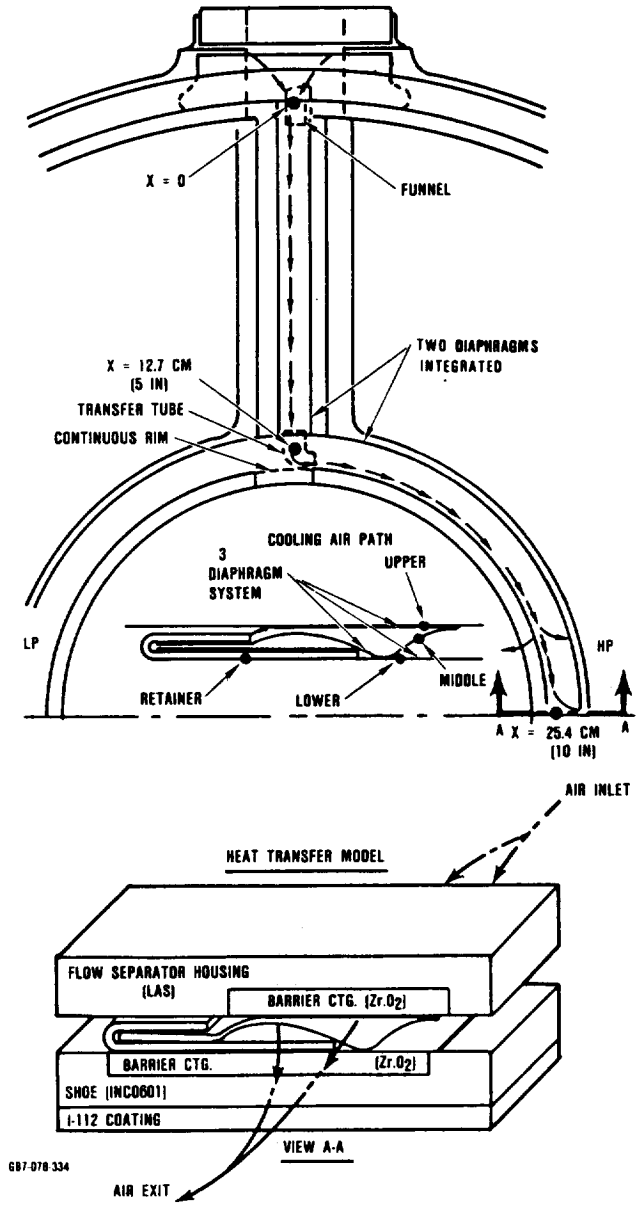

Figure 155. Inboard (Hot) Seal Crossarm Diagram Cooling Schematic.

axial direction in the middle diaphragm, the flow can be interrupted to prevent boundary layer build-up and promote localized turbulence, which increases the localized heat transfer coefficient. In addition, convection coefficients between the upper diaphragm and flow separator housing were also estimated based on leakage.

As illustrated on the model (Figure 155), the portion of the middle diaphragm, which is in contact with the upper and lower diaphragms, represents a direct conduction path between the FSH and the rubbing seal shoe. Consequently, a thermal barrier coating such as zirconium oxide was required on the back side of the rubbing shoe to reduce temperature in this region and minimize cooling air requirements. The inner circular portion of the FSH also required a thermal barrier coating, though in practice, this was not attempted due to development considerations of this LAS ceramic component.

The design concept was evaluated for cooling flows varying from 0.0004 to 0.0014 kg/s, which corresponds to 0.25 percent (minimum) and 0.85 percent leakage, respectively. For each cooling flow, the convection heat transfer coefficient was increased 20 percent to simulate interrupting the flow.

The middle diaphragm temperature distribution for axial locations of 130 mm and 250 mm as a function of cooling flow are illustrated on Figure 156. The barrier coating thickness for the seal substrate and FSH inner circular section were both 1.3 mm. The minimum cooling flow (0.25 percent) was sufficient to keep the middle diaphragm temperature below 927C (1700F) for the straight portion of the crossarm (X = 0 to 130 mm), as shown in Figure 156. In order to cool the circular portion of the crossarm (X = 130 mm to 250 mm) to the design temperature level, the cooling flow requirement was 0.85 percent. The original leakage objective of 3.6 percent included a 0.25 percent allowance for cooling the hot seal crossarm diaphragm. Based on this analysis, an additional 0.60 percent leakage was required to sufficiently cool

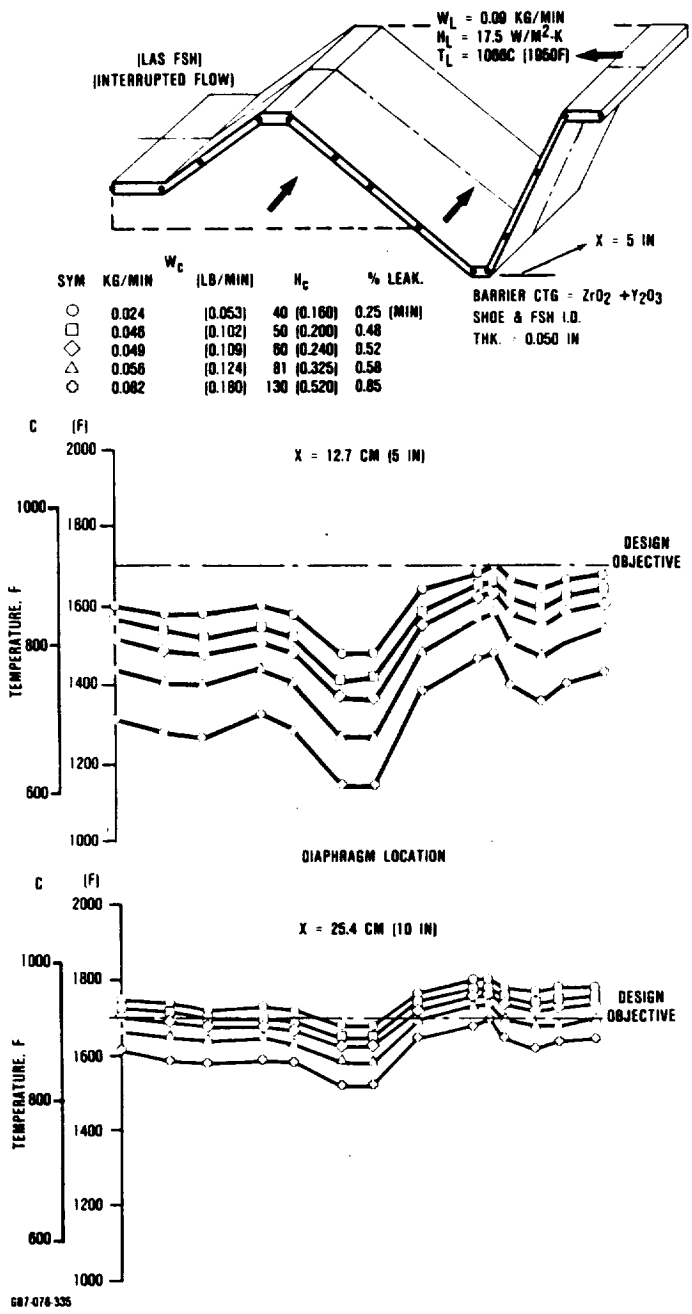

Figure 156. Middle (Support) Crossarm Diagram Temperature Distribution.

the circular portion of the crossarm diaphragm.

The cooling analysis shows that the middle diaphragm is coldest at the outboard end of the crossarm and progressively increases until it reaches a maximum at the center of the inner peripheral section. Core position analysis shows that the seal clearance in this region will be about 16 mm, and the average diaphragm stress level at this clearance, as estimated by MENTOR II, is about 139,000 kPa. Examination of Rene 41 creep data shows that this will cause some local yielding. This local yielding will be confined to the spring in the peripheral section of the crossarm where the metal temperatures are highest. It is doubtful that any yielding will occur in the straight section of the crossarm where the temperatures are much lower. As the spring yields the local stress is reduced to the point where further creep occurs at a very low rate. The spring will still provide containment for the cooling air and it will still separate the diaphragms so they can be pressure loaded. It is difficult to believe that any significant increase in leakage will occur.

In summary, the regenerator seals have been developed through six distinct phases and now appear capable of meeting the program leakage objectives. In addition, they have shown acceptable levels of drive torque and the capability of operating over a wide range of seal working heights with little change in leakage. Cooling air is required to keep the diaphragm temperature of the hot seal to acceptable levels. The cooling air requirements are modest and any diaphragm creep that occurs will be limited to a local region at the center of the inner, hot peripheral diaphragm. This creep is not expected to result in any significant increase in leakage.

5.4.1.2 Regenerator Seal Coating Development

The primary concern for achieving a 1090C regenerator system was the upper temperature limit of the hot seal crossarm wear face

coating I-112. This was the only Ford proprietary seal coating that did not have documented durability at the higher AGT crossarm temperature conditions. In order to establish the upper temperature limit for the I-112, an existing test rig was modified to increase the maximum test temperature from 815 to 1090C (Figure 157). The primary modification was replacement of the metal test sample holder with a ceramic holder.

The stationary test sample was loaded against the rotating test core by a compression spring. A lever arm, which was pinned to a center shaft, applied the torque reaction force against a calibrated load cell. By knowing the applied force (P), torque reaction force (F_R) and physical dimensions of the sample, the sliding coefficient of friction (μ) could be determined. Periodic measurements of sample thickness determined the seal coating were rate.

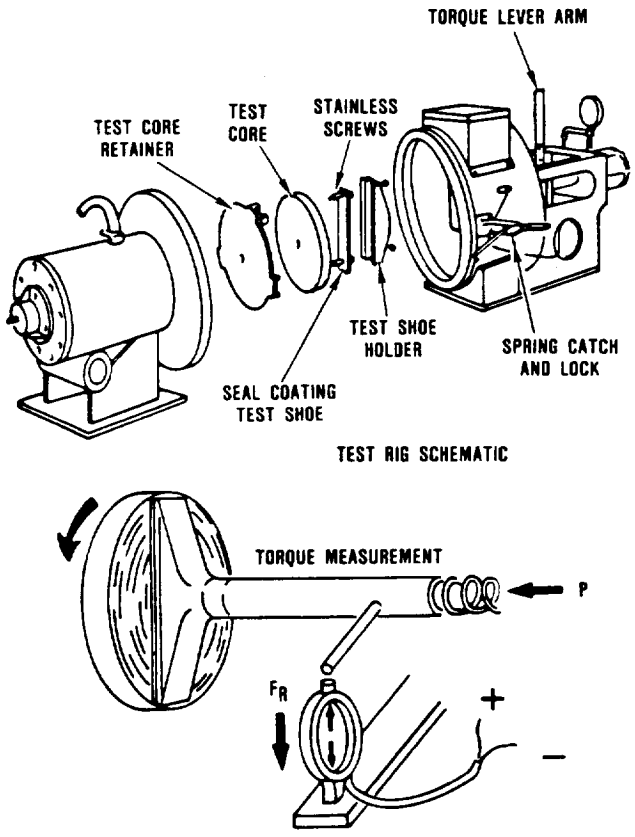

Figure 157. Regenerator Seal Coating Wear Test Rig.

In order to determine the upper temperature limit of the I-112 coating to be assured that it had 1090C capability and to be confident that its friction and wear characteristics could be controlled during processing, the following parameters were investigated:

1) Chemical composition and particle size distribution of the coating powder.

2) Spraying procedure for deposition of the coating powders on the metal substrate.

3) Interface coatings to accommodate the difference in thermal expansion between the I-112 coating and the metal substrate.

4) Substrate serrations to form a mechanical bond attachment of the coating.

Fourteen samples were tested for more than 2000 total hours in order to evaluate the above parameters.

All of the I-112 powder evaluated was processed by Ferro Corporation. In order to determine the optimum process for the I-112 powder using the equipment and facilities at Ferro Corp., three different batches of powder were processed. Each of these batches were within the Ford specification for chemical composition and particle size distribution.

The primary evaluation of the I-112 powder and plasma spray process was dependent on coefficient of friction and wear rate as measured in the seal wear rig. For the Ford 707 gas turbine engine, the acceptance criteria for the I-112 coating were as follows:

1) Coefficient of friction (μ): less than 0.35 at operating temperature and 68.9 kPa load

2) Wear rate (w): less than 0.020 mm/100 hr.

Since the loads in the AGT101 regenerator seals were approximately the same as those in

the 707 seals, a coefficient of friction less than 0.35 and a wear rate of less than 0.020 mm/100 hr. should result in acceptable drive torque and seal life in the AGT engine based on 707 experience. These same criteria were used, therefore, to establish the acceptability of the I-112 coatings that resulted from variations in composition, particle size, spraying procedure, etc.

For the 14 samples evaluated in the wear rig, which consisted of the three different batches of powder as well as variations in spraying process, the I-112 coating demonstrated friction and wear characteristics well with the Ford acceptance criteria for exposure up to 1090C and 68.9 kPa maximum load.

To evaluate the substrate bond coating, samples sprayed with commercially available METCO 443, METCO 447, and GE Superalloy in place of NiCr were evaluated. In order to evaluate the effectiveness of the deep serrations, additional samples without serrations were also tested. A summary of the temperature capabilities of the various test combinations are listed on Table 17. Some improvement was evident with METCO 443 and METCO 447, which appeared to increase the temperature capability approximately 28 to 56C. The GE Superalloy appeared to satisfy the 1090C objective.

The effectiveness of the deep serrations are clearly illustrated (Table 17). Temperature capability appeared to be increased 55 to 166C compared to a non-serrated sample.

Based on visual observations of hot flow path components tested in the initial hot structures rig and ceramic engine at 1090 to 1150C turbine inlet temperatures (TIT), the I-85 coating for the hot seal outer peripheral shoes appeared to be marginal. Although the copper based I-85 did not delaminate, soften or experience significant wear, trace amounts of copper were found to be the cause of sticking between other ceramic components. In order to increase the upper temperature limit, I-151 was evaluated as a replacement for the I-85 coating on these shoes. Based on wear rig tests at Ford in the early 1970's, the I-151 (zinc-oxide) had 112C higher temperature capability compared to I-85 (copper base).

The initial seals with I-151 installed in the ceramic engine at Garrett experienced delamination in the I-151+I-39 interface bond region. An evaluation of the I-151 coating was conducted which established that the coating powder used was not within specification. Since the coating vendor had difficulty producing this coating, it was decided that the I-151 would not be pursued.

Table 17. Test Sample Temperature Limit.

Interface Bond Coating	Maximum Temperature, C		Total Test Time, Hrs	
	Without Serrations	With Serrations	Without Serrations	With Serrations
NiCr (Standard)	920 - 950	980 - 1010	288	1108
METCO 443	870 - 900	1010 - 1040	45	135
METCO 447				160
GE Superalloy	920 - 950	1090 +	100	200

As a replacement for I-151 peripheral seal components, modified versions of I-85 with improved plasma spray parameters as well as I-112 peripheral components were assembled for engine evaluation at Garrett. Testing seal assemblies with improved I-85 or I-112 in the ceramic engines did not cause sticking between ceramic components. As expected, seal assemblies with I-112 in place of I-85 did, however, have higher drive torque requirements.

For the final AGT seal configuration (Phase VIB), the best combination of wear face coatings that would satisfy the 1090F regenerator inlet temperature requirement was as follows:

1) Hot (inboard) seal: I-112 on all components

2) Cold (outboard) seal: Improved I-85 on all components except for I-112 on the circular section of the crossarm.

In summary, two of the Ford proprietary wear face coatings (I-85 and I-112) have been adapted for the higher temperature requirements associated with the AGT program. Improved plasma spray parameters have prevented the I-85 wear face coating from delaminating at the higher temperature conditions of the outboard seal assembly. I-112 combined with GE superalloy bond coating on a serrated inboard seal crossarm substrate has satisfied the 1090C temperature requirement.

5.4.1.3 Regenerator Core

The AGT101 regenerator core was evaluated in terms of core performance, thermal and mechanical stress, and material thermal stability.

The design performance objectives for the AGT regenerator are 92.9 percent effectiveness with less than 7.5 percent pressure drop at 100 percent gas generator speed. To meet the 3.6 percent leakage objective, the through-wall porosity leakage in the core must be less than 0.5 percent. In order to satisfy the 1090F regenerator inlet temperature requirement, the regenerator matrix must have sufficient thermal stress capacity. Durability is dependent on matrix material stability at elevated temperatures for extended time.

During the AGT101 program, regenerator cores have been supplied by Corning Glass Works, and NGK-Locke. The Corning cores are fabricated as a two-sheet wrapping process with aluminum-silicate (AS) material. NGK-Locke utilize the extrusion process with magnesium-aluminum-silicate (MAS) material. Geometry and performance for each of these core configurations are compared in Table 18.

The Corning aluminum-silicate (AS) wrapped thin-wall sinusoidal matrix satisfied the pressure drop objective but is 1.0 percent low in effectiveness. Corning was provided additional funding to fabricate samples of an extruded AS matrix with a rectangular cell shape and 0.089 mm material wall thickness to meet the AGT101 regenerator effectiveness and pressure drop objectives. The wall thickness in the sample provided was thicker than anticipated. The estimated performance for this matrix geometry (Ext. 1) was 0.8 percent lower effectiveness than the original matrix geometry with equivalent pressure drop. Even though the extruded rectangular matrix is more efficient than the sinusoidal geometry, the thicker fin wall more than offsets any expected gain in effectiveness. Further development of the extruded Corning matrix would have extended beyond program termination.

In order to achieve the improved effectiveness required, new tooling was developed by NGK. NGK has fabricated full-size cores with three different matrix geometries, labeled C0.3, C0.7, and C0.9 and defined in Table 18. In addition, tooling was developed for a fourth fin geometry (C0.8). The C0.7 matrix geometry is an isosceles triangular fin with 0.089 mm wall thickness. The C0.8 and C0.9 structures, which have different aspect ratios, are rectangular with a nominal 0.114 mm wall thickness. Regenerator core performance can be projected based on estimating the heat transfer and pressure drop characteristics of

the fin geometry utilizing shuttle rig test data for similar geometries. The predicted performance for the four NGK fin geometries are listed on Table 18. Estimated performance predictions indicated the program performance objectives could be attained with the C0.7 fin geometry, provided a more dense material could be developed to reduce excessive wall porosity leakage.

Due to the greater wall porosity of the original NGK MAS regenerator matrix material, core leakage across the crossarm and through the inner and outer circumferential was higher when compared to the more dense Corning material. NGK took two approaches toward resolving this problem. First, they developed coatings for the inner and outer circumferences, in addition to impregnating the matrix walls. This method was not effective in reducing porosity in the thin wall C0.7 or C0.8 matrixes. Then, they fabricated full-size cores with their dense, less porous revised MAS material designated MAS-A.

NGK has demonstrated significant improvements in modifying their standard magnesium-aluminum-silicate (MAS) material in order to achieve the porosity leakage objective. The improved MAS-A incorporated in-

Table 18. Regenerator Core Performance.

	FIN ID	Wall Thickness, mm	Cell Density, Cells/cm^2	EFF, %	P/P, %	Porosity Leakage, %
Goal @ N_E = 100 Percent	--	—	—	92.9 Min.	7.5 Max.	0.5 Max.
Corning:						
Wrapped Sinusoidal	$T_{14.2}$	0.064	203.0	91.9	7.3	0.20
Extruded Rectangle	Ext.1	0.127	161.9	91.1	7.2	0.20
NGK:						
Extruded Isosceles	C0.3	0.140	142.6	90.1	6.0	0.30
Extruded Isoceles	C0.7	0.076	234.0	93.6	7.3	1.7
Extruded Rectangle	C0.8	0.109	215.4	93.3	9.2	1.0 (est.)
Extruded Rectangle	C0.9	0.119	172.8	91.4	7.2	0.60
Extruded Rectangle	C0.9*	0.109	190.0	92.1	7.7	0.40

NOTE: NGK leakage based on GE-cordierite coating and impregnation.

*MAS - A material with no coating or impregnation.

creased shrinkage during firing, which reduced wall porosity from 38 percent to 28 percent. Based on static seal leakage data for a full-size core with the rectangular matrix parameter (C0.9), the estimated leakage at full power conditions was 0.40 percent, which satisfied the porosity leakage requirement. In addition, the matrix wall thickness was reduced from 0.119 mm to 0.109 mm with a corresponding increase in cell density from 170.5 to 186 cells/cm^2. Further development of the C0.7 matrix with the MAS-A material would result in significantly improved core performance.

The regenerator thin wall AS matrix, made by Corning Glassworks, was examined for thermal stress using an axisymmetric stress analysis (2-D) for the cruise condition. This represents the worst case from the thermal stress viewpoint since the largest matrix thermal gradients are present in this operating mode. The analysis showed the operating tangential thermal stresses in the hub and rim do not exceed 413 kPa. This stress is well within the 1380 kPa capability of the material, so that no problems would be expected in regenerator matrix life with AS material at 1090C (2000F) operation.

A three-dimensional thermal stress analysis (SAP III) was completed (Figure 158) on a MAS regenerator matrix made by NGK. This matrix contained a number of tapered slots extending from the inside diameter of the rubbing seal shoe on the hot face to the matrix outside diameter on the cold face. Previous analysis and experimental work had shown that these slots were close to the optimum design for reducing tangential thermal stress. The objective of the 3-D analysis was to determine the number of these slots required to reduce the stresses to an acceptable limit. The results of this analysis indicated that 28 slots were required and that sufficient thermal stress capacity would be expected with NGK's MAS material at the cruise operating condition. Engine operating experience with MAS cores in the 707 engine has shown that MAS cores with thermal stress safety factors (modulus of rupture/maximum calculated elemental

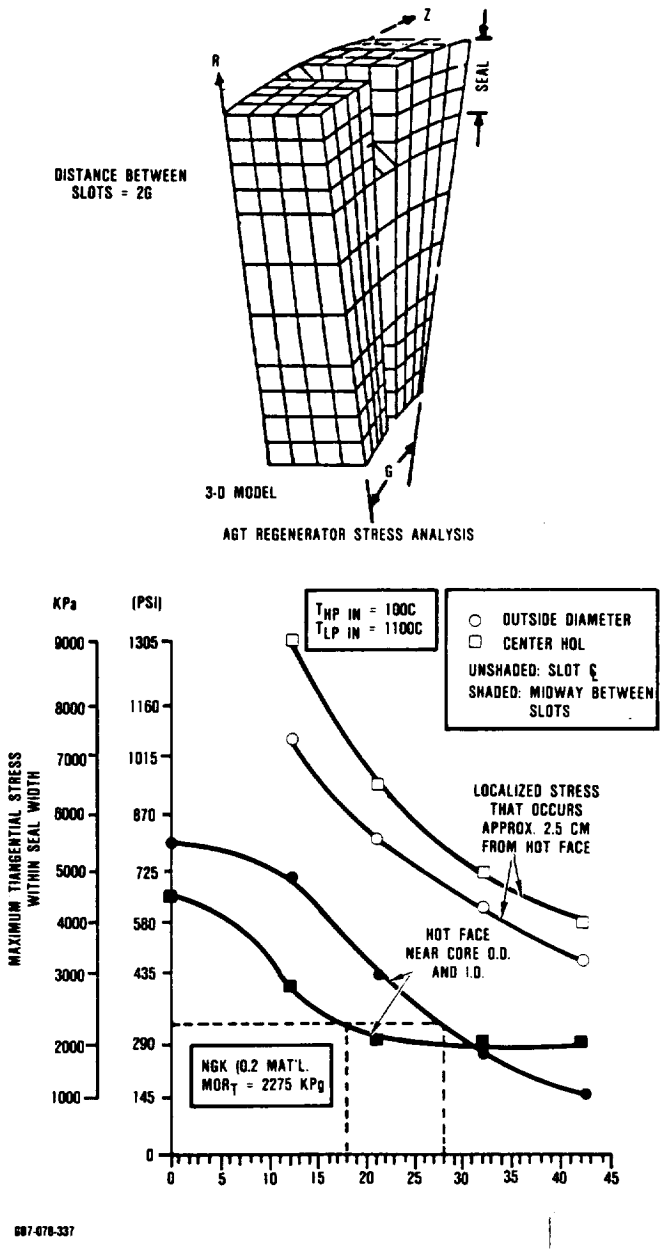

Figure 158. 3-D Thermal Stress Analysis.

stress) considerably less than unity have accumulated over 3500 hours of engine test with relatively minor rim thermal cracking. This was attributed to the fact that most of the rim is at low stress levels and the cracks tend to further stress relieve the rim. These cracks usually terminate below the rim where the

matrix is in compression. As the safety factor increases, the potential for the formation of rim cracks decrease. Since the safety factor for this NGK core with 28 slots is approximately 1.0, thermal rim cracking is not expected to be a problem.

The high temperature dimensional stability of the NGK original and improved MAS materials were evaluated by periodic measurement of specimen length change as a function of exposure time at 1000C (1832F) and 1100C (2012F) for 1008 hours (Table 19). In addition, the thermal expansion behavior between room temperature and 1000C (1832F) was determined for each material before testing and after completing the prescribed testing schedule. As a reference, the Corning AS material data generated in 1980 is included (Table 19). Both NGK materials exhibited equivalent stability when compared to reference data generated in 1977 for the NGK matrix that demonstrated 2500 and 250 hours at 800C and 1000C, respectively, in the Ford 707 engine.

The significant decrease in thermal expansion for the 1986 NGK materials compared to the 1977 material provides a significant decrease in thermal stress, which allows a substantial increase in dimensional stability tolerance. This is the main reason the Corning AS material has a high thermal stress capacity even though the AS is considerably less stable than the MAS materials.

Two full-size cores fabricated with the new improved MAS-A material were received from NGK near the end of this program. Ring gears were bonded to them for engine and test rig evaluation. One of these cores accumulated a total of 96 hours in Ford development test rig, with 53 hours at 1090C (1994F) exposure. This core demonstrated improved thermal stress capacity compared to cores fabricated with the original MAS material. The stress relief slots effectively eliminated radial thermal cracks at the outside diameter of the core on the hot face.

In summary, regenerator cores have been supplied by Corning Glass Works. and NGK-Locke. The Corning core, which is fabricated as a two-sheet wrap structure with aluminum-silicate material, is approximately 1 percent below the effectiveness objective. The most recent NGK extruded core with their improved magnesium-aluminum-silicate material is approximately 0.7 percent below the effectiveness objective. Both cores have sufficient thermal stress capacity for 1090C (1994F) system operating temperature.

Table 19. Regenerator Matrix Thermal Properties.

	Dimensional Change (ppm) After 1008 Hr. Exposure		Coefficient of Thermal Expansion ($X10^6/C$)	Thermal Expansion (ppm) at 1000C		
NGK Material	1000C	1100C	(20-1000C)	Before Test	After 1000C Test	After 1100C Test
MAS (1977)	-80	+400	1.5	1480	1380	1250
MAS (1986)	+60	+380	0.63	620	900	840
MAS-A (1986)	-60	+400	0.59	580	900	740
Corning AS	+300	+700	-0.05	-50	-400	-450

5.4.1.4 Drive and Support System

The regenerator mounting and drive system is a derivative of the Ford 707 engine support system. Support roller locations have been optimized, as shown in Figure 159, based on the interacting forces of the system as well as ring gear flexure. This optimum configuration minimizes the load concentrated on the pinion and support rollers and provides a durable system consistent with prior Ford engine experience.

Development efforts were concentrated on improving the graphite bearing design. The original design, which was based on the Ford 707 engine design that successfully replaced the grease packed ball bearing system, is shown in Figure 160. The revised design features the following improvements:

1) Elimination of costly shoulders on the original roller and pinion bearings.

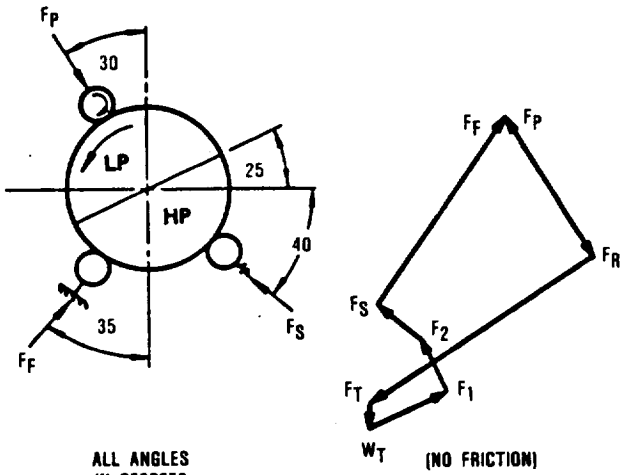

TORQUE = 271 Nm
WT = 9 Kg
F_R = GEAR SEPARATING FORCE = 39 Kg
F_T = GEAR DRIVING FORCE = 107
T_1 = PHERIPHERAL SEAL REACTION FORCE = 36 Kg
F_2 = CROSSARM SEAL REACTION FORCE = 22.7 Kg
F_S = SPRING ROLLER FORCE = 23 Kg
F_F = FIXED ROLLER FORCE = 91 Kg
F_P = PINION ROLLER FORCE = 29 Kg

G87-078-338

Figure 159. Regenerator Support Roller Locations.

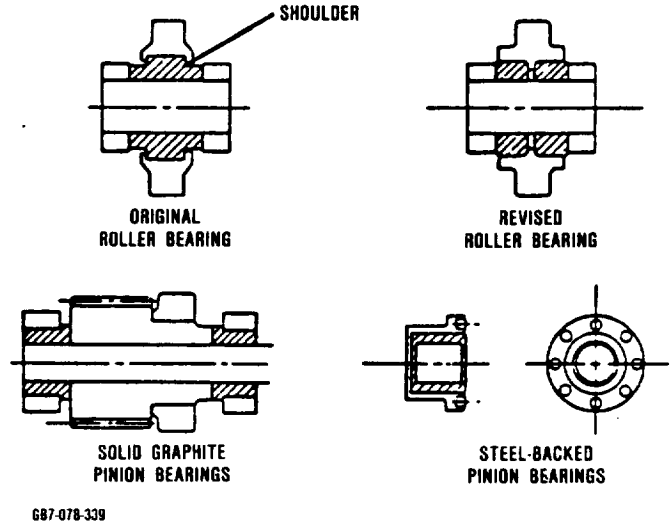

G87-078-339

Figure 160. Regenerator Drive and Support System Bearing Designs.

2) Total compressive support for the bearing by encompassing them with metal.

3) Simplified roller support design.

4) Steel backed pinion bearings can be press fitted without preheating the housing, which was required for the original design when the carbon bearing was press fitted directly to the housing.

5) Multiple bonded graphite buttons, which have been highly developed for other applications, are utilized as the thrust surface for the pinion assembly.

Test experience in the hot regenerator rig and engine have indicated no significant problems.

There are two key areas involved in the elastomer bonded ring gear to regenerator matrix design for the AGT application that fall within Ford regenerator system experience. These are: elastomer operating temperature and compliancy. One of the key elements for the elastomer bonded ring gear design is to minimize the temperature of the elastomer. Utilizing a two-dimension heat

transfer program, the results indicated that, by locating the ring gear near the cold face of the regenerator, the elastomer temperature will be comparable to those in the Ford 707 engine (Table 20). Consequently, this elastomer has had no difficulty meeting AGT engine cycle conditions.

Table 20. Calculated Elastomer Temperatures.

Configuration	Temp, C
Ford 707 Standard	288
Ford 707 Undercut Experimental	343
AGT AS Metro/Hwy	187
AGT AS Wide Open Throttle (WOT)	302
AGT MAS - Metro/Hwy	231
AGT MAS - WOT	344

From the standpoint of compliance, the equivalent modulus of the elastomer must be reduced to an acceptable level to accommodate the marginal radial compressive strength of the Corning AS matrix material. Since the metallic ring gear grows much more than the low-expansion matrix material, an elastomer attachment with a high modulus or low compliance will transmit a large outward radial force to the rim of the core. Ford experience has shown that if the ring gear is heated while the elastomer is being cured, a compressive pre-load can be applied to the rim of the core. If the compressive strength of the matrix is low, the amount of preload will be limited. A low modulus or highly compliant elastomer configuration is desirable to solve this problem. Several candidate configurations were evaluated based on prior Ford experience in the 707 engine. A three-dimensional finite element analysis of the Corning AS matrix required the highly compliant diagonal bond elastomer design configuration as illustrated on Figure 161.

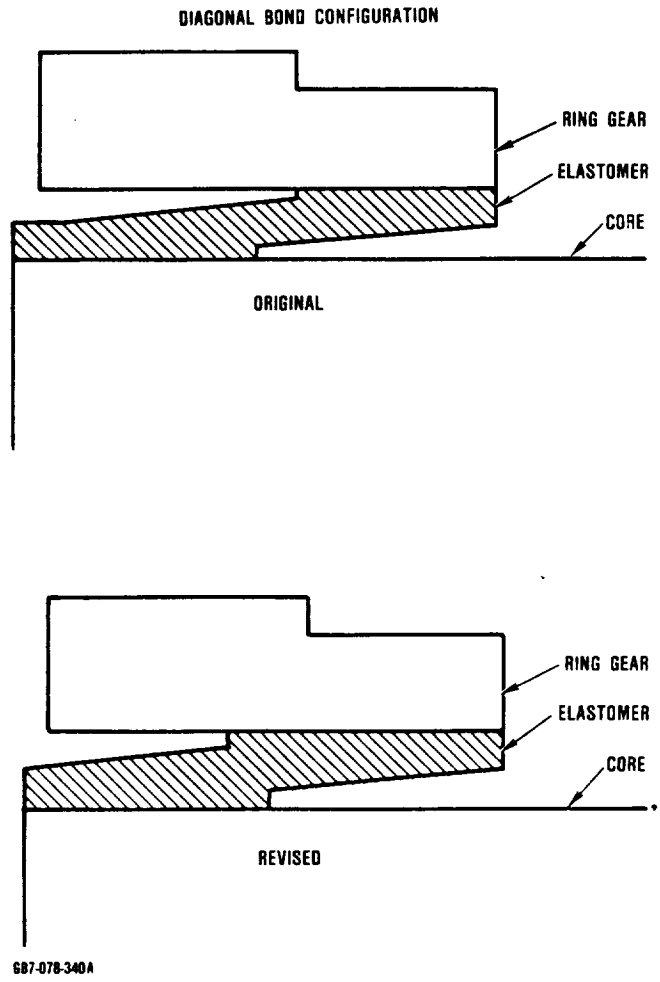

Figure 161. Diagonal Bond Configurations.

High torque levels generated by Phase IV seals operating at tight clearances caused ring gear separation from two NGK cores by shearing the elastomer. In order to improve elastomer shear strength, the diagonal bond configuration cross-section was modified as shown in Figure 161. Application of the GE cordierite coating to the outer peripheral surface created a very hard layer, which withstood the additional radial force associated with the modified design. Subsequent cores were bonded with this configuration for evaluation at Ford and Garrett without incident.

In summary, the three-point support drive system for the AGT engine which is a derivative of the Ford 707 system, has not indicated any significant problems in limited rig and engine testing. Attachment of the metal ring gear to the ceramic regenerator matrix with the diagonal bond configuration, which has a high degree of compliance, has minimized the drive system reaction forces imparted on the core.

5.4.1.5 Regenerator System Development Rig

AGT101 regenerator system rig testing has been performed during the AGT101 project at both Ford and at Garrett. The purpose of this testing was to evaluate the regenerator system under controlled conditions for development of the regenerator system components and evaluation of the regenerator system operating characteristics. Regenerator system leakage was evaluated at inlet temperatures up to 650C (1202F) and durability was evaluated at temperatures up to 1090C (1994F).

Leakage evaluations were performed in metallic structured rigs with flow paths similar to the engine configuration. The Garrett rig attempted to isolate the regenerator system from the outer system seals by welding or brazing the structural assembly together, eliminating many of the interpath seals. This rig incorporated a separate flow path for the high and low pressure sides of the regenerator system. Leakage was measured by seeding the high pressure inlet gas with helium and sensing the helium concentrations in the low pressure side gas discharge. The Phase V-A configuration seal was tested in this rig. Leakage was measured at the 6 percent level at the elevated temperature condition of 650C (1202F). Continued development was conducted in the Ford rigs.

Shown in Figure 162, the Ford rig was similar to the Garrett rig, though it could

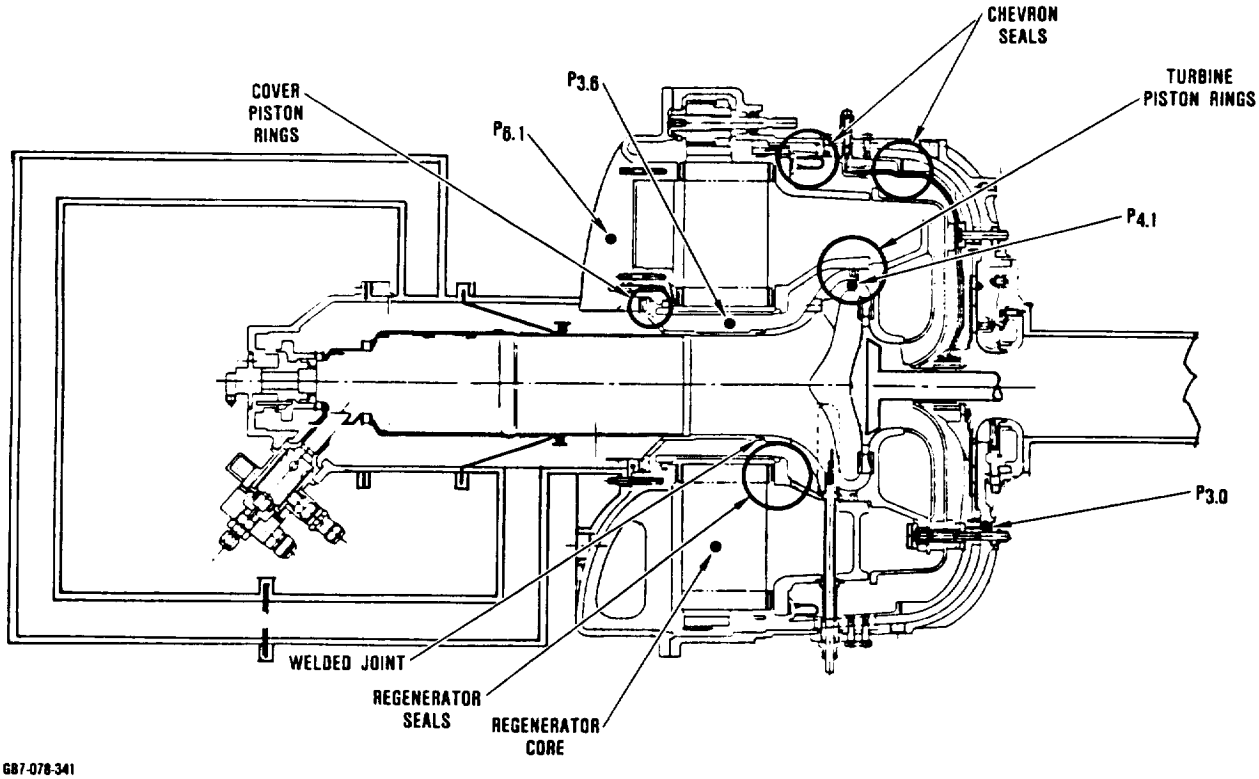

Figure 162. Leak Paths and Pressure Notations.

accommodate either metallic or ceramic structures. The leakages for each of the non-regenerator system seals were calibrated in cold, static testing and corrected for high temperature conditions. For measurement of overall rig leakage at operating temperature, this rig utilized a high temperature orifice measuring section between the regenerator high pressure discharge and rig combustor inlet. To simulate the pressure drop across the turbine this rig incorporated a valve which seated on the turbine shroud. The valve featured a power screw adjustment that allowed the valve position to be changed in the test cell for precise simulation of engine operating conditions. The operating temperature of the rig was limited to 590C due to the materials used in the orifice section. The regenerator leakage was determined by subtracting the system leakages from the overall.

Assembled in the ceramic configuration, this rig was characterized for leakage in cold static testing, and overall leakage measured up to the 590C temperature limit of the metallic interpath orifice section. This data was further reduced through analysis to determine how the regenerator seal leakage compared to the program goal of 3.6 percent.

An analytical model was developed to aid in understanding the different sources of leakage. The flow paths used in this model are illustrated in Figure 163. All the high pressure, cold air leaks (P3.0 and P5.1) were consolidated together and simulated by one leak, as were the high pressure, hot air leaks (P3.6 to P5.1). The unique high pressure, hot air leak, (P3.6 to P4.1) which is present in this rig but not in an engine, was also included. The components and leak paths were defined by a set of flow restrictions, as illustrated in Figure 163. Each restriction is an orifice having a specified flow area. The computer model iterates on this network of restrictions until it converges on a solution in which the sum of the pressure drops of the individual components equals the available pressure drop, P3.0 to P6.0. The following assumptions apply:

1) The flow is compressible.

2) The entire velocity pressure in each of the restricting areas is lost.

3) Reynolds Number effects are ignored.

4) Temperatures at the various points in the flow path were inputted from rig test data.

5) The flow areas used to eliminate the different leaks were determined from measurements made in the cold, static rig in the Build-Up Laboratory.

6) Other flow areas were estimated from pressure drop measurements made in the dynamic rig.

7) All flow areas, except that of the valve, were held constant in all calculations.

This model correlated well with the test data taken from the rig at inlet temperatures up to 590C (1094F). The regenerator system leakage at the hot, cruise condition was projected at 4.0 percent using the same model. This was close to the program objective of 3.6 percent. If a Phase VIA hot seal and a low leakage Corning core had been used, it was anticipated that the leakage objective would have been met.

Durability Testing

After completing the seal leakage evaluations, elevated temperature testing was conducted to evaluate the high temperature durability of the regenerator system. This testing was conducted in the ceramic version of the Ford Regenerator System Rig without the interpath orifice section installed. This rig was capable of operation of regenerator inlet temperatures up to the system design goal of 1090C (1994F).

During this test program the rig was assembled 13 times, accumulating 238 hours of testing, including 73 hours at 1090C (1994F) regenerator inlet temperature. This testing contributed to the design and development of the inner regenerator seal cooling configuration and evaluated improved materials and designs used in the regenerator core assembly.

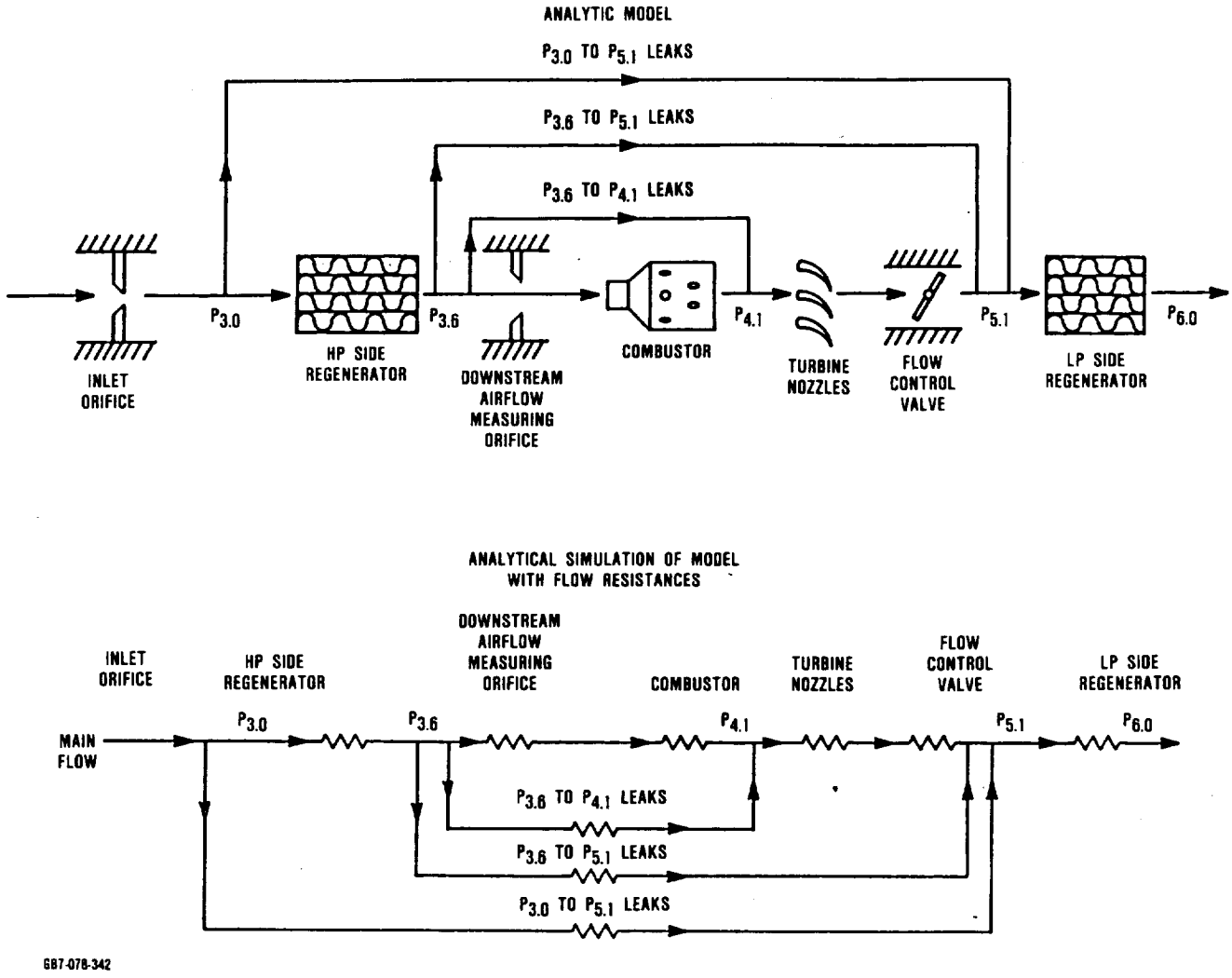

Figure 163. Analytical Model for Dynamic Rig Leakage.

The regenerator seal cooling system was developed through an iterative process. Seal diaphragms were instrumented with thermocouples and installed in the rig for each test. The resultant temperature data was recorded and evaluated, providing valuable information for seal design improvements such as the application of thermal barrier coatings to the seal shoes, finned support diaphragms etc.. The curves in Figure 164 show typical data from this testing.

Additional information was generated as a result of endurance testing in the ceramic configuration of the regenerator rig. Long term durability of the seal assemblies were evaluated in tests planned for 50 and 100 hours. Significant problems such as regenerator core thermal cracking, seal coating delamination, and shoe distortion were discovered and evaluated during extended durability testing.

The regenerator core thermal cracking problem was related to the thermal expansion of the MAS regenerator core material and the strength of the matrix. In cores assembled from extruded segments, the strength and

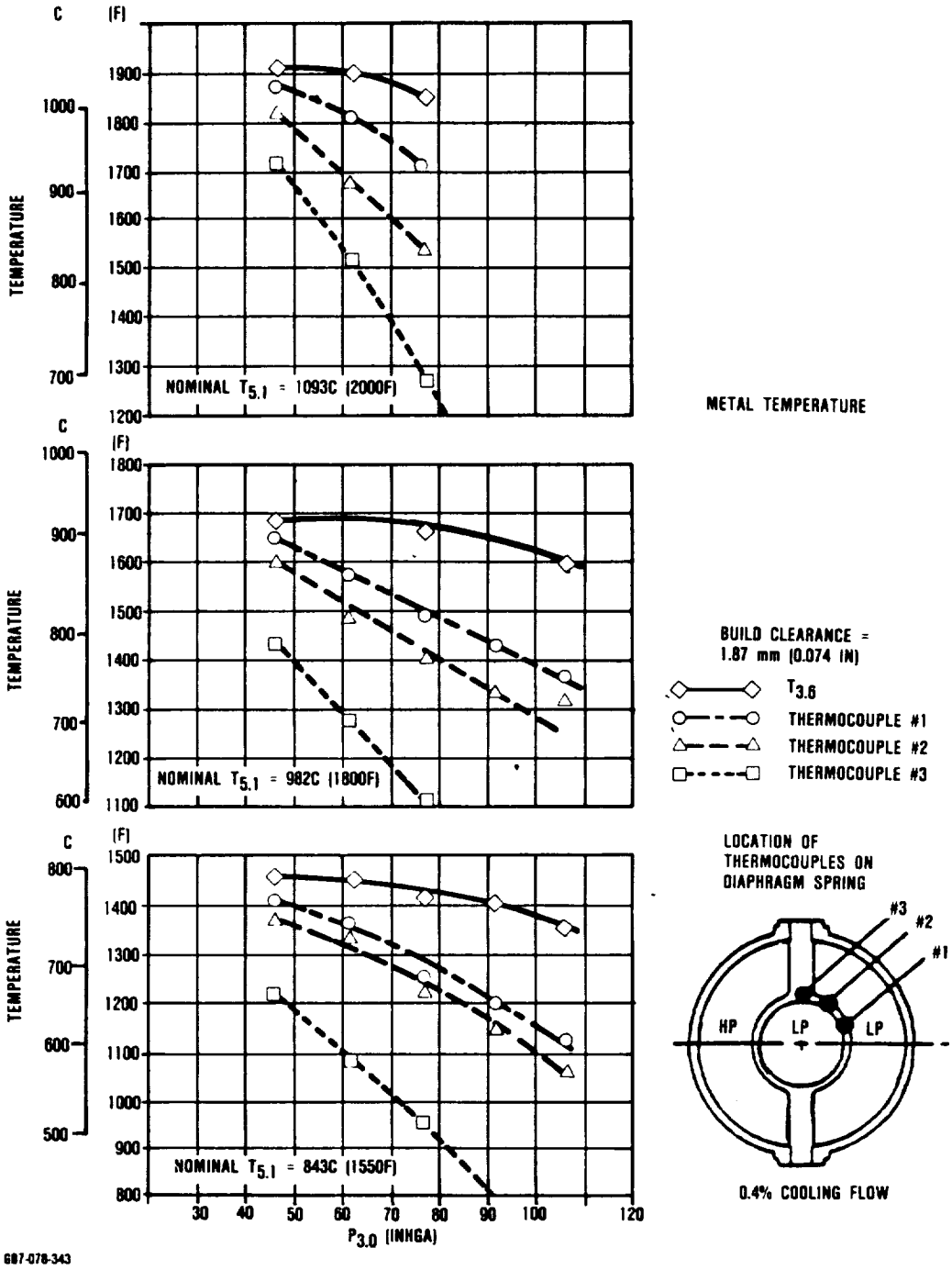

Figure 164. Seal Diaphragm Temperatures at 0.4 Percent Cooling Flow.

compatibility of the bonding cement was also a significant factor. Small matrix cracks form on the outer periphery of the hot face of the core after several hours of durability testing. In the most severe cases, the cracks would propagate with time and temperature across the face of the core to the center, generating large leaks, and core debris. The problem was solved through proper location of stress relief slots in the outer rim of the core and the use of improved MAS-A material from NGK.

The distortion of the regenerator seal shoes, and delamination of the seal coating during 1090C (1994F) operation are related phenomenon which were discovered during the last phases of the AGT regenerator seal development effort. The photograph in Figure 165 shows the crossarm shoe and how the coating delaminated from the inner periphery of the shoe wearface. Inspections of the seal indicated that the circular inner periphery was distorted to an oblong shape and that the coating was lost from the distorted portions of the shoe. Characteristically, the seal shoe was also bowed axially toward the coated side.

Subsequent investigation in the regenerator rig evaluated the coating delamination at temperatures up to 1090C (1994F). Seal design modifications were made to remove restrictions to seal thermal growth, however the distortion was evident in follow-up testing.

Regenerator System Summary

Based on test data and analysis accumulated at both Ford and Garrett, the current status toward achieving the three main program objectives are as follows:

1) 92.9 percent regenerator core effectiveness with less than 7.5 percent pressure drop at WOT engine conditions.

   Regenerator cores supplied by Corning Glass Works and NGK-Locke, Inc. are approximately 1.0 percent and 0.7 percent below the effectiveness objective, respectively, with a nominal 7.5 percent pressure drop. NGK has developed a thinwall isosceles triangular structure that will exceed the objective provided a more dense mate-

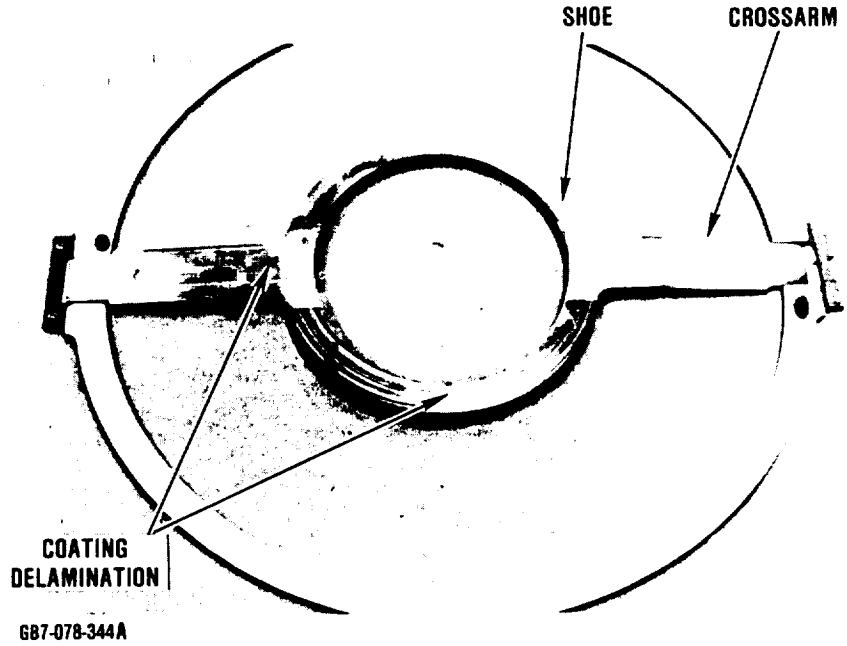

Figure 165. Seal Coating Delamination from Crossarm Shoe.

rial can be developed to have acceptable wall porosity leakage.

2) Regenerator System capable of operating at 1090C (1994F) regenerator core inlet temperature.

   Corning cores fabricated with AS material and NGK cores extruded with their improved MAS-A material have demonstrated the thermal stress capacity and matrix thermal stability required for 1090C engine conditions.

   Ring gear attachment to the regenerator with a compliant elastomer system design and the associated drive and support system has also demonstrated the system temperature objective.

   Outboard (cold) seal assemblies with all I-85 coated substrates, except for I-112 on the circular portion of the crossarm, have achieved the temperature objective.

   Although inboard (hot) seal assemblies have demonstrated the capability of the I-112 coating to operate in a 1090C (1994F) environment, distortion of the present substrate materials limits this component to a 1040C (1904F) system temperature. Substitution of 316 stainless and Haynes 230 material for 430 stainless peripheral and INCO 601 crossarm substrates, respectively, should achieve the 1090C (1994F) temperature objective.

3) Maximum regenerator system leakage of 3.6 percent at WOT engine condition.

   Based on static and dynamic leakage measurements in the Ford test rigs and supported by analytical models, the regenerator seal system appears to have achieved the leakage objective. In addition, the Corning and NGK cores have also demonstrated minimal porosity leakage that is essential for achieving the system leakage objective.

5.4.1.6 Non-Diaphragm Seals

As an alternate approach to cooling the inboard (hot) seal crossarm diaphragm, a feasibility study was initiated to eliminate diaphragms from this seal, as shown in Figure 166. The core would run against a wear face coating applied directly to the flow separator housing (FSH). The key requirements for a successful non-diaphragm seal are low friction and wear coatings combined with minimum leakage gaps resulting from compatible platform deformations of the core and FSH. The work plan for this study consisted of the following:

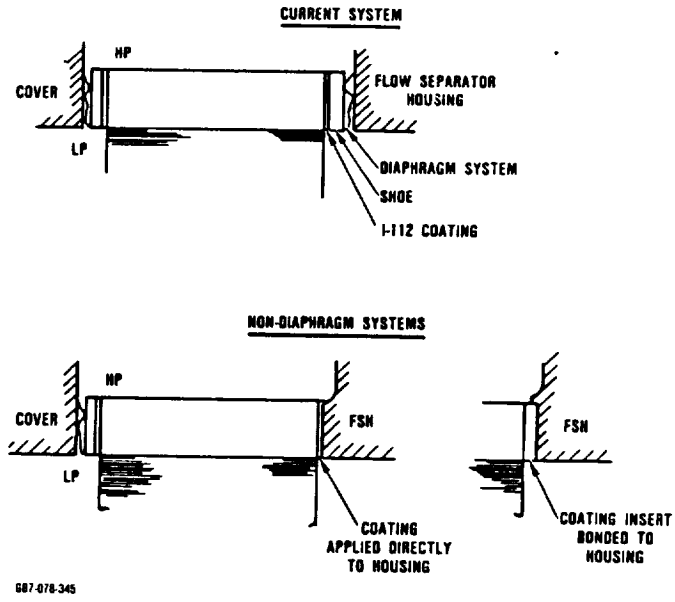

Figure 166. Seal Systems Comparison.

1) Thermal analysis

   a) Three dimensional finite element analysis of flow separator housing (FSH) distortion performed at Garrett

   b) Two dimensional finite element analysis of the regenerator matrix distortion performed at Ford

c) Labyrinth seal leakage analysis for regenerator core - FSH gap performed at Ford

2) Attachment of ceramic coatings to the FSH

3) Evaluate coating wear and friction characteristics in the seal wear rig.

An analytical model based on labyrinth seal theory was developed to evaluate non-diaphragm seal leakage as a function of regenerator core and flow separator housing (FSH) distortions. The inboard (hot) seal consists of six leak path components, as illustrated in Figure 167. Analytical expressions were developed for both the circular and linear components.

The hot face thermal distortion for the original Corning (AS) and NGK (MAS) materials was previously evaluated for cruise and full power conditions, which corresponds to engine speed of 60 percent and 100 percent, respectively. The results, shown in Figure 168, indicated that the Corning material had acceptable distortion variance (0.0152 mm), whereas the original NGK material variance (0.076 mm) was unacceptable for a nondiaphragm seal system.

The objective for the AGT regenerator system leakage is 3.6 percent maximum at the maximum power operating condition. Based on static leakage data and analysis, the total leakage consists of the following:

1) Inboard (hot) seal assembly - 1.9 percent
2) Outboard (cold) seal assembly - 1.2 percent
3) Regenerator core carry-over loss = 0.25 percent
4) Inboard seal diaphragm cooling allowance = 0.25 percent

Therefore a non-diaphragm inboard seal will have a design objective of 2.15 percent (1.9 percent seal + 0.25 percent cooling) as a replacement for the present diaphragm seal system.

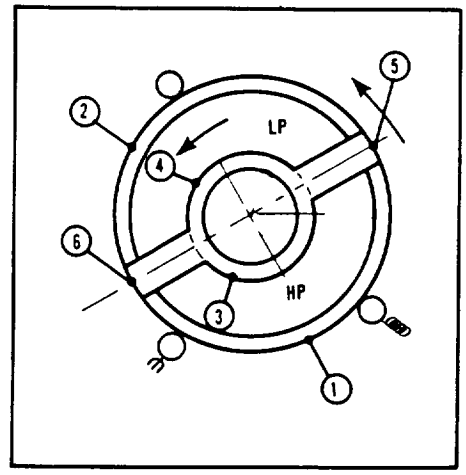

COMPONENT	SEAL LENGTH, CM (IN.)
1	67.5 (26.6)
2	67.5 (26.6)
3	27.4 (10.8)
4	27.4 (10.8)
5	10.9 (4.3)
6	10.9 (4.3)

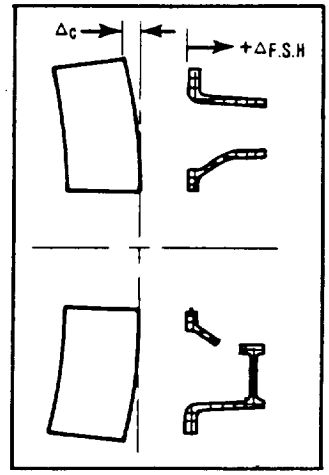

G87-078-346

Figure 167. Analytical Model Evaluating Non-Diaphragm Leak Paths As a Function of Component Distortions.

In order to evaluate seal system sensitivity, the initial study consisted of evaluating seal component leakage as a function of a uniform gap at cruise and maximum power operating conditions, which are listed on Table 21. The results at cruise, shown in Figure 169, and maximum power, shown in Figure 170, demonstrate the powerful influence of leakage air temperature. As expected, the leakage for components 1 and 4 are minimal since pressure drop at these locations is very small (less than

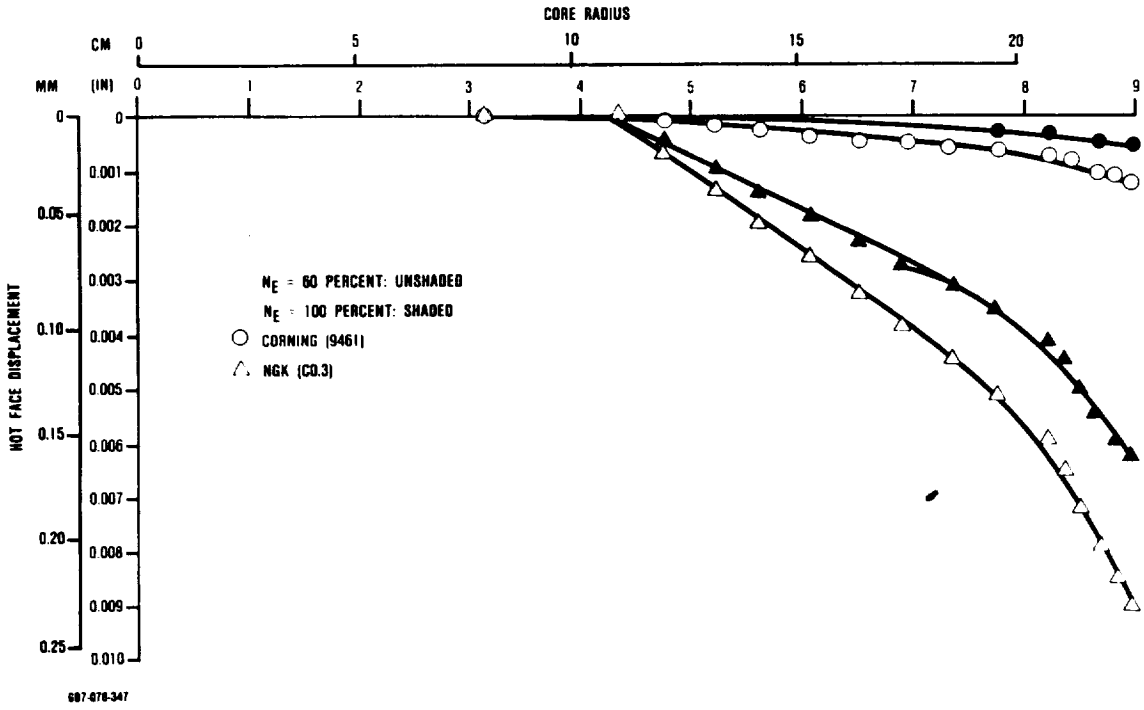

Figure 168. Regenerator Core Axial Distortion Effects.

Table 21. Leakage Air Flow Conditions.

Component	P_O	P_N	T_O
Speed = 60% W = 0.161			
1	205.5	204.1	99
2	205.5	104.8	99
3	204.1	101.3	1063
4	104.3	101.3	1090
5	204.1	104.3	1063
6	204.1	104.8	1063
Speed = 100% W = 0.377			
1	506.1	504.7	243
2	506.1	111.7	243
3	504.7	101.3	914
4	111.7	101.3	965
5	504.7	111.7	914
6	504.7	111.7	914

P_O: Leakage Inlet Pressure, KPaA
P_N: Leakage Exit Pressure, KPaA
T_O: Leakage Inlet Temperature, C
W: Engine Air Flow, kg/sec

10.28 kPa). Conversely, the leakage for Component 2 is substantially higher than Components 3, 5, and 6 even though pressure drop is approximately the same.

This is directly attributable to the much lower temperature of the compressor discharge air compared to the discharge air through the high pressure side of the regenerator. Component 2 leakage represents approximately 70 percent of the total leakage at both engine conditions (Figures 169 and 170). Leakage through component 3 is more than the crossarm (components 5 and 6) due to the following reasons:

1) The seal width of the crossarm (38.1 mm) in twice the width (19.0 mm) of the peripheral seals

2) For a wrapped process regenerator (Corning Glass) the crossarm will have a geometrical advantage due to a substantially higher number of sealing points (labyrinths).

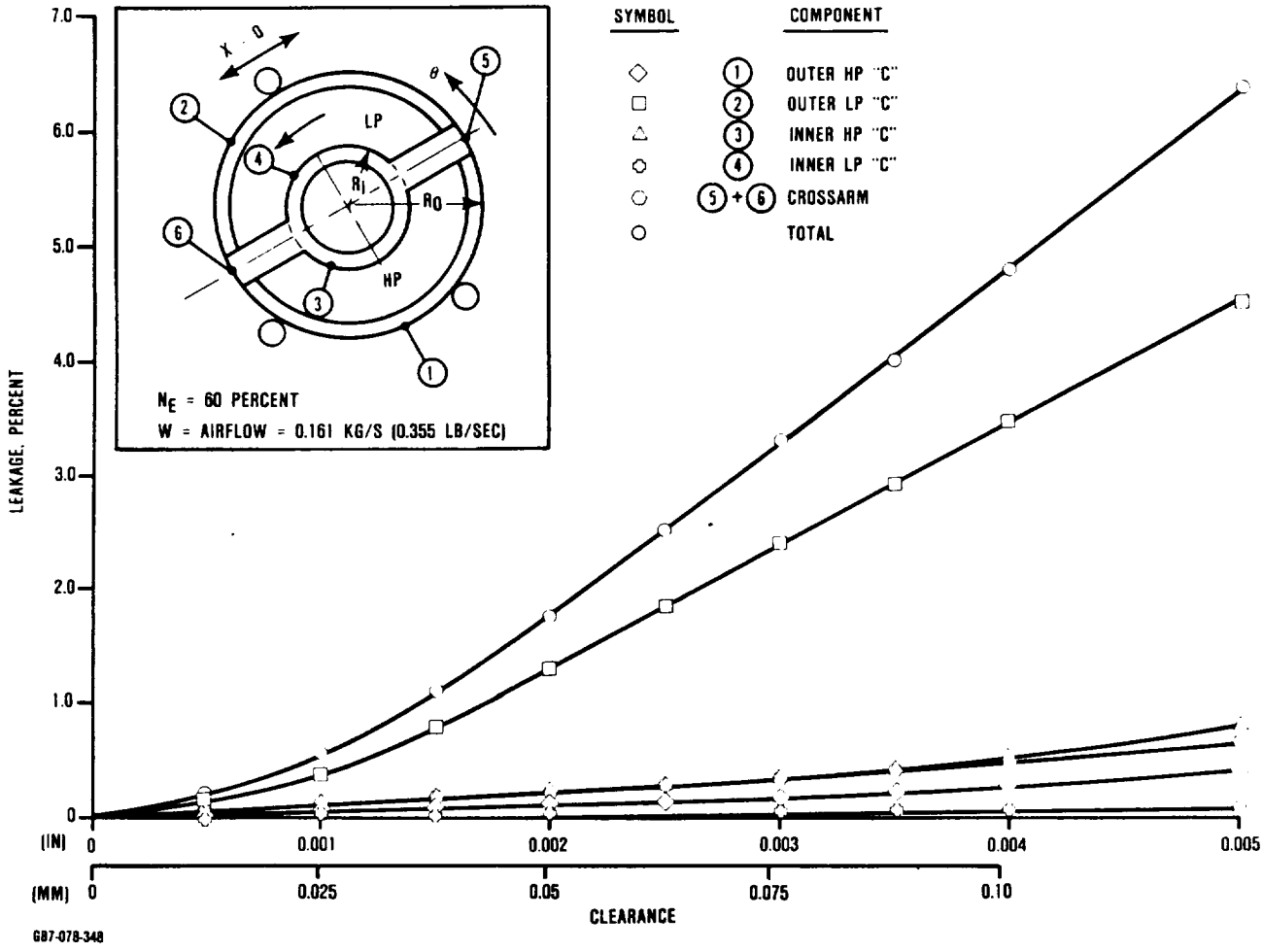

Figure 169. Non-Diaphragm Seal Leakage Versus Uniform Clearance.

To further demonstrate the importance of air temperature, the leakages at cruise and full power were estimated based on ambient air as a function of uniform clearance (Figure 171). In this case, the leakage with ambient air was approximately twice as high as leakage based on engine temperatures.

The next study consisted of evaluating seal leakage for the FSH distortions predicted by Garrett from their 3-D finite-element analysis, which is summarized on Table 22. For the current Garrett model, one of the boundary conditions assumes axial constraints at the ring support interface, which results in zero axial distortion of the outer ring of the FSH. Consequently, the distortions predicted are for the inner ring relative to the outer ring. In addition, to simplify the initial analysis, distortion due to temperature and pressure were evaluated separately. Distortion due to temperature was evaluated at engine cruise (N_E = 60 percent). Conversely, distortion due to pressure (isothermal) was evaluated at full power conditions (N_E = 100 percent).

A total of thirteen combinations were evaluated and summarized on Table 23. The

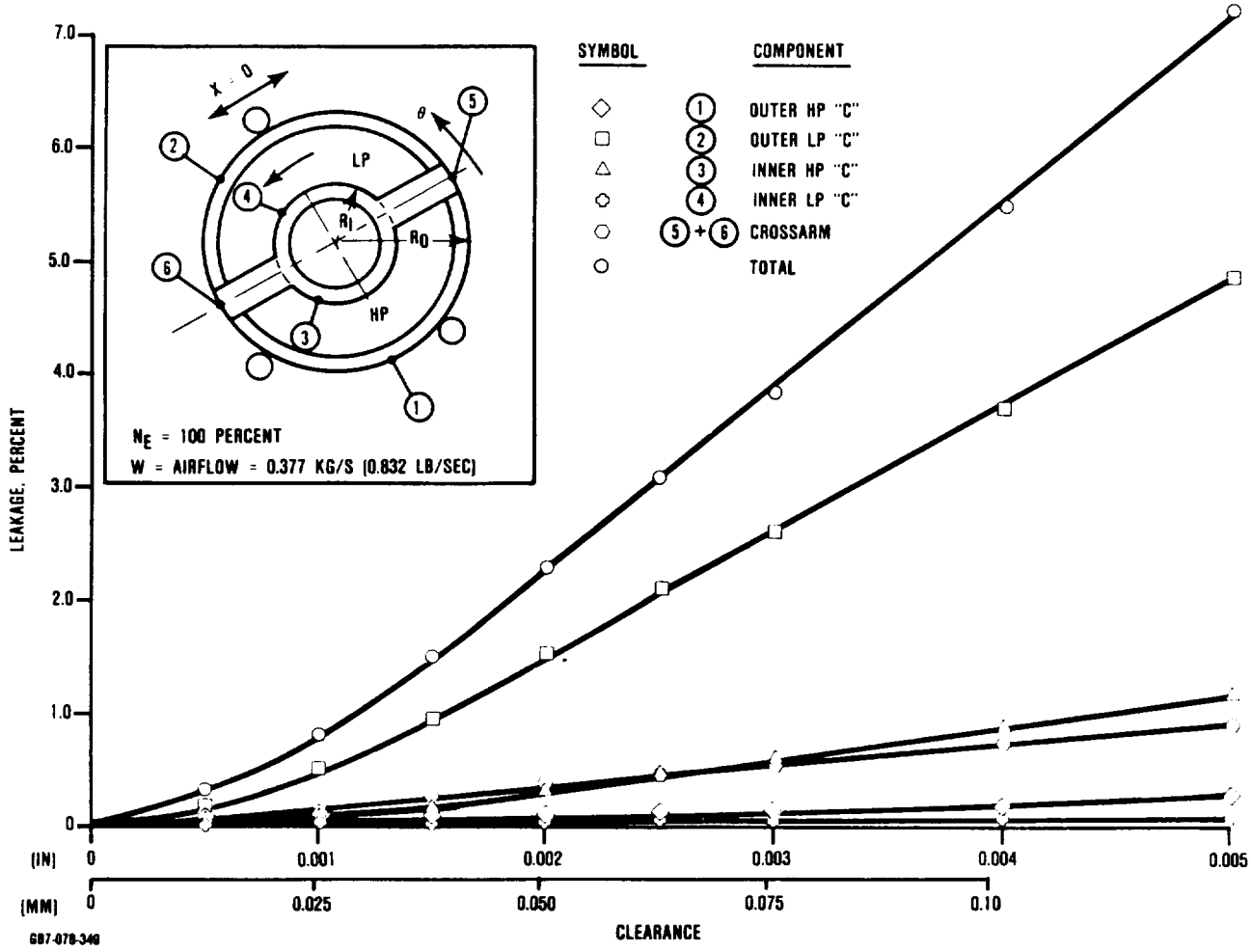

Figure 170. Non-Diaphragm Seal Leakage Versus Uniform Clearance.

maximum component gap is predicated by the contact point that results from meshing the axial distortion of the core with that of the housing (FSH). If the distortion of the core is greater than the FSH, then a gap will exist at the outer ring (components 1 and 2) and leakage will be substantial. Conversely, when the axial distortion of the core is less than the FSH, then the gap at the outer ring is zero and leakage will be minimized.

For the thermal distortions without pressure at cruise conditions, leakage was calculated for both the current configuration (H = 28.39 $W.m^2C$) and the simulation of a metal baffle (H = 5.68 W/m^2C) around the outer perimeter of the FSH. Initial results at Garrett indicated that, by allowing the mounting flange of a RBSN housing to heat up by baffling the compressor discharge flow around it, the distortion is reduced significantly. In addition, distortion of an RBSN housing due to pressure is reduced significantly with the incorporation of struts.

Based on these preliminary results, the leakage of a non-diaphragm inboard seal system was projected to meet the objectives, provided the clearance between the core and FSH at the outer ring was minimized. To ensure this condition is met, the axial distortion of the core should be less than the axial distortion of the FSH inner ring (components 3 and 4). In addition, to more accurately predict seal leakage, axial distortion of the FSH due to the combined effects of pressure and temperature must also be determined.

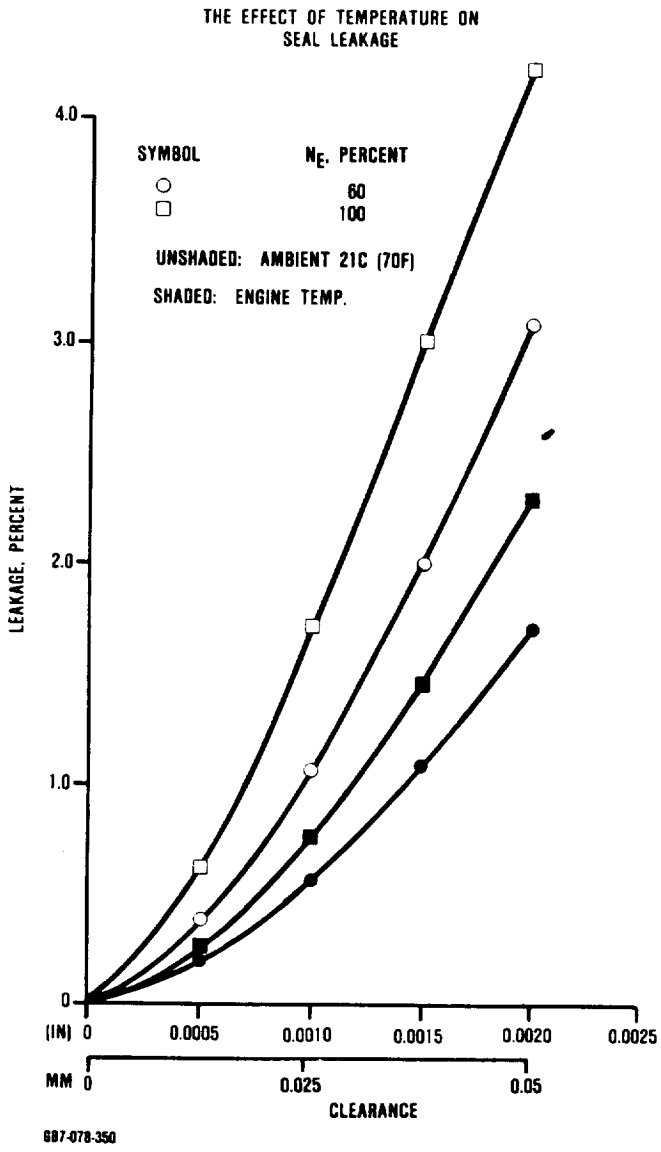

Figure 171. Effect of Temperature on Seal Leakage.

The evaluation of candidate coatings and method of attachment to LAS samples was investigated. Based on furnace exposure and seal wear rig testing, two wear face coatings developed at Ford continue to show promise. These coatings are zinc-oxide based and designated as I-112 and S-77.

A composite coating on a LAS ceramic wear rig substrate consisting of a pre-heat treated coating of Ford ATLAS glass frit, which provides an intermediate bond coating, and I-112 plasma sprayed wear face coating was subjected to 1090C (1994F) furnace exposure without failure. The sample accumulated 63 hours at temperatures up to 980C (1796F) in the seal wear rig against an LAS core without apparent difficulties. The coefficient of friction varies between 0.16 at 980C (1796F) and 0.22 at 815C (1499F) with negligible wear. A friction coefficient below 0.3 is considered excellent.

Another LAS sample with S-77 material applied without the Ford ATLAS intermediate bond coating accumulated 120 hours in the seal wear rig at temperatures up to 980C (1796F). The coefficient of friction varied between 0.15 and 0.20 with negligible wear. Minor chipping and delamination occurred after the 980C (1796F) exposure.

Since flow separator housings made from silicon nitride were being considered in the AGT program, S-77 coating was sprayed on a silicon nitride substrate. It accumulated 75 hours in the wear rig at temperatures up to 870C (1598F) without distress. The coefficient of friction varied between 0.08 and 0.13. The test was terminated when the ceramic sample holder failed while attempting to run the 980C (1796F) condition. A casting mold was fabricated to form reaction bonded silicon-nitride (RBSN) blocks as a replacement sample holder. One of these blocks was sintered and machined into a sample holder.

Garrett provided Ford additional funding to coat a thick-flange LAS flow separator housing with the special "non-diaphragm" seal coatings. The thick flange separator housing (FSH) with the plasma sprayed Ford wear face coating (S-77) was held at 1090C (1994F) for 24 hours in a kiln without difficulties. A cold seal was fabricated with thicker diaphragms to increase the mechanical loading to compensate for the diaphragms eliminated from the hot seal. This modification was required to

Table 22. Flow Separator Housing Axial Distortion.

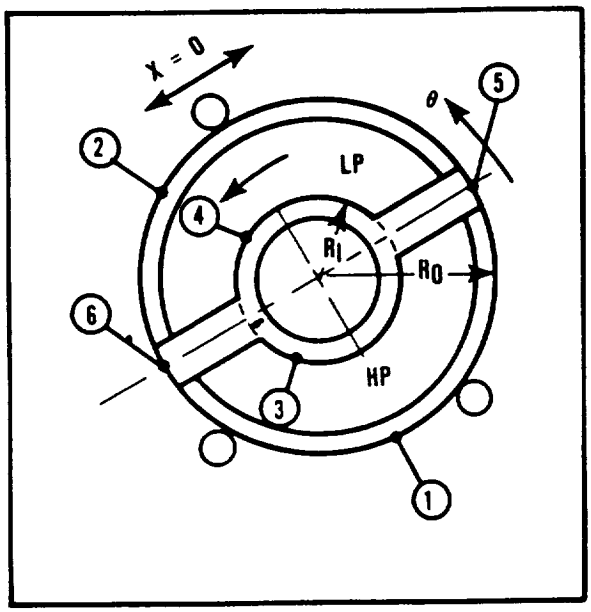

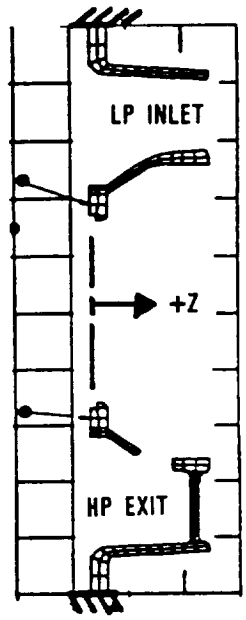

Speed %	Flow Sep Mat'l	Flow Sep Config	Film Coeff W/M^2C	Distortion (mm)					
				Loc #3		Loc #4		Loc #5 & #6	
				Max	Min	Max	Min	Max	Min
60	LAS	Non	31.2	0.147	0.143	0.147	0.147	0.139	0
60	LAS	NON	6.24	0.099	0.083	0.099	0.101	0.094	0
60	RBSN	NON	31.2	0.272	0.241	0.267	0.246	0.254	0
60	RBSN	NON	6.24	0.0914	0.0813	0.0889	0.0864	0.089	0
60	RBSN	Strutted	31.2	0.099	0.038	0.099	0.066	0.099	0
100	RBSN	NON	0	-0.046	-0.005	-0.099	0.046	0.046	0
100	RBSN	Strutted	0	0.018	0.0051	0.005	0	0.005	0
100	LAS	NON	0	0.069	-0.0457	0.0457	-0.069	0.046	0
100	LAS	Strutted	0	0.038	0.015	0.015	-0.005	0.015	0

GB7-078-351

Table 23. Non-Diaphragm Seal Leakage Analysis.

LEAKAGE
OBJECTIVE: 1.25 PERCENT MAX.

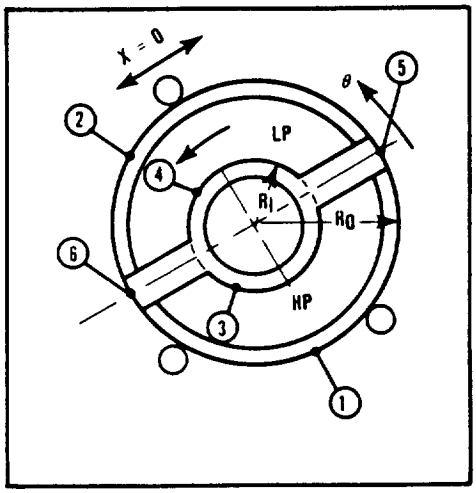

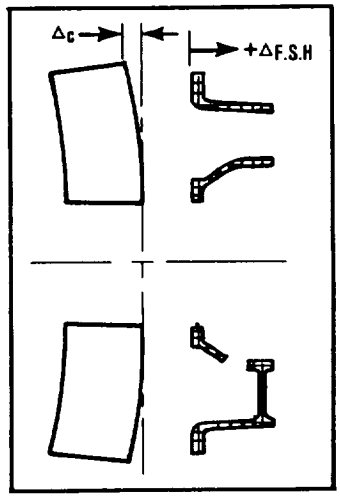

						Max Component Gap, mm					Total Leakage	
Speed, 4%	FSH Config	FSH Matl	Core Type	Core Dishing mm	Film Coeff, W/M^2-C	Loc 1	Loc 2	Loc 3	Loc 4	Loc 6	(kg/s)	(%)
60	No strut	LAS	Corning	0.03048	5.678	0	0	66.04	71.12	50.8	0.000612	0.38
60	No strut	LAS	Corning	0.03048	28.39	0	0	114.3	116.84	88.9	0.001421	0.88
60	No strut	LAS	NGK	0.2286	5.678	147.32	147.32	16.002	18.542	119.38	0.011338	7
60	No strut	LAS	NGK	0.2286	28.39	104.14	104.14	20.32	22.86	88.9	0.007256	4.5
60	No strut	RBSN	Corning	0.03048	5.678	0	0	58.42	58.42	43.18	0.000506	0.37
60	No strut	RBSN	Corning	0.03048	28.39	0	0	238.76	231.14	177.8	0.003930	2.4
60	No strut	RBSN	NGK	0.2286	5.678	147.32	147.32	8.382	6.35	114.3	0.011187	6.9
60	No strut	RBSN	NGK	0.2286	28.39	0	0	40.64	33.02	30.48	0.000226	0.14
60	Strutted	RBSN	Corning	0.03048	28.39	0	0	63.5	60.96	35.56	0.000453	0.28
100	No strut	RBSN	Corning	0.04064	0	114.3	114.3	88.9	35.56	83.82	0.021467	5.7
100	Strutted	RBSN	Corning	0.04064	0	17.78	17.78	16.51	5.08	12.7	0.001511	0.39
100	No strut	LAS	Corning	0.04064	0	152.4	152.4	20.066	7.874	12.192	0.033713	8.9
100	Strutted	LAS	Corning	0.04064	0	20.32	20.32	40.64	12.7	20.32	0.002418	0.64

G87-078-352

ensure that the core will contact the FSH. The FSH and associated cold seal with the thicker diaphragms were sent to Garrett for evaluation.

In summary, preliminary analysis of the non-diaphragm seal system indicates feasibility provided the clearance between the core and FSH is minimized. To ensure this condition is met, the axial distortion of the core should be less than the axial distortion of the FSH. Based on furnace exposure and seal wear rig testing, two wear face coatings continue to show promise for bonding to the FSH.

5.4.2 Garrett Regenerator Development

Two cold flow regenerator test rigs, low pressure (LP) and high pressure (HP), were designed and fabricated at Garrett in order to:

a) Determine circumferential and radial pressure profiles imposed by engine geometry on the regenerator core

b) Evaluate flow profile control mechanisms

c) Analytically predict the regenerator installed effectiveness based on the test profiles obtained in Steps 1) and/or 2)

Construction of an analytical flow and heat transfer model of the regenerator system in 3-D form was completed and is discussed in paragraph 5.4.2.3.

5.4.2.1 Regenerator Low Pressure (LP) Cold Rig

The LP regenerator cold rig design concept, Figure 172 is based on engine/model similarity in areas of flow path geometry, regenerator matrix frontal area, pressure drop, and engine corrected mass flow in the turbine discharge plane. Rig objectives include baseline turbine diffuser performance mapping and regenerator flow pattern mapping. Instrumentation requirements for the diffuser performance are shown in Figure 172. Special instrumentation (hot wire anemometery) was required for accurate low level velocity measurements in the regenerator core mapping test.

The hot wire technical capability required for testing was developed in a specially designed calibration tunnel (Figure 173). The calibration tunnel was utilized to calibrate a total of eight 2-D and two 3-D hot wire probes for use in the regenerator core survey test. Additionally, an in-house hot wire probe repair capability was developed to support the test.

Analytically predicted turbine discharge conditions had to be duplicated for the diffuser testing. Specifically, turbine exit swirl, radial pressure profile, and corrected flow rates were duplicated for idle, cruise, and maximum power engine conditions. Hardware configurations to meet these requirements are shown in Figure 174. Preswirl assemblies for idle (+55 degrees), cruise (0 degrees), and maximum power (-27 degrees), were fabricated along with various percent open areas screens to generate the analytically predicted 5-percent radial pressure gradient.

LP Rig Test Results

The main objectives of the LP cold flow rig tests were as follows:

- Determine circumferential and radial pressure distortion profiles imposed on the LP inlet core face by engine flowpath geometry
- Investigate and evaluate different flow influencing devices and the effect on overall regenerator performance

As previously stated, hot wire anemometry techniques were employed during initial testing. However, due to the geometry of the 3-D hot wire probe sensing elements, wherein discrete (matrix cell) velocity jets could impinge on an individual probe element, the results of testing were highly suspect. Therefore, hot wire anemometry data was used to ascertain flow trends within the plenums, and core pressure drop data was used during later testing for analysis.

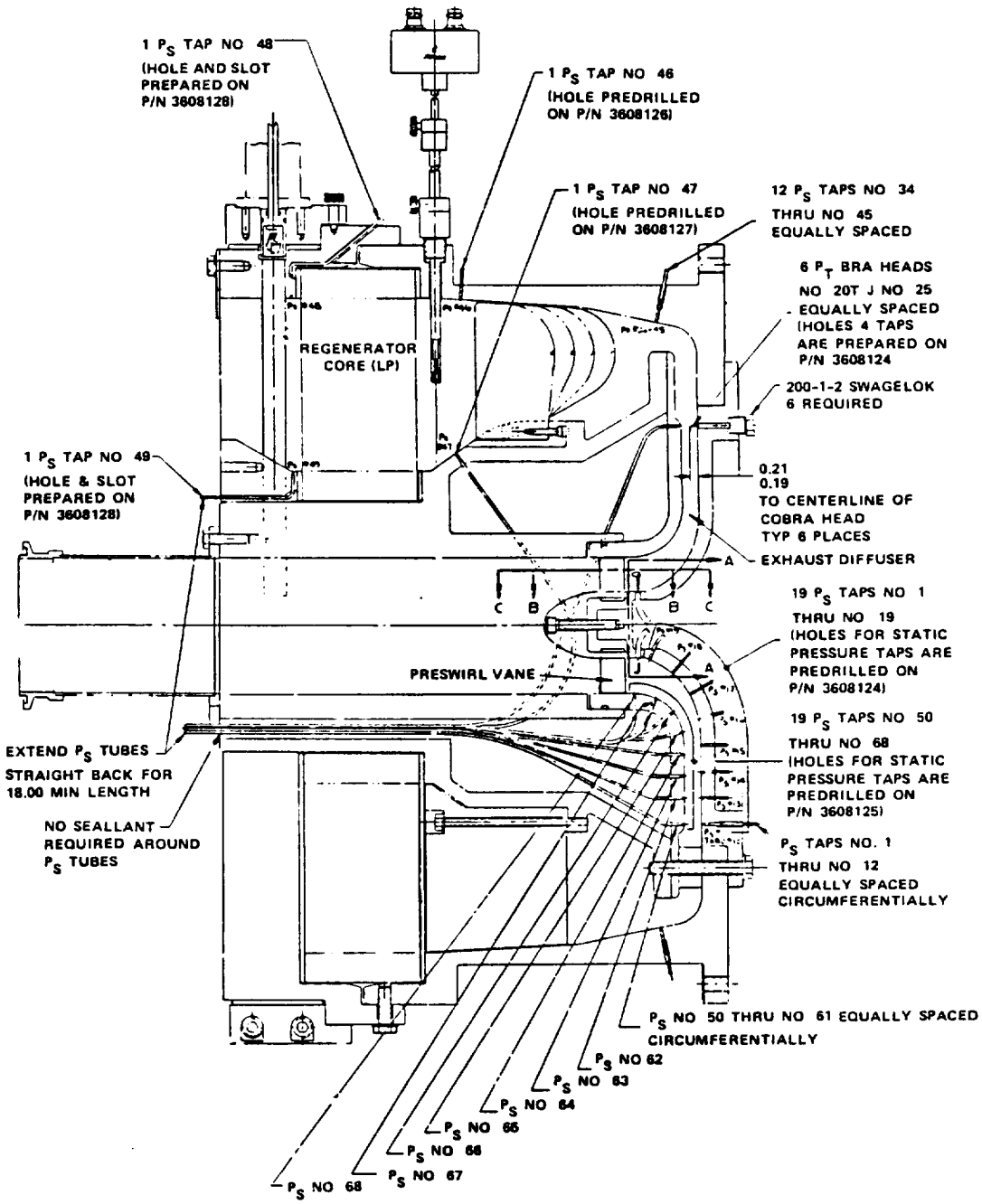

Figure 172. Regenerator LP Cold Rig.

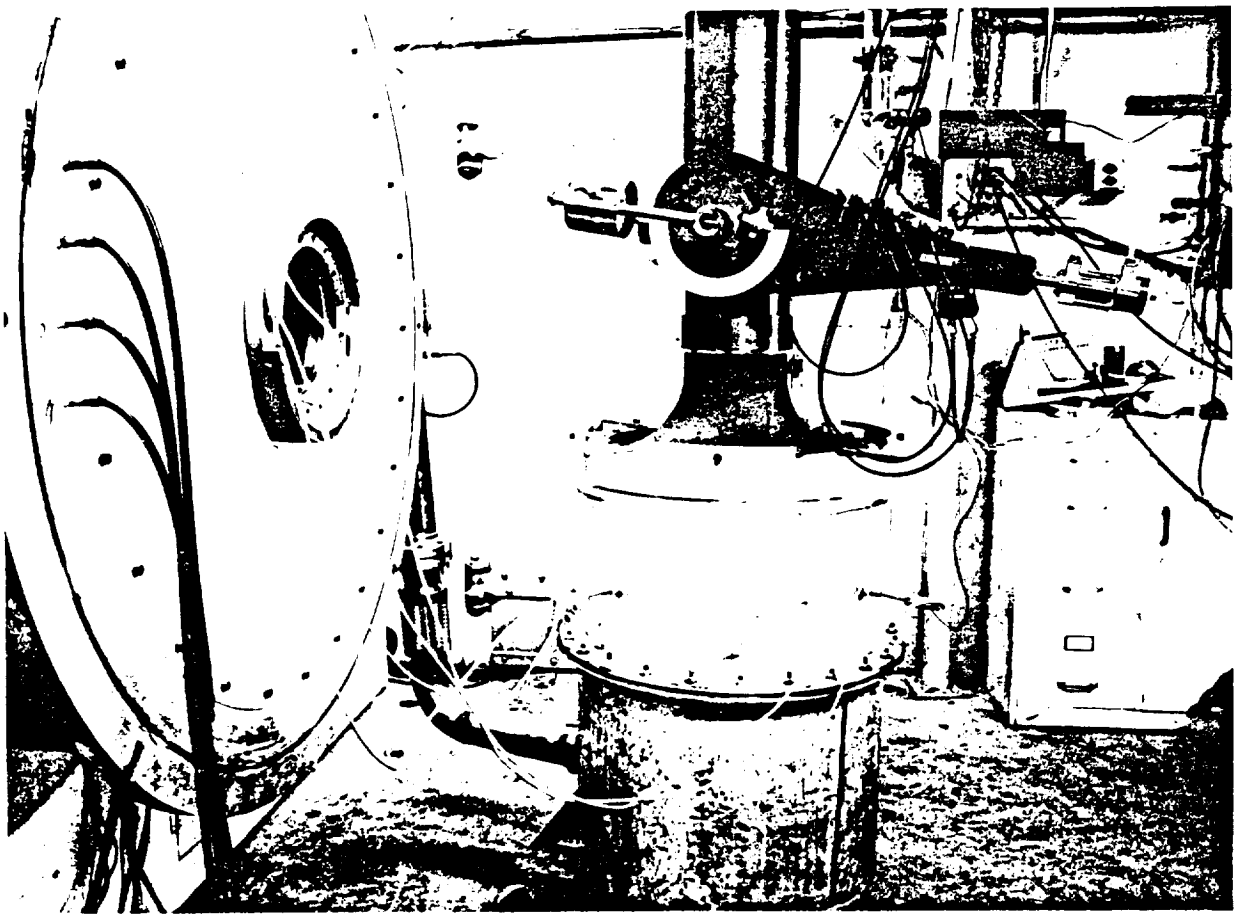

Figure 173. 3-D Hot Wire Calibration Tunnel.

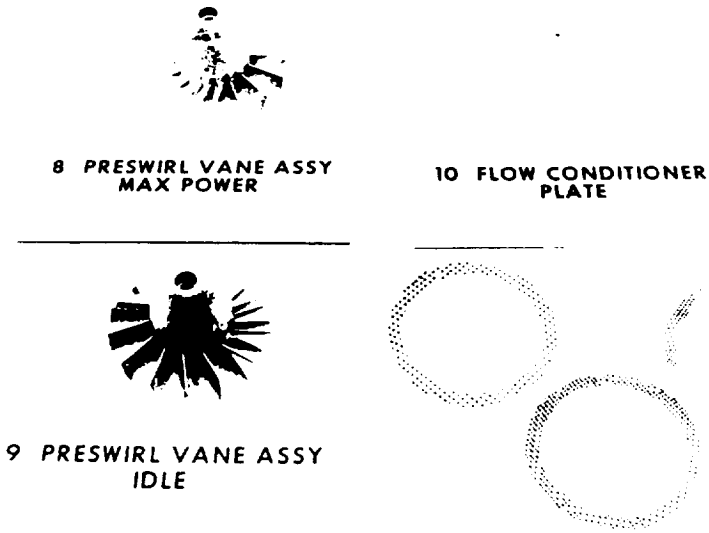

Figure 174. Regenerator LP Cold Rig Preswirl and Screen Assemblies.

A series of tests were conducted at simulated turbine rotor exit swirl angles and respective flows to determine the effect of swirl on regenerator LP inlet pressure distortion. Swirl angles of +55 degrees (idle), 0 degrees (cruise), and -27 degrees (maximum power) were induced at the rotor exit plane. Concurrent 3-D analysis showed that circumferential distortion of comparatively large magnitude has a negligible effect on regenerator effectiveness when gas/matrix heat transfer and core rotation effects are considered.

Tests also were conducted at various mass flows [hence Mach number and plenum head Q ($\theta V^2/2g$)] and 0 degrees swirl. These tests were conducted to determine effects of mass flow variations on regenerator LP-inlet pressure. Distortion magnitude remains approximately linear with inlet Q as mass flow rates increase.

Based on the above test results and the fact that the aggregate fuel consumed over CFDC in the upper 60-percent power range is negligible, all remaining cold flow pressure distortion testing (LP and HP) was conducted at cruise conditions.

Figure 175 presents the observed inlet pressure distortion (local cold core pressure drop) for the LP core face imposed by engine flowpath geometry at the simulated cruise condition.

Several flow influencing devices were evaluated to determine the potential of reducing LP inlet flow distortion. Downstream devices (baffles) showed limited potential for reducing LP inlet flow distortion. An upstream "diverter," Figure 176 showed good potential for redistributing the flow, as noted in Figure 177. The parameter U/V_{REF} seen in Figure 177 is based on 3-element anemometer data

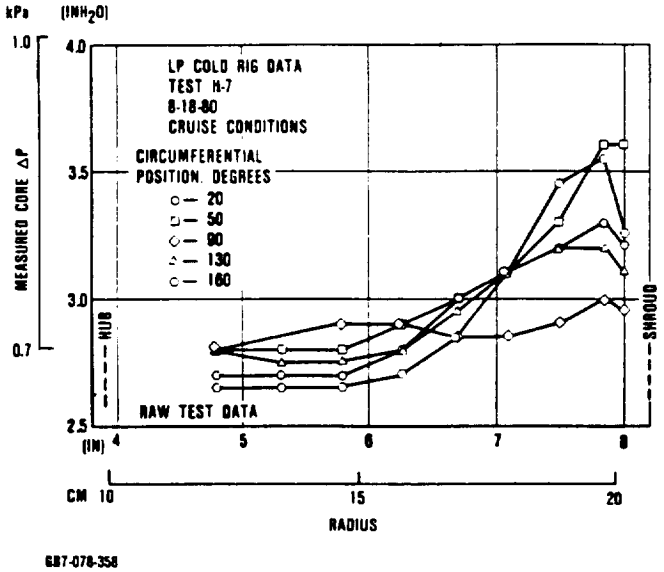

Figure 175. Measured LP ΔP Data From Regenerator Cold Rig.

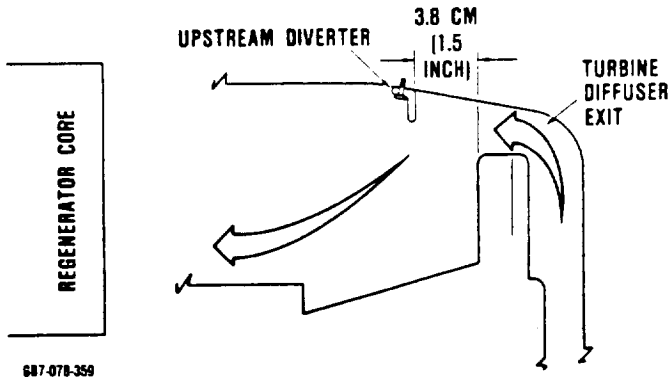

Figure 176. LP Regenerator Cold Rig Upstream Diverter.

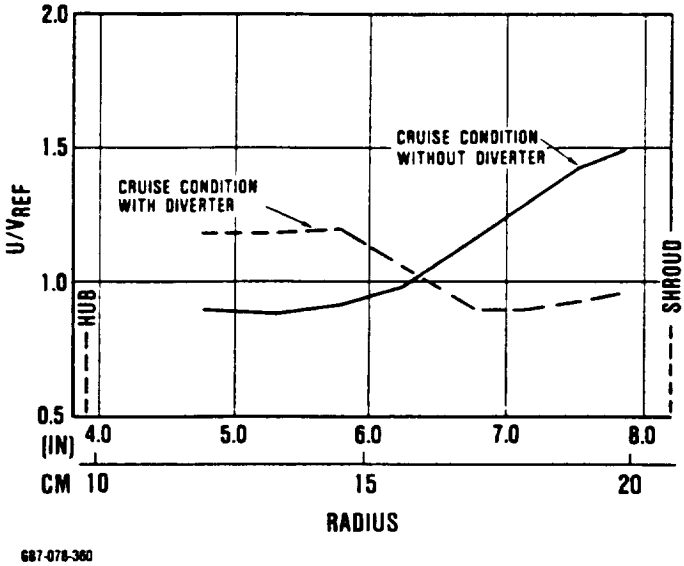

Figure 177. LP Regenerator Cold Rig, Effects of Upstream Diverter.

and is the ratio of local to average axial velocity at core inlet.

For the ceramic engines, placement of the upstream diverter requires ceramic fabrication tooling changes. Therefore, it was decided to await hot regenerator rig test results prior to any further evaluation or adoption of this upstream diverter for AGT101 application.

Data obtained from LP and HP cold rig testing were used to predict regenerator performance in the engine as described in paragraph 5.4.2.3.

5.4.2.2 Regenerator High Pressure (HP) Cold Rig

The HP side regenerator cold rig (Figure 178) has the same criteria for engine similarity as the LP side of the cold rig. The objectives of this rig are to match the flow patterns of the LP side such that the maximum heat transfer is optimized. Flow control techniques for this purpose include various hole patterns and radial web stiffeners in the exhaust housing and internal recontouring of the housing. Here again, a 3-D hot wire probe was installed immediately downstream of the core for direct low level velocity measurement. Additional instrumentation was in-

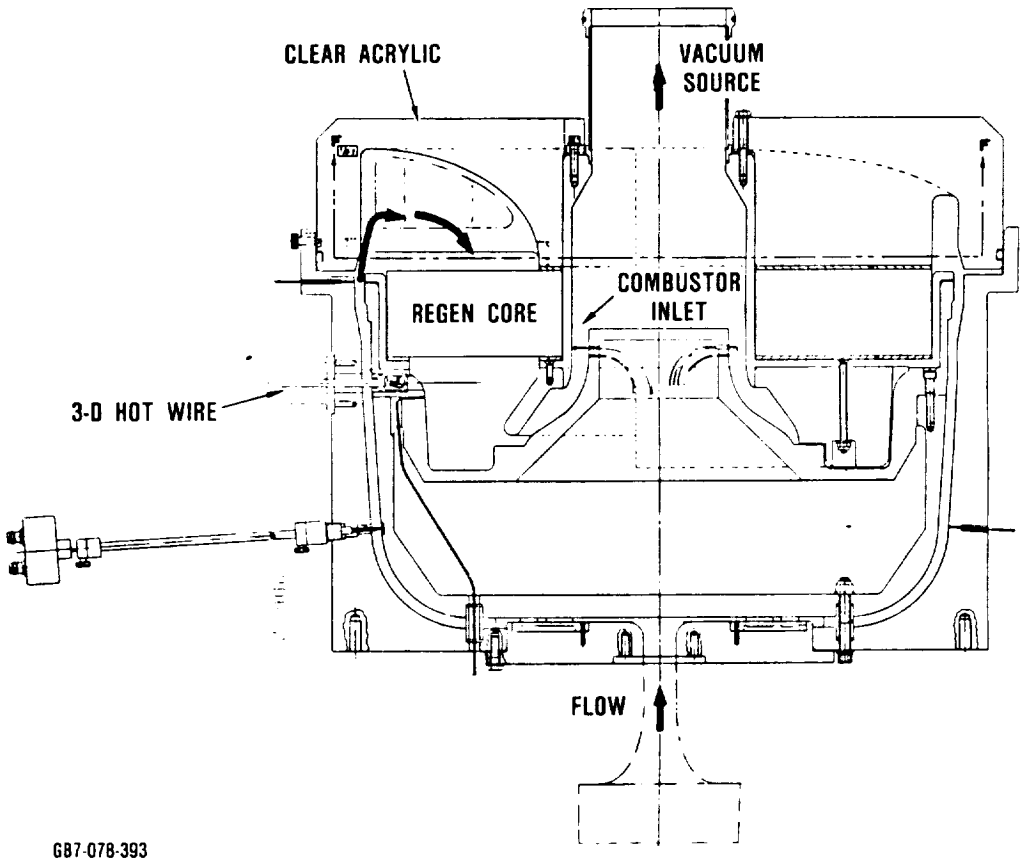

Figure 178. Regenerator HP Cold Rig.

cluded for the determination of the combustor annulus inlet velocity profile such that an optimum shape could be determined for the regenerator exit/combustor inlet guide vane configuration. A uniform circumferential flow profile is desired at the combustor inlet to assure the best flame control and primary/secondary mixing in the combustor. Effects of this guide vane selection on the regenerator flow profile were also determined.

Regenerator HP Rig Testing

Main objectives for the HP cold flow rig tests were the same as the LP cold flow rig tests.

Testing was initiated to determine HP inlet flow distortion at engine cruise operating conditions. Radial distortion (from hub to shroud) was measured for a bare, untreated HP flowpath.

Several flow influencing devices (bonnets) were evaluated on the downstream HP flowpath utilizing hot-wire anemometry. Figure 179 shows the dramatic influence of one of the bonnets on HP-flow conditions in terms of HP-discharge velocity ratios (U/V_{REF}).

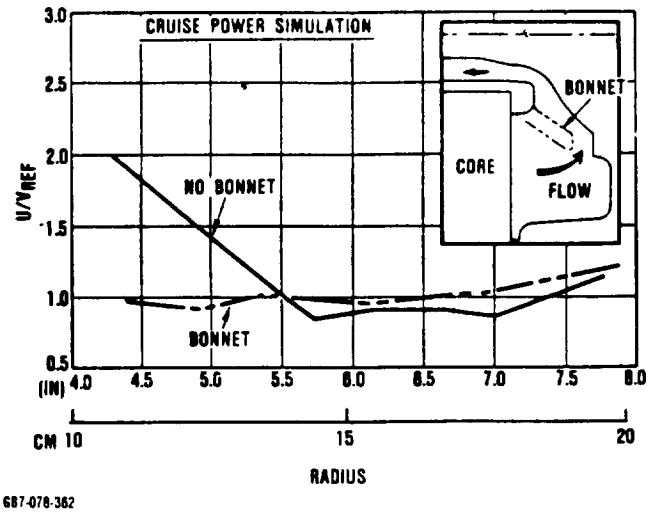

Figure 179. HP Regenerator Cold Rig Flow Effects of Bonnet.

Figure 180 shows the HP regenerator cold rig test data used for subsequent analysis. Testing was conducted both with and without the HP-inlet housing (exhaust housing) and confirmed that HP-inlet flow distortion is dominated almost solely by hot face flow separator housing geometry (downstream bonnet).

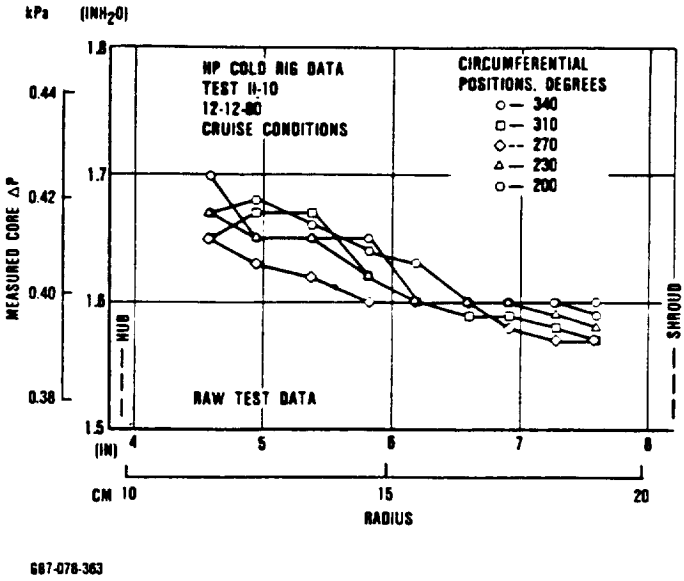

Figure 180. Measured HP ΔP Data From Regenerator Cold Rig With Bonnet.

5.4.2.3 3-D Finite Element Analysis of Regenerator Cold Rig Data

Regenerator Analysis

To predict regenerator effectiveness based on cold flow test data, an analytical model using 3-D finite element techniques was used. The core matrix was divided into 10-radial stations, 20-axial stations and 360-rotational increments. Core matrix geometry and pressure drop/heat transfer characteristics were program inputs.

Care should be exercised when comparing quoted regenerator effectiveness associated with engine performance results presented herein. Engine performance includes effects of regenerator seal leakage and, therefore, represents the mixed flow effectiveness for

the entire regenerator system. The results described here refer only to core effectiveness. Mass flows used in the 3-D analysis for both the LP and HP flowpaths have been adjusted for predicted seal leakages.

Analytical Model

Regenerator core effectiveness was analytically predicted by imposing measured or prescribed core inlet face pressure distortion profiles on the rotating 3-D heat transfer mode. Figure 181 shows the principle features of the analysis wherein matrix geometry, Colburn number characteristic, Fanning friction factor characteristic and core rotational speed are program inputs. Heat transfer and core pressure drop calculations, within the core matrix, are determined using local properties (i.e., local Reynold's Number, viscosity, etc). The analytical model also includes effects of local radial and axial conductive heat transfer to neighboring elements. Individual elements are analyzed for heat transfer along five paths (four core conduction and one gas convection path). Time integration is used to arrive at a steady-state heat transfer solution that is consistent with this pressure distortion profile imposed at the HP and LP inlet planes.

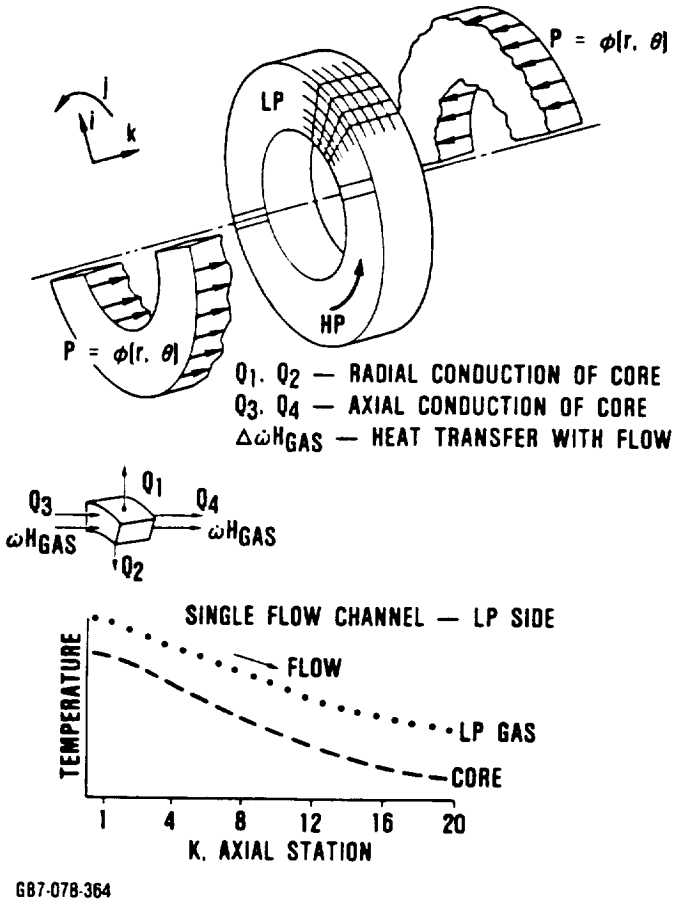

Figure 181. Measured Analytical Flow Distortion Model.

Sample Procedure

As an aid in explaining the test and analytical procedures, the following paragraphs describe the steps involved in obtaining an analytical prediction of regenerator performance in the engine. Since the cruise condition is of most interest, it is the subject of the example case.

Step 1: Cold Rig Testing

Cold rig tests were performed using the LP and HP cold flow rigs. The salient corrected flows (and therefore the Mach numbers) predicted for engine operation at cruise were supplied to the respective rigs. The corrected flows simulated were LP inlet and HP discharge since these are the locations generating the bulk of the pressure distortion.

Data were taken in the form of core pressure differential. Data for the LP rig were obtained by stagnating small core areas [0.64 cm (0.25 inch) diameter] from the exhaust side. The upstream stagnation pressure was then measurable through the core matrix. Static pressure data from the HP cold rig were obtained in similar fashion from the HP inlet core face.

Assuming that the core face stagnation pressure is essentially unaffected by the instrumentation measurement technique, the axial velocity through the core corresponds to only about 0.25 mm (0.01-inch) H_2O velocity head (approximately one percent of the peak-to-peak distortion level).

Figures 182 and 183 describe the raw cold rig ΔP (local cold core pressure drop) data for the HP and LP rigs. Note the excellent agreement between the theoretical (calculated from the core matrix Fanning friction factor data) ΔP for uniform flow and the average measured ΔP in both cases.

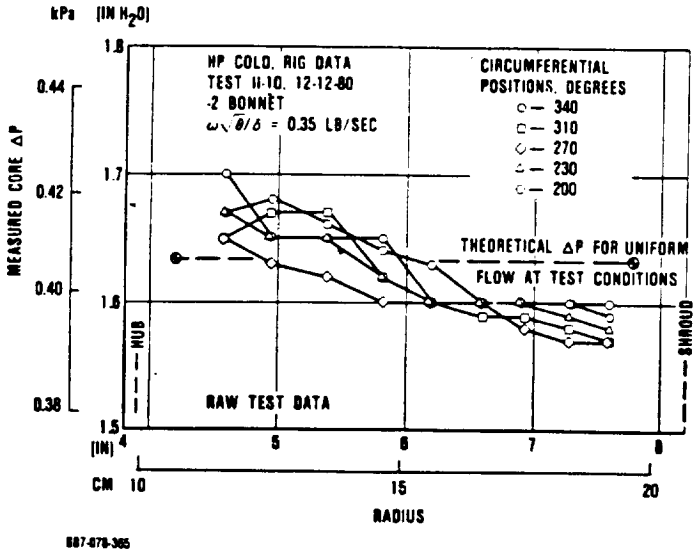

Figure 182. Measured HP ΔP Data From Regenerator Cold Rig.

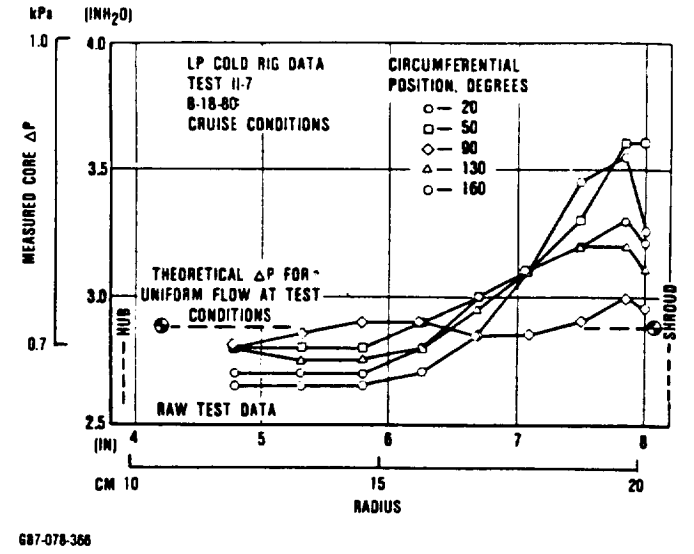

Figure 183. Measured LP ΔP Data From Regenerator Cold Rig.

Step 2: Test Data Preparation

The ΔP data shown was scaled slightly upward [by the ratio of $P(\omega\sqrt{\theta}/\sigma)^2$] to match the latest predicted engine hot face corrected flow and Mach number at the cruise condition. This step is required solely because engine predicted stage points had changed slightly between test and analysis stages.

Step 3: Analytical Input

The scaled HP and LP pressure field data were input to the 3-D analysis as hot face pressure boundary conditions. The analysis allows a uniform pressure drop bias to pass the required flow rates. However, the variable portion of the pressure profile is preserved. The gross level of pressure drop is a result of core matrix pressure drop while the variable (profile) portion is the result of flowpath geometry and flow redistribution patterns.

Step 4: 3-Dimensional Analysis

The analysis was run with the above pressure profiles as boundary conditions and the predicted engine flow, temperature and pressure data as input. The analysis iteratively arrives at a heat transfer solution and HP- and LP-flow profiles, which satisfy the heat transfer, energy balance, and pressure drop boundary conditions.

Step 5: Interpretation of Analysis

Figure 184 shows the analytical prediction of capacity rate ratio (CRR) and LP and HP mass velocities ($F = \rho V$), which result from the imposed (test) pressure fields and flow conditions. The mass velocities and CRR are circumferentially averaged at each radial station in Figure 184. Note that CRR is defined here as the ratio of LP-capacity rate divided by HP-capacity rate and is not necessarily equal to C_{Min}/C_{max}. Figures 185 and 186 summarize the analytically predicted cruise discharge face gas isotherms and mass flux contours.

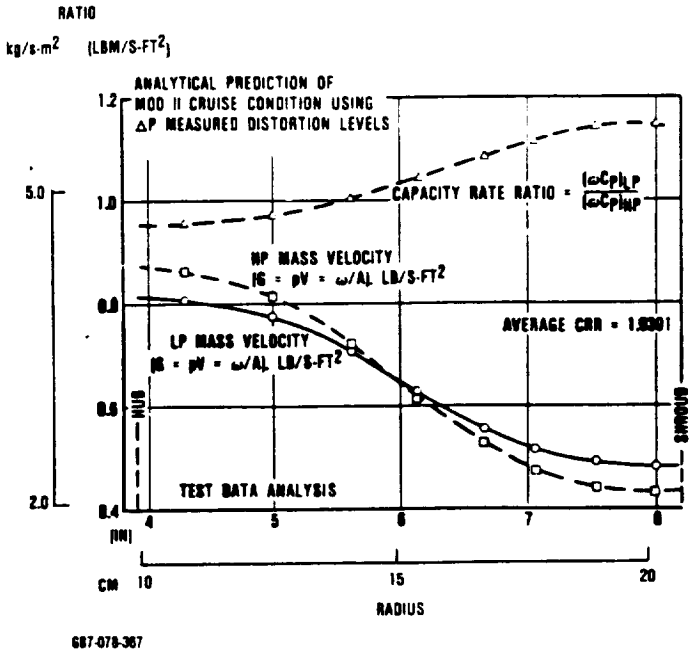

Figure 184. Capacity Rate Ratio and Integrated Mass Flux Versus Radial Position.

Observe that even nominal distortion generates a significant (55.5K/inch) radial discharge gas temperature gradient at the LP and HP carryover point (about 170- and 350-degrees angular position). The idealized case (no pressure distortion) yields essentially radial isotherms (no radial gradient) except for slight asymmetry introduced by the crossarm seals.

The analysis predicts a HP-side temperature effectiveness of 0.9662 with the imposed distortion levels. This compares with the ideal effectiveness of 0.9779 in the absence of pressure distortion. The predicted loss in effectiveness due to distortion is, therefore, 0.0117 at the cruise condition. No significant effect on performance is anticipated from the slight predicted increases in core pressure drop. These small increases in pressure drop are manifestations of residual flow kinetic energy which is already considered lost in the engine performance predictions.

Analysis of distortion effects was similarly accomplished for operating points along the

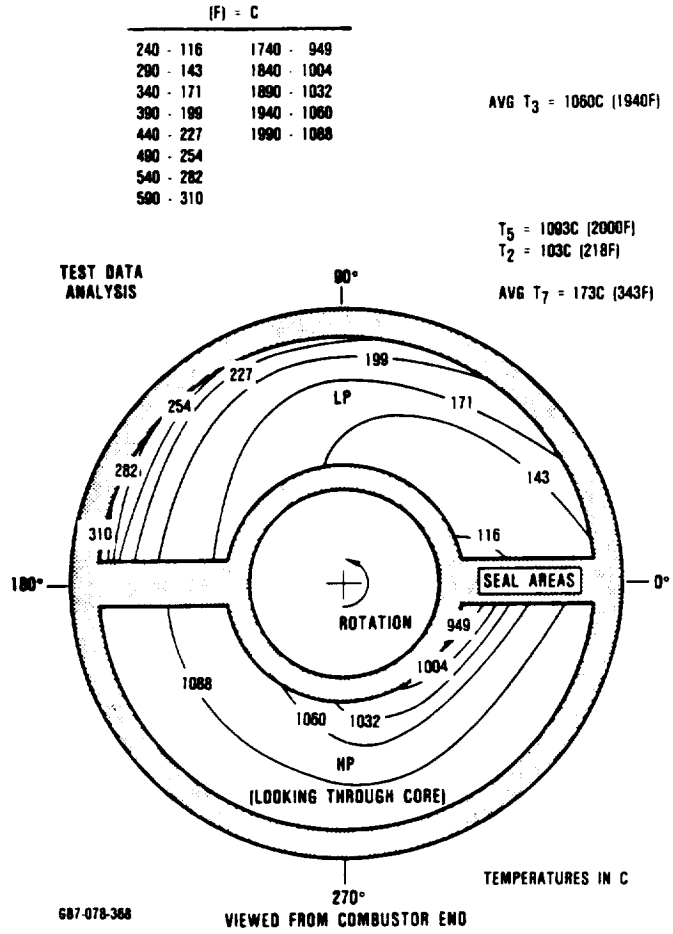

Figure 185. Predicted AGT101 Regenerator Discharge Gas Isotherms for the Cruise Condition Based on Cold Rig Pressure Distortion Patterns.

engine operating line from idle to maximum power. The penalty, in terms of fuel flow, was then correlated to engine output power as described in the following section.

Analytical Results

Table 24 summarizes the regenerator analysis results. Cases 1 through 7 and 14 are hypothetical cases using prescribed distortion profiles. Cases 9 through 13 and 15 through 18 are evaluations with measured distortion profiles based on LP and HP testing. Initial work

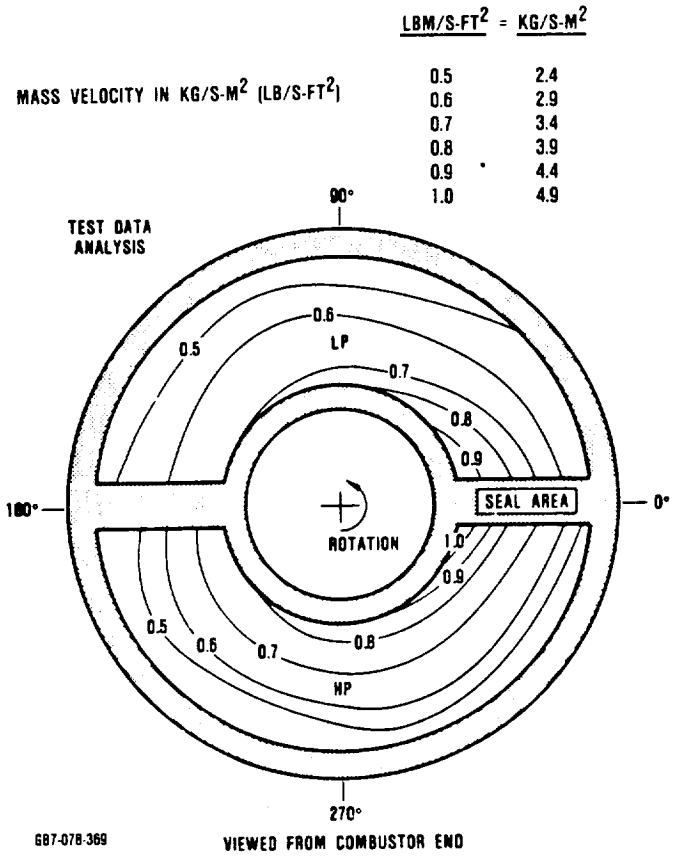

Figure 186. Predicted AGT101 Regenerator Local Core Mass Velocities for the Cruise Condition Based on Cold Rig Pressure Distortions.

(cases 1 through 8) was conducted using early engine cycle statepoint data corresponding to a low cruise 11.2 kw (15 hp) condition. Subsequent work (cases 9 through 18) was performed using current 1371C (2500F) engine statepoints.

Results of case studies showed good agreement between the traditional 1-dimensional (1-D) solution and the 3-dimensional (3-D) finite element solution for undistorted cases.

Figure 187 presents results of cases 2 through 8. These case studies, with hypothetical distortion were configured to evaluate and quantify the effect of radial inlet distortion profiles. The prescribed inlet distortion profile for these cases is linear with radius from hub to shroud. Note the difference in LP and HP sensitivity.

Early measured LP-cold flow data for the low cruise condition was analyzed with a uniform (ideal) HP inlet flow. Case 8 results, shown in Figure 187, indicates that the distortion measured on the LP rig yields an effectiveness degradation of (0.0043) equivalent to a linear radial LP inlet distortion profile of 0.14 kPa (0.56-inch) H_2O.

Cases 9 through 18 summarize the analysis for idle, cruise, and maximum power using current 2500F engine cycle statepoints. Cases 13 and 14 can be used to evaluate the effects of LP-circumferential pressure distortion. Case 14 is a case with a hypothetical circumferential pressure distortion of 0.55 kPa (2.23 inches H_2O) (positive gradient in the direction of rotation). This magnitude is two to ten times greater in peak-to-peak magnitude than the observed cold flow radial distortions, and yet results in a negligible (Δ = 0.0001) degradation of effectiveness. Other cases (HP side and negative gradients), not included in Table 24 show equal or lesser impact. Circumferential distortion of any reasonable magnitude is not considered to impact regenerator performance.

Cases 9, 12, and 16 are traditional 1-D analyses and are provided for comparison with Cases 10, 13, and 17, which are 3-D analyses. Cases 11, 15, and 18 are analytical evaluations using distortion profiles measured during LP and HP cold flow testing. Both the LP and HP inlet flowpaths are untreated (no baffles or flow diverters) and the magnitude of distortion is corrected from cold test conditions to engine operating conditions by the ratio of $P(\omega\sqrt{\theta}/\delta)^2$.

Cases 11, 15, and 18 results are utilized in the construction of Figure 188, where effectiveness and fuel flow penalties are projected as a function of engine horsepower. These projections are determined through the use of engine performance and CFDC computer models. Since the majority of fuel consumed over the CFDC occurs in the 0 to 29.8 kw (0 to

Table 24. Regenerator Analysis Summary.

Case	Engine Power	LP Core Inlet Distortion	HP Core Inlet Distortion	Effectiveness $\Delta T/\Delta T_{MAX}$)	
				E_{HP}	E_{LP}
1	Low Cruise	1-D Ideal	1-D Ideal	0.9823	--
2		Ideal (3-D)	Ideal (3-D)	0.9837	0.9473
3		0.42 in-H_2O Radial**	Ideal	0.9810	0.9445
4		1.00 in H_2O Radial**	Ideal	0.9734	0.9359
5		1.95 in-H_2O Radial**	Ideal	0.9607	0.9212
6		Ideal	0.21 in-H_2O Radial**	0.9814	0.9449
7		Ideal	0.976 in-H_2O Radial*		0.9648
8		ΔP Map 8-18-80	Ideal	0.9794	0.9426
9	Idle	1-D Ideal	1-D Ideal	0.9849	—
10	Idle	Ideal (3-D)	Ideal (3-D)	0.9841	0.9632
11	Idle	ΔP Map 8-18-80*	ΔP Map 8-12-80*	0.9808	0.9603
12	Cruise	1-D Ideal	1-D Ideal	0.9750	—
13	Cruise	Ideal (3D)	Ideal (3-D)	0.9779	0.9430
14	Cruise	2.23 in-H_2O Circumferential	Ideal (3-D)	0.9778	0.9429
15	Cruise	ΔP Map 8-18-80*	ΔP Map 8-12-80*	0.9662	0.9299
16	Max	1-D Ideal	1-D Ideal	0.9506	—
17	Max	Ideal (3-D)	Ideal (3-D)	0.9549	0.8996
18	Max	ΔP Map 8-18-80*	ΔP Map 8-12-80*	0.9421	0.8858

*ΔP maps scaled from cold flow rig for appropriate corrected flow
**Linear variation of (P_{SHROUD}-P_{HUB}) in inches H_2O.

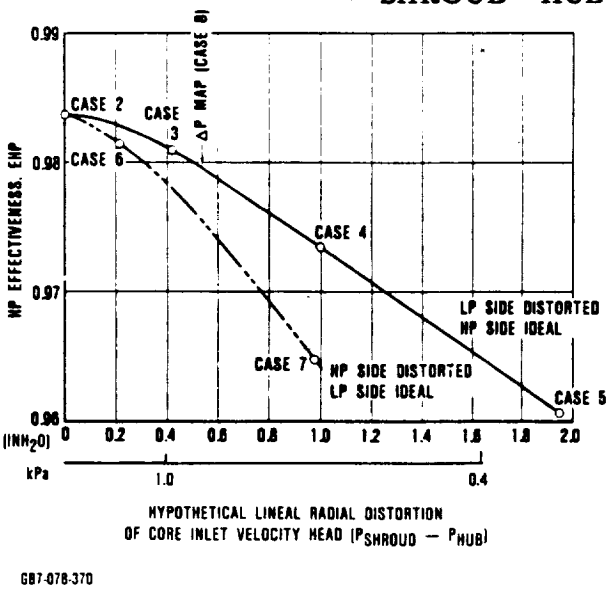

Figure 187. Effect of Linear Radial Distortion on Regenerator HP Effectiveness.

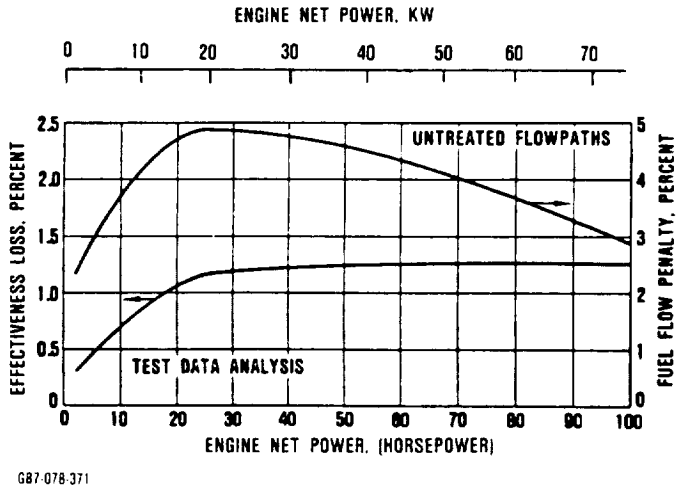

Figure 188. Effect of Measured HP and LP Distortion on Effectiveness and Fuel Flow.

40 hp) range, the expected fuel consumption penalty for an engine without regenerator distortion treatment is predicted to be approximately 3.5 percent.

5.4.2.4 Regenerator Hot Rig

The regenerator hot rig objectives are summarized below:

- o The hot regenerator rig is designed to measure regenerator seal leakage by the use of an inert gas (helium) seeding/detection system
- o The regenerator hot rig will be utilized to optimize flow distortion treatment geometry
- o The matrix effectiveness will be determined at optimum core rotational speeds for idle, cruise, and maximum power simulated conditions. Seal leakage will be factored into the core performance
- o Core drive torque will be determined under the following conditions:
  - New seal breakaway torque
  - New seal break-in interval (ideal conditions for approximately 10 hours)
  - Core drive torque during engine start sequencing
  - Steady-state torque at idle, cruise, maximum power engine conditions.
- o Verify matrix ΔP/P (HP/LP) at idle, cruise, maximum power simulated engine conditions
- o Measure cavity pressure at core ID under idle, cruise, maximum power simulated engine conditions, and size-bleed orifice to LP discharge to limit pressure in this area

The regenerator hot rig design is shown in Figure 189. The rig was designed to minimize leakage paths (at seal locations) by eliminating

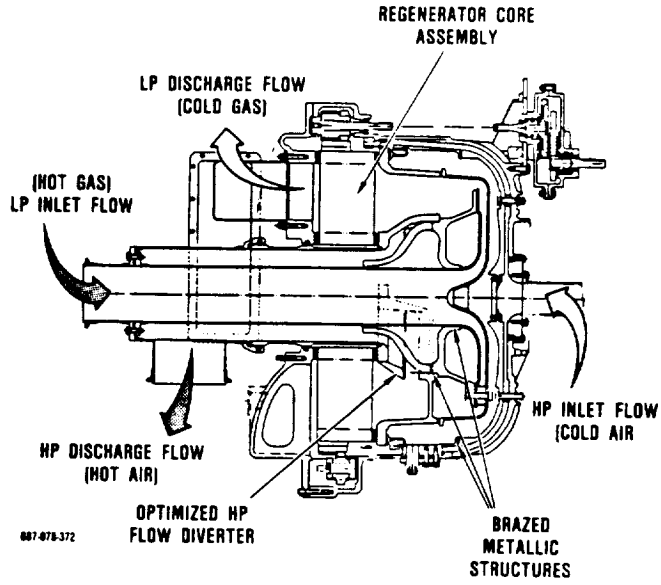

Figure 189. Hot Regenerator Rig Schematic.

all seals not required for unit assembly. Braze joints replace seal joints so that leakage from the HP side of the rig to the LP can only occur across the static side of the regenerator seal, flipper seal, and the dynamic face of the regenerator seals.

Hot Regenerator Test Results

The regenerator hot test rig was assembled and installed in the test facility. During rig Builds 1 and 2, minor assembly and laboratory problems precluded testing. Build 3 of the rig was completed and testing initiated. With the NGK core and first-generation Ford regenerator seals, static leak checks showed excessive leakage (≈25 percent of compressor inlet flow). The unit was disassembled and a series of vacuum leak tests were conducted. Several areas were noted as contributors with a significant leakage found in the NGK core. This core exhibited excessive through wall porosity resulting in approximately 40 percent of the total cold leakage noted earlier. Subsequent testing of the Corning thin wall cores exhibited negligible leakage. Modifications were incorporated to the test rig and the Corning core installed for Build 4.

Build 4 was completed and the unit installed in the test cell. Initial operation of the rig was conducted at ideal conditions [equivalent to 870C (1600F) TIT] for approximately 4 hours to break in (or glaze) the seals prior to performance mapping.

Further testing was conducted at simulated engine conditions. Instrumentation was located upstream and downstream of the HP and LP core faces. Thermocouple rakes were located in equal area planes at five radial locations, spaced approximately 35 degrees apart.

Dynamic seal leakage was determined using a unique helium flow seeding technique depicted in Figure 190. Helium is injected and

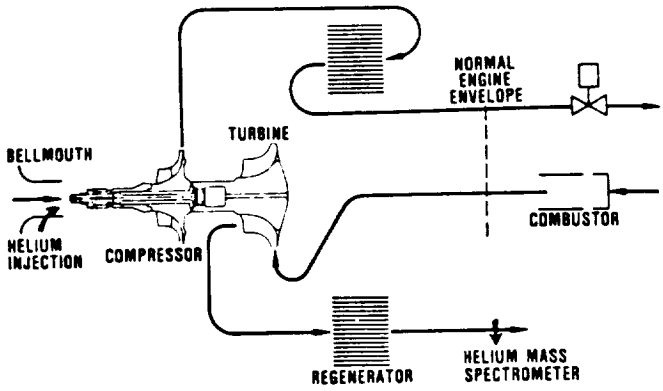

Figure 190. Schematic of Helium Seeding Technique for Measuring Regenerator Leakage.

mixed at selected stations upstream of the HP inlet. Flow passing through the HP side of the core is then ducted overboard. Conditioned LP flow is then introduced to the slave burner to maintain proper LP and HP flow match. Fuel is introduced and combustion initiated. Regenerator seal leakage from the HP side (helium seeded flow) to the LP side (unseeded) can then be determined using a mass spectrometer to measure helium concentration levels at the LP exhaust. Leakage is measured accurately to approximately 0.2 percent of the HP inlet flow.

Due to requirements of the 871C (1600F) engine test program, testing was limited to an idle condition only. Additional testing will be conducted following engine testing.

At points near idle conditions, leakage was measured at 0.26 kg/min (0.576 lb/min), approximately 5.2 percent of test compressor flow. Figure 191 shows the LP and HP core exhaust temperature profiles at the simulated idle condition. The tested temperature effectiveness of the HP side of the regenerator was 95.9 percent at idle conditions (Table 25).

Figure 191 shows that the radial temperature gradients of the discharge gases at the carryover points (170- and 350-degree arcs) are minimal indicating insignificant flow distortion effects.

Temperature effectiveness of the regenerator system is shown to be one percent lower than the goal. This deficiency may be solely the result of the additional interpath leakage.

Ford fabricated three sets of seals for test evaluation:

- o Baseline Phase IV seals
- o Phase IV with increased inner peripheral seal loading plus tapered thickness hot crossarm shoe
- o Phase IV with increased seal loading plus welded seal diaphragms

Each of these seal sets were installed and tested in the hot regenerator rig under nominal operating conditions ($T_{3.1}$ ≈120C or 250F, $T_{5.1}$ ≈650C or 1200F).

The third seal set with welded diaphragms exhibited such high seal loading resulting in excessive drive torque and prohibited the measurement of useful data. In fact, while attempting to test these seals, the ring gears were separated from two regenerator cores as

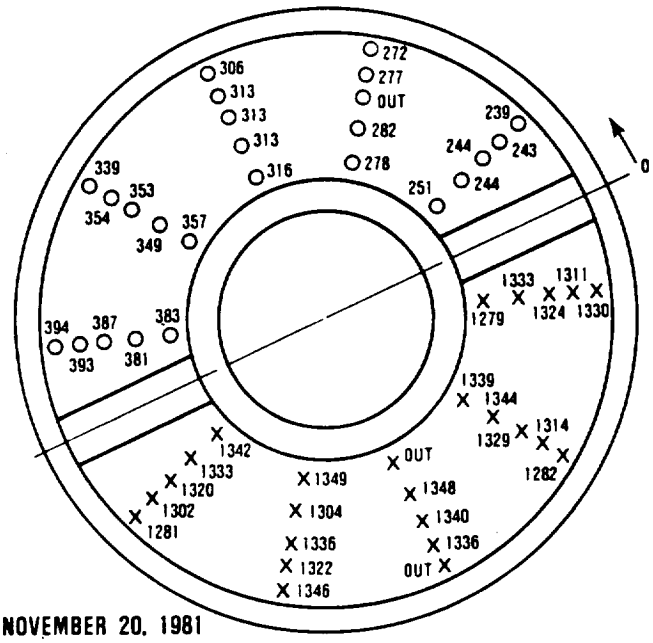

Figure 191. Steady State Regenerator Discharge Temperature Distribution.

a result of drive torques in the 41 to 62 kg-m (300 to 450 ft-lb) range.

Successful tests were completed on the baseline and tapered seal sets. The drive torque and leakage characteristic for these seals are shown on Figures 192 and 193, respectively.

Table 25. Regenerator Rig Test Results.

	Metal Engine (871C - 1600F) Predicted	Regenerator Rig Test Test Results
Regenerator HP Inlet Pressure, kPa (psig)	42.3 (6.14)	37.4 (5.42)
HP Side Inlet Flow kg/min (lb/min)	4.57 (10.07	5.03 (11.08)
LP Side Inlet Flow kg/min (lb/min)	4.48 (9.88)	5.05 (11.13)
HP Inlet Temperature C (F)	70 (158)	74 (165)
LP Inlet Temperature C (F)	788 (1451)	746 (1375)
LP Exhaust Temperature C (F)	115 (239)	157 (314)
HP Exhaust Temperature C (F)	766 (1411)	718 (1325)
HP Temperature Effectiveness	0.969	0.959
Interpath Leakage kg/min (lb/min)	0.196 (0.431)	0.261 (0.576)

The baseline seal set exhibited lower drive torque requirements and substantially higher leakage than the tapered seal set. The disparity in seal performance is probably a result of the higher seal stiffness of the tapered seal set.

Relative to the best of the earlier seal configurations neither of these seal sets exhibited improvement.

Instrumentation was added to this rig to measure the variations in seal clearance at the

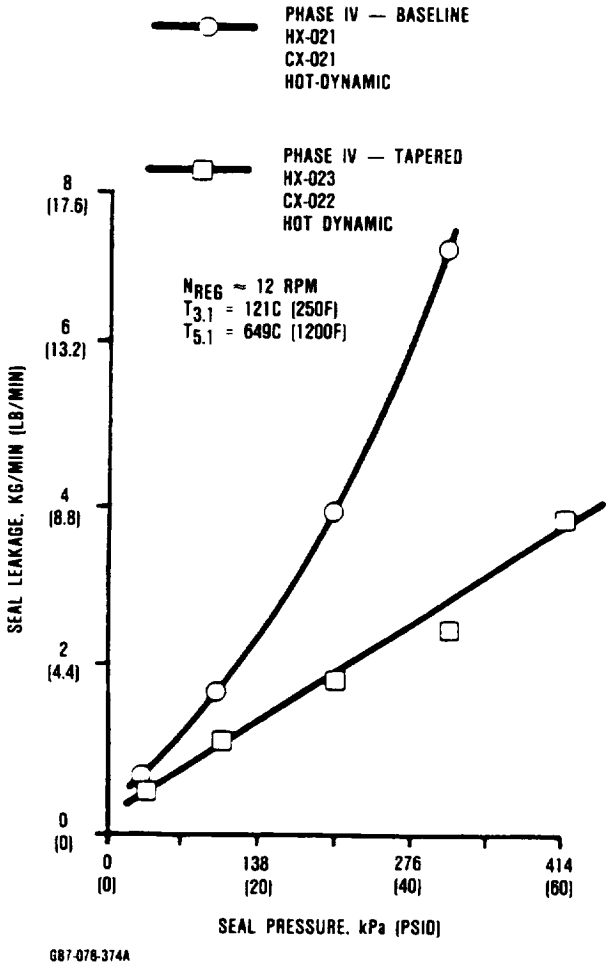

Figure 192. Regenerator Seal Leakage.

regenerator seal inner periphery crossarm positions. This instrumentation consisted of a set of Bentley clearance probes mounted on a bracket anchored to the exhaust cover bolt circle. The Bentley targeted a "finger" fixed to the regenerator shield. Another Bentley targeted the flat land of the exhaust cover. By comparing these clearance measurements, taking into account thermal growth of the regenerator shield, and the thermal effects on the Bentley calibrations the local variations in regenerator pocket can be calculated.

The data from this clearance probe instrumentation was inconclusive due to the lack of information on the thermal growth of the regenerator shield. Qualitatively however, these data seemed to indicate an opening of

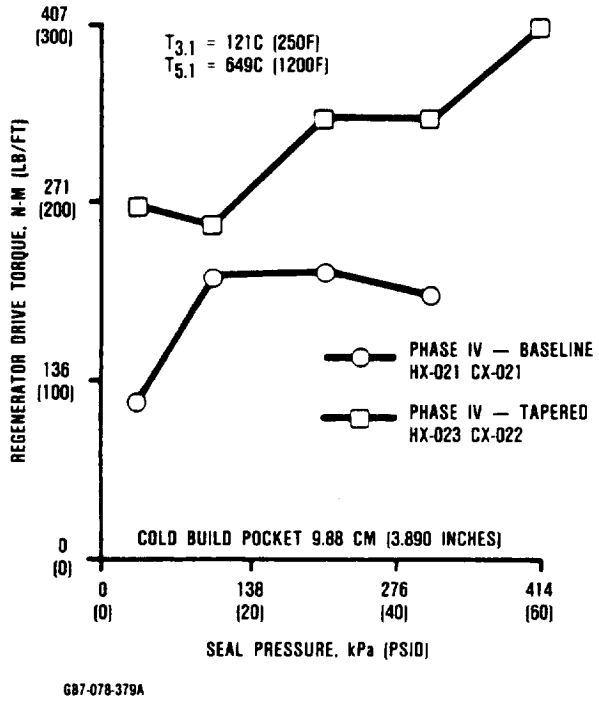

Figure 193. Regenerator Drive Torque.

the inner peripheral regenerator pocket with increased rig pressure.

Several tests were run and the cold build seal clearance was varied to determine optimum clearance with respect to seal leakage and drive torque. Figures 194 and 195 show seal leakage and regenerator drive torque plotted versus rig pressure for 1.35 mm (0.053 inch) seal clearance (optimum) and also for a 1.55 mm (0.061 inch) seal clearance. Leakage at low pressures proved insensitive to seal clearance while, at high pressures, sensitivity to leakage increased dramatically. Seal clearances smaller than 1.35 mm (0.053 inch) were tested, but excessive drive torques precluded gathering data at the higher pressures and the data that was obtained showed no improvement over the leakage with 1.35 mm (0.053 inch) seal clearance.

Unlike earlier generation seals, the drive torque at the optimum seal clearance is almost constant with respect to rig pressure.

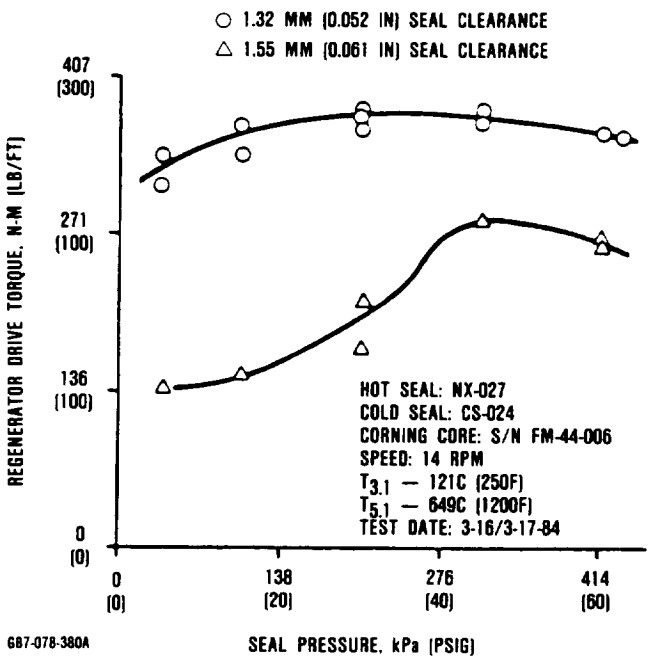

Figure 194. Phase V Regenerator Seal Drive Torque Versus Seal Pressure.

Relative to the best of the earlier generation seals, the Phase V seals represent an improvement in leakage. A comparison is shown with Phase III leakage curves in Figure 196. The seal leakage, measured at two values for total seal clearance, is shown plotted versus rig pressure.

Phase V seal drive torque is also shown compared with earlier seal (Figure 197) configurations. Although improved over Phase IV, these seals still have excessive drive torque.

5.5 Gearbox/Transmission

Single-shaft gas turbine engine optimization for automotive applications requires the use of a continuously variable speed transmission, (CVT) with high ratio reduction. Because the AGT101 was designed with an automotive application in mind, early phases of the project included design of a continuously variable transmission. An ideal CVT will allow

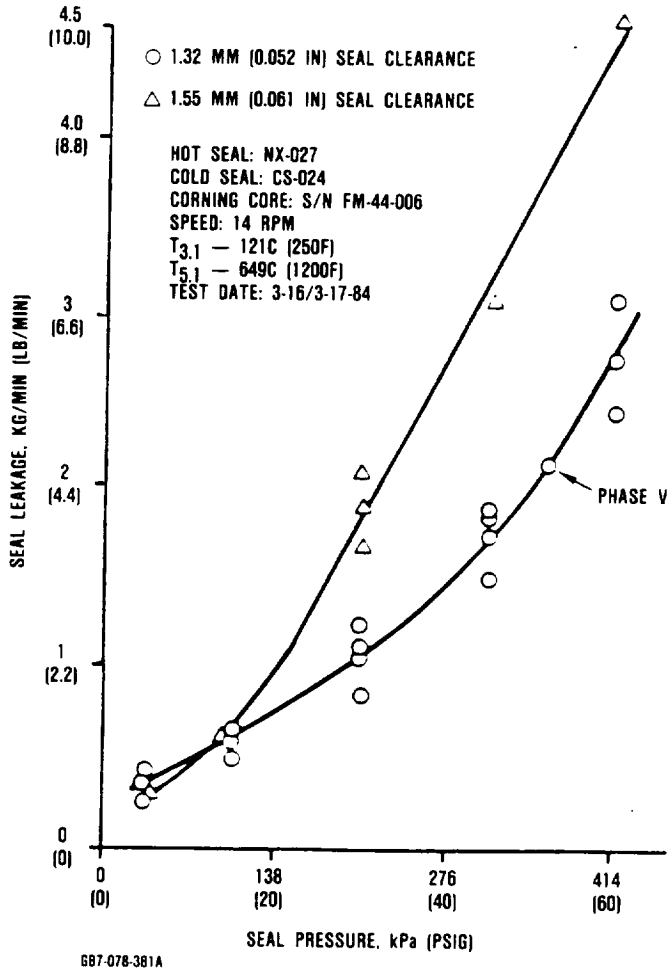

Figure 195. Phase V Regenerator Seals Clearance Test.

engine operation at efficient peak cycle temperatures for all power levels while operating over a limited speed range of approximately 50 percent speed at idle to 100-percent speed at full power.

The transmission system selected for the AGT101 consists of a high-speed variable single-stage differential planetary gearbox in conjunction with a modified Ford four-speed automatic overdrive (AOD) transmission. This combination results in a nearly stepless, continuously variable speed transmission required for single-shaft gas turbine vehicle system optimization.

The planetary gearbox incorporates a differential in which power is split into two

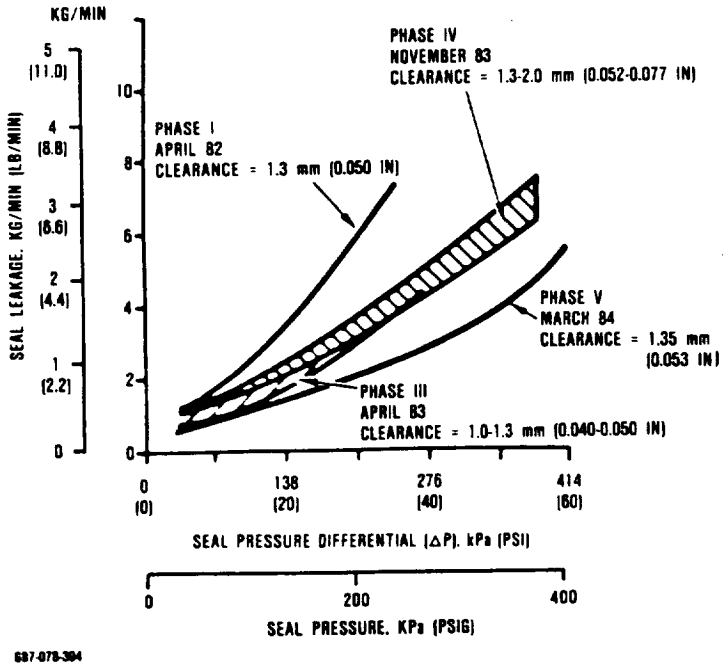

Figure 196. AGT101 Regenerator Seal Leakage.

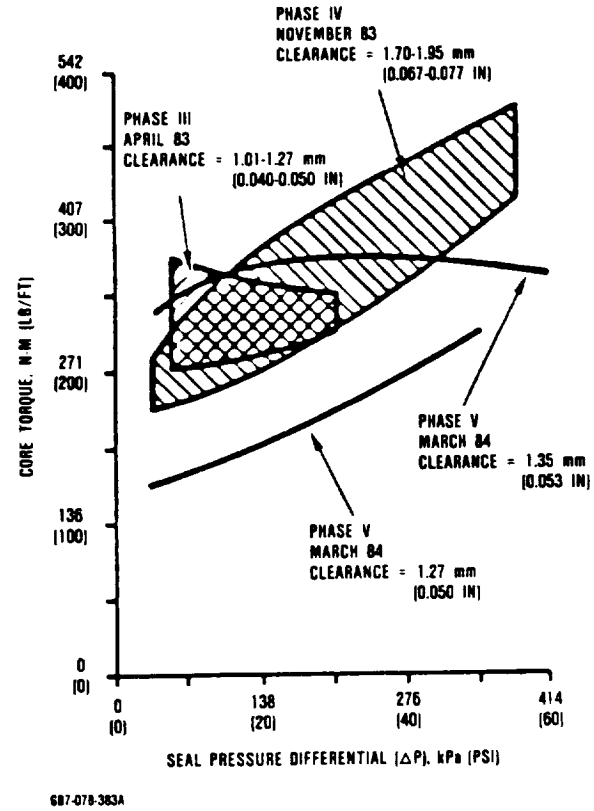

Figure 197. AGT101 Regenerator Core Torque.

paths. Power is input at the planetary sun gear and extracted from the planetary carrier. In this planetary system, all elements rotate and the relative speeds are interdependent. One power path extends directly from the sun gear to the carrier; the second power path passes through the planetary ring gear to a variable stator torque converter (VSTC) that is used as a speed changing device. The torque converter variable output speed is connected to the carrier through a clutch that is open during vehicle idle operation and closed during normal driving modes. Speed ratio modulation across the VSTC results in a variable output speed of the planetary carrier, which in turn is geared directly into the AOD transmission. Step ratio changes in the AOD are phased with off-setting speed ratio changes in the variable speed gearbox to produce a continuously variable drive line system.

The AGT101 drive system schematic is shown in Figure 198.

The AGT101 transmission system cross section is shown in Figure 199. The gearbox geartrain has been emphasized by solid black shading for clarification.

A 23.3 cm (9.18-inch) diameter VSTC of Ford design and manufacture was tested to generate a performance map covering the extended speed ranges, ratios, and stator blade angles required for the AGT101 application. The VSTC map is shown in Figure 200. Efficiency islands as high as 95 percent were identified and the gearbox differential ratios were selected to operate the VSTC in the most efficient areas over the CFDC.

In March 1981, when budget cuts occurred and the new Administration dictated that the Government should sponsor long-range high-technology programs that industry could not afford, the transmission and vehicular tasks were deferred for industry sponsorship, with remaining funds oriented at developing the AGT101 high-risk technology elements.

The variable stator torque converter for the AGT101 concept had been fabricated,

drawings were completed for the Ford AOD transmission modifications, and drawings for the differential gear and housings had been made at the time of curtailment of the transmission and vehicle phase of the AGT101 program. Consider that although the transmission arrangement illustrated in Figure 199 represents new technology, the components including variable stator torque converter consist of proven technology.

5.6 Controls and Accessories

The engine electronic control unit (ECU) and the fuel control unit evolved significantly during the course of the program. Initial design of these components was made assuming an automotive installation. The ECU software and hardware provided for many vehicle powertrain functions such as transmission operation in addition to engine control, and the

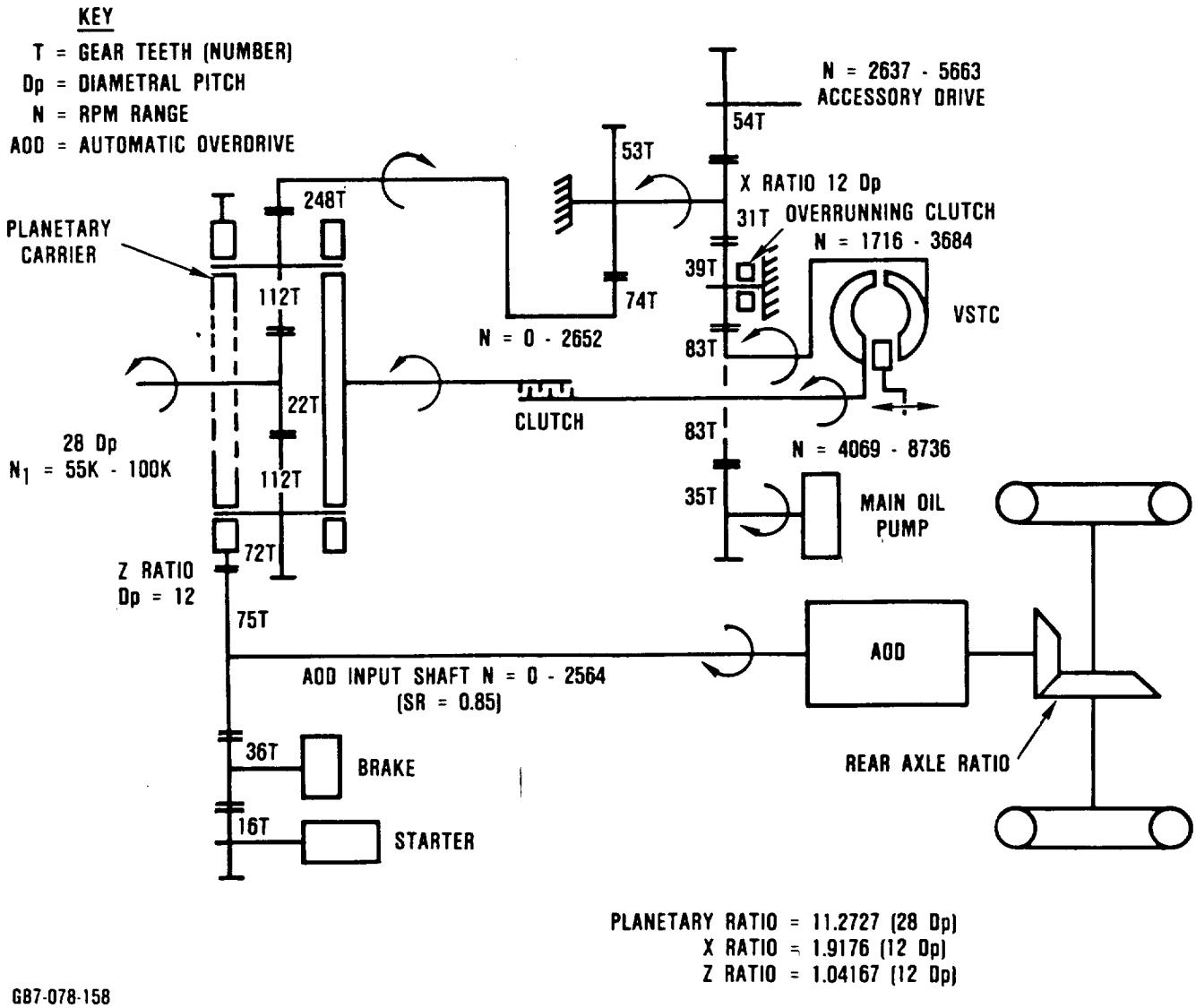

Figure 198. AGT101 Drive System.

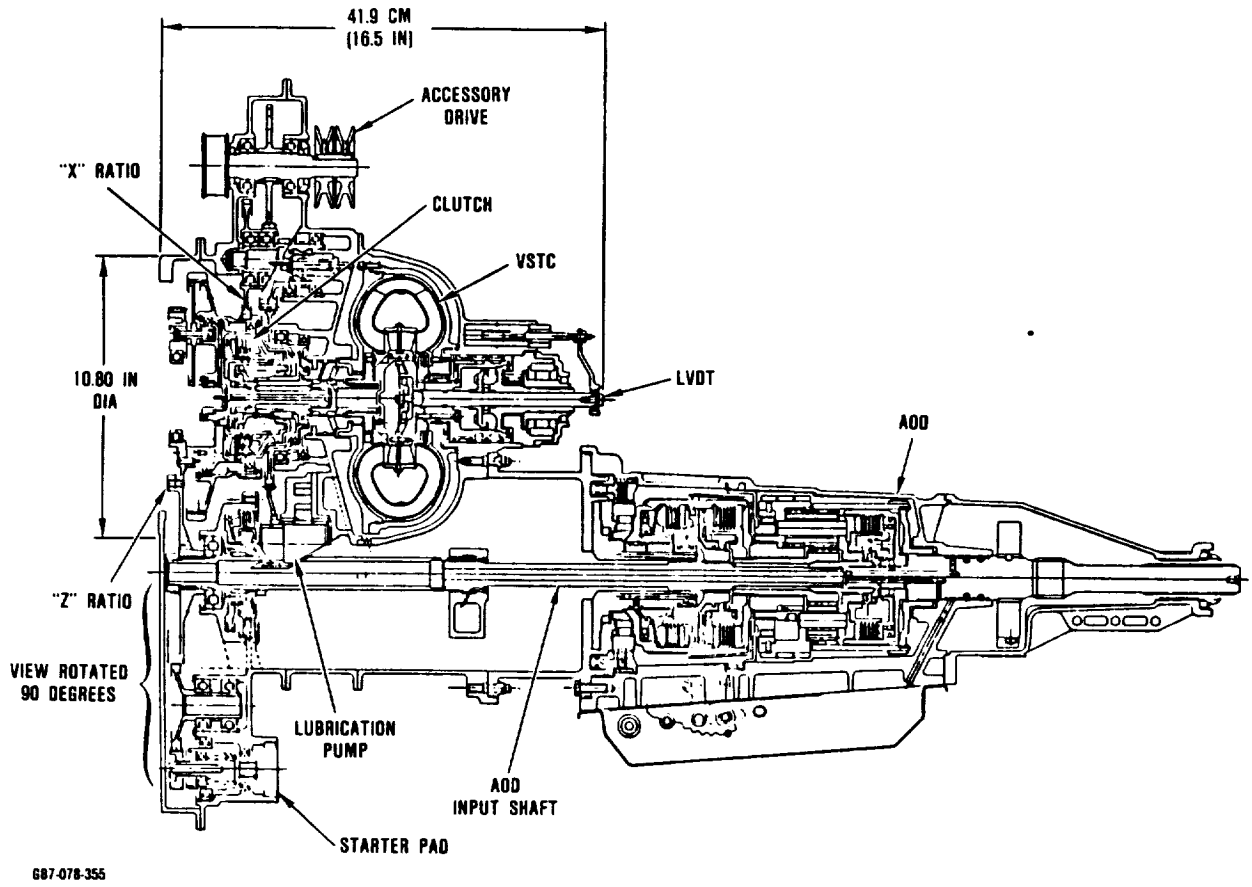

Figure 199. AGT101 Transmission System.

fuel control was designed as a compact unit for vehicular installation that operated on a 12 volt dc electrical system. Though they represented the state of 1980 technology, these components lacked the flexibility required for a laboratory test program. As a result, both components were redesigned to delete the vehicular features and enhance the flexibility required for laboratory testing.

5.6.1 Engine Electronic Control Unit

The initial ECU was based on an Intel 8086 microprocessor and incorporated 10 analog and 2 digital control boards. This unit featured both static (manual) and dynamic (automatic) control software and monitored all aspects of the vehicle powertrain operation controlling the transmission as well as the engine. This unit became obsolete as control technology progressed during the course of the program and the demands of laboratory ceramic engine testing became more and more difficult to meet.

A new ECU was designed and fabricated which featured improved flexibility over the original ECU. The new ECU, shown in Figure 201, consisted of 3 standard off-the-shelf boards, 1 iSBX board, 5 custom driver boards, a standard card cage and a RS232 adapter. By utilizing the commercial boards the ECU will be easily supported or expanded in the future to include new functions as they are needed. The commercial boards used in this new design are:

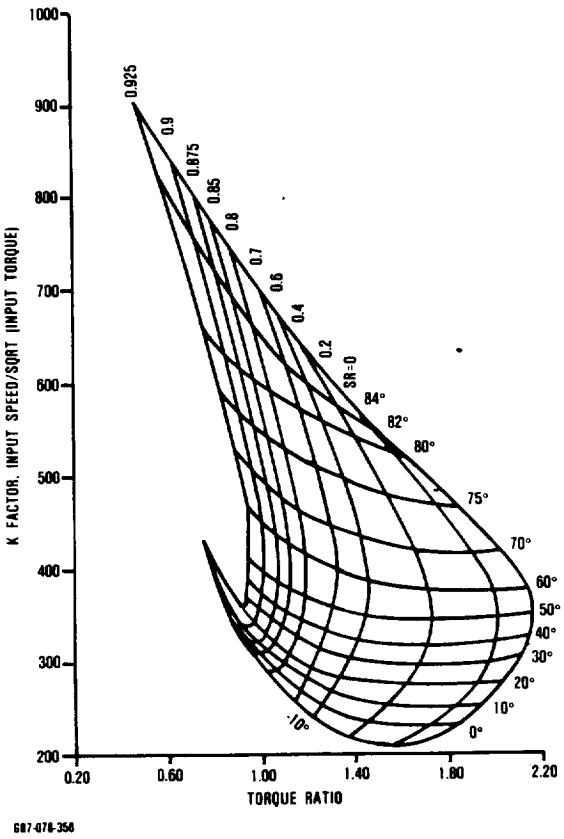

Figure 200. VSTC Test Results.

- o Systek 8810C CMOS CPU STD board
- o Intel iSBX 328 analog output board
- o MSI C412 CMOS Analog I/O board
- o Prolog 76C14 CMOS Digital I/O board
- o Prolog BR16-T card cage with 7102 STD Motherboard
- o Systek CA-101 RS232 serial adapter

The software for the new ECU consists of background and foreground modules. The foreground modules contain the control logic. The background modules in the final product are used to monitor and change the various setpoints and tables. During the ECU development phase the background modules were also used as tools for debugging and testing the foreground control logic.

Three important features were incorporated in the software to faciliate future support and modification of the ECU. First the entire software file was written in PL/M 86, a high-level programming language. The ECU control logic flow is clear and easy to understand from an examination of the program listing. Second, all setpoint variables and tables are defined and all RAM variables are grouped according to their function in the same programming module. Third, the ECU control logic is divided into different functions with each function programmed in a different module consisting of various related subroutines.

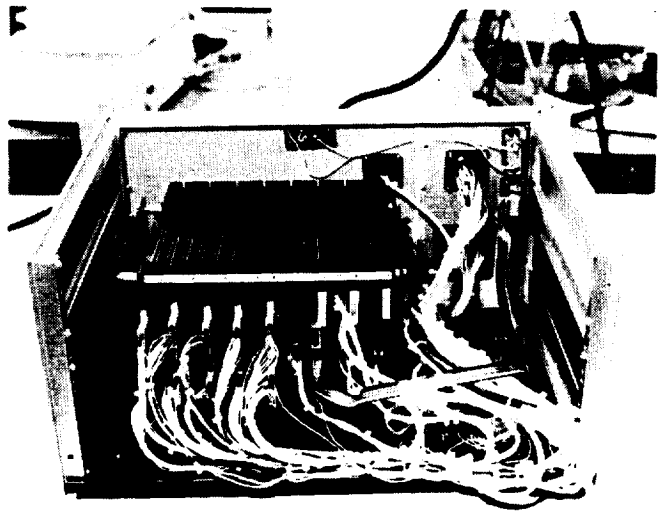

Figure 201. Engine Electronic Control Unit (ECU).

To enhance the capability of the ECU, up to 24 different sets of setpoints and tables can be saved, each containing 340 bytes of data. Different setpoint and table values can be input to the ECU through an external keyboard terminal, stored in internal memory and recalled as they are needed during the course of a test series. This allows different control parameters to be used from one run to another without physical modification to the ECU. A control software self-test mode was implemented to test the torque motor drivers and solenoid functions.

The ECU logic provides for full authority control of the engine during testing. Engine fuel flow and variable inlet guide vanes (VIGV) are modulated according to operator changes in engine speed setpoints and dynamometer load conditions. The ECU will provide for either manual or automatic operation of the VIGV and start functions. Engine protection is provided for low oil pressure, high oil temperature, overspeed, underspeed, and extreme engine station temperatures (turbine inlet, turbine discharge, regenerator LP discharge). The ECU logic diagram is shown in Figure 202.

5.6.2 Engine Fuel Control

The original AGT101 engine fuel control was a three piston pump with a pulse width modulated (PWM) fuel metering unit. This system was compact, driven by a 0.09 kw (1/8 hp) 12 vdc motor and mounted on the engine test cart. Repeatability, hysteresis, linearity, and frequency response were all improved over existing proportional metering systems. Difficulty arose when attempts were made to measure fuel flow with the PWM system.

The fuel flows required for engine testing ranged from 0.36 to 20.4 kg/hr (0.8 to 45 lb/hr). This exceeded the range of the turbine flow meters available and necessitated the use of a Coreiolis type mass flow measurement unit such as the one provided by Micromotion ®. The pulse frequency of the PWM system with the piston pump, interfered with the mass measurement of Micromotion system causing erroneous readings. Since fuel flow measurement was required for laboratory evaluations, an equivalent fuel control was designed and fabricated for use in the laboratory.

The new fuel control was based on the design used in Garrett's GTCP36-100 APU. The schematic in Figure 203 shows the fuel circuit in this design. This unit featured a gear pump with an internal bypass circuit and a combination of 70 micron filter screen and a cartridge filter. Fuel was metered with a torque motor specially selected to allow a range of fuel flows from 0 to 20.4 kg/hr (0 to 45 lb/hr). The system was driven by a constant speed 440 vac motor and mounted in its own cart for easy access and transportation.

5.6.3 Variable Inlet Guide Vane Actuator

The variable inlet guide vane actuator used during AGT101 engine testing was a torque motor actuated hydraulically driven unit. The actuator design was identical to that used in Garrett's GTCP331 series APUs and no development or modification was required.

5.6.4 Electrical Accessories

Engine temperature measurement for control and monitoring are provided by standard Garrett laboratory thermocouples. Type K (Chromel/Alumel) thermocouples are used for all temperature locations except for turbine inlet which used Platinum/Platinum-10 percent Rhodium thermocouples. These probes are a shielded open bead design which optimizes thermocouple response with respect to radiation error.

The hydraulic system low oil pressure switch incorporates a "shunt disc" actuating element. A resistive element temperature sensor is specified to monitor high oil temperature and ambient air temperature.

Engine speed sensing is accomplished using an eddy current killed oscillator transducer with a miniature 1.78 mm (0.070 inch) diameter probe tip supplied by Bently, Nevada Corp. This probe is mounted in the engine inlet housing and targets the stepped surface of the compressor shaft OD.

Connectors selected for development use are MIL-C-5015 threaded connectors with 16 gauge contacts. The ECU and engine harness had two connectors with 48 and 36 contacts for total of 84 terminations. The 48 and 36 contact connectors were common with the boom cables and interface connectors in the Garrett test facilities.

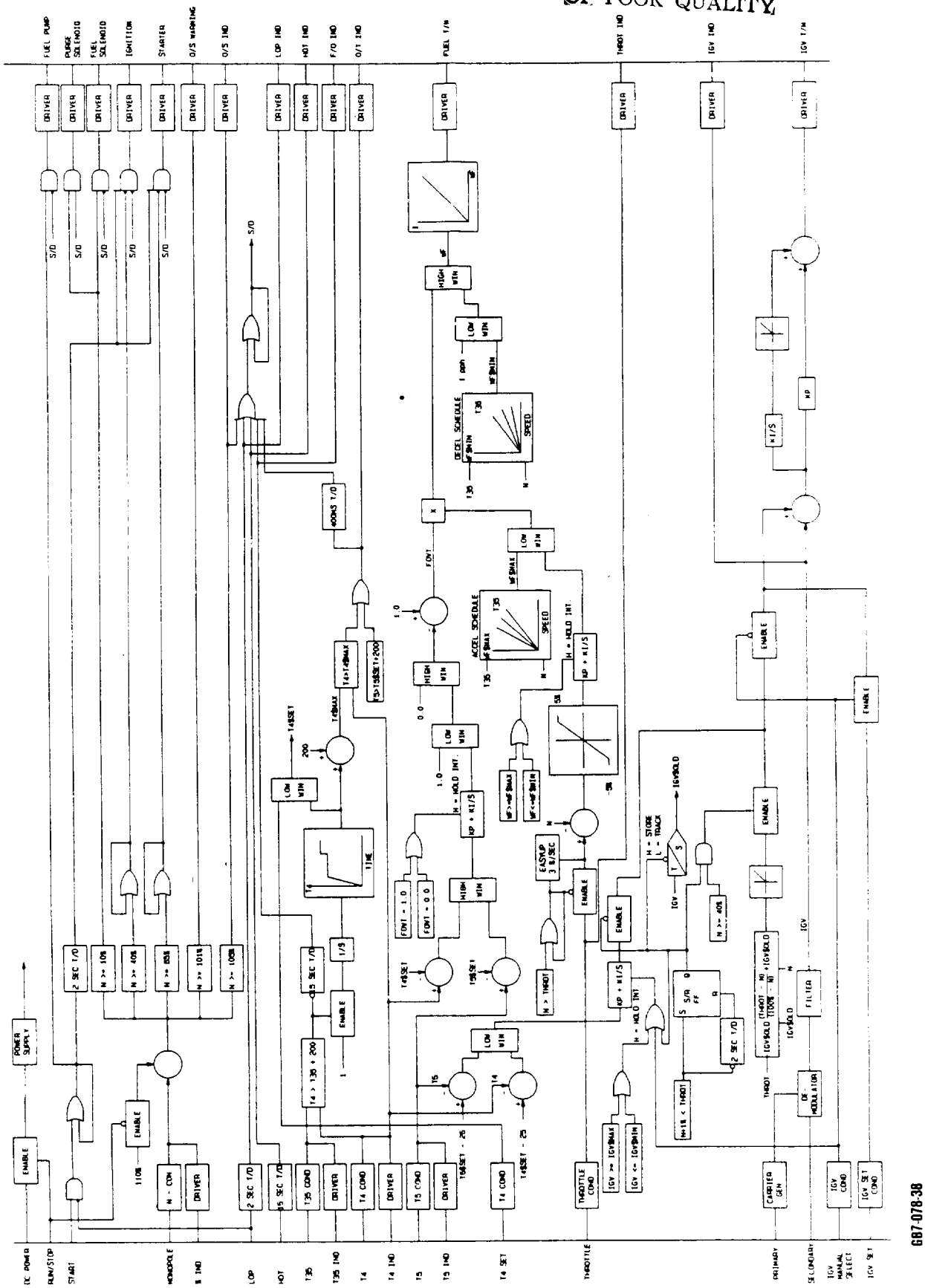

Figure 202. ECU Logic Diagram.

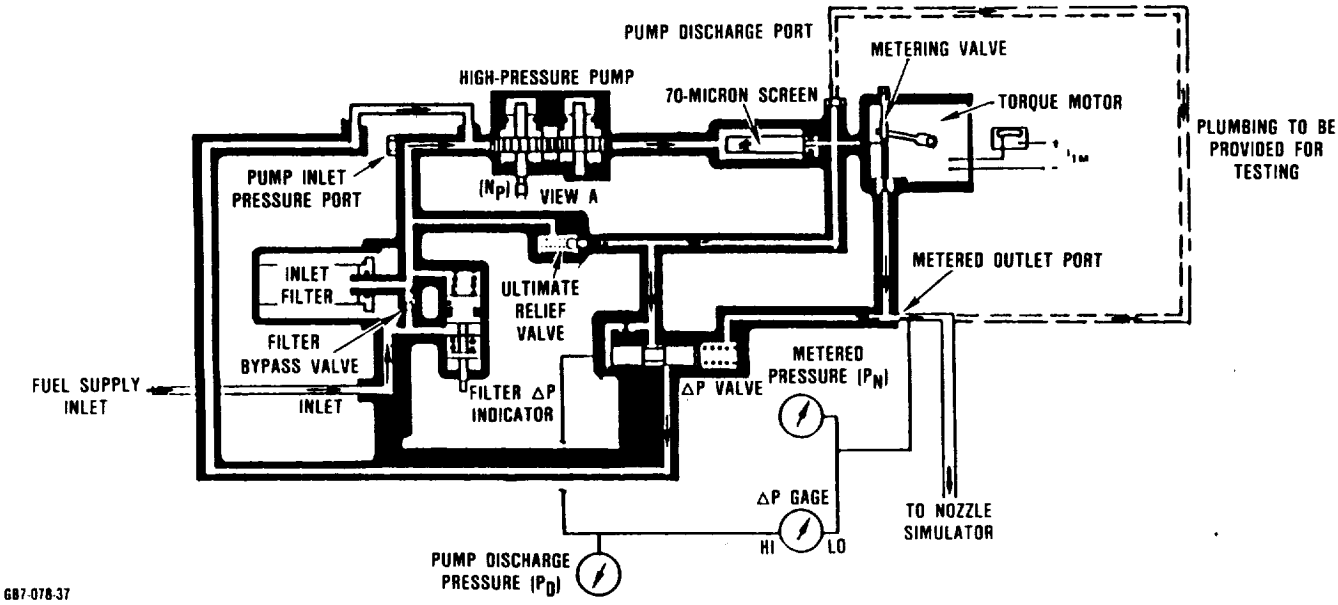

Figure 203. Fuel Control Test Setup (P/N 3601500).

ORIGINAL PAGE IS
OF POOR QUALITY

6.0 CERAMIC MATERIALS AND COMPONENT DEVELOPMENT

6.1 Ceramic Materials Testing

6.1.1 Fast Fracture and Stress Rupture Testing

The fast fracture, four-point flexure strength of ceramic materials used for components in the AGT engine have been continuously monitored over the AGT program. Both fabricated test specimens and specimens machined from components have been tested.

All four-point flexure testing was conducted using self-aligning metal (for room temperature) and hot pressed SiC (for elevated temperature) fixtures. The outer span dimension is 38.1mm (1.5 inches) and the inner span dimenson is 19.1mm (0.75 inch). The load is applied using a crosshead speed of 0.5mm/min (0.02 inch/minute). Specimen cross sections were typically 3.2 x 6.4mm (0.125 x 0.250 inch) except where noted.

Test specimens were machined with 320 grit diamond wheels longitudinal to the specimen length unless noted otherwise. The specimen corners were chamfered 0.127-0.254mm (0.005 - 0.010 inch) at a 45 degree angle. Test data generated during the first five years of the AGT program is summarized in Table 26. In general, the strength of fabricated test specimens has been very close to the strength of specimens cut from components.

During the last two years of the program more extensive material property testing was initiated to characterize the advanced silicon nitride and silicon carbide materials. Typically, fast fracture testing was conducted at up to ten temperatures with between five and thirty specimens per temperature. In addition flexural stress rupture testing was conducted at typically three temperatures and at four stresses chosen to result in stress rupture lives of $\leq$150 hours. The materials, test and specimen sources are listed in Table 27.

Many silicon nitride materials were tested to determine suitablity for AGT rotor use. Many materials such as ASEA, Ford RM-20, Kyocera SN 220M, NGK SN-73, and SN-81 were eliminated for rotor use based on the inadequate elevated temperature properties. Four more advanced materials, NGK SN-82, NGK SN-84, Kyocera SN 250M and Kyocera SN 270M did have adequate properties for rotors based on the testing of fabricated test bars. Unfortunately, two of the four materials, NGK SN-82 and Kyocera SN 270M could not be successfully formed into the complex rotor configuration. The remaining two materials Kyocera SN 250M and NGK SN-84 were successfully fabricated into the AGT101 rotor shape. Rotors of both materials were cut into test specimens. The specimens were tested for both fast fracture strength and stress rupture. The material cut from the Kyocera SN 250M rotors has considerably lower strength at elevated temperatures (Figure 204, View G) and two- to three-orders of magnitude lower stress rupture life than specimens fabricated as test specimens (Figure 204, View H). The poor elevated temperature material properties of the Kyocera SN 250M rotors makes them unsuitable for long term, 1371C (2500F) TIT engine testing.

Two NGK SN-84 sintered silicon nitride rotors were cut into test specimens to compare the fast fracture strength and stress rupture life to that of fabricated test specimens. The fast fracture strength of rotor S/N 135 material (Figure 204, View Q) is slightly lower than the fabricated specimens (Figure 204, View P), at elevated temperature but is still >689.5 MPa (100 ksi) at temperatures $\leq$1260C (2300F). The fast fracture strength of rotor S/N 136 is lower than measured on rotor S/N 135 but the elevated temperature fast fracture strength at temperature $\leq$1260C (2300F) is greater than 586MPa (85 ksi). The flexural stress rupture life of the rotor specimens are approximately one order of magnitude less than the stress rupture life of the fabricated test specimens.

Table 26. AGT101 Component And Material Summary.

Supplier	Material	Process	Condition	Qualification Bar							Ceramic Component						
				Room Temperature			Elevated Temperature				Room Temperature			Elevated Temperature			
				σ_C[2]	M[3]	Population	σ_C[2]	M[3]	F	Population	σ_C[2]	M[3]	Population	σ_C[2]	M[3]	F	Population
ACC																	
Inner Diffuser Outer Diffuser Turbine Shroud Baffle	RBSN (RBN104)	Slip Cast	As-Fired Longitudinally Ground Heat Treated	49.7 53.2 54.8	4.5 5.5 8.5	30 10 29	52.1	10.1	2200	10	44.3[4] 46.3 59.0 31.1	8.0 5.3 15.4 5.7	21 ID 27 OD 17 T5 5 B				
Stator	RBSN (RBN124)	Injection Molded	As-Fired[1]	40.1	4.8	19	44.5	8.4	2200	23							
Rotor	Sintered Si_3N_4[7] Code 1	Slip Cast	Longitudinally Ground								123.9	16.4	10	98.6 71.0	5.7 36.8	1800 2200	5 5
	Sintered Si_3N_4[7] Code 2	Slip Cast	Longitudinally Ground	89.8	7.2	9	50.3	13.0	2200	10	119.0	21.4	10	99.0 63.7	10.3 9.3	1800 2200	5 5
Standard Oil																	
Turbine Shroud, Stator	SASC	Injection Molded	As-Fired	48.6	9.5	30	45.0	5.0	2500	10	55.4[5]	7.1	9				
Combustor Baffle	SASC	Slip Cast	Longitudinally Ground	49.4	5.8	30	41.4	6.7	2500	10	53.0 51.6	7.3 8.9	9 4				
Transition Duct, Regenerator Shield, Backshroud	SASC	Isopressed	Longitudinally Ground	57.7[9]	7.7	30	56.2	11.9	2500	10	54.4 34.3 41.8	6.2 9.1 14.2	5 23 12	36.9	6.8	5	
Ford																	
Rotor	SRBSN (RM-2)	Slip Cast	Longitudinally Ground	109.3	19.8	6	73.1	16.4	2200	6							
Rotor	SRBSN (RM-3)[8]	Slip Cast	Longitudinally Ground	98.6[6]	19.0	10	77.6[6] 71.6[6] 70.8[6]	10.9 12.9 11.3	1832 2192 2552	5 5 5							
Rotor	SRBSN (RM-20)[8]	Slip Cast	Longitudinally Ground	130.4	13.3	10											
Stator	RBSN	Injection Molded	As-Fired	43.1	9.2	39	45.8	7.7	2200	10							
NGK																	
Backshroud, Transition Duct, Diffusers	Sintered Si_3N_4 (SN-50)	Isopressed	Longitudinally Ground	87.6	10.5	10	47.1	13.6	2000	7							
Turbine Shroud	Sintered Si_3N_4 (SN-54)	Isopressed	Longitudinally Ground	109.5	10.3	5	67.9 53.0 40.7 23.2	3.6 6.1 25.0 7.0	1800 2000 2200 2500	2 5 5 2							
Kyocera																	
Turbine Shroud	Sintered SiC SC201	Isopressed	Longitudinally Ground	65.4	5.2	5											
			Ground and Heat Treated	78.5	10.4	5					66.5 70.5	19.7 12.0	5 5				
Corning																	
Flow Separator Housing	LAS	Slip	Longitudinally	14.0	18.8	11	13.5	9.7	2000	12	12.9	5.3	10	13.4 15.4 16.0	3.4 8.1 7.7	1800 2000 2050	5 10 9

All test bars 0.250 x 0.125 inch cross section unless noted. Bars tested in 4-point flexure, 1.50 inch outer span and 0.75 inch inner span. Cross head speed, 0.02 inch/minute

[1]Test bar cross section 0.31 x 0.15 inch

[2]Characteristic strength, ksi

[3]M = Weibull Modulus

[4]Test bar cross section 0.236 x 0.1 inch

[5]As machined, longitudinally ground

[6]Average flexure strength, ksi

[7]Code 1 = 8%-Y_2O_3, 4%-Al_2O_3
Code 2 = 6%-Y_2O_3, 2%-Al_2O_3

[8]Data supplied by vendor

[9]Not heat treated

Table 27. Fast Fracture and Stress Rupture Data was Measured for Many Advanced Si_3N_4 and SiC Materials.

(Figure 204)

	Fast Fracture		Stress Rupture	
	Test Bar (View Ref)	Component (View Ref)	Test Bar (View Ref)	Component (View Ref)
Silicon Nitride				
ASEA	A	--	—	—
Ford RM-20	B	—	—	—
Kyocera SN 220M	C	—	D	—
Kyocera SN 250M	E	G	F	H
Kyocera SN 270M	I	—	J	—
NGK SN-73	K	—	—	—
NGK SN-81	L	—	M	—
NGK SN-82	N	—	O	—
NGK SN-84	P	Q	R	R
Silicon Carbide				
Kyocera SC201	S	--	--	--
Standard Oil SASC	T	--	--	--

Based on this data SN-84 appears to be a material that can be used for limited 1371C (2500F) TIT engine testing.

Over the seven years of the AGT101 program large improvements have been made in high performance ceramic materials. Additional work must be done to increase the elevated temperature material properties, fracture toughness and shape capability.

6.1.2 Ceramic Compatibility Testing

In conjunction with ceramic component tests, an interface compatibility study was conducted. All interface conditions for the AGT101 have been identified, as shown in Figure 205, along with respective stress and temperature environments for the three engine operating conditions [871, 1149, and 1371C (1600, 2100, and 2500F) TIT]. Test bars of as-machined or as-processed material were stacked with a 6.4 x 6.4mm (0.25 x 0.25-inch) contact area. The specimens were heated to the appropriate temperature while dead weight loaded at a minimum simulated engine assembly load. Once at temperature, additional dead weight loads were applied, as required, to simulate engine aerodynamic or mechanical loads and held for 20 hours. Unloading and cooldown followed. The specimens then were inspected for sticking phenomena. Three classifications were assigned; no stick or reaction (NSR); light sticking (LS) upon cooldown, ie, came apart during handling; and hard sticking (HS), not separable by hand. Concern is raised for LS and HS conditions due to the following:

- LS - longer exposure may result in hard sticking
- HS - could result in component fracture if the parts thermally expand or cool down at differing rates

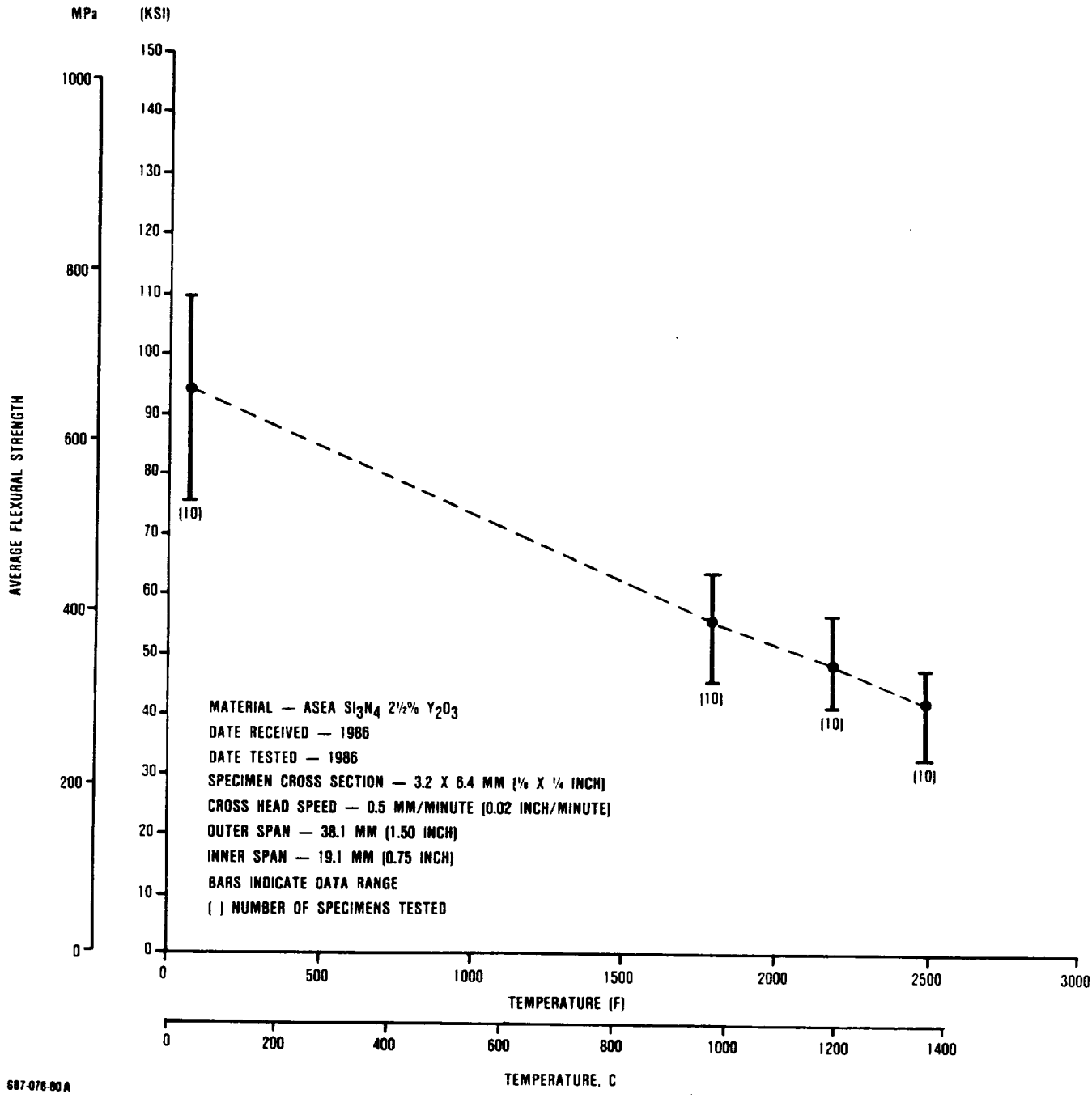

Figure 204. View A. Four-Point Flexure Strength of ASEA Si_3N_4-2½ Percent Y_2O_3.

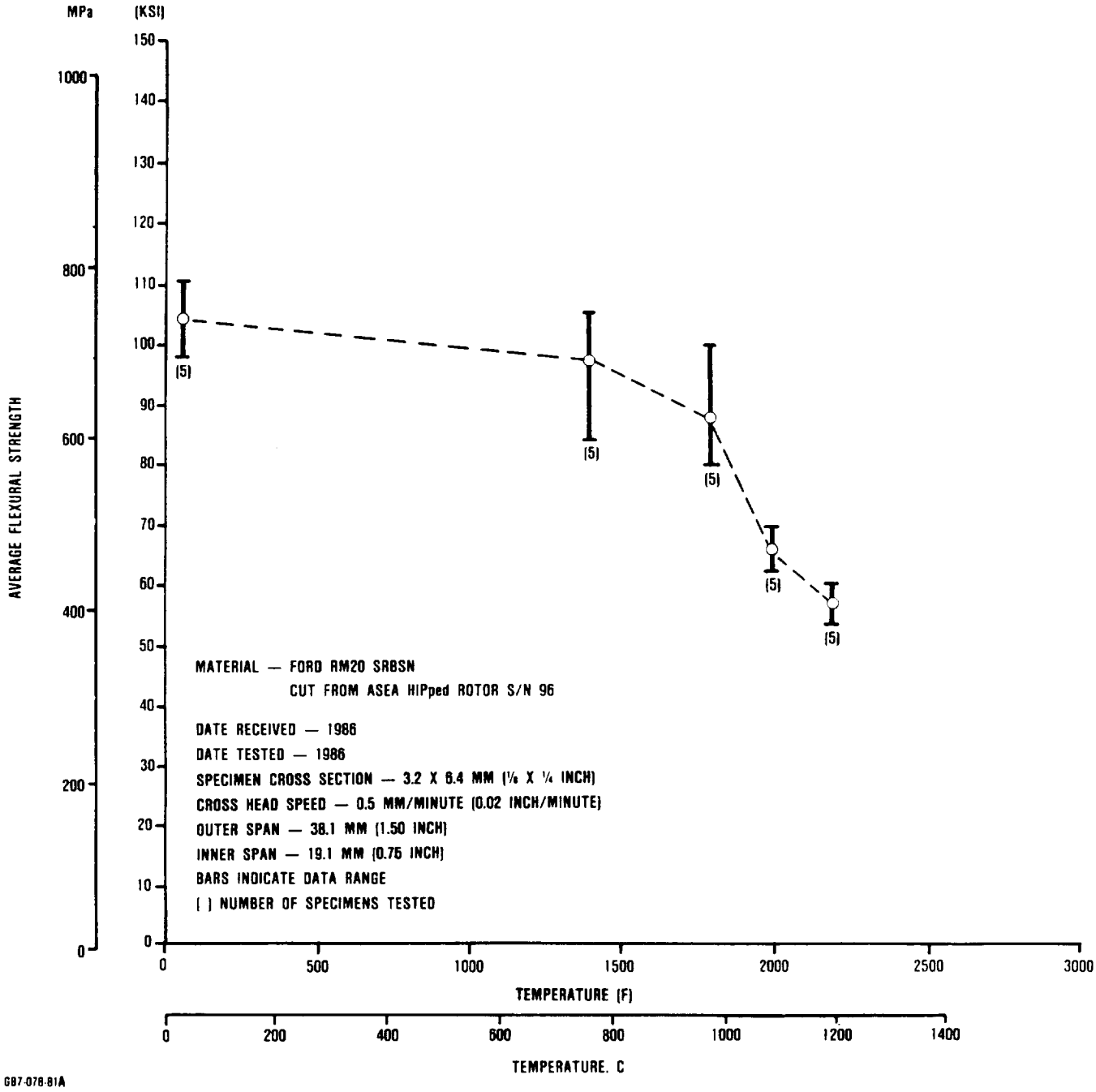

Figure 204 (Contd). View B. Four-Point Flexure Strength of Ford RM-20, HIPped by ASEA, Cut From Rotor S/N 96 .

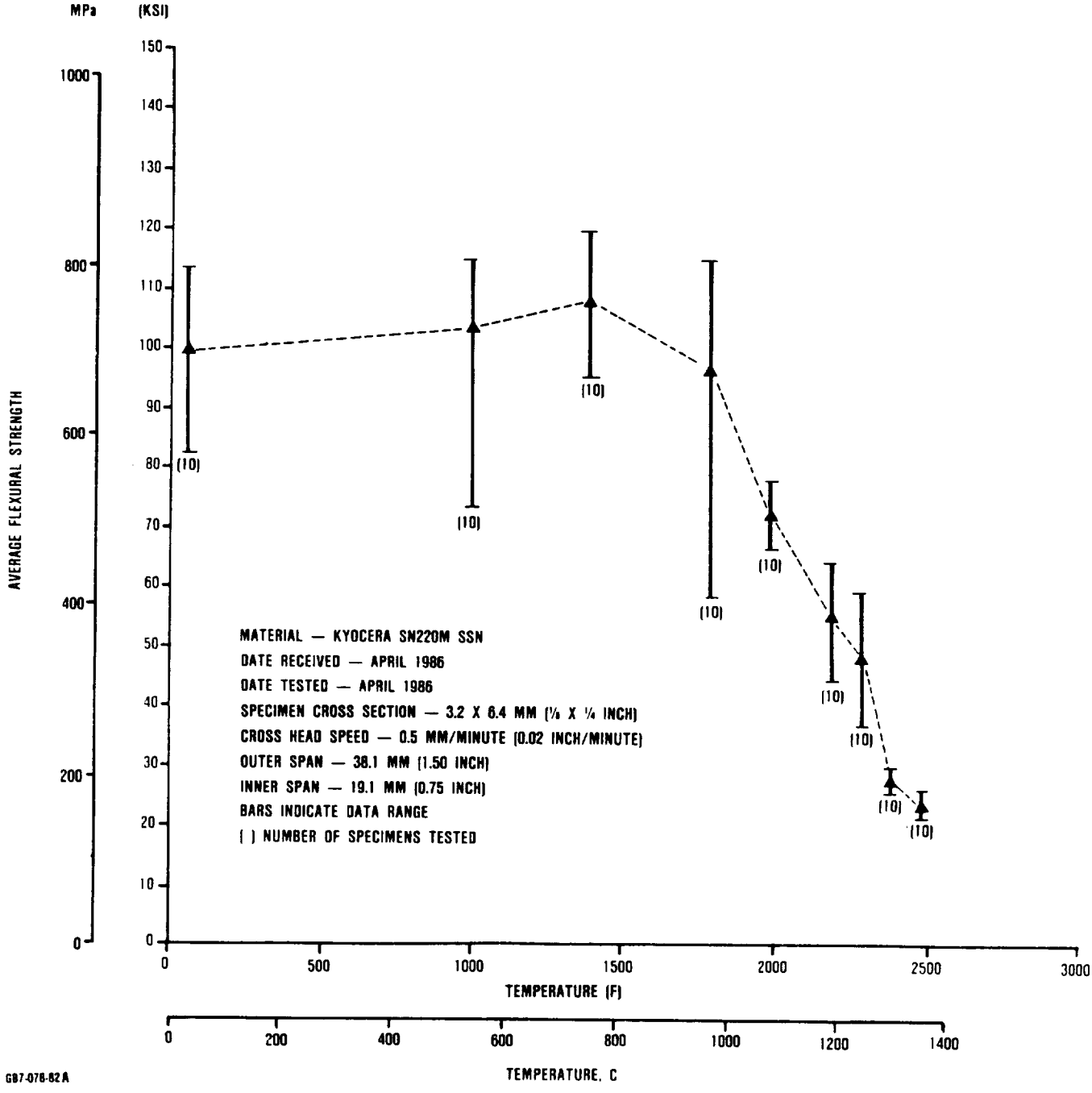

Figure 204 (Contd). View C. Four-Point Flexure Strength of Kyocera SN 220M Sintered Silicon Nitride.

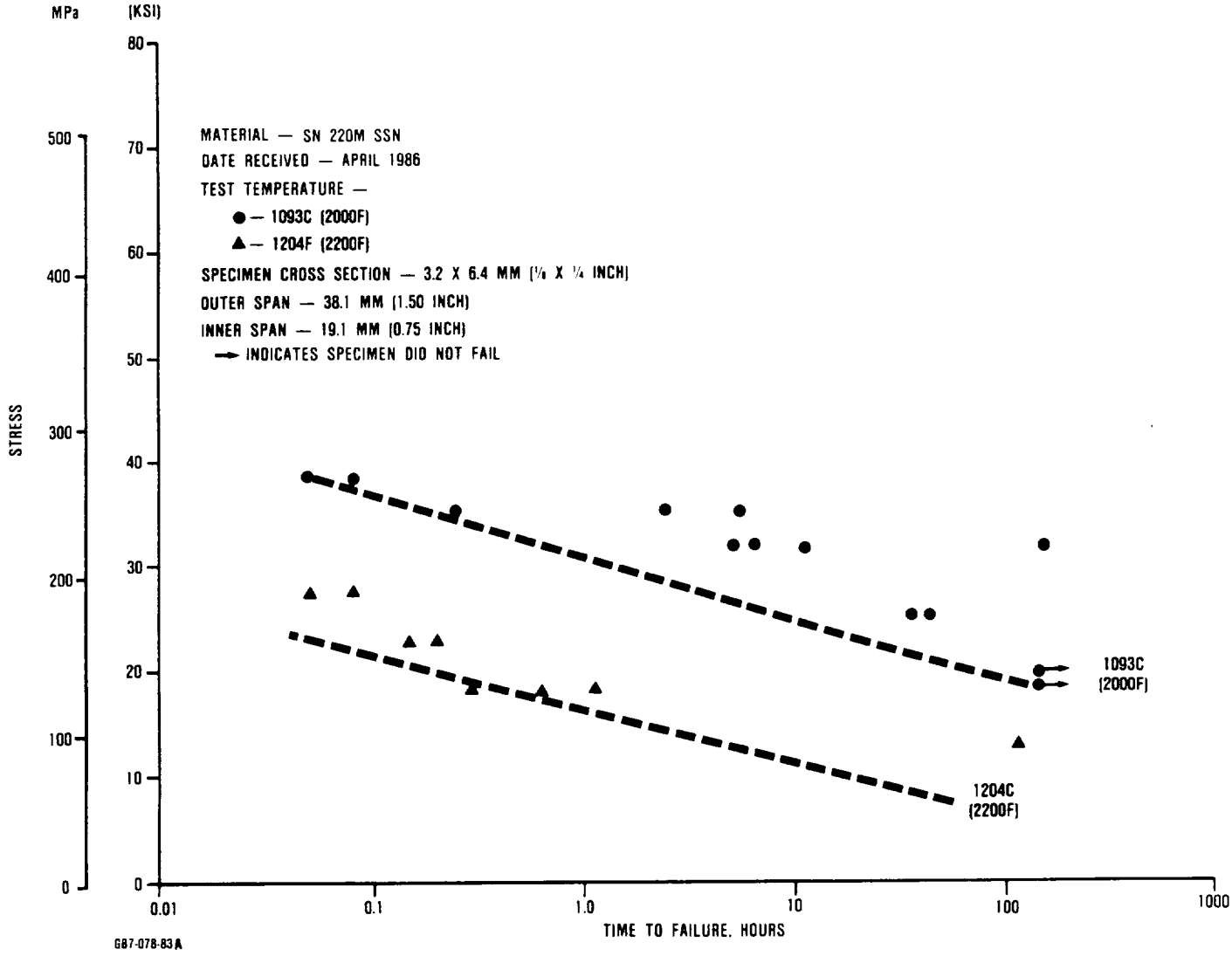

Figure 204 (Contd). View D. Kyocera SN 220M Flexural Stress Rupture.

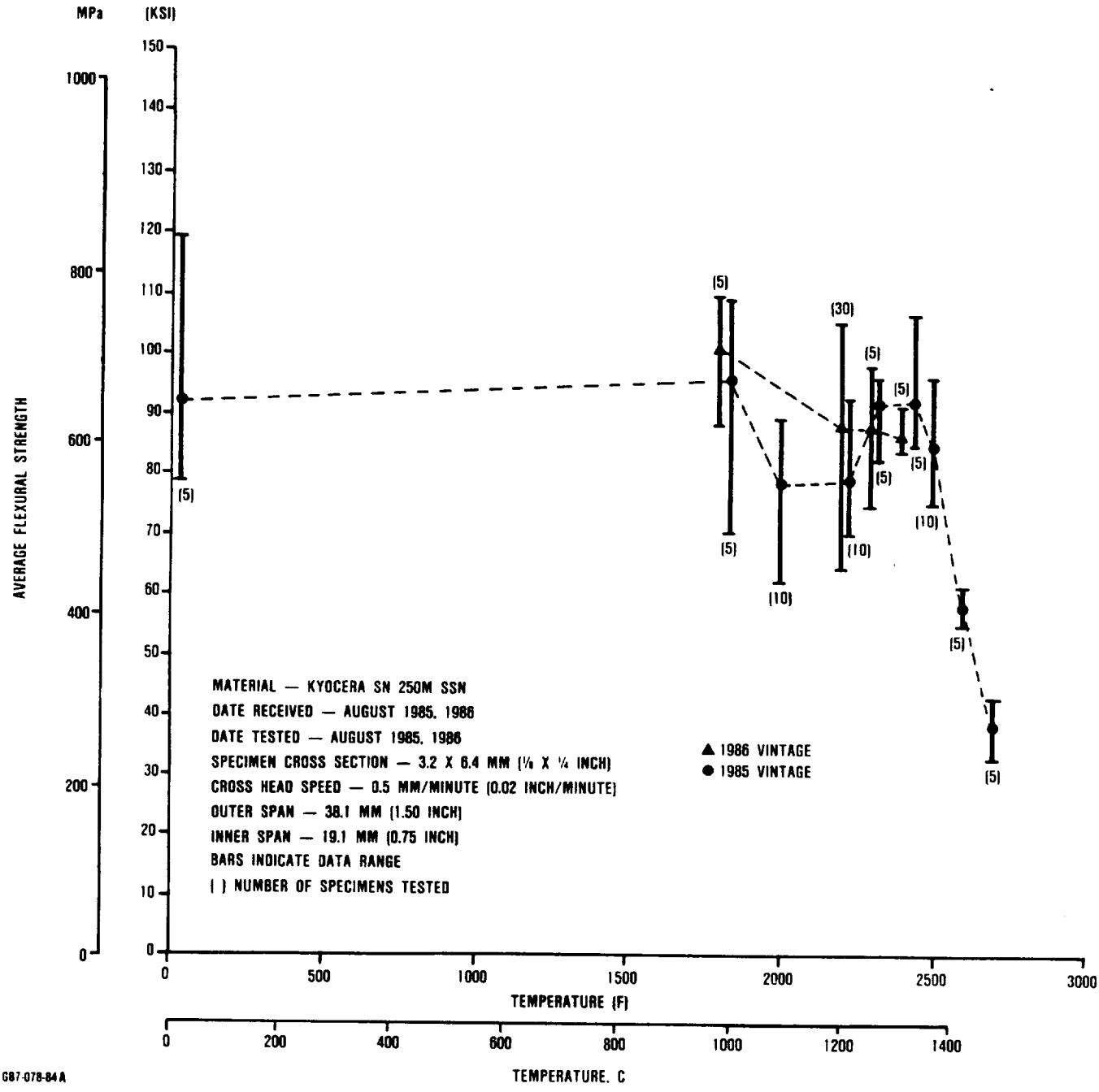

Figure 204 (Contd). View E. Four-Point Flexure Strength of Kyocera SN 250M Sintered Silicon Nitride.

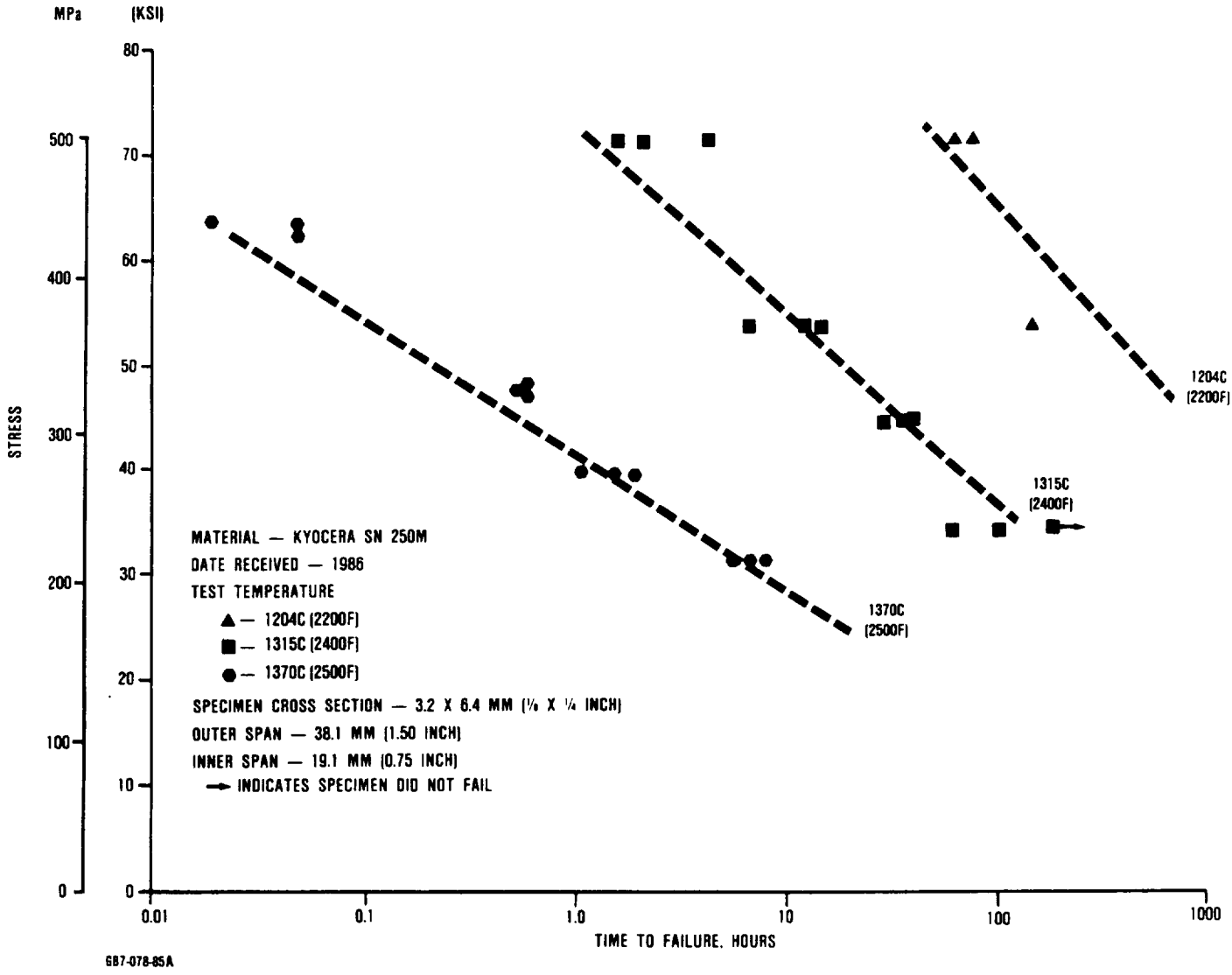

Figure 204 (Contd). View F. Kyocera SN 250M, Flexural Stress Rupture.

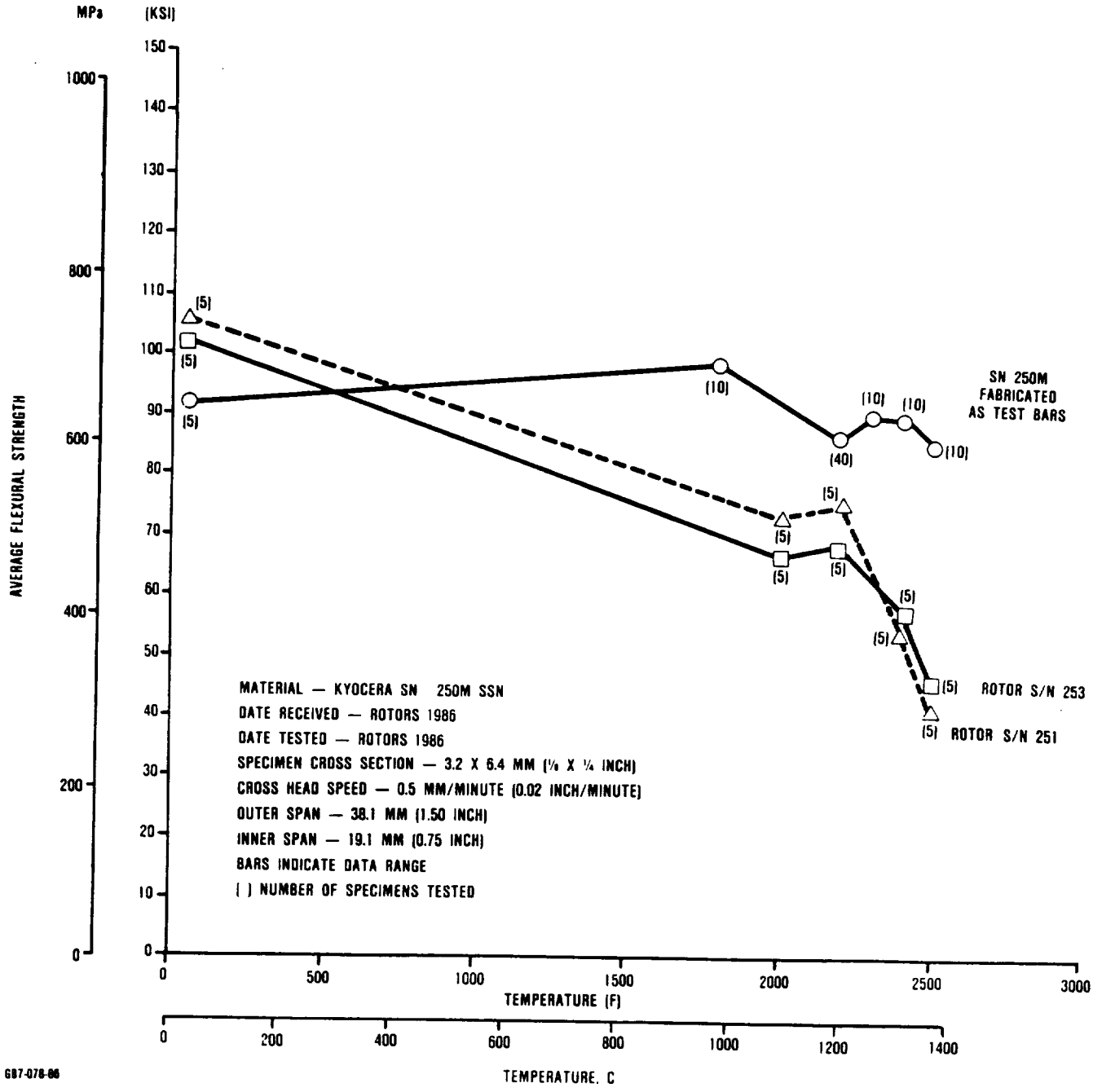

Figure 204 (Contd). View G. Four-Point Flexure Strength Comparison of Kyocera SN 250M Cut From Rotors and Fabricated as Test Bar Specimens.

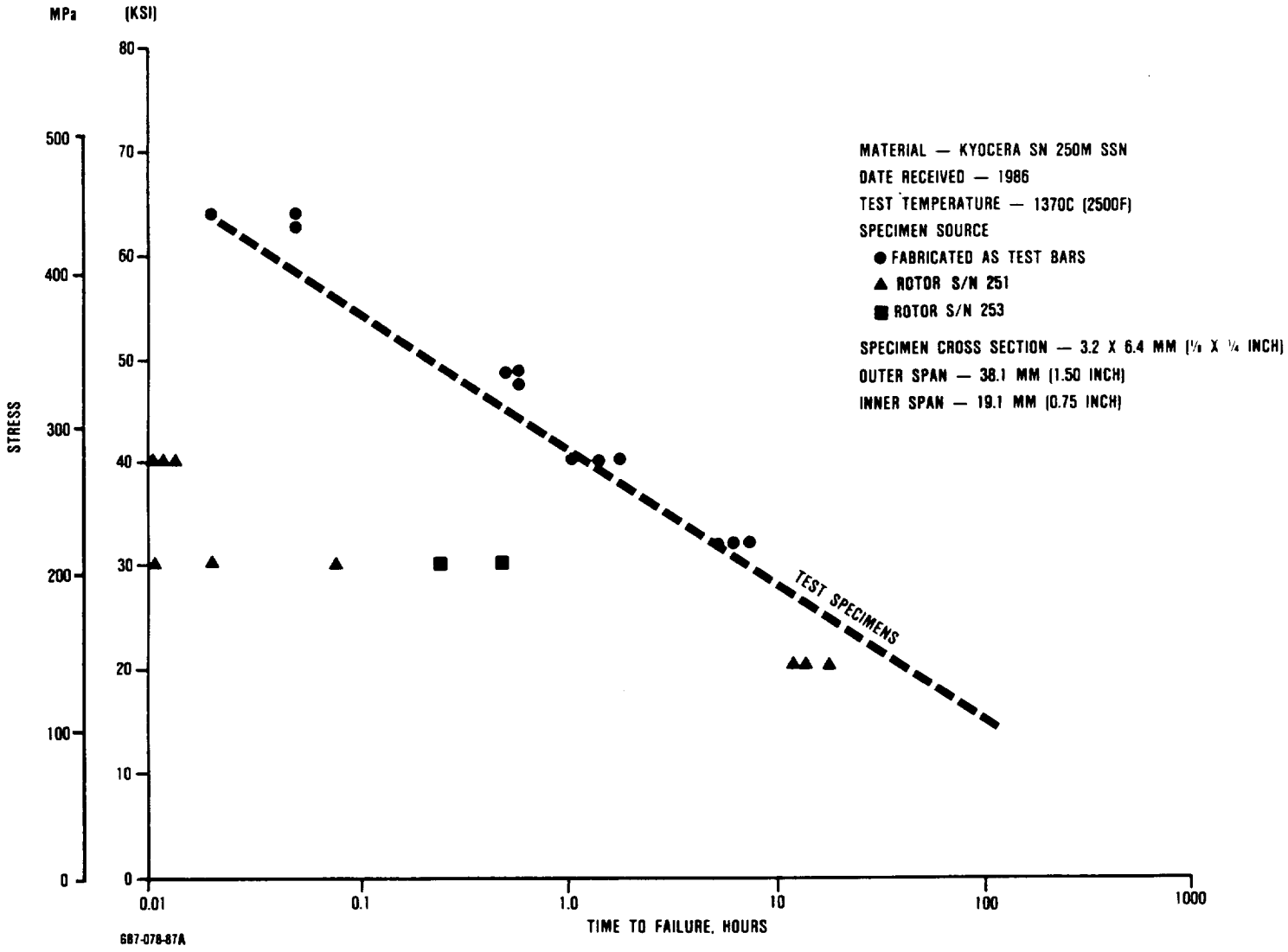

Figure 204 (Contd). View H. Stress Rupture Lives of Kyocera SN 250M From Rotors is Considerably Less Than That Fabricated as Test Bars.

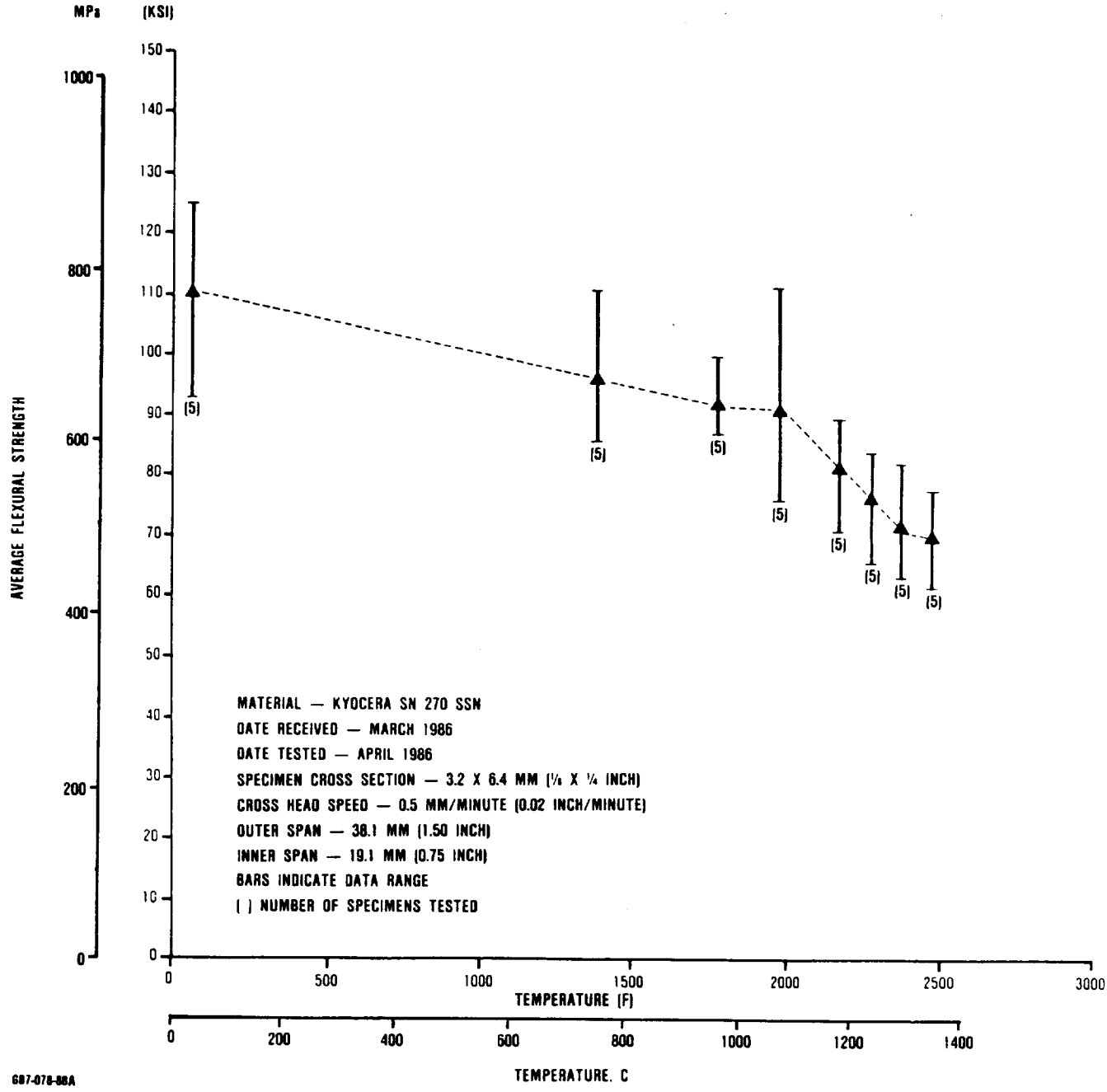

Figure 204 (Contd). View I. Four Point Flexure Strength of Kyocera SN 270M Sintered Silicon Nitride.

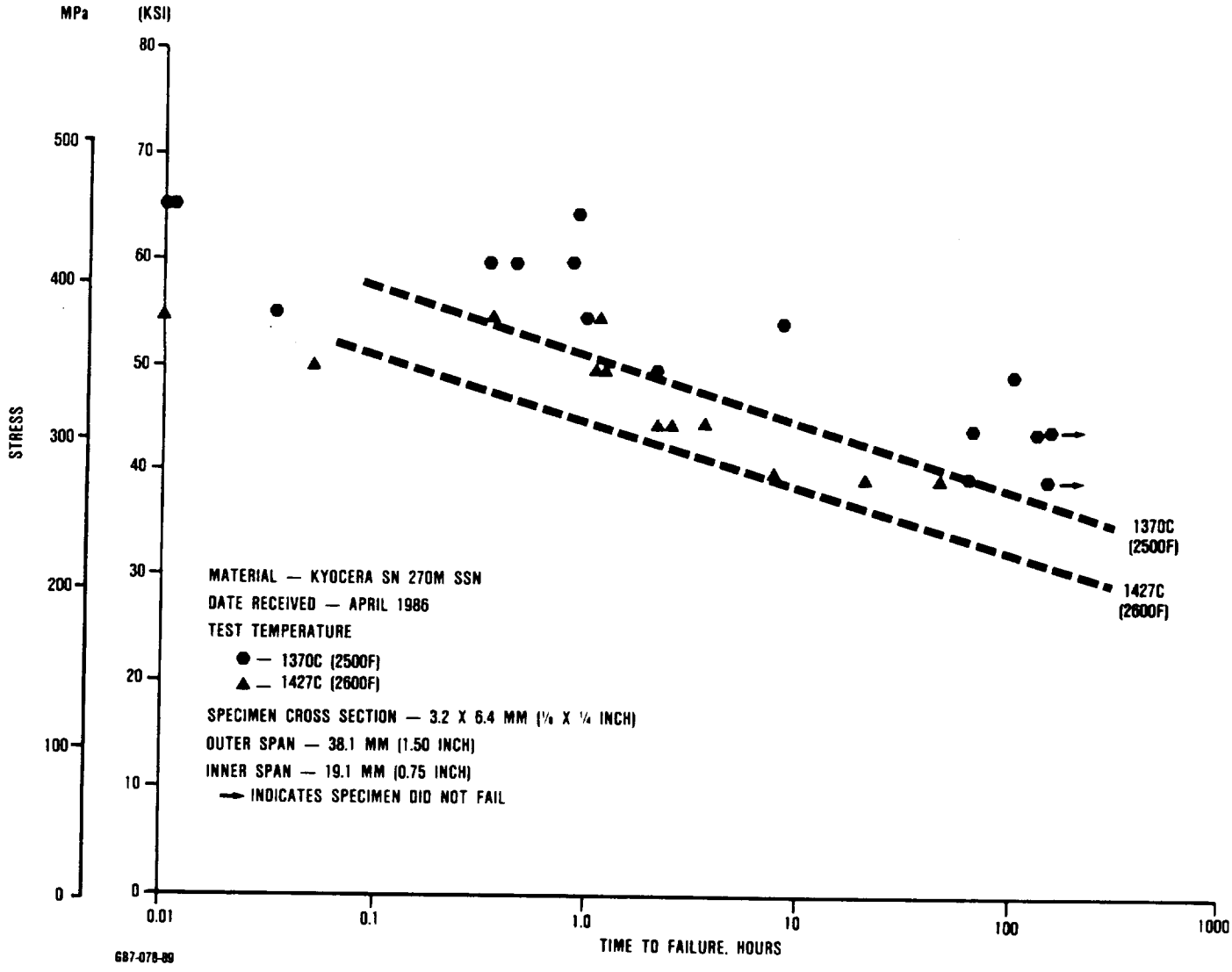

Figure 204 (Contd). View J. Kyocera SN-270M, Flexural Stress Rupture.

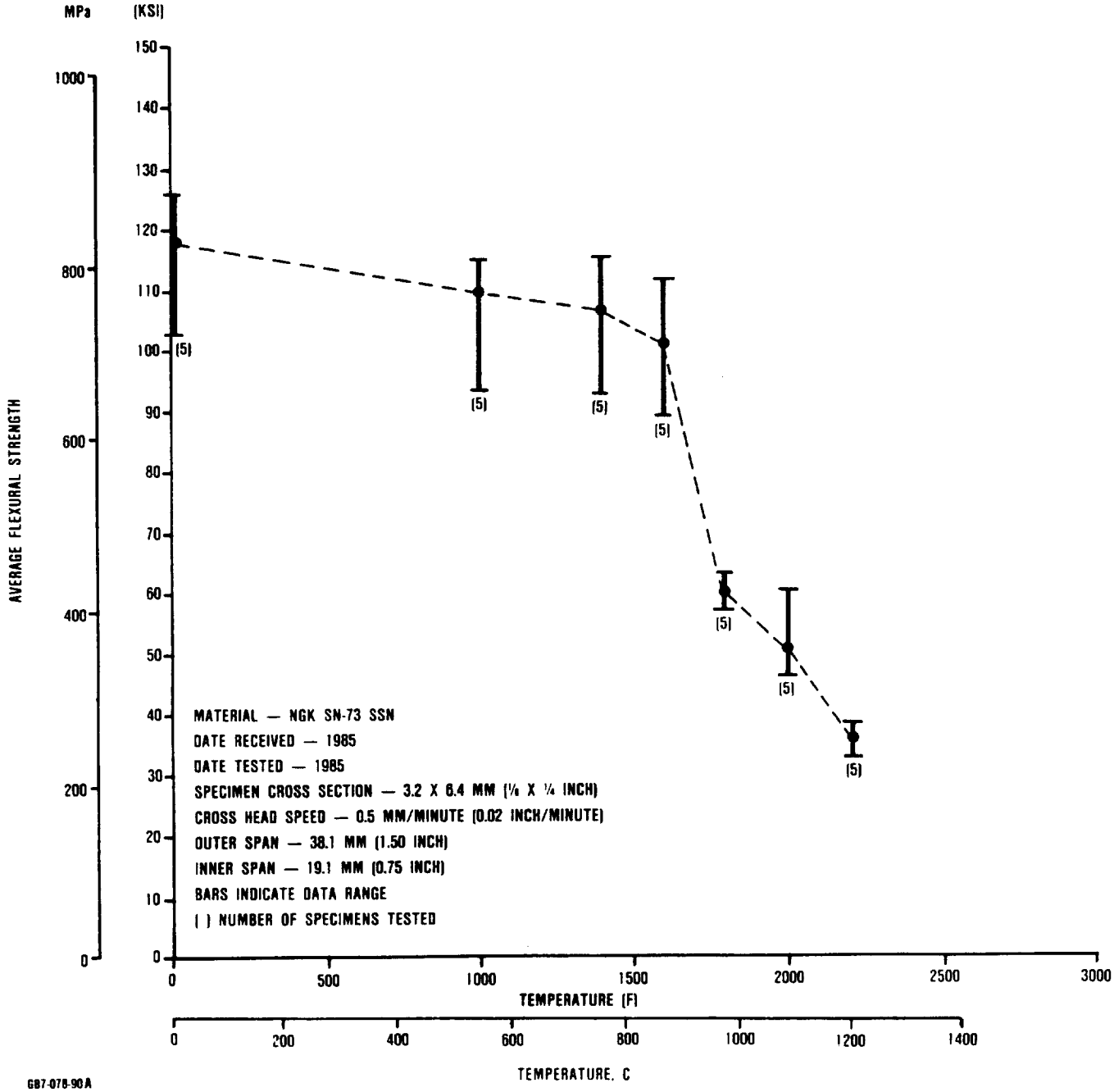

Figure 204 (Contd). View K. Four-Point Flexure Strength of NGK SN-73 Sintered Silicon Nitride.

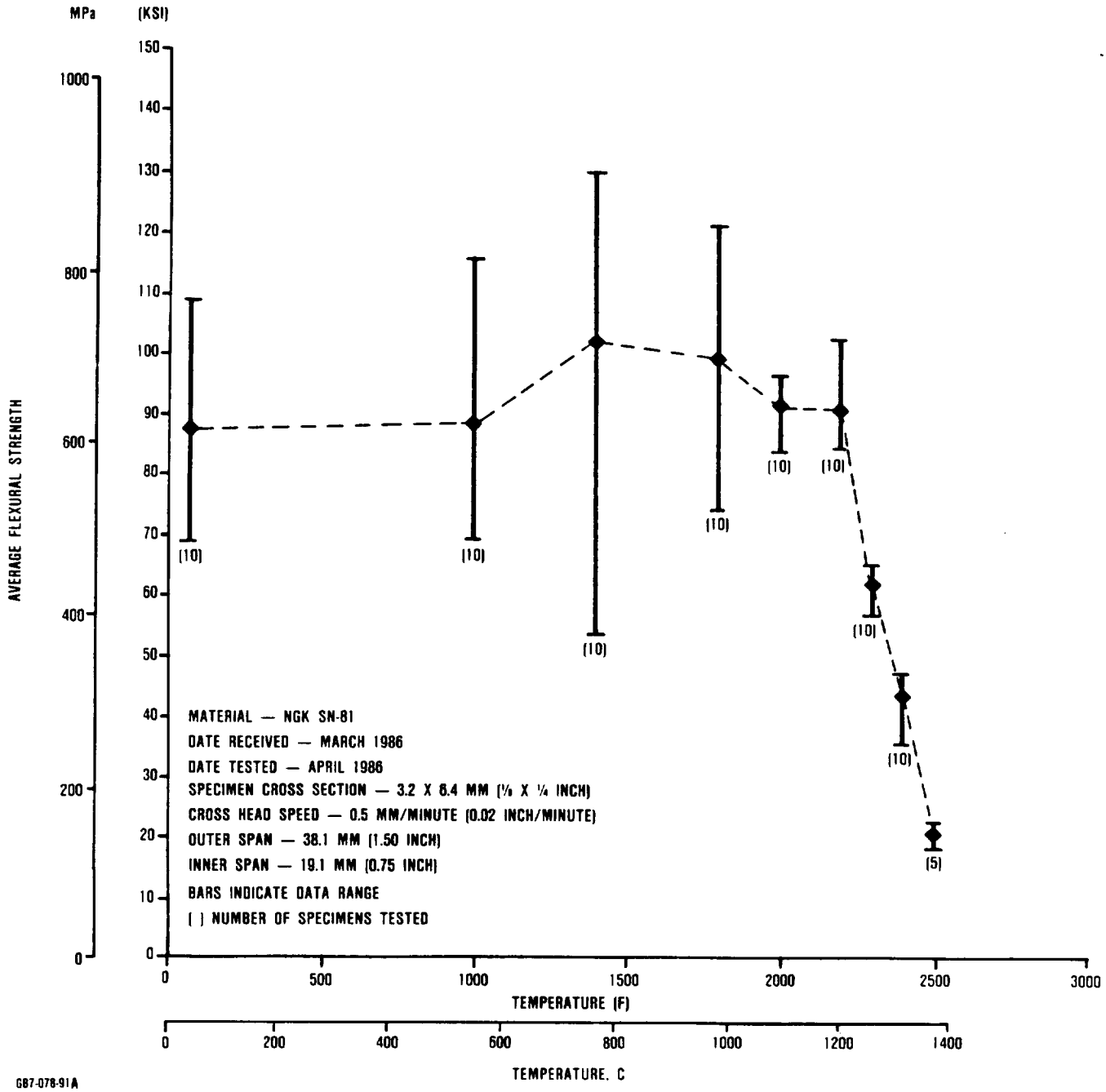

Figure 204 (Contd). View L. Four-Point Flexure Strength of NGK SN-81 Sintered Silicon Nitride.

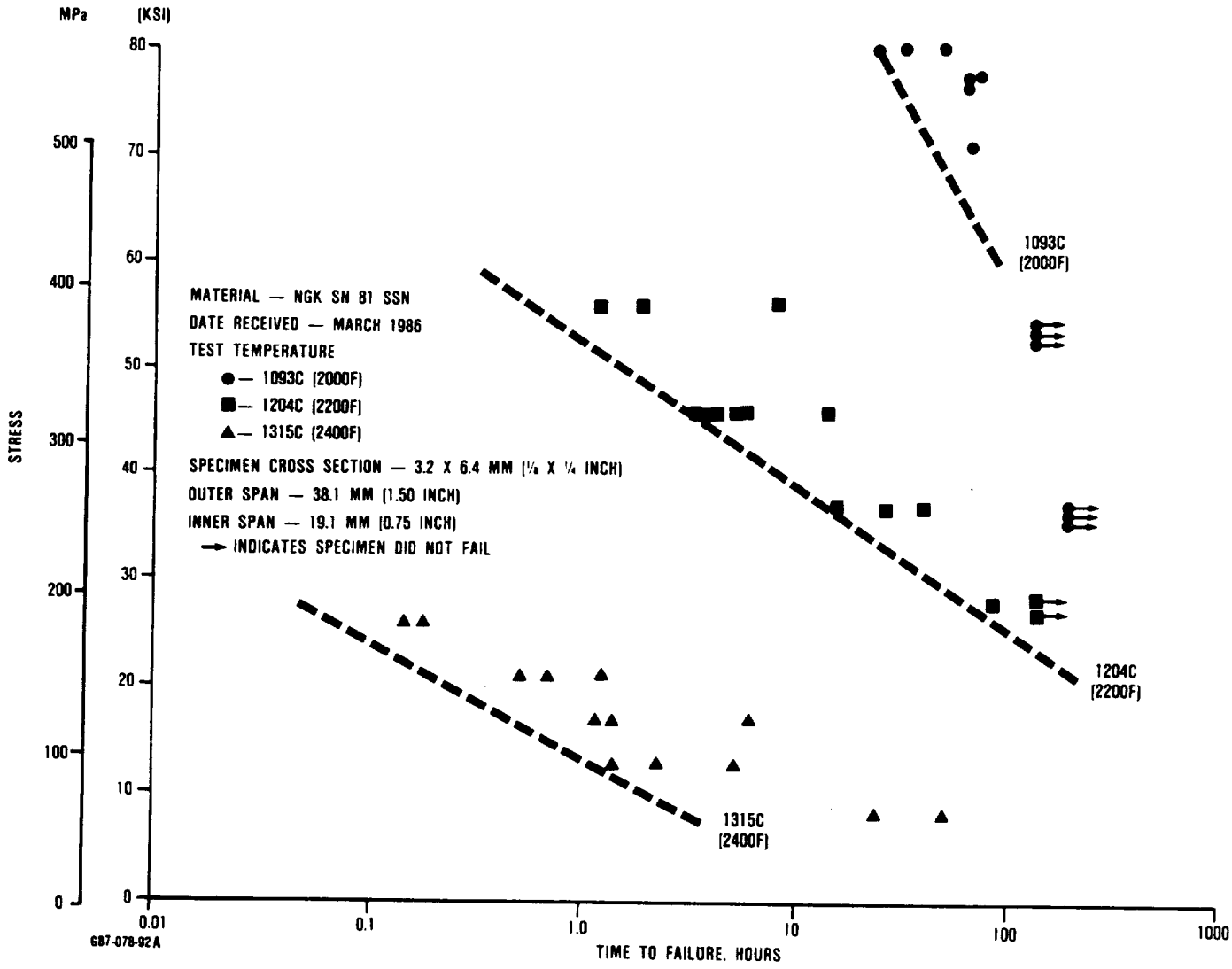

Figure 204 (Contd). View M. NGK SN-81, Flexural Stress Rupture.

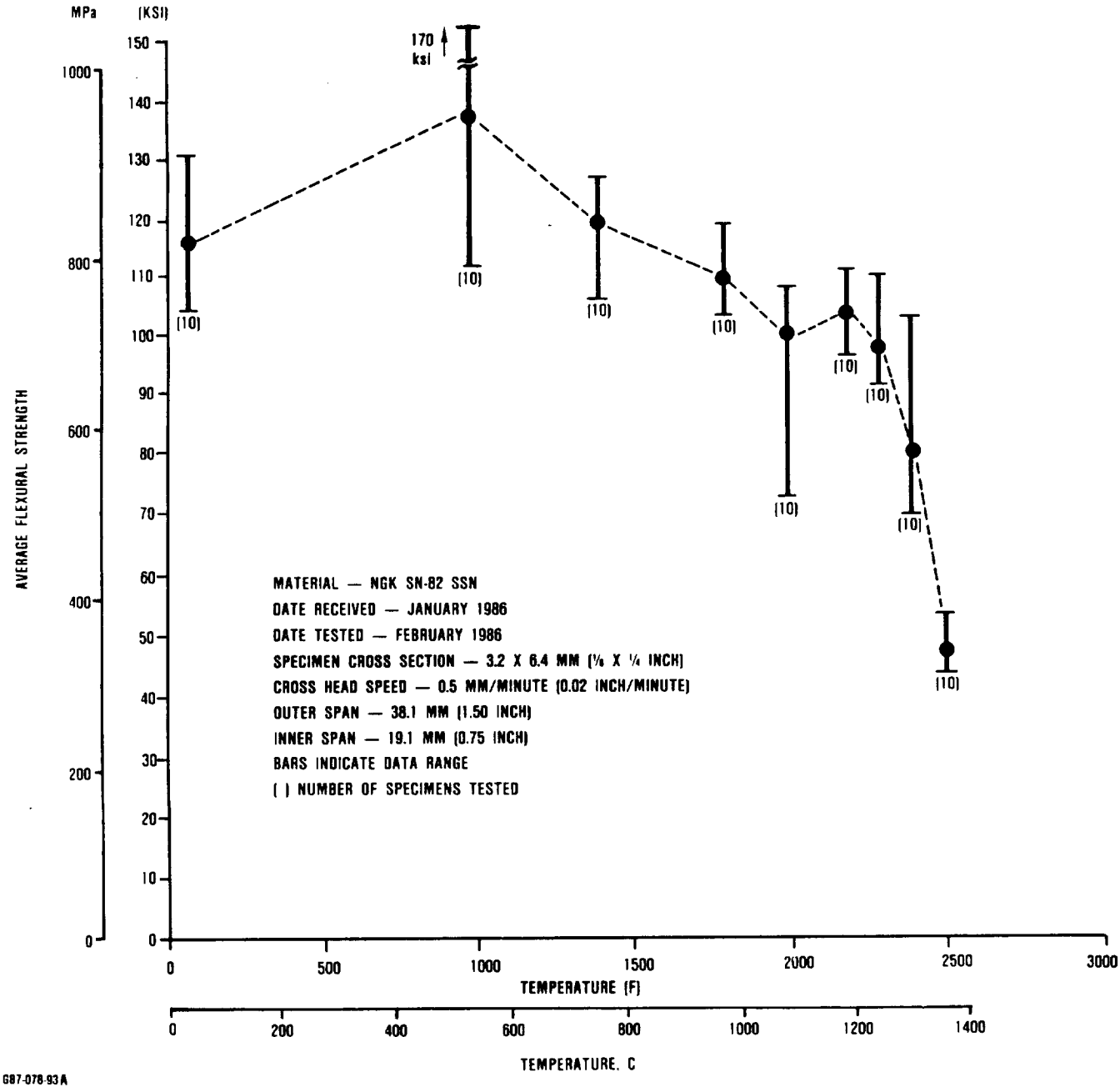

Figure 204 (Contd). View N. Four-Point Flexure Strength of NGK SN-82 Sintered Silicon Nitride.

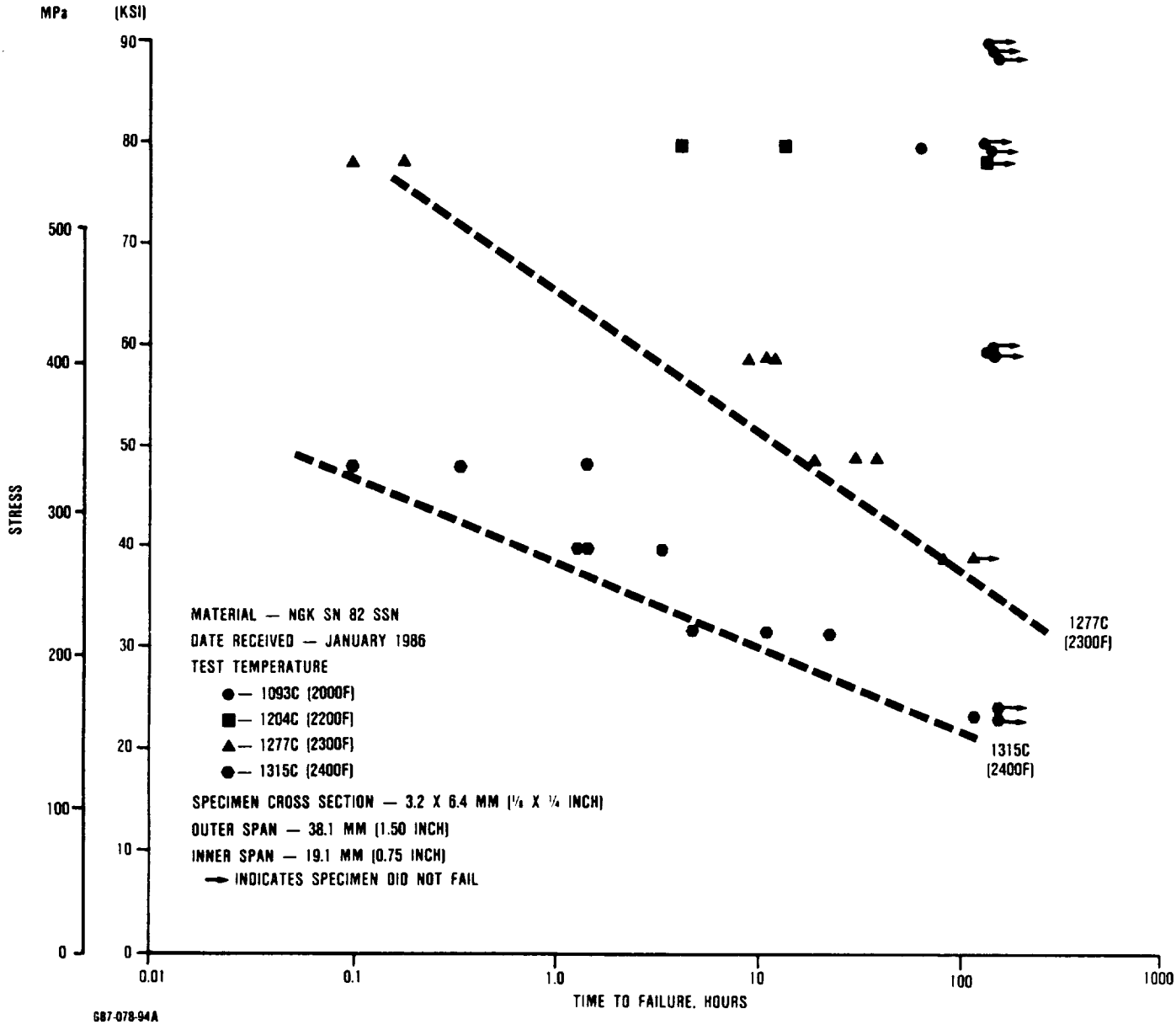

Figure 204 (Contd). View O. NGK SN-82, Flexural Stress Rupture.

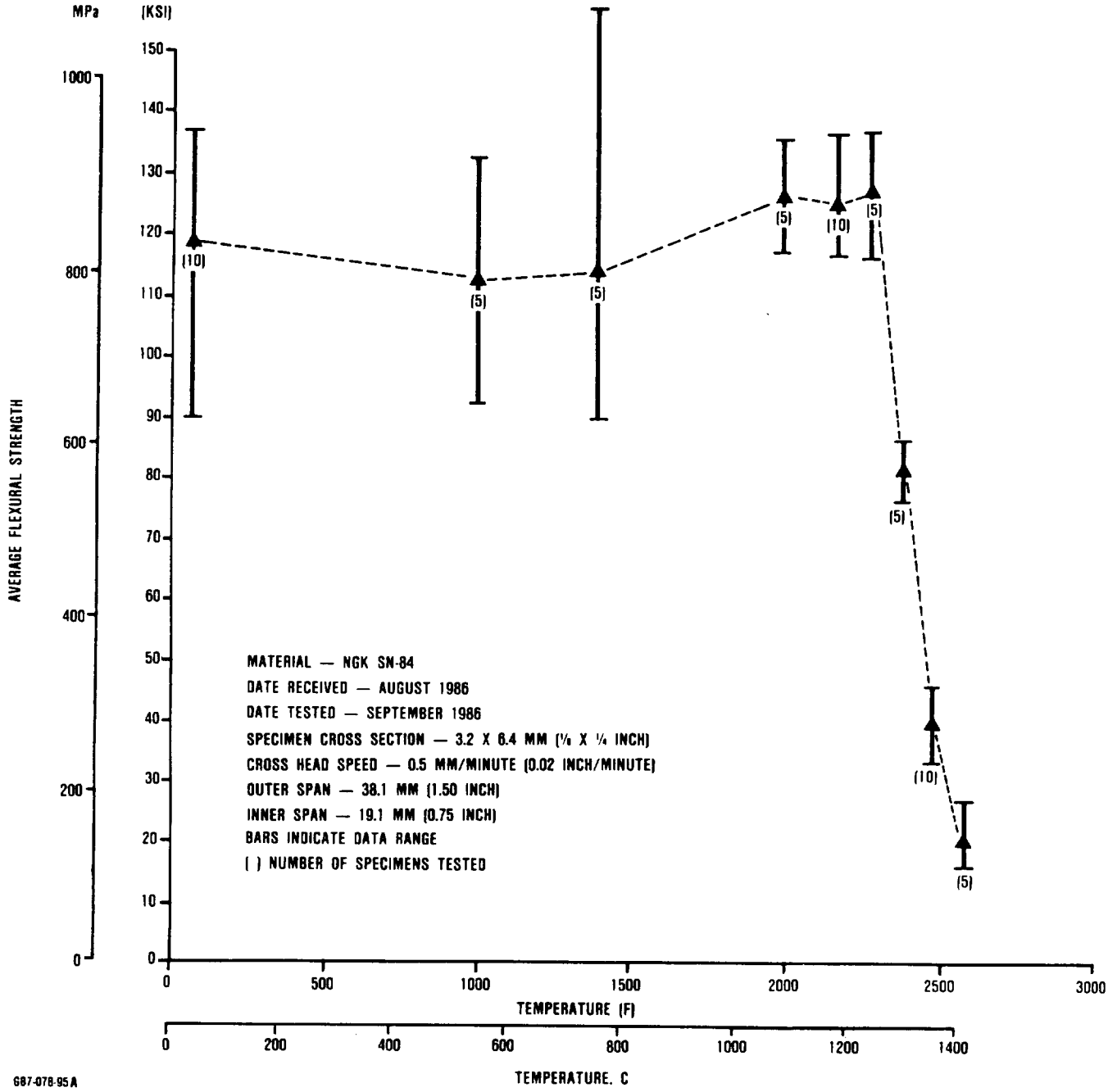

Figure 204 (Contd). View P. Four-Point Flexure Strength of NGK SN-84 HiPped Silicon Nitride.

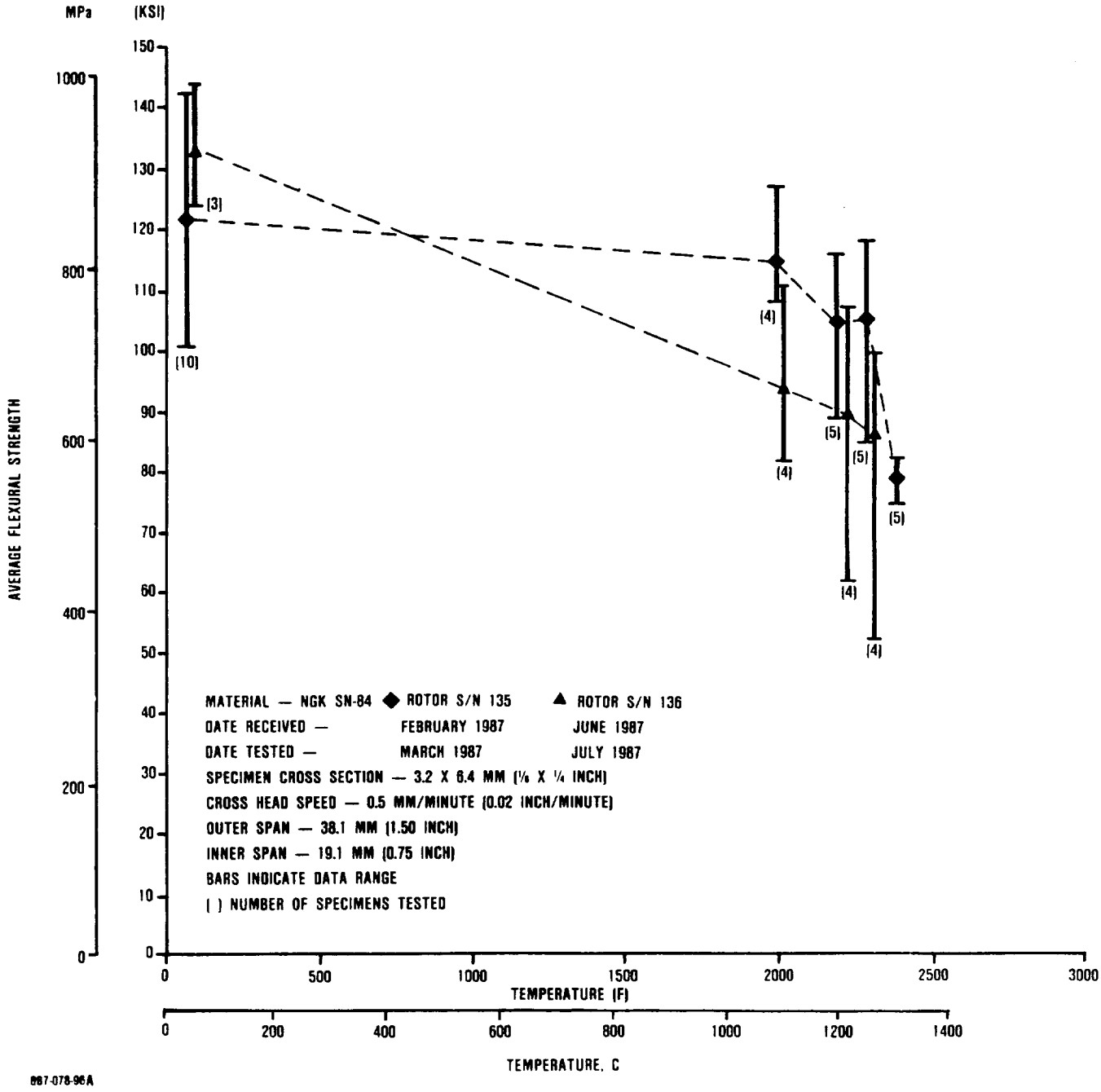

Figure 204 (Contd). View Q. Four-Point Flexure Strength of NGK SN-84 HIPped Silicon Nitride Cut From Rotors S/N 135 and S/N 136.

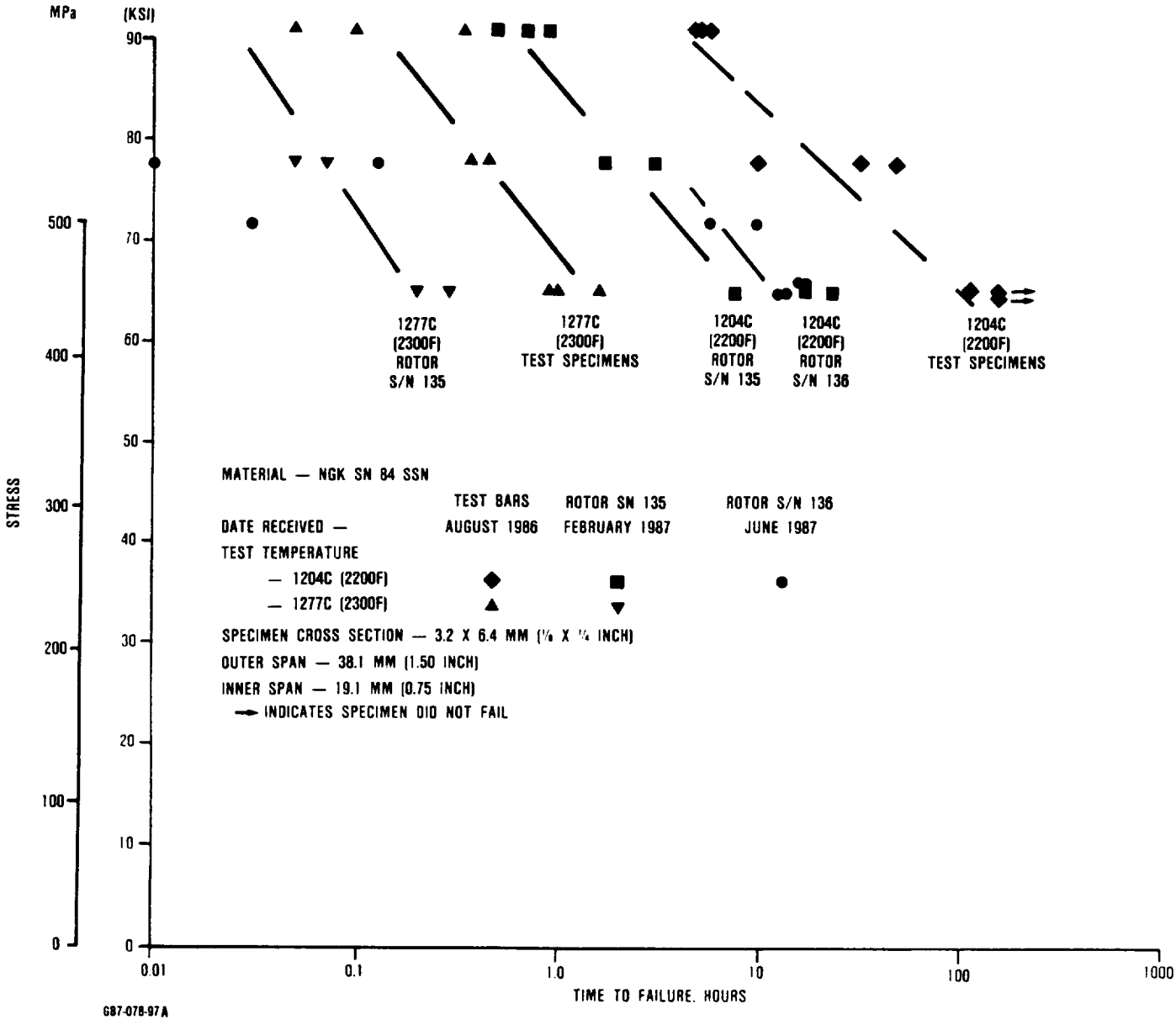

Figure 204 (Contd). View R. NGK SN-84, Flexural Stress Rupture of Test Specimens and Rotors.

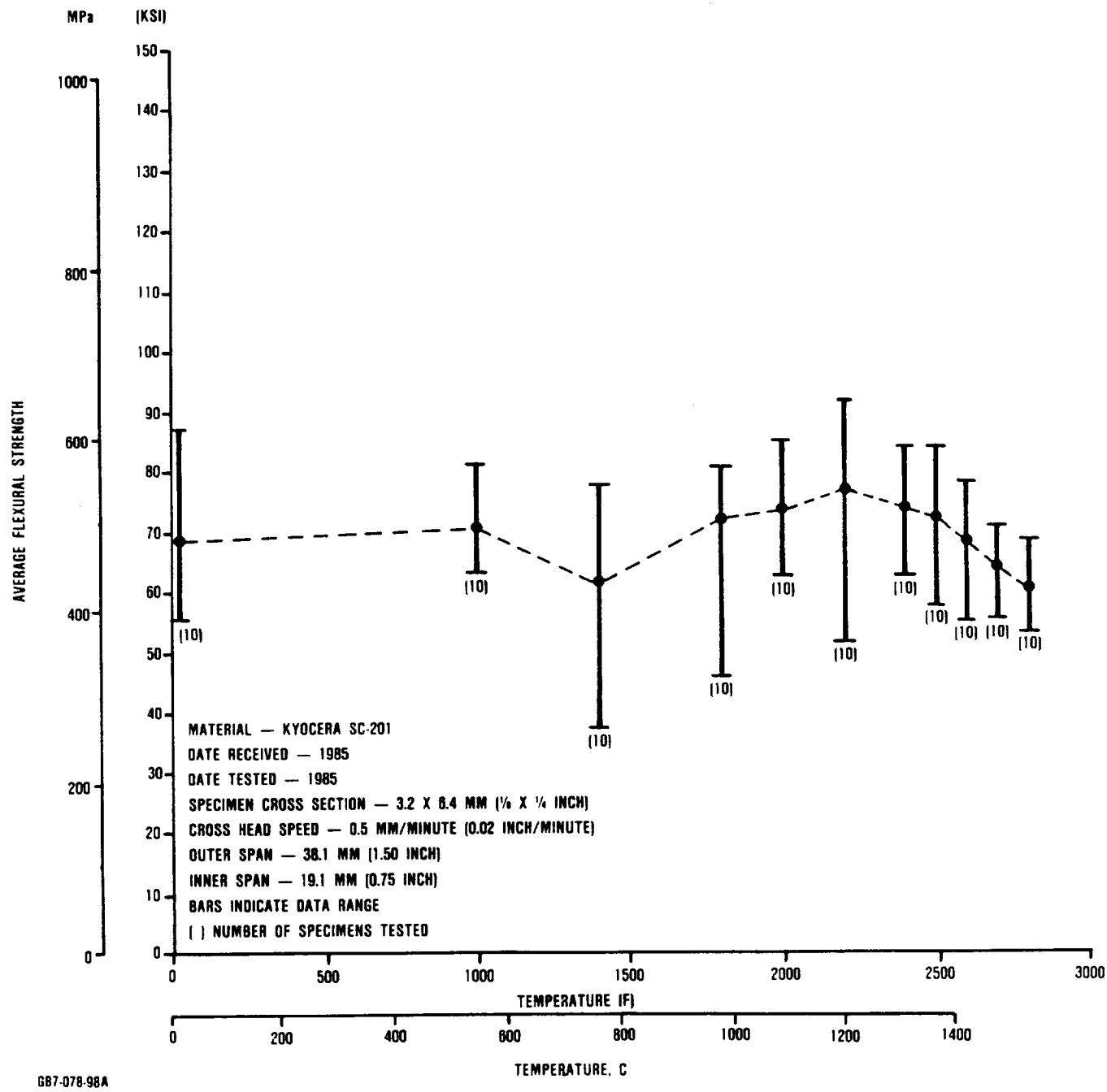

Figure 204 (Contd). View S. Four-Point Flexure Strength of Kyocera SC201 SSC.

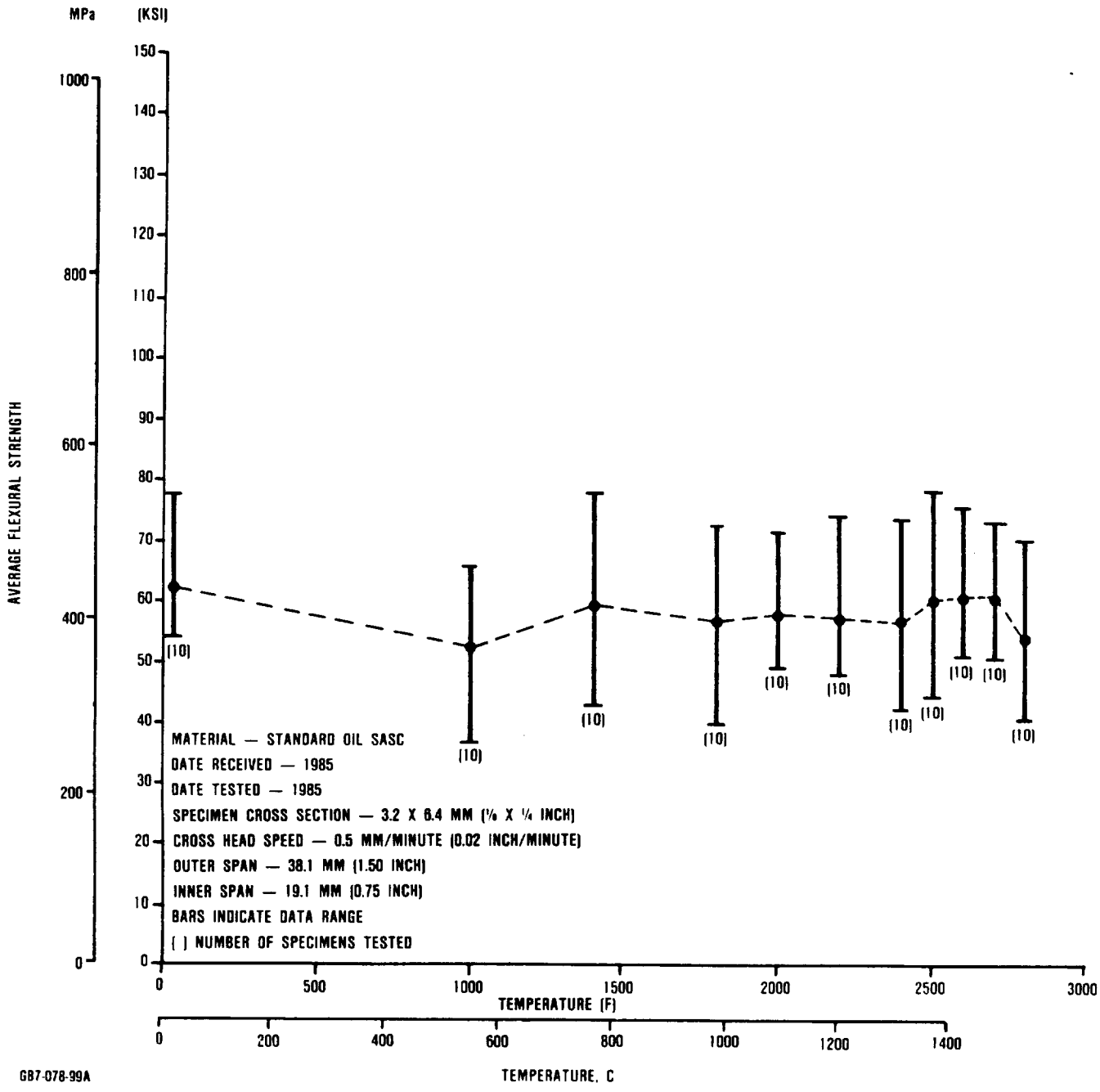

Figure 204 (Contd). View T. Four-Point Flexure Strength of Standard Oil SASC.

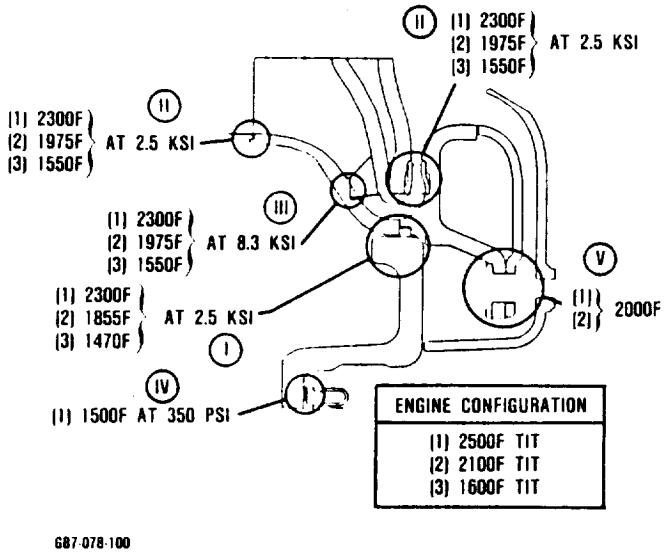

Figure 205. Interface Conditions for 871, 1149, 1371C (1600, 2100, 2500F) TIT Engines.

Table 28 summarizes the testing for interface conditions I, II, and III. Testing at condition III, depicted in Figure 206, was conducted under a constant 36.9kN (8.3-ksi) load (engine assembly preload) and results showed no sticking or reaction. Materials tested include ACC RBSN, Standard Oil SASC, Kyocera SC201 SSC, Standard Oil SiSiC, Corning LAS, and NGK SN-50 SSN.

As noted in Table 28, several material combinations result in sticking under conditions I and II. Additional testing was conducted for these combinations using flame-sprayed mullite coating on one interface surface. Results indicate that no sticking or reaction occurred with flame-sprayed mullite-coated surfaces.

Test results indicate that the AGT101 ceramic engine testing can be performed under the following guidelines:

- Attention must be given to material combination selection
- Coated SASC or RBSN can be used for selected interface combinations
- Detailed inspection after test must be conducted to identify problem areas
- Crowned surfaces appear to help in alleviating sticking phenomena

Alumina - LAS Sticking Study

Alumina thermocouple spacers and seals have been fabricated for use on the T_4 thermocouple. These spacers and seals seat against the LAS flow separator housing and the SASC transition duct and are exposed to a peak temperature of approximately 1093C (2000F). To evaluate the potential of sticking at these interfaces, a stack of LAS, Al_2O_3, and SASC materials was exposed to 1093C (2000F) for approximately 20 hours with a compressive 15-pound load simulating engine assembly. After completion of exposure and cooldown, no sticking between the LAS and alumina or between the SASC and alumina was observed.

6.1.3 Ceramic Interface Evaluation

Studies under the DARPA*/NAVY/Garrett Ceramic Engine Demonstration Program show that chipping and cracking of static components, which ultimately led to engine failure, were due to a contact stress mechanism at interfaces. This mechanism was identified in the DARPA program and a parallel ONR** program as localized high tensile stress due to biaxial loading resulting from a combination of axial aerodynamic loading and radial thermal expansion relative movement.

Based on the DARPA and ONR program studies, contact stress appears to be one of the most critical considerations of static-structure component design and material evaluation. In summary, these studies show that for high sliding contact loads a large strength reduction resulted when bare surfaces were in contact, moderate strength reduction resulted with high temperature lubricants present, and

*Defense Advanced Research Projects Agency
**Office of Naval Research

Table 28. Ceramic Interface Test Summary

Material Combination	Interface[1] I			Interface[1] II			Interface[2] III		
	799C (1470F)	1010C (1850F)	1177C (2150F)	843C (1550F)	1077C (1970F)	1260C (2300F)	843C (1550F)	1077C (1970F)	1260C (2300F)
RBSN/RBSN	-	-	-	NSR	NSR	NSR	NSR	NSR	NSR
RBSN/SASC	-	-	-	NSR	NSR	NSR	NSR	NSR	NSR
SASC/SASC	-	-	-	HS[3]	HS[3]	HS[3]	NSR	NSR	NSR
SASC/SC201	-	-	-	-	LS[4]	-	-	-	-
SASC/SiSiC	-	-	-	NSR	NSR	HS[3]	-	-	-
SASC/RBSN	-	-	-	NSR	NSR	NSR	-	-	-
RBSN/LAS	NSR	NSR	NSR	-	-	-	-	-	-
LAS/SASC	NSR	NSR	HS/CHIP	-	-	-	-	-	-
SASC/SN-50	-	-	-	NSR	Dis	NSR	NSR	NSR	NSR
SN-50/RBSN	-	-	-	NSR	Dis	NSR	-	-	-

[1] Evaluated at 0.889, 4.89, and 11.1kN (0.2, 1.1, and 2.5 ksi)

[2] Evaluated at 36.9kN (8.3 ksi), crowned

[3] Mullite coated - NSR

[4] Evaluated at 0.889kN (0.2 ksi)

Test Cycle

Heat at 0.889kN (0.2 ksi)

Load

Hold 20 Hrs

Unload

Cool at 0.889kN (0.2 ksi)

NSR = No stick or reaction

HS = Hard stick

LS = Light stick

Dis = Discolored

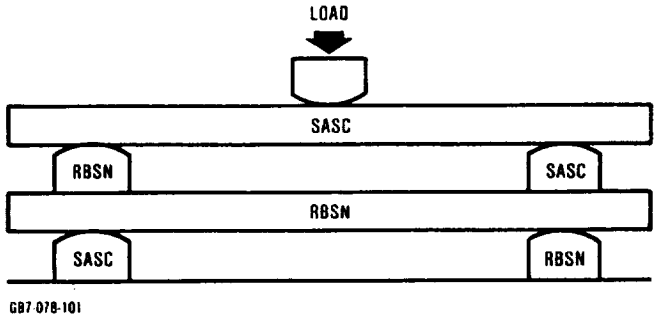

Figure 206. Compatibility Test Condition III, Interface Material Combinations.

little or no strength reduction resulted with a suitable metal compliant layer between the surfaces. The test apparatus developed in the DARPA program (shown in Figure 207) for interface evaluation was used to evaluate the materials and estimated contact conditions of AGT components. (The test procedure is described in the First AGT semiannual report.)

Initial tests on ACC's RBSN and Standard Oil's SASC were conducted with point contact 6.4mm crown against a 6.4mm crown (1/4-inch crown against 1/4-inch crown) at loads ranging from 44.48 to 254.8N (10 to 57.3 pounds) normal force (F_N) and at temperatures ranging from room temperature to 1093C (2000F). For the elevated temperature tests, the specimens were held at temperature for 30 minutes prior to application of the tangential force (F_T). A relative movement of 1 mm (0.04 inch) was applied at a rate of 0.5mm/min (0.02 in/min) to allow calculation of the static and dynamic coefficients of friction.

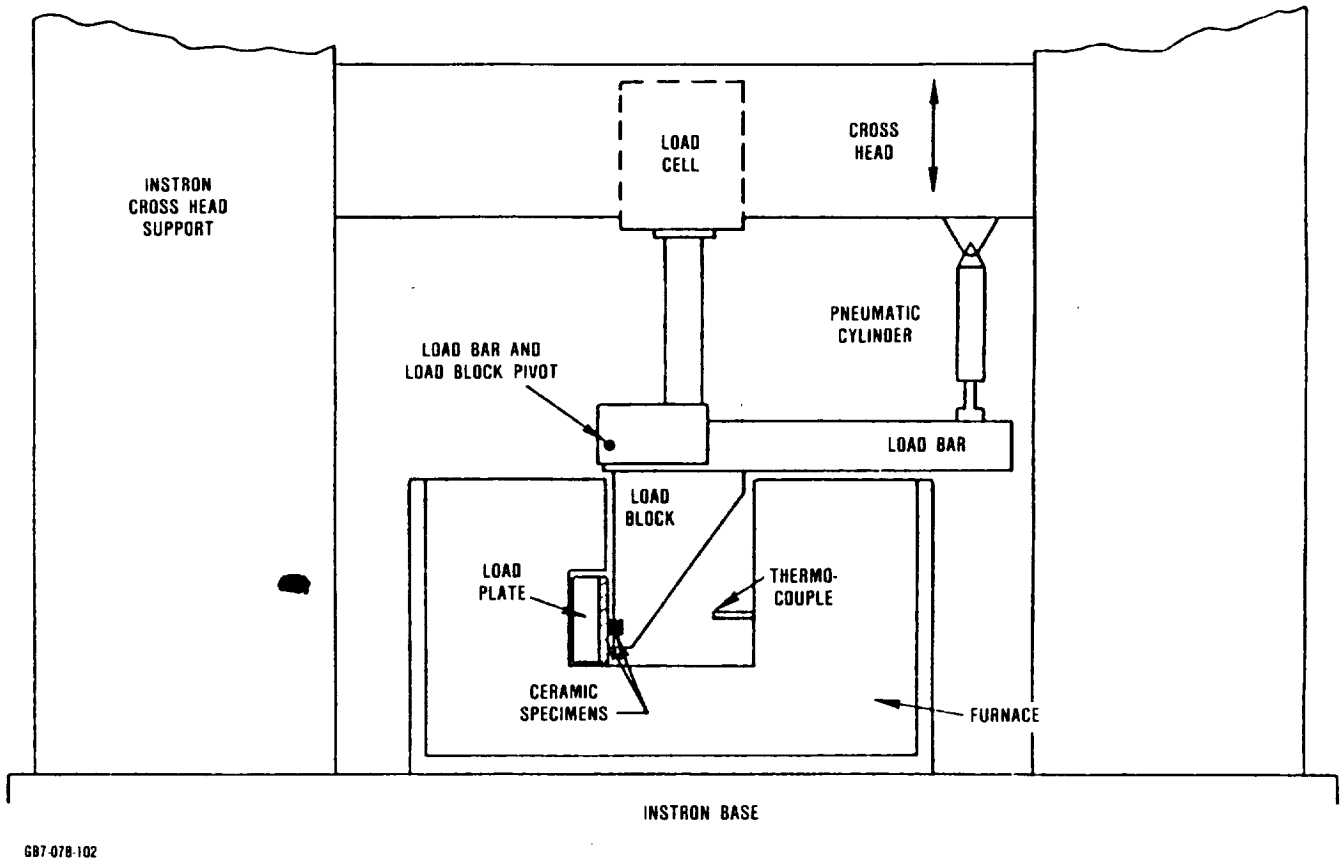

Figure 207. Interface Test Apparatus.

Each test was repeated six times to verify the test rig reproducibility and to provide a good data base for the RBSN and SASC. Figure 208 shows the degree of data scatter for the static coefficient of friction versus the normal load at room temperature. The scatter is not excessive. The most important observations are that the SASC has a substantially lower room temperature static coefficient of friction than does the RBSN, and the static coefficient of friction does not vary significantly over the load range evaluated for the point-contact condition.

Further information is available by comparing the actual F_T versus contact traverse distance curves for each material at each temperature. These curves for RBSN and SASC under 6.8 kg (15 pounds) point-contact are shown in Figure 209 with coefficient of friction values. These curves were reproducible from specimen to specimen; the following observations were noted:

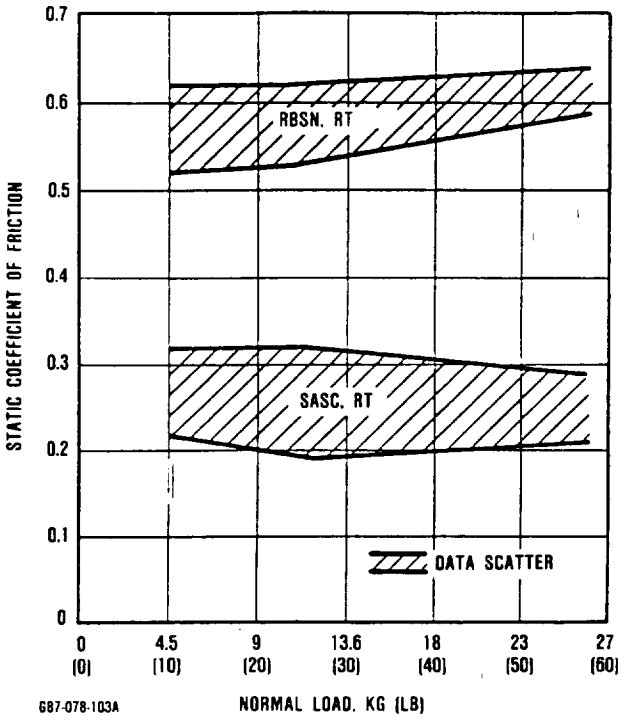

Figure 208. Static Coefficients of Friction Versus a Normal Load for RBSN and SASC at Room Temperature.

a) At room temperature, the curves for both materials were continuous with no abrupt change between static and dynamic coefficients of friction. The curve for RBSN gradually increased and then decreased. Examination of the contact surface suggested that surface damage had occurred and that particulate debris was being pushed ahead of the contact interface, which could explain the steady increase in friction. Once a sufficient amount of debris was present, it could begin acting as a dry lubricant, which could explain the later decrease in friction. Very little surface damage was visible on the SASC stationary specimen, but a roughening had occurred on the moving specimen. The accumulation of surface damage on the moving specimen could account for the continuous increase in friction.

b) At elevated temperatures, the curves for both materials had a discontinuity between the static and dynamic friction, representative of a breakaway condition. The mechanism has not been fully identified, but is suspected to be associated with sticking due to surface oxidation. Contact surface examination suggests that oxidation is enhanced in the contact region and that, once breakaway occurs, the oxide acts as a viscous lubricant.

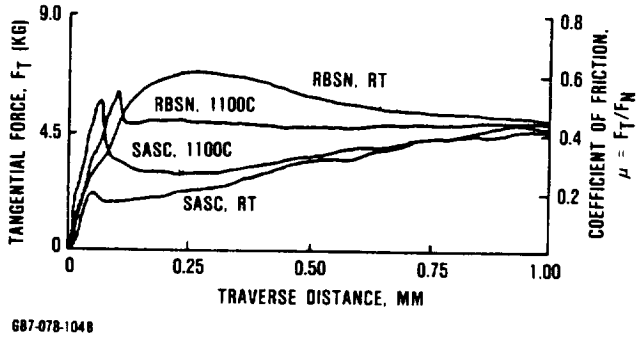

Figure 209. Friction Versus Relative Motion for Bare SASC and RBSN Under the Point Contact Condition With a Normal Load of 25 Pounds.

c) The dynamic coefficient of friction for RBSN is lower at 1093C (2000F) than at room temperature and is approximately constant at 0.45 for normal loads of 4.5 to 26 kg (10 to 57.3 pounds). The dynamic coefficient of friction for SASC increases with traverse distance at 1093C (2000F) and room temperature to the 0.45 range. Friction also appears to increase with normal load at 1093C (2000F).

Most engine components are pre-oxidized prior to rig and engine testing. Figures 210 and 211 summarize contact data for pre-oxidized RBSN and SASC. The RBSN and SASC were pre-oxidized for 2 hours at 1204C (2200F). Pre-oxidation appeared to decrease the room temperature coefficient of friction but had little effect for elevated temperatures.

The point-contact tests at 11.36 kg (25 pounds) are considered more severe than the static structure components will be exposed to in the AGT101 engine. Current estimates are that the load will not exceed 1.6 kg (3.5 pounds) over a comparable point-contact area. The purpose of the exaggerated contact loads was to identify the mechanisms of contact damage and to determine the sensitivities of the candidate ceramic materials to surface damage.

Additional tests were conducted at 11.36 kg (25 pounds) or less with line contact. Initial tests suggest that the data scatter is larger for line-contact than for point-contact. The high-temperature friction data are almost identical for both RBSN and SASC contact conditions. The room temperature coefficient

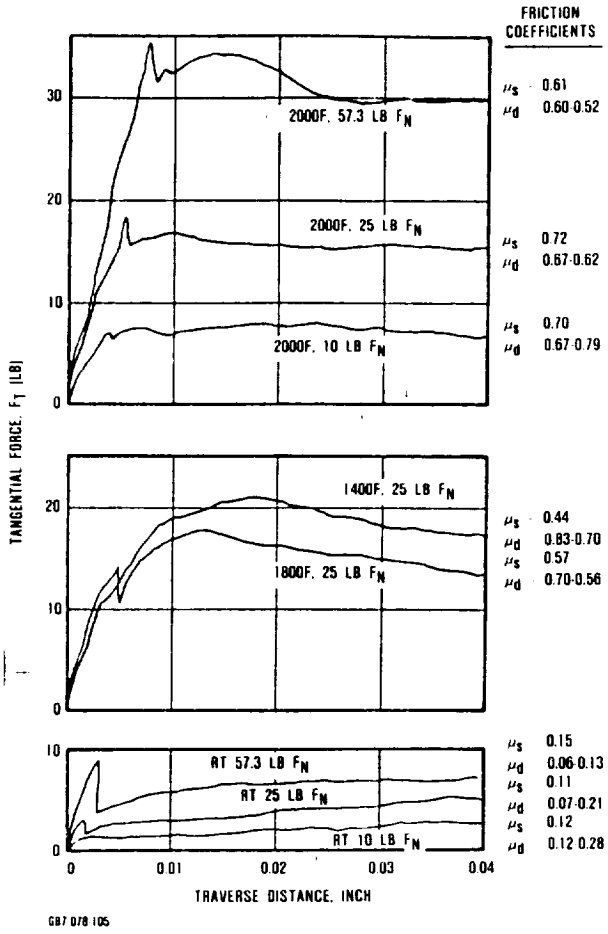

Figure 210. Coefficients of Friction for Oxidized RBSN Point Contact.

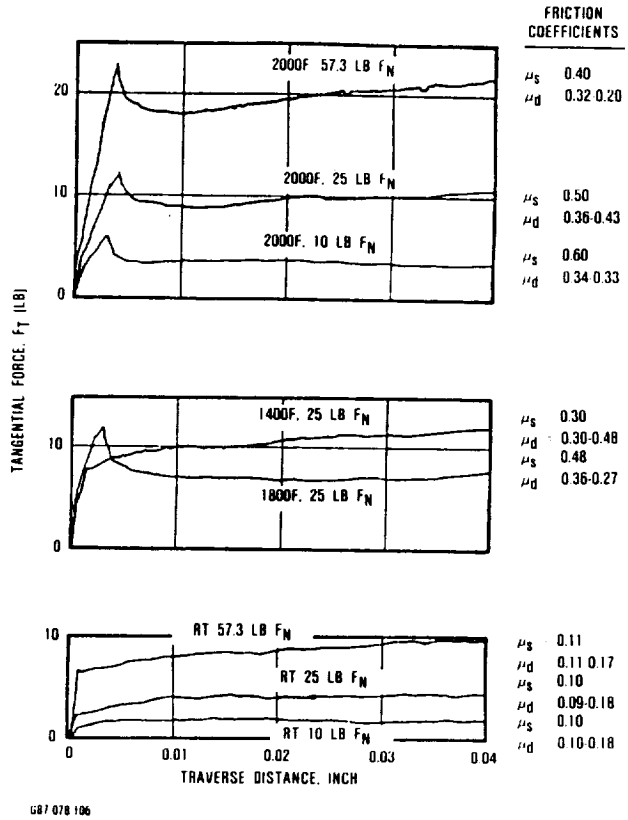

Figure 211. Coefficients of Friction for Oxidized SASC in Point Contact.

of friction appears to be substantially lower for the line-contact condition for both materials. The line contact friction data for RBSN and SASC for the 11.36-kg (25-pound) normal load are shown in Figure 212.

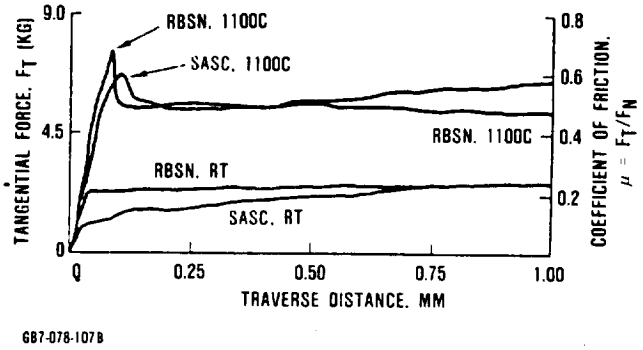

Figure 212. Friction Versus Relative Motion for Bare SASC and RBSN Under the Line Contact Condition With a Normal Load of 25 Pounds.

After contact testing, each specimen was fractured in four-point bending. The strength data are plotted in Figure 213 for point-and line-contact conditions. Obviously, the RBSN material has lower residual strength than SASC, and the point-contact results in lower line-contact conditions. Obviously, the RBSN material has lower residual strength than SASC, and the point-contact results in lower strength than line-contact. More specifically, the RBSN exposed to point-contact biaxial loading, has a residual strength of 121 MPa (17.5 ksi). Strengths of RBSN prior to contact typically ranges from 275 to 380 MPa (40 to 55 ksi). Strength degradation in the range of 60 percent has occurred.

The line-contact strength curve in Figure 213 for RBSN intersects the point-contact curve, although most of the individual line contact data points are higher. Examination of the line-contact surfaces shows that con-

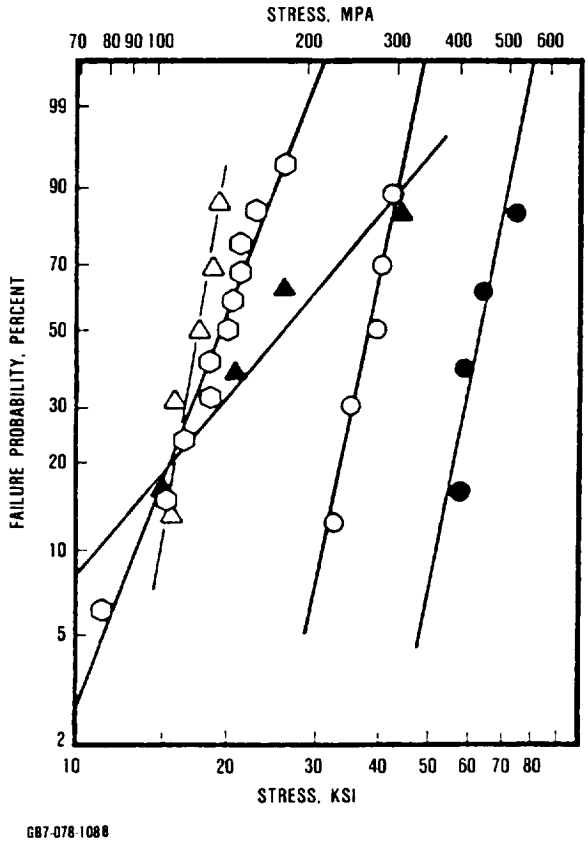

LEGEND

	MATERIAL	CONTACT	CONTACT TEST TEMPERATURE	AVERAGE 4 POINT MOR. MPA
△	RBSN (RBN104)	POINT	1100C	121
▲	RBSN (RBN104)	LINE	1100C	186
⬡	RBSN (NC350)	POINT	RT AND 1100C	132
○	SASC	POINT	1100C	258
●	SASC	LINE	1100C	433

Figure 213. Room Temperature Strength RBSN and SASC After Line and Point Contact Tests.

tact (and the resulting damage) only occurred at high points and varied from specimen to specimen. Specimens having a low residual strength typically had contact only along a small segment of the line. As the degree of contact along the line increased, the residual strength increased, suggesting that load distribution and load sharing are important in minimizing contact damage in RBSN.

Figure 213 shows that SASC has higher residual strength than RBSN. Specifically the average strength of SASC after point-biaxial contact is 258 MPa (37.4 ksi). The average strength prior to contact exposure for the configuration tested is approximately 450 MPa (65 ksi). The resulting strength degradation for the SASC, therefore, is approximately 43 percent for point-contact and 4 percent for line-contact.

To estimate the actual tensile stresses applied at the ceramic surfaces during biaxial contact loading, the contact apparatus data for RBSN and SASC were run through a contact stress analysis computer program developed under an ONR Program. The results for room temperature and 1100C point- and line-conditions are summarized in Table 29. The 1100C results are plotted in Figure 214 and compared with baseline four-point flexural strength data for the line-contact configuration.*

The predicted stresses for the point-contact condition considerably exceed the baseline strengths of both RBSN and SASC and would be expected to produce the degree of surface damage that would yield the severe strength degradation measured. Peak stresses for line contact are substantially reduced, only

*Specimen-oriented in the four-point test fixture with the flat surface in tension and the 0.63-cm radius surface in compression.

Table 29. Predicted Contact Tensile Stresses For Point- and Line-Contact Conditions.

Material	Normal Load, lb	Contact Test Temperature, C	Point-Contact		Line-Contact	
			μ_s*	σ** ksi	μ_s*	σ** ksi
RBSN	10	Room	0.62	148	0.18	10
	25		0.62	219	0.22	20
	57.3		0.64	293	0.22	31
	10	1100	0.64	152	0.54	32
	25		0.60	212	0.68	64
	57.3		0.52	236	0.53	75
SASC	10	Room	0.25	67	0.25	20
	25		0.19	77	0.09	11
	57.3		0.26	154	0.15	28
	10	1100	0.66	170	0.62	5
	25		0.51	200	0.61	75
	57.3		0.51	290	0.70	131

* μ_s = static coefficient of friction

** σ_p = calculated peak tensile stress

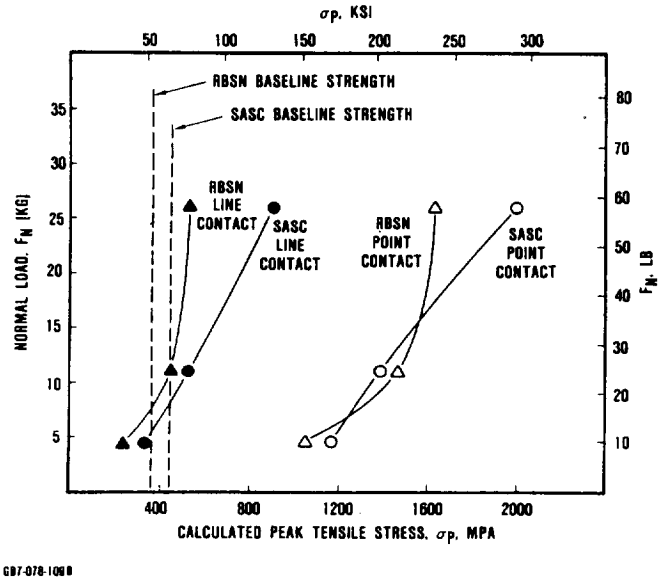

Figure 214. Calculated Peak Tensile Stresses for 1100C Contact Tests of RBSN and SASC.

exceeding the baseline strengths of RBSN and SASC at normal loads above 7.0 kg (15.4 pounds) for the configuration studied.

Correlation between analytically estimated peak stresses (see Figure 214) and retained strength are not as good for SASC in line-contact. Estimated contact stresses substantially exceeded the base-line strength of the material, yet very little strength degradation occurred.

6.1.4 RBSN Spalling Study

Spalling damage has occurred on three ACC RBSN (RBN104) turbine shrouds when these parts were exposed to temperatures ranging from 871 to 1204C (1600 to 2200F). In two instances the spalling resulted in complete destruction of the component. In the third instance only limited spalling occurred and the turbine shroud subsequently passed 10 simulated lightoff cycles to 871C (1600F).

Spalling typically has been attributed to thermal stress generated within RBSN when residuals of Si remain un-nitrided during processing. The amount of free Si required to induce spalling has not been quantitifed, however a review of Garrett in-house data suggests that spalling of RBSN parts may occur if weight gains, which occur during the nitriding process, are below 59 percent. A weight gain below this figure indicates that a significant portion of Si has not been converted to Si_3N_4 during the reaction process. In addition, high green densities and thick cross sections inhibit free N_2 passage to the interior, which is necessary for complete reaction. Green densities and part thickness limitations must typically be experimentally determined as this fabrication approach is applied to larger or thicker engine components.

Additional influences on complete nitriding include Si purity. Contaminants such as carbon will react with the Si at the elevated nitridation temperatures to form undesirable compositions. Thus, any component processing between green fabrication (ie, casting or molding), may adversely affect the final Si_3N_4 product if contamination may occur.

Fabrication processing of the ACC turbine shroud requires that green machining occur prior to part nitriding. If mounting compounds and machining coolants are used, the result may be contamination of the porous Si part.

The significance of these and other variables on spalling were suspected, but not determined with certainty. RBSN fabrication techniques were nonetheless modified with the intent of reducing spalling. Parts were fabricated with lower green densities and green machined with no coolant, and with minimal or no mounting compound. In cases where mounting compounds were used, they were subsequently machined off the Si surfaces prior to the final cleaning operation to prevent compound penetration into the green part. Turbine shrouds processed using these methods were thermally cycled to 1204C (2200F) after nitriding without any occurrence of spalling.

6.1.5 Laser Marking of Ceramic Materials

The effect of laser marking on the strength of five ceramic materials was investigated to

determine whether this technique would be suitable for permanently marking AGT101 parts. Positive identification of engine hardware for the AGT program is necessary to keep component traceability. Samples of the five ceramic materials (RBSN, SASC, LAS, HPSN and SSN) were used to determine the laser parameters that would clearly mark the ceramic surface without visible damage. Only laser marking of the LAS materials was unacceptable, due to visible damage of legibly marked materials. Subsequently, test bar samples were marked with a series of XHs along the length of the test bars to simulate worst case marking orientations. One-half of the test bars from each material were given the established heat treatment for healing surface flaws. All test bars were flexure tested at room temperature with the laser marked surface in tension. Table 30 summarizes the flexure strength data of laser marked specimens. Standard oil SASC and ACC RBSN laser-marked and heat-treated materials showed no reduction in strength due to the laser marking and did not fracture in the laser marked area, as long as the materials were heat treated. The flexure strength after laser marking of these materials without heat treating showed a reduction in strength and all fractures originated at the laser marking.

ACC SN-501 SSN and Norton NC132 HPSN test specimens failed at the laser marking, both with and without heat treatment. But the flexure strength of the specimens was adequate in all cases.

In summary, laser marking parameters have been established for marking four ceramic materials frequently used on the AGT101 program. Properly processed laser marked materials show little or no material strength loss as a result of laser marking.

6.1.6 Slip Casting Rheology Studies

Two subcontracts were initiated during the summer of 1983 to study the rheology of Si and Si_3N_4-Y_2O_3-Al_2O_3 particulate dispersions in water. The program objectives are briefly discussed in subsequent paragraphs and the results are presented in detail in Appendices D and E to the ninth AGT semiannual progress report.

Table 30. Flexure Strength and Fracture Origins of Laser Marked Test Bars

	Laser Marked		Laser Marked and Heat Treated	
	Mean Strength MPa (ksi)	Fracture Origin	Mean Strength MPa (ksi)	Fracture Origin
Standard Oil SASC	225.5 (32.7) (5 samples)	At laser marking	352.3 (51.1) (5 samples)	Not at laser marking
ACC RBN104 RBSN	228.9 (33.2) (5 samples)	At laser marking	263 (38.2) (5 samples)	Not at laser marking
ACC SN-501 SSN	676.4 (98.1) (7 samples	At laser marking	583 (84.6) (7 samples)	At laser marking
Norton NC-132 HPSN	615 (89.2) (8 samples)	At laser marking	723 (105.0) (8 samples)	At laser marking

The Si slip program was subcontracted to Dr. M.D. Sacks of the University of Florida to support reaction-bonded Si_3N_4 processing at ACC.

Objectives/tasks included:

- o Baseline characterization of ACC-supplied Si powder
  - Particle size distribution
  - Powder surface area measurement
- o Electrophonetic mobility versus pH
- o Zeta potential versus pH
- o Shear stress versus shear rate as a function of solids contact, pH, and ultrasonic agitation
- o Viscosity versus shear rate as a function of solids content, pH, and ultrasonic agitation
- o Total porosity and median pore radius of cast samples as a function of slip solids content, pH, and ultrasonic agitation
- o Screening study of potential dispersants

The study report "Dispersion of Silicon Powder", covering June through September 1983, is included as Appendix D to the ninth semiannual AGT progress report. A technical paper was subsequently prepared by Dr. Sacks and submitted (after NASA approval) to the American Ceramic Society for publication.

The Si_3N_4-Y_2O_3-Al_2O_3 slip program was subcontracted to Dr. I.A. Aksay of UCLA and subsequently of the University of Washington to support sintered Si_3N_4 rotor processing technology.

Objectives/tasks included:

- o Baseline characterization of commercial Si_3N_4, Al_2O_3 powders
  - Agglomerate content and structure
  - Particle size distribution
  - Particle size control by elutriation
- o Electrophonetic mobility for each powder in aqueous suspension
- o Zeta potential versus pH
- o Preparation of cast specimens for sintering and evaluation at Garrett

The study report, "Development of Homogeneity in Si_3N_4 Ceramics by Colloidal Filtration", was co-authored by I.A. Aksay and C.A. Ambarian of UCLA and covers June through September, 1983. The report is included as Appendix E of the ninth semiannual AGT progress report.

6.1.7 Turbine Diffuser Insulation Evaluation

The use of a fibrous insulation in the turbine diffuser was stimulated by the successful use of Babcock and Wilcox vacuum-formed 3000 material in rig testing. Results of the rig testing indicate that a fibrous insulation could withstand high temperature, high gas velocities for a short period of time. However, surface erosion on the insulation indicated that a more durable system would be required for longer term exposure and higher gas velocities. In pursuit of an improved insulation system, several samples of Lockheed High Temperature Protection (HTP) were obtained for evaluation. The sample consisted of cylinders of sintered and machined high purity SiO_2 and Al_2O_3 fibers. The samples were machined to form cylinders with a 7.87cm (3.1-inch) bore and a 7.62cm (3-inch) length. As-machined cylinders, and cylinders partially coated with a boro-silicate glass, designated by NASA and Lockheed as reaction cured glass (RCG), were provided by Lockheed and shown in Figure 215.

Two samples, one uncoated and one coated, were exposed to combustor discharge gases as illustrated in Figure 216. During this test, vitiated air at 1149C (2100F) was directed through the cylinder bore at 9 kg/min (20 lb/min) [approximately 76.2 m/sec (250 ft/sec)] for 46 minutes. This condition exceeded

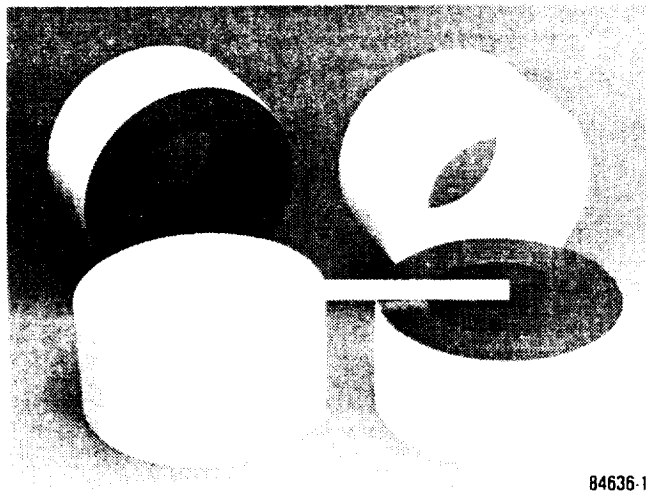

Figure 215. RCG Coated and Machined HTP Insulation From Lockheed.

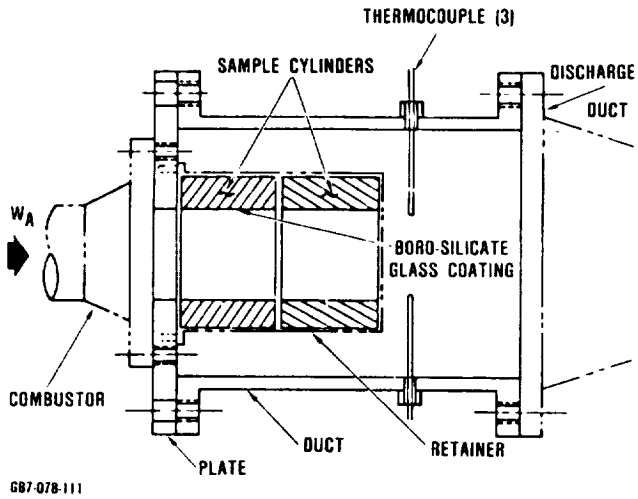

Figure 216. AGT101 Insulation Test Rig.

the 22.9 m/sec (75 ft/sec) gas velocity predicted for the turbine exhaust diffuser dump region currently utilizing the Babcock and Wilcox fibrous insulation.

Post test visual examination did not reveal any damage to the coated sample and only minor surface erosion on the uncoated sample. This erosion was judged a result of local surface damage resulting from the machining operation rather than the exposure conditions. These preliminary results indicate that coated or uncoated HTP may be suitable for use in the current AGT101 engine configuration and that the RCG coated HTP may be suitable for use in higher gas velocity locations. Additional testing was directed toward evaluating insulation capabilities under representative turbine rotor discharge conditions, simulating gas velocities and temperatures rather than at the turbine diffuser dump location. Two test conditions were selected representative of engine maximum power [966C, 304.8 m/sec (1770F, 1000 ft/sec)] and idle [1093C, 106.7 m/sec (2000F, 350 ft/sec)] flow conditions. To perform these tests, additional RCG-coated and uncoated test cylinders were obtained from Lockheed. The cylinders were 7.62 cm (3-inches) long with a 6.4 cm (2.75-inch) inner diameter (needed to attain the higher gas velocity conditions). The new cylinders were a higher density HTP-16 (16 lb/ft^3)than the HTP-12 material previously tested.

Testing was performed for 7 cycles profiled in Figure 217. The test rig was disassembled for inspection after completion of Cycles 1, 3, and 7. At completion of Cycles 1 and 3, no material distress was observed. Following Cycle 7, however, disassembly revealed coated sample shrinkage, uncoated sample shrinkage, and melting (illustrated in Figure 218). Based on previous testing at both Garrett and Lockheed, these results did not correlate with 1093C (2000F) exposures. Thus, the two samples were returned to Lockheed for post-test analysis. Meanwhile, the test conditions were reviewed at Garrett, including recalibration of the three control thermocouples located downstream of the test cylinder discharge. Three conditions were identified that may have contributed to the atypical results. These included the use of a gas discharge water quench downstream of the test cylinders for rig ducting protection. This discharge may have provided recirculated contamination or vapor that could conceivably have reached the test articles. Contaminants

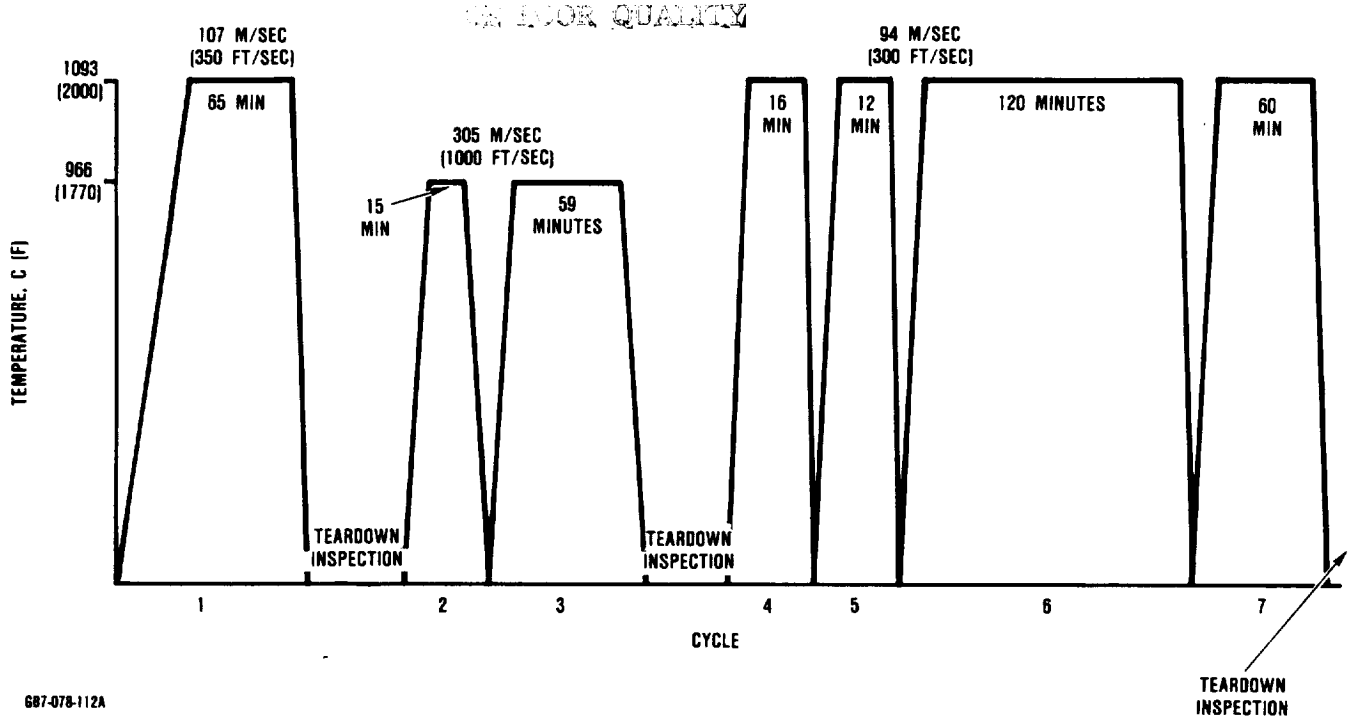

Figure 217. Maximum Power and Idle Condition of Lockheed HTP-16 Insulation.

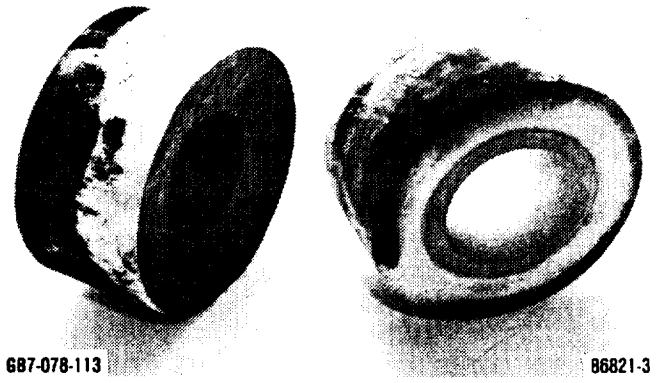

Figure 218. Lockheed HTP-16 Cylinders After Cyclical Flow Testing.

may have contributed to a reduction in the melting temperature of the insulation materials. Water quenching was used only in test cycles subsequent to Cycle 3.

Another possible contributor was the occurrence of wet starts in which unburned fuel may have been sprayed onto, and by, the insulators. Subsequent operation would have produced local burning and hot spots, which would have contributed to insulation melting.

The most likely contribution to insulation damage probably occurred at overtemperature test conditions. Post-test calibration of the three Type S thermocouples indicated that one thermocouple was reading substantially lower microvolt output than the others. Due to the averaging of the output of these thermocouples by the control and recording systems, there is a strong possibility that temperatures 500C over the 1093C (900F over the 2000F) desired test condition occurred in the cycles subsequent to Cycle 3. Thermocouple deterioration is believed to have occurred during the final phases of testing (Cycles 6 and 7).

Continuing discussions with Lockheed regarding these results confirmed the typical occurrence of HTP material shrinkage at 1593C (2900F), supporting the indications of an over-temperature condition. Nonetheless, encouragement is gained in that the test samples demonstrated short-term durability during the first 3 cycles, and that even under the excessive conditions of Cycles 4 through 7, only limited deterioration occurred.

6.2 Ceramic Turbine Rotor

The AGT101 radial turbine rotor has required extensive development in design, material, and fabrication. Through close involvement with AGT101 ceramic suppliers, Garrett was able to define the barriers to successful rotor fabrication and determine possible solutions. The material strength requirements were determined through detailed analysis. High-temperature materials with the required strength were selected for rotor fabrication development. Initial development concentrated on fabrication of bladeless simulated rotor hubs to demonstrate that thick-section hubs of the required strength could be fabricated. Suppliers successfully achieving this task were released to pursue bladed rotor development.

6.2.1 Initial Evaluations

Garrett selected four ceramic suppliers to develop the AGT101 turbine rotor: AiResearch Casting Co. (ACC), Pure Carbon Co., Standard Oil, and Ford. Difficulties in fabrication were expected due to the large volume and thick cross section of the rotor. For this reason, suppliers were requested to provide bladeless simulated rotor hubs for evaluation to demonstrate the capability to fabricate thick-section rotor hubs of the required strength. A typical simulated rotor is shown in Figure 219.

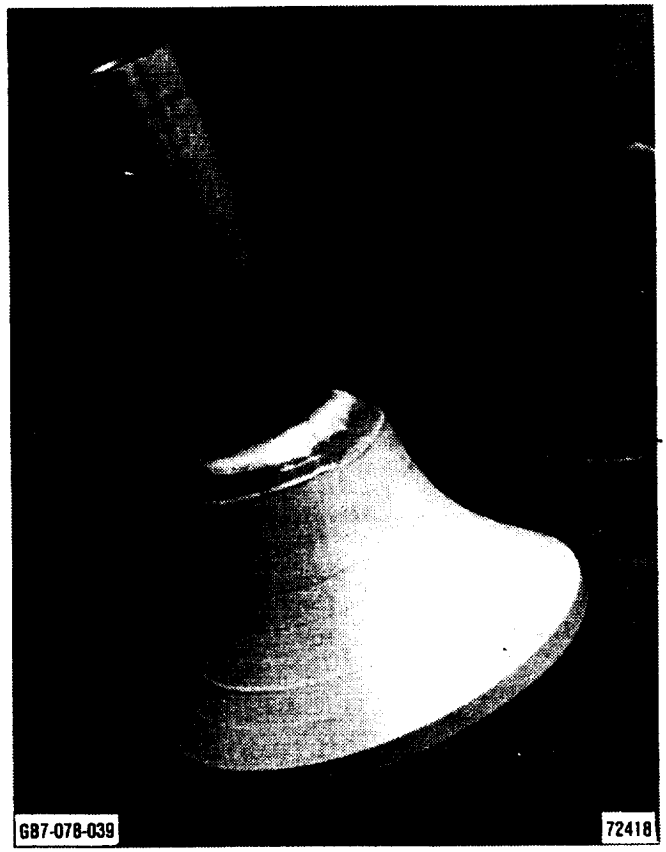

Figure 219. Simulated Rotors Were Used to Demonstrate Thick Section Fabrication Capability.

Rotor materials evaluations indicated that the majority of candidate rotor materials met, or nearly met, the first-year material strength goals. Nominally, these goals were a characteristic strength of 469 MPa (68 ksi) and a Weibull modulus of 12 at 1093C (2000F). These goals were based on a rotor stress distribution that peaks at approximately 207 MPa (30 ksi) within the rotor hub. Final material goals were a characteristic strength of 552 MPa (80 ksi) and a Weibull modulus of 14. Suitable candidate rotor materials were demonstrated for first-year rotor development for three materials: Ford Sintered RBSN, ACC Sintered Si_3N_4, and Pure Carbon Refel Reaction-Sintered SiC. In addition, Standard Oil hot-pressed alpha-SiC material met the strength requirements and was a possible rotor candidate material if a suitable fabrication method could be found.

All four suppliers successfully demonstrated simulated rotor shape capability using a variety of fabrication techniques. ACC approached the challenge with a slip casting technique. Ford also concentrated on a slip-cast approach. Standard Oil selected an initial two-piece fabrication approach in which a hub and shell were isopressed, baked-out, and bonded (hot pressed) together. Standard Oil selected this approach due to the difficulties in binder bake-out of cross sections greater than one inch. Improved binder removal methods allowed Standard Oil to later abandon the two-piece approach in favor of a solid

injection-molded rotor. Pure Carbon, in conjunction with British Nuclear Fuels, Ltd (BNFL), fabricated rotors from reaction sintered SiC.

Although advancements in rotor fabrication were made by all suppliers, only minimal rotor deliveries were made early in the program. Standard Oil produced a "spin quality" SASC simulated rotor, i.e., free of x-ray indications and significant visual defects. Garrett spin-tested the rotor, obtaining good correlation between analysis and material properties. A room temperature burst speed of 72,400 rpm was achieved. Pure Carbon successfully fabricated a simulated rotor from reaction sintered SiC. One simulated rotor, successfully formed, reacted, and inspected, was delivered for evaluation. Evaluation indicated that the Pure Carbon Refel material would require additional development for AGT101 rotor application; thus it was discontinued from the program.

During the first half of 1981, simulated rotors were received from ACC and Standard Oil. Evaluation of the ACC simulated rotors demonstrated rotor hub integrity. Additional evaluation was required to determine the reproducibility of the demonstrated rotor integrity. This was achieved late in 1981. ACC was given approval to fabricate bladed AGT101 rotors, with initial bladed rotor deliveries received in early 1982. Initial testing of Standard Oil's SASC material showed it did not meet the initial required strength goals when fabricated into simulated rotor shapes and was deleted from future consideration. Two additional Standard Oil materials--hot-pressed alpha SiC and reaction-sintered SiC--were evaluated. These materials also did not meet strength goals when fabricated into rotor shapes and were also deleted from consideration. Efforts by Standard Oil on AGT101 rotor development were postponed until Standard Oil could demonstrate sufficient rotor material properties.

Ford encountered difficulties in forming simulated rotors, due primarily to density gradients, which resulted in internal cracking. Through changing the slip rheology (viscosity and specific gravity) Ford was able to obtain a more consistent density throughout the rotors, eliminating the cracking problem. Further improvements in simulated rotor quality were obtained through controlled drying. These improvements could be seen in the successful spin testing of simulated rotors.

6.2.2 Bladed Rotor Fabrication

Initial bladed rotor fabrication began in early 1982, with the suppliers demonstrating limited success. As discussed in paragraph 5.2.4, the blade cross section was redesigned to improve fabricability (ref. Figure 136). Nominal rotor thickness at the inducer blade tip was modified from 0.762 to 0.774 mm (0.030 to 0.040 inch). These changes reduce the difficulty encountered in achieving complete blade fill. Late in the AGT101 program, another design iteration was made, shown pictorially in Figure 220. This change resulted

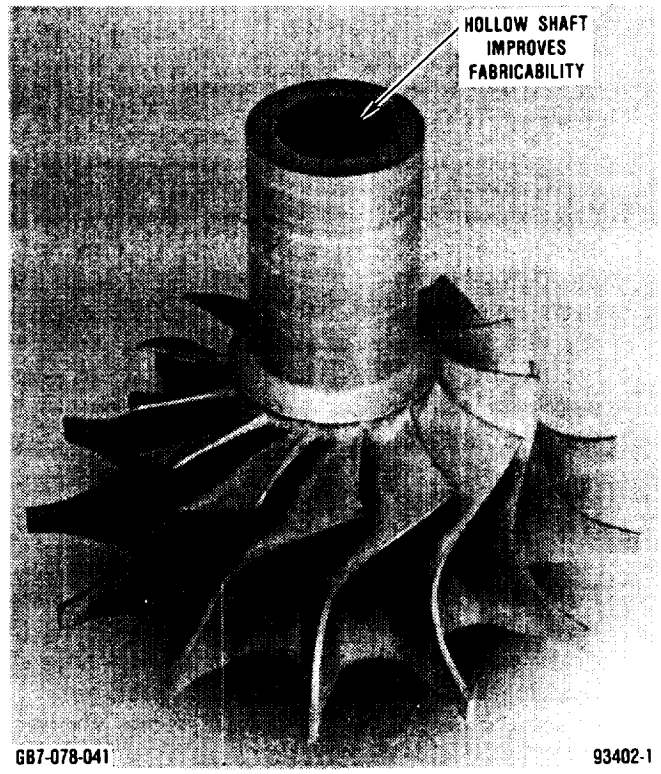

Figure 220. Hollow Shaft Design Improved Fabricability.

in both an improved bearing surface and rotor/compressor attachment. Rotor/compressor attachment methods will be discussed later in section 6.2.4.

The remainder of the AGT101 rotor effort focused on fabrication by ACC and Ford using a slip cast Si_3N_4 approach. Problems were encountered in slip preparation, casting, and densification.

To consistently prepare a high quality slip for casting, the starting powder must be consistent with respect to purity and particle size distribution. While the powder may meet the powder supplier's specifications, there is usually batch-to-batch variations for which the user must compensate, normally through additional powder processing. Powder impurities can degrade the material properties by affecting grain boundary chemistry and/or in the formation of strength reducing inclusions. A controlled optimum particle size distribution is required to consistently achieve high strength and minimize shrinkage and porosity. To optimize strength, a powder that can be densified quickly with minimal grain growth is desired.

Casting is affected by the slip properties. The viscosity must be low enough to allow complete mold fill, yet the solids content must be high enough to achieve a reasonable casting rate and green density. AGT101 experience showed that too-slow a casting rate would result in density variations due to particle segregation, while too-rapid a casting rate would result in blockage of narrow passages in the mold when casting under atmospheric pressure conditions.

Problems specifically encountered by ACC included powder purity, partical size distribution, incomplete blade fill and cracking during densification. The powder particle size distribution and purity was not consistent from batch to batch as received from the powder supplier. Powder impurities resulted in contaminant migration to the blade tips, causing laminar platelet formation and subsequent blade tip cracking. Several approaches were investigated to clean both the powder and the slip prior to casting but the problem was not solved. This experience emphasized the requirement for a clean-room processing environment. Incomplete blade fill also remained a problem (Figure 221) despite centrifugal spinning during casting. While ACC was not able to solve blade breaking during densification, it was attributed to non-uniform green density and/or furnace thermal gradient and/or non-optimized sintering cycle. Despite this, ACC did achieve near theoretical densities and produced rotors capable of passing 115,000 rpm spin testing. The high temperature properties of the materials developed by ACC, however, did not meet AGT101 RPD temperature goals.

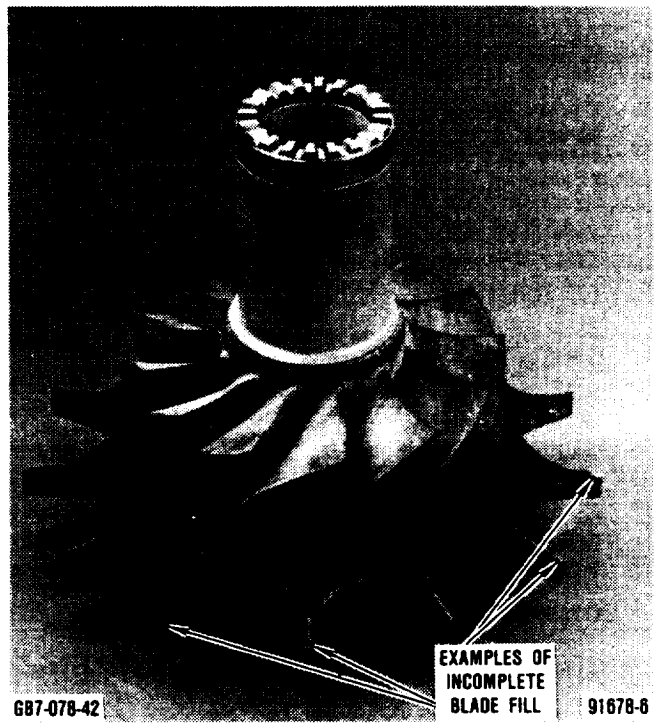

Figure 221. Example of Incomplete Blade Fill.

Ford encountered similar problems, including poor tip definition, poor blade resolution, and cracks at the blade roots and in the hub region. The tip definition and blade resolution problems were improved by using a centrifugal casting technique that forced slip into the

blade cavities. Blade root cracking appeared to be improved by modifications in the wax removal technique. The hub cracking problem was improved by more careful removal of the plaster base. Internal cracks were determined to be caused by density gradients, similar to the problem encountered in simulated rotor fabrication. This was corrected through use of an organic suspending agent and greater control of slip viscosity to eliminate slip settling during casting.

In addition, as Ford improved material high temperature properties, changes were made to the slip. One problem this caused was a low green strength and thus a greater risk of handling damage. However, by adding a presintering step to the densification process, handling strength was increased. This allowed minor machining operations to be carried out on the rotor in the green state, precluding the need for expensive, time-consuming diamond grinding of the fully dense rotor.

ACC bladed rotor S/N 10191, cast in October 1981, was judged suitable for spin test evaluation based on visual inspection, x-ray radiography, and density evaluation, despite incomplete blade fill. Spin testing was performed to verify rotor hub integrity in a bladed rotor. Initial spin testing resulted in the loss of two blades at 83,000 rpm. A secondary blade tip fracture occurred in one blade adjacent to that of the two blades; no hub or shaft damage occurred. Visual and 30x microscopic analyses revealed that both blades fractured at surface casting defects. The second spin test achieved 95,300 rpm at which time complete rotor destruction occurred. Partial reconstruction was possible since several large pieces of rotor remained. This indicated that although the specific origin was missing, the primary fractures initiated at surface locations with secondary fractures propagating inward to the hub. Examination of interior fractures revealed no internal defects.

Two encouraging facts came from this test. First, the fact that the rotor fractures initiated from surface sites, and the lack of observable interior defects confirm the rotor hub integrity. This initial bladed rotor testing indicated the successful transfer of simulated rotor technology to the bladed rotor. Second, the surface features responsible for the rotor failure were easily observable prior to spin testing. This fact implied that casting and sintering processes which produce good surface finish rotors will increase spin speed capability. From these results, both Ford and ACC were directed to apply fabrication processes to improve visual appearance (surface finish) to rotors being fabricated.

The end-of 1982 saw three additional bladed rotors from ACC judged suitable for cold spin testing to assess rotor development progress. All three rotors were slip cast at ACC and sintered by Ford under a Ford/ACC agreement. Table 31 gives the densities and spin test speeds of the rotors. One rotor failed due to a surface flaw while the remaining two survived the spin test and were selected for hot turbine rig testing.

Table 31. ACC Bladed Rotor Test Results.

S/N	Density g/cm^3	Speed, krpm	
213	3.17	102.0	Burst due to surface flaw
277	3.27	115.0	Successful overspeed test
211	3.09	80.0	Qualified to 80.0 krpm hot turbine rig testing

Although both Ford and ACC continued rotor fabrication development efforts, neither was able to produce rotors with the quality required for engine testing. In order to fulfill contractual requirements for engine demonstrations, Garrett began purchasing rotors from Kyocera and NGK towards the end of the AGT101 program.

Initial rotors received from NGK were fabricated from both SN-73 and SN-81 (sintered

silicon nitride materials). The first rotor failed the 115,000 rpm spin proof test, bursting at a speed of 112,000 rpm. The second rotor was proof tested to 100,000 rpm, which it successfully passed. The remaining two rotors were returned to NGK for further processing. This processing included additional heat treatment to recrystallize the grain boundaries in an attempt to improve the high temperature strength. Both were re-spin tested by NGK prior to shipment to Garrett. One burst during the spin test, the second was spin tested to 95,000 rpm. This rotor was never used for engine testing due to the availability of improved rotor materials. (Rotor material properties are discussed more fully in paragraph 6.1).

Initial rotors received from Kyocera were fabricated from SN 220M (sintered silicon nitride). These wheels were proof spin tested to 110,000 rpm at Kyocera. This was lower than the desired proof spin speed of 115,000 rpm due to concerns of the material strength of SN 220M. In response, engine testing was limited in speed and temperature when testing the SN 220M wheels. Later rotors received from Kyocera were fabricated from SN 250M, also a sintered silicon nitride material. These wheels were proof spin tested to 115,000 rpm at Kyocera. The SN 250M material has a higher room temperature strength than the SN 220M material and could thus be spin tested to the higher speed.

Results of ceramic engine testing utilizing these SN 250M wheels are discussed fully in paragraph 4.3.3, Ceramic Engine Development. Results pertaining directly to rotors will be discussed here. In two engine tests, the inducer blade tips were damaged on the two SN 250M rotors, rendering them unacceptable for further engine testing. These rotors were sectioned into test bars for fast fracture and stress rupture property evaluation. Results indicated that the material in these excised sections exhibited lower strength properties than those measured in bars provided as test specimens of the same material. These lower material properties in SN 250M rotors were deemed unacceptable for performance engine testing. The remaining ceramic engine tests utilizing SN 250M rotors were limited in speed and temperature in an attempt to avoid stress rupture failures due to the lower material properties.

The SN 250M rotor (S/N 256) which had been used in the 85-hour, 1204C (2200F) endurance test (engine S/N 004C, Build 6) was spin tested to burst, which occurred at 108,600 rpm. The rotor had been spin tested twice prior to engine operation: once at Kyocera to 115,000 rpm before shaft bore machining, and again at Garrett to 105,000 rpm after the shaft bore was machined.

The failure mode of rotor S/N 256 (spin pit tested) was similar to that of rotor S/N 259 from engine testing in S/N 002C, Build 18. These failures are compared in Figure 222. In both rotors, the hub centerline remained

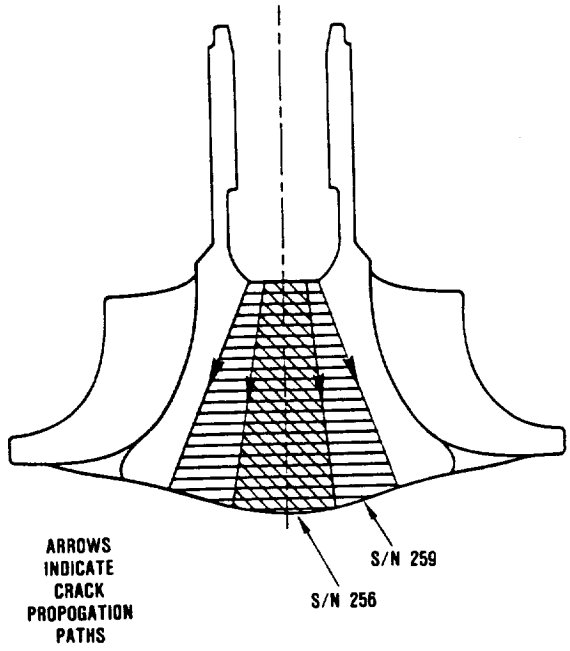

Figure 222. Rotor S/N 256 Failed During Spin Test in Mode Similar to Previous Engine Failure.

intact and the fracture surface propagated from the exducer hub zone to the rotor backface. A close examination of rotor S/N 256 revealed that the fracture originated near the interior surface of the shaft bore in the area of some transverse grinding marks. The stress concentration characteristic of the machining marks could have caused the rotor to fail.

Rotor Density

Testing showed a definite correlation between rotor density and burst speed (Figure 223). Rotors with a density of 98.5 percent

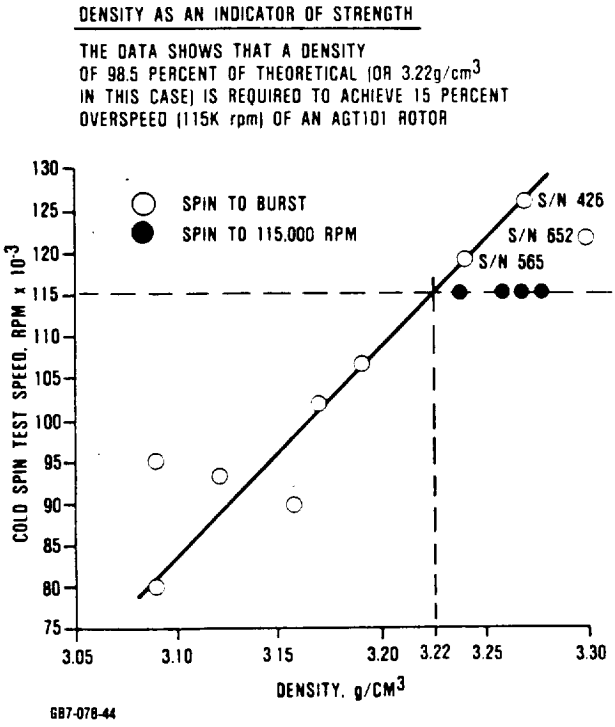

Figure 223. Increasing Consistency Evident in Cold Spin Test.

theoretical typically have sufficient strength to pass the cold spin test. Low density rotors can be immediately rejected, thus eliminating costly inspection and testing. As part of the continuing materials evaluation, rotors S/N 652 and 688 (ACC, Si_3N_4) were selected as spin-to-burst candidates. Rotor S/N 652, due to its high density, was selected to provide an additional data point to correlate burst speed with density. Burst occurred at 121,000 rpm resulting in a maximum principal stress of 332.3 MPa (48.2 ksi). As shown in previous Figure 223, this correlates favorably with previous high density rotor data. Ultrasonic inspection of rotor S/N 688 revealed a large flaw, approximately one inch from the backface, rendering this rotor unsuitable for engine testing. Due to the size of the flaw, expectations were that the rotor would burst in the 70,000 to 80,000 rpm range. The actual burst speed was 101,000 rpm, with a maximum principal stress of 235.8 MPa (34.2 ksi). The failure of rotor S/N 688 reinforced the reliability of ultrasonic inspection in revealing flaws and the need for additional data correlating flaw size with burst speed and density to determine a maximum allowable flaw size.

6.2.3 Hot Turbine Rig

The hot turbine rig was designed, fabricated, and mechanically tested using metal engine turbine rotors. The objective of the hot turbine rig tests was to subject ceramic turbine rotors to transient thermal and mechanical loads simulating startup and shutdown in the AGT101 engine. These transients were designed to induce blade stresses equivalent to engine-like operational stresses, thus providing further screening of the ceramic rotor prior to engine testing. Initial rig testing using a metal rotor showed that the rotor could be controlled at all speeds. Thermal transients approximating expected engine conditions could be simulated with the rig.

After initial rig checkout, the rig was reassembled with an ACC silicon nitride turbine wheel which had been cold spun to 80,000 rpm (S/N 211). Three cycles of rig operation were completed. Each cycle imposed stresses in the ceramic wheel that were 2 to 3 times more severe than would be expected in a normal shutdown cycle when operated in the 871C (1600F) metal engine. Inspection after disassembly revealed no damage or signs of distress to the ceramic components. As a result of this testing, the rotor could be used in a metal engine restricted to 80,000 rpm.

A second ACC turbine rotor, cold spun to 115,000 rpm was tested in the hot turbine rig. A cycle was defined to simulate a combustor flameout while operating at 100,000 rpm at full load. Three cycles were accomplished on the wheel. After teardown inspection showed no evidence of any cracking, rubbing, or other distress on the turbine wheel. As a result of this testing, the wheel could be used in a 871C (1600F) metal engine without speed restrictions.

As confidence was gained in rotor hub integrity and material properties, it was determined that the hot turbine rig was no longer necessary. Rotors could be successfully screened for engine testing through visual inspection, density determination and cold spin pit testing.

6.2.4 Turbine Rotor Attachment

Attachment mechanisms of the ceramic turbine rotor to the metallic rotating group were analyzed and a "shrink fit" coupling arrangement was selected for initial evaluation. This type of arrangement was necessary due to the initial solid shaft turbine wheel design. Detailed thermal and stress analyses indicated that a low expansion, high-strength alloy could be used with the ceramic rotor to effect the attachment. IN-907 material was selected for testing based on the strength and thermal expansion coefficient in the temperature range of interest 1120 MPa at 0.2 percent yield and 1.05 and 1.67/C x 10^{-6} coefficient of expansion (162.5 ksi at 0.2 percent yield and 4.5 to 5.0 in/F x 10^{-6} coefficient of expansion).

Preliminary assembly tests confirmed that diametral interferences between 0.11 and 0.12 mm (0.0045 and 0.005 inch) could be made without subjecting the IN-907 to temperatures in the recrystallization range and further, no apparent damage to the ceramic shaft was observed. Therefore, a series of thermal cycling tests were conducted to determine dimensional stability after assembly. IN-907 sleeves of two different thicknesses, 1.9 and 3.0 mm (0.075 and 0.120 inch), were assembled on silicon nitride shafts (Figure 224, View A). Thermal cycling consisted of 15 minutes of soak at 538C (1000F). Coupling environment temperatures were measured at the coupling surface using a standard thermocouple. Since a limited number of test specimens were available, the ceramic shaft was removed and then reinserted into the sleeve at different circumferential orientation to avoid single-assembly effects during testing.

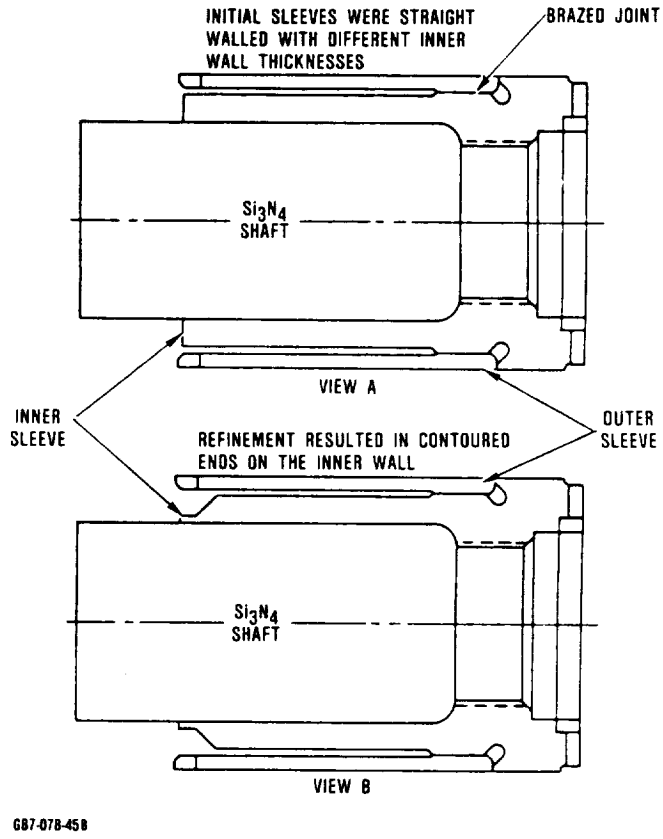

Figure 224. IN907 Ceramic Test Sleeves.

Initial thermal cyclic testing showed that thermal "ratcheting" and consequent variations in length of the coupling assembly were concerns of the sleeve design. Based on these results, a coupling was designed, as shown in Figure 224, View B, to include a straight inner wall and a contoured open end. Testing was resumed. The -1 version, 3.53 mm (0.139 inch) wall thickness and 22.5 mm (0.886 inch) diameter ceramic shaft, showed essentially no racheting after 350 thermal cycles. The -2 design, 1.9 mm (0.075 inch) wall thickness and

25.8 mm (1.015 inch) diameter shaft racheted toward the contoured end (shrunk) from 0.058 to 0.21 mm (0.0023 to 0.0083 inch) in each 50 cycles out to 350 cycles; thus the -1 version was selected for further evaluation. Additional testing was conducted on the foil bearing and rotor dynamic test rigs, including thermal cycling tests, to evaluate the coupling. It should be noted that since the AGT101 utilizes an air lubricated bearing located over the coupling area, a second sleeve is brazed to the inner sleeve to reduce thermal input to the bearing and to maintain a uniform journal diameter. (ref. Figure 224.

Initial rotors were of the stub shaft configuration, shown in Figure 225. The initial coupling attachment method, shown in Figure 226, was difficult to perform because of the attachment apparatus. Close control of the coupling temperature during installation was required. Installation had to be performed in a vacuum due to oxidation of the coupling at the temperatures required for successful installation. Radial positioning of the coupling relative to the rotor shaft was difficult due to misalignment in the fixturing. Due to the necessity of assembling the rotor/coupling in a vacuum, axial positioning of the coupling relative to the rotor shaft had to be done blind. These problems were solved through a modification to the coupling. Electroless nickel was plated onto the couplings, eliminating the oxidation problem. This in turn eliminated the positioning problems through removal of the vacuum chamber requirement. A new attachment tool (Figure 227) eliminated the radial and axial positioning difficulties.

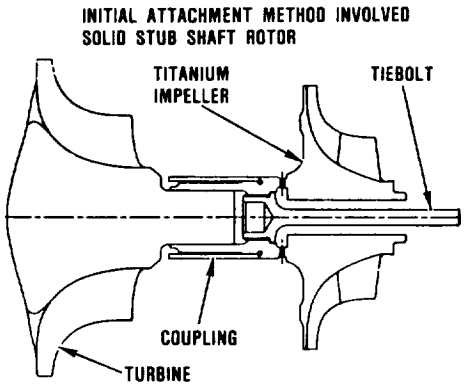

Figure 225. Initial Attachment Method Involved Solid Stub Shaft Rotor.

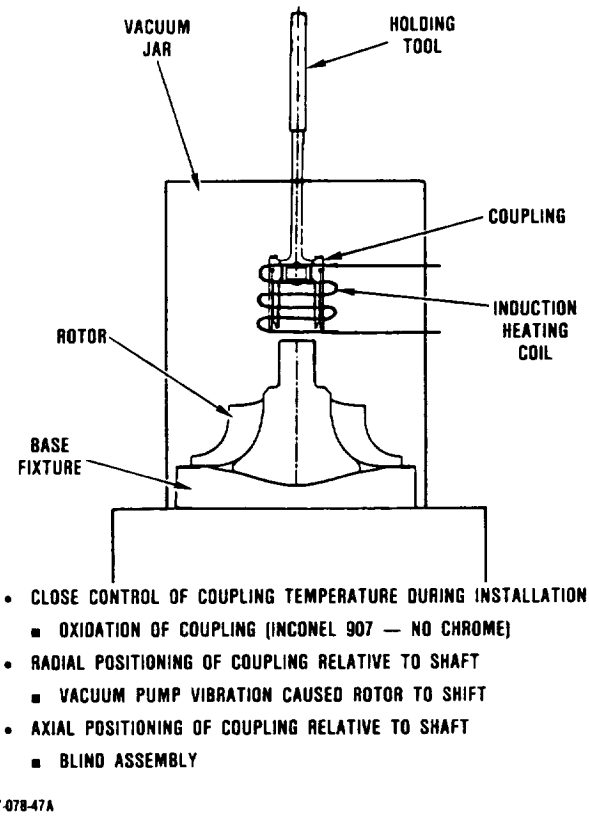

Figure 226. Installation Difficulties with Initial Attachment Method.

Further foil bearing development work indicated that sintered silicon nitride, when properly polished, made an excellent load bearing surface. A rotor design modification was made with the resulting rotor/compressor attachment configuration shown in Figure 228. This design has two major benefits over the stub shaft design: (1) the hollow shaft reduces the amount of heat transferred to the journal area, keeping the journal surface cooler, and (2) ceramic journal/gold plated foils is a very durable foil bearing combination with high load carrying capabilities.

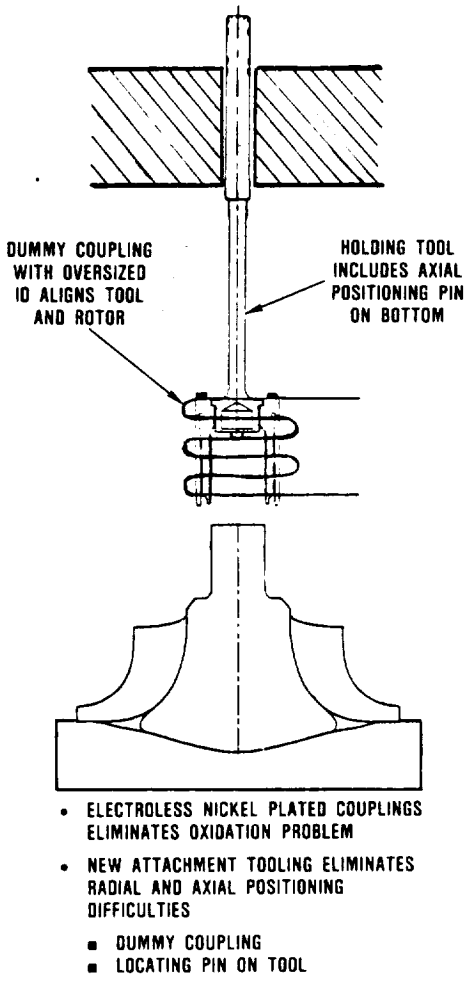

Figure 227. Installation Difficulties Solved with New Method.

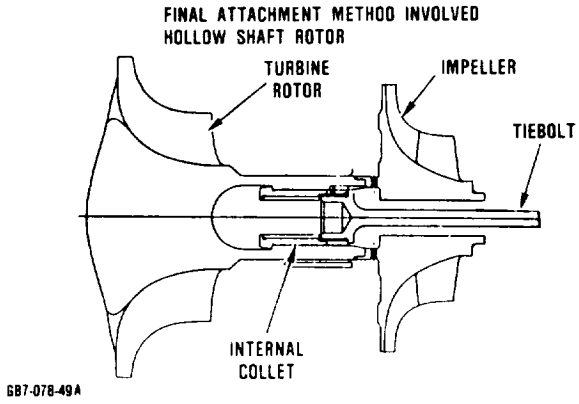

Figure 228. Internal Collet Attachment Method.

6.2.5 Cold Spin Testing

Discussion of cold spin testing is incorporated into the discussion of bladed rotor fabrication and test activities, paragraph 6.2.2.

6.2.6 Rotor Blade Vibration

Natural frequencies, mode shapes, and strains were predicted and verified for the AGT101 sintered silicon nitride rotor. Finite element model (FEM) modal analysis was used to predict natural frequencies, mode shapes, and normalized stresses and strains. Results from shaker table, acoustic ring, holography, and cold motored engine tests were used to verify room temperature frequencies, mode shapes, and vibratory strains.

6.2.6.1 Rotor Blade Modal Analysis

Finite element models were generated both from tooling layouts (TLs), and hardware inspection data. Inspection data were used to generate a second model because Kyocera's SN 250M rotor geometries were noticeably discrepant from TLs.

A typical 3-D AGT101 blade FEM model used for the modal analysis is shown in Figure 229.

A Zeiss series 500 coordinate measuring machine was used to inspect blade surfaces (both pressure and suction sides). Side screen inspection was used to define the blade outline in the axial-radial plane. An SN 220M rotor (S/N-0005-6), and an SN 250M rotor (S/N 254) were inspected.

The Zeiss machine was programmed to measure surface locations along blades in planes normal to the axis of rotation (Z section cuts) and normal to the radial reference axis (L section cuts). Comparisons of inspection data to TLs at a Z section for both SN 220M and SN 250M rotors are shown in Figures 230 and 231.

Zeiss inspection showed a major geometric discrepancy in the SN 250M blade exducers. The blade exducers leaned toward the pressure

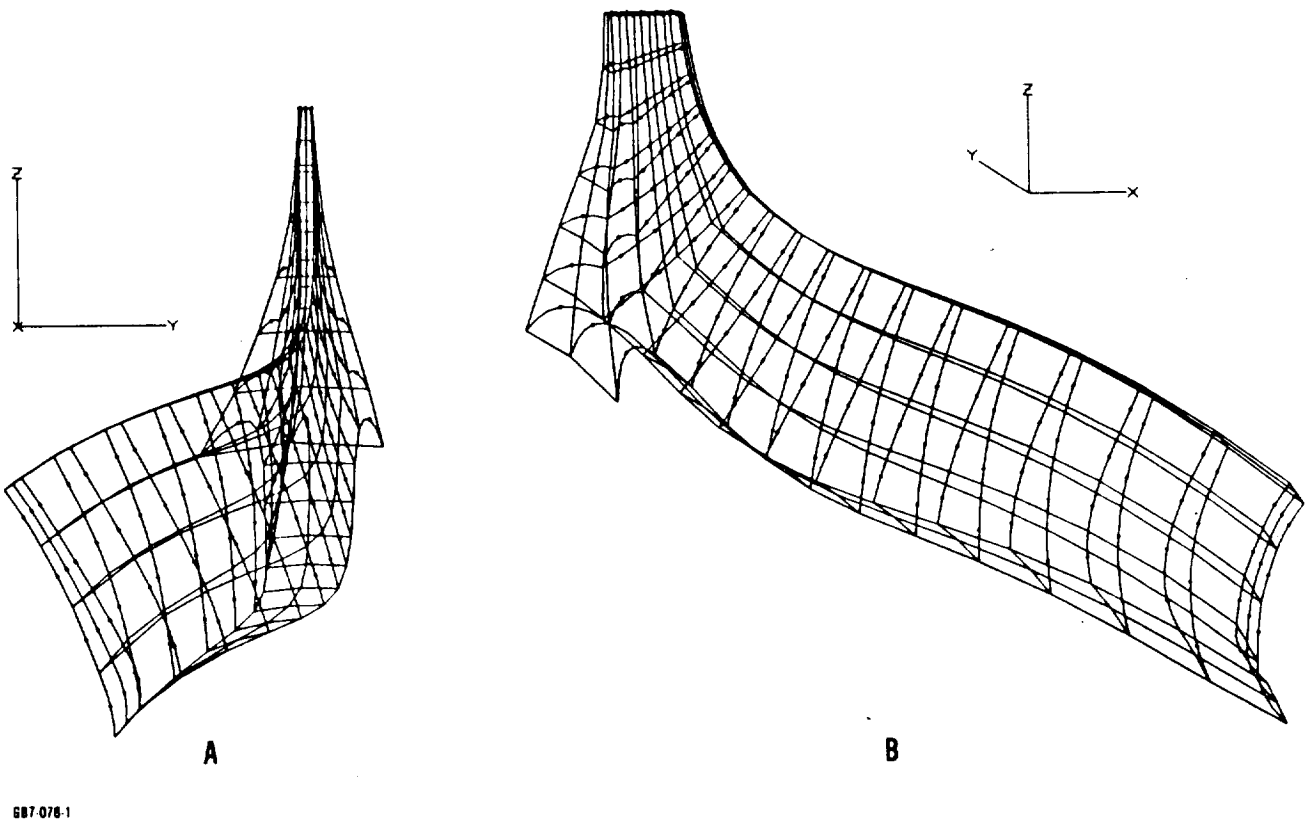

Figure 229. Typical 3-D Views of the Finite Element Blade Vibration Model.

side, so that the blade cross section is no longer radial. This SN 250M exducer discrepancy is apparently caused when exducers droop under their own weight during densification. The SN 220M rotor did not exhibit this droop. Inducers of the two rotors appeared very similar.

Turbine blade inspection data were used to generate a 3-D finite element blade model. First, a 2-D blade grid was created from side screen inspection data. Then, using a least squares fit, 3-D polynomial surfaces for the pressure side and suction side were generated from Zeiss inspection data. The 2-D grid was projected onto the pressure and suction side surfaces to create a 3-D FEM.

Finite element models of the SN 220M rotor blade, SN 250M rotor blade, and nominal blade were generated with skewed exducer elements. Another SN 250M and nominal blade model were constructed with normal elements after the problem with skewed elements was identified.

The Campbell diagram, shown in Figure 232, was generated for the SN 250M rotor blade at 1371C (2500F) T_4 and 100,000 rpm. Operating temperatures and stresses were included to account for thermal softening and centrifugal stiffening. Rotor temperatures used for the 1371C (2500F) T_4 case are the same temperatures used in the complete rotor stress analysis and are discussed in paragraph 6.2.7.2 Rotor Stress Analysis.

Garrett analysis programs ISOVIB and EIGEN were used to set up and solve the eigen problem for each of the seven analysis models listed in Table 32. Solutions consisted of natural frequencies predicted for the first three modes for the seven models, in Table 32.

6.2.6.2 Blade Vibration Testing

Rotor vibration tests were performed to measure natural frequencies, verify mode

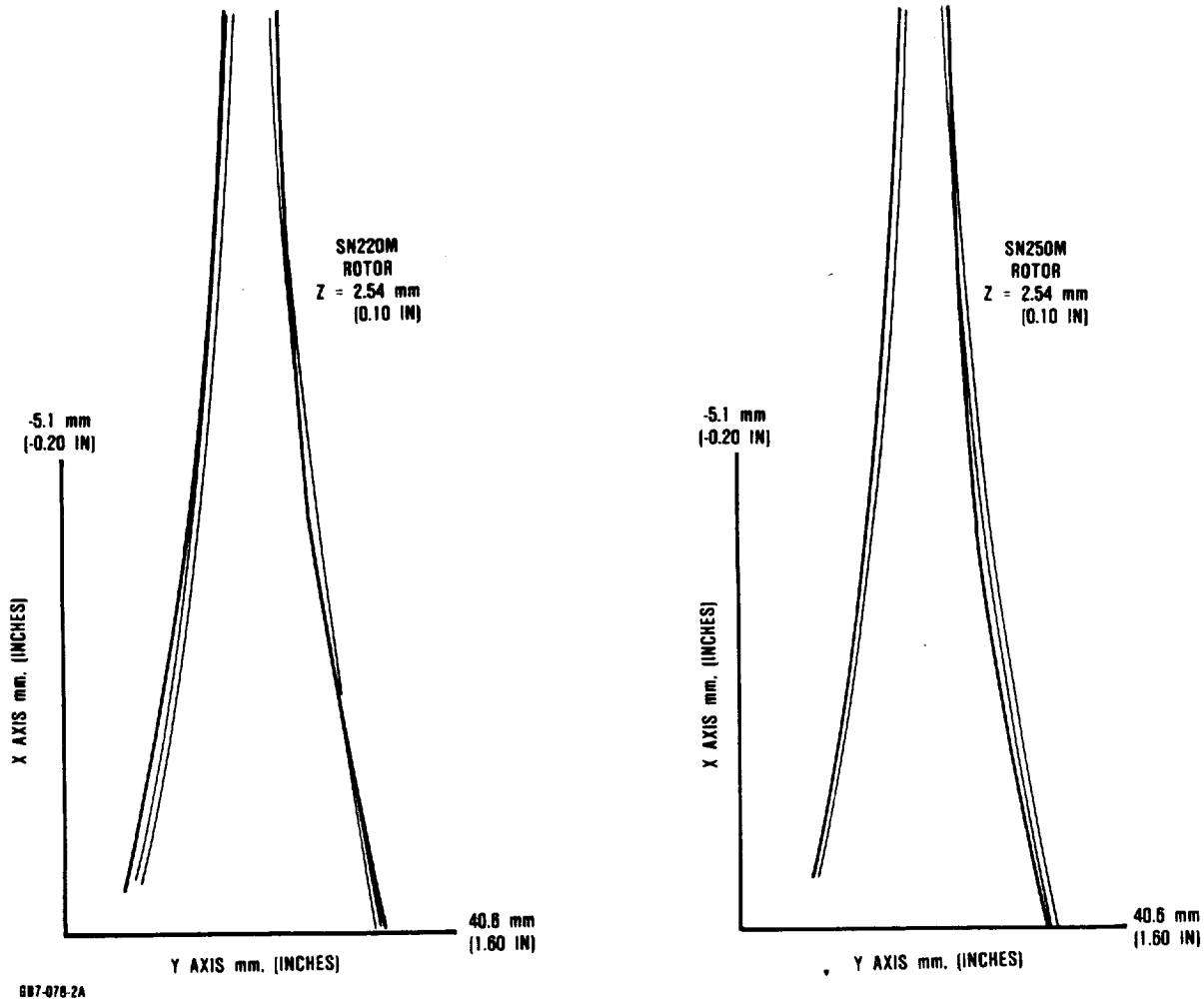

Figure 230. Comparison of Inspected Z Sections (heavy lines) to TLs at 2.54 mm (0.10 inch) From Inducer Backface.

shapes, and measure vibrational strains. The type of tests run and rotors tested include:

- o Acoustic Ring (SN-73, SN-81, SN 220M, and SN 250M)
- o Holograph (SN 250M - S/N 252)
- o Bullen (SN-73 - S/N-1001, and SN 220M - S/N-1-1000)
- o Cold engine (SN-73 - S/N-1001)

Description and results of each test method are given in the following discussion.

Acoustic Ring Testing

Due to concerns of possible blade vibration problems during engine operation, acoustic ring testing was used toward the end of the program to determine natural frequencies of each blade of each rotor. The frequencies can be converted to equivalent engine speeds based on the assumption that the blades are excited by the wake of the 19 stator segments. This provides a guideline to avoid dwelling at resonant speeds. In addition, blade frequency response data could be used as a quality check to confirm blade shape and uniformity of mass distribution. A rotor with consistent blades

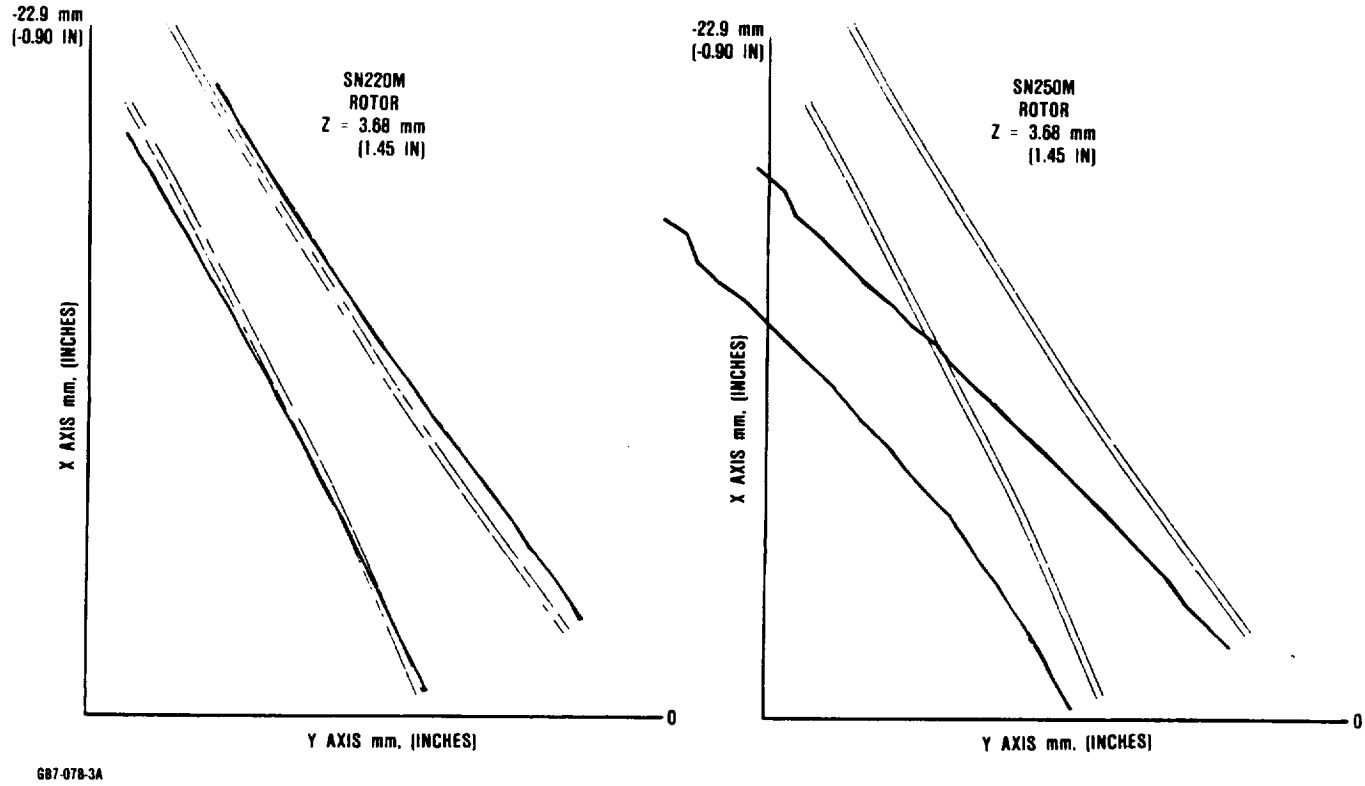

Figure 231. Comparison of Inspected Z Sections (heavy lines) to TLs at 3.68 cm (2.45 inch) From Inducer Backface.

has very little blade-to-blade variation in frequencies. Rotors from the same supplier fabricated from the same material and by the same process also have very little rotor-to-rotor variations in frequencies, as illustrated by Figure 233.

Data collected from acoustic ring tests are given in Table 33. These data indicate that rotors of the same material had nearly the same blade natural frequencies. However, SN 250M blades and SN 220M blades had significantly different natural frequencies. Since these materials have nearly identical densities the difference in natural frequencies was attributed to geometry differences associated with the different shrink factors of the two materials in densification.

Holography

Holography was used to verify predicted mode shapes. Natural frequencies were excited with a piezoelectric transducer glued to the blades. Holography results are compared to predicted mode shapes in Figures 234, 235, and 236. The close match between predicted and observed mode shapes provided increased confidence in the accuracy of the finite element model.

Bullen Test

A test plan was developed to address concerns about blade vibration in engines. Two different tests were conducted: a magnetorestrictive shaker (Bullen machine) test (to determine strain-to-failure), and a (cold) engine motoring test (to assess strain during engine operation).

The Bullen machine is a 1600 watt magnetorestrictive shaker capable of frequencies up to 40,000 Hz. It was used to find the vibratory strain magnitude at which blades fracture.

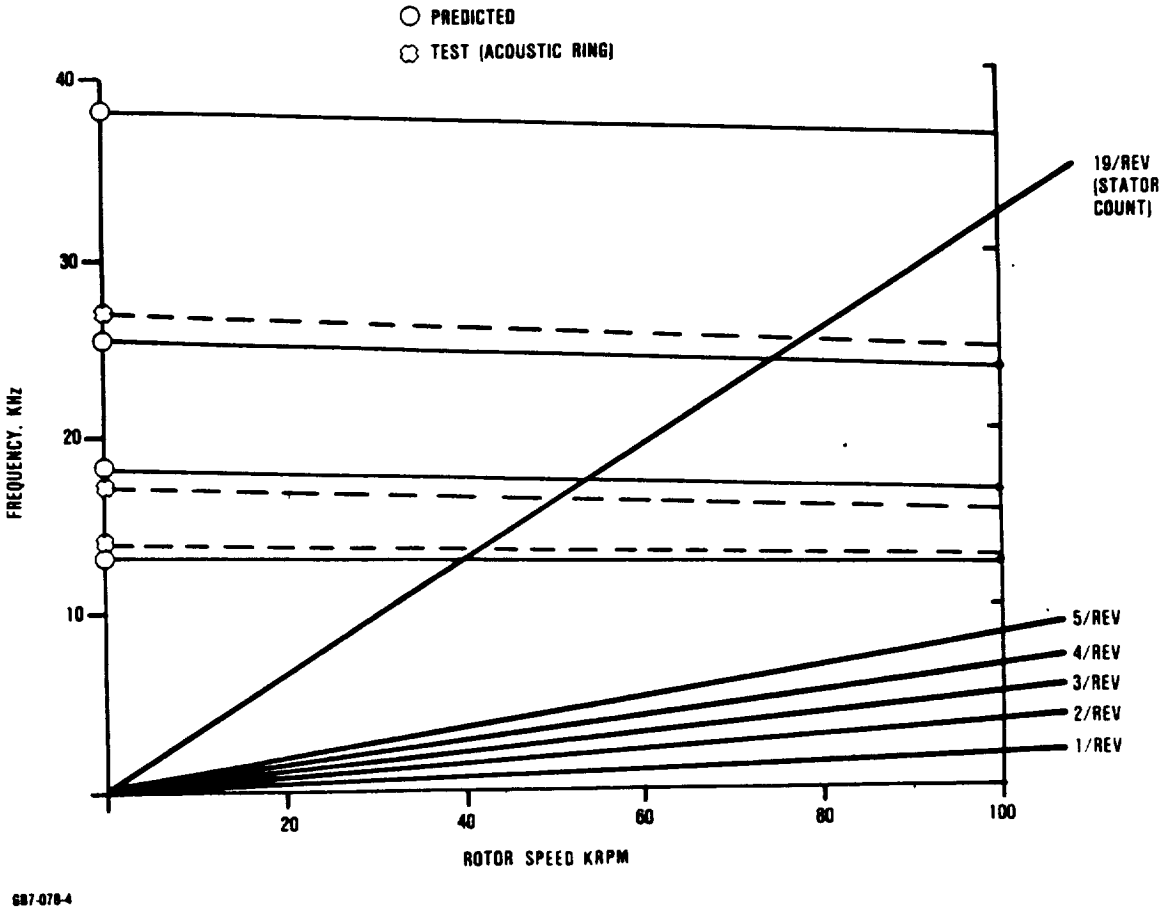

Figure 232. Campbell Diagram for SN 250M Rotors Showing 19/Rev Stator Excitation Line.

Table 32. Analytical Results.

Geometry	rpm	Mode 1 T_4	Mode 2 Freq	Mode 3 Freq	Freq	Elements
Nominal	0	70	15356	21738	34974	Normal
Nominal	0	70	16167	21796	44700	Skewed
SN 250M	0	70	13189	18265	25785	Normal
SN 250M	0	70	13999	20581	41012	Skewed
SN 250M	0	2500	12649	18010	36850	Skewed
SN 250M	100,000	2500	12998	18359	37008	Skewed
SN 220M	0	70	16941	23079	44958	Skewed

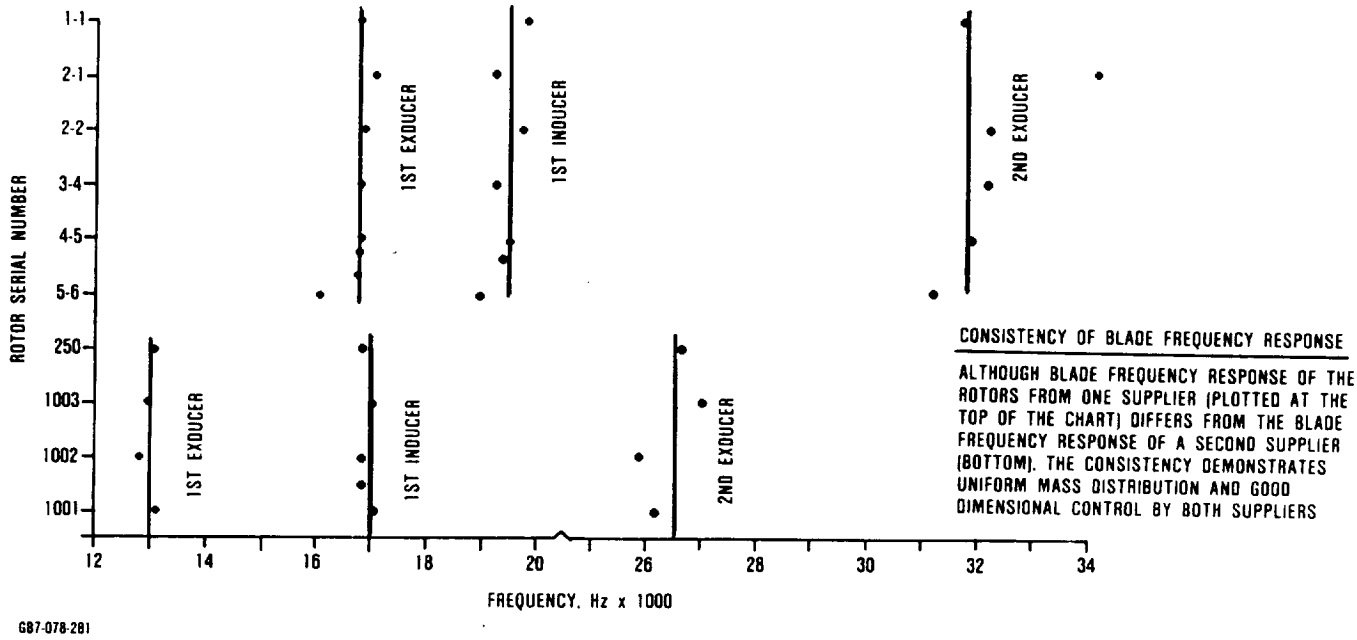

Figure 233. Consistency of Blade Frequency Response.

Table 33. Acoustic Blade Ring Results.

Material	S/N	Freq 1, Hz (Std Dev)	Freq 2, Hz (Std Dev)	Freq 3, Hz (Std Dev)	Additional Testing
NGK SN-73	1001	13094 (271)	17163 (210)	26167 (529)	Cold Engine test and Bullen test
NGK SN-81	1002	12826 (320)	16884 (222)	25625 (561)	
Kyocera SN 220M	1-1000	16826 (115)	19836 (173)	31836 (187)	Bullen test
Kyocera SN 220M	0002-1	17144 (108)	19230 (353)	34298 (222)	
Kyocera SN 220M	0005-6	16192 (181)	19009 (173)	31250 (343)	Zeiss Inspection
Kyocera SN 250M	252	13438 (95)	16923 (243)	27009 (211)	Holography
Kyocera SN 250M	254	13759 (166)	17076 (78)	27038 (165)	Zeiss Inspection
Kyocera SN 250M	255	13798 (167)	17163 (133)	27385 (292)	

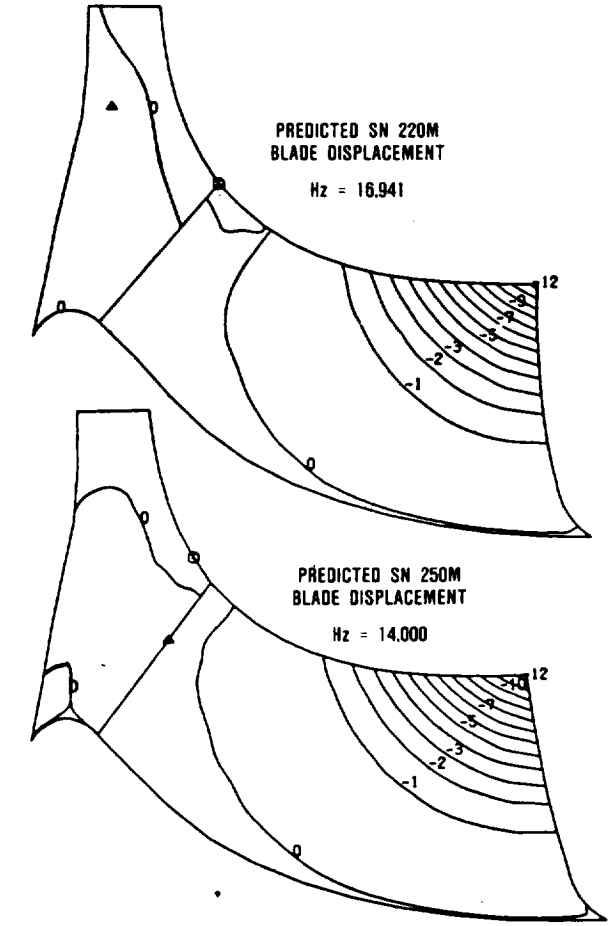

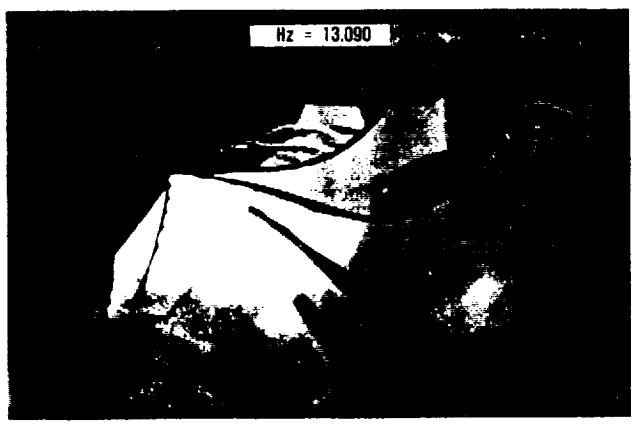

HOLOGRAPHY OF AN SN 250M ROTOR BLADE

G87-078-5

Figure 234. Comparison of Holography Results with Predicted First Exducer Mode.

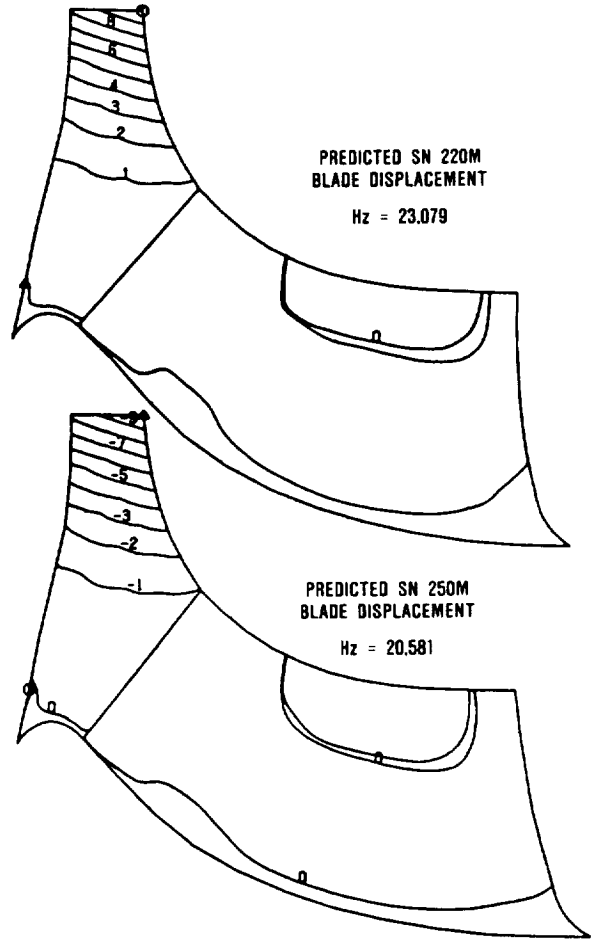

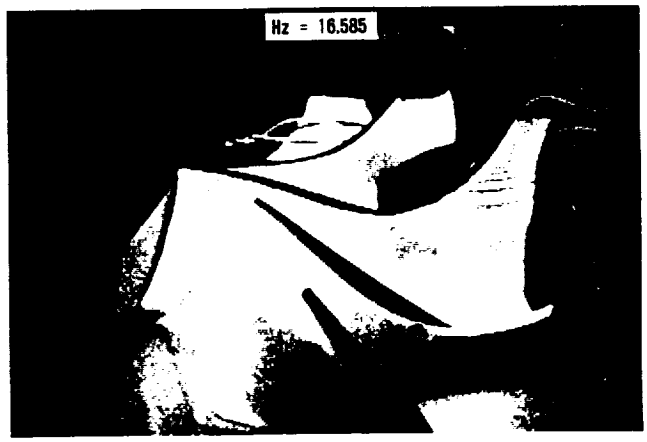

HOLOGRAPHY OF AN SN 250M ROTOR BLADE

G87-078-6

Figure 235. Comparison of Holography Results with Predicted First Inducer Mode.

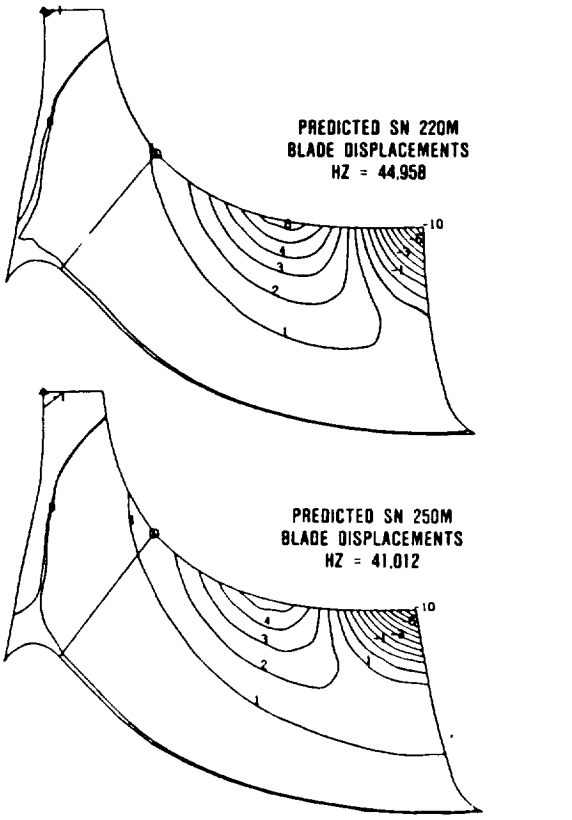

HOLOGRAPHY OF AN SN 250 ROTOR BLADE

GB7-078-7

Figure 236. Comparison of Holography Results with Predicted Second Exducer Mode.

In this test, selected blades on the rotor were stress mapped and instrumented with cold strain gages at the point of peak stress.

The rotor was rigidly mounted on the machine, and the frequency band was swept at low amplitude to find the blade natural frequencies. The amplitude was then increased at each natural frequency. Four Bullen tests were conducted on an SN 220M and an SN-73 rotor.

The SN 220M rotor was mounted axially, as shown in Figure 237, and tested. This orientation primarily excited the exducer tips. No blades broke even at the highest input levels. The rotor was mounted transversely in the second test, as shown in Figure 238, to excite the inducer blades more efficiently. One blade broke at the inducer, but it was not one of the gaged blades. This test was repeated and a gaged blade broke at 2280 micro inches/inch. The NGK SN-73 rotor was mounted transversely and tested, but blade failures could not be induced.

Cold Engine Vibration Tests

Following the Bullen test, a similar rotor (NGK S/N-1001 of SN-73 material) was strain-

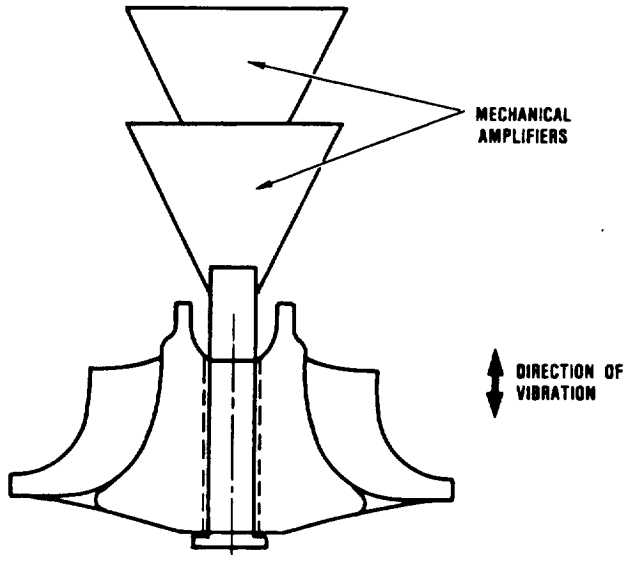

GB7-078-278

Figure 237. Initial Rotor Orientation Excited Exducer Tips (Bullen Test).

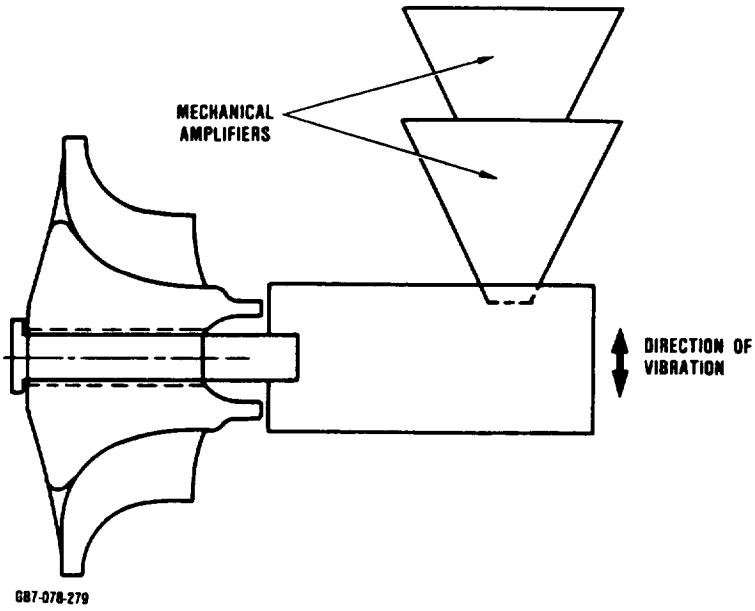

Figure 238. Rotor Re-oriented to Excite Inducer Tips (Bullen Test).

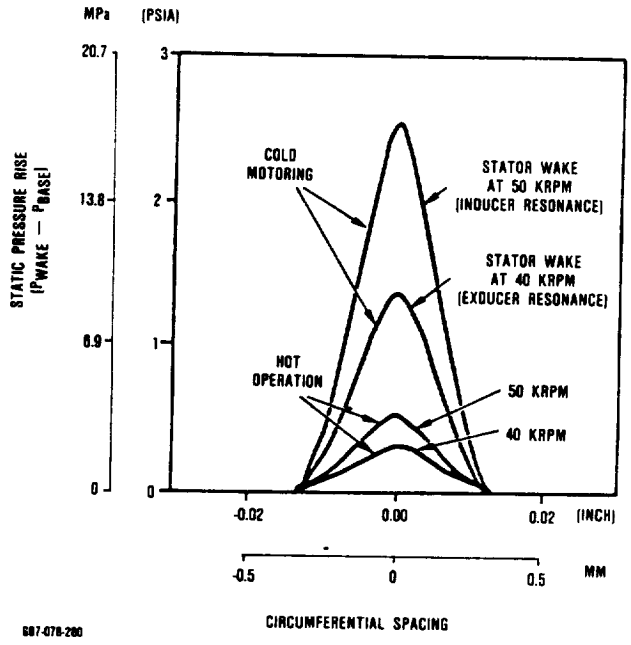

Figure 239. Cold Motoring Test Analysis Results.

gaged and installed in a metallic-structured engine (S/N-001, Build 40). The engine was then motored with ambient temperature air through the blade resonant speeds. The blade vibration amplitudes were recorded.

A turbine stator wake analysis was performed to establish the pressure profile at the stator discharge for the cold test case and a similar profile for the predicted hot operating conditions. On the assumption that the blade response is proportional to the pressure wake, the blade resonant amplitudes measured in the engine motoring test were corrected to predicted engine conditions. Result from the wake analysis are illustrated in Figure 239.

The resulting predicted blade stresses are shown in Table 34. This indicates a low hot operational cumulative stress which combines the vibratory peak-to-peak stress to the centrifugal and thermal stresses in the blade.

At around 43,000 rpm the exducer resonates at its first natural frequency with a peak-to-peak vibratory stress of 33.1 MPa (4.8 ksi). During operation this stress is superimposed on a steady state stress of 13.1 MPa (1.9 ksi). In comparison with the 620.5 MPa (90 ksi) stress, calculated from the measured 2280 micro inches/inch strain, that caused failure in the Bullen test, fracture is highly unlikely.

Table 34. Predicted Ceramic Blade Stresses.

Mode	Measured Strain, μin/in P-P	Cold Vibratory Stress, MPa (ksi P-P)	Hot Vibratory Stress Range, MPa (ksi P-P)	Hot Cumulative Tensile Stress, MPa (ksi)
Exducer	460	138 (20)	33 (4.8)	30 (4.3)
Inducer	1730	538 (78)	101 (14.6)	130 (18.8)

At about 53,000 rpm the inducer resonates at its first natural frequency with a peak to peak vibratory stress of 101 MPa (14.6 ksi). This is superimposed on a steady state stress of 79.2 MPa (11.5 ksi). Again vibratory failure is not expected at this stress level.

Analysis indicates that the cold condition is much more severe than the hot operating condition with larger driving forces; however, this condition can be avoided in engine testing by limiting the speed of the engine without a flame in the combustor.

6.2.7 Rotor Stress Analysis

AGT101 rotor stresses were predicted for partial power 70,000 rpm and 1204C (2200F) T_4, maximum power 100,000 rpm and 1371C (2500F) T_4, and 115,000 rpm proof test conditions.

6.2.7.1 Model Development

An initial model without a fillet between the hub and blade was developed to help guide engine test plans specifically for the proposed 100-hour endurance test. A later model with a fillet was developed to generate a more complete stress solution for failure risk assessment as discussed in the following paragraph 6.2.8. These models are shown in Figure 240.

Blade and hub geometries measured from the SN 250M rotor, S/N 254, were used to develop both models. The models thus included the exducer blade "droop" anomaly shown by the "Z-section" measurements (reference paragraph 6.2.6, Figure 231). Because this anomaly introduces non-radial blade elements, bending stresses are present at speed which would not be present in a rotor made to blueprint.

Thermal boundary conditions for partial power and maximum power conditions were determined from analyses and engine test results. Analyses were done for maximum power, steady-state conditions then corrected according to rotational speed, turbine inlet temperature, compressor discharge temperature, and mass flow for partial power conditions. The maximum and partial power thermal distributions are shown in Figure 241 and Figure 242 respectively.

6.2.7.2 Stress Analyses

Stresses predicted with these models are a function of applied rotational speeds and thermal boundary conditions. Blade pressure loads were assumed minimal and were not evaluated.

Stresses from the first model were determined using the Garrett finite element program IS03DQ. The principal stress distribution

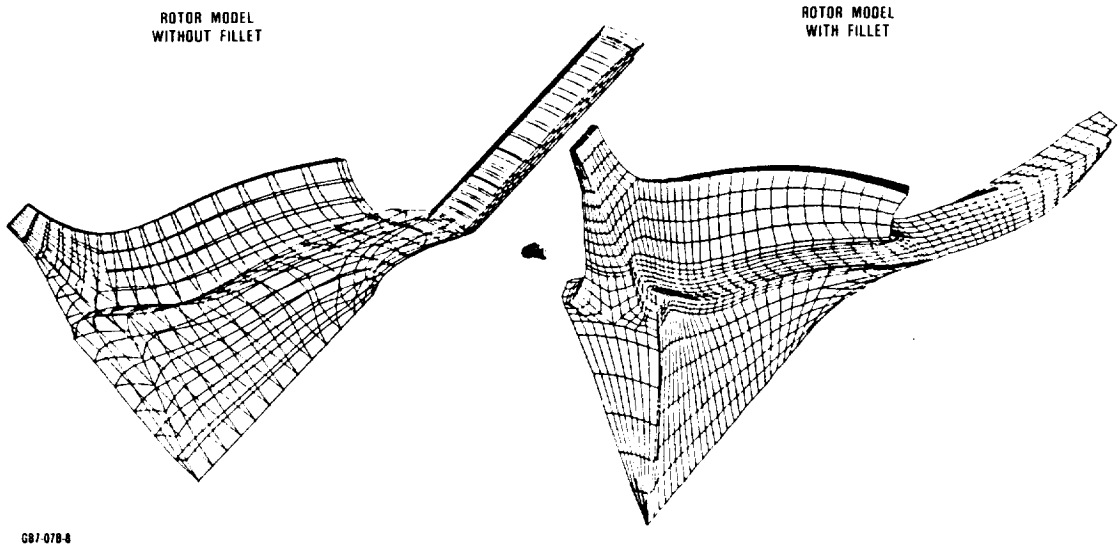

Figure 240. AGT101 Rotor Finite Element Stress Models.

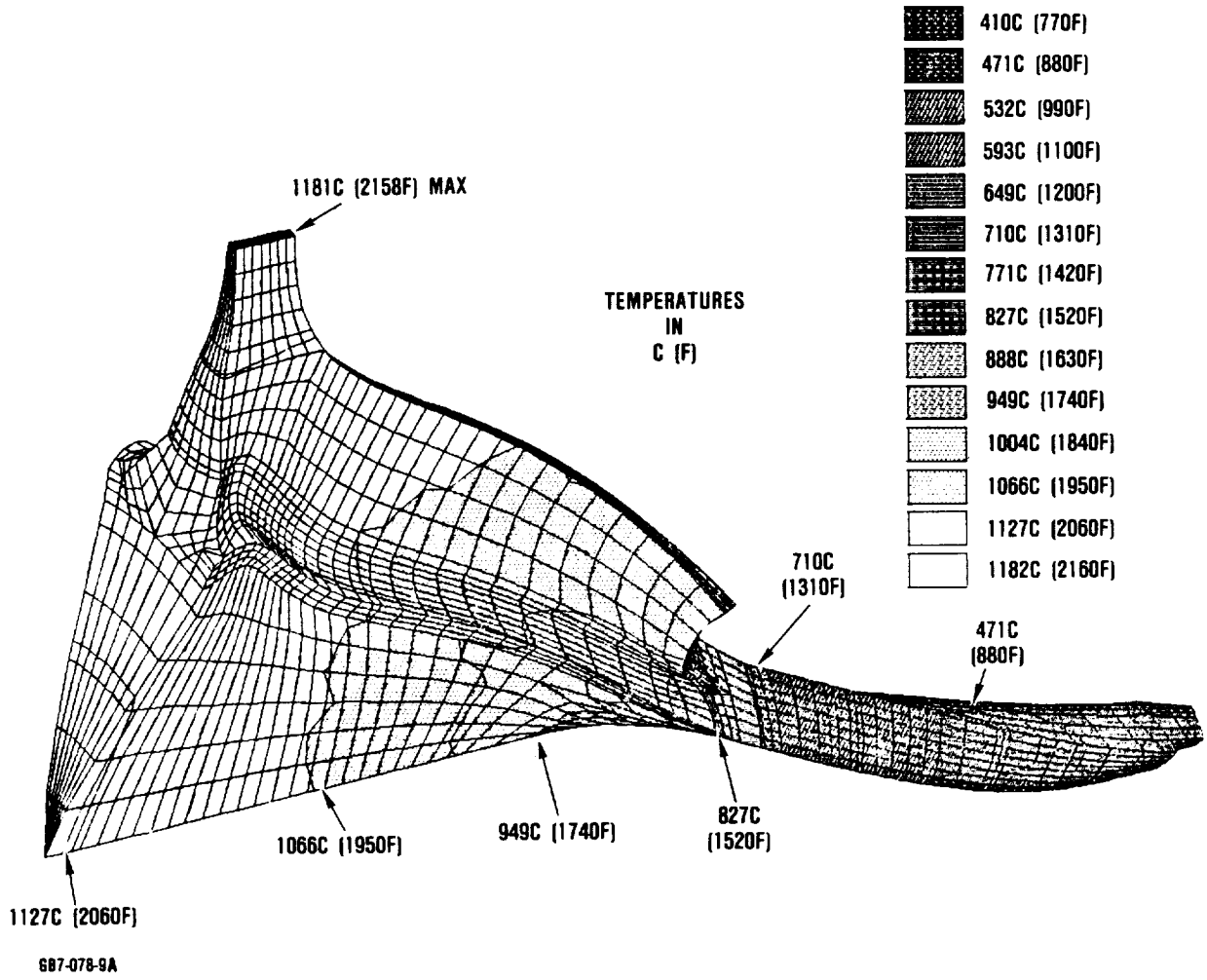

Figure 241. Maximum Power Thermal Distributions, T_4 = 1371C (2500F).

for the room temperature 115,000 rpm proof test, maximum power operating condition, and for partial power conditions are shown in Figures 243 and 244.

Stress analysis showed the largest maximum principal stress location occurred in the blade exducer, where the off-design geometry induces bending stress.

6.2.8 Rotor Life Prediction

Garrett applied probabilistic design methods to evaluate the risk of rotor failure during partial power 70,000 rpm and 1204C (2200F) TIT, and maximum power 100,000 rpm and 1371C (2500F) TIT, conditions for which stress solutions had previously been generated (paragraph 6.2.7). Life predictions were made by integrating the risk of fast fracture and time dependent failure (slow crack growth) over the area and volume of the AGT101 rotor. These results have helped define the capabilities of current ceramic probabilistic methods and have laid the ground work for future verification efforts. These results also provide an assessment of current ceramic materials capabilities and their suitability for heat engine applications.

Kyocera SN 250M sintered silicon nitride material properties were calculated for rotor failure analyses. Fast fracture and slow crack growth properties were obtained from bend test results. Fast fracture failures were identified with optical microscopy and cate-

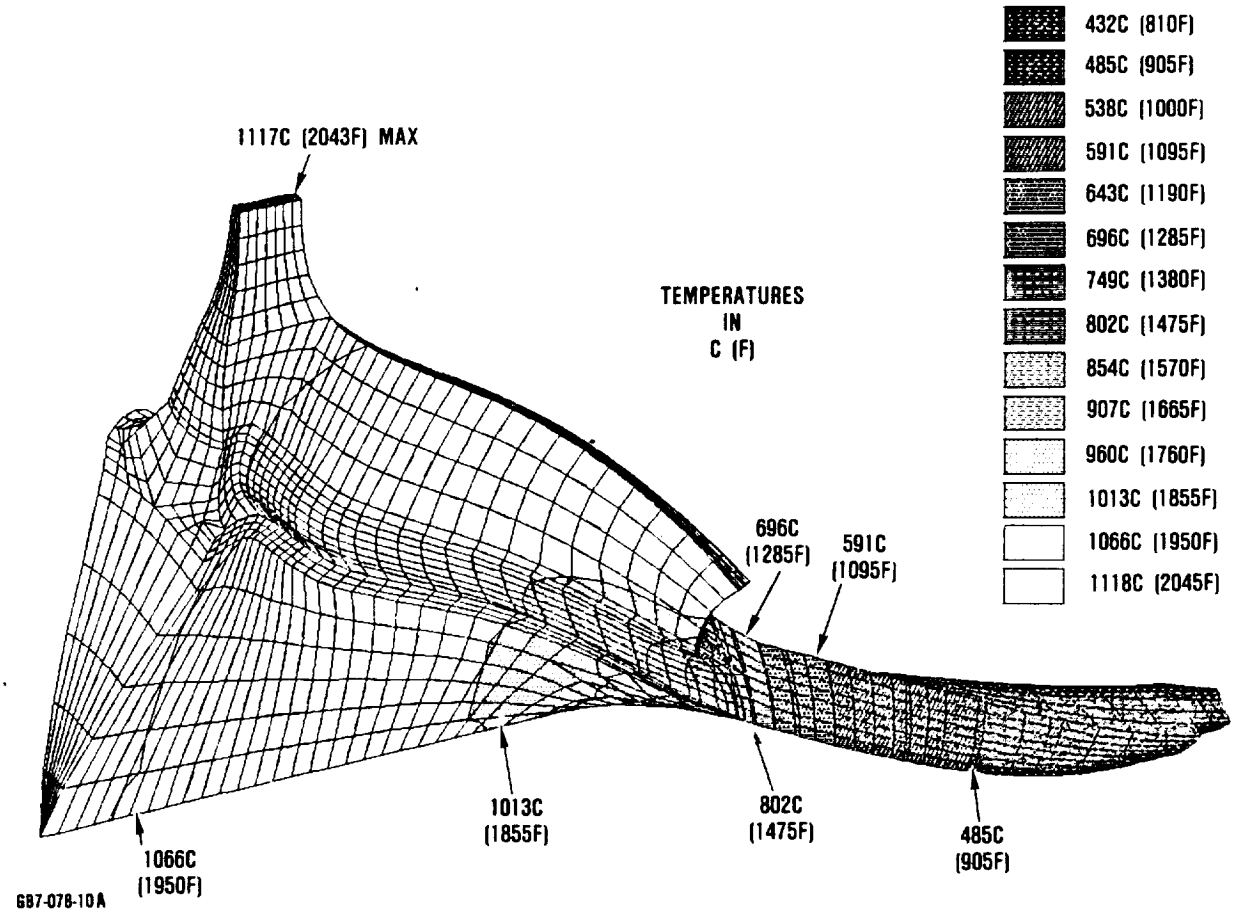

Figure 242. Partial Power Thermal Distributions, T_4 = 1227C (2240F)

gorized as surface or internal. Details about test procedures are given in paragraph 6.1.

Independent surface and volume strength properties were required to predict the combined probability of surface and internal initiated rotor failure. The probability of survival when these failure modes are concurrent is the product of the probabilities of survival of each failure mode.

Independent surface and volume Weibull characteristic strength and modulus cannot be simply determined from test data that contains both modes of failure. The interdependence of combined failure modes tends to mask their underlying independent failure distributions. This is demonstrated in Figure 245. Monte Carlo methods were used to generate the curves in Figure 245 based on a hypothetical surface characteristic strength and Weibull modulus of 621 MPa (90 ksi) and 20 respectively, and a volume characteristic strength and Weibull modulus of 689 MPa (100 ksi) and 10. These material properties were used to generate independent surface and internal failure occurrence curves A and B. When both failure modes occur in the same population, curve C is observed. The apparent surface and volume curves D and E were generated by separately plotting surface and internal failure data used to plot curve C. The reason for different independent and apparent failure distributions can be explained by examining the volume failure distributions. At 724 MPa (105 ksi), 20 percent of the population would survive volume failures. When both surface and volume failures are present the

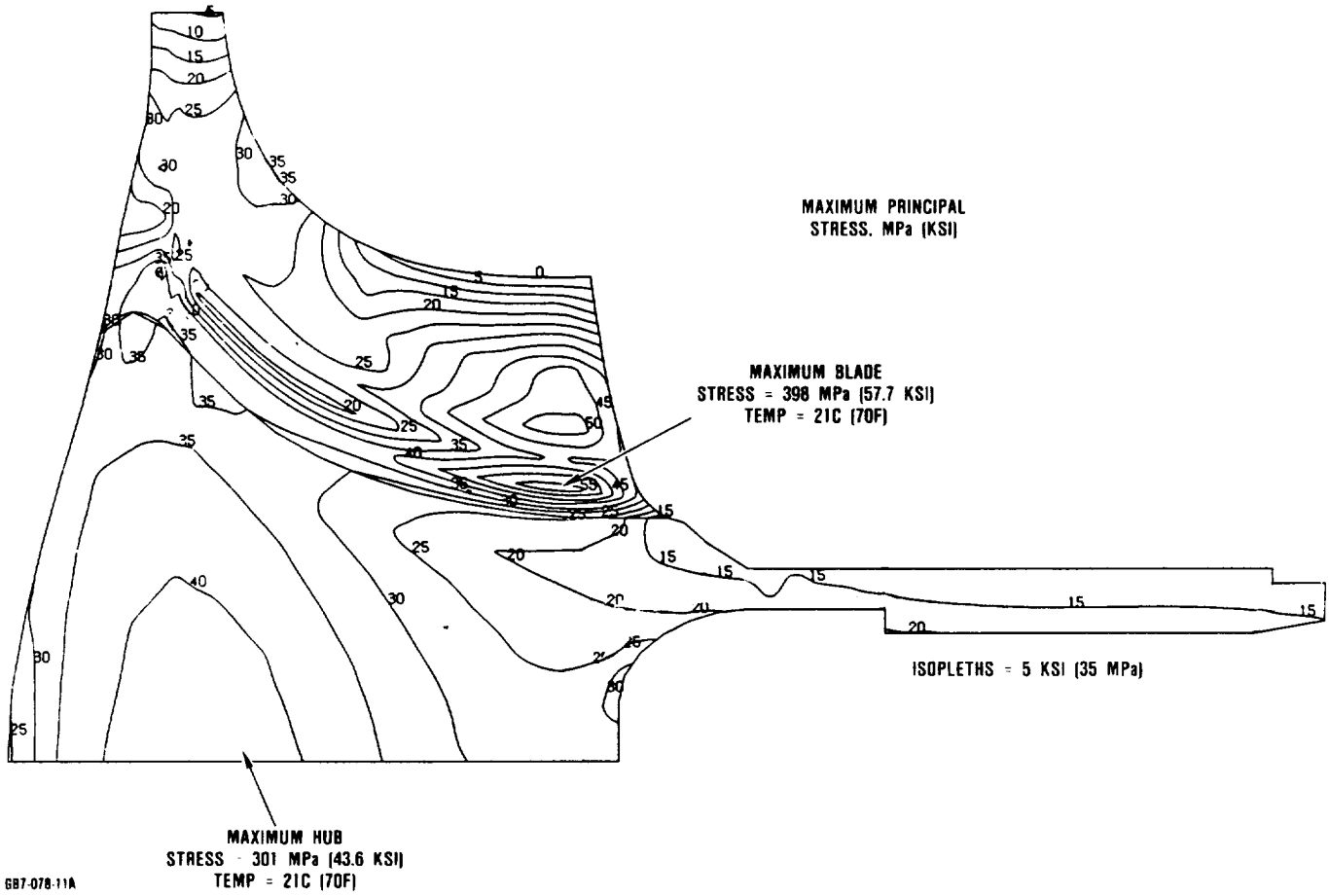

Figure 243. Principal Stresses for Room Temperature 115,000 RPM Proof Test Predicted From No-Fillet Model.

entire population fails by 689 MPa (100 ksi). Therefore, the apparent volume failure distribution is truncated to zero at 689 MPa (100 ksi) which is significantly different than the independent volume failure distribution. Curves D and E demonstrate the distributions of data that would be observed from testing this material with both failure modes present. Data for the curves A and B, however, are needed to determine the independent surface and volume Weibull strength properties for risk analysis.

Determination of independent surface and volume strength distributions was accomplished through data censoring. Surface and volume Weibull strength parameters for SN 250M, determined with censoring, are given in Table 34.

Slow crack growth and fast fracture material properties were determined from specimens tested under uniaxial stress conditions. Batdorf's multiaxial fracture criteria was used to predict risk of failure in the AGT101 rotor, which has largely biaxial stresses. The ratio of multiaxial risk to uniaxial risk with respect to increasing biaxial stress ratio is plotted in Figure 246.

A multiaxial correction factor, mx, was selected from these curves according to the principal stresses at the location being evaluated with the Weibull modulus of the material.

At elevated temperatures the risk of fracture increases with time due to slow crack growth. Slow crack growth causes cracks to propagate from existing flaws according to the

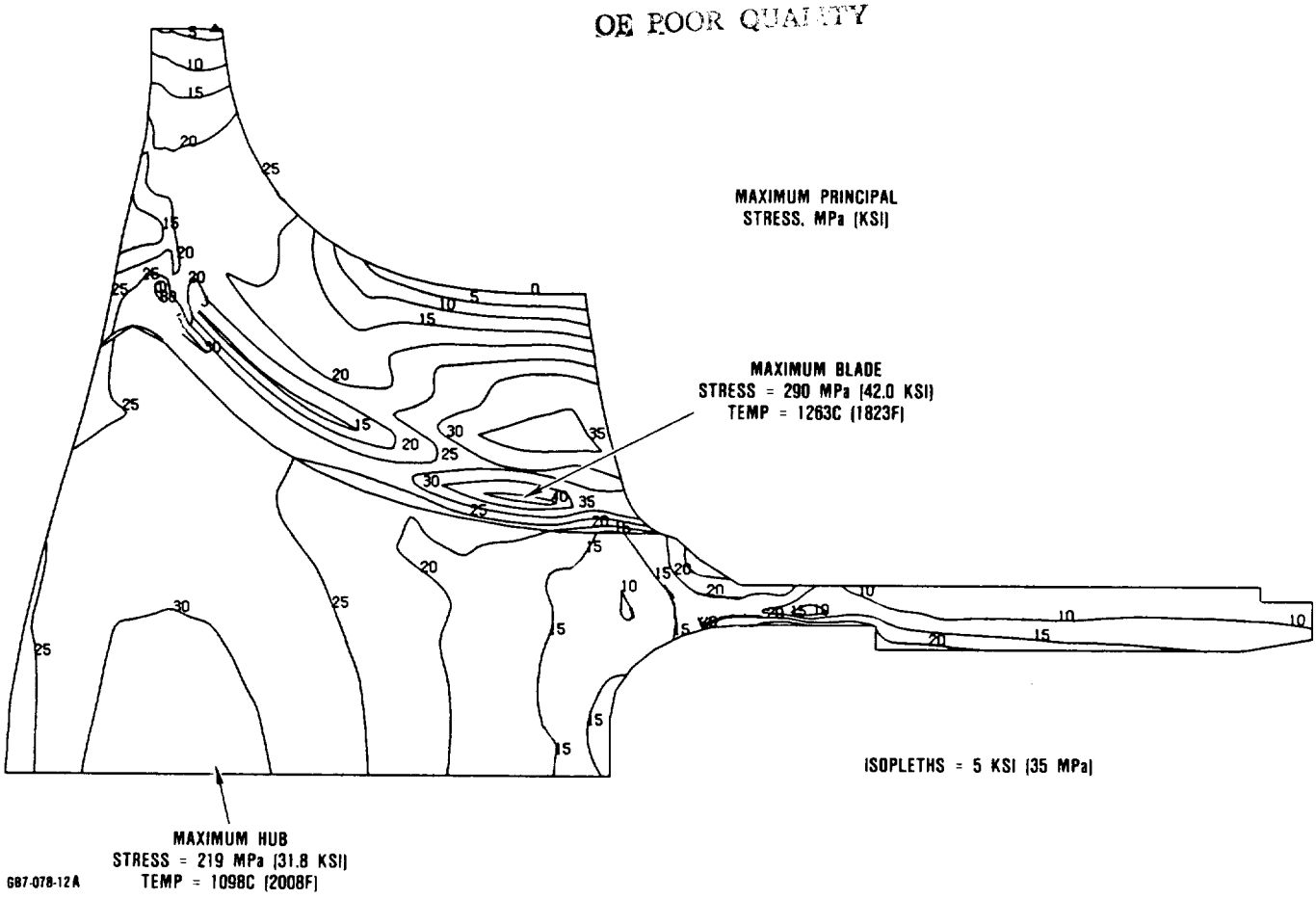

Figure 244. Principal Stresses for Maximum Power, Predicted From No-Fillet Model.

slow crack growth power function. The crack growth rate power function was combined with the equation for the critical stress intensity to derive the time to failure equation.

The time to failure relationship was combined with the Weibull fast fracture equation to calculate the risk of fast fracture at any time.

The risk of AGT101 rotor failure was evaluated with a Garrett developed program that performs Gaussian integration of risk over each element from a finite element stress solution. The product of all element survival probabilities was calculated to determine the total survival probability.

The predicted risk of fast fracture for partial power 70,000 rpm and 1204C (2200F) TIT, and maximum power 100,000 rpm and 1371C (2500F) TIT, are given in Table 35.

The risk of failure in each of the rotor regions and over the total rotor volume and area for the partial power condition are shown in Figure 247. SN 250M (as-fabricated) specimen slow crack growth data were used for these analyses. At part power, the hub does not have the highest stress in the rotor but it does have significantly higher initial failure risk than the other regions. This is due to the high relative volume and biaxial nature of the stress. Only the hub exhibits higher internal failure risk than surface failure risk, high enough to initially give the entire rotor a greater internal failure risk. Later in the rotor life, surface failure risk exceeds internal failure risk, due to the higher temperature at the rotor surface.

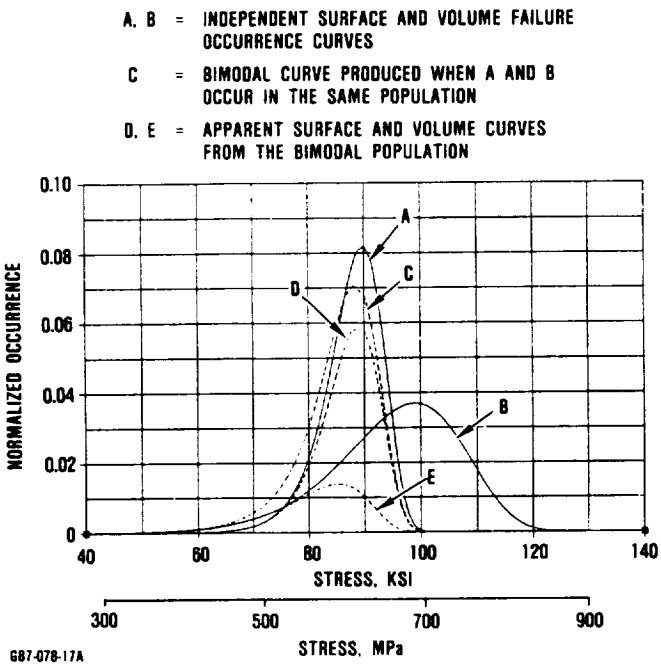

Figure 245. Comparison of Concurrent and Independent Surface and Internal Failure Distributions.

Similar risk analyses were performed for maximum power conditions using specimen slow crack growth data. These results are shown in Figure 248. The same trends observed at partial power conditions were seen here. However, the effect of these higher stresses and temperatures is an order of magnitude reduction in rotor life.

An additional set of analyses were run for the partial power case using slow crack growth properties determined from cut up rotors shown in Figures 249. These life predictions were significantly different than predictions made using specimen slow crack growth data. Specimen data predicted a 10 percent failure probability after more than 10,000 hours operation at part power (reference Figure 249).

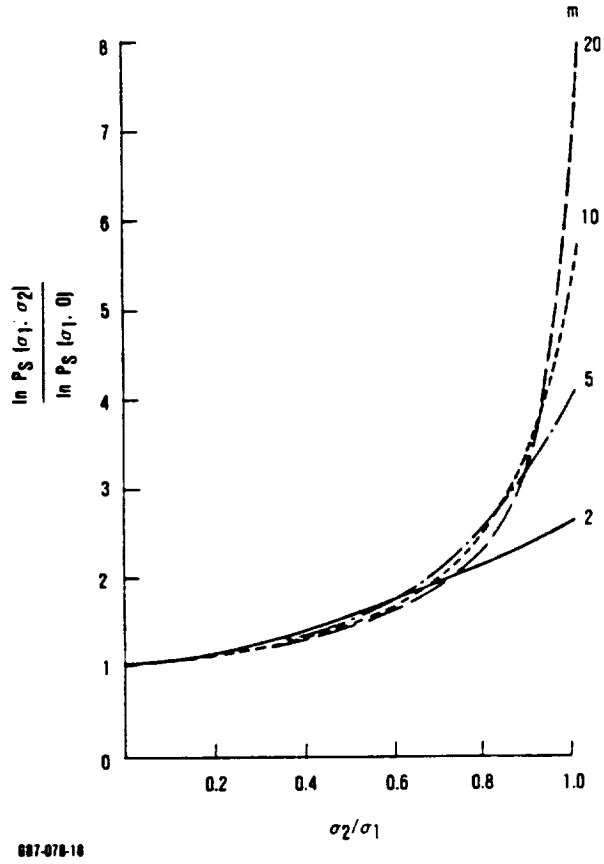

Figure 246. Effect of Biaxial Tension on Fracture Risk According to Batdorf's Criteria.

When the rotor data was used a 10 percent probability of failure was reached in just one hour (reference Figure 249). The overall life was thus several orders of magnitude less than predicted from specimen data.

While test bar data will continue to be the primary indicator and comparator by which

Table 35. Rotor Fast Fracture Predictions.

Load Condition	Percent Failure Probability		
	surface risk	internal risk	total risk
Partial Power	0.006	0.006	0.014
Maximum Power	1.42	3.09	4.47

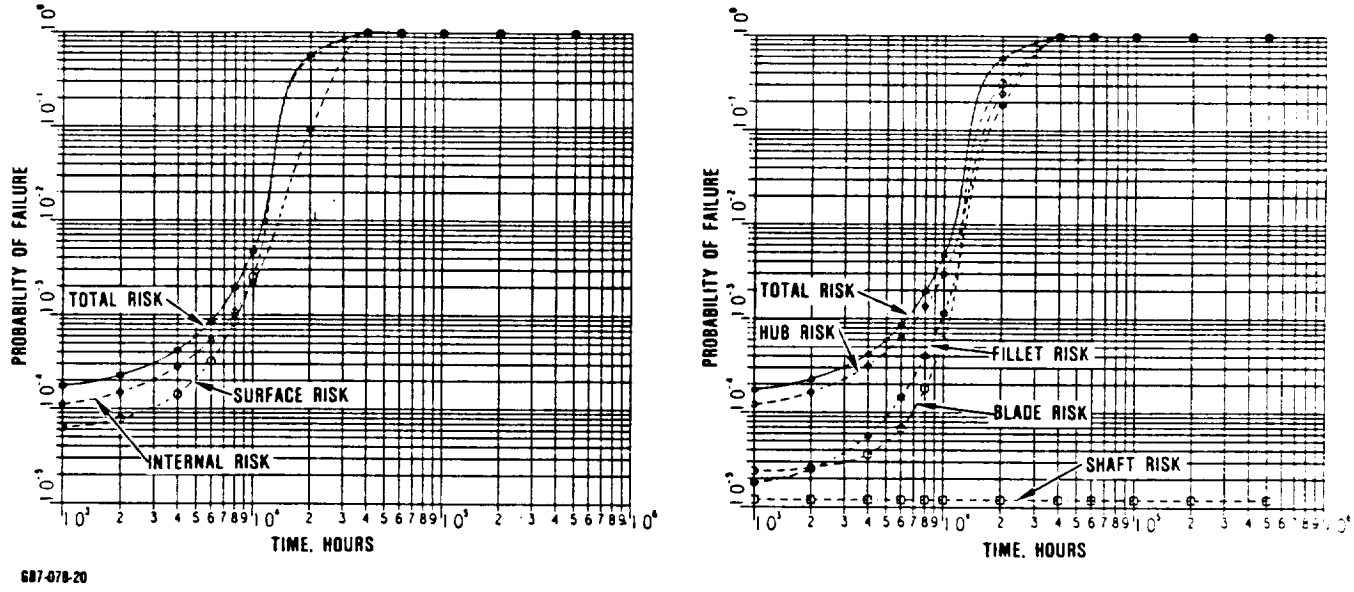

Figure 247. Rotor Failure Probability for Partial Power Operating Conditions.

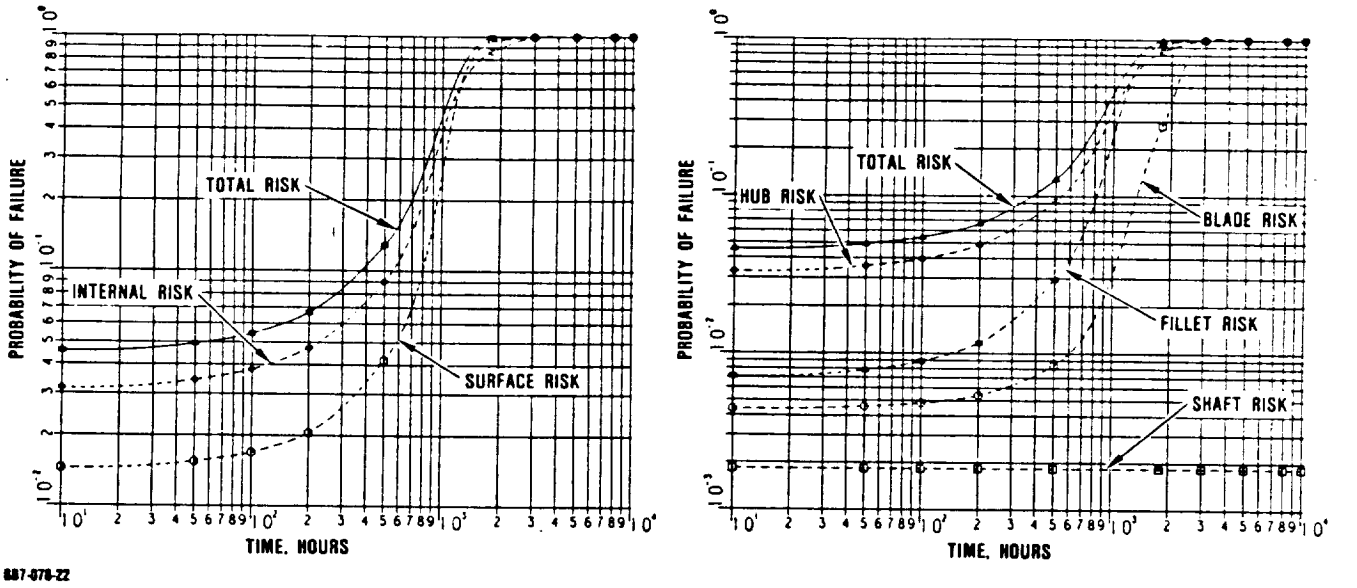

Figure 248. Rotor Failure Probability for Maximum Power Operating Condition.

advanced materials are measured, the findings presented here give reason for caution. The severe reduction in predicted rotor life, as a result of the decreased properties of the material as fabricated in the rotor, is an indication of the importance of verifying properties of components, rather than relying exclusively on test bar data.

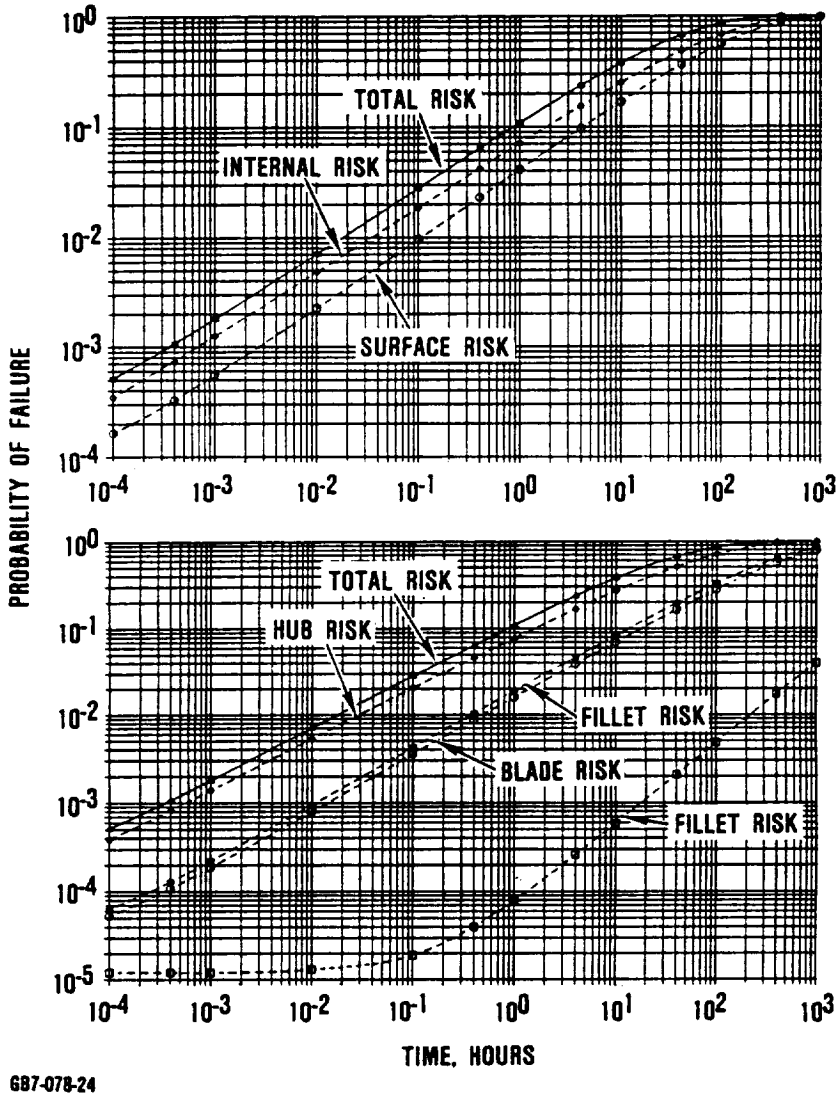

Figure 249. Rotor Failure Probability for Partial Power Conditions Based on Properties of SN 250M Rotors.

6.3 Ceramic Structures

The AGT101 ceramic hot section consists of 75 static structural and support system components, and a ceramic radial inflow turbine rotor, as illustrated in Figure 250. Static structural components are predominantly stressed from start transient induced thermal gradients with pressure loading imposed as a comparatively low stress.

In the initial design phase, the probabilistic design prediction method developed by Weibull[1], commonly used to characterize the flaw distributions in ceramics, was used to establish an allowable stress level. This method is based upon the weakest link theory, which assumes that a given volume of ceramic under a uniform stress field will fail at the most severe flaw. To account for the fracture statistics of a polyaxial stress distribution, the probabilistic method was modified by an approach used by Batdorf[2].

[1]Weibull, W.A., "Statistical Distribution Function of Wide Applicability," Journal of Applied Mechanics, Vol. 18, September 1951, pp. 293-297.

[2]Batdorf, S.B., "Some Approximate Treatments of Fracture Statistics for Polyaxial Tension," International Journal of Fracture, Vol 13, No. 1, February 1977, pp. 5-10.

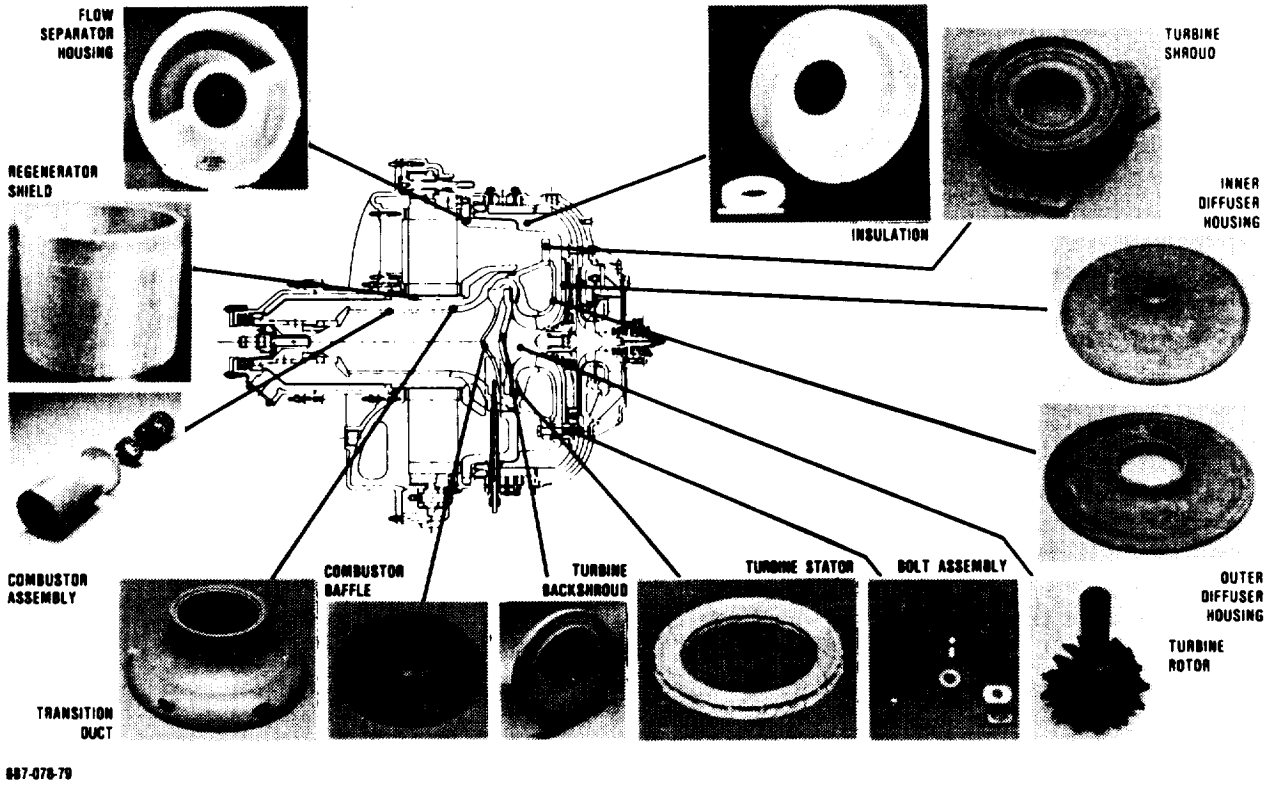

Figure 250. AGT101 Ceramic Components.

At the beginning of this program, correlation between probabilistic prediction methods (especially for polyaxial stress distributions) and the limited test data had not been established. As a result, the realistic design criteria had to be established by testing--initially by extensive tests in engine simulated mechanical and thermal screening rigs, and finally, in actual engine conditions.

The overall design/development philosophy, therefore, has been to define problem areas and initiate design changes based on feedback from component testing. Continuous feedback has been made to the analytical process and material selection throughout all stages of rig and engine testing to arrive at a viable and optimized component design.

6.3.1 Component Design/Analysis

6.3.1.1 Introduction

Development of AGT101 ceramic components was initiated during the engine configuration conceptual design study phase. Twenty-three different engine concepts were reviewed.

Based on experience in earlier ceramic programs, component symmetry, both in geometry and loading, was pursued in the basic design strategy to eliminate circumferential stress variations and to reduce the complexity of the finite element analysis. This simplification resulted in reduced cost, both in manpower and computer demands, and rapid analysis turnaround that allowed for extensive design iterations. The engine symmetry also provided the capability to fabricate and rig-test components early in the program, thereby allowing test data feedback into the design program. The flow separator housing is the only exception to the concept of symmetry. This component will be discussed in detail in the component design section.

Individual component geometries were defined to minimize stresses and to provide ease of component fabrication and engine assembly while maintaining the required piloting control. Design and fabrication of state-of-the-art structural ceramic components of the size and shape required for the AGT101 had not heretofore been attempted. Therefore, the design of simple component configurations with uniform wall thicknesses were pursued. Whenever a deviation from a uniform wall thickness was required, a gradual contour change was used to minimize the stress concentration effects. The large thermal expansion differences between ceramic and metallic structures dictated the use of unique and innovative piloting systems. To accurately predict component stresses for this program, extensive engine instrumentation and data reduction were necessary to develop the proper analytical thermal boundary conditions. By creating a high degree of analytical confidence, a selection criteria was established for various component configuration/material options. For example, a component design utilizing varying wall thickness to reduce excessive thermal gradients during transient thermal conditions could only be accomplished by accurately knowing the flow path heat transfer coefficients (HTCs). Likewise, only by instrumenting the various rigs and components could confidence be placed in the fact that these rigs were properly simulating engine conditions and proof testing the ceramic components to a predetermined stress level.

A wide variety of available ceramic materials was considered in this program. To eliminate extensive design optimization on each material/component combination, a preliminary evaluation was performed for each component to identify primary and alternate materials. Subsequently, design optimization was performed using a prime material candidate for each component. After design optimization was achieved, alternate candidate materials again were evaluated, at which time all acceptable material/component combinations were assessed.

Because of the lack of ductility in ceramics, localized stress concentrations cannot plastically redistribute stresses. Consequently, conducting detailed finite element modeling and eliminating known stress concentra-

tions from the design wherever possible becomes of paramount importance. When component analysis revealed significant tensile stresses near known stress concentrations, additional analyses using a finer substructure model mesh were performed.

Stresses were analyzed for three modes of loading enountered during the normal engine operation; one pressure (maximum power) and two thermal (steady-state operation and light-off transient). Shutdown transient conditions were initially considered but were insignificant due to the thermal inertia effects of the regenerator core.

Detailed discussion of the design and development of the ceramic components follow. Specific components are addressed although overlapping occurs due to the interrelation of one component upon the others, for example: the finite element model to evaluate the turbine shroud included the outer diffuser. Results from these analyses, both for outer diffuser and turbine shroud are addressed in the turbine shroud section.

6.3.1.2 Diffusers

A thermal stress problem was encountered during light-off conditions on the inner and outer turbine diffuser housings (Figure 250). Rig testing of the diffuser housings resulted in recurring failures originating from the pilot slots in the outer diffuser and the pilot holes in the inner diffuser. These failures were identified as being thermal fractures primarily caused by the high radial transient thermal gradient occurring during light-off condition.

A 2-D plane stress model of a π Radian (180 degree) angular sector of the outer diffuser was created to evaluate the localized effect of the rim pilot slot. Two light-off cycles were evaluated; the initial cycle was the existing worst case engine light-off cycle (Figure 251) and the latter was for a 871C (1600F) screening rig cycle (Figure 252). The material evaluated for all analyses was RBSN.

A comparison between the stress results obtained for the original and a scalloped con-

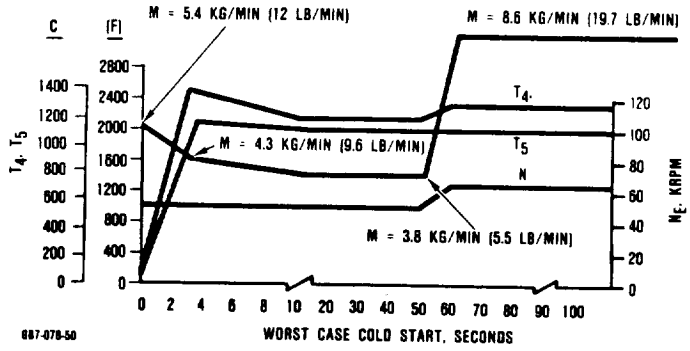

Figure 251. Worst Case Light-Off Cycle (1282C).

figuration are shown in Figure 253. A predicted maximum principal stress of 391.5 MPa (56.8 ksi) for the worst case engine lightoff cycle was reduced 54 percent with the scalloped configuration.

Both a slotted and a two-piece configuration were found to offer substantial further reductions in stress but to realize this potential a loss in piloting capability would have to be taken. The design solution finally chosen was found by eliminating the radial piloting slots, and instead pilot the diffusers by sleeves on the rocker assembly (Figure 254). Anti-rotation would be maintained by frictional loading against the diffuser assembly by an axially spring loaded mechanism. The outer diffuser thus became a completely axisymmetric structure. A 41-percent reduction in maximum principal stress from the scalloped configuration was estimated for this configuration.

The analytical effort on the inner diffuser proceeded on a parallel path to outer diffuser analysis. A 2-D finite element model was made of the existing inner diffuser, which extended along the flow path from the turbine rotor exit to the flow separator housing. An additional finite element model was made of a truncated inner diffuser, scalloped about the pilot bolts. All analyses were made using RBSN as the inner diffuser material. Thermal stresses only were considered.

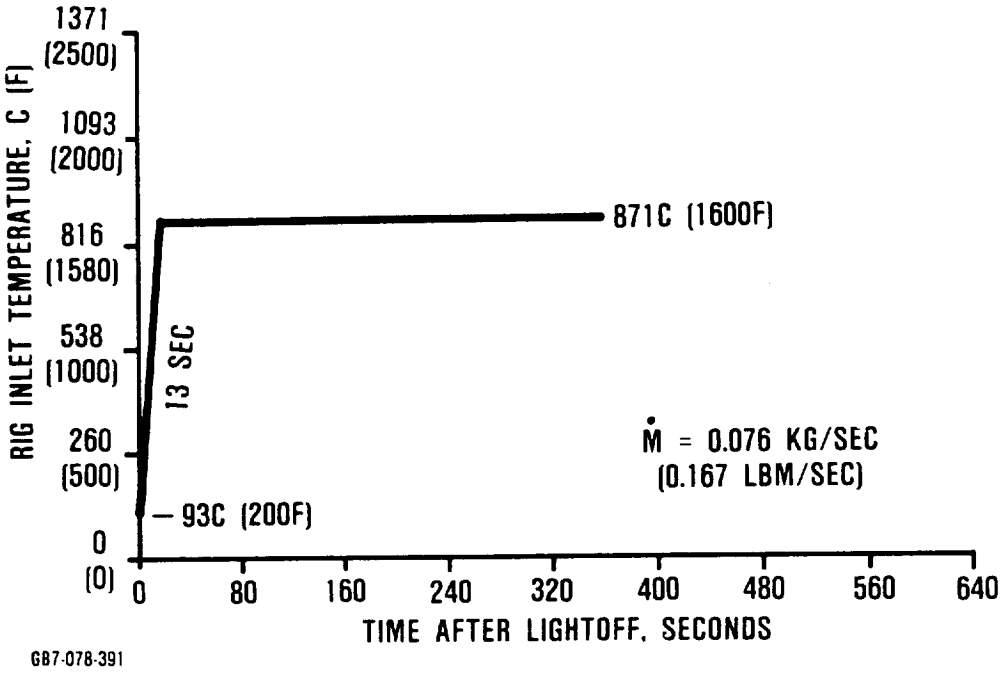

Figure 252. Rig Cycle 871C (1600F) Static Structures.

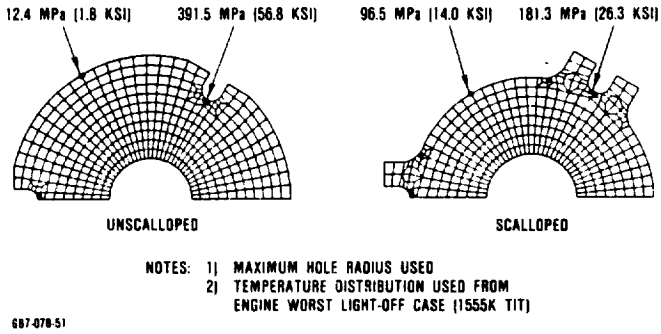

Figure 253. Effect of Scalloping Outer Diffuser.

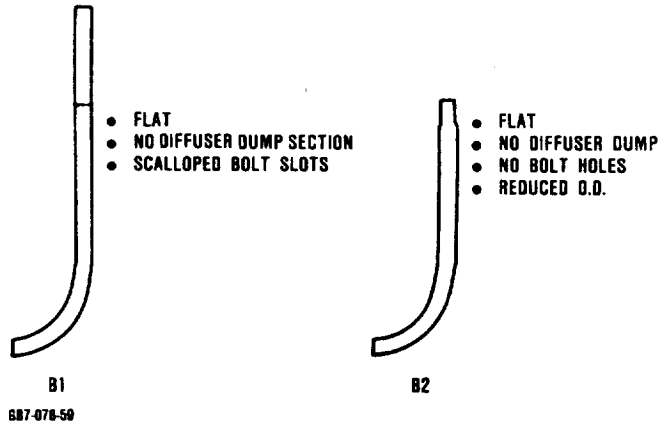

Figure 254. Outer Diffuser B1 and B2 Configurations.

The stress analysis results for the initial inner diffuser is shown in Figure 255. To simulate 3-D effects on this 2-D model, the outer section of the inner diffuser was modeled as a thick rim and parametrically plotted with principal stresses at three locations. The results show that the effect of the increased rim thickness is to reduce stresses at the pilot hole.

The stress analysis results for the scalloped inner diffuser was done for both the maximum and minimum tolerances on the pilot slot. As shown in Figure 256 the singular effect of the tolerance within the pilot slot radius accounted for approximately a 10 percent varia-

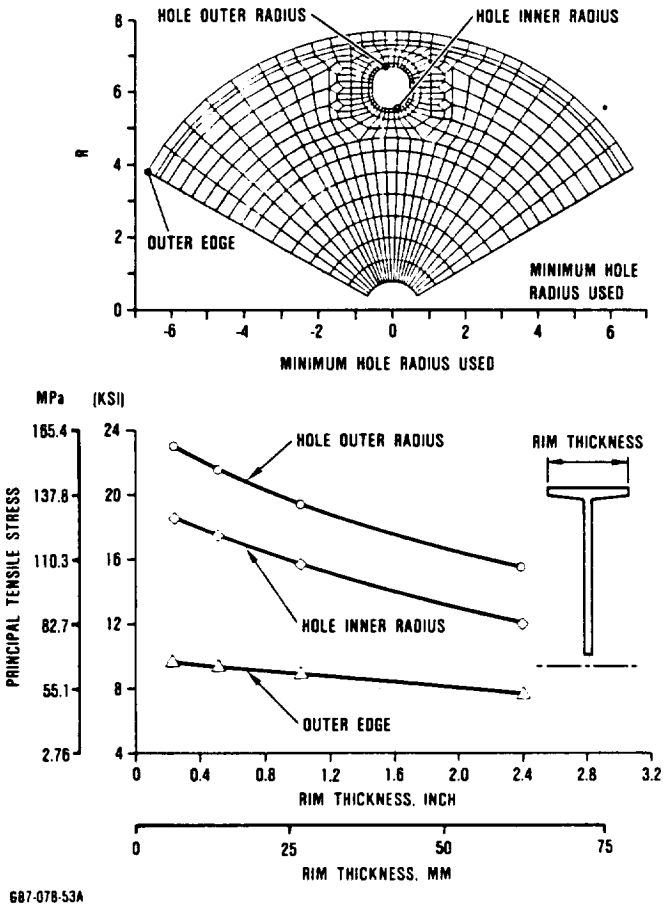

Figure 255. Inner Diffuser Initial Configuration Stress Analysis Results.

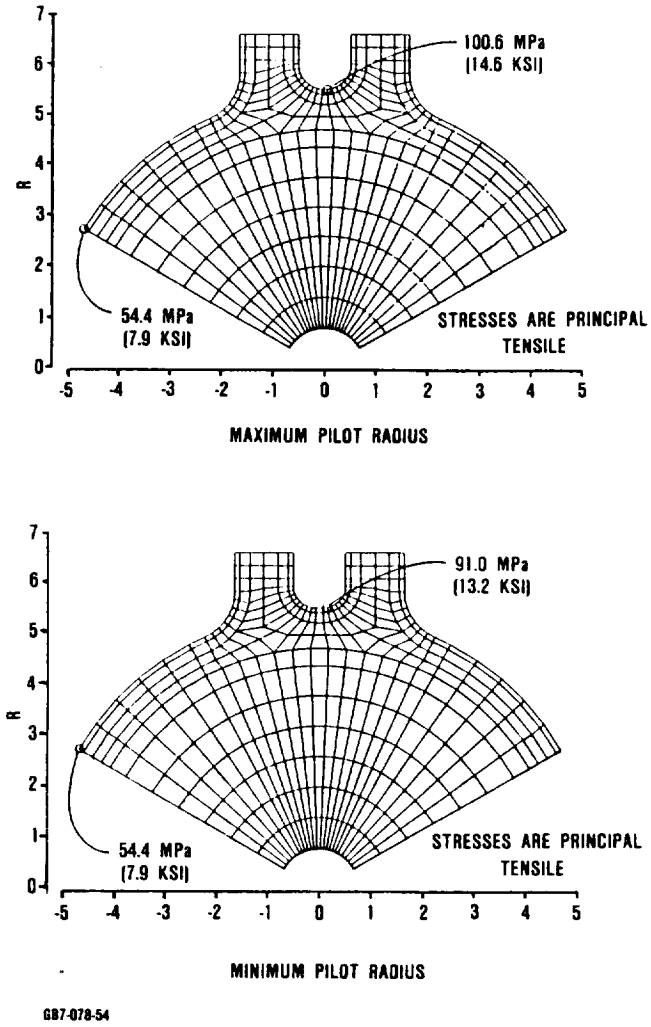

Figure 256. Inner Diffuser Scalloped Configuration Stress Analysis Results.

tion, the higher stress being predicted for the larger radius. The higher stress for the larger radius initially appeared contrary to the common rules of thumb concerning stress concentrations. This apparent contradiction was rationalized by realizing that the smaller fillet radius between the sides and the bottom of the slots produced a flat at the bottom, where the peak stress occurred. The larger radius produces a full radius at the bottom of the slots. Compared to the initial configuration, the scalloped configuration was estimated to offer a 34-percent improvement.

The design finally chosen for the inner diffuser to meet the program goal had a configuration similar to that chosen for the final outer diffuser design. The component was truncated to inside of the pilot bolts to form a completely axisymmetric design. Piloting is maintained by frictional loading from an axially spring loaded mechanism. A 60-percent reduction in maximum principal stress has been estimated by the total culmulative design changes on the inner diffuser.

The truncated inner diffuser required the design and fabrication of an additional component to provide the outer flow path between the outer diffuser to the flow separator housing. The 1093C (2000F) gas temperature,

lack of mechanical loading, and the low peak gas velocity of 15.2 to 22.9 m/sec (50 to 75 ft/sec) allowed materials other than monolithic ceramic components to form this gas path surface. Babcock and Wilcox, Inc., vacuum formed Al_2O_3 fiber insulation, coated with Johns-Manville Cerakote at the surfaces exposed to the hot turbine exhaust gases, was selected for this component and is currently being used.

6.3.1.3 Turbine Shroud

The turbine shroud design (Figure 250) was the most substantial design challenge of all the ceramic static structural components. Functionally, this component must maintain the outer turbine flow path as energy is converted into power through the turbine rotor.

The turbine shroud design, therefore, must survive the thermal transient stresses that are induced as local boundary condition change along the meridional flow path. These non-uniform boundary conditions result in high thermal gradients and polyaxial stresses within the shroud, predominantly during engine light-off conditions. The greatest influence on the thermal gradients is the variation in heat transfer coefficients. Although not of primary concern, it also withstands a significant pressure load at maximum power conditions. Additionally, stress concentrations are imposed due to the discontinuities required for turbine stator vane piloting and pressure sealing. The classical solution to the reduction of high thermal stresses, the multiple piece approach, was not feasible in the AGT101 application due to the performance requirement for close rotor clearance control and static sealing complications.

Two-dimensional finite element programs were the primary tools used to design the turbine element. Three primary models were created to represent the static structure rig, the thermal screening rig, and the engine.

6.3.1.3.1 Static Structure Rig Shroud Analyses

The static structure rig model used to analyze the turbine shroud, as shown in Figure 257 consisted of the shroud, outer diffusers, the seal area, and portions of the transition duct, stators, and flow separator housing. Heat transfer coefficients on the turbine shroud and the outer diffuser were modeled to reflect the absence of the turbine rotor.

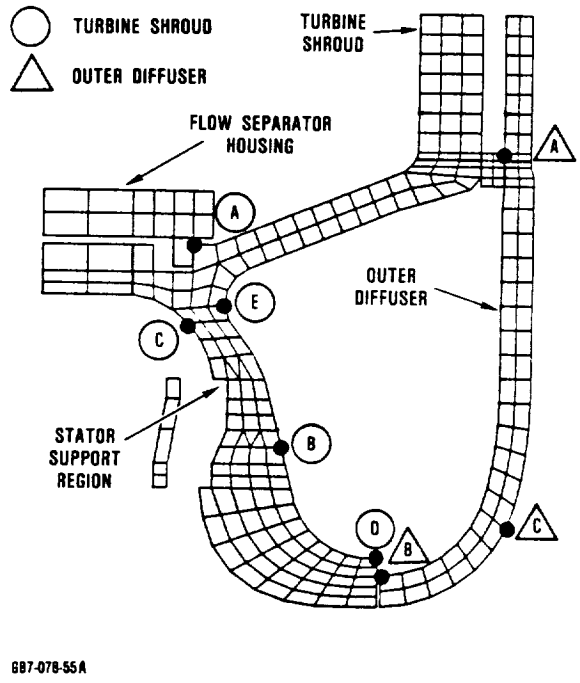

Figure 257. Turbine Shroud/Outer Diffuser Critical Stress Areas (Static Structures Rig Model).

Early optimization of the turbine shroud configuration used the static structure rig model. High thermal stresses during light-off were found at the junction of the shroud outer cone with the stator support (Figure 257). The stresses in this area were from high hoop stresses coupled with axial-radial bending. The primary cause was attributable to the large variation in heat transfer coefficients along the shroud structure. High heat transfer coefficients are generated at the turbine section from the high velocity core flow, whereas, low heat transfer coefficients are generated at the diffuser exit.

Various configurations, as shown in Figure 258, were investigated and the results are shown in Table 36. All stresses are for a light-

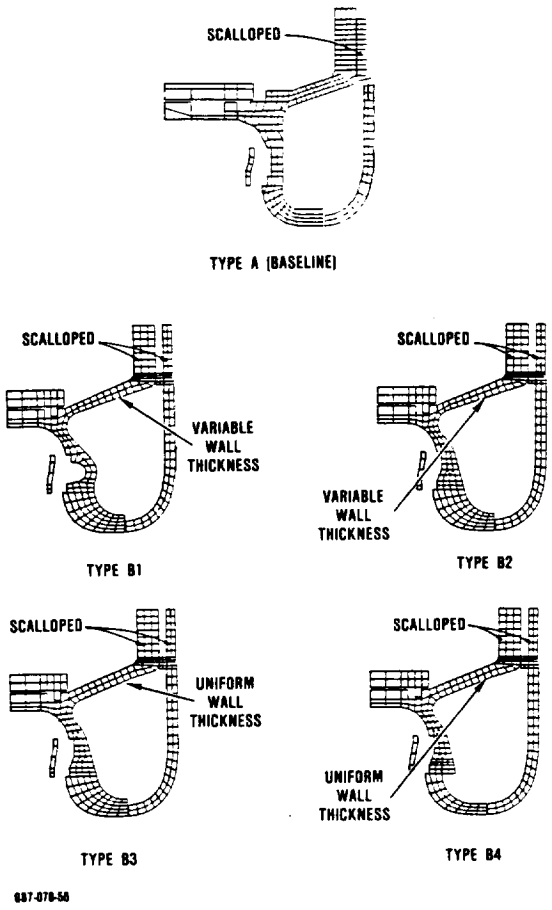

Figure 258. Phase B Turbine Shroud Configurations.

off transient to 871C (1600F) as shown in Figure 252. The comparisons were made assuming RBSN as the primary shroud material. The heat transfer coefficients were based upon aerodynamic analyses.

The Type B1 thru B4 configurations had a scalloped flange whereas the baseline configuraton (Type A) did not. In addition, all Type B configurations attempted to increase the structural flexibility to relieve the thermal growth mismatch between the outer and inner sections of the turbine shroud during transient light-off conditions. The Type B4 was a two-piece configuration with the interface at the stator support.

The following results were found from this investigation:

- o The Type B3 configuration had the lowest predicted stress 54.4 MPa (7.9 ksi) for a 28-percent reduction from the baseline configuration
- o Compared to the baseline, the B3 configuration increased the time to critical stress from 175 to 240 seconds, whereas the B4 decreased the time to critical stress from 175 to 120 seconds
- o Types B1 and B4 moved the location of critical stress from the seal area (location A) to behind the stator pocket (location B)
- o A material change from RBSN to SASC resulted in a 76 percent higher stress

As a result of this study, a design change was made on the turbine shroud to reflect the Type B3 configuration.

The next area to be considered was the effect of various light-off and operating cycles on the shroud stresses in the static structure rig. Six different cycles were considered. Three of these cycles were light-off cycles to 1149C (2100F), all at idle mass flow conditions but at different transient rates as shown in Figure 259. In addition, three other operating cycles were considered, as shown in Figure 260. These included a light-off to steady-state conditions (cycle 2), a light-off followed by a shutdown after a 1-minute hold at maximum temperature (cycle 3), and a shutdown from steady-state conditions (cycle 6). Again mass flow was at idle condition during the cycle until the rig was shutdown, then mass flow was reduced 50 percent.

Table 37 shows the results for the effect of cycle variations. Both the turbine shroud and outer diffuser were assumed to be RBSN. The heat transfer coefficients were based on a first set of thermocouple data from a metal engine test.

The screening rig cycle was selected after this study to include a long hold period

Table 36. Phase B Shroud Configuration Study.

Shroud			Maximum Principal Stress (MPS)			
Case No.	Type	Material	Location*	Magnitude MPa	(ksi)	Time After Start, sec
1	A	RBSN	A	75.8	(11.0)	175
2	B1	RBSN	B	73.1	(10.6)	240
3	B2	RBSN	A	57.9	(8.4)	240
4	B3	RBSN	A	54.4	(7.9)	240
5	B4	RBSN	B	59.3	(8.6)	120
6	B3	SASC	A	95.8	(13.9)	240
B1 Configuration Outer Diffuser (RBSN) Analytical heat transfer coefficients (HTCs) used Static Structure Rig Model						

*For locations see Figure 257.

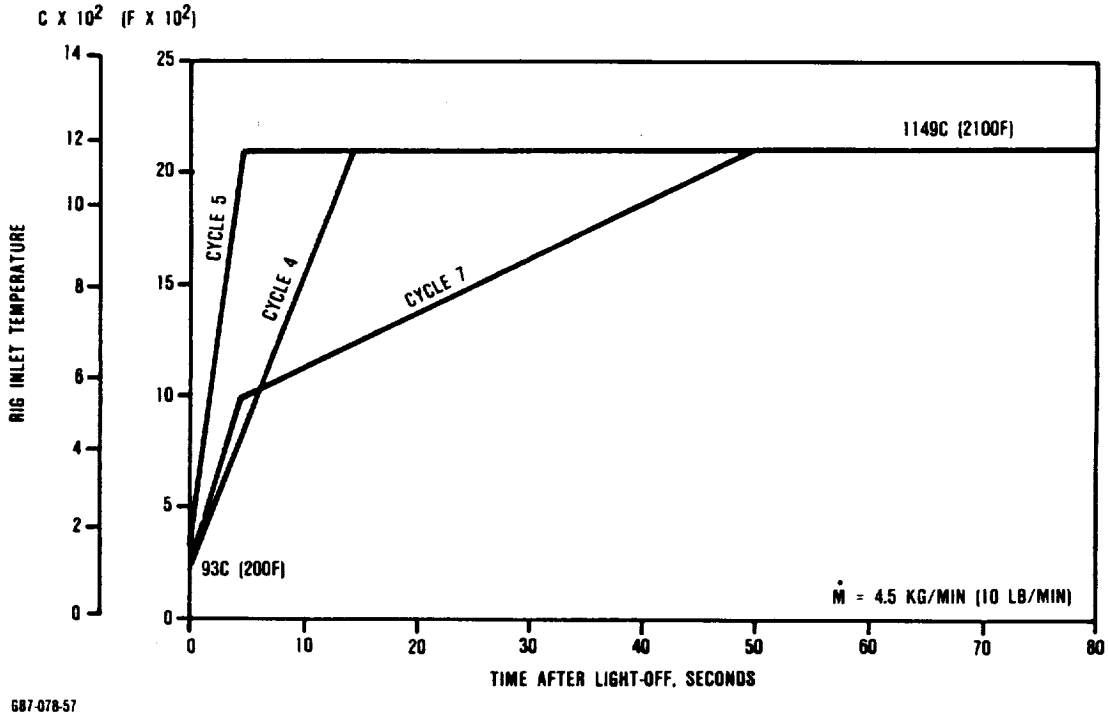

Figure 259. Static Structure Rig Light-off Cycle.

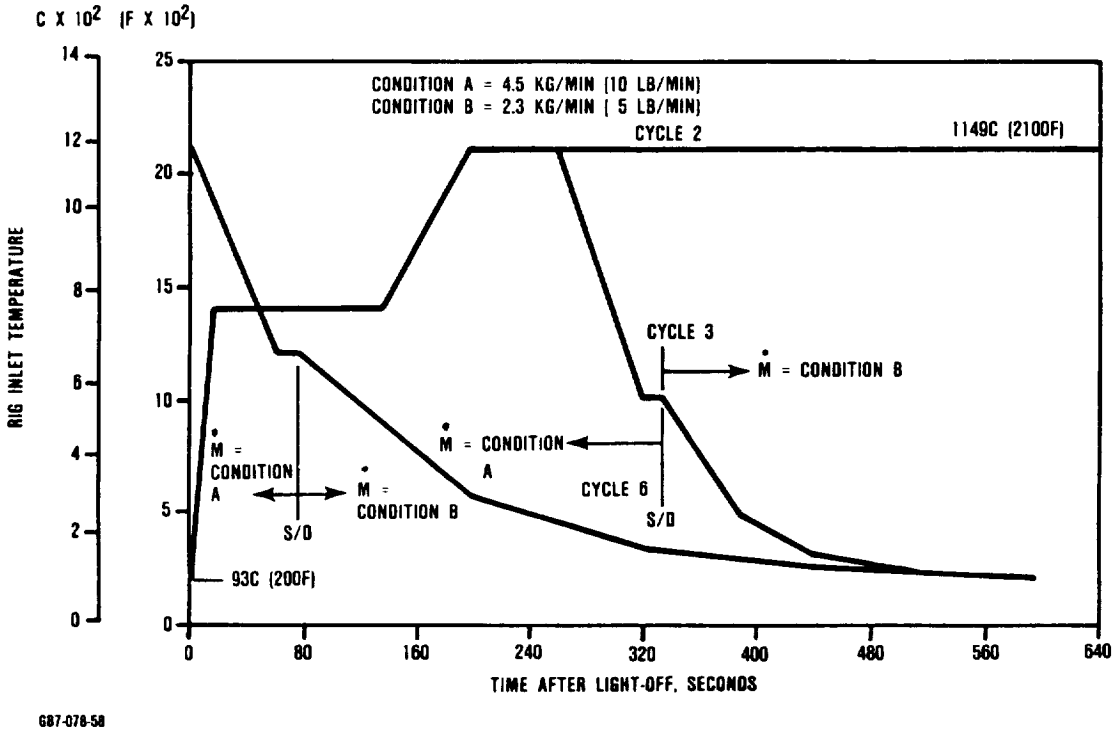

Figure 260. Static Structure Rig Operating Cycle.

(6 minutes) to ensure that the maximum principal stress was realized during lightoff. In addition, the cycle ensured that the cool-down was less severe than the lightoff. The potential for high cool-down stresses occur only in the rigs since the regenerator system on the engine negates the possibility of significant cool-down rates.

6.3.1.3.2 Shroud Screening Rig Analyses

In the fall of 1983 turbine shroud failures in the screening rig were noted that were inconsistent with analysis. Fractography revealed that the failure origins began in the seal radius rather than radially inboard on the flow path surface predicted by analysis (Areas A2 and C respectively in Figure 261). As a result, investigation was directed toward validating the rig heat transfer coefficients and refining the finite element model.

The shroud screening rig is similar to the static structures rig as concerns the absence of a turbine rotor but different in regard to the absence of flow around the shroud flange and cone. The screening rig also had been used to screen turbine shrouds initially without the use of stators and a backshroud. After passing this initial test, the stator assembly and backshroud were added to the assembly and the turbine shroud was retested. Consequently, the initial turbine shroud screening rig test did not include the stator exit swirl flow effect encountered in the latter test.

Rig testing in January 1984 with a metallic turbine shroud instrumented with thermocouples allowed for empirical evaluation of heat transfer coefficients. As expected, higher heat transfer coefficients occurred in the shroud region aft and inboard of the stator exit when the stator assembly and backshroud was added to the screening rig. But after the heat transfer coefficients were revised in the analysis, the results still were unable to confirm the location of the failure origin with the existing model. Model refinements were necessary to confirm the failure origin.

Table 37. Static Structure Shroud Cycle Study.

Case No.	Thermal Cycle No.	Type Cycle	Light-off Time, sec	Hold Temperatures, C	Mass Flow, g/sec	Maximum Principal Stress (MPS)					
						Turbine Shroud			Outer Diffuser		
						Location*	Magnitude, MPa (ksi)	Time After Start, sec	Location*	Magnitude, MPa (ksi)	Time After Start, sec
7	2	Light-off	15	93/760/1149	75.5	A	75.1 (10.9)	300	A	88.2 (12.8)	240
8	7	Light-off	5	93/538/1149	75.5	A	80.6 (11.7)	180	A	106.8 (15.5)	120
9	4	Light-off	15	93/1149	75.5	A	81.3 (11.8)	180	A	108.9 (15.8)	120
10	5	Light-off	5	93/1149	75.5	A	81.3 (11.8)	180	A	108.9 (15.8)	120
11	3	Light-off/ Cooldown	5	93/760/ 1149/538/ 93	75.5/ 37.8	A	73.1 (10.6)	240	A	88.2 (12.8)	240
12	6	Cooldown	—	1149/93	75.5/ 37.8	E	93.0 (13.5)	360	C	53.8 (7.8)	240

Static Structure Rig Model
B3 Type Shroud (RBSN)
B1 Type Outer Diffuser (RBSN) —
First Revision HTCs Used (engine conditions)

*For locations see Figure 252.

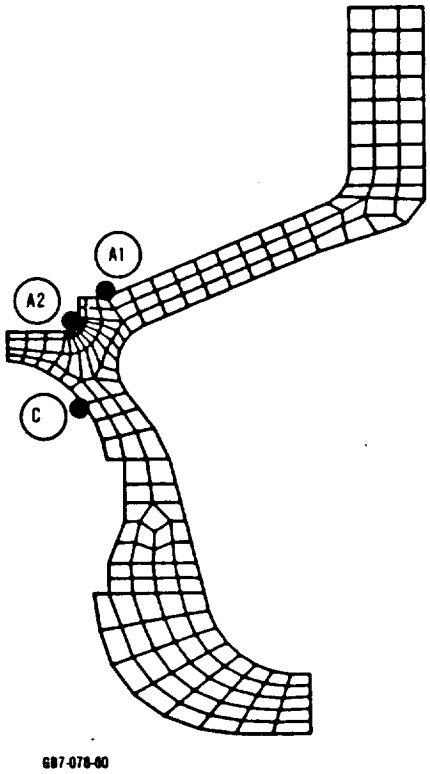

Figure 261. Turbine Shroud Critical Stress Areas (Shroud Screening Rig Model).

Since the shroud failures occurred in a rig test without the stator assembly and backshroud the finite element model was likewise configured. Table 38 shows the results of this study. The model light-off (cycle 13, shown in Figure 262) corresponded to the test cycle that caused shroud failures. Heat transfer coefficients and shroud material (RBSN) also reflected test conditions. Two levels of model refinements were made, the second is shown in Figure 263. In addition, one design modification was considered. The shroud seal area was to be moved toward the combustor 6.1 mm (0.240 inch) to increase the neck cross section adjacent to the shroud seal. The results were as follows:

- o The analyses with model refinements predicted the shroud failure origin. Maximum principal stress increased a total of 68 percent (182 percent at location A2)
- o The configuration change in the shroud seal area resulted in a 31-percent reduction in maximum principal stress.

Concurrent with this effort, a revised rig test was developed. To more accurately simulate engine conditions all subsequent turbine shroud screening tests were conducted with the backshroud and stator assembly. Insulation was modified within the rig housing to improve radiation cross connections between the shroud cone and flange. The screening cycle was modified to subject the turbine shroud in the rig to 125 percent of the maximum predicted principal stress in the engine. Testing was resumed and the Type B3 shroud survived.

Table 39 shows the effect of different ceramic component materials. RBSN, SASC, and SSN were considered for the turbine shroud and SASC and SSN were considered for the backshroud. Following are the results:

- o The lowest shroud maximum principal stress (154.4 MPa) was predicted using an RBSN turbine shroud.
- o SSN turbine shroud was next at 86 percent higher than RBSN.

- o SASC turbine shroud was highest at a maximum principal stress 145 percent higher than RBSN.
- o A SSN backshroud had a maximum principal stress 23 percent higher than a SASC backshroud.

6.3.1.3.3 Shroud Engine Analyses

The engine model for the turbine shroud structurally is the same as the static structure model except the boundary conditions are modified to include the effect of the turbine rotor on the heat transfer coefficients.

The initial use of this model was to evaluate various thermal cycles. Table 40 shows three cycles considered. The first analysis considered the same cycle (cycle 5), used in the static structure rig. Another considered cycle 8 shown in Figure 264. This cycle corresponds to a normal engine lightoff in an operational environment. Cycle 11 shown in Figure 265 was considered to assess the effect of a slow ramp instead of a step increase to

Table 38. Turbine Shroud Seal Radius Study.

Case No.	Type	Material	Maximum Principal Stress (MPS)			Case Description
			Location*	Magnitude MPa (ksi)	Time After Start, sec	
14	B3	RBSN	C	108.9 (15.8)	600	Baseline Model
15	B3	RBSN	A2	164.7 (23.9)	660	First model refinement in seal
16	B3	RBSN	A2	182.6 (26.5)	660	Second model refinement in seal
17	B3	RBSN	A1	126.1 (18.3)	660	Seal land decreased 6.10 mm (0.240 inches)
Shroud Only Screening Rig Model First Revision HTCs Used (Rig Condition) Cycle 13 Light-off						

*For locations see Figure 261.

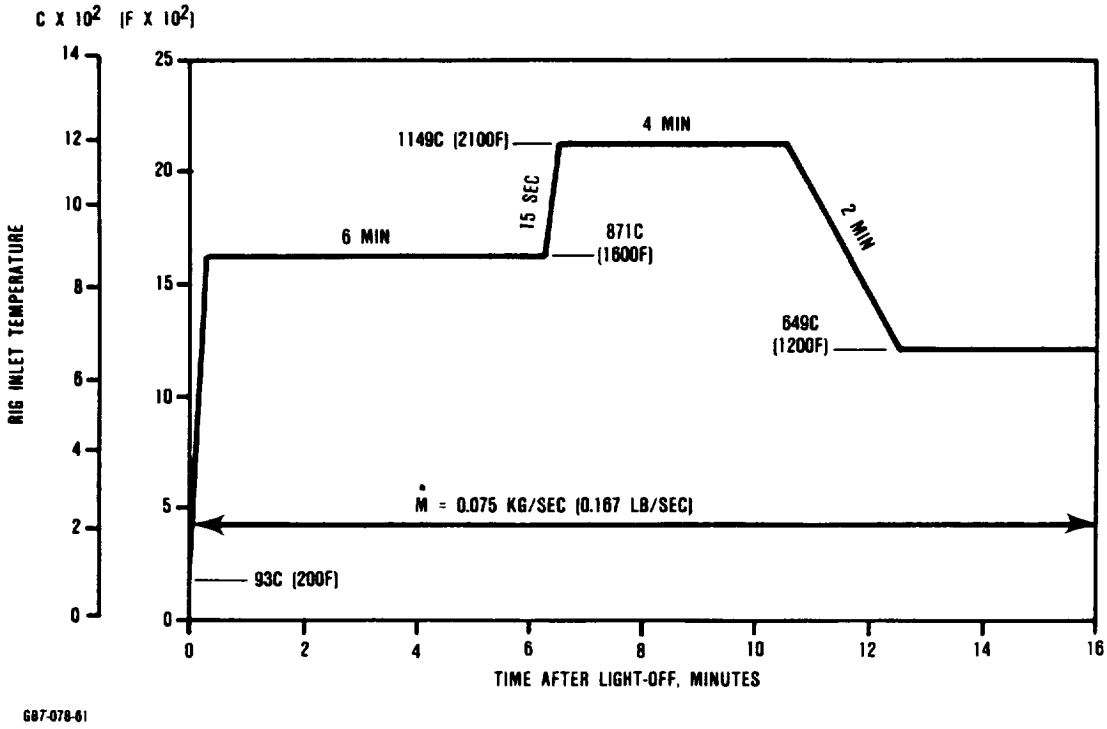

Figure 262. Screening Rig Cycle 13.

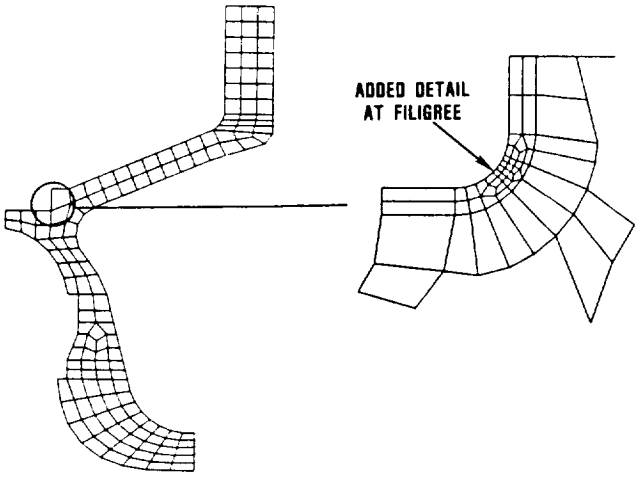

GB7-078-62A

Figure 263. Second Model Refinement to Shroud Fillet Radius.

operating temperatures. The first engine test with all of the ceramic structural components would use a similar type light-off. The analyses were all done assuming an RBSN turbine shroud and heat transfer coefficients (first revision) generated from metal engine S/N 002/Build 4 test data. The shroud model in these analyses was based on the original model without the refined seal radius. Critical stress locations for the engine model are shown in Figure 266. The results have been summarized as follows:

- o The effect of the turbine rotor causes the turbine shroud maximum principal stresses in the engine to be 25-percent higher than those in the static structure rig for the same light-off cycle.

- o The predicted maximum tensile stress for normal engine light-off was 115.8 MPa (16.8 ksi) based on the first revision heat transfer coefficients.

- o The maximum principal stresses predicted for a ramp type engine cycle occurred two minutes after light-off resulting from the initial step change in gas path temperature, as shown in Figure 267. Maximum principal stresses during the ramp heatup and cooldown were marginally lower.

The significance of the last item was that the maximum stresses could be controlled to occur during the initial light-off where the environment is more fully characterized and the remainder of the cycle would function at a lower stress level. The first ceramic engine light-off (engine 002C/Build 1) had a similar cycle to cycle 11 except stresses were controlled to a 25-percent lower stress level by decreasing the initial light-off step and ramp rate.

Concerns about the viability of the existing type B3 shroud led to a Phase C turbine shroud redesign effort. The engine model was updated to reflect the refined stresses at the shroud seal radius and updated heat transfer coefficients (Figure 268). The outer diffuser was changed from a type B2 to A3 configuration as shown in Figure 269. Stresses were calculated for an RBSN turbine shroud and outer diffuser for a normal engine lightoff. In addition, the radiation from the shroud outer cone to rig insulation was considered as shown in Figure 270.

The various shroud configurations considered are shown in Figure 271. The primary objective in the C type configuration was to increase the heat transfer coefficients in the outer portion of the shroud from the seal area to the flange. This was to be achieved by reducing the hydraulic diameter of the flow over the shroud by increasing the diameter of the shroud outer section and decreasing the diameter of the opposing outer duct wall. The type D configuration was an attempt to decrease the bending stresses at the seal area by providing a more direct path from the stator support to the flange. All of the various cases considered are shown in Table 41. The significant results are as follows:

- o The finite element model refinements in the shroud seal area was less significant in the engine model (increasing maximum principal stress 36 percent) than in the thermal screening rig model.

- o Increasing the heat transfer coefficients on the cone area of the type B3 configuration

Table 39. Material Sensitivity in Screening Rig.

Case No.	Shroud	Backshroud	Stators	Maximum Principal Stress (MPS)						
				Shroud			Backshroud			
				Location*	Magnitude, MPa (ksi)	Time After Start, sec	Location*	Magnitude, MPa (ksi)	Time After Start, sec
22	RBSN	SASC	SASC	A2	154.4 (22.4)	210	B	56.5 (8.2)	30
23	SASC	SSN	RBSN	A2	377.7 (54.8)	200	B	69.6 (10.1)	60
24	SSN	SSN	RBSN	A2	286.7 (41.6)	240	B	69.6 (10.1)	60

Backshroud/Stator/Shroud Screening Rig Model
First Revision HTCs Used (Rig Condition)
Cycle 16 lightoff
Revised Rig Configuration
B3 Type Shroud
A Type Backshroud
A Type Stators

*For locations see Figure 261.

Table 40. Engine Shroud Cycle Study.

Case No.	HTC Revision No.	Thermal Cycle No.	Type Cycle	Hold Temperatures, C	Mass Flow, g/sec	Maximum Principal Stress (MPS)					
						Turbine Shroud			Outer Diffuser		
						Location*	Magnitude, MPa (ksi)	Time After Start, sec	Location*	Magnitude, MPa (ksi)	Time After Start, sec
27	1	5	Light-off	93/1149	75.5	A	101.3 (14.7)	120	A	91.7 (13.3)	120
28	1	8	Light-off	93/1218	95.2	A	115.8 (16.8)	120	A	97.2 (14.1)	120
29	1	11	Light-off	52/538 1149/538	75.5	A	35.1 (5.1)	120	A	33.8 (4.9)	120

Shroud/Outer Diffuser Engine Model
B3 Type Shroud (RBSN)
B2 Type Outer Diffuser (RBSN)
First Revision HTCs Used (Engine Condition)
Original Model Configuration in Shroud Seal Area

*For locations see Figure 266.

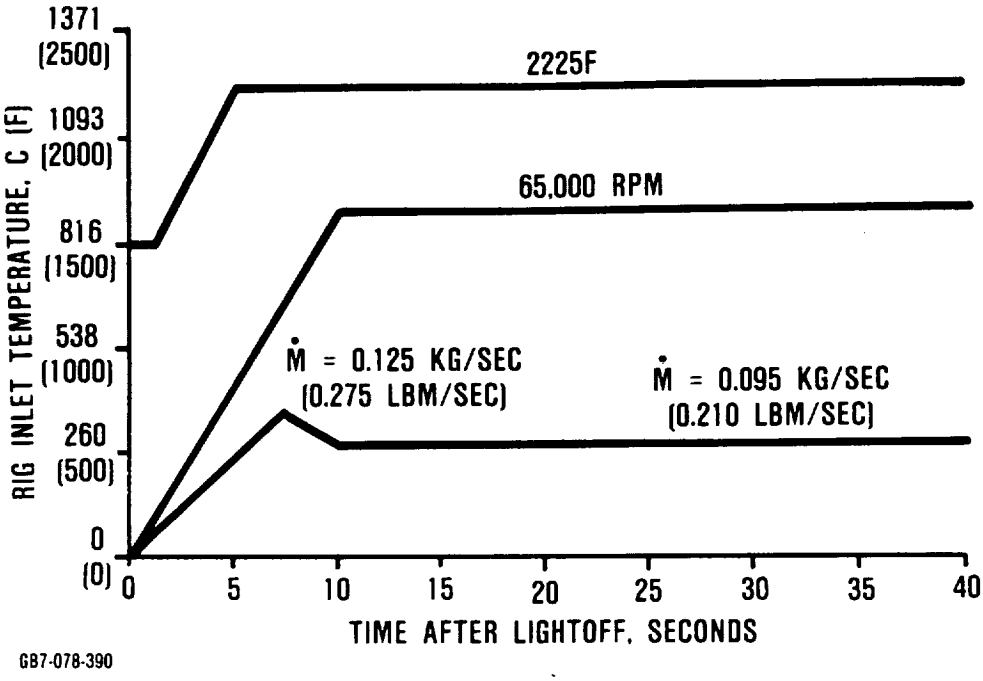

Figure 264. Normal Engine Light-Off, (Cycle 8).

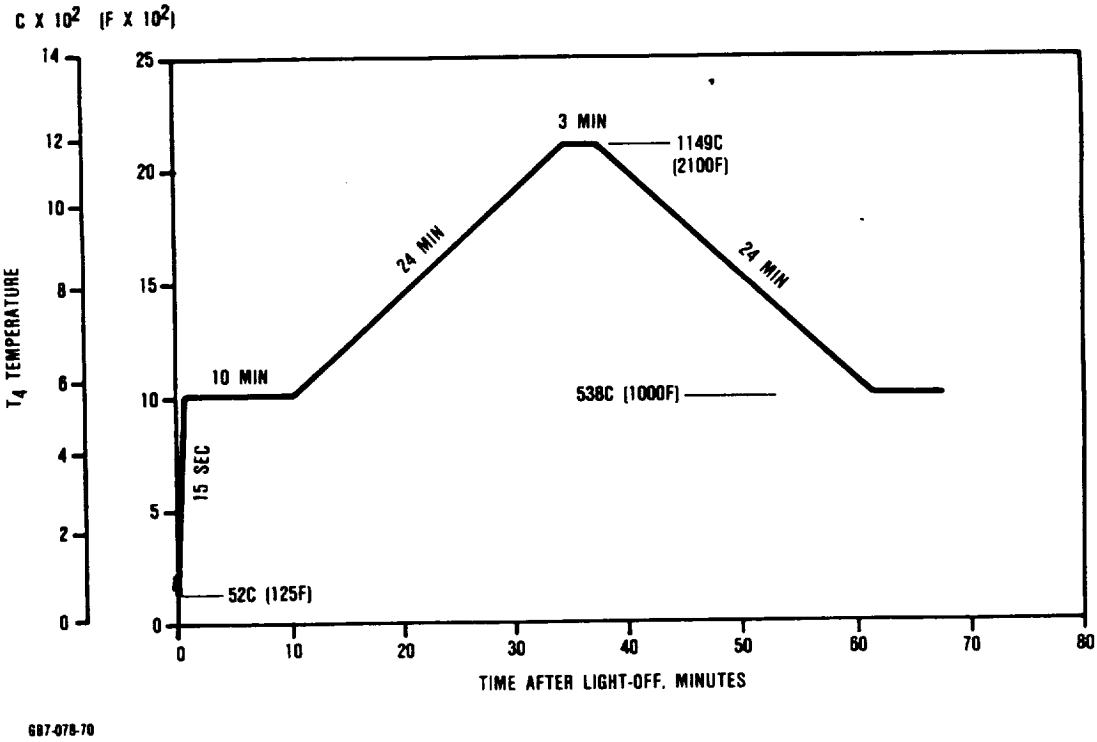

Figure 265. Ramp Type Engine Cycle 11.

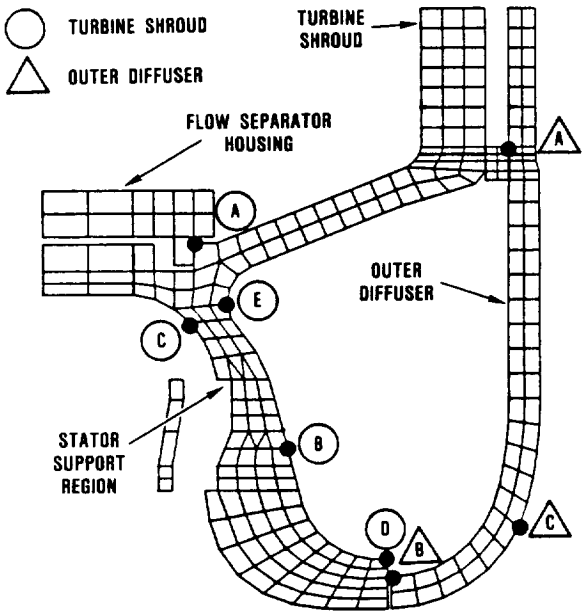

Figure 266. Turbine Shroud/Outer Diffuser Critical Stress Areas (Engine Model).

reduced maximum principal stresses by 63 percent (without radiation effects from the shroud to the rig insulation considered).

- The type C3 configuration shroud had the lowest predicted maximum principal stresses of all configurations considered (29 percent reduction).
- Changing from the first revision to the second revision set of heat transfer coefficients resulted in an 18-percent reduction in MPS.
- Changing the model boundary conditions to consider the effect of radiation to the rig insulation resulted in an 11-percent reduction.
- Modeling radiation to the rig insulation reduced the sensitivity of the MPS from the HTCs over the shroud cone area.
- The outer diffuser MPS decreased 15 percent by changing from a type B2 to A3 configuration.

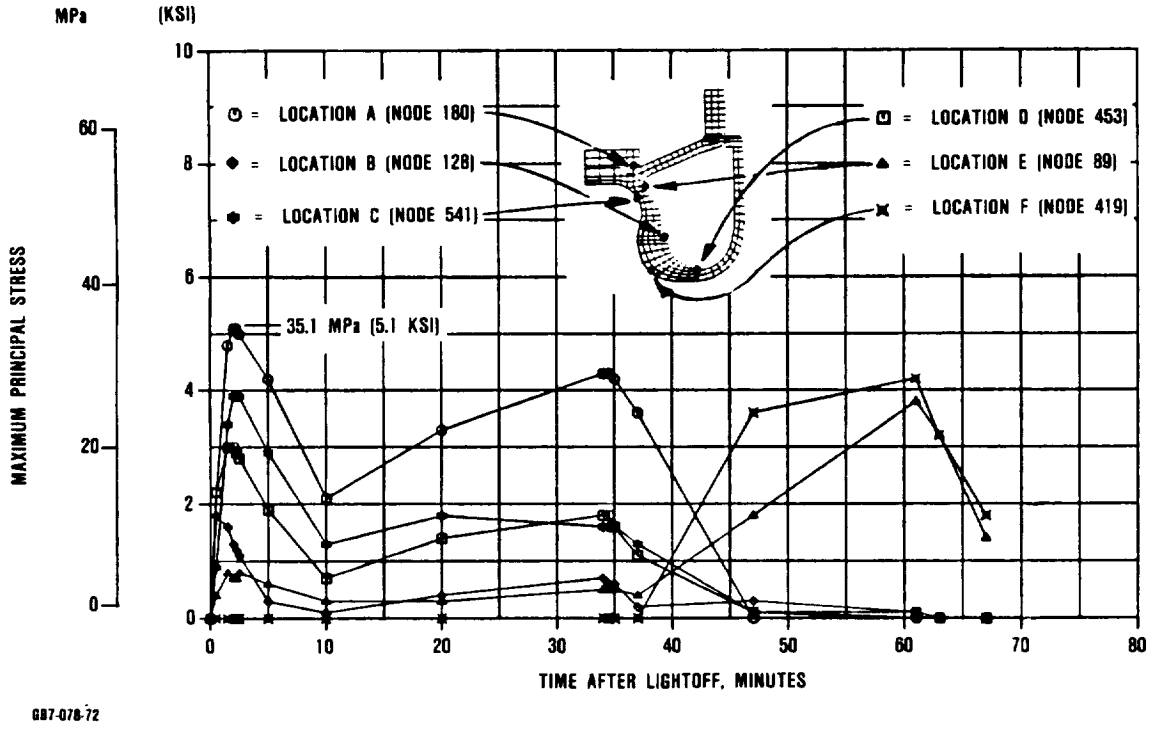

Figure 267. Turbine Shroud Stress Response for Ramp Type Cycle (Engine Cycle 11).

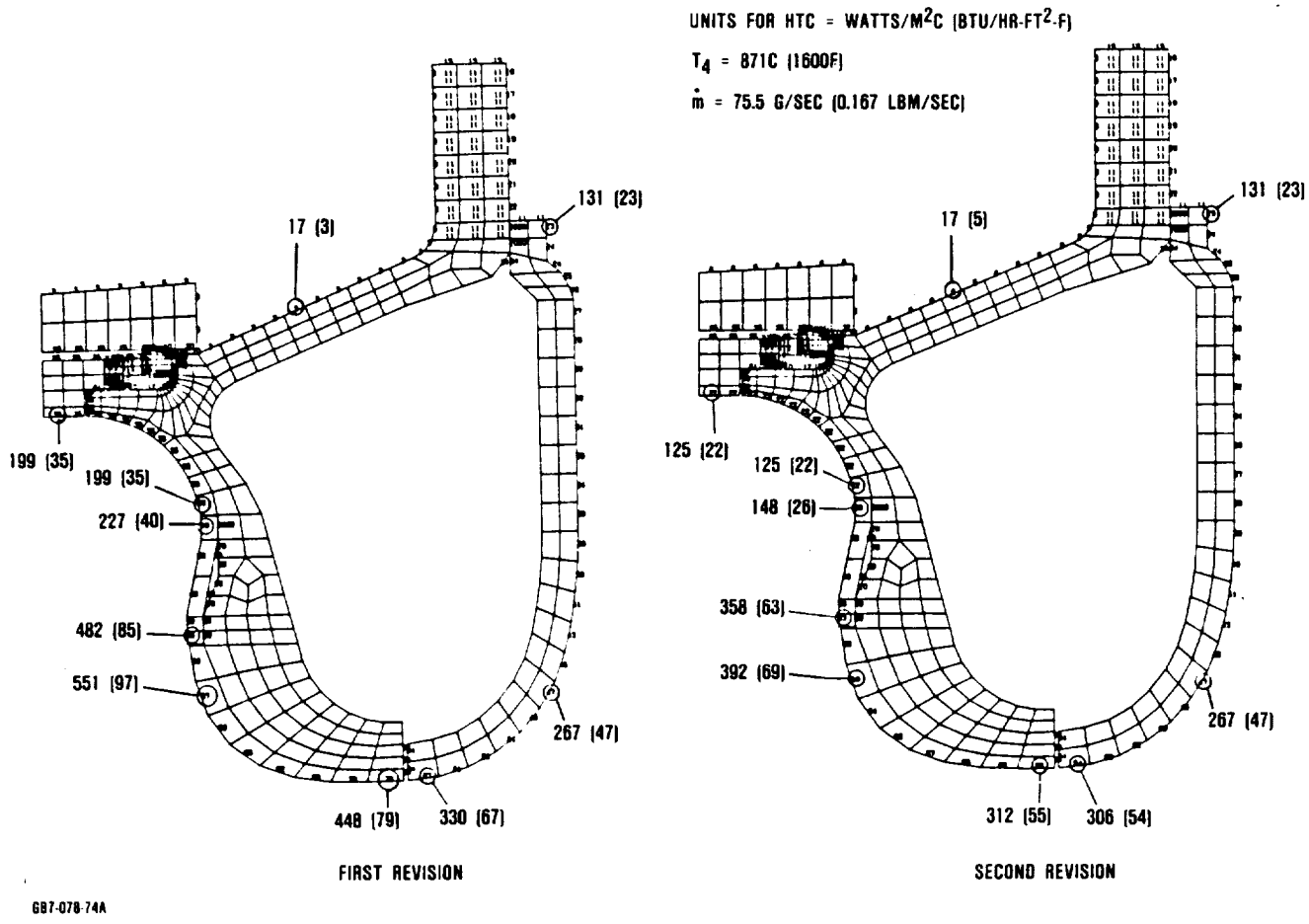

Figure 268. Engine Heat Transfer Coefficients on Turbine Shroud/Outer Diffuser Model.

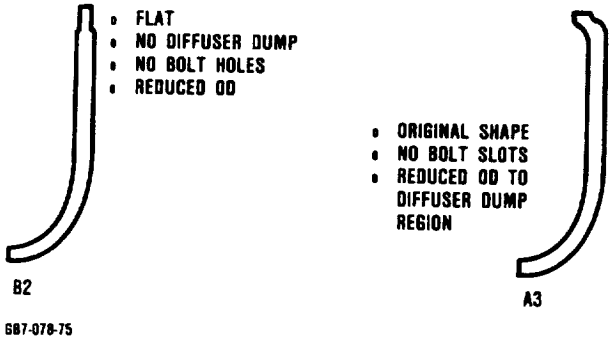

Figure 269. Design Change From Type B2 to Type A3 Outer Diffuser.

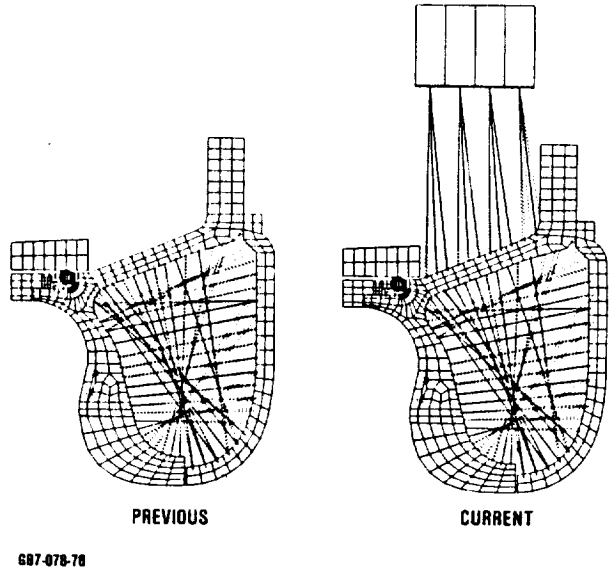

Figure 270. Shroud Cone to Insulation Radiation.

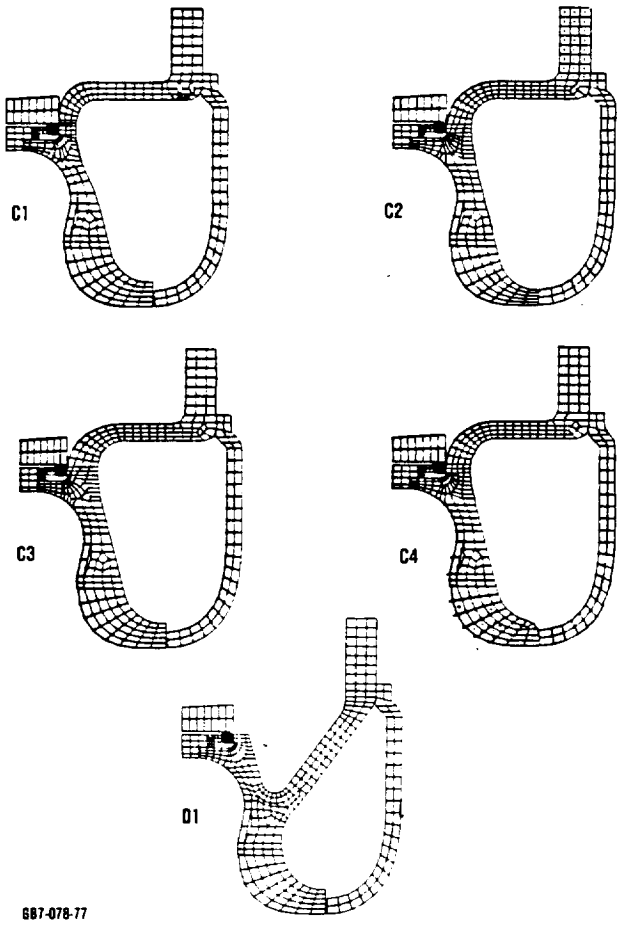

Figure 271. Shroud Configurations Investigated in Phase C Study.

- Considering radiation to the rig insulation and the second revision of heat transfer coefficients resulted in a total reduction of 12 percent in the MPS on the outer diffuser.
- The change from a type B3 to C3 turbine shroud results in a 36 percent reduction in the outer diffuser MPS.

Various materials were also considered for the turbine shroud and outer diffuser and are presented in Table 42. The analyses considered the latest refinements in the model and boundary conditions and represented the thermal conditions for a normal engine lightoff. The current type B3 turbine shroud and type A3 outer diffuser was used in the analyses. The results are as follows:

- The RBSN turbine shroud had the lowest MPS (115.1 MPa) of the three materials considered.
- The SSN turbine shroud had the next lowest MPS (104 percent higher than RBSN)
- The SASC turbine shroud had the highest MPS (188 percent higher than RBSN).
- The outer diffuser MPS was affected by the choice of shroud material. The MPS was 38 and 46 percent higher for an SSN and SASC turbine shroud respectively.

Development engine testing normally operates with the inlet guide vanes (IGV) fully open as opposed to being partially closed in a normal engine lightoff. To achieve the same stress level as in the normal engine lightoff, light-offs must be made to lower temperatures to account for the higher core flow. The light-off cycle to 982C (1800F) shown in Figure 272 has been determined to be the development engine light-off to simulate the normal engine lightoff. Figure 273 shows the MPS response of the turbine shroud for the development engine lightoff. For comparative purposes the MPS response from the screening rig and normal engine lightoffs are also shown.

6.3.1.4 Transition Duct/Combustor Baffle/ Turbine Backshroud

The transition duct, combustor baffle, and the turbine backshroud (reference Figure 250) are addressed collectively in this section. Since they are closely interrelated, they were analyzed in a common finite element model.

The transition duct provides the outer flow path between the combustor and turbine shroud. It axially supports the combustor baffle with a standoff midway along the component. Three holes are provided to monitor the turbine inlet temperature. Mechanically, the component must carry a radially inward pressure load and an axially compressive load due to engine pressure loading. Thermally, the component is exposed to both a through-the-wall and axial thermal gradients. Pressure loading is normally negligible, compared to thermal loading.

Table 41. Phase C Shroud Configuration Study

Case No.	Shroud Type	HTC Revision No.	Shroud Case HTC Multiplier	Maximum Principal Stress (MPS)						Case Description
				Turbine Shroud			Outer Diffuser			
				Location**	Magnitude, MPa (ksi)	Time After Start, sec	Location**	Magnitude MPa (ksi)	Time After Start, sec	
30	B3	1	1	A	19.3 (2.8)	150	A	79.9 (11.6)	90	Baseline
31	B3	1	10	B	58.6 (8.5)	60	A	70.3 (10.2)*	90*	
32	C1	1	1	A	144.7 (21.0)	140	—	—	—	
33	C1	1	6	A	64.1 (9.3)	120	B	45.5 (6.6)	40	
34	C1	1	10	E	59.3 (8.6)	110	—	—	—	
35	C1	1	4	A	85.5 (12.4)	135	—	—	—	
36	C2	1	4	A	79.9 (11.6)	130	B	45.5 (6.6)	40	
37	C3	1	4	A	73.7 (10.7)	120	B	46.9 (6.8)	60	
38	D1	1	0.33	B	111.0 (16.1)	160	A	82.7 (12.0)	80	
39	B3	2	1	A	129.6 (18.8)	150	A	76.5 (11.1)	90	Revised HTC's
40	B3	2	1	A	115.1 (16.7)	160	A	70.3 (10.2)	80	Added Radiation from outer cone to insulation
41	C3	2	1	D	81.3 (11.8)	100	B	44.8 (6.5)	60	
42	C3	2	2	D	74.4 (10.8)	100	B	44.1 (6.4)	60	
43	C3	2	3	D	70.3 (10.2)	80	B	44.1 (6.4)	60	
44	C3	2	4	A	66.9 (9.7)	100	B	44.1 (6.4)	60	
45	C4	2	1	A	86.8 (12.6)	120	B	51.0 (7.4)	30	

Shroud/Outer Diffuser Engine Model
Cycle 8 Lightoff
RBSN Shroud
A3 Type Outer Diffuser (RBSN)
Refined Model Configuration in Shroud Seal Area
*B2 Type Outer Diffuser Used

**For locations see Figure 266.

Table 42. Shroud Material Sensitivity in Engine

Case No.	Turbine Shroud	Outer Diffuser	Maximum Principal Stress (MPS)					
			Turbine Shroud			Outer Diffuser		
			Location*	Magnitude, MPa (ksi)	Time After Start, sec	Location*	Magnitude, MPa (ksi)	Time After Start, sec
40	RBSN	RBSN	A	115.1 (16.7)	160	A	70.3 (10.2)	80
46	SASC	RBSN	A	331.5 (48.1)	160	A	102.7 (14.9)	90
47	SSN	RBSN	A	2350.0 (34.1)	180	A	97.2 (14.1)	100

Shroud/Outer Diffuser Engine Model
Second Revision HTCs Used (Engine Condition)
Cycle 8 Lightoff
B3 Type Shroud
A3 Type Outer Diffuser
Refined Model Configuration in Shroud Seal Area

*For locations see Figure 266.

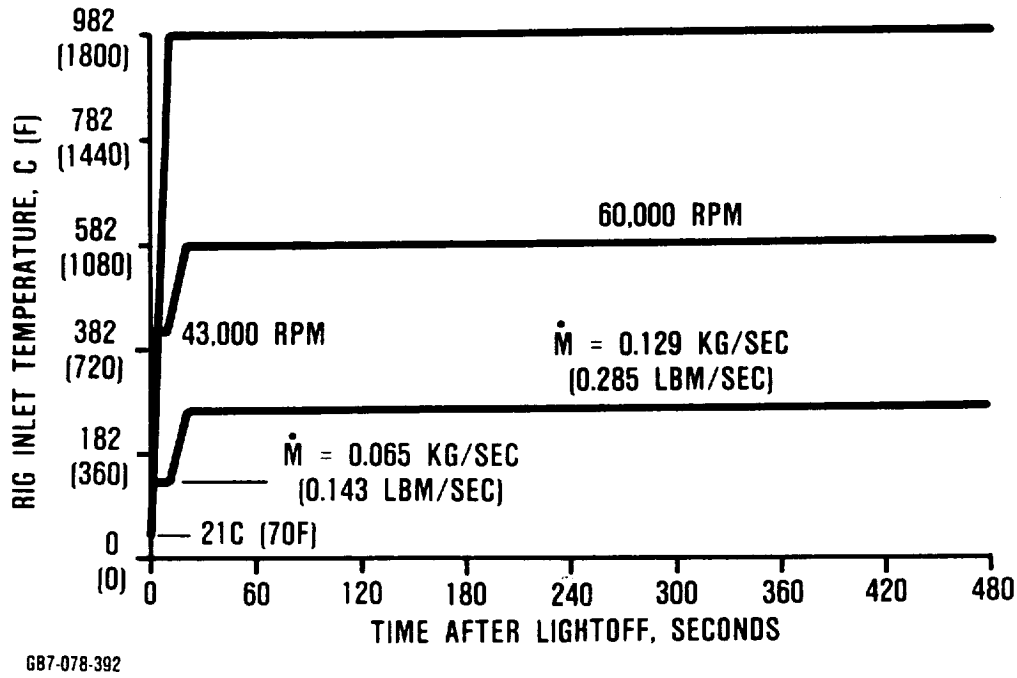

Figure 272. Development Engine Lightoff (Cycle 17).

The combustor baffle diverts the flow from the can combustor into an annulus flow circulation for the turbine section. It is axially contained between the transition duct and turbine backshroud. The baffle utilizes three struts to interface with the transition duct through the flow path. Mechanically, the component must carry a small pressure drop across the component and a spring load. Normally, mechanical loads are negligible. The thermal environment consists of radiant heat from the combustor and convective heat transfer along the flow path, peaking at the stagnation point on the centerline.

The turbine backshroud provides the flow path boundary at the axial backface of the radial turbine rotor. The backshroud has a circular disk geometry with concentricity to the engine centerline provided by a pilot diameter at the turbine stators. The pressure stresses acting on this component are negligible when compared with the thermal stresses. The temperature distribution in the backshroud is significantly influenced by the turbine rotor. The heat transfer coefficients along the backshroud reflect a complex interaction between the rotor speed, blade backface clearance, hub backface clearance, and the resulting hub backface flow distribution. Additionally, the large mass of the rotor hub provides a radiation heat sink during light-off transient conditions.

A 2-D finite element model as shown in Figure 274 was created to evaluate transient thermal stresses. The model was initially used to evaluate component stresses in the static structure rig. Two transient cycles were analyzed, the light-off (cycle 9) and the shutdown (cycle 10) shown in Figures 275 and 276 respectively. Two different materials, RBSN and SASC, were considered for the combustor baffle material. The cases considered and their results for the combustor baffle and transition duct are shown in Table 43. High stresses were found on the combustor baffle struts during shutdown. To reduce

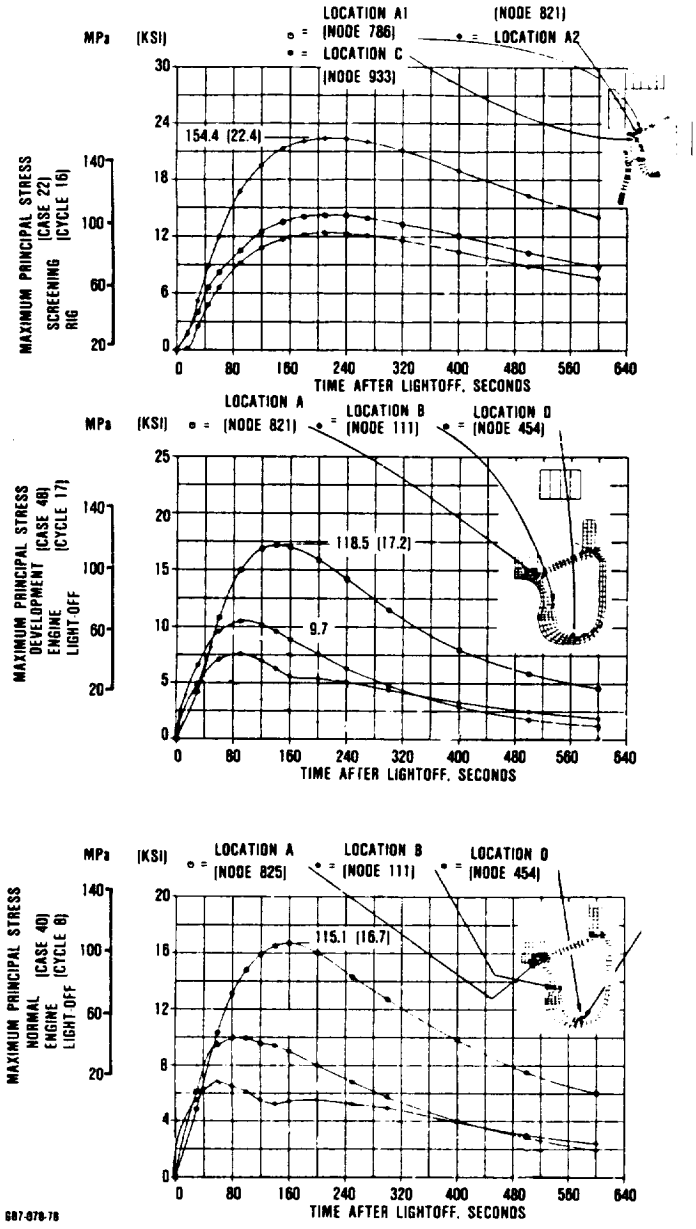

Figure 273. RBSN Shroud Stress for Various Stages of Development.

these stresses, two alternate design configurations for the combustor baffle were considered. The first had struts with the chord reduced 33 percent and the second had struts with wall thickness doubled. The results are summarized as follows:

- o Maximum principal stresses (MPS) of 100.1 and 27.6 MPa (14.6 and 4.0 ksi) were found

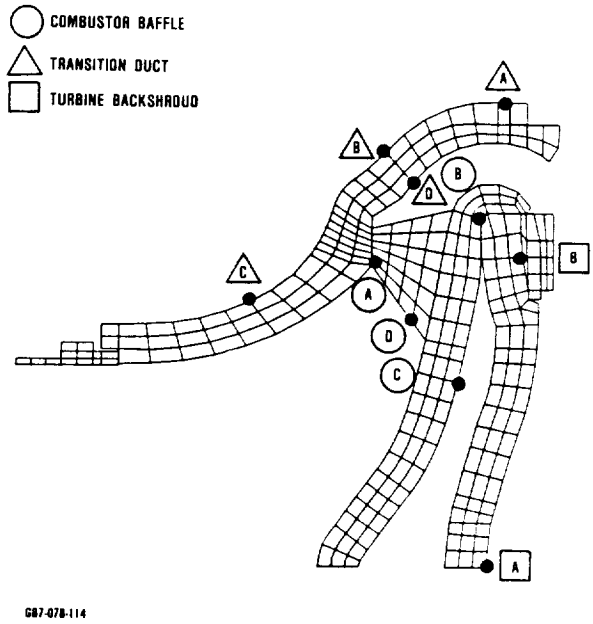

Figure 274. Transition Duct/Combustor Baffle/Turbine Backshroud Critical Stress Areas.

respectively for an SASC combustor baffle and transition duct during light-off.

- o An RBSN combustor baffle has a MPS 34 percent lower than a SASC combustor baffle.
- o The MPS is higher during shutdown (cycle 10) than during light-off (cycle 9) for the combustor baffle.
- o The MPS on the combustor baffle is highest on the struts during both light-off and shutdown.
- o The MPS occurs more rapidly during shutdown than light-off on both the transition duct and combustor baffle.
- o The combustor baffle MPS during shutdown could be reduced 22 percent by decreasing the strut chord by 33 percent.
- o The combustor baffle MPS during shutdown could be reduced 33 percent by doubling the strut thickness.

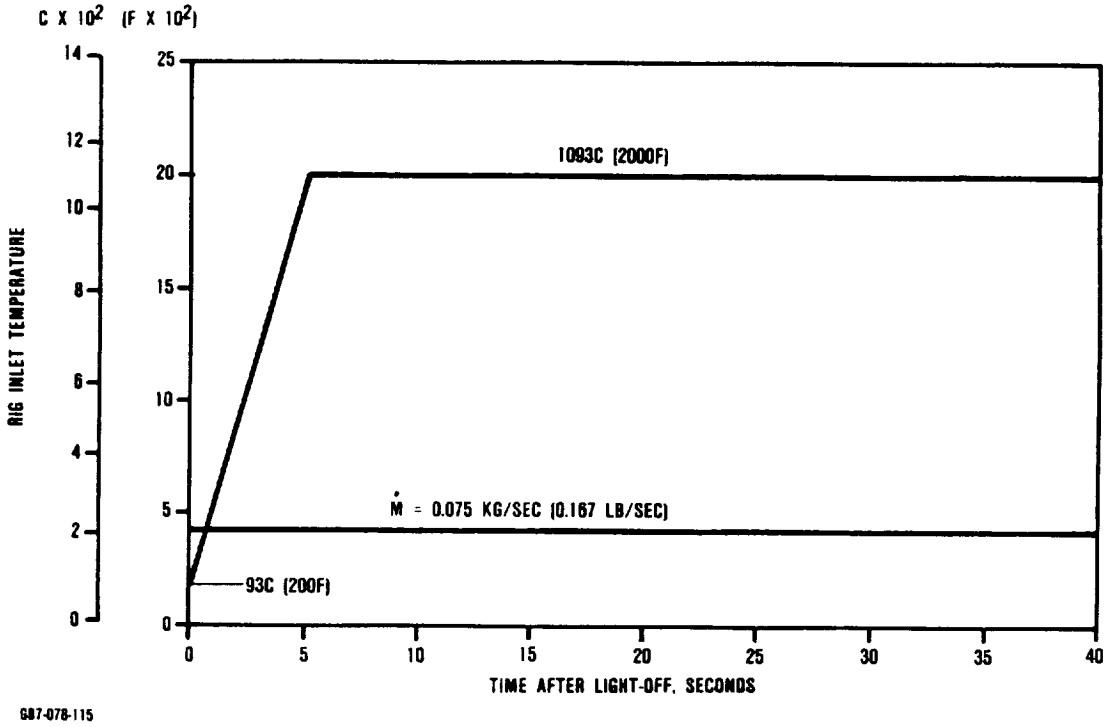

Figure 275. Static Structure Rig Light-off Cycle 9.

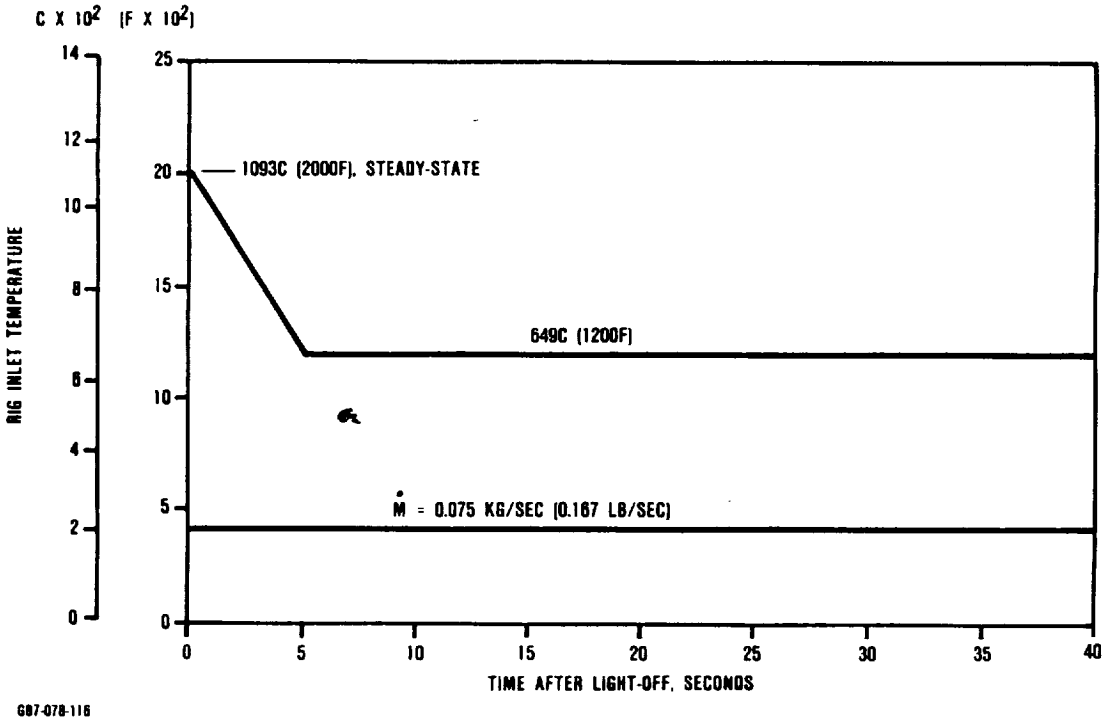

Figure 276. Static Structure Rig Cool-down Cycle 10.

Table 43. Transition Duct/Combustor Baffle Analyses in Static Structure Rig Configuration.

Case No.	Thermal Cycle Type	Thermal Cycle No.	Combustor Baffle Material	Maximum Principal Stresses (MPS)						
				Transition Duct			Combustor Baffle			
				Location*	Magnitude, MPa (ksi)	Time After Start, sec	Location*	Magnitude, MPa (ksi)	Time After Start, sec	Case Description
1	Lightoff	9	SASC	A	27.6 (4.0)	120	A	100.6 (14.6)	240	
2	Lightoff	9	RBSN	A	28.3 (4.1)	120	A	66.2 (9.6)	120	
3	Shutdown	10	SASC	D	26.2 (3.8)	30	D	122.7 (17.8)	30	
4	Shutdown	10	SASC	D	26.2 (3.8)	30	D	95.1 (13.8)	30	33% reduced chord combustor baffle struts
5	Shutdown	10	SASC	D	26.2 (3.8)	30	D	82.0 (11.9)	30	Doubled thickness combustor baffle struts

SASC Transition Duct
SSN type A1 Turbine Backshroud
Type A1 Combustor Baffle
*For location see Figure 274

Changes to the combustor baffle strut design were not made since shutdown conditions during engine operation have been made much less severe than the shutdown cycle analyzed. To ensure against failures in the static structure rig, the shutdown cycle was made more gradual. The combustor baffle alternate design configurations were kept as backup designs.

The transition duct/combustor baffle/turbine backshroud model was then modified to reflect engine conditions. The primary difference consists of including radiative and convective heat transfer to the turbine rotor. The turbine rotor component has a large thermal inertia and acts as either a heat sink or source during transient operating conditions. In addition for the 1149C (2100F) development engine with the dual alloy metallic turbine wheel, turbine bore cooling would impinge upon the backshroud.

Table 44 shows the results of a study on the dual alloy rotor effect on the transition duct, combustor baffle, and turbine backshroud stresses. For MPS locations refer to Figure 274. The study considered effects with and without turbine bore cooling, backflow circulation between the rotor and backshroud, and mixing of the circulation. Midway through the study the analysis was updated to include the change from an A1 to A2 type combustor baffle (Figure 277) and an SSN to SASC turbine backshroud. All results are for a light-off cycle to 1149C (2100F) maximum power condition (cycle 15), as shown in Figure 278 to evaluate rotor backflow effect with engine speed. Following is a summary of the significant results:

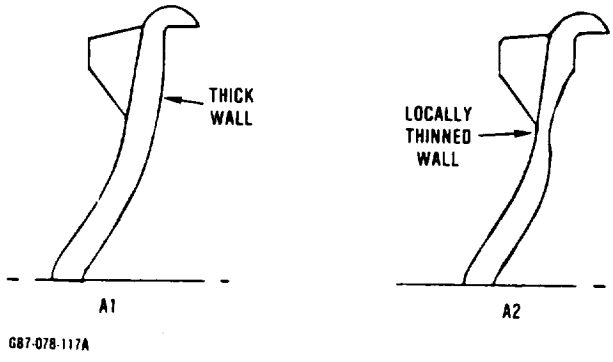

Figure 277. A1 and A2 Configurations Combustor Baffle.

- o High turbine backshroud MPS were found in all cases with the rotor modeled.
- o The consideration of turbine bore cooling significantly increased the MPS (66 to 70 percent increase) on the turbine backshroud. MPS occurs after engine speed reaches 100,000 rpm.
- o The effect of rotor backflow circulation reduced the MPS on the turbine backshroud.
- o The effect of mixing in rotor backflow circulation increased the MPS on the turbine backshroud.
- o The effect of the rotor on the transition duct and combustor baffle stresses is insignificant.
- o The MPS on the transition duct does not occur during the initial light-off, but after rotor speed reaches 100,000 rpm.

Table 45 shows the results for various component materials considered for the all ceramic engine with an SSN turbine rotor. The analyses assumed rotor backflow circulation with mixing, but no rotor bore cooling. For comparative purposes the operating cycle (cycle 15) was the same as for the previous engine analyses. The results for these analyses are as follows:

- o The transition duct MPS is almost independent of the choice of materials for the combustor baffle or turbine backshroud.
- o An RBSN combustor baffle has the lowest MPS followed by SSN and SASC with the highest.
- o The turbine backshroud MPS decreases 6 percent when an SSN combustor baffle is substituted for an RBSN combustor baffle.

Table 44. Transition Duct/Combustor Baffle/Turbine Backshroud Analyses with Rotor Effect

Case No.	Combustor Baffle Type	Turbine Backshroud Material	Turbine Rotor Bore Cooling	Turbine Rotor-Backshroud Circulation	Mixing of Circulation	Maximum Principal Stress (MPS)								
						Transition Duct			Combustor Baffle			Turbine Backshroud		
						Location*	Magnitude, MPa (ksi)	Time After Start, sec	Location*	Magnitude, MPa (ksi)	Time After Start, sec	Location*	Magnitude, MPa (ksi)	Time After Start, sec
6	A1	SSN	No	No	--	A	44.8 (6.50)	310	A	126.8 (18.4)	120	A	280.5 (40.7)	120
7	A1	SSN	Yes	No	--	A	45.5 (6.6)	310	A	126.1 (18.3)	120	A	466.6 (67.7)	420
8	A2	SASC	No	Yes	No	B	37.9 (5.5)	600	A	181.9 (26.4)	180	A	178.5 (25.9)	120
9	A2	SASC	No	Yes	Yes	B	38.6 (5.6)	600	A	178.5 (25.9)	180	A	186.8 (27.1)	120
10	A2	SASC	Yes	Yes	Yes	B	37.9 (5.5)	600	A	179.2 (26.0)	180	A	317.7 (46.1)	420

Engine Configuration
Dual Alloy Metallic Rotor
SASC Transition Duct
SASC Combustor Baffle
Type A Backshroud
Cycle 15 Lightoff

* For location see Figure 274

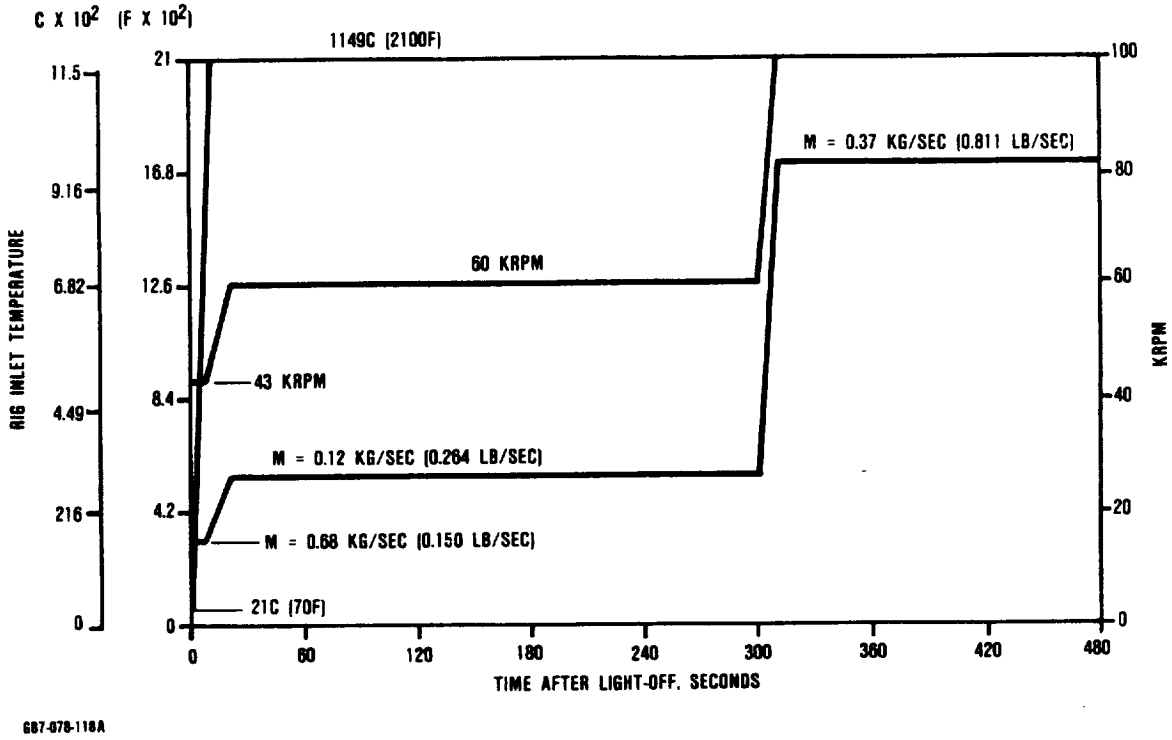

Figure 278. Engine Cycle 15 (Light-Off to 1149C Max Power).

Fracture of a ceramic turbine backshroud during a structures rig qualification test in August 1984 led to a design change which incorporates a hole in the center of the turbine backshroud. In this way, the highly stressed area of the part was, in fact, physically eliminated from the design. A piece of insulation was installed between the backshroud and the baffle to avoid thermally stressing the combustor baffle. This is particularly significant in the 1149C (2100F) configuration engine, where bore cooling is used to cool the dual-alloy rotor.

The results for an analysis of this configured backshroud are shown in Table 46 along with the original and another proposed configured backshroud. The original, the truncated center configuration, and the recontoured turbine backshroud have been designated as the A1, A2, and B1 type as shown in Figure 279 respectively. The contoured backshroud was analyzed for both an SSN and SASC material. All analyses are for the engine with an SSN turbine rotor. The significant results are:

- An A2 type turbine backshroud has a MPS 82-percent lower than for the original (A1) configuration.
- A B1 type turbine backshroud has a MPS 23-percent lower than for the original (A1) configuration.
- A SASC type B1 turbine backshroud has a MPS 8-percent lower than a SSN backshroud. The corresponding MPS in the combustor baffle increases 7 percent.

6.3.1.5 Flow Separator Housing

The flow separator housing (Reference Figure 250) is the largest asymmetrical ceramic component in the AGT101. This housing provides the flow path split between the high pressure and low pressure portions of the engine to accommodate the regenerator waste heat recovery system. The low pressure (gas side) of the flow separator housing is rapidly heated after lightoff while the high pressure (air side) heating lags due to the regenerator core thermal mass. Pressure loading of this

Table 45. Transition Duct/Combustor Baffle/Turbine Backshroud Model Material Study

Case No.	Transition Duct	Combustor Baffle	Turbine Backshroud	Maximum Principal Stress (MPS)								
				Transition Duct			Combustor Baffle			Turbine Backshroud		
				Location	Magnitude, MPa (ksi)	Time After Start, sec	Location*	Magnitude, MPa (ksi)	Time After Start, sec	Location*	Magnitude, MPa (ksi)	Time After Start, sec
11	SASC	SASC	SSN	B	39.3 (5.7)	510	A	175.7 (25.5)	165	A	206.8 (30.0)	105
12	SASC	SSN	SASC	C	39.3 (5.7)	480	A	150.9 (21.9)	120	A	186.1 (27.0)	90
13	SASC	RBSN	SASC	C	39.3 (5.7)	460	A	111.0 (16.1)	120	A	198.5 (28.8)	90

Engine Configuration
Ceramic (SSN) Turbine Rotor
Type A2 Combustor Baffle
Type A1 Turbine Backshroud
Cycle 15 Lightoff
Turbine Rotor/Backshroud Circulation with mixing

* For locations see Figure 274

Table 46. Turbine Backshroud Alternate Configuration Study

Case No.	Turbine Backshroud Material	Type	Maximum Principal Stress (MPS)								
			Transition Duct			Combustor Baffle			Turbine Backshroud		
			Location*	Magnitude, MPa (ksi)	Time After Start, sec	Location*	Magnitude, MPa (ksi)	Time After Start, sec	Location*	Magnitude, MPa (ksi)	Time After Start,)sec
11	SSN	A1	B	39.3 (5.7)	510	A	175.7 (25.5)	165	A	206.8 (30.0)	105
14	SASC	A2	C	40.0 (5.8)	600	A	183.3 (26.6)	180	A	36.5 (5.3)	60
15	SSN	B1	B	39.3 (5.7)	480	A	169.5 (24.6)	180	A	159.2 (23.1)	120
16	SASC	B1	—	—	—	A	181.9 (26.4)	180	A	146.8 (21.3)	90

Engine Configuration
Ceramic (SSN) Turbine Rotor
Type A2 Combustor Baffle (SASC)
SASC Transition Duct
Cycle 15 Lightoff

* For locations see Figure 274

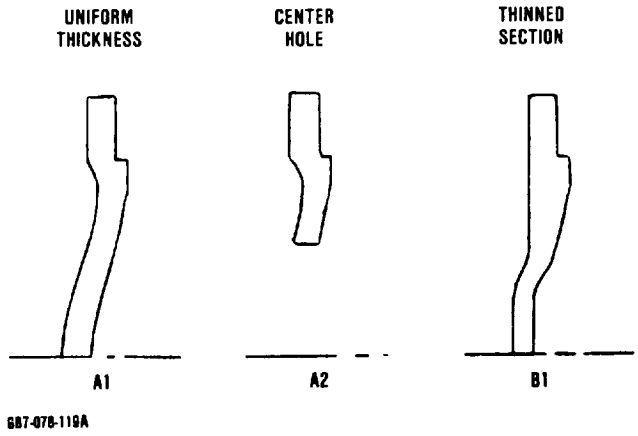

Figure 279. Alternate Configurations of the Turbine Backshroud.

housing further complicates the stress field as the high pressure (air side) is asymmetrically loaded at higher engine pressure ratios. Due to the complex shape and the locally varying thermal and pressure environment, 3-D finite element analysis were utilized to evaluate component deflections along sealing surfaces and associated stresses. Two material candidates were evaluated for this component, LAS and RBSN, although LAS was the only material from which actual components were made.

Strain gage testing of a LAS flow separator housing was done in May 1981 at Corning Glass Works. Fourteen uniaxial and seventeen triaxial strain gages were attached to S/N-7 housing in critical stress areas determined from earlier 3-D finite element analyses. Strain gage data were taken up to 414 kPa (60 psi) in increments of 27.6 kPa (4 psi) both in air and water environments in the flow separator housing mechanical screening rig.

Figure 280 shows the stress values at similar housing locations for a comparison between the stresses attained during the strain gage tests and the earlier 3-D stress analysis. In both cases, high stresses occur on the pressure half of the housing. The three notable similarities are along the outer rim (location 2), in the center of the inner side of the rim (location 1), and along the fillet radius at the corner of the HP slot (location 4). There are two reasons for the discrepancies. First, the

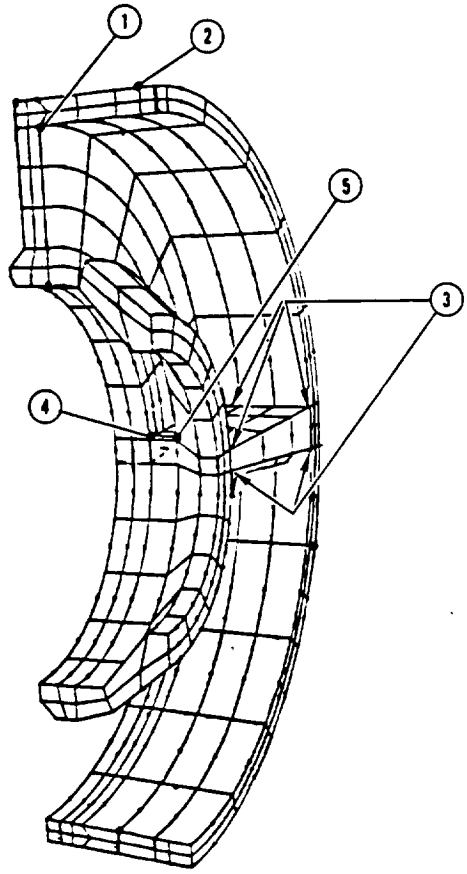

STRESS VALUES AT SIMILAR HOUSING LOCATIONS

LOCATION		STRESS MPa (KSI)		
		GARRETT	FORD AT 366.1 kPa (53.1 PSI)	
①	1.5	(2.3)	13.8	(2.0)
②	13.1	(1.9)	15.2-17.2	(2.2-2.5)
③	6.3-13.8	(1.0-2.0)	3.1-7.9	(0.45-1.15)
④	15.2	(2.2)	17.6-19.3	(2.55-2.8)
⑤	11.7	(1.7)	2.8	(0.4)

887-078-120

Figure 280. Flow Separator Housing Strain Gage Test Correlation.

physical characteristics of the test and analytical model differ, and secondly, the stress locations may not be exactly coincident.

Due to the considerable difference in material properties, the RBSN component design was sized to have considerably thinner walls to take advantage of its higher strength.

A 3-D finite element model was created of the thin wall configuration and stresses and deflections were determined. The model was constrained against rigid body motion only for evaluation of thermal stresses. For evaluating pressure stresses, the model was axially constrained at all of the circumferential row of nodes that interface with the flow separator housing support ring. In addition, nodes at the location of the piloting slots were constrained against rigid body radial motion. Pressure stresses and deflections were found acceptable, but both thermal stresses and deflections at the regenerator seal surface were found to be excessive. The thermal stresses and deflections during light-off increased with time during the transient interval and were found to be maximum at steady-state operating condition. To reduce the deflections at the regenerator seal surface, a strutted configuration was created. Four struts were located 60 degrees apart, two in the HP side, and two in the LP side. The finite element model of the strutted configuration is shown in Figure 281 alongside the original configuration.

The strutted housing was analyzed and was found to have improvements in seal deflection but not in thermal stresses. Large, thermal gradients were being created in the housing from the heat sink effect of the outer flange being exposed to compressor discharge air. To eliminate this heat sink, another configuration (type X1) was created without this flange. The axial support was thereby removed to the diffuser end of the flow separator housing as shown in Figure 282. Insulation would be applied at the outer diameter of the flow separator housing to shield the component from compressor discharge air impingement. Axial pins would extend from the axial support to provide piloting for the component.

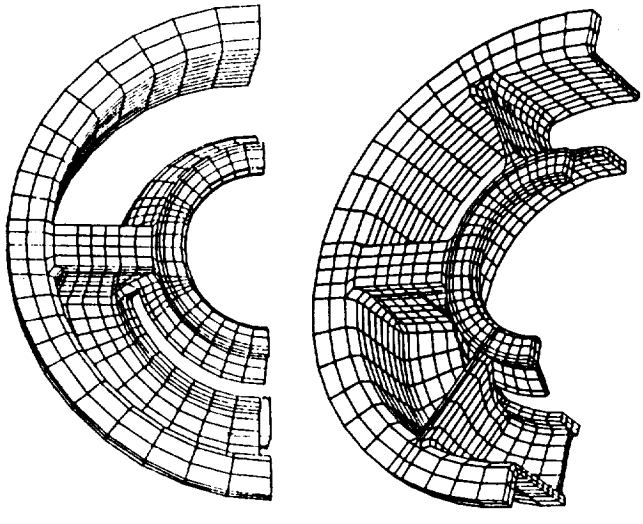

687-078-121

Figure 281. The Original and Strutted RBSN Flow Separator Housing FEMS.

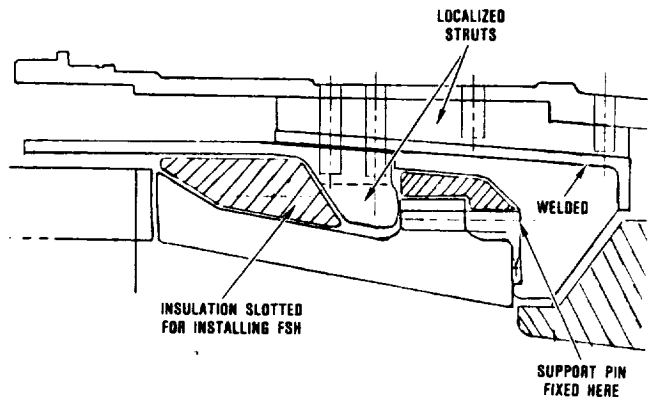

687-078-122

Figure 282. Flangeless Flow Separator Housing Outer Cone and Attachment Configuration (Type X1).

Table 47 shows the results of the finite element analyses for the maximum power pressure conditions. All three configurations have been evaluated with RBSN; the first two configurations have also been evaluated with LAS material. The location of the critical stress areas are shown in Figure 283. Comments regarding pressure stresses on the flow separator housing follow:

- Pressure stresses are almost independent of component material.
- The MPS due to pressure loading is 8 percent lower in the strutted (B2) configuration compared to the original (B1) configuration.

Table 47. Flow Separator Housing Pressure Stresses.

Case No.	Configuration Type	Material	Maximum Principal Stress (MPS)	
			Flow Separator Housing	
			Location	Magnitude, MPa (ksi)
01	B1	RBSN	A	47.6 (6.9)
02	B2	RBSN	B	44.1 (6.4)
03	X1	RBSN	C	18.5 (2.7)
04	B1	LAS	A	47.6 (6.9)
05	B2	LAS	B	43.4 (6.3)
1371C (2500F) Maximum Power Condition 100,000 rpm				

*For locations see Figure 283

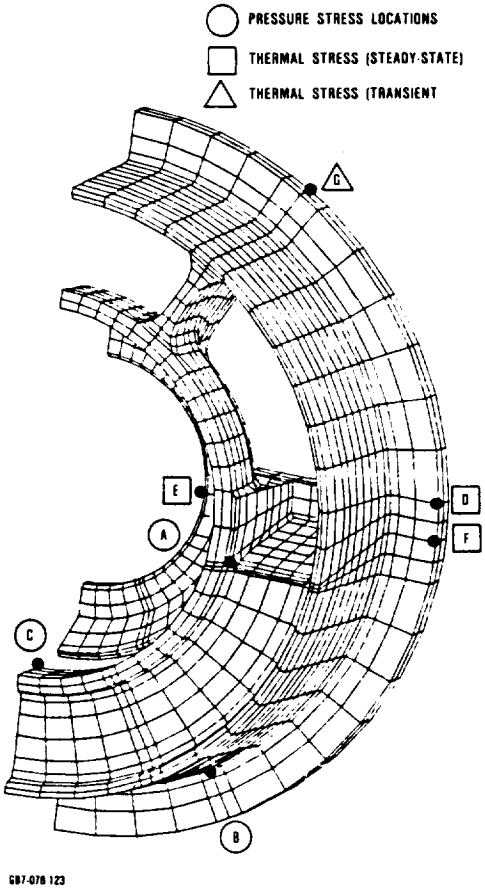

Figure 283. Flow Separator Housing Critical Stress Areas.

- Because the axial loading due to pressures is reacted out directly behind the HP cavity in the flangeless (X1) configuration as opposed to being reacted out at the flanges in the original (B1) configuration, pressure stresses are much lower (61 percent) in the flangeless configuration.

- Because of the lower strength of LAS, pressure stresses are more critical for the LAS material.

An acceptable design for the flow separator housing must be able to provide a flat platform for the regenerator seal surface as well as provide a low MPS. The corresponding regenerator seal platform deflection for the previous pressure analyses are shown in Figures 284, 285, and 286. These curves trace the axial deflection of the inner platform circumferentially 180 degrees from the HP to the LP side of the component. Figure 286 also traces deflections along the outer platform since the type X1 configuration is supported at the opposite side from the platform. Concerning pressure deflections on the flow separator housing, the following conclusions are drawn.

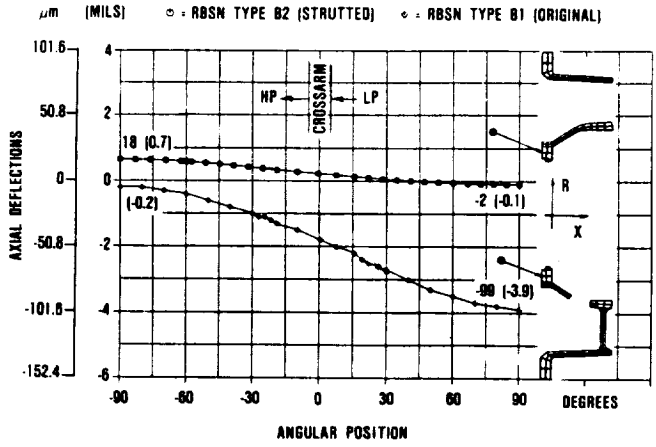

687-078-124

Figure 284. Pressure Deflections at the Regenerator Seal for Types B1 and B2 RBSN Flow Separator Housings.

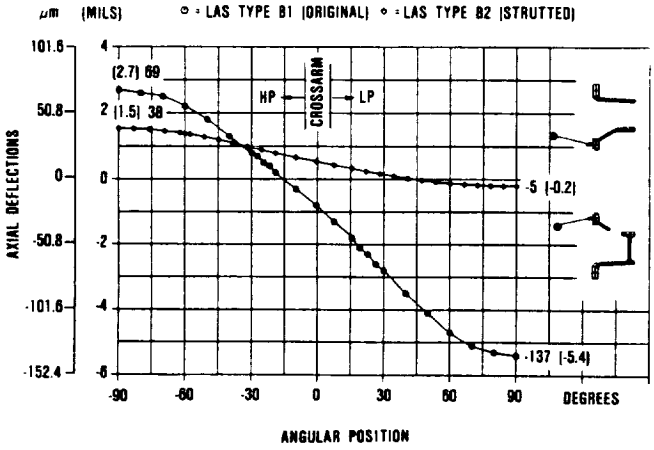

687-078-125

Figure 285. Pressure Deflections at the Regenerator Seal for Types B1 and B2 LAS Flow Separator Housings.

- The material with the highest modulus of elasticity (RBSN) had the least variation in deflections at the inner regenerator seal platform for the type B1 and B2 configurations.

- The B2 configuration had 81 percent less variation in the inner regenerator seal platform deflection than the B1 configuration.

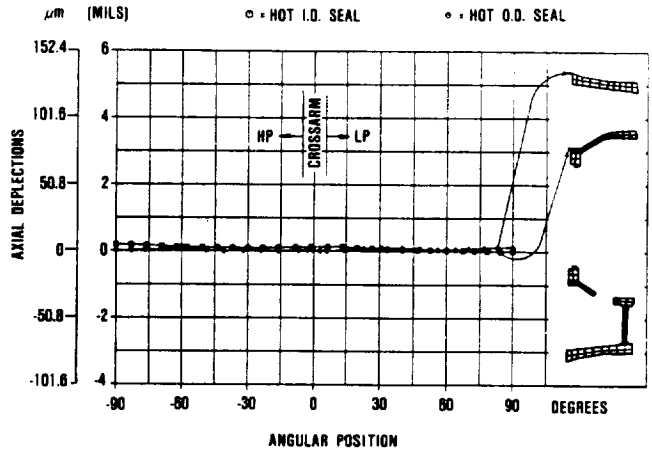

687-078-126

Figure 286. Pressure Deflection at the Regenerator Seal for Type X1 RBSN Flow Separator Housing.

- The X1 configuration had 95 percent less variation in the inner regenerator seal platform deflection than the B1 configuration.

- The low spot on the inner regenerator seal axial surface is located midway between the crossarms on the HP side of the flow separator housing.

The thermal stresses and deflections were also investigated at steady state cruise condition [1218C (2225F) T_4]. Circumferential thermal gradients are created by the difference in turbine exit temperature ($T_{5.1}$) and combustor inlet temperature ($T_{3.5}$) at the LP and HP side respectively. Radial gradients are created by the combustor inlet temperature ($T_{3.5}$) and the inner diameter and the compressor discharge temperature ($T_{3.1}$) at the outer flange. Radial gradients were found to contribute most to the overall thermal gradient. Figure 287 shows the variation in steady-state temperature along the crossarms of an LAS flow separator housing. The sensitivity of thermal stresses and deflections to

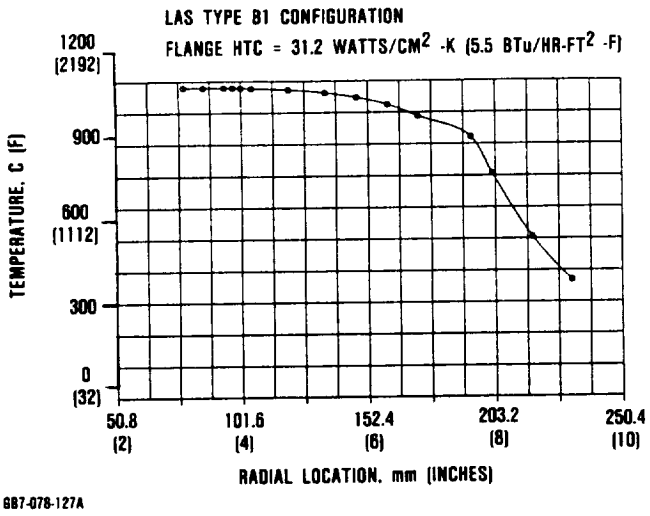

Figure 287. Steady-State Cruise Radial Temperature Distribution Along the Flow Separator Housing Crossarm.

the heat transfer coefficients over the outer flange were assessed by analyzing two different sets of heat transfer coefficients. The results of the stress analyses are shown in Table 48. The type X1 flow separator housing was not analyzed since the worst case thermal stresses and deflections occurs during light-off for this configuration. The results are summarized as follows:

- The MPS is very sensitive to the assumed heat transfer coefficient between the flow separator housing flange and the compressor discharge temperature. The MPS is more sensitive for components made from RBSN than LAS.
- The strutted (B2) configuration MPS is significantly higher than the MPS for the original (B1) configuration.
- The MPS occurs at the outer surface of the outer flange except for the single case with high heat transfer coefficients on LAS where the MPS occurs on the inner surface of the inner cone.

The type B1 flow separator housing regenerator seal thermal deflections are shown in Figure 288 for both the RBSN and LAS material at steady-state cruise conditions. The axial deflections at the regenerator seal inner surface are plotted against the angular position for two different sets of heat transfer coefficients over the outer flange. Figure 289 shows the regenerator seal surface deflection results for the type B2 RBSN flow separator housing. The deflection results for the steady state thermal cruise condition are summarized as follows:

- The effect of the heat transfer coefficient over the outer flange on the platform

Table 48. Flow Separator Housing Steady-State Thermal Stresses.

Case No.	Configuration Type	Material	Flange Heat Transfer Coefficient, Watts / cm^{2}C	Flange Heat Transfer Coefficient, Btu / Hr - ft^2-F	Maximum Principal Stress (MPS) Flow Separator Housing Location*	Magnitude, MPa	(ksi)
06	B1	RBSN	31.2	(5.5)	D	133.0	(19.3)
07	B1	RBSN	5.7	(1.0)	D	42.0	(6.1)
08	B1	LAS	31.2	(5.5)	E	26.9	(3.9)
09	B1	LAS	5.7	(1.0)	D	20.0	(2.9)
10	B2	RBSN	28.4	(5.0)	F	192.3	(27.9)
Steady-State Cruise 1218C (2225F)							

*For locations see Figure 283

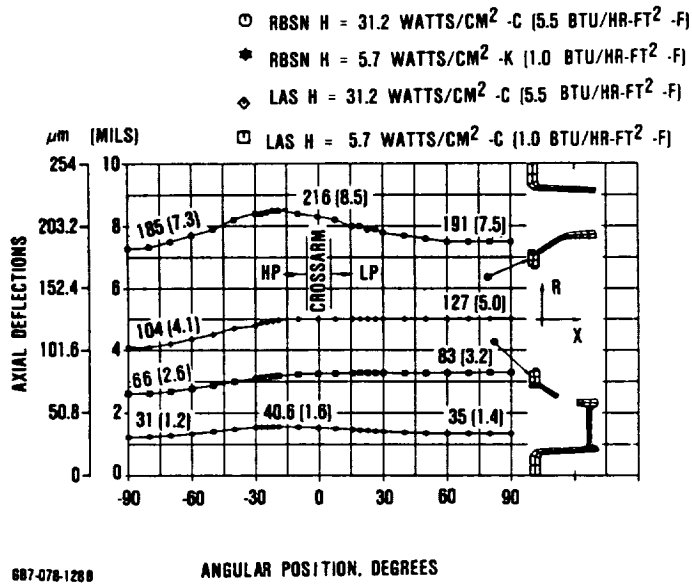

Figure 288. Steady-State Cruise Thermal Deflections at the Regenerator Seal for Type B1 RBSN and LAS Flow Separator Housing.

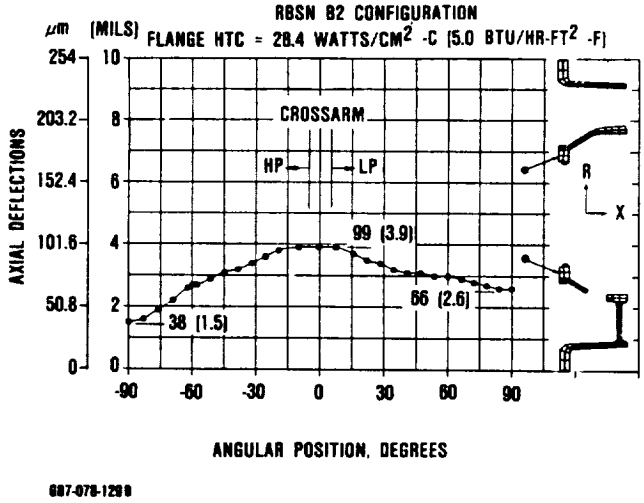

Figure 289. Steady-State Cruise Thermal Deflections at the Regenerator Seal for the RBSN Type B2 Flow Separator Housing.

deflection is similar to the MPS. Specifically, the deflections are very sensitive to the assumed value of heat transfer coefficients, greater for RBSN than for LAS.

- At the higher value of heat transfer coefficients (31.2 watts/cm^{2}C) the regenerator seal platform deflections are greater for housing. At the lower value of heat transfer coefficients (5.7 watts/cm^{2}C) the opposite is true.

- The strutted (B2) configuration has a significantly lower level of regenerator seal platform deflections (68 percent on the average) than the original (B1) configuration but has a higher variation (100 percent) in-deflections.

The transient light-off to cruise condition (cycle 8 in Figure 264) was also evaluated for the flow separator housing. The maximum thermal gradient for both the B1 and B2 type flow separator housings occurred at steady state conditions. Consequently, the MPS for these configurations also occurred at the steady state condition. Figure 290 shows the

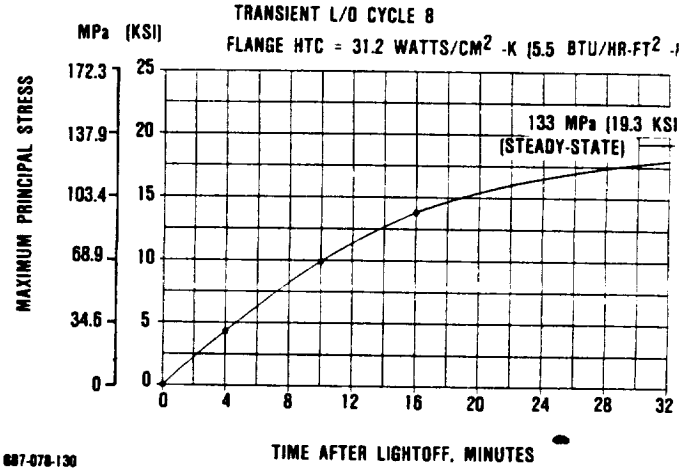

Figure 290. Type B1 Flow Separator Housing Thermal Stress Response During Lightoff.

transient MPS response for the type B1 configuration, which was typical for the configurations with the outer flange exposed to the compressor discharge air. The MPS for the flangeless (X1) configuration was found to occur during the transient light-off interval of the operating cycle. Table 49 shows the MPS for two cases that were considered. The first model, as with the steady-state analyses

Table 49. Flow Separator Housing Transient Thermal Stresses

Case No.	Configuration Type	Material	With Inner to Outer Cone Radiation	Maximum Principal Stress (MPS) Flow Separator Housing		
				Location	Magnitude, MPa (ksi)	Time After Start, sec
11	X1	RBSN	No	G	186.1 (27.0)	900
12	X1	RBSN	Yes	G	104.8 (15.2)	600
Cycle 8 Lightoff						

*For locations see Figure 283

neglected the radiation between the inner and outer cones of the flow separator housing. The latter analysis included this radiation. The results are summarized as follows:

- Without cross radiation from the inner to outer cone, the MPS is higher for the flangeless (X1) compared to the original (B1) RBSN flow separator housing at steady-state conditions.
- With cross radiation, the MPS is lower for the flangeless compared to the original RBSN flow separator housing at steady-state conditions.
- Including cross radiation reduces the transient time to MPS.

In September 1985, the metal engine (S/N 001/Build 34) was tested with 32 thermocouples attached to a metallic flow separator housing. Additional instrumentation was used to monitor the inlet guide vane setting, flow path temperature, and engine speed. Data was recorded and reduced for three transient light-offs to low cruise (60,000 rpm) condition. The boundary conditions and light-off cycle was duplicated with an analytical model of a metallic flow separator housing and resulting transient temperature responses were compared to the test results. Initial comparison showed a significant lag in the temperature response in the analytical model compared to test results. Inclusion of cross radiation between the inner and outer cone of the flow separator and increased heat transfer coefficients helped but still were insufficient to show correlations. The most reasonable hypothesis is that combustor heat reradiating from the transition duct should have been modeled since it apparently provides a significant heat input to the flow separator housing. The foregoing conclusion is that the transient response and perhaps the MPS is less than determined from analyses.

6.3.1.6 Turbine Stators

The design and development of the turbine stators (reference Figure 250) is primarily controlled by its severe thermal environment. High core flow velocities produces high heat transfer coefficients, which coupled with the required nonuniform vane profile, creates high thermal stresses at the vane trailing edge during engine light-offs. High reliability and survivability is also essential to ensure that even minor stator damage does not lead to secondary impact failure of the turbine rotor.

The initial development effort concentrated on the segmented stator concept designed in 1980. Both RBSN and SASC stators were fabricated. In November 1984 a stator thermal screening test was run using the turbine shroud screening rig. The test objective was to thermally shock stator segments (RBSN) to normal engine start conditions (plus 25-percent stress margin). Following the test, no cracks were found in the stator trailing edge.

In February 1985, a segmented stator set (SASC) was again run to the same screening rig cycle used to proof the RBSN stators. The test was unsuccessful; nearly all of the stator segments were fractured, and two were fully parted down the vane centerline. Fractures were seen to initiate from the stator vane trailing edge area, which is the most highly stressed portion of the part. As a result of this testing, it became apparent that survivability of stators is a concern under thermal transient conditions. In order to improve the survivability of stators a design modification was made which incorporated a 3 mm (0.120-inch) radius cutback at the trailing edge. This scallop of the trailing edge represents approximately a 1-percent penalty in performance, but appeared to improve the survivability of the stators under thermal transient conditions. This was seen in subsequent testing, as for example, an RBSN stator set on March 6, 1985 and another SASC stator set on May 3, 1985. The cutback employed is illustrated in Figure 291.

An analytical effort was initiated to assess the merit of a cutback trailing edge compared to the original configuration stator vane. Finite element analysis models as shown in Figure 292 were created for both configurations. The thermal model included adjacent sections of both the shroud and backshroud as shown in Figure 293 to provide the correct transient heat fluxes at the stator support interfaces. Radiation and convective heat transfer were considered at the non-contacting interfaces between the stator and shroud, and stator and backshroud. Adiabatic wall conditions were assumed at the remaining surfaces of the backshroud and shroud. In conjunction with this thermal model an ANSYS stress model was created.

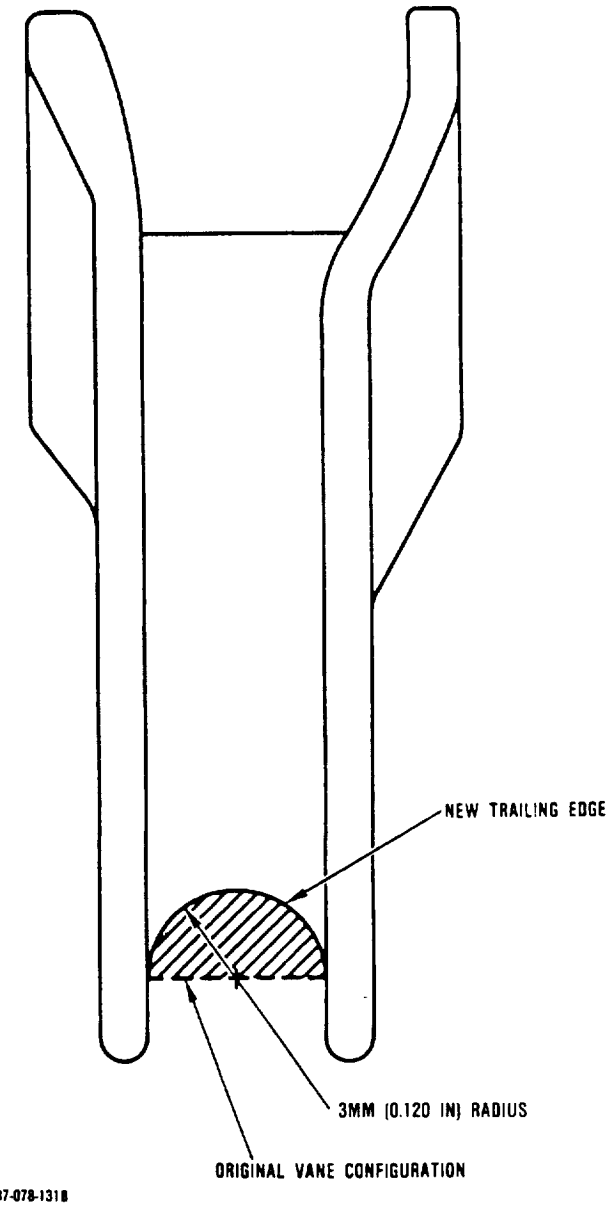

Figure 291. Turbine Stator Cutback Vane Trailing Edge Redesign.

Before any analysis was made for the ceramic stators, verification of the stator flow path heat transfer coefficients was first accomplished. The metal engine, S/N 001/ Build 34, was run in September 1985 with 23 thermocouples attached to an integral

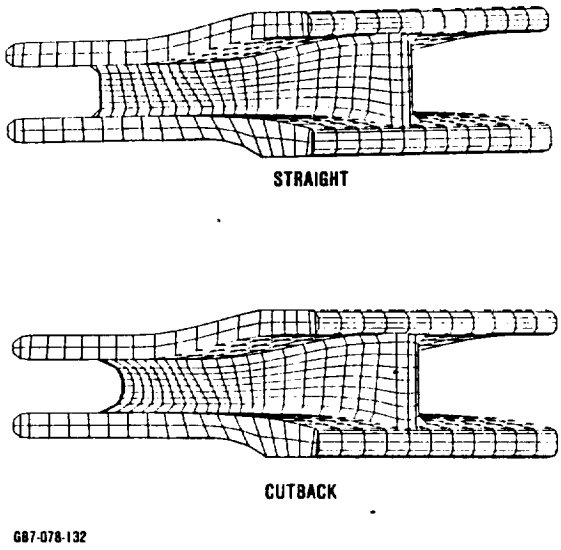

Figure 292. Turbine Stator Finite Element Stress Models.

metallic stator assembly as shown in Figure 294. This run occurred in conjunction with a similarly instrumented flow separator housing. The transient thermal response for three light-

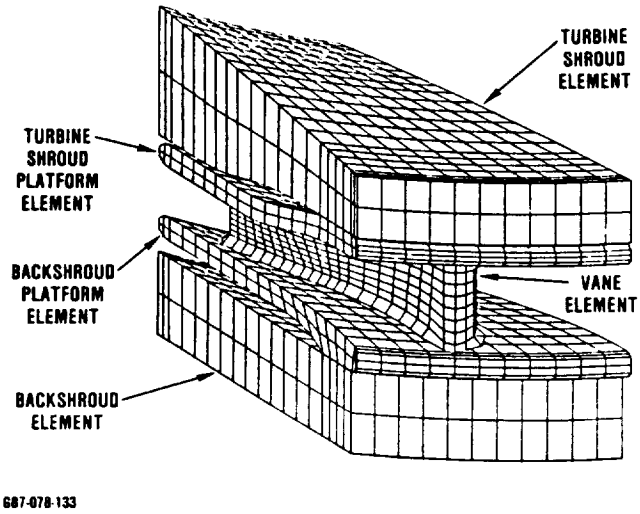

Figure 293. Turbine Stator Finite Element Thermal Model.

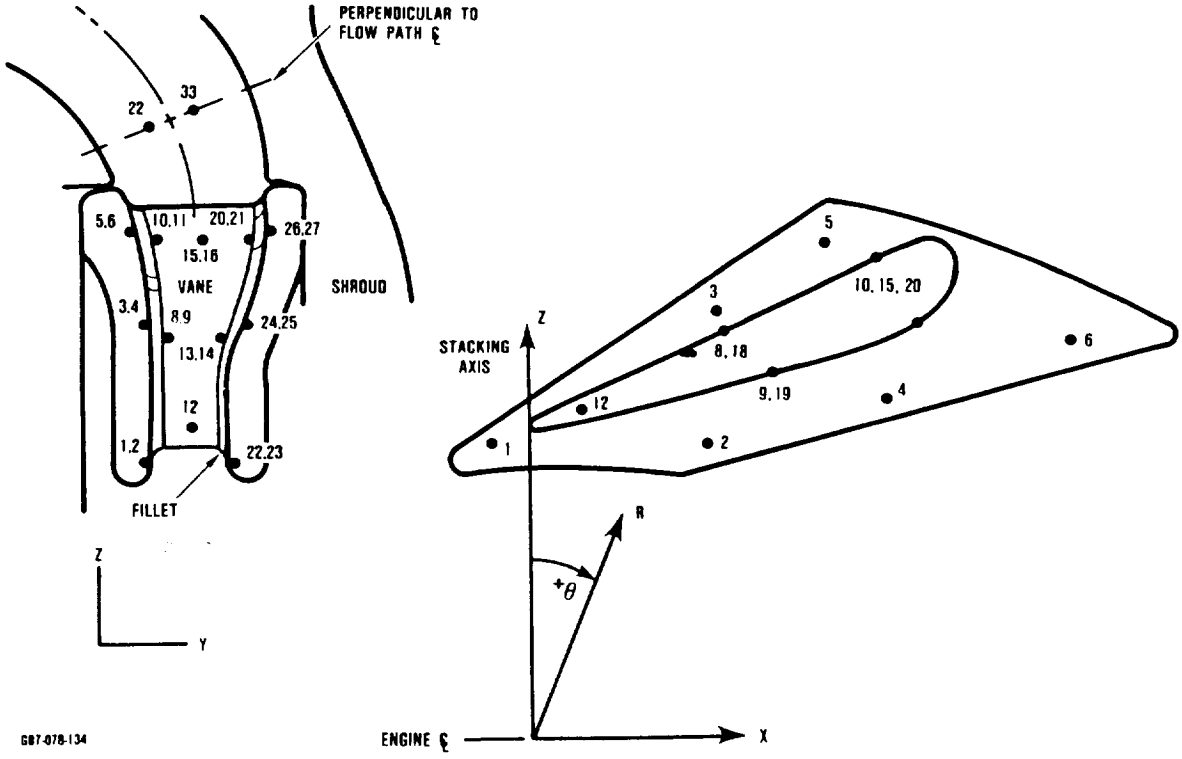

Figure 294. Metallic Stator Assembly Thermocouple Locations.

offs were recorded and reduced. Engine light-off parameters were then simulated in a 3-D thermal analysis of the metallic turbine stator model. Temperatures from the analysis were than compared to the measured test results. A good correlation was found using the originally calculated heat transfer coefficients if the measured thermal response was assumed to lag due to thermocouple limitations. Two representative comparisons between the measured and calculated thermal responses are at the mid-span leading and trailing edges as shown in Figure 295.

The analytical comparison between the original straight and the cutback trailing edge stators was then done using the foregoing verified heat transfer coefficients. The thermal analyses assumed the turbine stator, backshroud, and shroud was RBSN. The engine start cycle (cycle 17) corresponded to the development engine cycle as shown in Figure 272. Both the original and cutback vanes were analyzed. The results were almost identical. The temperature distribution at 20 seconds after lightoff is shown in Figure 296. The peak temperature occurs at the mid-span of the vane trailing edge and cools off spanwise and chordwise along the vane.

Stress analyses were then conducted at various times after lightoff to determine the

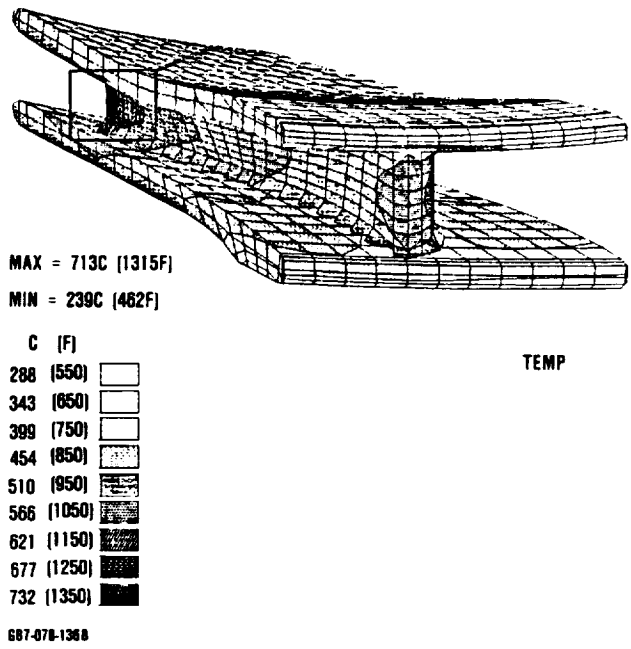

Figure 296. Turbine Stator Temperature Distribution 20 Seconds After Light-Off.

stress response. The MPS was found to occur at the mid-span of the vane trailing edge for both stator configurations. As shown in Figure 297 the MPS response at this location was very similar; the MPS for the original configuration was slightly higher (88.7 MPa compared to 88.3 MPa). No discernible difference was

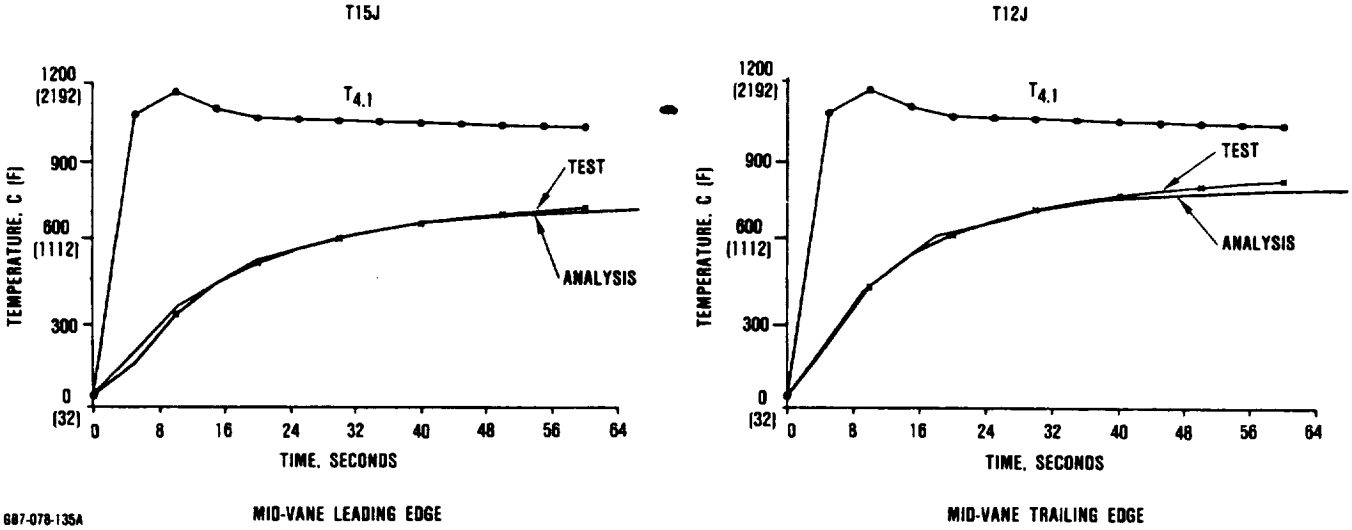

Figure 295. Typical Correlation Between Test and Analytical Turbine Stator Thermal Response.

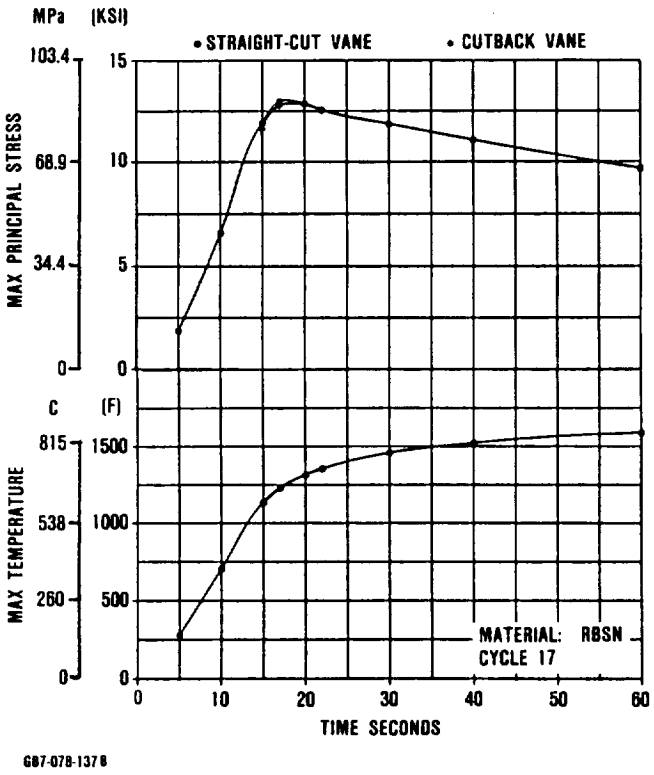

Figure 297. Turbine Stators Maximum Temperature and MPS Response (at Mid-Span Trailing Edge).

found in the temperature response at the mid-span trailing edge. The MPS occurs 17 to 20 seconds after lightoff. The 3-D plots of the MPS at this time (20 seconds after lightoff) are shown in Figures 298 and 299 for the original and cut-back trailing edge turbine stators respectively.

To resolve this apparent discrepancy between analysis and test results further testing needs to be conducted. For these tests, a significant sampling of stators should be carefully inspected and documented in the critical stress areas then destructively tested under increasingly severe thermal transient conditions. Only after correlation between inspection data and test results have been made can an opinion be formulated as the whether this discrepancy between analysis and test is due to analysis error or non-nominal effects of the component geometry and/or material processing.

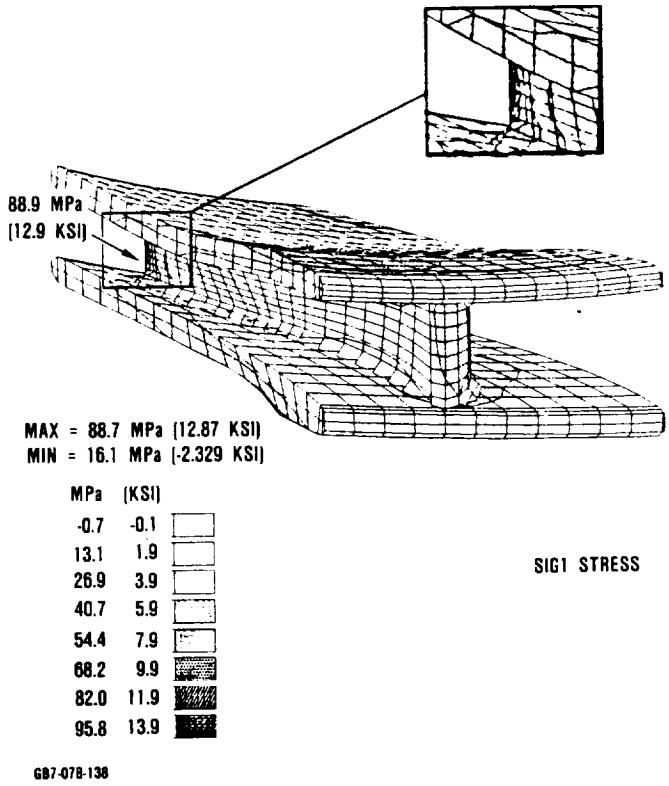

Figure 298. Original Turbine Stator MPS Distribution 20 Seconds After Lightoff.

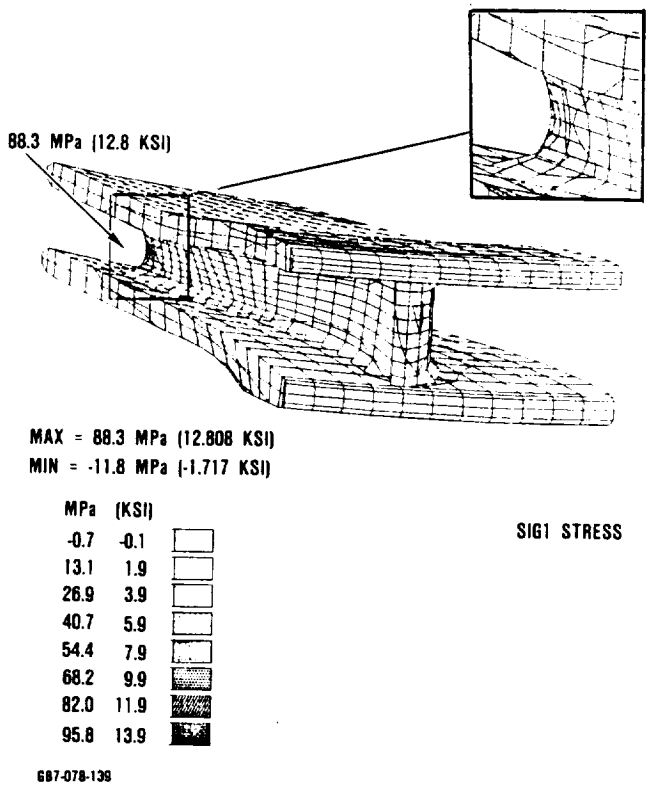

Figure 299. Cutback Turbine Stator MPS Distribution 20 Seconds After Lightoff.

6.3.1.7 Combustor Assembly

The combustor assembly (Reference Figure 250) was designed to have a low emissions and specific fuel consumption (SFC) capabilities. To meet these goals a lean burn concept was utilized in conjunction with a regenerative combustor inlet air source. The lean burn concept creates a uniform lean fuel-air ratio that minimizes NO_x. The high inlet temperatures cause the CO and HC to be oxidized to an acceptable level.

Development of the combustor design has evolved to the existing combustor assembly configuration as shown in Figure 300. The modular main fuel nozzle incorporates an axial ignitor. It includes a pilot combustor with a full open radial inflow swirler at the pilot exit. The absence of holes in the liner walls and the low temperature differential between combustor inlet and discharge temperatures minimizes thermal stresses.

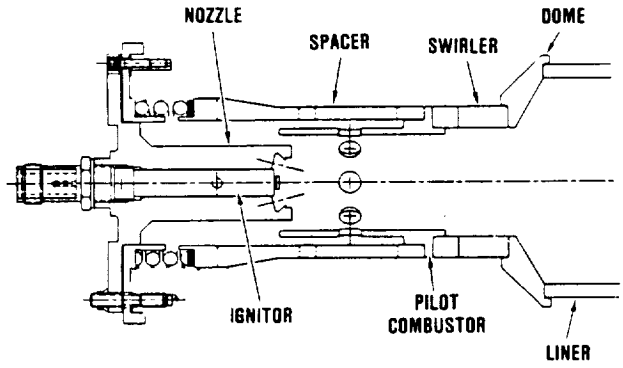

Figure 300. Combustor Assembly Design.

The critical design loading for the combustor component is thermal loading. Mechanical loading consists of small axially compressive loading from the combustor spring and compressive hoop loading from the small radially inward combustor pressure drop. The thermal loading is induced by the flame radiation and gas convection of the combustor. Circumferential and axial hot spots can also be created, the severity of which depends upon the fuel nozzle performance.

To evaluate thermal stresses in the combustor assembly, the axisymmetric finite element model shown in Figure 301 was used. The model consisted of the combustor end of the engine that included all components from the engine housing inward. The finite element model was based upon an earlier design that did not include the pilot combustor component. Convective heat transfer coefficients were analytically derived and applied as boundary conditions. Flame radiation was considered as well as radiation between engine components and to the engine external environment.

The temperature distribution determined for steady-state maximum power condition is shown in Figure 302. The peak temperature 1465C (2669F) was found at the lip of the nozzle holder. The corresponding MPS for the combustor assembly components are shown in Figure 303. The components with the highest MPS (61.3 and 66.2 MPa) were found at the outer edge of the nozzle holder and combustor support respectively. Both of these components were analyzed as RBSN.

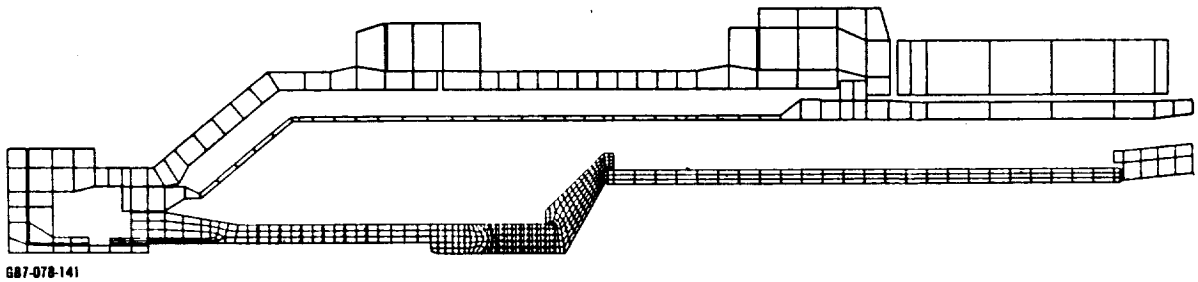

Figure 301. Combustor Assembly Finite Element Model.

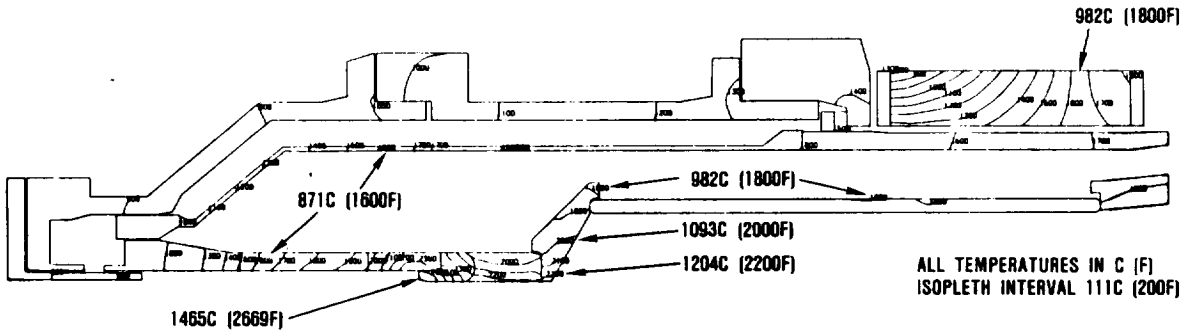

G87-078-142A

Figure 302. Combustor Assembly Steady-State 1371C (2500F) Max Power Temperatures.

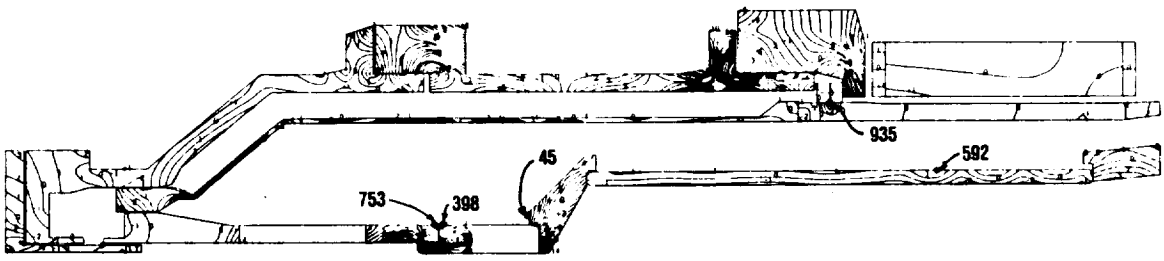

COMPONENT	MATERIAL	NODE	MAXIMUM PRINCIPAL STRESS MPA	(KSI)
SPACER SLEEVE	RBSN	753	44.1	(6.4)
NOZZLE HOLDER	RBSN	398	61.3	(8.9)
COMBUSTOR SUPPORT	RBSN	45	66.2	(9.6)
COMBUSTOR LINER	SASC	592	12.4	(1.8)
REGENERATOR SHIELD	SASC	935	32.4	(4.7)

G87-078-143

Figure 303. Combustor Assembly Steady-State 1371C (2500F) Max Power MPS.

The transient start stresses were evaluated with the lightoff cycle to 1281C (2337F) cruise condition as shown in Figure 304 (cycle 22). Shutdown stresses were not analyzed due to the benign effect of the regenerator system. The MPS responses are shown in Figures 305, 306, 307, and 308 for the four ceramic combustor assembly components. The highest MPS was 32.4 MPa (4.7 ksi), located at the outer edge of the combustor support, and which occurred 180 seconds after lightoff.

In summary, the analyses showed very low thermal stresses for the assumed combustor burner condition. Axial or circumferential variations of the flame or gas within the combustor were not considered in these analyses. Consideration of these variations would probably make significant increases in MPS levels but was not evaluated due to the uncertainty of the actual combustive environment.

6.3.1.8 Component Assembly/Sealing

The design of ceramic components must take into consideration the interfacing of high temperature brittle material into an assembly. This section specifically addresses these design considerations. They include designing

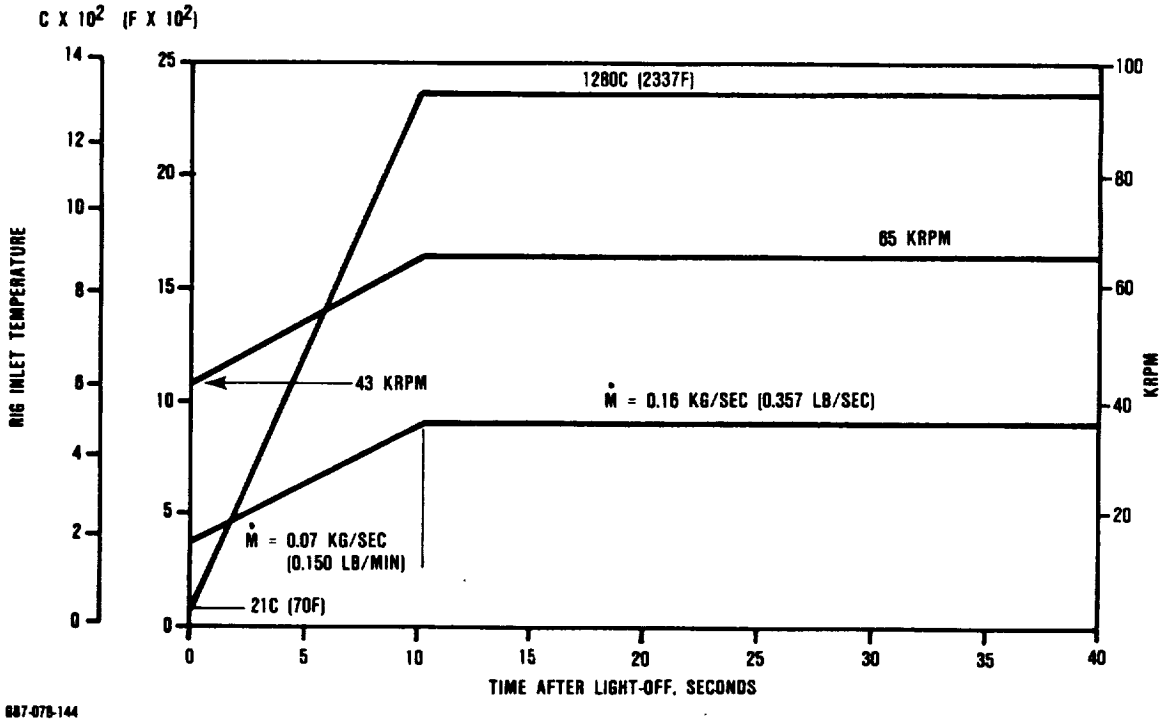

Figure 304. Engine Start to Cruise (Cycle 22).

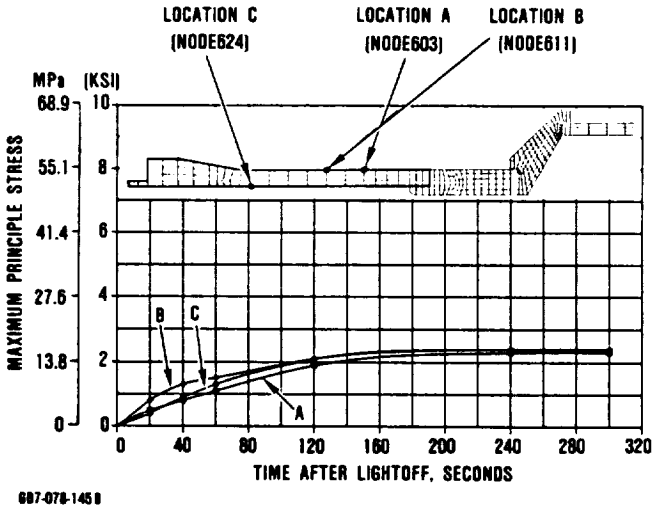

Figure 305. Spacer Sleeve (RBSN) Start Transient MPS.

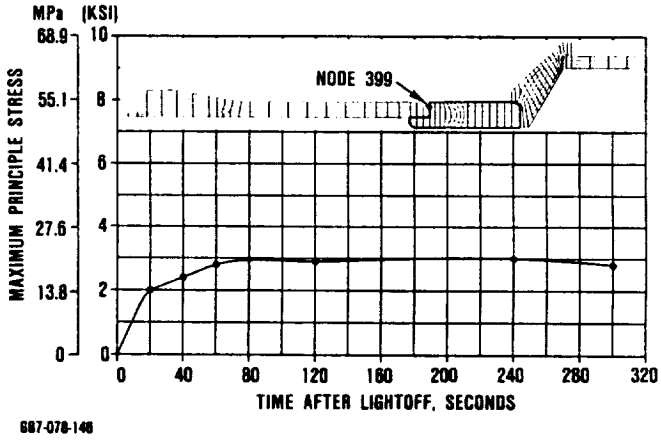

Figure 306. Nozzle Support (RBSN) Start Transient MPS.

the axial and radial support system, sizing and controlling the critical dimensions to ensure against interference between ceramic components, and designing the sealing interfaces to obtain optimum engine performance. To address these design considerations, it is a prerequisite necessity to have a thorough understanding of the mechanical and thermal growth of the overall engine during its duty operation. On the AGT101 program initial

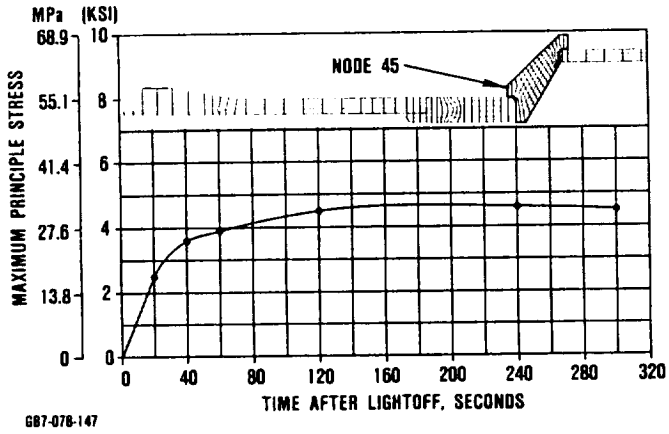

Figure 307. Combustor Support (RBSN) Start Transient MPS.

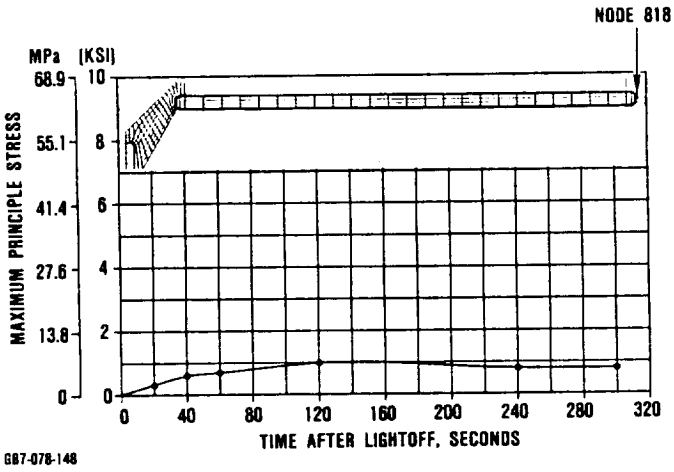

Figure 308. Combustor Liner (SASC) Start Transient MPS.

design effort was accomplished using analytically determined growth and was updated as engine test data became available.

To control the axial positioning of the ceramic components, springs have been used to axially load these components against controlled surfaces. This thereby eliminates the possibility of component failure due to thermal interference between the ceramic and supporting metallic components. Five sets of ceramic component stackup as shown in Figure 309 are found on the engine. These are the inner ceramic stackup, the outer ceramic stackup, the regenerator stackup, the combustor baffle/backshroud/stator stackup, and the diffuser stackup.

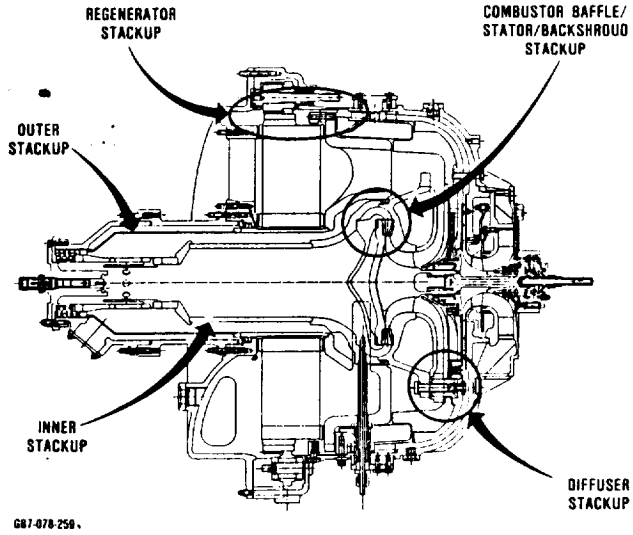

Figure 309. Ceramic Components Stackup Load Paths.

The inner stackup consists of the rocker assembly, turbine shroud, transition duct, and combustor assembly. They are supported by the inner combustor spring that has been sized to provide stability under a 6-g lateral shock load throughout the engine operating cycle. The spring was also sized to provide adequate travel to compensate for the relative thermal and pressure growths between the inner stackup and engine housing.

A subassembly of the inner stackup is the combustor baffle/turbine backshroud, and turbine stators stackup. The inital design for this engine did not have this subassembly stackup, but had the inner ceramic loadpath going directly through these three ceramic subassembly components. The incorporation of this subassembly stackup design was a consequence of seal improvements, as discussed later in this section, made at the flow separator housing, transition duct, and turbine shroud interface.

The outer stackup includes the regenerator shield and the flow separator housing, although

the flow separator housing is axially piloted by the regenerator stackup. The regenerator shield was designed to be loaded by an outer combustor spring more lightly loaded than the inner stackup. Again, this spring was sized to meet a 6-g lateral shock load and to allow for growth differential between the outer stackup and the engine housing.

The diffuser stackup consist of the inner and outer diffusers and is loaded by a compression spring against the turbine shroud. As shown in Figure 310 changes have been made to the first generation support system. The first generation load spacer in a series of tests had a tendency to become cocked and wedged in the guide sleeve. The load spacer was changed to a ceramic ball supported by a conical spring. A stiffer spring was also used to increase the axial support load from 9.5 kg (21 lbs) to 36.3 kg (80 lbs) force. On previous testing (static structure build 9) failure of the outer diffuser was attributed to vibratory energy from this spring-mass system.

The regenerator stackup consists of the regenerator core and flow separator housing. The components are axially loaded by the two regenerator diaphragm seals. The flow separator housing support ring was constructed to minimize the thermal growth differential between the engine housing and the regenerator components. This provided a more uniform seal performance and regenerator drive torque.

The radial support for ceramic components must be able to maintain the concentricity of these components without introducing any mechanical interference. Two types of piloting methods were used to maintain concentricity of the ceramic components to the engine centerline. One of these, an eccentric pin in a radial slot, was used to pilot the flow separator housing. This system consists of three radial slots in the outer rim of the flow separator housing through which three metallic eccentric pins, mounted to the main engine housing, maintain component concentricity. A more innovative method is used to pilot the turbine shroud module. This method consists of a three support rocker assembly (Figure 311) that replaces sliding friction with rolling friction at a highly loaded interface.

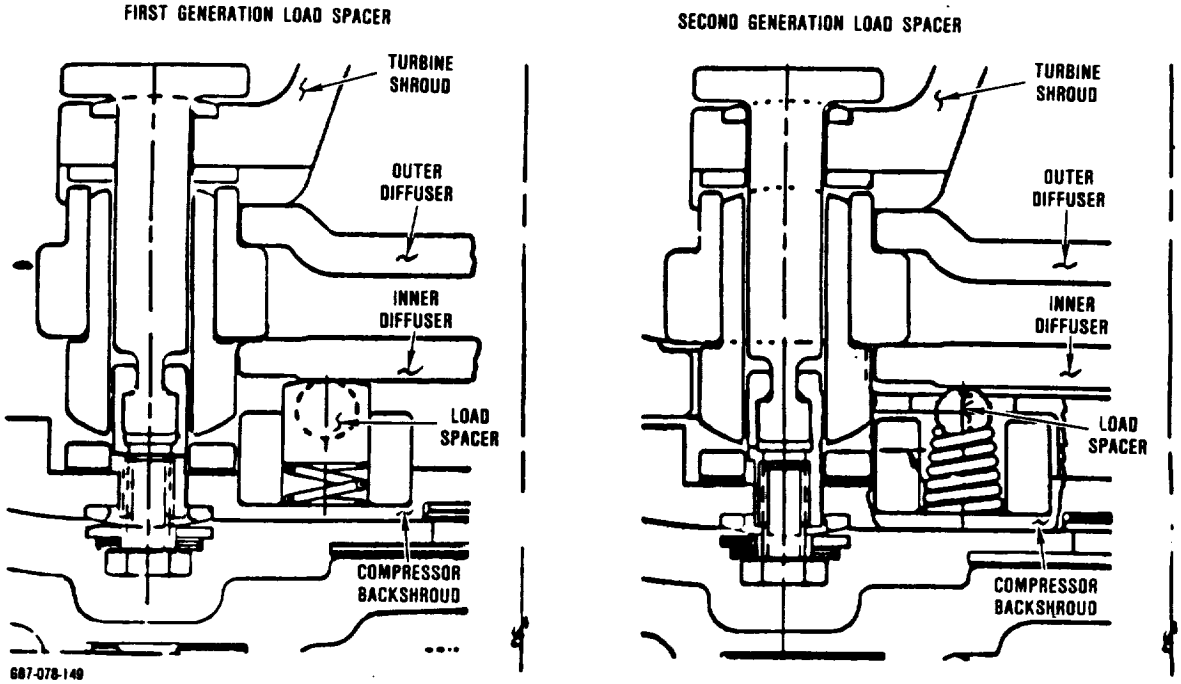

Figure 310. First and Second Generation Diffuser Support System.

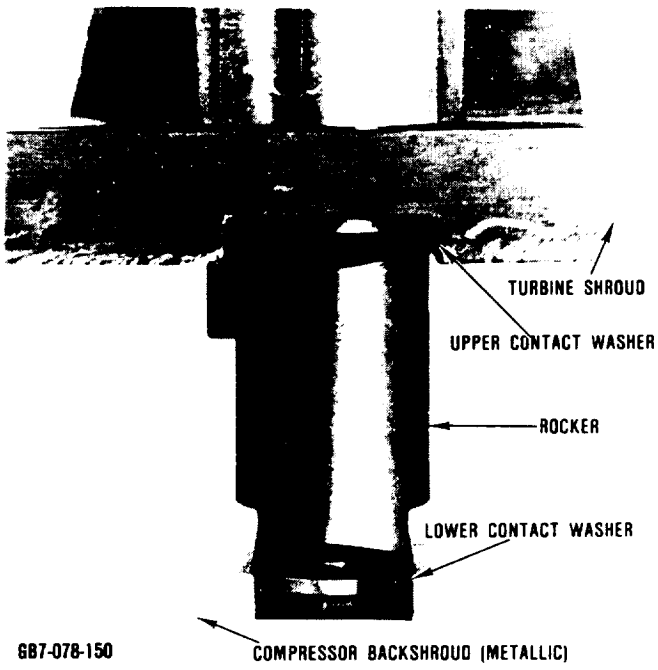

Figure 311. Inner Ceramic Support Rocker Assembly.

Component concentricity is maintained in this configuration through interfacial friction at the rocker contact zone.

Figure 312 shows the change in the rocker assembly as a result of development testing. The rocker was modified to eliminate a thermal interference problem of the outer diffuser between the shroud and rocker. The rocker assembly was therefore eliminated from the diffuser stackup in the axial direction. The rocker assembly still remained as the radial pilot for the diffusers.

In the turbine shroud mechanical screening rig test the turbine shroud is axially loaded and reacted (supported) by the rocker assembly. Repeated failures during simulated engine maximum power pressure condition led to a design change in the turbine shrouds. The locating slots at the turbine shroud mounting flange were eliminated as shown in Figure 313. The turbine shroud mounting system, which includes the rocker and bolt assemblies, was

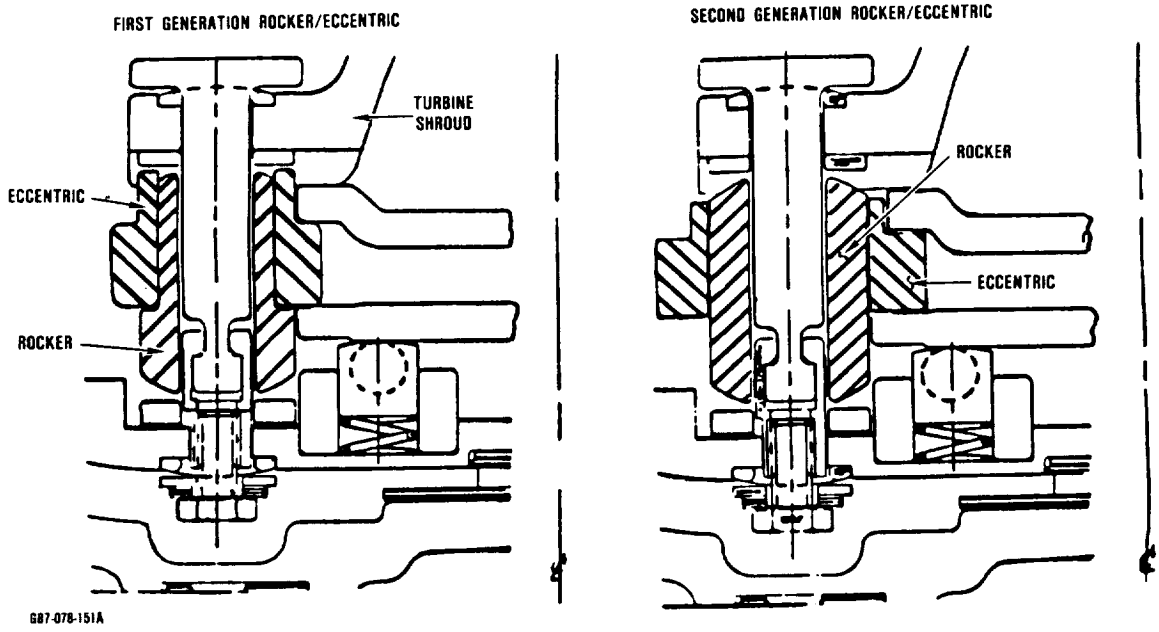

Figure 312. First and Second Generation Rocker/Eccentric Design Comparison.

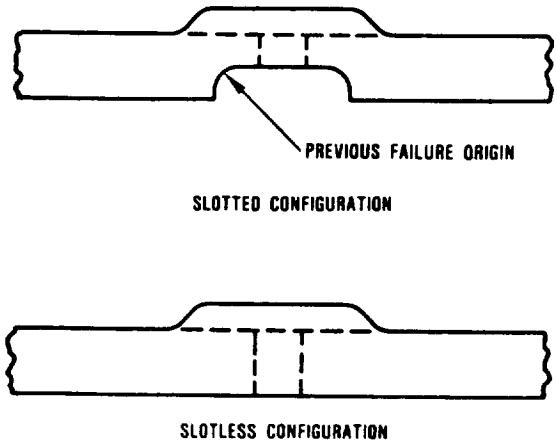

Figure 313. Slotted Versus Slotless Turbine Shroud Configuration.

shown to adequately retain the turbine shroud in position in a shake-table test. The slotless configuration, which relies upon frictional loads alone to maintain turbine shroud position, withstood a 12-g load.

The radial clearance between ceramic components was also sized to eliminate potential thermal interference during engine operations. The stackup of ceramic components has to be designed for unconstrained thermal growths without any radial interference between adjacent stackups. In addition, corner and fillet radii had to be sized to preclude the possibility of mating components contacting within the radii. An example of this occurred during development assembly of static structure rig, build 7 when the flow separator housing failed. Disassembly and inspection of the fractured component revealed the presence of an interference between the fillet radius of the flow separator housing inner lip and the corner radius of the mating regenerator shield. The corner radius was increased to a larger value than the fillet radius in the mating part, thereby eliminating the possibility of localized contact within the radii.

Axial clearances between the rotor to backshroud interface and axial and radial clearances between the rotor to shroud interface were determined for transient and steady-state operating conditions. Since close turbine running clearances are critical to optimum engine performance, instrumented engine testing is normally conducted to verify analysis. This criticality is compounded with the low rub tolerance of ceramics compared to metallics. On metallic engines, verification is usually made by using capacitance probes between the turbine shroud and rotor to measure clearances. On ceramic components, capacitance probes do not function. Therefore, the approach followed was to measure running clearances with the early metallic version of this engine. These clearances were then adjusted to account for the difference in materials and higher operating temperatures of the all ceramic engine. Further discussion of the turbine clearance evaluation can be found in engine design and development (Section 4).

There are three high temperature leak paths from the HP to the LP cavities in the static structure of the engine as shown in Figure 314 that require the use of ceramics. These seal areas are:

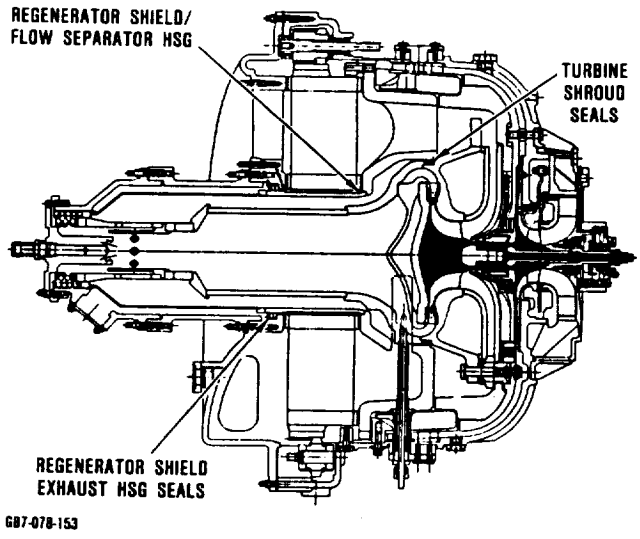

Figure 314. High Temperature Ceramic Seal Areas.

- o Turbine shroud/flow separator housing seal
- o Regenerator shield/flow separator housing seal
- o Regenerator shield/exhaust housing seal

Early testing (static structure rig, build 4) investigated the usage of a ceramic fiber seal between the turbine shroud and flow separator housing. The rig was assembled and a static leak check performed. The results indicated a gross internal leak at the fiber seal area. The fiber was replaced with ceramic ring seals for all subsequent testing.

To investigate the performance of ceramic ring seals, static seal leakage rigs were designed. These rigs were designed to measure seal leakage as a function of seal force and pressure differential at the three high temperature seal areas. In addition, each rig has the capability of establishing the degree of concentricity between parts being sealed so that seal performance can be measured and compared to predetermined amounts of eccentricity.

For the baseline configuration the leak path at the turbine shroud/flow separator housing area was found to be the most critical in terms of performance loss. The baseline configuration consisted of a single LAS piston ring between the turbine shroud and flow separator housing axially loaded by a ceramic wave washer. The following results were noted.

- o The effect of the axial spring load on the seal performance in the baseline seal configuration was negligible.
- o The effect of eccentricity between the turbine shroud and flow separator housing on the seal performance of the baseline seal was significant.
- o A dual piston ring seal configuration reduced seal leakage by 50 percent compared to the baseline line configuration, as shown in Figure 315.

The dual piston ring configuration was adopted for the turbine shroud/flow separator housing area. Because of space limitation, the wave spring was removed and the piston ring was loaded by the inner combustor spring. To allow the for differential thermal growth between this seal area load path and the combustor baffle, backshroud, and stator load path, a wave spring was inserted into the latter load path as shown in Figure 316.

The axial interface between the regenerator shield and the flow separator housing relies upon the outer combustor spring load to control the seal leakage. Testing of this seal area indicated a very low leakage rate that met design criteria.

The two piston ring seal concept was adopted for the regenerator shield/exhaust housing seal area. The axial load was provided by a ceramic wave spring in the stackup.

6.3.2 Rig Design/Development

6.3.2.1 Introduction

The ceramic structural parts received from AGT101 program suppliers are qualified for engine testing according to the flow chart shown in Figure 317. The iterative design/inspection/test/redesign approach in developing engine quality hardware is designed to eliminate discrepant parts before they reach the engine test phase. Each component is, therefore, subjected to 40X visual and dimensional inspection, non-destructive evaluation (NDE), and series of rig tests for final qualification prior to engine installation. A list of all of the rig tests used in this qualification process is shown in Table 50.

Structural components which are subject to high mechanical loads, such as the regenerator shield, flow separator housing, turbine shroud and rocker assembly components, are tested in mechanical rigs to simulate the pressure and contact loading encountered in engine operation. Likewise, components which are subjected to significant thermal stresses are proof tested in thermal screening rigs to simulate the maximum principal thermal stresses encountered in engine operation. The thermal

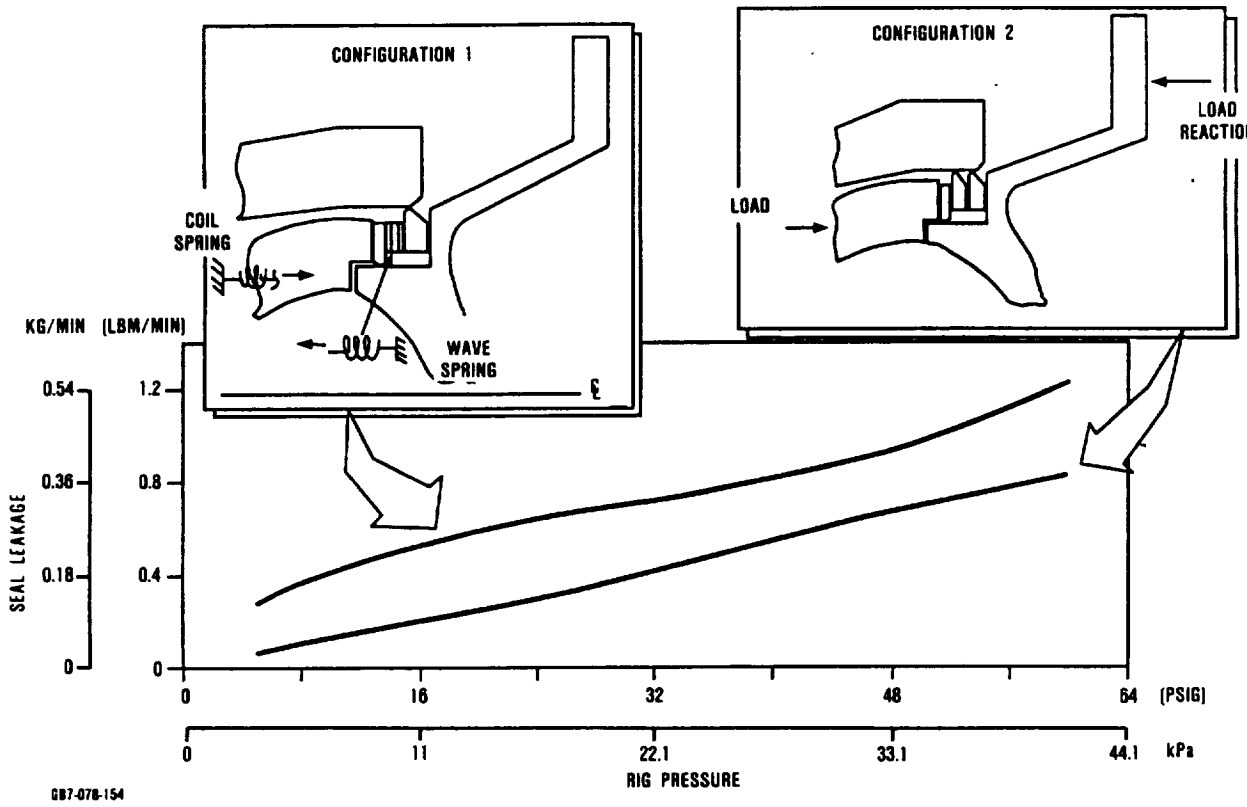

Figure 315. Dual Piston Ring Seal Performance Benefit.

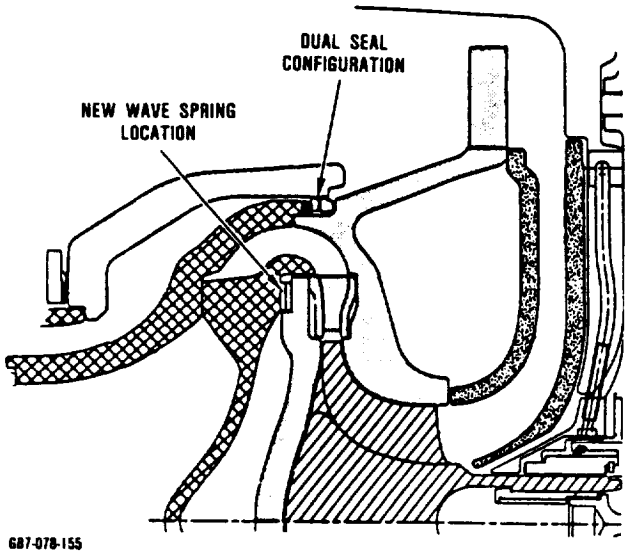

Figure 316. Combustor Baffle/Backshroud Wave Spring Location.

cycles for the screening rigs are defined so as to simulate stresses which exceed predicted engine stresses under normal start conditions by 25 percent.

Thermal screening is intended to eliminate components with gross internal defects and/or smaller defects located in regions of high bending or tensile stress. These lower quality components will fracture during thermal screening allowing only the highest quality parts to continue through qualification testing and subsequent engine tests. The thermal screening rigs provide a screening test bed for various components, configurations, and material changes and have an upper temperature limit of 1149C (2100F).

The static structure rig test utilizes all of the ceramic components in an assembly of the engine structure, without the rotor, and checks the mechanical functioning of the as-

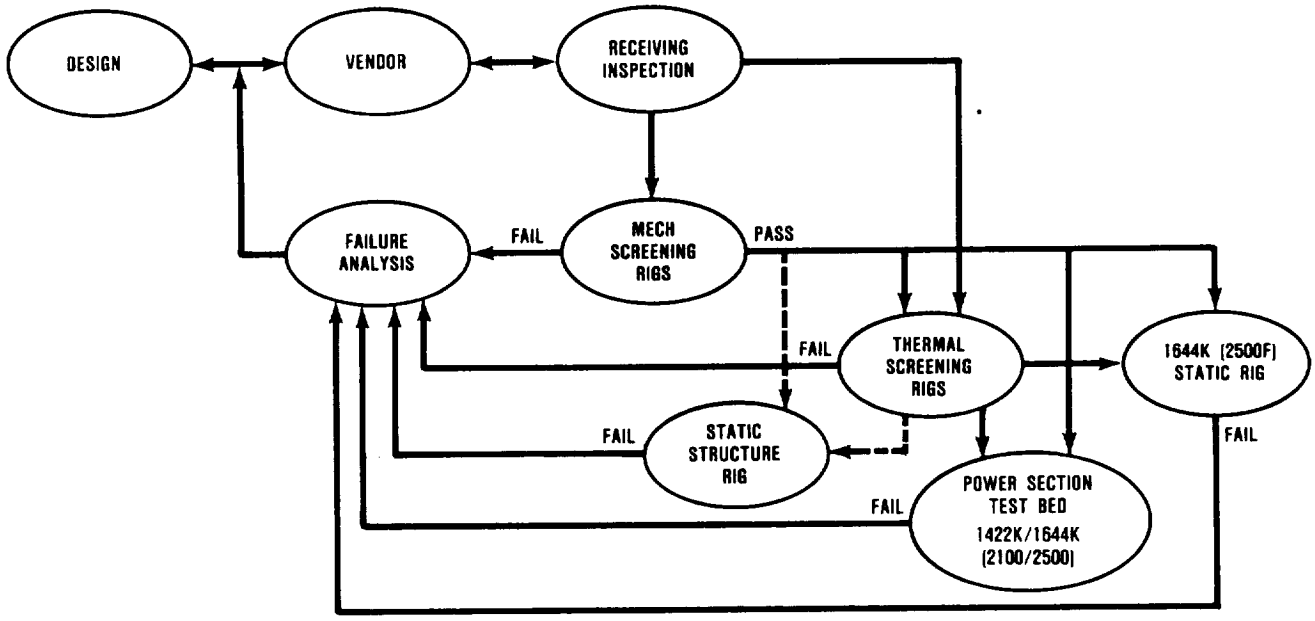

Figure 317. Ceramic Component Qualification Sequence.

sembly. Further, the static structures rig evaluates the sealing capability, component capability, axial and radial pilots, contact loading, and stresses at elevated temperature. Components that fracture during any phase of this evaluation undergo intensive fractography and analytical reevaluation to determine the cause and recommended solutions. The maximum operating condition for this rig was set at 1093C (2000F), which corresponds to the maximum operating temperature of the regenerator in the AGT101 engine.

To evaluate ceramic structures upstream of the turbine exhaust, such as the turbine, stator, shroud, backshroud, combustor baffle and transition duct at the higher flow path temperature of the engine, another rig, the 1371C (2500F) static rig is used. Long-term testing at 1371C (2500F) temperatures is performed in this rig to investigate the high temperature effects on ceramics, such as static fatigue, contact loading, and endurance.

In addition to screening substandard components, the component test rig provide a data base for evaluating thermal, stress, and risk analysis tools and methodologies.

6.3.2.2 Mechanical Screening Rigs

Mechanical screening tests have a dual purpose; establish overpressure capability and measure strain, and qualify parts. Initial tests were performed on the flow separator housing, regenerator shield, and those components that provide the attachment between the ceramic turbine shroud and metal compressor backshroud. These parts have low thermal stresses due to a combination of uniform heating or to a low thermal expansion coefficient (i.e., lithium aluminum silicate material).

The test fixture for the regenerator shield screening rig is shown in Figure 318. The initial regenerator shield test incorporated the use of strain gages to measure strain distribution and magnitude during pressurization. This instrumentation was installed as a checkout of the test procedure. Pressure was applied until a strain level equivalent to 137.8 MPa (20 ksi) was achieved. This stress level was selected

Table 50. Ceramic Component Rig Tests.

Name	Function	Description
Regenerator Shield Rig	Mechanical screening of regenerator shields	Internal pressure proof test
Flow Separator Housing Rig	Mechanical screening of flow separator housings	Internal pressure proof test of HP cavity
Turbine Shroud/Rocker Assembly Rig	Mechanical screening of turbine shrouds and rocker assemblies	Axial static load test of the ceramic inner stackup support system
Stator Torch Test	Low-cost thermal screening of turbine stators	Lightoff thermal shock testing using oxacetylene torches
Diffusers Rig	Thermal screening of inner and outer diffusers	Lightoff thermal shock testing using an external combustor
Transition Duct/Combustor Baffle Rig	Thermal screening of transition duct and combustor baffle	Lightoff thermal shock testing using an external combustor
Backshroud/Stator/Shroud Rig	Thermal screening of turbine backshroud, stators, and shroud	Lightoff thermal shock testing using an external combustor
Static Structure Rig	Short term maximum temperature interface evaluation of turbine section static structure components	Elevated temperature testing up to 1371C (2500F) with a gentle lightoff and cool-down cycle
	Long term elevated temperature interface evaluation of all static structure components	Elevated temperature testing up to 1093C (2000F) with a gentle lightoff and cool-down cycle. Uses an internal combustor.
1371C Static Rig	Long term maximum temperature interface evaluation of turbine section static structure components	Elevated temperature testing up to 1371C (2500F) with a gentle lightoff and cool-down cycle. Uses an external combustor.

Figure 318. Strain Gaged Regenerator Shield and Mechanical Screening Rig.

because it exceeded the predicted combined thermal and mechanical stress exposure in operation and is less than one-half of the material characteristic strength.

To screen and qualify ceramic components the proof pressure was reduced to a magnitude that would simulate 48.2 MPa (125 percent of the maximum operation stress encountered in engine operation). Strain gages were not used in the screening tests.

The flow separator housing test fixture in the assembled condition is shown in Figure 319. The test fixture was designed to support the housing, simulating engine mounting conditions while sealing the housing to the fixture with rubber gaskets. The fixture was designed to use water to apply pressure loads within a containment vessel. The upper plate is provided with fittings for a pressure line and an

Figure 319. Flow Separator Housing Mechanical Screening Rig.

air bleed valve. Using gaskets and o-rings, the high pressure cavity is sealed so that pressure can be applied to simulate engine operating pressures. The flow separator housings are screened at pressure levels that represent 125 percent of the maximum mechanical loads exerted in the engine at maximum power condition.

The flow separator housing mechanical test fixture not only serves as a screening apparatus but also permits the correlation of 3-D stress analysis with mechanical stresses encountered in engine operation. Fourteen uniaxial and seventeen triaxial strain gages were attached to S/N-8 flow separator housing in critical areas for this purpose.

The attachment between the turbine shroud and the compressor backshroud must survive a large pressure induced axial load during engine operation. To proof these components, a mechanical rig is used as shown in Figure 320. The rig consists of a turbine shroud attached by three sets of rocker components to an aluminum plate which functions as the compressor backshroud. The objective of this test is to subject the three rocker assemblies and shroud attachment area to a 1814 kg (4000 lb.) axial load. This represents a pressure load 25 percent greater than the maximum power pressure load.

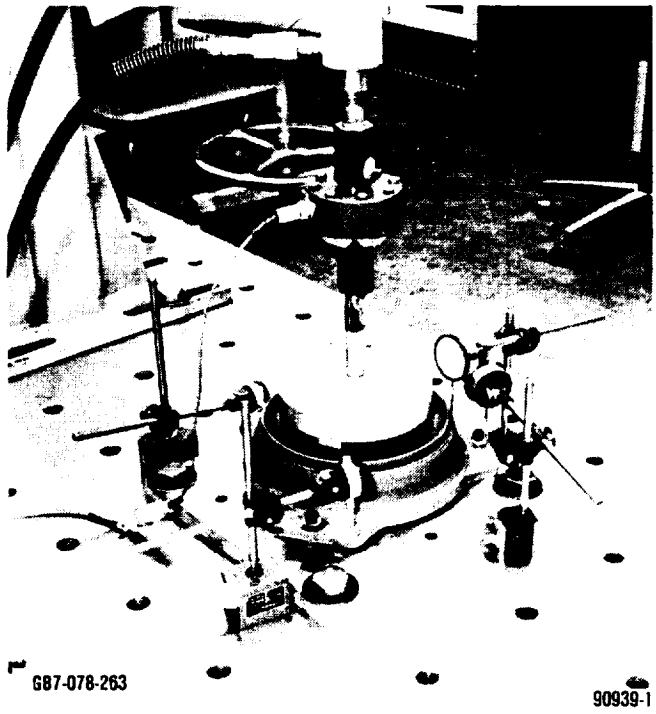

Figure 320. Turbine Shroud/Rocker Assembly Mechanical Screening Test Setup.

A variation of this rig has been used to serve two other functions in this program. Both used the turbine module assembly with the compressor backshroud replacing the aluminum plate. The first function arose early in the program when verification was needed to ensure that the rocker assembly could sustain relative radial differential thermal growth motion without compromising the shroud axial stack or alignment dimensions. This test consisted of subjecting the turbine module assembly with compressor bolt loading to thermal cycles from room temperature to 232C (450F). After testing, the contact washers and rocker interfaces were inspected for damage.

The other use for the turbine module assembly came when demonstration of the rocker assembly capability under shock loading was needed. The module was mounted thru the compressor backshroud to a shaker table and submitted to a 10-g lateral load.

6.3.2.3 Thermal Screening Rigs

The thermal screening rigs are designed to subject critically stressed (thermal) hot gas flow path components to simulated engine starting transients to 1149C (2100F). These rigs duplicate engine flow path geometry, thus close approximation of actual heat transfer coefficients is achieved for idle and cruise conditions. This defined operating envelope provides a remote test bed for the testing of individual and/or multiple components in the desired start transient condition. Components are thereby screened on a pass/fail basis for any given thermal transient.

An external combustor provides the heated air supply to the rigs which is monitored with rig inlet and exit thermocouples.

The ceramic components that have been designated as critically stressed components consist of the transition duct, combustor baffle, turbine backshroud, turbine stators, turbine shroud, outer diffuser and inner diffuser. Three rigs have been designed and dedicated to qualify (proof) these components. These are the transition duct/combustor baffle rig, the backshroud/stator/shroud rig, and the inner/outer diffuser rig.

An acoustic emission monitoring system is utilized on all thermal screening rigs in which high frequency response acoustic transducers are mounted to a waveguide in direct contact with the ceramic component being tested. Component screening is monitored in real time so that if a fracture occurs, the event can be correlated with thermal transient conditions. This equipment allows for diskette recording of acoustic emission (AE) data and hard copy graphics display of the AE data generated by the test. Additionally, this monitoring approach provides in-situ component diagnosis so that unnecessary disassembly/inspection/build time and secondary damage due to continued rig operation are minimized.

A torch test designed to simulate stator lightoff thermal response was used prior to the development of the thermal screening rigs. This rig was used to identify potential material deficiencies of the first stator sets from ACC and Standard Oil. The objective of the experimental effort was to duplicate the worst-case stator trailing edge heating curve for RBSN and sintered α-SiC vanes with the Garrett thermal shock test rig.

The general thermal shock test arrangement consisted of two castable alumina stator vane holders (each designed to hold three stator vanes), one or more oxyacetylene torches, two airblast cooling tubes, a timer-actuated slide table and a small-focal-spot infrared pyrometer. Test setup is illustrated in Figure 321.

A number of iterations were required to identify the setup and torch conditions that simulated the analytically-predicted thermal

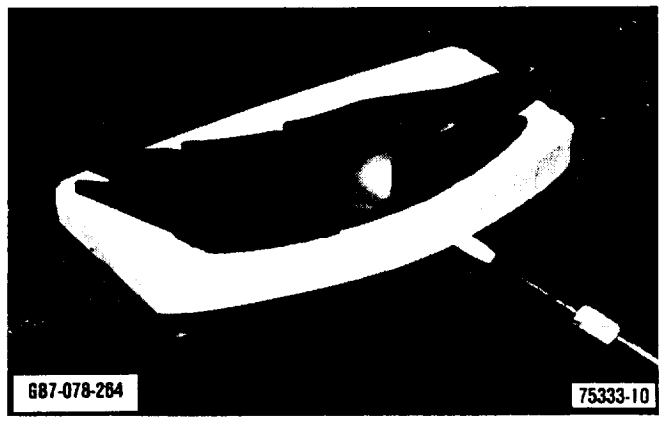

Figure 321. Standard Oil SASC Stator Vanes in the Thermal Shock Test Rig.

response of the stator vane trailing edge in the engine. Initial attempts with one torch did not produce a realistic temperature profile on the vane or an acceptable thermal response curve. The use of two torches yielded a response that closely simulated the stator lightoff and was used for all torch testing. Although the torch testing proved very simple and quick to use, its effectiveness to adequately simulate the engine conditions was questionable. After the component screening rigs were developed, torch testing was terminated.

The inner/outer diffuser screening rig as it currently exists is shown in Figure 322. The rig was designed to screen both the inner and outer diffuser for short term lightoffs up to 1149C (2100F). The diffuser assembly is mounted within the rig, as in the engine with a ceramic rocker assembly, and the flange section of a modified ceramic turbine shroud. Hot gas from a 76.2mm (3 inch) diameter natural gas burner at an engine idle flow rate provide the heat source. Flow is ducted to the diffuser assembly by a metallic nose cone and outer liner. Purge air enters thru the nose cone to simulate the foil bearing cooling of the engine. The inner walls of the housing are lined with insulation to keep the housing temperature within acceptable levels. The rig test is monitored and controlled by two thermocouples located at the burner exit. The integrity of the ceramic components is mon-

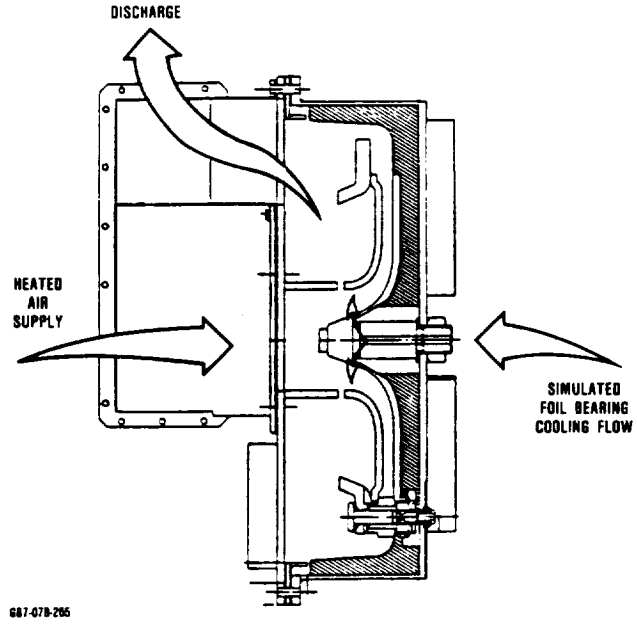

Figure 322. Inner and Outer Diffuser Screening Rig.

itored by an acoustic emission probe positioned off the back side of the inner diffuser.

The existing rig has evolved from the original design with only minimal changes. As the engine design changed the rig was concurrently updated. These include such changes as modifying the load spacer design, the rocker assembly eccentric design, and the ceramic bolt design. In addition, the rig insulation material was improved. The previous material Fiber-Frax formable insulation was replaced with Babcock and Wilcox 3000 alumina-silica insulation which additionally was coated to increase strength with Ceracote, where exposed to the turbine discharge gases.

The second thermal screening rig, the transition duct/combustor baffle rig as shown in Figure 323 uses spring loaded pushrods to axially load the transition duct and combustor baffle assembly against a strutted standoff. It uses the same laboratory burner as the inner/outer diffuser rig uses. In addition to monitoring the combustor discharge temperatures, two thermocouples monitor the flow temperature at the $T_{4.1}$ ports on the transition duct. The acoustic emission probe is positioned onto the transition duct at the third T_4 port.

The original design for this rig utilized a metallic strutted standoff for the combustor baffle. This proved inadequate for the elevated temperatures encountered in this rig. Consequently, the recent rig configuration

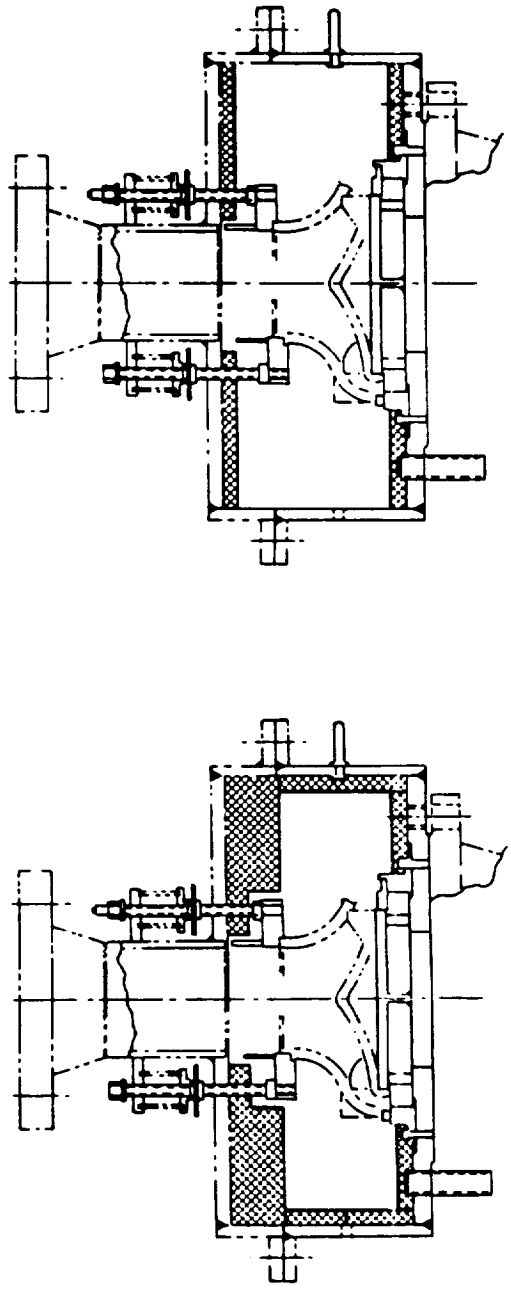

Figure 323. Transition Duct and Baffle Screening Rig With Original (top) and Final (bottom) Configurations.

C-4

uses as a support platform a piece of Lockheed HTP-12 insulation which is formed to provide both the support and a portion of the discharge flow path. This also has proved inadequate due to erosion in the flow path ahead of the struts. Other changes in this rig include increased insulation along the rig inner walls, change from aviation fuel to natural gas, and the addition of a viewport to visually monitor the mechanical integrity of the transition duct. The change was made from a liquid fuel burner to a natural gas burner for better lightoff characteristics and more stable operation under severe transient conditions, leading to more repeatable screening tests.

The third thermal screening rig, shown in Figure 324, is the backshroud/stator/turbine shroud rig. It uses the same spring axial loading mechanism and combustor used on the transition duct/combustor baffle rig. Temperatures were monitored at both the combustor discharge and at the stator inlet ($T_{4.1}$) locations. The lightoff is controlled from a $T_{4.1}$ thermocouple. Since this rig does not closely simulate the engine (no diffused flow around the shroud flange) two separate test cycles must be used to proof the different ceramic components. A shorter and greater transient thermal shock cycle is used to qualify the stators. A longer and less severe thermal shock cycle is used to qualify the turbine shrouds.

In January 1984, the backshroud/stator/turbine shroud screening rig was tested to determine the effect of various rig insulation configurations on the heat transfer rate into the turbine shroud. A metal turbine shroud, instrumented with thermocouples, was used to model the heat transfer coefficients. The purposes of the test series were to evaluate the effect of a new more heavily insulated configuration that was in use when two shrouds fractured during screening, and to determine a suitable rig insulation configuration (and thermal transient cycle) for future ceramic shroud screening.

Tests were run using improved insulation both with and without stators. The rig was then reconfigured to the previous insulation arrangement. Again, tests were run with and without stators. Finally, the new insulation piece, which nests behind the turbine shroud, was installed with the remainder of the rig employing the former insulation. This configuration was run to provide data on any effects that this single change may have. The

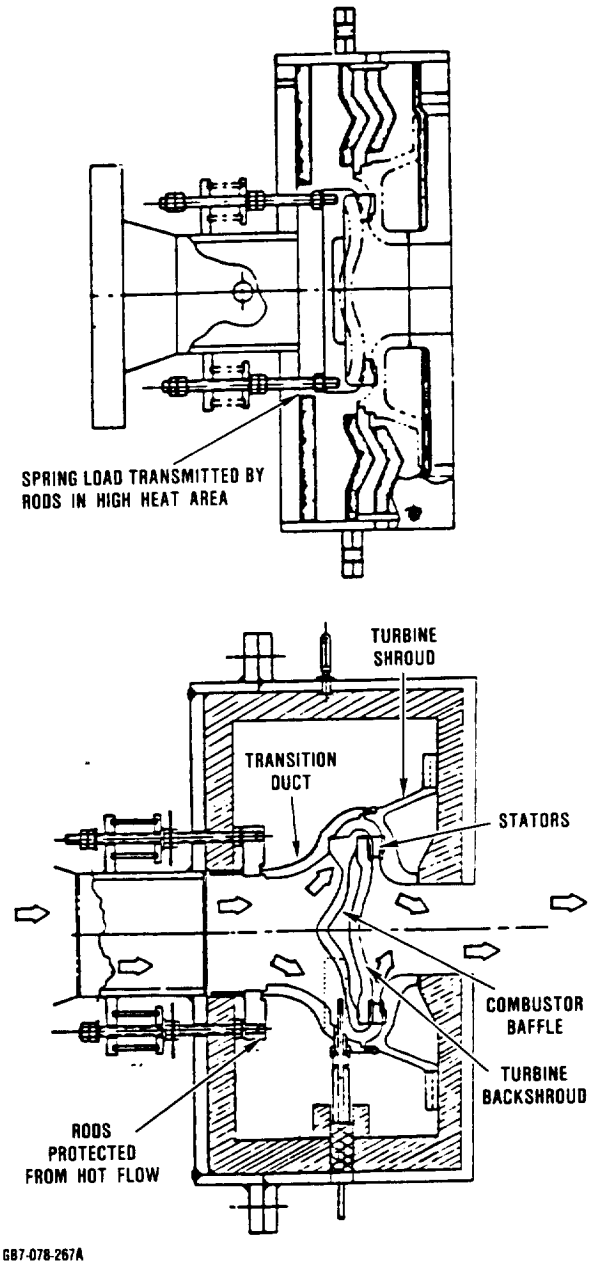

Figure 324. Turbine Shroud Screening Rig Original (top) and Final (bottom) Configuration.

results of this test are discussed further in the analysis and design section on the turbine shroud (paragraph 6.3.1.3.2).

As a result of rig testing with a metallic shroud the following changes were made:

- The lightoff cycle required to proof the turbine shroud was made less severe and became dependent on the shroud material being tested [changing from 93 to 1149C (200 to 2100F) to approximately 93 to 871C (200 to 1600F)].
- The housing cavity insulation was reduced to allow for more cross-radiation between sections of the turbine shroud.

Continued rig improvements were made as a result of further rig problems. Some changes were made only to be later discontinued. A chronological order of these problems and changes are covered in detail in a previous report*. The design changes made that have been incorporated into the final rig configuration include:

*Ninth Semiannual Report - Advanced Gas Turbine (AGT) Technology Development -NASA CR - 174886

- Rig modification was made to include a ceramic transition duct, combustor baffle and seal rings into the flow path. This was done to more closely simulate engine heat transfer coefficients on the turbine shroud.
- The rig discharge section of the insulation was replaced with Lockheed HTP-12 type insulation.
- Two ceramic waveguides are now utilized in this rig test; one in direct contact with the turbine shroud mounting flange and the other in contact with the transition duct.
- A viewport has been added at the forward end of the rig to allow for visual inspection of the turbine shroud and transition duct interface area.

The thermal cycles for the screening rigs are defined so as to simulate stresses which exceed analytically predicted engine stresses under normal start conditions by 25 percent. A normal engine start in defined as ambient to 1218C (2200F) in five seconds at idle air flow. These proof cycles are given in tabular form in Table 51. The test cycles for the turbine shroud have been rigorously developed by determining heat transfer coefficients for

Table 51. AGT101 Static Components Proof Test Cycles.

Component(s)	Material	$\dot{m}$ g/sec (lbm/min)	T_o, C (F)	T_{rig}, C (F)	$\Delta t_{l/o}$, sec	$t_{s/D}$, sec
Transition Duct, Baffle	All Materials	171 (22.6)	21 (70)	982 (1800)	10	500
Inner/Outer Diffusers	RBSN SSN	129 (17.1)	21 (70)	1093(2000) 1093(2000)	10	600
Turbine Shroud	RBSN	76.0 (10.0)	93 (200)	859(1575)	15	600
	SSN SASC			878(1630) 938(1720)		
Stators	All Materials	129 (17.1)	294 (70)	1218 (2225)	10 10	35

both the engine and rig from test data and verifying or updating the accuracy of the finite element thermal and stress analyses. The cycles for the other components were developed assuming similar flow conditions occur in the engine and rig.

6.3.2.4 Static Structure Rig

The ceramic structures rig is a high temperature test bed for the complete set of ceramic structural components. The purposes of the ceramic structures rig are:

- To evaluate the durability of the ceramic assembly under the following conditions:
  1) Normal engine start conditions for the 871C (1600F) TIT configuration and 1093C (2000F) TIT configuration with a dual alloy metallic wheel.
  2) Steady-state engine conditions for 871C (1600F) and 1149C (2100F) TIT configurations at idle and cruise
- To evaluate ceramic interface compatibility at idle and cruise conditions.
- To evaluate the ceramic turbine shroud support/alignment system under start, cruise, and idle conditions.
- To demonstrate the ceramic assembly durability for ten normal start cycles for the 871C (1600F) and 1149C (2100F) configurations.

The rig utilizes AGT101 metallic engine outer compressor and exhaust housings with the hot gas flow path constructed of 49 individual ceramic static structural components. As a ceramic static structures test bed, the rig has a maximum low pressure (LP) inlet temperature limit of 1093C (2000F) due to the absence of a turbine rotor and the attendant temperature drop during simulated engine operation. This 1093C (2000F) limit is a function of the maximum gas temperature immediately downstream of the turbine rotor and is the maximum regenerator temperature.

The original and final configurations for the ceramic static structure rig are shown in Figure 325. The original static structures rig had two air inlet supplies that simulated compressor discharge (HP), and turbine inlet conditions (LP) in an open loop configuration. A

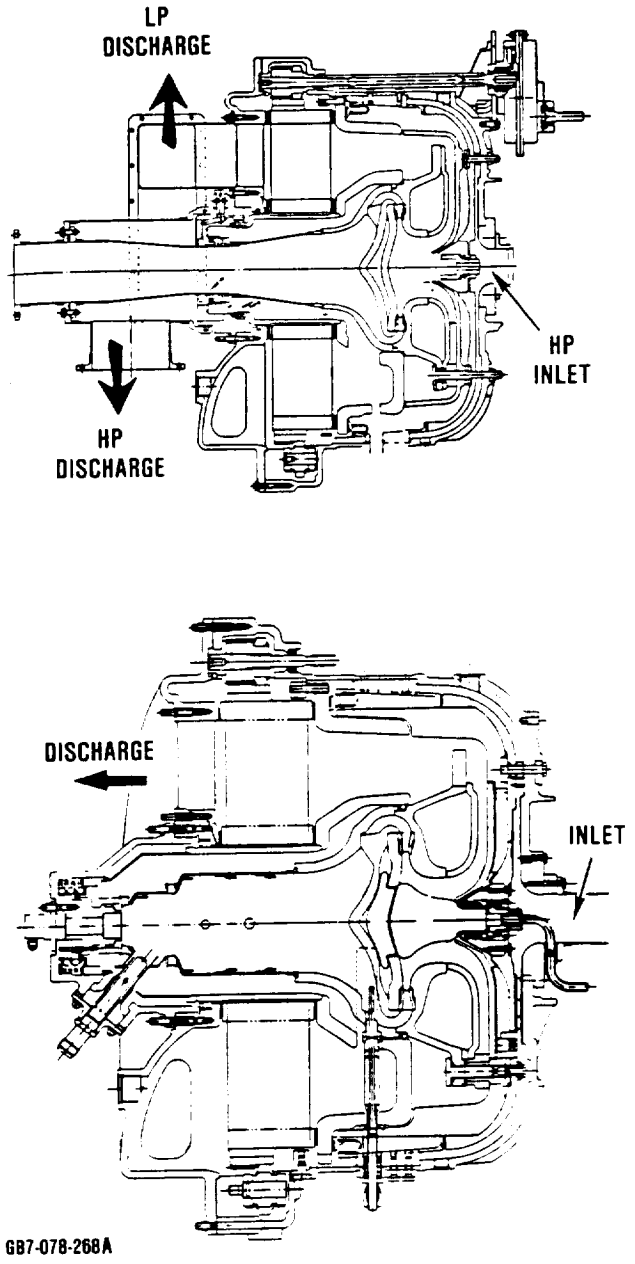

Figure 325. Static Structure Rig Original (top) and Final (bottom) Configurations.

three inch lab combustor provided thermal start transient and steady-state conditions under AGT101 simulated engine idle and cruise airflow conditions.

Air, as hot as 1093C (2000F), entered the structures rig through the inlet duct and then diffused through the ceramic transition duct; thus heating the combustor baffle, turbine shroud piston rings, segmented turbine stators, turbine backshroud, inner and outer turbine diffusers, and LP side of the flow separator housing. The air then passed through the regenerator.

The cold, HP air entered the rig at temperatures up to 93C (200F), flowed along the compressor backshroud and compressor housing, turned in the exhaust cover, and was heated through the regenerator. The air then flowed over the HP side of the flow separator housing, around the transition duct through the regenerator shield, and out of the rig.

Initial testing of the original static structure configuration showed a combustor instability problem related to an improper pressure drop across the burner. This can result in a lack of flame containment within the primary zone of the burner and, in fact, "allow" the flame to extend well into the turbine flowpath region. The ceramic structural components would thereby be locally heated in an atypical manner.

Attempts were made to alleviate this problem by modifying the combustor to operate at a higher burner pressure drop, but satisfactory combustor performance was never fully attained. The solution to this problem was achieved by using a singular flow arrangement with the engine metallic combustor. The final rig configuration, used since August 1984, therefore simulates engine conditions more completely.

An acoustic emissions monitoring system was used on all ceramic test rigs which provided a "real time" component integrity assessment. Two acoustic waves guides are installed on the structures rig; one on the ceramic bolt assembly, the other on the flow separator housing. These locations were selected so that all components could be continuously monitored through one of the two component assembly locations. The acoustic monitor detects ceramic component fracture incidence through a high frequency transducer. The system eliminates rig disassembly between thermal start transients in which no high energy acoustic events are detected.

The last static structure rig test (Build 13) was run in March 1985. Sufficient confidence was gained in the ceramic static structures rig testing so that ceramic structural components are now considered qualified for engine use without passing through this phase of screening. The static structures rig was therefore modified for use as a hot regenerator seal leakage test rig.

6.3.2.5 1371C (2500F) Static Rig

The intent for this rig was as a vehicle for performing tests at 1371C (2500F) of major structural components, including transition duct, combustor baffle, turbine backshroud, stators, and turbine shroud. During maximum operating conditions, those components being forward of the rotor where work is extracted from the flow will be exposed to temperatures up to 1371C (2500F). Those components aft of the rotor will never be exposed to temperatures higher than 1093C (2000F) in the engine. Therefore, components such as the diffusers, flow separator housing and regenerator core are fully evaluated in the aforementioned static structures rig.

The 1371C (2500F) milestone was initially achieved in a backshroud/stator/turbine shroud screening rig in April thru May 1984, although only for a short term cycle. To demonstrate survivability over an extended time period a separate rig was developed.

The original configuration as given in Figure 326 incorporated a flow separator housing. This configuration was used for the first build of the 1371C static rig. Note that the flow path of the incoming air to the rig differs

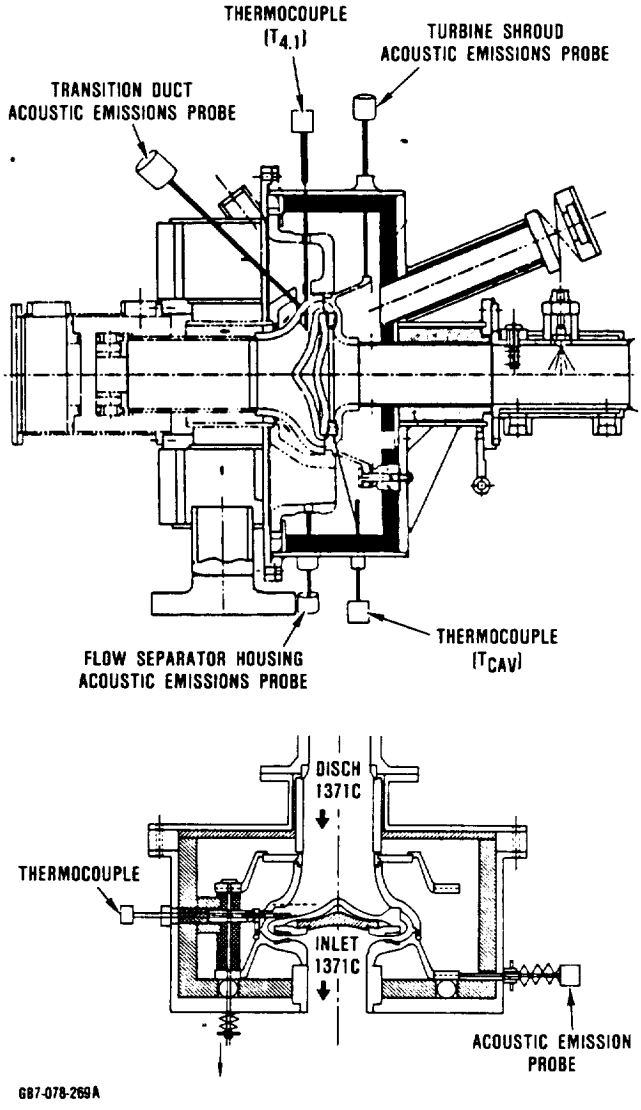

Figure 326. 1371C (2500F) Static Turbine Rig Original (top) and Final (bottom).

from previous screening rigs in that the incoming air enters via the flow separator housing "smile" prior to combustion in the rig burner. For this initial test a natural gas preheater was not used, as originally intended, due to concerns about rig inlet housing integrity when exposed to heated inlet air. This means that incoming air prior to combustion was in the range of 93-121C (200-250F). The heating effect of the regenerator core was not simulated in this test.

This rig was first used in August 1984, but was unable to meet the 1371C (2500F) objective because of the fracture of ceramic components. Testing on this rig was terminated and development of an improved rig was initiated. In the interim, until a replacement rig was developed, 1371C (2500F) testing was done using the backshroud/stator/turbine shroud screening rig. This was done for two reasons: to avoid thermal growth damage to the 1371C static rig inlet housing due to different heating rates in different areas, and to avoid risking the flow separator housings, which are not required for the 1371C (2500F) testing.

In April 1985, further 1371C (2500F) testing was conducted, this time employing the new 1371C static rig design similar in configuration to the turbine shroud screening rig, but oriented in a vertical position. This was done for two reasons: 1) to allow a dead weight to supply the required load to the ceramic stack, and 2) to preclude the possibility that discharge quench water will back up into the rig. In addition, the rig eliminated the flow separator housing, an expensive and long lead time item, which would have been unnecessarily placed at risk in the previous rig design.

The dead weight employed was made of 300 Series stainless steel, insulated for protection. Unfortunately, it reached a high enough temperature at approximately 25 minutes after achieving the 1371C (2500F) test temperature, that premature shutdown of the rig was thought prudent.

In May 1985, additional testing at 1371C (2500F) was attempted. To extend the running time at the 1371C (2500F) temperature condition, the dead weight system was changed to incorporate ceramics. However, the amount of weight that can be physically installed in the rig envelope was found insufficient. A pressure differential at light-off between the flow path and the cavity surrounding the test pieces caused the transition duct to move upward (axially) and then bounce back down upon the rest of the stack of parts. Further modifications to the loading system for this

rig were made to allow extended operation at 1371C (2500F) test temperature. These modifications included a component loading system where a spring load is transmitted through three air-cooled metal bolts. These bolts then load a modified turbine shroud and thus the stack of ceramic parts. This arrangement is illustrated in Figure 326 (bottom view).

6.3.3 Component Rig Testing

6.3.3.1 Mechanical Screening Rig Testing

Testing was conducted on three mechanical screening rigs; namely, the regenerator shield rig, the flow separator housing rig, and the turbine shroud/rocker assembly rig.

The initial testing with the regenerator shield rig subjected the ceramic shields to an internal pressure loading that would screen out material flaw sizes that had strength less than 137.8 MPa (20 ksi). Four regenerator shields from Standard Oil (SASC) were tested and one failed at a pressure loading equivalent to 124.1 MPa (18 ksi).

Subsequent regenerator shields were tested at a lower internal pressure that induced stresses (48.2 MPa) equivalent to 125 percent of the maximum stress level encountered in a normal engine operation. Fifteen regenerator shields made out of SASC from Standard Oil were received and tested and all passed without any damage.

The flow separator housings were tested in a pressure rig at the vendor (Corning) before shipping to Garrett. Pressures were specified for this test to simulate the maximum pressure loading in the flow separator housing during engine operations (44.8 MPa). In addition to the testing at the vendor, testing was also conducted at Garrett, in another duplicate rig, to substantiate that no strength degradation had occurred whenever the flow separator housing was reworked. In all cases whenever components were reworked and retested, the components passed the rig test without damage.

In November 1984, all turbine shrouds were mechanically tested along with the rocker assembly to proof these components against engine maximum pressure loading. A hydraulic press was used to incrementally apply a load up to 1814 kg (4000 lbs). This corresponds to 125 percent of the maximum pressure loading of the engine. The first two shrouds to be tested were an RBSN shroud from ACC and an SN-54 shroud from NGK. The SN-54 shroud passed the test undamaged while the RBSN shroud failed at 1315 kg (2900 lbs). The origin of the fracture was located in the radius of the piloting slot on the shroud flange.

During December 1984, two additional shrouds, an RBSN, and SN-54 shroud were subjected to the mechanical proof test. Again, the SN-54 turbine shroud passed the test while the RBSN shroud failed at approximately 1315 kg (2900 lbs). The origin of the fracture was located in the same area as the previous failure.

Due to the two failures of slotted RBSN turbine shrouds during mechanical screening, a design modification was implemented to strengthen the area where these failures initiated. This modification resulted in removing the slots on the flange of the shroud. Mechanical shock testing of the turbine shroud/supports/compressor backshroud assembly had shown that these slots, initially designed for piloting, were not needed to control piloting. The first modified RBSN turbine shroud was mechanically screened during April 1985. The shroud passed the test, the first RBSN shroud to do so, and indicated that eliminating the stress concentration of the slot increased the load carrying capability to the required level.

All turbine shrouds were henceforth fabricated without the slots on the shroud flange. Of the remaining shrouds tested, only one, S/N 726 (RBSN), failed below the required load. Failure was attributed to a pre-nitriding crack in the shroud flange. Shroud S/N 744 (RBSN) did pass the test but was rejected for further use because of the presence of a crack/flow line found on the shroud flange. All the SN-54 turbine shrouds from NGK and SN 250M tur-

bine shrouds from Kyocera passed the mechanical screening test.

A variation of this rig was used in April 1987 for a series of tests to assess the structural integrity of the lower contact washers in the rocker assembly. Washers supplied by NGK (SN-54) and Kyocera (SN 220M) were tested to load up to 1814 kg (4000 lbs) through the turbine shroud, one at each of the three rocker supports.

Initially, nine lower contact washers from NGK were successfully tested on both sides to a 1814 kg (4000 lb) load. Following this, a series of tests was performed with Kyocera lower contact washers in which three failures were encountered out of 15 test attempts (each test setup can proof three contact washers on one side).

Following this, additional testing was performed to determine if a primary failure of one contact washer would lead to a secondary failure of an adjacent contact washer. To induce a premature failure of one contact washer, a washer was scribed on the lower side. The test showed that once the scribed washer had failed, an additional washer failure would occur in the 1134-1361 kg (2500-3000 lb) range.

It was later discovered that the supporting surfaces in the aluminum test fixture, which support the lower contact washers and the rockers did not all have perfectly flat faces. In at least one case, a visible depression was observed, that was later measured at 38-51 microns (0.0015 -0.002 inches). Preliminary analysis indicated that the local depressions below the contact washers would induce high bending stresses in the washers. The aluminum test plate was subsequently remachined to eliminate the surface depressions. On June 15 and 16, 1987 ten contact washers made out of NC132 were tested on both sides to 1814 kg (4000 lbs). In the eight tests required all contact washers survived without any damage.

The results to date for the mechanical screening rigs are shown in Figure 327. A high

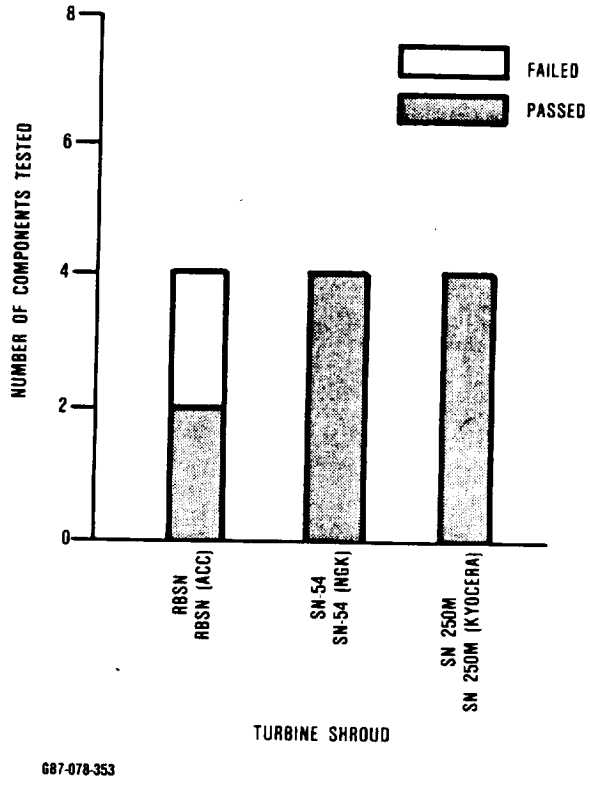

Figure 327. Mechanical Screening Component Test Results.

rate of success has been experienced for all material/component combinations except for the turbine shroud made out of RBSN. These failures have been traced to material processing flaws and are not design related.

6.3.3.2 Thermal Screening Test Results

Thermal shock test results were first obtained from the torch test of RBSN and SASC stators. All stators tested were from the first batch made by ACC and Standard Oil and were tested in the as-sintered condition with no final machining. In addition all the stators were reject components. The ACC stators were rejected due to voids in the leading edge while the Standard Oil stators were rejected due to dimensional problems. The objective was to identify potential design or material deficiencies as early as possible. Because of the lack of close simulation between the thermal response of the test and analysis, this test

was intended only as an interim test until the more refined thermal screening rigs became available.

Some of the stator vanes from both ACC and Standard Oil survived the worst case start simulation. Those made out of RBSN tended to fail at processing defects that were detected by radiography, others failed at the mold line at the radius between the trailing edge and the platform. The SASC stators tended to fail at the radius between the trailing edge and the platform. Those stators that survived the thermal shock test gave reassurance to the adequacy of the existing stator design.

Initial testing of inner and outer diffusers resulted in fractured components starting from the bolt holes in the inner diffuser and bolt slots in the outer diffuser. Progressive design changes were made in conjunction with analysis to increase test success. Design changes on the outer diffuser included scalloping the outer ring, slotting from the inner to outer diameter, and finally eliminating all of the outer rim and bolt slots by piloting off the inside of the rocker assembly (Figure 328). Likewise with the inner diffuser, slotting from the inner to outer diameter, removing the outer rim and changing to bolt slots, was tried before the final change was made to truncate the outer diameter to below the rocker assem-

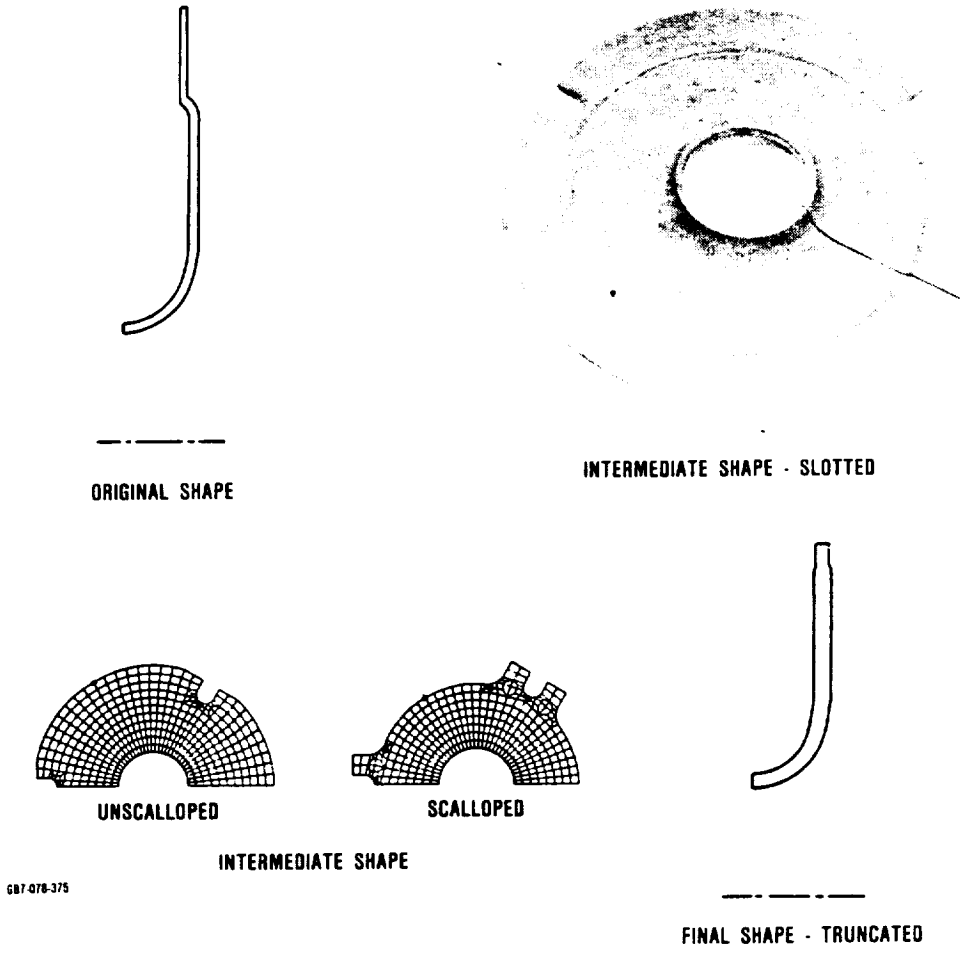

Figure 328. Outer Diffuser Housing Design Evolution.

bly, thereby eliminating the bolt slots in the component (Figure 329). The initial goal was to screen a few components for application in the static structure rig before a rigorous test cycle was used to proof components for normal engine use. These components were qualified and on February 5, 1985 proof testing was initiated. To insure component traceability, laser marking of all ceramic components was also initiated. No deterimental effects from the marking were noted (see also paragraph 6.1.5).

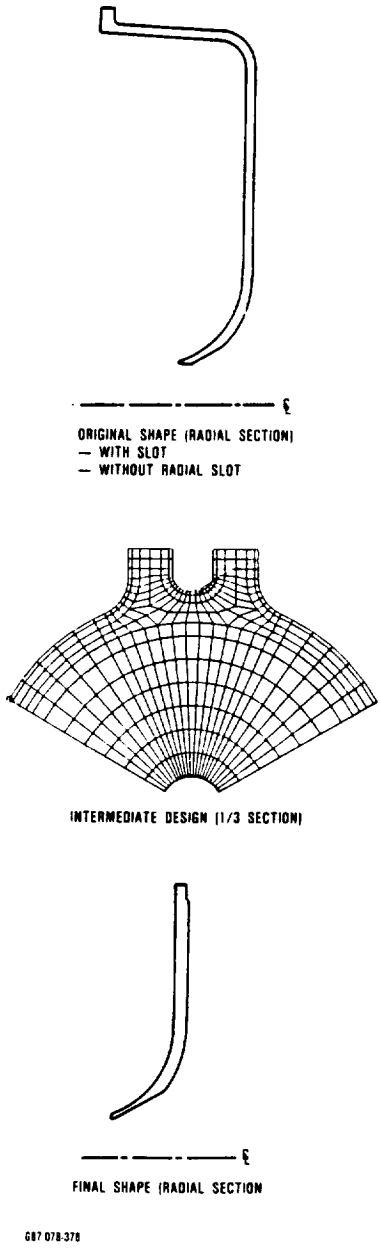

Figure 329. Inner Diffuser Housing Design Evolution.

The test history for the other screening rigs also proceeded on a similar and concurrent path, whereby early testing took place in conjunction with analysis to optimize the component design. Numerous design evaluations were made with the transition duct/combustor baffle thermal screening rig. Design evaluations on the transition duct centered around the design of the standoff for the combustor baffle struts and the T_4 thermocouple holes. The primary justification for the final design choice was based on manufacturability and functionality since, except for one design choice, no degradation in test results was evident for any choice. Degradation in component strength was noted in testing of two components with thermocouple bosses brazed to the transition duct. The braze material was moly-disilicide. Brazing was discontinued after this trial and all following components utilized a slip fit design.

The combustor baffle design activity primarily focused on the effect of wall thickness. A higher rate of test success was achieved with a uniformly thin wall that was 5.08 mm (0.200 inch) thick. All subsequent combustor baffles were changed to this design.

Initial testing of the turbine shroud was done without any stators in the rig. This was quickly discontinued when it became apparent that stators were required to simulate the thermal response of the shroud along the flow path. In addition, since no flow occurs on the outboard of the shroud as in the engine, the thermal shock was much greater in the rig than in the engine for the same combustor discharge temperature rise rate. Consequently, the proof cycle for the turbine shroud was adjusted to maintain a maximum thermal shock stress 25 percent higher than for a normal engine lightoff. The proof cycle was based on measured transient temperature responses in the rig and engine.

Initial design activity on the turbine shroud focused on the effect of wall thickness. When poor results were obtained for both the thin or regular wall thickness components, a completely new design concept study was initiated. The outcome of that analytical study was the varied wall thickness turbine shroud design which would provide for a more uniform thermal response (Figure 330). Initial testing

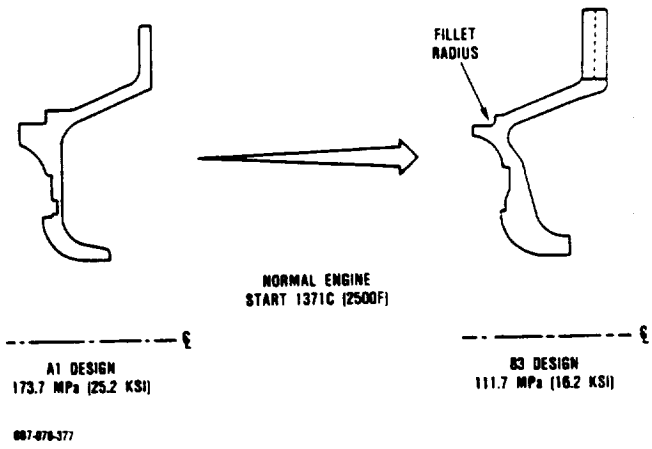

Figure 330. Turbine Shroud Design Evolution.

of this design was not encouraging due to the presence of a large stress concentration at the seal land radius that was not detected in the analysis. Subsequent testing of this design was made successful by a combination of a larger seal land radius, a better control of the finish within the seal land radius, and improved material properties.

An attempt was made to improve the marginal capability of the original design by machining a full radius cutback in the stator vane trailing edge. An apparent improvement in strength was noticed in testing. All subsequent stators were made with the cutback trailing edge. Three integral stator assemblies from Ford were also tested and all resulted in failures.

As the component designs became finalized along with the proof cycle requirements, a data base evolved that allowed for comparative evaluation of the performance of various ceramic materials in a simulated engine environment. Figure 331 shows the test results for RBSN (AiResearch Casting Company, SN-54 (NGK-Locke), SASC (Standard Oil) and SN-250M (Kyocera) materials used on the AGT101 engine components. Both SN-54 and SN-250M showed better consistency, although their data base was somewhat smaller. SASC showed better success with the combustor baffle application than with the transition duct, perhaps, because of fewer stress concentrations in the combustor baffle design. RBSN tended to do better on components aft of the stator, when combustor pattern factors are less pronounced.

6.3.3.3 Static Structure Rig Testing

Static structures rig testing was initiated in July 1982, with primary intent to simulate steady-state engine idle conditions at a 871C (1600F) T4.1. The initial build suffered the fracture of an outer diffuser along a radial line. Thereafter, the rig was rebuilt substituting an updated outer diffuser design, containing a radial stress relief slot (reference paragrapha 6.3.1.2). Another (partial) teardown and rebuild ensued, this time due to a suspicious acoustic event, before the rig was successfully run (as Build 03) of the metallic engine. This successful series was run at turbine inlet temperature of 871C (1600F) at airflow rates of 75.6 and 113.4 g/sec (10 and 15 lb/min), to simulate engine test bed idle and cruise flow conditions. A total of 15 start and shutdown thermal transient cycles were completed, with an average start transient time of 120 seconds. In addition, shorter thermal start transients were run in the range of 15 to 25 seconds to 871C (1600F) demonstrating the capability of the ceramic static structural components to withstand current metallic engine test bed start transients.

At test completion, the rig was disassembled and none of the 49 ceramic components were damaged. Also, no areas of interface deterioration were detected.

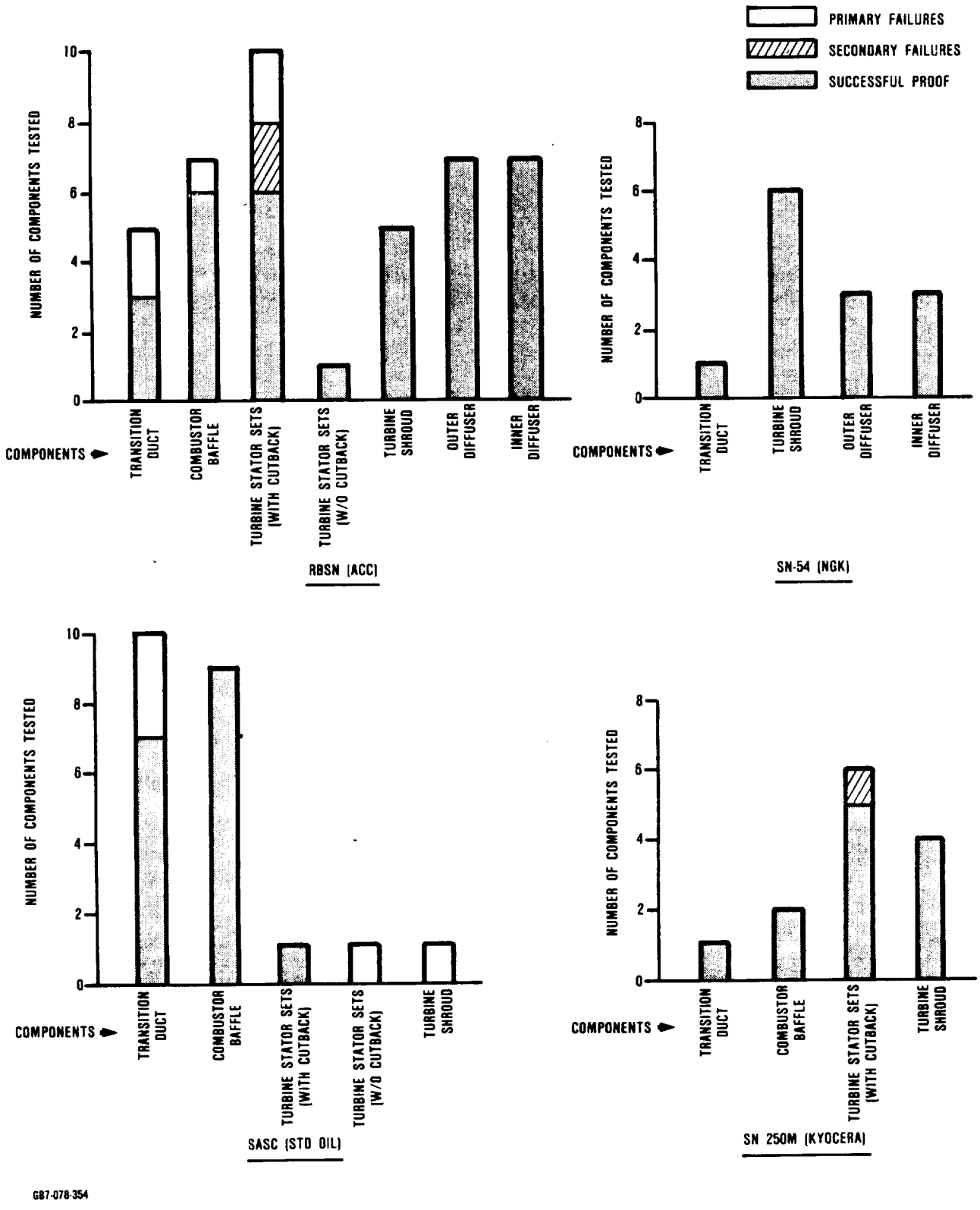

Figure 331. Thermal Screening Component Test Results.

Subsequent builds again encountered setbacks. In one case, an experiment with a fibrous seal between the turbine shroud, transition duct, and flow separator housing gave unfavorable leakages when compared with the ceramic seal rings they replaced. In another case, instability of the rig combustor due to the inadequate control of the pressure drop across it resulted in a typical heating of the ceramic components and consequent fracture. In still, another case, a stack calculation error resulted in a "thermal jack", or interference between parts as they grew at differing thermal expansion rates during the course of testing, and thus catastrophic failure of several ceramic components. And in the subsequent build (Build 07) a radius mismatch between the regenerator shield and the mating pocket or platform in the flow separator housing was the cause for failure of the flow separator housing during assembly.

The replacement flow separator housing for Build 08 had a fillet smaller than the corner radii in the mating regenerator shield. In August 1983 a complete set of ceramic structures was tested to a cycle 25 percent more severe than the cycle defined for the first set of 1149C (2100F) engine testing with ceramic components. Seven cycles were completed. On the lightoff for the eighth cycle rig testing was terminated due to excessive high-to-low pressure internal leakage. The rig was disassembled and inspected for component damage.

Minor chipping was noted on the following components: combustor baffle strut, eccentric spacers, flow separator housing ID seal ring, and $T_{4.1}$ (TIT) thermocouple load spacers. None of the noted chipping was a result of material interface sticking. The excessive leakage that terminated the test was due to the collapsed diaphragms on the regenerator inner seal as a result of overheating.

Turbine shroud alignment is of paramount importance in maintaining proper turbine rotor running clearance within close tolerances. The ceramic rocker/eccentric assembly successfully maintained cold assembly runout dimensions of 38.1 microns (0.0015 inches) total-indicated-reading (TIR) through the cyclic testing of Build 08.

Rig Build 09 incorporated a completely new set of ceramic hardware and was conducted to the same test cycle as Build 08. At two minutes into the second cycle the acoustical emission monitor picked up a continuous high energy output from a rocker assembly sensor. Due to high energy indications, the test was terminated and the rig disassembled.

Upon disassembly, component inspection revealed a fractured turbine shroud and a chip from the outer diameter of the outer diffuser. The turbine shroud fractured at a surface defect approximately 3.18 mm (0.125 inch) in depth. In addition the outer diffuser housing stackup was loose due to apparent sticking at the number two and three bolt locations. It is believed that the vibratory energy from the outer diffuser to the turbine shroud driven by the recirculating flow behind the outer diffuser, contained sufficient energy to propagate the existing surface defect and chip the outer diffuser. To preclude the potential for this problem to reoccur, the spring load across the inner and outer diffuser stackup was increased from 9.5 kg (21 lbs) to 36.3 kg (80 lbs).

The rig was reassembled with a replacement turbine shroud as Build 10 and run to the same cycles as with Builds 08 and 09.

At 19 minutes, 20 seconds into the first transient cycle (1093C) a 91 db event was recorded on the flow separator housing acoustic emission monitor. The count rate for the event (approximately 450 counts) indicated a probability of fracture. However, no changes were noted in rig HP or LP inlet pressures, and there was no fluctuation in regenerator drive torque following the event, therefore, the test was continued. After the successful completion of ten cycles the rig was disassembled.

At disassembly it was noted that the inner diffuser and the flow separator housing had fractured. It is believed that the flow separator housing fractured at the time indicated by

the acoustic monitor and was caused by a radial interference between the flow separator housing and the ring support housing. Inadequate diametral clearance between the insulation preform (in its coated and hardened condition) and the inner diffuser has been determined to be the primary cause of the fracture of the inner diffuser. The anti-erosion coating on the insulation preform is applied by brush, and so coating thickness is difficult to control. Also, the insulation material is subject to shrinkage in use, another obstacle in controlling its geometry.

The objective for Builds 11 through 13 was to subject the ceramic static structure components to a start 25 percent more severe than the development engine start, which would be equivalent to the normal engine start. The initial test for Build 11 utilized the two flow path rig configuration used on all previous static structure rig test. A three inch laboratory burner is located in-line of the low pressure air supply. This burner had never been used at the higher mass flows required for this start cycle and was unable to maintain the proper burner control to achieve the desired lightoff. The rig was consequently reconfigured to include the engine combustor by using a single flow configuration as in the engine.

A successful lightoff was achieved with the new rig configuration but was terminated prior to achieving the desired maximum temperature of 982C (1800F). The test was terminated due to the occurrence of coupled acoustical emissions from the two probes and a simultaneous drop in rig inlet pressure. Disassembly revealed that the transition duct, stator assembly, shroud, outer diffuser, and backshroud had fractured.

Fractography results in conjunction with thermal and stress analysis for monitored rig conditions have concluded the cause of failure to have originated from thermally induced stress in the turbine backshroud. The components are believed to have reached fracture stress as a result of a rig burner/control instability at the time of maximum (transient) stress in the above listed components. The shock wave created by the strain release in the backshroud at fracture is believed to have caused the failure in the interfacing components.

The solution to the rig failure was twofold. First, the turbine backshroud was partially stress-relieved by redesigning, and machining a 3-inch diameter hole through the center of the component. The void area was then filled with Lockheed HTP-12 insulation. The 3-inch diameter hole removes the current peak stress area of the component, effectively lowering the maximum principal stress by 88-percent. Secondly, an improved fuel metering system was installed to preclude burner/control instability, thereby minimizing the probability of a rig induced failure.

In September 1984 another set of static structure rig components was assembled as Build 12 and run with the same test objectives as for Build 11.

Five cycles to 982C (1800F) were accumulated, after which the rig was removed from the test cell and disassembled. All major ceramic components were intact; only a few minor discrepancies were observed. These included chips on two of the three spacers separating the inner and outer diffusers; two very small chips on the inner diffuser, and a small chip due to contact stress on the flow separator housing seal ring. Successful completion of this test represented the first time that a full set of ceramic static structure components were proof tested to such severe thermal shock conditions.

Rig Build 13 was assembled from another set of ceramic components and tested in April, 1985. Three successful test cycles were run to same conditions required for Builds 11 and 12.

Late in the third cycle, high level AE was noted, indicating a possible fracture of ceramic components. The test was terminated. Subsequent rig disassembly revealed only a chipped stator segment (reusable) and erosion of the high temperature ZAL-45 fiber insula-

tion. The high level AE indications may be attributed to the insulation breaking up, or perhaps to the effect of a too rigidly mounted AE probe sweeping a surface as the rig expands and contracts. The test was considered completed.

After Build 13 confidence had reached a level that a check screen of the entire ceramic structural assembly was no longer felt necessary as long as components were still qualified on smaller subassembly thermal and mechanical screening rigs. The static structure rig was therefore modified and used as a hot regenerator seal leakage test rig.

6.3.3.4 1371C (2500F) Static Rig Testing

This section covers the high temperature testing of ceramics to investigate effects such as static fatigue, contact loading, sticking, and endurance. Testing was conducted in three different rigs throughout the duration of the program before a specific rig for high temperature testing was finalized.

The initial testing was done in the backshroud/stators/turbine shroud screening rig with improved insulation in mid-April, 1984. The objective was to subject the ceramic transition duct, combustor baffle, turbine backshroud, stator assembly, and turbine shroud to the high temperature cycle defined in Table 52. The first two cycles only reached 1149C (2100F) and 1260C (2300F) respectively. The third cycle reached 1371C (2500F). After 3.5 minutes at 1371C (2500F) a high acoustical emission event occurred.

Table 52. Test Cycle for Initial 1371C (2500F) Testing in the Stator/Shroud Screening Rig.

Time, min,	Temperature C (F)
6	649 (1200)
4	815 (1500)
4	982 (1800)
4	1149 (2100)
4	1260 (2300)
4	1371 (2500)
5 ramp	down to 649 (1200)
4	649 (1200)
Shutdown	

*Light-off to 649C (1200F) in 15 seconds; 15 second ramps

Disassembly revealed fractures to the turbine shroud and the integral stator ring. The stator failure was secondary to the turbine shroud fracture. The most likely explanation of the fracture was that the pressure difference across the stators created a force sufficient to counteract the spring load holding the ceramic stack together. Thus, the assembly was sensitive to any fluctuations in pressure. Initiation of fracture was at the turbine shroud seal land outer diameter (OD) where contact was made with the transition duct. Prior to further testing the rig underwent modifications to the axial spring loading mechanism.

In mid-May, 1984 another set of ceramic components was assembled in the modified rig and tested to a maximum temperature of 1371C (2500F) according a cycle similar to that used for the previous test. Although acoustical emissions indicated a high energy output after shutdown, rig teardown revealed all components intact, with the exception of a spalled wave spring. Wave spring spalling had been traced to the quality of the powder used in the manufacture.

The design of the backshroud/stator/shroud screening rig limited the 1371C (2500F) testing to short term exposure. The hot static rig was designed for long term exposure of elevated temperatures to the ceramic components. The original configuration for this rig had the flow path of the incoming air different from the flowpath of previous screening rigs in that the incoming air enters via a ceramic flow separator housing prior to combustion in the rig burner. Goals for this initial test were to establish proper rig setup in the test cell, verify rig build procedure and operation, and achieve a 1371C (2500F) temperature. The intended maximum temperature of 1371C (2500F) was not achieved because of component failures during start. Rig disassembly revealed a failed turbine shroud, integral

stator assembly, seal assembly. The most likely cause for the fracture was contact loading near the fillet area of the shroud where it mated with the flow separator housing seal ring.

Further testing at 1371C (2500F) was conducted in October 1984 using the backshroud/stator/shroud screening rig as a test bed in lieu of the previous hot static rig. The ceramic hardware in the backshroud/stator/screening rig Build 06 was subjected to 30 minutes of operation at 1371C (2500F) and 75.6 g/sec (10 lb/min) airflow. No fractures occurred during the operation.

Two significant observations were made during rig disassembly. Insulation which supports the turbine shroud and the rest of the ceramic hardware, consisting of a silicon dioxide insulation with an alumina based rigidizer, yielded during the test, allowing the parts to drift axially by approximately 1.3 to 2.5 mm (0.050 to 0.100 inch). The insulation also stuck to the turbine shroud when the latter was removed from the rig. Further, examination under magnification on the three struts on the combustor baffle and the mating areas of the transition duct revealed glazing in these areas, although no component sticking was observed (the parts were freely disassembled). Successful completion of this test represented the first time that these components had been exposed over a long period (30 minutes plus) to 1371C (2500F) temperatures.

A subsequent attempt to repeat the test, (backshroud/stator/shroud screening rig, Build 07), but substituting a turbine shroud of RBSN for the SSN turbine shroud, was aborted approximately 5 minutes after reaching the 1371C (2500F) temperature. The rig was shut down after a shift in the stack of the ceramic parts was noted. Subsequent disassembly revealed that this was due to relaxation of the insulation, as had previously occurred. Unfortunately, quench water used to cool the discharge ducting backed up into the rig, passed a dam intended to contain it, and as a result the turbine shroud and backshroud both were fractured. The fractures originated in areas where high stress levels normally would not occur. Also, several stators were noted to have stuck to the turbine shroud. This phenomenon was analyzed and it is felt that the sticking was due to metallic deposits emanating from the metal-sheathed thermocouples employed in the rig.

In April 1985, further 1371C (2500F) testing was conducted, this time employing a new rig design similar in configuration to the backshroud/stator/shroud screening rig, but oriented in a vertical position. This was done for two reasons: 1) to allow a dead weight to supply the required load to the ceramic stack, and 2) to preclude the possibility that discharge quench water would back up into the rig. This rig would be used for all subsequent 1371C (2500F) testing. This rig's first test was identified as the 1371C (2500F) static rig Build 01.

The dead weight employed was made of 300 Series stainless steel, insulated for protection. Unfortunately, it reached a high enough temperature at approximately 25 minutes after achieving the 1371C (2500F) test temperature that premature shutdown of the rig was thought prudent. Upon disassembly four RBSN stators were found lightly stuck to the RBSN turbine shroud and the LAS spacer ring melted. The melting of the LAS spacer ring was believed to be caused by a combination of a hot spot in the flame and leakage through the seal assembly.

Build 02 incorporated an RBSN spacer ring and a stator assembly consisting of both RBSN and SASC stator segments. To extend the running time at the 1371C (2500F) temperature, the dead weight system was changed to incorporate ceramics. However, the amount of weight that could be physically installed in the rig envelope was found insufficient. A pressure differential, at the test light-off, between the flow path and the cavity surrounding the test pieces caused the transition duct to move upward (axially) and then bounce back down upon the rest of the stack of parts. Because of this failure no test time at 1371C (2500F) was accumulated for this build.

Rig modifications to allow for 1371C (2500F) testing were completed in early July 1985. An external spring loading mechanism was used to provide the axial force to contain the ceramic components. This rig configuration was tested for the first time in late July 1985 (Build 03) and was successfully operated at 1371C (2500F) for 2 hours. Stators made of silicon carbide (SiC) and reaction-bonded silicon nitride (RBSN) were alternately used to evaluate interfacial sticking. Teardown inspection of the rig revealed glass formation, primarily on the stator and baffle feet surfaces; however, there was no evidence of sticking.

The next build (Build 04) incorporated an all RBSN stator set and RBSN turbine shroud to evaluate interfacial sticking at the shroud/stator interface. No results were obtained. A light-off was attempted using an off-the-shelf automatic control system. Thermocouple response in this rig (the thermocouples are shielded in a ceramic sheath) was too slow for adequate control, and as a result ceramic fracture ensued.

Builds 05 and 06 each accomplished 12 hours at 1371C (2500F). Build 05 showed sticking at the stator/turbine shroud and stator/stator interfaces. No damage was seen at either interface. Previous builds had showed the transition duct/baffle interface to be a problem when using the same material for both parts. This problem can be eliminated by using an SASC transition duct/RBSN baffle combination.

Build 06 showed no sticking. Unlike the RBSN stators in Build 05, the SASC stators did not stick to either the turbine shroud or to each other. As in Build 05, alternating materials at the transition duct/baffle interface eliminated problems encountered in earlier builds.

The test objective of stator rig Build 07 was to determine the effectiveness of Al_2O_3 Sol-Gel coating on SASC parts to prevent sticking. Preliminary results using test bars have shown this to be an effective coating. In this test the coating was not satisfactorily evaluated due to failure of the turbine shroud. This was caused by inadequate clearance between the SASC turbine shroud and the RBSN transition duct to allow for the differential thermal growths.

The test objective for Build 08 was to evaluate SN 250M material in an assembly with SASC material. After 13 hours of testing at 2500F three pairs of SN 250M stator segments were found stuck to each other but not at the stator to shroud interface. In addition, a glassy deposit was found at the center portion of the SASC turbine backshroud.

Build 09 consisted of a complete set of ceramic components made out of SN 250M. The rig was run for 14 hours at 1371C (2500F) and similar results to build 08 test were found on disassembly. The glassy deposit was again found on the center portion of the backshroud, but this time the backshroud was made out of SN 250M. This would seem to indicate that the glassy deposit was not reacted from the backshroud surface. Two pairs of stator segments were also found stuck to each other and one stator stuck to the turbine shroud.

To date, limited sticking at 1371C (2500F) has been seen. No failure has occurred due to sticking. Interfacial distress seen between the transition duct and combustor baffle can be eliminated by using an alternating material stack in this area. More time at temperature is needed before drawing any conclusions about possible detrimental effects of the stator/stator and stator/shroud sticking that was seen.

6.3.3.5 Ceramic Seals Testing

Performance measurements made during engine testing of the ceramic-structured and all ceramic engines indicated power output was below design calculations. Excessive leakage through the ceramic sealing areas was suspected as a primary reason for the lack of power. The three sealing areas of interest included the turbine shroud/flow separator piston ring seal, the regenerator shield/flow

separator housing butt joint seal, and the regenerator shield/exhaust housing piston ring seal. These seal areas are shown in Figure 332. In order to isolate and measure leakage through these areas, three cold static seal rigs were designed and fabricated. Each of the rigs made extensive use of engine hardware in order to simplify fabrication. By measuring cold seal leakage, the rigs were able to generate performance data for new seal designs which could be compared to performance of existing configurations. The rigs were also successful in measuring the effects of seal loading, concentricity between sealed parts, and effects of pressure distortion on seal performance.

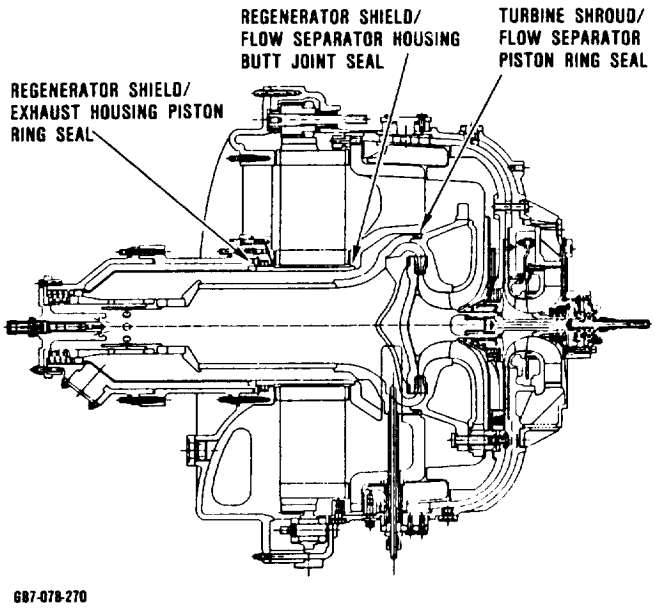

Figure 332. Turbine Shroud Piston Ring Seals.

Since the turbine shroud/flow separator piston ring seal was believed to be most critical with regard to engine performance, this rig design was fabricated initially and is shown in Figure 333. Baseline leakage measurements using the turbine shroud piston ring seals rig were obtained using the single LAS flow separator seal configuration shown in Figure 334. This configuration was compared to a new dual seal configuration shown in Figure 335.

The dual seal configuration utilized two LAS flow separator housing seals and a turbine shroud piston ring seal solid stack arrangement in the turbine shroud seal pocket. The spring load was transferred from the turbine shroud stack to the baffle/backshroud/stator stack by inserting a 17.8 cm (7-inch) ceramic wavespring between the baffle and backshroud. Rig measurements of the new configuration showed a 50-percent reduction in leakage over the single LAS configuration as shown in Figure 336.

Leakage testing with the single LAS seal configuration was done to determine the effects of axial load on the seal performance. Seal loading was varied from 2.27 to 25 kg (5 to 55 lbs) over the range of engine pressures. As shown in Figure 337 there was no significant benefit from increased loading.

Single LAS seal testing also indicated that eccentricity between the turbine shroud and flow separator has a significant effect on seal performance. This increased leakage up to 25 percent in a position of 1.52 mm (0.06 inch) eccentricity over the concentric position.

Overall, a 50-percent reduction in turbine shroud/flow separator housing piston ring seal leakage was accomplished by maintaining eccentricity below 1.0 mm (0.04 inch) and creating the dual seal configuration. More recently, a triple seal configuration was designed and fabricated using sintered silicon nitride. The seals have a split end gap to account for the difference in thermal growth between the LAS flow separator housing and the silicon nitride seals. Although testing has not yet begun, the seals will have increased temperature capability over the LAS design and should exhibit improved performance.

The regenerator shield/exhaust housing seal is a piston ring type seal shown in Figure 338. The dual seal is axially loaded onto the cast iron exhaust housing through a ceramic wavespring. The primary purpose of the test was to determine the effect of load applied to the seal on seal performance. The results from this testing indicated that axial load had a critical effect on seal performance. The seals are a split end gap configuration which

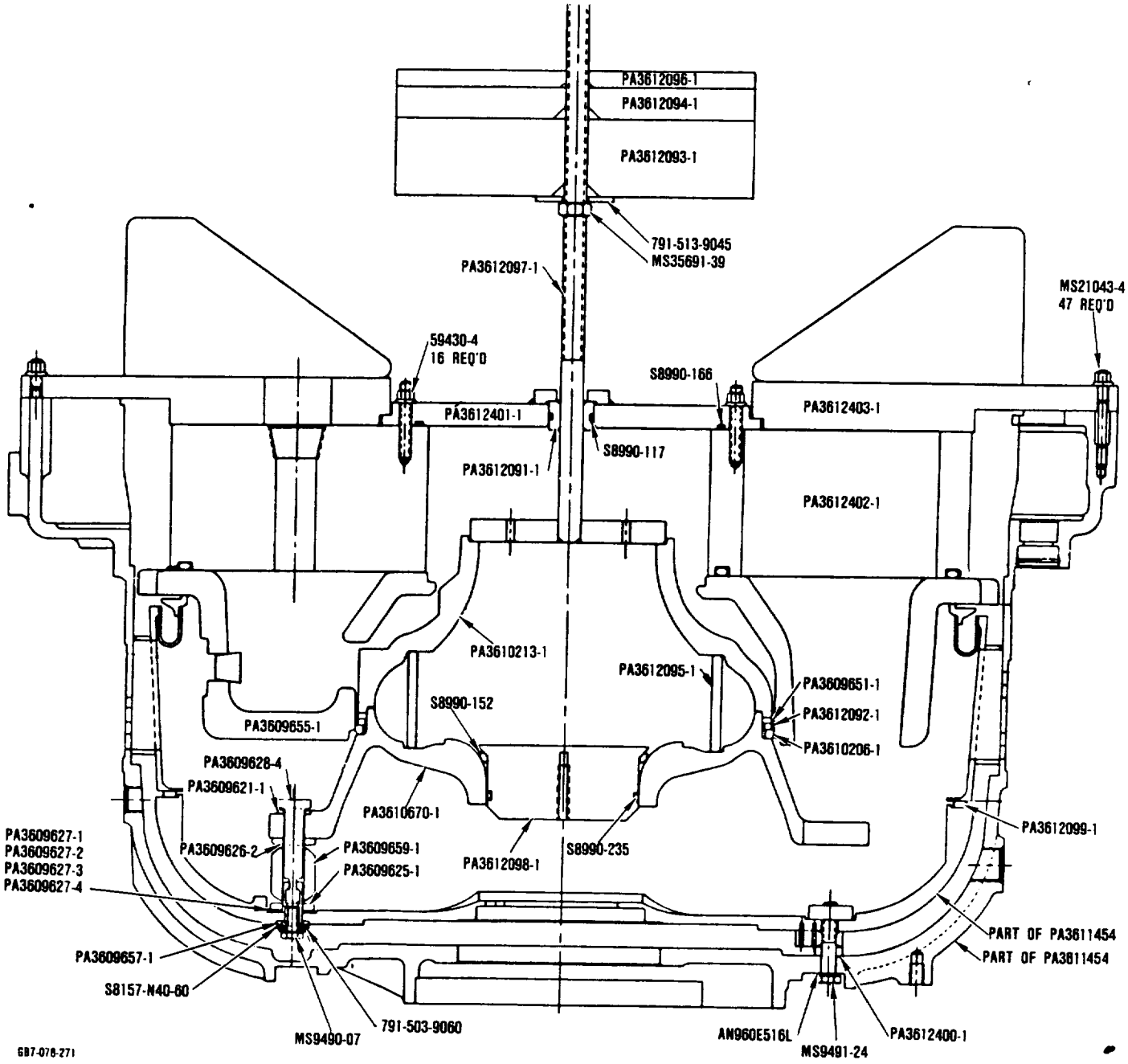

Figure 333. Turbine Shroud Piston Ring Seals.

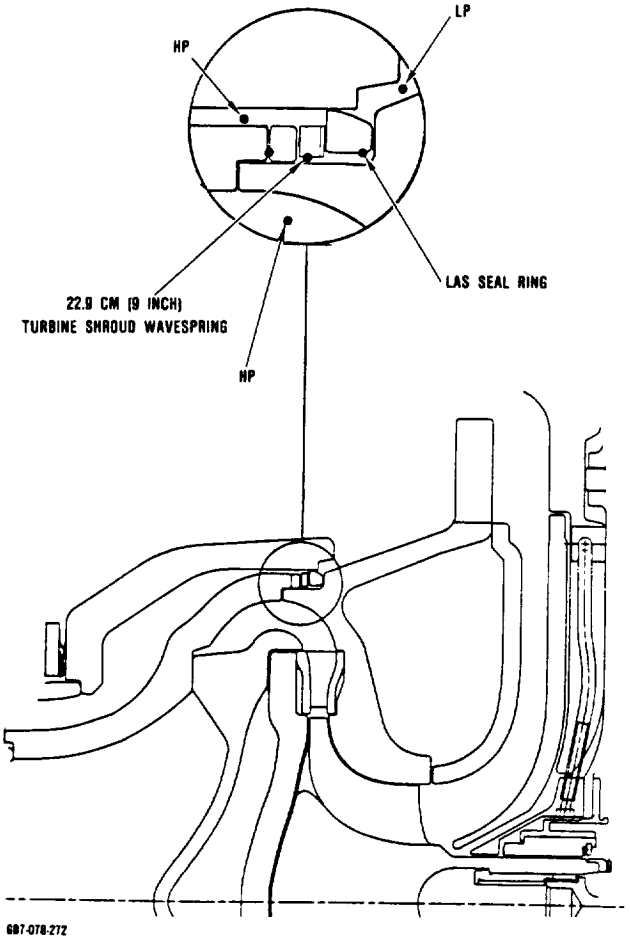

Figure 334. Single LAS Flow Separator Seal Configuration.

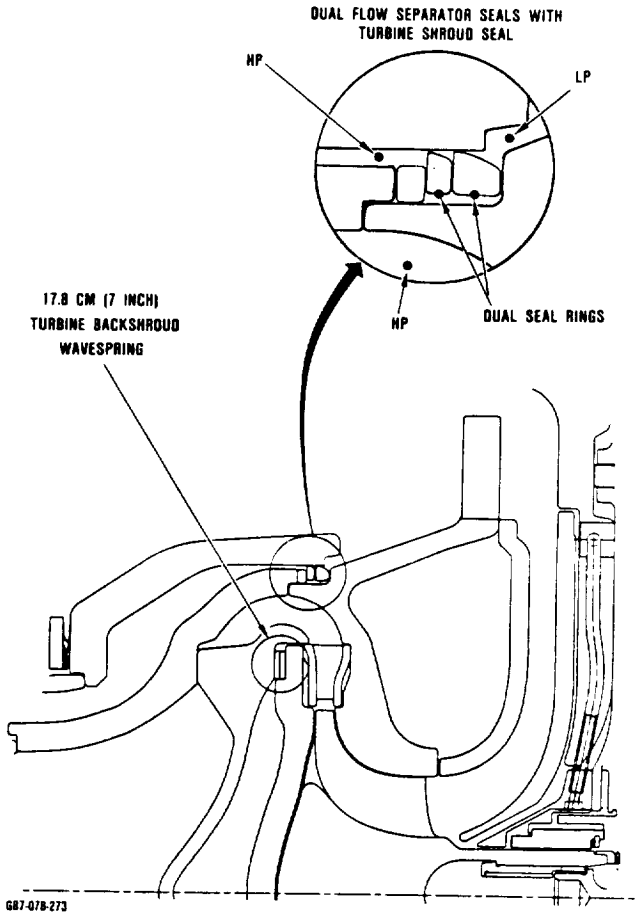

Figure 335. Dual LAS Flow Separator Seal Configuration.

allows for thermal growth of the regenerator shield and uses pressure to conform the seal to the surface of the shield. Testing showed that seal performance needs improvement at lower pressures where the seal is not pressure-activated. Optimum axial load was less than 2.27 kg (5 pounds). A typical seal leakage curve is shown in Figure 339. Further seal testing will focus on methods of improving this seal's low pressure performance.

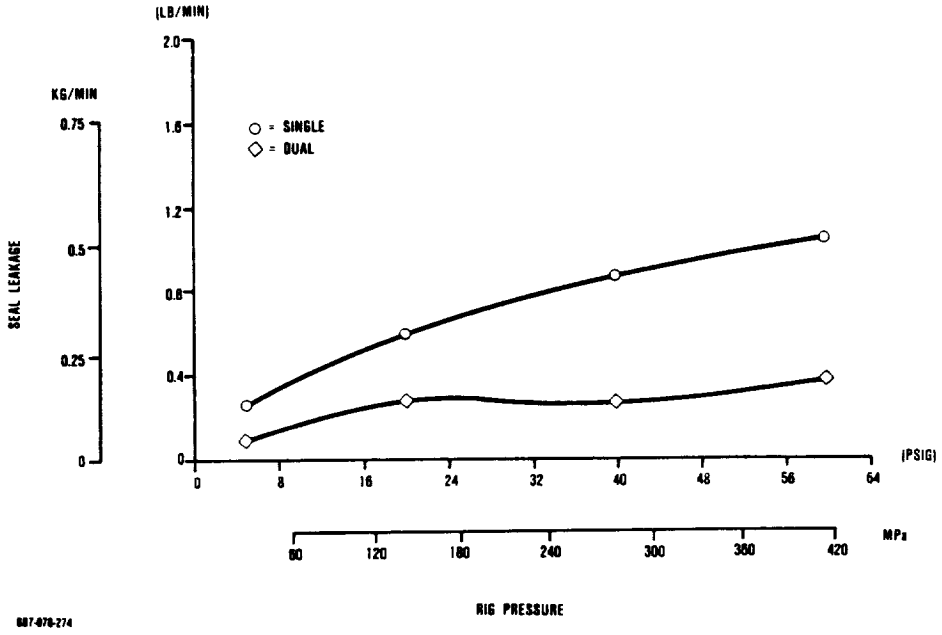

Figure 336. Single vs. Dual Piston Ring Seals.

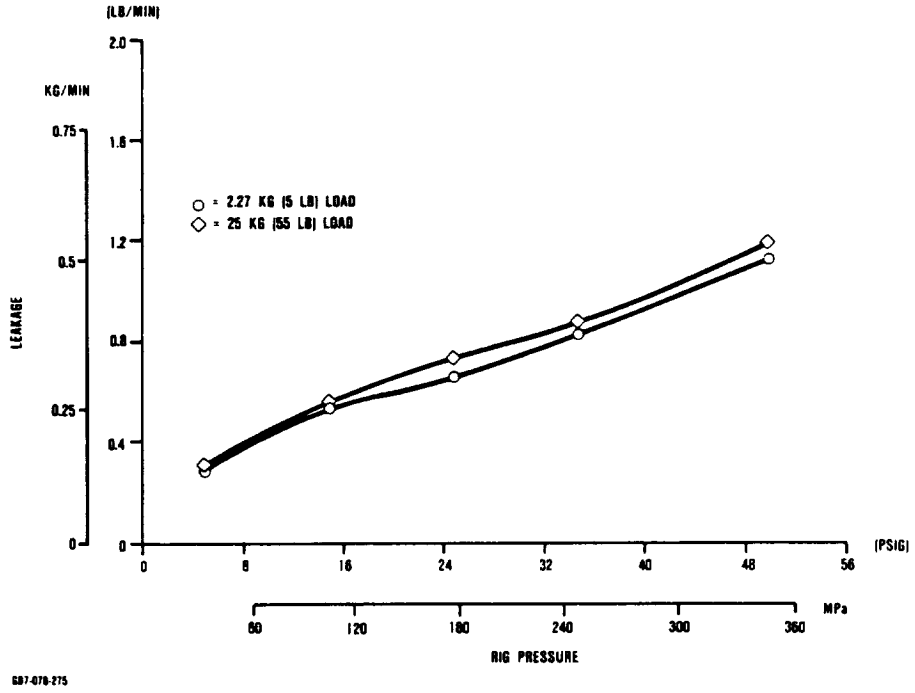

Figure 337. Increased Loading Effect on Single LAS Seal - 5-28-86.

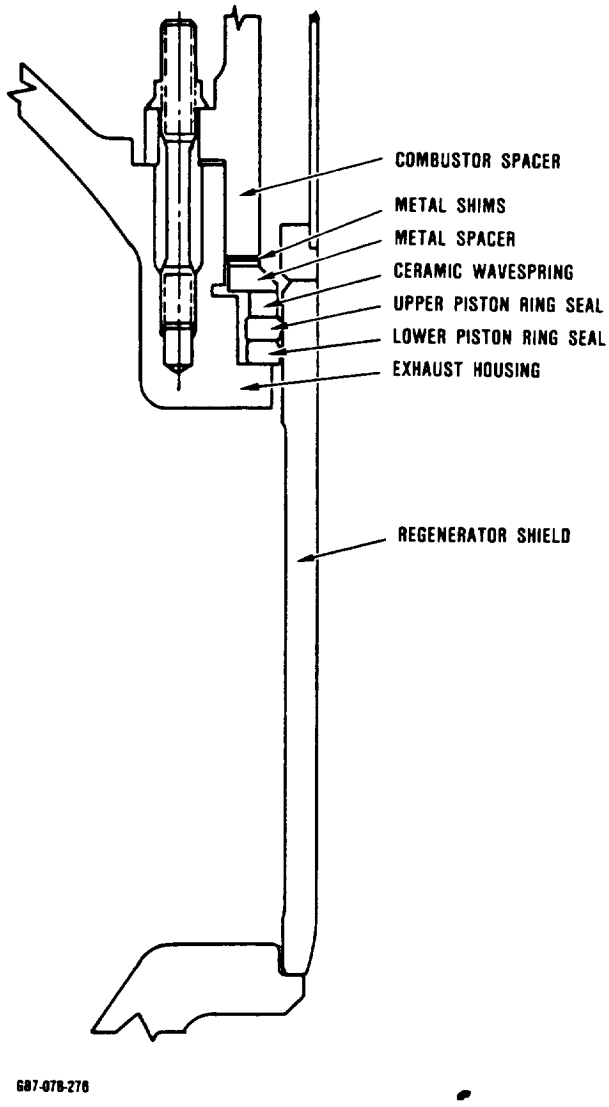

Figure 338. Regenerator Shield Piston Ring Seal Configuration.

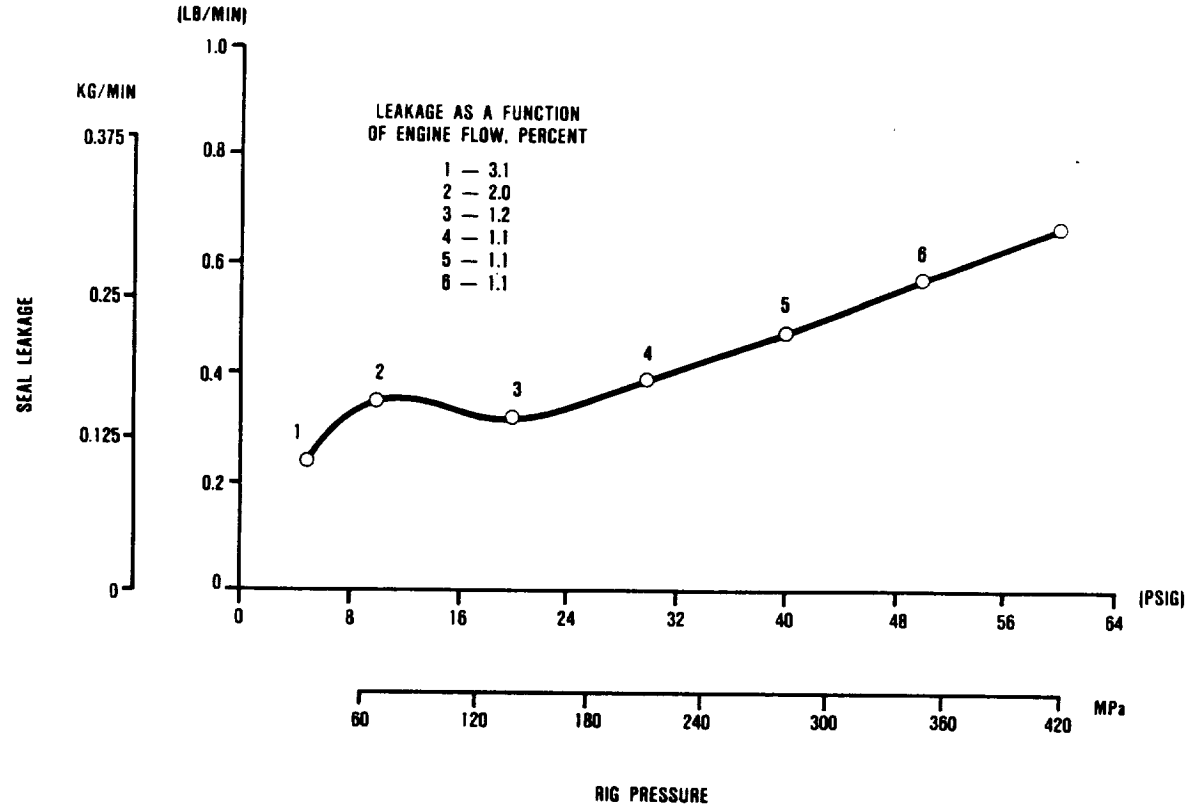

Figure 339. Regenerator Shield Seal Leakage over Operating Pressure Range.

APPENDIX A

AIRESEARCH CASTING COMPANY ADVANCED GAS TURBINE (AGT) TECHNOLOGY DEVELOPMENT PROJECT FINAL REPORT

1.0 INTRODUCTION

This report, submitted by AiResearch Casting Company (ACC), covers the efforts of ACC in support of the Advanced Gas Turbine - 101 Program (AGT101). This program was conducted as a subcontract to the Garrett Turbine Engine Company (GTEC). This report covers ACC's materials and fabrication development efforts. These efforts are concerned with the materials development and fabrication or rotors and ceramic structures by slip casting and the fabrication of stator vane assemblies by injection molding.

2.0 ROTOR - MATERIALS AND FABRICATION PROCESS DEVELOPMENT

2.1 Introduction

Net shape fabrication of an AGT101 turbine rotor was considered to be the most challenging task of the whole AGT program. No baseline rotor fabrication technology was available at the beginning of the program in 1979. Every aspect of materials and processing procedures had to be developed.

Initially, a rotor fabrication process was developed based on GTE SN502 Si_3N_4 powder. In the last two years, GTE has not been able to produce powders with consistent quality. Consequently, new materials and processing procedures were required.

The following section describes the progress made in developing the standard processing procedures using GTE SN502 powder, the material properties of the rotors, and the more recent efforts of developing alternate materials and processing procedures.

2.2 Pre-Casting Materials Preparation Development

Proper materials preparation to produce a desirable slip is the foundation to the successful casting of the rotor. It involves the optimization of milling procedures (particle size control), slip property adjustments (pH, viscosity, solids contents, etc.), and green density. The materials composition selected for investigation at the beginning of the program (1979) was GTE SN502 Si_3N_4 + 8 percent Y_2O_3 + 4 percent Al_2O_3 (Code 1 composition). A rubber lined steel mill jar with Si_3N_4 media was used to blend the powders and control the particle size distribution. The milling time was 72 hours. The initial slip preparation procedures resulted in a slip with low solids contents (31-66 percent) and having a high tendency to gel, and a very high viscosity (500 cps). A subsequent series of iterative experiments resulted in a more desirable slip which had a solids content of 78 percent and a viscosity of 120 cps. This involved the reducing of milling time from 72 hours to 24 hours, the introduction of Daxad 30 as a defloculant and some other improvements. Before reaching these optimized slip properties, many factorial designed experiments were conducted to explore the effects of calcination temperature, wet milling versus dry milling, mill jar type, type of defloculants, the use of KOH, etc. on slip viscosity, gellation tendency, casting rate, green density and sintered density.

In 1983, a new composition (92 percent GTE SN502 + 6 percent Y_2O_3 + 2 percent Al_2O_3) was introduced. This composition, designated as Code 2, was developed in an AMMRC contract "Low Cost, New Shape Ceramic Radial Turbine Program" (Contract

No. DAAG46-81-C-0006). Because of the lower Y_2O_3 and Al_2O_3 contents, this new composition was believed to have superior high temperature properties. Optimization experiments were then conducted to establish a procedure to achieve desirable slip properties. The procedure produced well dispersed slip with consistent properties when materials were taken from the same lot of GTE SN502.

A series of slips was tested using the Haake viscometer at 25C, with the CV100 measuring drive, and the AZ30 measuring system. Yield points of the slips were then determined on the shear stress versus shear strain rate curves. Table 53 seems to indicate a correlation between yield point and gelling. This investigation led to the use of the Haake viscometer to control the quality of the slip prior to casting.

Table 53. Yield Point of Slip and Quality of Casting.

Slip ID No.	Test Date	Yield Point, Pa	Remarks
06044	06-13-84	0.14	Good casting
06124	06-19-84	0.13	Good casting
05314	06-12-84	0.29	Slip gelled; rotor cracked
04274	05-14-84	0.22	Good casting
04184	05-10-84	0.24	Good casting
04164	04-26-84	0.24	Good casting

In April 1985, the characteristics of GTE SN502 Si_3N_4 were changed significantly due to several changes in the powder manufacturing process implemented by GTE. This required another series of process modifications before desirable slip properties were once again obtained.

2.3 Mold Fabrication and Casting Procedure Developments

Net shape casting of a bladed rotor requires an organic shell mold with the correct configuration, dimensions, and a defect free inner surface. A procedure was developed to fabricate such a mold from either a rubber pattern or a water soluble wax pattern. The development effort was primarily performed using rubber patterns. This development was aided by the expertise that exists in the Wax Department at ACC.

Several shell mold materials were evaluated with varying degrees of success. A paraffin based material, optimized for wax patterns, was initially used for mold fabrication with rubber patterns. The paraffin based material was opaque and did not coat the blade edges well. Ethyl cellulose and butyrate based dip seal materials provided transparent molds helpful in obtaining complete fill and excellent edge coating but were not dimensionally reproducible. Subsequently a translucent mold material (LN 209-218) was developed, similar to the original material, with improved edge coating capability.

All organic shell molds were produced by one technique. The reusable pattern is dipped into the advanced shell mold material, LN 209-218. The mold is built up further by continued dipping into a molten batch of water-soluble wax. The reusable pattern is then pulled from the mold and the water-soluble wax is dissolved away.

The wax mold is placed on a plaster base which provides the configuration for the dome and also removes the water from the slip. Initially there were problems with poor dome surface quality and the presence of pour lines. A procedure to treat the plaster mold with a 0.5 percent ammonium alginate solution was established which produces a smooth dome surface.

The initial experimental castings experienced air entrapments, high porosity and high concentrations of agglomerates. To solve

these problems, a screening and de-airing of the slip immediately before casting was incorporated.

In addition, a pouring device was developed whereby slip is withdrawn from the bottom of the container. This was to eliminate the contamination from the foaming foreign substance which always appears on the skin layer of the slip and produced defects in the initial experimental castings.

Incomplete fill near the upper blade tips was one of the major problems when bladed rotor casting efforts were first introduced. To overcome this problem a procedure to spin the mold during slip pouring was incorporated. Another improvement in casting procedure was the control of pouring rate by using a separatory funnel.

The as-cast rotor often exhibited cracks on the dome because of a fast casting rate in the dome area where the slip is in direct contact with the plaster mold. This cracking problem was eliminated by soaking the plaster mold in water prior to use.

2.4 Drying and Pre-Sintering Developments

Cracks often developed during drying of a ceramic part. This is particularly true for large size rotors with varying thicknesses. Improper drying also would result in cracking during pre-sintering or sintering. At the beginning of this program even the bladeless simulated rotors cracked consistently. Figures 340 and 341 show two examples. Consequently, a major effort was devoted to solving this problem.

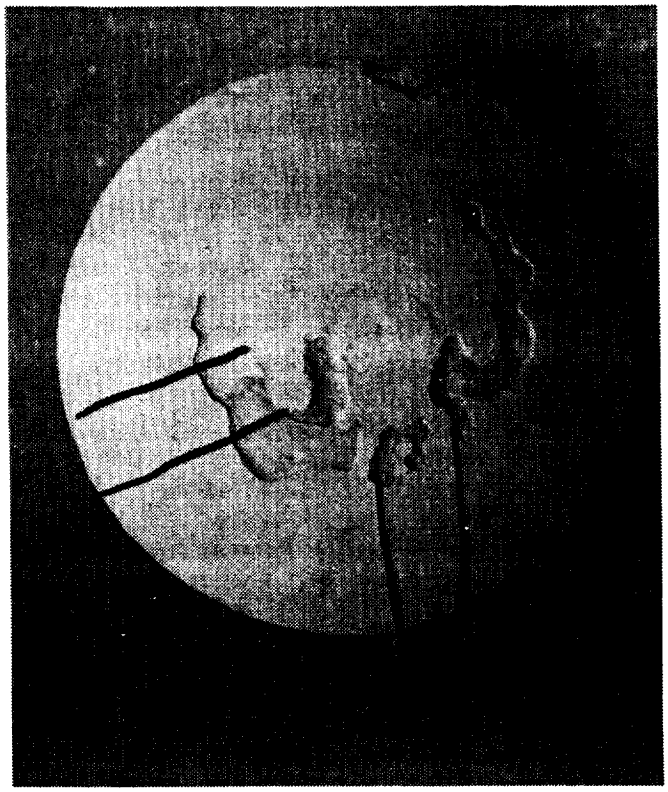

Figure 340. Cracked Dome On a Bladeless Rotor Casting After Drying.

Figure 341. Part After Sintering Cracked Into Several Pieces Due to Incomplete Drying.

The initial experiments included the use of a desiccant to absorb moisture from the part and oven drying at 150F as the final step in the drying procedure.

This procedure was not successful even with the simulated rotors. Another experiment involved drying the part at room temperature for one day followed by vacuum drying for three days. Again the parts cracked into several pieces. Additional experimental trials included drying the parts in a plastic box, with or without venting holes for a period of up to several weeks and the use of manually controlled humidity oven. This was then followed by oven drying at 90F. None of these experiments showed any significant improvements.

The major breakthrough occurred when a programmable humidity oven was introduced. This humidity oven enabled more systematic control of the drying environment. A successful cycle for the rotor was developed. The cycle starts at a high humidity (80 percent relative) and low temperature (77F) and ends with a low humidity (20 percent relative) and high temperature (185F). Final drying is accomplished in an air oven due to the temperature limitation of the humidity oven. This drying cycle shortened the previously unsuccessful long cycle to 9 days and produces consistently crack-free bladed rotors.

Prior to the demonstration of ACC's sinter/HIP capability, dried castings were shipped to Ford or ASEA for densification. To avoid shipping damages, a pre-sintering cycle was developed. This sintering cycle was to impart sufficient strength to the rotor without causing cracking or noticeable sintering. The cycle was successfully established with the 100 psi furnace. This pre-sintering cycle has beome a standard procedure prior to sintering even for rotors sinter/HIP'ped at ACC.

2.5 Configuration Evolution

Rotor efforts at ACC were initially directed toward fabrication of both injection molded and slip cast rotors. a simulated rotor configuration (bladeless rotor) was used in both approaches before a bladed rotor configuration was introduced.

Injection Molding

A Tempcraft plunger type injection molder was used in this effort. A large number of silicon nitride simulated rotors were injected to evaluate the wide variety of molder adjustments. These included variations in injection pressure, tool clamp pressure, flow control, barrels and nozzle temperature, injection and cooling time. In spite of the wide choice of parameter variations, a problem of air entrapment within the rotor persisted.

It was decided to modify the simulated rotor tool configuration. Originally, the base portion of the tool was made in two halves in order to permit future simulated vanes at the vertical parting lines. However, it was found that the tool could not be clamped with sufficient pressure to resist flashing. This caused release of injection pressure resulting in poor surface and incomplete mold fill. A new one-piece base section was built which eliminated the flashing problem and improved surface cosmetics but did not eliminate air entrapment.

The next tool modification designed to solve the problem of entrapped air was to provide the capability to evacuate the cavity prior to injection. It was found that the vacuum had to be turned off simultaneously with material injection or the material would flow into the vacuum system requiring extensive clean-up. However, even with the ability to evacuate the mold cavity, air within the injection molder barrel enters the mold with the batch material when injected.

Originally, the entrapped air in injection molded simulated rotors was assumed to be the major reason for the inability to produce a satisfactory rotor. In an effort to determine the actual material flowpath during injection, a clear plastic was substituted for the Si_3N_4. The material flowed from the backface (where it entered the tool), moved along the tool wall, and on into the shaft end and sealed off the air trapped in the center.

As a result of this experiment, much of the problem encountered with voids in the injection molded rotors was traced to the fact that the rotor was not cooled sufficiently within the tool to solidify the binder before holding pressure was lost. Pressure time was thus increased from 6 minutes to 30 minutes. When the resulting rotor was split open, it was solid throughout, showing no evidence of voids. Subsequently more rotors were injected that did not have any flaws as determined by visual inspection and X-ray radiography. However, cracks developed in the rotor in the initial binder removal experiments.

To solve the binder removal problem, many studies were conducted. Initially, a study was performed to determine whether rotor hub size is a critical factor. For this evaluation, crack-free molded bladeless rotors were reduced in size by lathe turning and evaluated in the vacuum dewax cycle. Again, dewax cycles resulted in rotor cracking, indicating that rotor size was not a major controlling variable.

Additional experiments using various thermal cycles in a nitrogen atmosphere at 10-12 psig pressure were tried, but results were inconclusive. The injection molding approach was discontinued in 1981.

Slip Casting

The very first castings were made using the bladeless rotor or simulated rotor configuration. The first casting was made in a metal mold with a plaster base. In subsequent castings, the metal mold was replaced by plaster and then by rubber.

Bladed rotors were fabricated using rubber patterns based on an actual metal rotor until a metal pattern with allowance for 14.5 percent sintering shrinkage was obtained. Scale-up was successful. All castings, by November 1981, were aimed at producing parts with the 14.5 percent shrinkage.

Mold design changes were made in 1985. The present rubber pattern was changed from 14-5 percent (A1 generation) to 17.0 percent (A2 generation) shrinkage allowance.

Another modification affected blade thickness at the saddle area, blade to hub filled radius, transition changes at the saddle area between the blades and a belled saddle to hub line radius definition. This modified design was named the "B" generation. Another difference between the "A" & "B" generation is the "A" generation utilizes reusable rubber patterns while the "B" generation uses injection molded water-soluble wax patterns.

2.6 Densification Process Development

Prior to 1983, the only high temperature furnace available to this program for densification of slip cast parts was the 100 psi N_2 furnace at ACC. Many cycles were experimented with in this furnace using Code 1 composition test plates as well as rotors. The theoretical density of Code 1 is 3.30 g/cm^3 (based on the rule of mixtures). Typically the test plates achieved densities in the range of 3.18-3.22 g/cm^3, while the rotors could only achieve 2.78-3.04 g/cm^3. Parameters investigated included soak temperature and time, heating rate, furnace load, and kiln furniture history. In addition to the sample densities (plate versus rotor) effect noted above, it was found that kiln furnitures previously exposed to an oxidizing environment had a detrimental effect on densification. It was also found that samples with lower weight loss exhibited high strength at room temperature.

Due to the low densities obtained at ACC using the 100 psi furnace, an arrangement was made to densify rotors at Ford and ASEA. Ford has a 1500 psi furnace and ASEA has glass frit encapsulation plus HIP'ping technology. Initially Code 1 rotors could be densified only to 3.20 g/cm^3 at Ford. As a result of continued materials/process development at ACC and cooperative efforts at Ford, bladed rotors were sintered to 3.27 g/cm^3 in November 1982 and further increased to 3.30 g/cm^3 in October 1984. Similar densities were also obtained in rotors densified at ASEA. In June 1983, ACC had demonstrated a capability to sinter/HIP bladed rotors to 3.26 g/cm^3 (Code 1 and Code 2). The Code 2 composition has a theoretical density of 3.26 g/cm^3. In 1984 the

densification processes at ACC, Ford and ASEA all could densify rotors to densities higher than 98.8 percent of theoretical. As a result of the good ACC sinter/HIP densification results, shipments of rotors to Ford and ASEA were discontinued.

2.7 Alternate Raw Materials Development

Limited availability, inconsistency in quality, and the higher cost of GTE SN502 Si_3N_4 powder have been the impetus for the search for alternate sources of Si_3N_4. Various silicon nitrides were investigated as potential replacements for GTE Si_3N_4. Some of the results are described in the following paragraphs.

Denka 9S Si_3N_4 was milled with additives, prepared as slip and cast into rotors. Sintered rotors yielded final densities of 3.23 to 3.26 g/cm^3. However, more optimization experiments are required before a stable and consistent slip can be routinely prepared.

UBE SN E02 and SN E05 Si_3N_4 were evaluated as a replacement for GTE. 100 percent SN E02, 100 percent SN E05 and blends of E02 and E05 (25-75, 50-50, and 75-25, percent by weight) all exhibited lower viscosities and faster casting rates than baseline castings. However, all developed cracks prior to sintering.

Starck H-2 Si_3N_4 showed little discoloration on rotor blades but was difficult to make into a consistent slip. A new procedure was recommended by Allied Central Lab. This involved preparing the slips of Starck Si_3N_4 and the premilled additives (Y_2O_3 and Al_2O_3) separately and then blending them together after adjusting them to a common pH. However, slips continued to be very viscous. No improvement in slip viscosity occurred after pH adjustments and lower solids content.

2.8 Alternate Casting Procedures Investigated

Long casting time, poor casting surface quality, incomplete fill and discoloration problem were addressed by trying a variety of alternate casting techniques or mold designs.

One of the original slip-cast mold configurations consisted of a plaster base that contained the backface shape and an all-rubber, two-piece mold for the hub and shaft. An iteration designed to reduce the length of casting time involved changing the all rubber portion of the mold to one-half rubber and one-half plaster. Several rotors were cast in this dual-material mold, but the portion of the casting in contact with the rubber face exhibited what could be classified as an outgassing condition with extensive surface porosity. A thin wax coating was applied to the rubber face portion of the mold, which improved the condition only marginally. The casting surface in contact with the plaster was excellent.

Another mold was prepared that was entirely plaster. The shaft portion was coated to render it non-absorbent in order to prevent preliminary casting in this area inasmuch as slip is poured through the shaft end of the mold. The casting appeared to be free of flaws both visually and by X-ray radiography. The above two experiments were conducted in 1981 on simulated rotors.

An all plaster mold using plaster inserts between the blades was tried. For the purpose of initial evaluation, the plaster inserts were made individually without proper tooling. Most blades were damaged while the inserts were being removed. It suggested that precisely fabricated plaster inserts and a controlled plaster insert removal mechanism should be developed before the potential of this technique could be truly evaluated.

An inverted wax shell mold, to form the blades, hub, and shaft was attached to a plaster base. A wax pattern dome with a funnel at the top center was welded to the upper wax shell that formed the blades (1981). This technique resulted in visually crack free rotors but it required a much longer casting time. In addition, it was difficult to form a precise dome contour. The wax dome in the above arrangement was replaced by a plaster plate with the dome contour. The slip was fed in both from the top and bottom, in separate experiments; all castings were cracked (1985).

Evacuation through the plaster mold base was aimed at reducing casting time, especially for the B generation rotor configuration. This approach was discontinued due to the lack of proper equipment.

Hydrostatic pressure casting was accomplished by placing a just poured casting and mold into a 1500 psi maximum pressure vessel. The vessel was then pressurized to various pressures and held for different lengths of time without heating. No obvious improvement in rotor quality was observed.

2.9 Blade Discoloration

As the casting procedures were established and drying cracks had been routinely eliminated, more attention was paid to other aspects of rotor fabrication problems, such as a blade discoloration. An interesting observation was first made in 1981 that a darker band always appeared near the tip of each blade. This discoloration first shows up in the green rotors as a dark grey color. Upon presintering this discoloration turns to black while the base material becomes white. After sintering, this discoloration remains black while the base material turns to the normal dark grey. When examined under a 30X microscope it was found that, after sintering, there were always mud-like cracks associated with the discolored area. These mud-like cracks were judged to be the cause of failure in the spin test performed at Garrett. Consequently, the elimination of the discoloration was identified as a major program objective.

Two parallel approaches were taken to combat this discoloration problem, namely 1) analysis and 2) process variation. The first approach was aimed at determining, chemically and microscopically, the difference between the discolored area and the normal area. The second approach was empirically to observe the effect of processing parameters on the degree of discoloration and the movement of the discolored area. Some major findings are described in the following:

1) Analysis

Many organizations have been contributing to this effort. Table 54 summarizes the results.

- **Garrett - SEM/EDX, 1982**

  Green as well as sintered blades were examined (Figure 342). The discolored area appears denser in the green state and contains heavier atomic number elements.

  EDX (energy dispersive X-ray) was used to compare the discolored area with the normal area. EDX shows that the discolored area has higher concentrations of Al and Y. It should be noted that EDX at Garrett could not, in 1982, detect elements with atomic numbers less than 11 (sodium). In the same investigation, a flower-like structure was found in the discolored region. EDX found that the flower structure contained higher concentrations of Mo and Y than the normal area. This was the only time that Mo was found in the material.

- **Seal Lab - SEM/EDX**

  Several green rotor blades were analyzed at Seal Lab with a more sensitive EDX (wavelength based) in an attempt to compare the concentrations of lower atomic number elements ($N<11$) between the discolored and normal areas. Several energy levels were used. Table 55 lists the results. It shows that oxygen, Na (or Zn) and Y were detected or existed in higher concentrations in the discolored region that in the normal area. Carbon was only found to be higher in the discolored region at 20 KV, thus is considered inconclusive.

- **Oak Ridge National Lab (ORNL) - Super Microprobe**

  A sintered rotor blade was examined at ORNL using their high sensitivity super

Table 54. AGT101 Rotor Discoloration Analysis.

Analyzed by	Method of Analysis	Discolored Area Compared with Normal Area	Stage of Process
Garrett (1982)	SEM-EDX Higher Al and Y	Higher Al, Sintered (AGT)	Green (AGT)
ORNL (November 1985)	Super Microprobe	Higher Y	Sintered (T-2)
Allied (March 1986)	SAXPS (Small Area X-Ray Photo Electron Spectroscopy)	Lower Y_2O_3	Pre-Sintered (AGT)
	SEM-EDS	Higher Al and Y Higher Al Higher Al and Y	Green (T-2) Pre-Sintered (AGT) Sintered (AGT)
Seal Lab (September 1984)	SEM-EDX	O, Na/Zn, Y	Green (AGT)
NASA (March 1986)	SEM-EDX	*	Sintered (AGT)

*No elements were significantly higher in the discolored area.

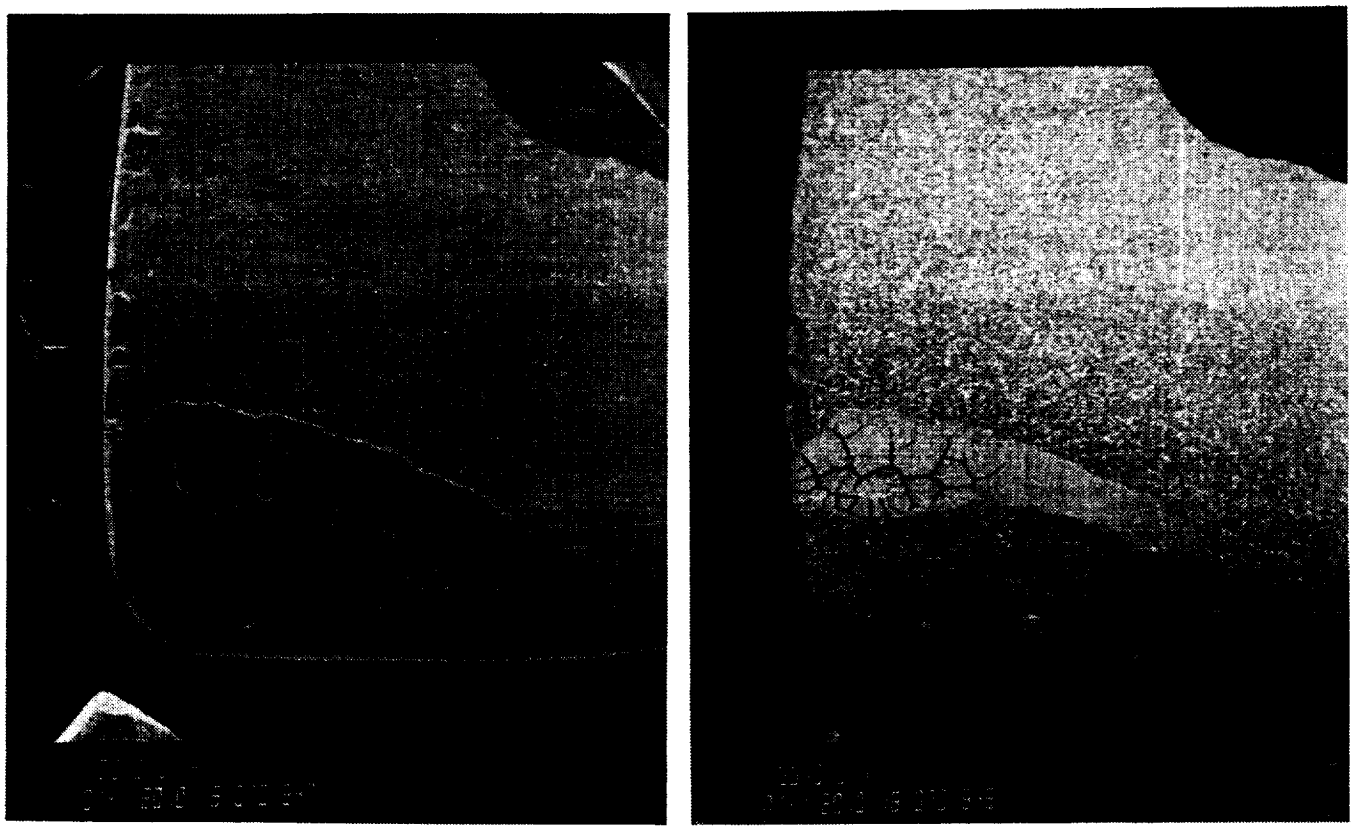

Figure 342. Green Vane Tip Showing Discolored Area.

Table 55. Discoloration Analysis of a Green Rotor.

EDX Voltage (KV)	Elements Detected	
	Discolored Area	Normal Area
4	C, O, Na/ Zn, Si, Y	C, Si
7	C, O, Na/ Zn, Si, Y, Al	C, Si, Al
20	C, O, Na/ Zn, Si, Y, Al	Si, Al
39	Si, Y, Al	Si, Al, Y

microprobe. The mud-like crack feature was found similar to the one reported by Garrett. The super microprobe showed that the only difference between the discolored region versus the normal region is the Y concentration being higher in the discolored region.

- o **NASA-Lewis Research Center**

  Both pre-sintered and fully sintered blades were analyzed by several techniques. Similar mud-like cracks were found in the discolored region. However, river-like cracks were found in the back face of a blade examined. Y concentration was found to be segregated in small islands which were uniformly distributed throughout the blade. No detectable difference between the discolored area and the normal area was found.

- o **Allied Central Research Lab (ACRL) - Methods (1986)**

  Green, presintered and sintered blades were analyzed by X-ray diffraction (XRD), X-ray photoelectron spectroscopy (XPS) and SEM - EMPA techniques. Although there were some differences in results found by different techniques, the most consistent results are that the discolored area contains higher Al and Y concentrations than the normal area.

2) **Process Variation**

Several experiments were conducted to determine if the cause of the blade discoloration was a result of a processing problem.

- o **Rubber Lined Steel Mill Jars Versus Al_2O_3 Miller Jar**

  To avoid undesirable oxide contaminations, rubber lined steel mill jars with Si_3N_4 mill media were used to prepare the powder. Due to the darker color of the discoloration, it was suggested that the rubber lining might be the source of the black substance. The rubber liner steel mill jar was replaced by porcelain mills (primarily Al_2O_3). The discoloration problem still exists.

- o **Upside Down Casting**

  The discoloration showed up on the back face of the blade instead of on the top face near the tip. This suggested that the discolored substance is lower in density tending to float to the top, then is trapped on the curved portion of the blade. However, finer particles also have a tendency to float. Thus, the discolored area might have a higher concentration of finer particles which may turn out to be Al_2O_3.

- o **Spin Casting Versus Stationary Casting**

  No difference was found between spin cast rotors and stationary cast rotors. In both cases, blade discoloration was evident.

- o **Reversed Spinning**

  A rotor was spin cast with the rotation direction reversed. Again, blade discoloration was present.

This experiment and the above experiment indicated that the discoloration phenomenon occurred after the mold was filled, i.e., during the casting period. The segregation or migration of certain species which resulted in discoloration occurred during the casting time which ranged from one to four days.

- **Plaster Patched Blade Tip Mold**

One-half of the blade edges of a wax mold were cut off and then sealed with plaster. This was to provide faster casting time (minimizing materials migration/segregation) near the blade area where discoloration occurred. This experiment resulted in a broader band of darker color parallel to the plaster seal on each blade which was sealed with plaster. The remaining unmodified blade of the same rotor showed the usual pattern of discoloration.

- **Additive Effects**

A rotor was cast with no additives in the slip. No discoloration was observed on the blades.

Another rotor was cast with a slip containing Y_2O_3 but no Al_2O_3. It also did not show any discoloration.

The above two experiments seem to suggest that Al_2O_3 causes discoloration.

Subsequent castings with reduced Al_2O_3 content (1 percent instead of the baseline 2 percent), no noticeable reduction in discoloration was observed.

2.10 Rotor Particle Size Distribution

A uniform particle size distribution (PSD) in a green rotor would normally result in uniform sintering shrinkage (thus no distortion), microstructure and mechanical properties through the rotor. The baseline process has produced rotors with very uniform PSD in the green rotors. To verify this particle size distribution measurements were made at different locations on several rotors to determine whether there is any variation in particle size distribution within dried green rotors. The results from one randomly selected rotor showed that no significant difference in PSD was found within the rotor (Table 56).

Table 56. Particle Size Variation Within a Green Rotor.

	Percentiles of Particle Size, μm		
Location	90th	50th	10th
Dome	2.62	0.90	0.36
Leading Edge	2.61	0.90	0.36
Blade	2.64	0.90	0.36
Trailing Edge	2.58	0.90	0.36
Shaft	2.60	0.89	0.36

Rotor Deliveries

During the AGT program, 50 turbine rotors were shipped to Garrett. Many of these rotors were spin tested and exceeded the 115K rpm proof test requirement. None of the rotors could be considered "engine quality" due to missing blades, surface porosity, and dimensional deviations from the print.

3.0 CERAMIC STRUCTURES- MATERIALS AND PROCESSES DEVELOPMENT

3.1 Summary

The objective of this portion of the AGT101 program at ACC was to supply static components to Garrett in support of the engine test program. At the outset, ACC was responsible for providing the turbine shroud, transition duct, turbine stator, turbine baffle, turbine inner diffuser and the turbine outer diffuser housing. Since that time, other components were added which included the turbine backshroud, flow separator housing, wave spring and flow separator housing seal rings.

The stator vanes were to be injection molded, and all the other parts were to be slip cast reaction-bonded Si_3N_4. The technology base at ACC prior to the start of this program was the establishment of a silicon slip, designated as RBN-104, and the demonstration of the net shape casting capability of various small engine components under several government programs. It was initially assumed that this baseline technology could be transferred to the fabrication of large AGT components without any significant developmental efforts. As the program proceeded, it became apparent that improved materials and processing procedures would need to be developed. It was also found that slip casting and other processing steps were very sensitive to tooling/design changes.

3.2 Materials Development

The original baseline compositions were established using silicon powder supplied by Kawecki Berylco Industries (KBI). Later in the program KBI discontinued operations necessitating evaluation of other sources of supply. Silicon was then obtained in lump form as ore directly from the mine which reportedly supplied KBI's material. The ore was pulverized by an outside source and returned in powder form. Analysis revealed high impurity levels and slip preparation was difficult and not reproducible. Other sources of high purity silicon powder were evaluated and Kemanord, Sweden, was finally selected as most reliable with respect to purity, consistency of product and availability of supply.

3.3 Pre-Casting Materials Preparation Development

Materials preparation prior to actual casting underwent continuous evaluation. Particle size distribution (PSD) and surface area (SA) of silicon powder are important parameters in controlling slip rheology. Experiments were conducted using the air classifier to separate the powder into different PSD fractions and observing slip behavior as a function of particle size.

Other parameters also affect slip behaviors. Experiments aimed toward density control of silicon slips prepared with various fractions of air classified powder were performed. Limits exist between pH and green density such that the controllable range of green density by pH and adjustment alone appears to be between 1.65 and 1.75 g/cm^3.

It was also recognized that small amounts of impurities such as calcium, deleteriously affected slip rheology and subsequent casting and nitriding results.

3.4 Casting Procedure Development

A flow chart of the overall slip casting process is shown in Figure 343.

One slip casting iteration was tried in efforts to eliminate center line shrink in the backshroud. The backshroud was cast to a thickness of one to one and a half inch using a net shape form one surface of the backshroud. The backshroud plaster mold to an otherwise solid ingot, as is shown in Figure 344 and 345. This is an effective method to produce the backshroud avoiding flow lines, centerline shrink and air entrapment, but requires considerable green machining.

3.5 Drying and Prenitriding

Drying of large, slip cast components, especially those with non-uniform wall thickness, has proven to be one of the more crucial steps in processing. Extensive evaluation of drying and prenitriding cycles were conducted. It is apparent that components such as the turbine shroud and transition duct must remain in the plaster mold after casting for a length of time to achieve good green strength. Subsequent to removal from the mold, it is essential that the casting be permitted to dry slowly and completely before attempting to prenitride. Several techniques have been used which include controlled humidity drying, drying in an enclosure and subsequent exposure to warm dry air, slowly heating in an oven over a long period of time to the boiling point of

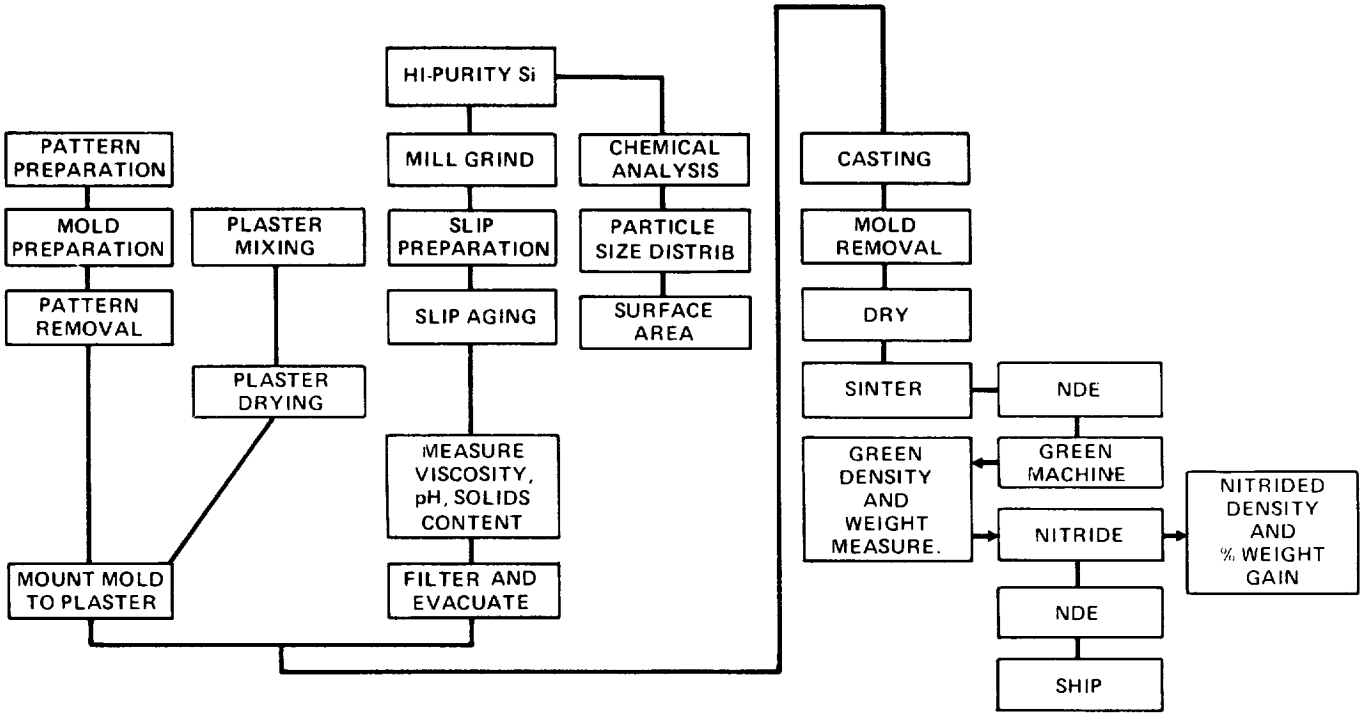

Figure 343. Flow Chart Showing Slip Casting Procedure.

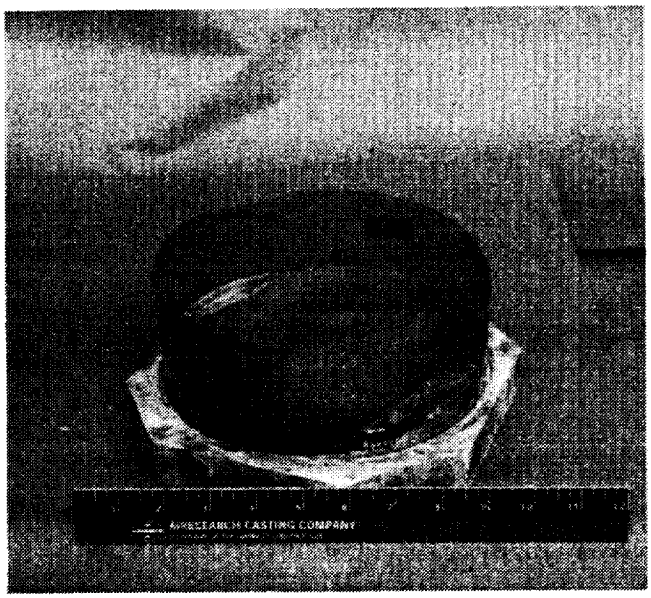

Figure 344. Plaster Base and Mylar Ring for Casting Solid Ingot.

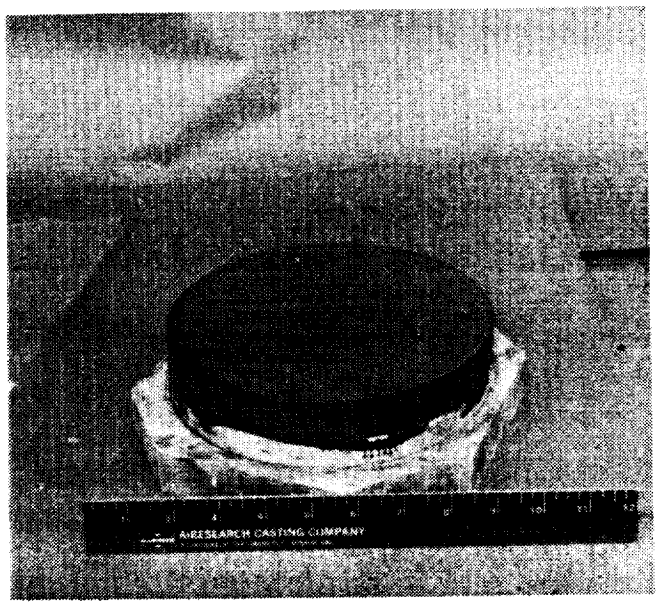

Figure 345. Ingot After Casting.

water and, allowing the part to remain in vacuum for several days prior to prenitriding. Several backshrouds and some transition ducts have survived prenitriding and machining but the turbine shroud continues to crack during prenitriding.

3.6 Nitriding Development

Early work investigation nitriding capability included nitriding thick sections, nitriding aids, and the effect of a 4-percent helium addition to the normal H_2-N_2 nitriding atmosphere.

Test plates of RBN-104 material were cast in thickness ranging from 1/4 inch to 1 3/4 inches to evaluate the nitriding capability of the standard cycle. These plates were nitrided and were evaluated for the presence of unreacted silicon. The nitriding of thick sections indicated that sections in excess of 1/2 inch thickness contained mostly unreacted silicon in the center. However, these evaluations were conducted with little mass of material in the furnace and a relatively short cycle. Since then it has ben found that nitriding is far more efficient when a large load mass and longer cycles are used.

Plates were cast to determine the effect of nitriding aid. Compositions investigated include the baseline 3 percent Fe_2O_3, 1.5 percent Cr_2O_3 and 1.5 percent Fe_2O_3 plus 1.5 percent Cr_2O_3.

The nitriding aid billets were machined into test bars. One-half of each of the specimens was nitrided in standard nitriding cycle and the remaining half was nitrided in an atmosphere containing a 4 percent helium addition.

The results are tabulated below.

Nitriding Aid Chemistries	H_2-N_2 MOR (ksi)	H_2-N_2-He MOR (ksi)
Baseline (RBN-104, 3 percent FeO_2)	47.0	47.0
1.5 percent Fe_2O_3	39.7	41.7
1.5 percent CR_2O_3	38.8	38.8
1.5 percent Fe_2O_3 + 1.5 percent Cr_2O_3	41.8	41.0

The new nitriding aids and nitriding cycle showed no improvement over the standard nitriding cycle and the baseline material, RBN 104.

This Page Intentionally Left Blank

APPENDIX B

FORD MOTOR COMPANY
ADVANCED GAS TURBINE (AGT)
TECHNOLOGY DEVELOPMENT PROJECT
FINAL REPORT

INTRODUCTION

Prior to initiation of the AGT program in 1979, Ford was involved in the early development of the various aspects of ceramic turbine technology. Much of this work was conducted under an ARPA-sponsored program entitled "Brittle Materials Design, High Temperature Gas Turbine"[1]. The broad objective of this program was to encourage wider use of ceramic materials in engineering systems; the more specific objective was to develop ceramic materials, designs, processes and test methods for a high temperature, automotive gas turbine and demonstrate 200 hours of ceramic component durability. Even though these goals were met on each of the ceramic flow path components, including the rotor, it became evident that development of the highly stressed, ceramic turbine rotor for widespread application was a most difficult and formidable task. A recommendation was made for a focussed research program that would investigate and develop materials, processes and designs and define reliability limits to establish "realizable potential" in this critical component.

In the AGT101 program, appreciable resources were allocated to the development of this critical component. Realizing the importance of ceramic materials, fabrication processes and components, as well as development of the regenerator system, Ford teamed up with the Garrett Turbine Engine Company as a subcontractor on the DOE/NASA/AGT101 Program. This report appendix covers activities in the ceramic materials and processes area.

Initially, the ceramic materials/processes tasks included materials and process development of the ceramic turbine rotor, the one-piece ceramic stator and the ceramic flow separator housing. As the AGT Program evolved, the Ford efforts on the one-piece stator and the flow separator housing tasks were terminated, because the work had reached a satisfactory plateau and the overall program was faced with funding reductions. In the critical ceramic rotor task, Ford retained its interest throughout the program, though there were, from time to time, budgetary reductions in all aspects of the program.

In this report, the ceramic materials and fabrication processes activities are covered according to the task breakdown in the subcontract, as shown below:

Task 2.3 - Ceramic Rotor

Task 2.7 - Ceramic Stator and Flow Separator Housing

Task 2.3 - Ceramic Rotor

Introduction

Pressureless sintered silicon nitride was the material selected for the fabrication of monolithic rotors for the AGT101 program. Two processes were proposed: the primary approach utilized sintered reaction bonded silicon nitride (SRBSN), with the more conventional sintered silicon nitride powder (SSN) serving as a backup material.

In both approaches, various developmental tasks had to be completed prior to producing a turbine rotor. These tasks included material and process improvement efforts. The fugitive wax slip casting method was employed to fabricate rotors from both materials.

SRBSN Material Development and Characterization

Sintered Reaction Bonded Silicon Nitride (SRBSN) describes a class of material combining reaction bonded silicon nitride and sintered silicon nitride technologies.

The consolidation process, outlined in Figure 346, begins with the addition of a sintering aid to a fine-grained, high purity silicon powder. Components are fabricated from this mixture using standard green forming processes including slip casting and injection molding. The part is then nitrided and sintered to near-theoretical density.

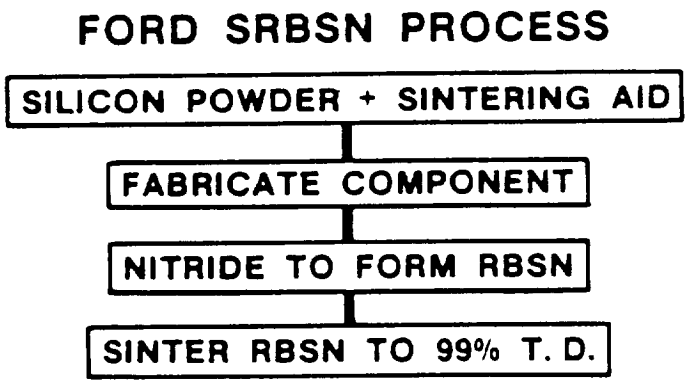

Figure 346. Ford SRBSN Process.

The inherent advantages of this process are availability and low cost of the raw material (silicon rather than silicon nitride) and lower sintering shrinkage.

Sintered reaction bonded silicon nitride has been under development at Ford since the late 1970s[2]. In the interim, SRBSN has undergone many iterative improvements in both material and fabrication processes, resulting in significantly improved microstructural and mechanical properites. This report will describe the material characterization techniques employed to identify the problem areas which prompted each iteration.

Slip cast SRBSN was developed for use in the advanced gas turbine engine, specifically for the highly stressed turbine rotor. Yttrium oxide was selected as the sintering aid for these materials as good strength at high temperature was retained by early hot pressed silicon nitrides containing this additive[3]. However, the Y_2O_3 - Si_2N_4 system is susceptible to oxidation, particularly with applied stress at intermediate temperature regimes. Consequently, time-dependent property determination also became an important aspect of the material characterization. These two characteristics, strength (flexural stress rupture) and oxidation resistance, dominated the evaluation program and determined the developmental iterations of this material.

Four grades of slip cast, yttria-doped SRBSNs were developed at Ford, code numbered RM-0 RM-1(4), RM-2(5) and RM-3. The properties of each of these grades are summarized in Table 57.

RM-0 Material

The first generation material (RM-0 had potentially high strength and Weibull modulus, despite significant batch-to-batch inconsistencies. Elevated temperature strength was acceptable. Oxidation behavior was evaluated at 700 and 1000C, the temperatures described in the literature as most critical in yttrium-containing silicon nitrides. Oxidation tests were performed for 300 hours in a static air environment. Visual inspection revealed surface discoloration, although no cracking had occurred. This was a significant improvement over the earlier Y_2O_3/Si_3N_4 which cracked severely after short exposure (<29 hours) at these temperatures[6].

RM-1 Material

The objective of the development of this material was reduction of the batch-to-batch strength variability exhibited by RM-0. This was accomplished through modification of the sintering cycle. The RM-1 material had high room temperature strength (91.5 ksi) with a Weibull modulus of 13.3. These characteristic values are a compilation of a number of sintering runs. Batch-to-batch variability was significantly reduced.

Table 57. Slip Cast SRBSN Material Properties.

	1979 RM-0	1980 RM-1	1981 RM-2	1982 RM-3
Density (g/cm^3)	3.05 - 3.31	3.20 - 3.25	3.26 - 3.31	3.26 - 3.34
MOR (ksi) and Weibull				
Room Temperature	65.7 - 107.5 (7.5 - 17.8)	91.5 (13.3)	107.6 (21.1)	98.6 (19.0)
1000C				77.6 (10.9)
1200C	78.3 - 84.6 (11.3 - 21.1)	81.9 (14.9)	91.7 (15.4)	71.6 (12.9)
1400C				70.8 (11.3)
Oxidation MOR				
700C	No cracking	-58% (700 hr)	0% (700 hr)	+7% (300 hr)
1000C	No cracking	-4% (300 hr)	-15% (700 hr)	-5% (300 hr)
1200C			-7% (300 hr)	-10% (364 hr)
1400C			-8% (300 hr)	-16% (300 hr)
Stress Rupture				
	—	—	1000 - 1200C up to 90 ksi: No time dependent failures (600 hrs)	≤40 ksi at 8000 - 1000C: No time dependent failures
	—		1000C, 20 ksi time dependent failure (57 hrs avg)	

Oxidation testing was again performed at 700 and 1000C. Exposure times were increased, up to 700 hours, and two new tests were introduced. Oxidation kinetics were determined by sequential weight gain measurements and the strength after oxidation was ascertained. This testing revealed that the reaction kinetics were different for each test temperature (Figure 347). At 700C, the kinetics were linear, and influenced by the testing sequence, while at 1000C, parabolic behavior was observed. Lower weight gains were recorded for samples exposed for 700 hours without removal for weight measurements. Again, no visible cracking was observed under any test condition; however, discoloration was noted. These data suggested that an oxidation problem still existed.

Residual strength after oxidation exposure was measured. Figure 348 shows the strength decreasing substantially when samples were oxidized at 700C, but deteriorating only slightly after the 1000C exposure. Additionally, the strength decrease at 700C was dependent on the testing sequence, as evidenced by the uninterrupted data point. A

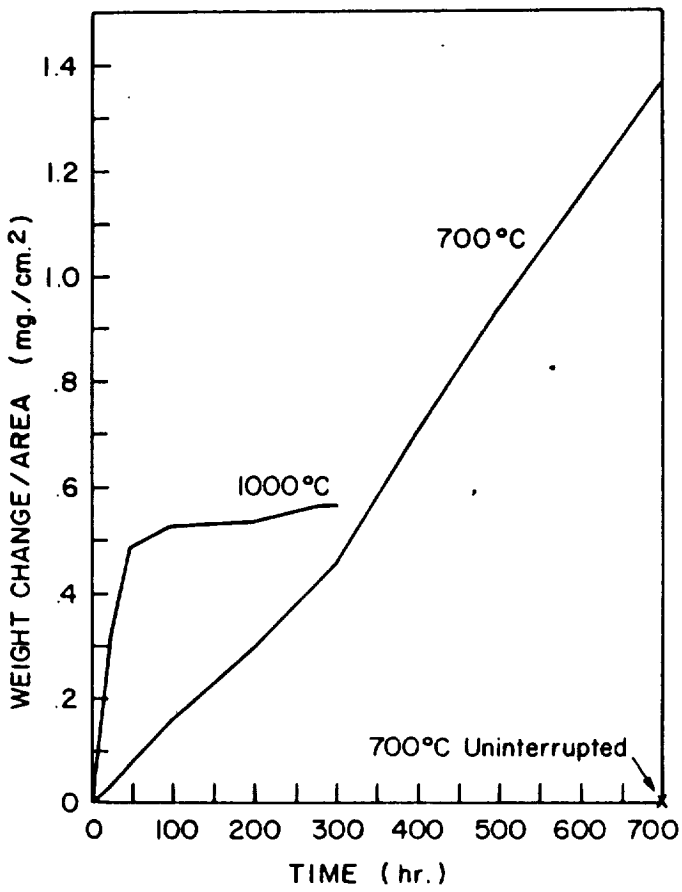

Figure 347. Oxidation Kinetics in RM-20.

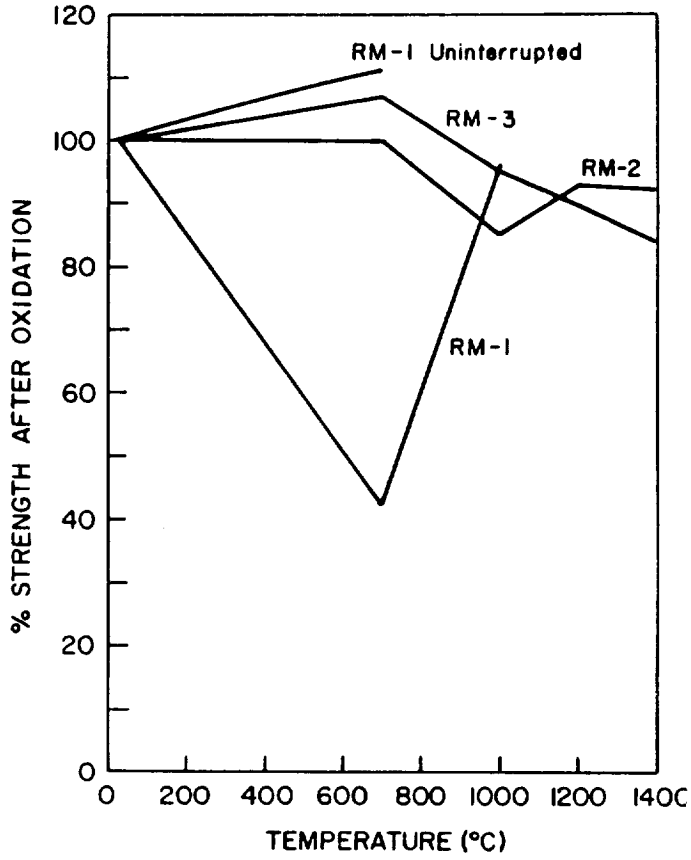

Figure 348. Strength After Oxidation of RM-1.

correlation was obtained between the oxidation kinetic and the strength after exposure. The strength dependence on test conditions also suggested a potential thermal shock problem.

RM-2 Material

The objective of this development iteration was improvement of the low temperature properties of the material as a function of both the oxidation kinetics and factors controlling the strength reduction after oxidation. This was accomplished through control of the secondary Y-Si-O-N phases present in the material via further refinements in sintering conditions and enhanced quality control.

This material itertion yielded a higher characteristic strength (107 ksi) and Weibull modulus (21.1). These improvements were attributed to a superior microstructure consisting of a matrix of interlocking needle-like grains (Figure 349), a structure found to result in optimum properties in hot pressed silicon nitride[7]. Increased process control also contributed significantly to these improved results.

The oxidation kinetics at 700C are parabolic, as are the 1000, 1200 and 1400C data (Figure 350). However, the 1000C data continue to reflect anomolous behavior with noticeable weight gains. The strength- after-oxiation data (Figure 348) show that the severe 700C problem of RM-1 was solved; only a minor strength reduction was measured at 1000C.

Testing to this point revealed no serious problems with the RM-2 material. Additional testing was undertaken to examine the material's thermal shock resistance (in response to

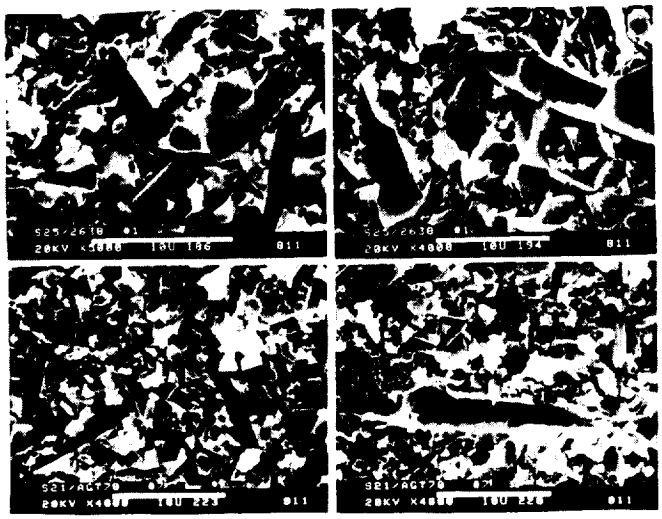

Figure 349. Microstructure of RM-2.

test results obtained for RM-1) and stress rupture behavior.

The thermal shock resistance of the material was measured by rapid cycling from room temperature to 1000 and 1200C using the procedure by Johnson and Hartsock(8). Although heating and cooling rates exceeding 2400C/min were employed, no visible damage was observed. Fracture evaluation after 1,000 and 10,000 cycles of thermal shock testing showed no strength degradation.

Stress rupture tests were conducted in four-point flexure at temperatures between 1000 and 1200C. Between 1100 and 1200C, no time-dependent failures were observed for stress up to 90 ksi (specimens tested in stepped stress rupture fashion) and times exceeding 600 hours. However, the testing at 1000C revealed another problem. Failures occurred in an average period of 357 hours (based on an average of 10 tests; data ranged from 19 hours to 93 hours) at a stress level of only 20 ksi. While a slight strength reduction was observed after static oxidation (15 percent), stress rupture testing in air revealed a reduction in strength of approximately 80 percent. In vacuum, there were no failures at 1000C and 40 ksi (twice the stress levels fo the air tests). These results revealed that

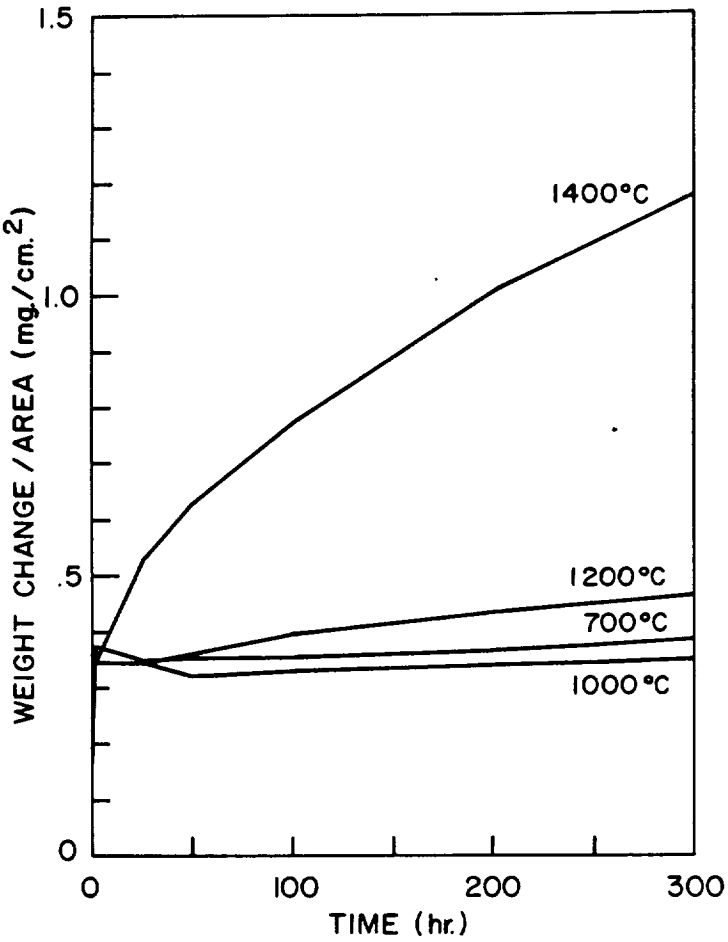

Figure 350. Oxidation Kinetics in RM-2.

SRBSN is subject to a stress-enhanced degradation due to oxidation similar to stress corrosion cracking, a finding not previously reported. Again a correlation was found relating this strength reduction to another oxidation behavior. Complete details regarding strength characterization of RM-2 were published recently by Govila, Mangels and Baer (9).

RM-3 Material

The goal in developing this material was improvement in the stress rupture characteristics at intermediate temperatures, without degrading the strength (Weibull modulus or microstructure of RM-2 SRBSN. This was accomplished through the use of a post-sintering heat treatment of the MR-2 SRBSN.

The strength and Weibull modulus are 100 ksi and 19.0 respectively, essentially the same as in RM-2. Again, these data consolidate the results of numerous batches. Figure 351 compares the strength/temperature data for RM-1, RM-2 and RM-3, showing slightly lower strengths for the RM-3.

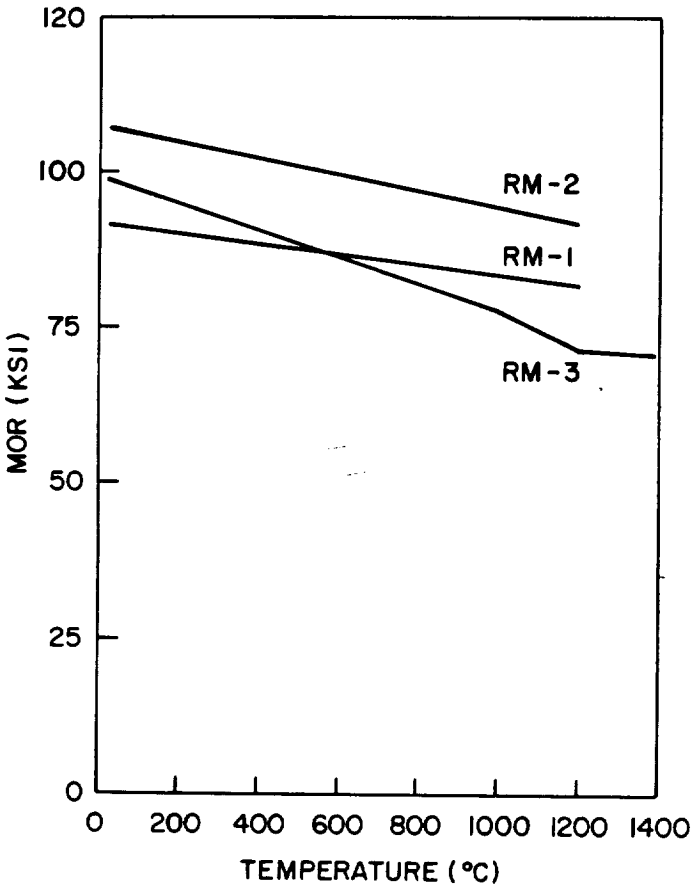

Figures 351. Strength at Temperature Data for RM-1, 2 and 3.

The oxidation kinetics for RM-3 are shown in Figure 352. The data at all temperatures describe parabolic curves, with the weight gains generally increaisng with temperature, as expected, for a dense material. The initial weight gain is a result of the post-sintering heat treatment given to this material. The strength after oxidation exposure is shown in Figure 348 as a function of temperature. The data show no degradation in strenght for temperatures up to 1000C with only modest losses at 1200 and 1400C. Both of these measure-

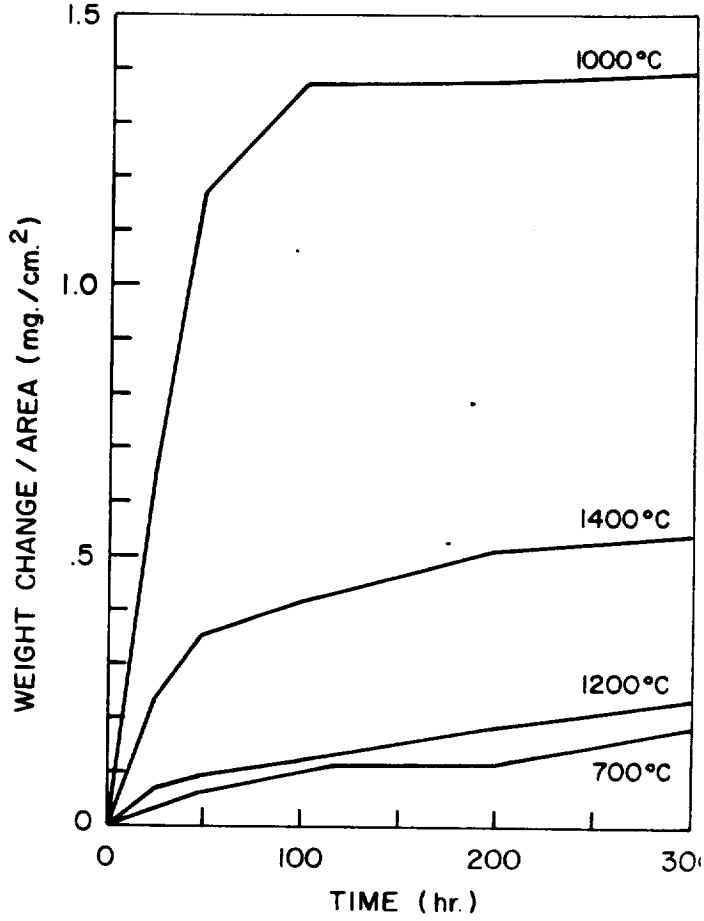

Figure 352. Oxidation Kinetics in RM-3.

ments, oxidation kinetics and strength after oxidation, reflect improvements over all other grades of SRBSN's tested.

The stress rupture behavior of RM-3 was evaluated between temperature of 800 and 1000C and stress levels between 40 and 62 ksi. Limited testing (800C at 62 Ksi for 100 hrs. and 1000C at up to 40 ksi for 500 hrs) produced no time-dependent failures. Detailed strength characterization of the RM-3 material was recently reported by Govila (10).

The properties of RM-3 exceed the criteria for the AGT101 turbine rotor as defined by the Garrett Engineering Project, who are responsible for overall engine development. It has good strength and Weibull modulus, consistent oxidation behavior with low weight gains and experiences no degradation with oxidation

exposure. Additionally, it presents no time-dependent stress rupture problems for stress levels up to 40 ksi and temperatures betwen 800 and 1000C.

While RM-3 exhibits significantly improved properties over earlier SRBSN materials, further advances are still possible and appear desirable. Post-sintering heat treatment results in a coating and the material becomes subject to the limitations imposed by coatings. The principal drawback is nonuniformity of coating thicknes which could lead to nonuniform oxidation of the base material and premature time-dependent failures. Non-uniform coatings are also a potential source of defects resulting in strength reduction. This may account for the slightly lower room temperature strength and the reduced high temperature strength of RM-3 relative to RM-2, the matrix material.

SSN Material Development, Characterization, Fabrication and Testing

a) RM-20 Introduction

Prior to 1985, SRBSN was the prime candidate for AGT101 turbine rotor fabrication at Ford. Inherently, this material was preferred because its low sintering shrinkage would permit the fabrication of rotors to near net shape. Efforts to fabricate crack-free rotors using the silicon-water slip cast system, however, were mostly unsuccessful. Problems were encountered with stability of the silicon-water base slip, and as a result of these problems, and the inherent weakness of the silicon castings, SRBSN components could not be made free of blade cracks.

Material iteration RM-20, a sinterable silicon nitride (SSN), provided a solution to some of the problems encountered with SRBSN.

The following sections characterize the RM-20 SSN material, and describe the Ford effort associated with fabricating a crack-free AGT rotor. During this phase of the program the rotor material composition was held constant, and the primary objectives of the program were:

1) Development of process techniques for casting crack-free turbine rotors using the fugitive-wax process.

2) Fabrication of rotors of the RM-20 mate rial with identical physical properties to those of test bars.

b) RM-20 Silicon Nitride Process

RM-20 is a derivative of a silicon nitride-based material originally developed by Ford for cutting tools and other wear type applications. This material is made by the pressureless sintering of a silicon nitride chemical composition. The process concept involves a form of SRBSN, and the use of yttria as a major sintering aid. Property data based on test bar specimens (Table 58), and the inherent process flexibility of RM-20 indicate that this material is suitable for slip casting of the AGT rotor.

Table 58. Physical Properties RM-20 Material.*

Flexural Strength (RT)	**126 ksi**
Weibull Modulus	**13**
Density	**3.29 g/cm^3**
Strength (2200F)	**82 ksi**

***Strength data are reported here for a cold pressed material nitrided and sintered. Complete processing details are given elsewhere (11).**

Figure 353 shows the process for fabricating RM-20 SSN gas turbine rotors. This process consists of dry ball milling selected silicon powders and additives to produce an intimate mix and cold pressing round plates under unilaxial pressure. These plates are nitrided to yield silicon nitride contents greater than 89 percent by weight and

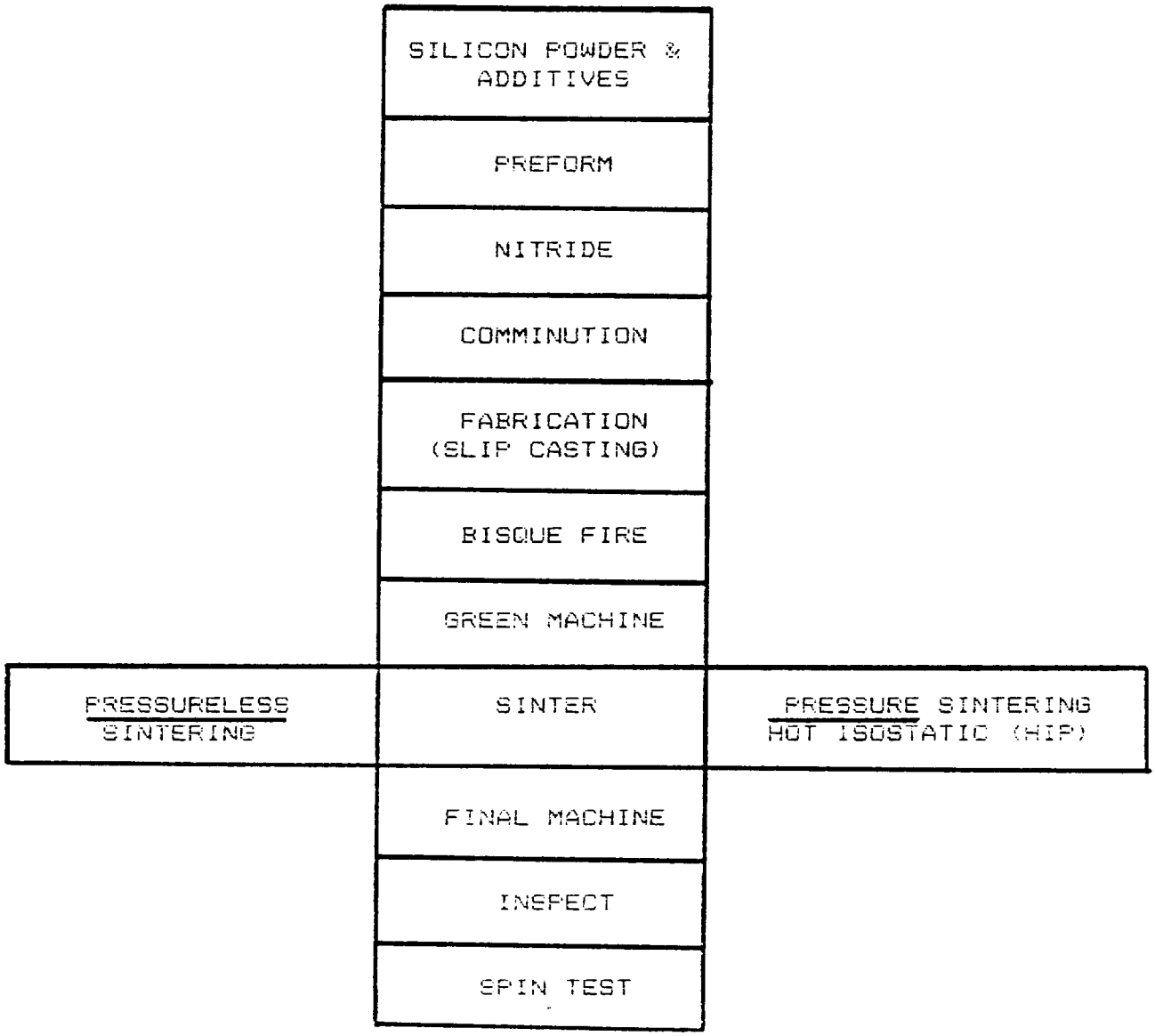

Figure 353. Sintered Silicon Nitride Process for Fabrication of Advanced Gas Turbine Rotors.

second phase oxynitride crystallites of $Y_{10}Si_6O_{24}N_2$ composition. Thereafter, the plates are broken into coarse particles (14 mesh) suitable for primary reduction by roll crushing.

Ball milling is sued to further reduce the particle size after roll crushing. By most standards the resultant powder is relatively coarse for slip castings, but a stable slip can be prepared using deflocculant systems that provide both physical and chemical suspension mechanisms. These deflocculant systems are covered in the following section of RM-20 slip preparation.

As in the case of SRBSN, slip casting - combined with the fugitive wax process - was used to fabricate RM-20 rotors. After slip casting, rotors are dried to remove the residual water, bisque fired for green strength, premachined and sintered. Both pressureless sintering and hot isostatic pressure were employed.

b) **RM-20 Rotor Fabrication**

Slip Cast Material Preparation

Early studies (12) examined the production of stable slips for the casting of RM-20 rotors. The objective of this work was the development of a slip, free of outgassing, with good flow characteristics, stability within the casting time period and demonstrating little thixotropic behavior. Slip deflocculants evaluated were a) Keltex, b) Dispex A-40, c) Dispex N-40, and d) California 226/35.

Of this group, Dispex A-40, in concentrations of 0.26 percent, produced the best results. Figure 354 shows the viscosity relationship with spindle rpm for various levels of Dispex A-40. Initially, a problem was encountered in casting the shaft (the last portion of the rotor cast), wherein the slip became thixotropic, causing slumping and distortion. This problem was eliminated by substituting Displex N-40 deflocculant for approximately 50 percent of the A-40 deflocculant.

One problem associated with slip consistency is the presence of agglomerates in the slip. These agglomerates are formed during dry milling of the RM-20 powder. The agglomerated powder, when placed into slip suspension, would break down over a long period of time, resulting in poor viscosity control. Wet milling and screening experiments were designed to eliminate agglomerates in the RM-20 casting slip. Screening was only partially effective, and wet milling drastically changed the powder particle size distribution. The best result was achieved with a combination of dry ball milling and limited amount of wet milling.

Table 59 summarizes this procedure which calls for 48 hours of dry milling, followed by removal of the balls and the addition of water. This suspension is then tumbled 72 hours. The mill is recharged with grinding media and the suspension is wet milled for 1.25 hours. The grinding media are removed, the viscosity of the slip is adjusted to 125-150 cps via water addition and the slip is tumbled 16 hours.

Table 59. Improved RM-20 Slip Preparation Procedure.

- 48 hours dry milling
- 72 hours tumbling, no milling media
- 1.25 hours wet milling with grinding media
16 hours tumbling, no milling media

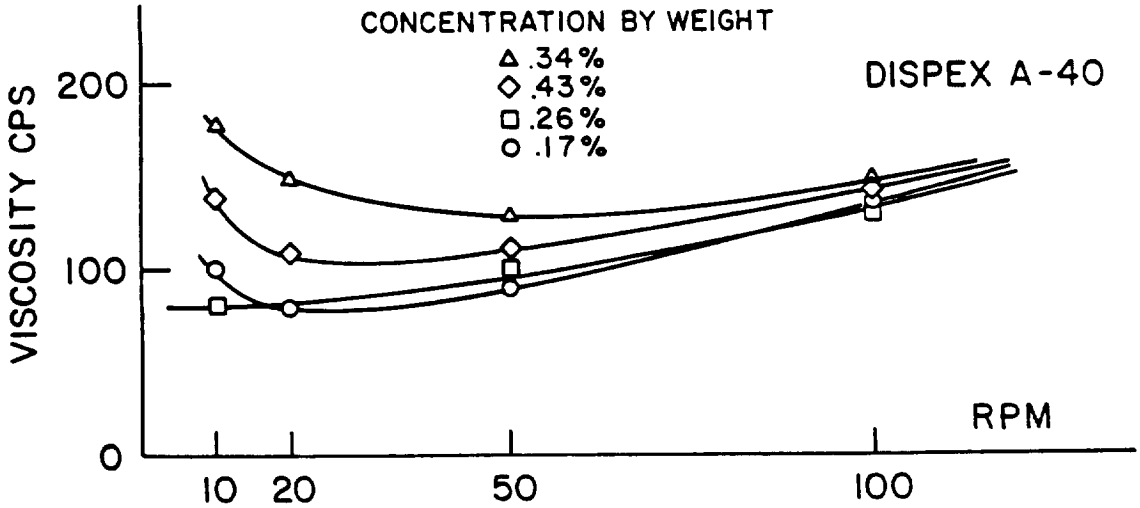

Figure 354. Relationship of Viscosity Vs. Spindle Speed for Various Concentrations of Dispex A-40 Deflocculant.

This procedure produced a casting slip of good stability and excellent consistency. Several rotors were cast with this improved technique.

Rotor Slip Casting

Historically, blade cracks and inferior microstructures in blade tip regions resulted in low rotor yield. Also, a high proportion of spin pit failures originated in blades that appeared sound, which suggested that subsurface defects were controlling quality, even in rotors that passed visual and Zyglo inspections. To overcome these problems, a systematic review of all the steps in the casting process was undertaken, starting with the composition of the waxes used to make the molds.

Thermal Expansion of Negative Fugitive Wax

The wax used for casting molds at Ford was a product of the Freeman Company, called "Dip Seal". In 1985 Freeman ceased marketing this product and an analysis of the wax was made to determine whether it could be duplicated "in-house". By analysis the wax was primarily paraffin (65 percent) and 35 percent methyl stearate. The later was deemed undesirable due to its' insolubility in toluene, the solvent used to remove the wax from the casting. A large change in the thermal expansion rate of paraffin occurs at rather modest temperatures (28 - 34F). This is caused by a solid-phase change in the crystal structure of the wax and results in a five-fold increase in an already high thermal expansion rate. Therefore, casting and wax removal is now done at constant temperature to avoid any expansion damage to the casting.

To replace the Freeman Dip Seal wax, a casting wax (LN-209-218) was purchased from J.F. McCaughin Co. This material is a beeswax-paraffin-carnauba mixture with a melting temperature of 150F.

Mechanical Strength of Negative Fugitive Wax

Because of the low elastic moduli and strength of waxes, slight forces or loads caused large deflections in thin sections of the casting molds. The molds had the form of a rotor sitting on a flat disc and clamped to a plastic base which loaded the wax mold on the webs formed between blade tips. Mismatches between the plaster and mold caused distortion in the wax. This type of mold, and the technique used to clamp it, were changed to eliminate distortions in the wax.

A new method of dipping the wax mold, using an aluminum contoured plate, was developed. The plate matched the base contour of the water soluble positive wax and had the web sections between blades machined away, leaving a ledge of aluminum 0.060 inches wide. The positive wax was held down loosely with a bolt and a cap. Any stress on the positive wax could cause a crack which would translate into a web inside the wax mold and a corresponding crack in the cast part. The contour of the aluminum dipping plate wax was produced in a computer-controlled mill. The same program was used to mill this exact contour into the surface of the plaster on which the wax mold sits, thus assuring a perfectly matched interface. The first molds, produced by three dips in a 155F McCaughin dip wax, were heavy enough to allow filling of the mold without mechanical clamping. This arrangement was slightly modified when the thickness and weight of the molds were changed; however, the unstressed mold feature (except for stress caused by the slip itself) was retained.

Wax Removal

While the triple-dip molds produced a high percentage of crack-free rotors, 24 hours were required to dissolve the wax. Removal was accomplished by immersing the wax-covered casting in toluene without agitation and at constant temperature. Thinner molds could be expected to dissolve quicker and less time in toluene would be a desirable result. It was also suspected that soaking the wax caused it to swell slightly, stressing the blades of the casting. Hence, thicker molds could be expected to stress the castings more than thin ones. Initial attempts at a single dip, thin mold produced problems in the wax positives.

Positive Wax Preparation

Polishing the wax with 4-0 steel wool eliminated surface defects and improved wax removal from the casting. Two new problems occurred in the thin wax molds; splitting of the mold down the blade edges and surface contamination by traces of lubricant used in the injection molding of the wax positive. The lubricant was elimiinated by two consecutive cleanings in an organic solvent.

The problem of mold splitting was caused by the uneven coating of wax around the edge of the blades. At the corners the wax deposits are very thin. Chamfering this edge on all blades caused a more even layer of wax and reduced this tendency to split.

Single Dip Molds

Initial attempts to use single dip molds proved difficult. The wax molds were 70-80 grams lighter than previous molds. Unless the slip was poured into the mold slowly and carefully, a leak would start at the mold/plaster interface, quickly draining the slip and ruining the casting. To overcome this, a steel ring about 6 inches in diameter, 1 inch high and 0.060 inch thick was fabricated. This ring weighed 70 grams and, when placed on the wax mold at the tip of the blades, held the mold down (Figure 355). Because of the perfect fit of the wax to plaster, there was no deflection of the wax.

Wax removal was accomplilshed in 6 to 8 hours (versus 24 hours for the triple-dip wax mold).

Material Quality In Rotor Blades

Spin pit tests of visually sound rotors produced a large percentage of blade failures. This suggested that the blades had subsurface cracks initiating failure(s) at speeds well below those at which hub failures occurred. To assess the qualify of the subsurface blade material, the sound blades were lightly glass-beaded after the rotors had been bisque fired. Removal of the surface disclosed porous material at the blade tips. To overcome this, the castings were spun at 100 rpm while pouring. This application of centrifugal force enhanced the migration of the material to the tip and significantly reduced the number of blade failures.

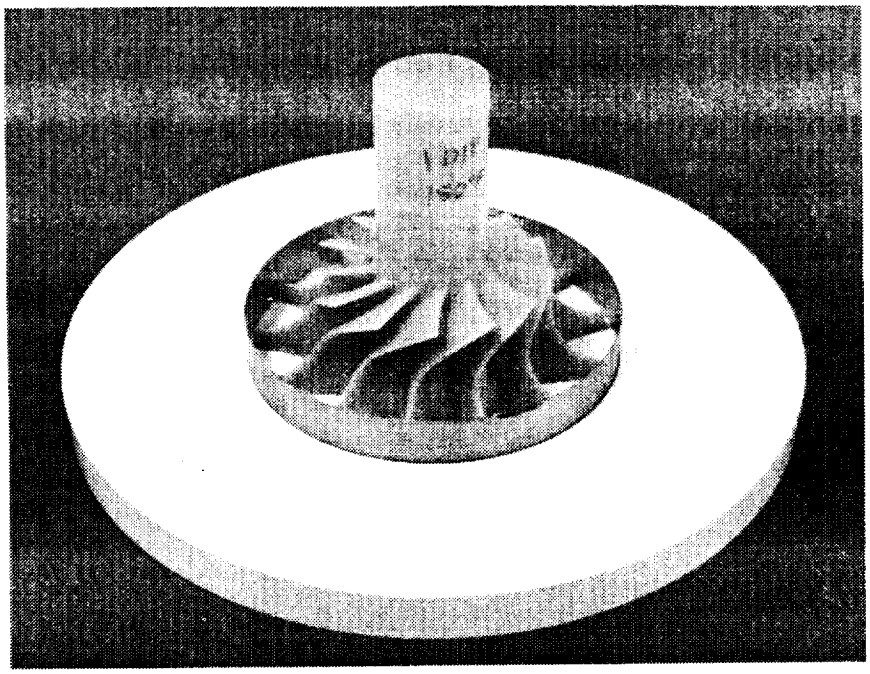

Figure 355. Single Dip Wax, Plaster Base and Steel Retaining Ring.

Remaining Problems With Wax Molds and Wax Positives

Two problems remain with the wax systems. First, the positive has a tendency to distort with shelf time. This tendency to stress-relieve and hence distort is well understood in the dental profession where critical dimensions in wax patterns must be maintained. This problem has not been addressed, but it will be a deterrent to accurate blade forming. This deformation also causes the shaft diameter of the wax positive to ovalize by 0.010 to 0.020 inch over a few weeks. Blade deformation has not yet been defined. Possible solutions for this problem include refrigerating the wax positives until they are useds or using them immediately after they are molded.

Secondly, the inside surface of the wax mold develops a rough surface even though the wax positive is polished smooth before dripping. Apparently, the 150-160F melting temperature of the water soluble wax is too close to the 150F melting temperature of the dip wax. Lowering the temperature of the dip wax to its lowest usable point improves the surface texture, whereas raising the temperature or holding the positive in the dip wax longer than required heightens the effect. These bumps on the casting not only destroy the smoothness of the component surface, but give the mold wax a rough surface, making removal more difficult. The surfaces can be smoothed after bisque firing by sanding, but this is a tedious job and should be avoided.

In summary, the process modifications described have produced a marked improvement in rotor fabrication. Approximately 70 percent of slip cast rotors have been crack free. There is, however, a need to improve the quality of the material in the blade tip region of the rotor.

Rotor Heat Treatment and Equipment

Pre-Sintering of Rotor

The dried RM-20 rotor castings are extremely fragile and difficult to handle through inspection and subsequent sintering. This problem is most severe during the placement or "packing" of the rotor in the power blanket for sintering. Therefore, a presintering or "bisque" firing treatment was developed to partially consolidate the casting and provide adequate handling strength.

The bisque firing cycle consists of slowly ramping in a nitrogen atmosphere to 1500C and holding at temperature for 2 hours. During this cycle the casting undergoes partial consolidation, as indicated by a 2.5 percent linear shrinkage, which is sufficient to impact suitable handling strength. An additional advantage of bisque firing is that it permits machining of the casting with standard high speed tool steel, and thus reduces costly diamond grinding of the final component. This pre-sintering cycle does not impede the final sintering kinetics. This process is now used on all castings.

Sintering of Rotor

The sintering time/temperature profile initially developed was a single-step cycle. This cycle was adequate for the densification of the original platformed rotors but yielded unpredictable blade distortion in the redesigned rotor castings. In addition, considerable fusion of the packing powder occurred, increasing the difficulty of removal, particularly between the blades. Packing powder compositional changes reduced but did not eliminate the problem.

A two-step sintering cycle was developed to reduce blade distortion and facilitate removal of the packing powder. The first step of the dual cycle incorporated a packing powder (boron nitride, silicon nitride, yttria and silica) and a 12 hour temperature ramping schedule that had three discrete temperature holds: 0.5 hours at 1520C, 0.5 hours at 1620C, and 4 hours at 1720C. Neglilgible fusion occurred within the packing powder.

The second step of the sintering cycle utilized a compositional change in the packing powder and a single temperature hold of 12

hours at 1800C. This compositional change and increased temperature and hold time provided greater availability of $SiO_{(g)}$ to maintain the required oxynitride composition within the rotor, resulting in full densification. This packing powder was easily removed.

At the completion of the two-step cycle, a nominal 18 percent sintering shrinkage and final densities of 3.24 to 3.28 g/cm^3 were obtained. Observed blade distortion was minimal.

The two-step cycle approach, although greatly improved over the earlier one-step cycle, considerably increased the process complexity and total time needed to complete the sintering cycle. Each step required a complete temperature cycle with re-packing of the rotor between cycles. In addition, an undesirable extra handling of the fragile rotor was incurred.

Consequently, a new cycle was developed for the final rotor iteration. Its main features were:

a) A one-step sintering cycle

b) A 36-hour hold (compared to the 12- hour hold) at the maximum temperature

c) Two discrete temperature holds: 1 hour at 1500C and 36 hours at 1800C.

d) Two discrete temperature ramp rates: 300C/hr up to 1500C, followed by 50C/hr to 1800C.

e) The packing powder, which included 24 percent boron nitride, was packed loosely.

In this one-step sintering cycle, shrinkage was nominally 18 and a final density of 3.28 to 3.29 g/cm^3 was obtained. The packing powder was readily removed and blade distortion was minimal.

Post Sintering Heat Treatment of RM-20 Rotor

All of the pressureless sintered rotors had a duplex zoning structure. The exterior casing was generally dark in color and has a well-crystallized secondary phase. The interior region of the rotor is lighter in color and shows (by x-ray diffraction) a predominantly glassy second phase. Scanning electron microscopy indicates that the densities and chemical compositions of both regions are identical. Cold spin testing of several rotors produced blade separation failures at the intersection of the two regions. Fracture origins could not be identified but separation occurred near the interface of the duplex zones in all of the blades. This zoning interface may have acted as a stress riser and produced premature failures.

An investigation of heat treatment techniques to crystallize the interior region of the rotor, and the elimination of the duplex interface, was undertaken. A half-fraction of a 2^{4-1} statistically-designed experiment was used to study four variables (nucleation temperature and time, growth temperature and time) at two levels each, requiring 8 heat treat cycles.

Test bars cut from sintered rotor #40 were heat treated. A 0.025 inch layer was ground from each test bar. X-ray diffraction analysis revealed that all eight heat treatment cycles resulted in a crystallized second phase. However, when the 0.063 inch-level (maximum depth of test bar) was examined, four of the eight bars retained some glassy phase.

Table 60 summarizes the eight heat treat cycles and the x-ray diffraction results. These initial test results indicate that devitrification of the glassy second phase throughout the rotor (over 1 inch depth) would require further cycle modifications.

Full size rotors were heat treated, sectioned and examined by x-ray diffraction to determine phase composition. One rotor (#64) was heat treated using a cycle similar to cycle #HT4; however, the hold time at the "growth" temperature of 1450C was increased from 4 hours to 96 hours. Rotor #63 was heat treated using a cycle similar to cycle #HT7 with an identical increase in hold time. The relevant

Table 60. Summary of Heat Treat Cycles and X-Ray Diffraction Results.

Cycle #	Bar #	Nucleation		Growth		Glassy 2nd Phase
		Temp C	Hours	Temp C	Hours	
HT1	8A	1050	1	1300	1	Some
HT2	9B	1200	1	1300	4	Some
HT3	6B	1050	1	1450	4	No
HT4	6A	1200	1	1450	4	Some
HT5	5A	1050	4	1300	4	No
HT6	8B	1200	4	1300	4	Some
HT7	7B	1050	4	1450	4	No
HT8	7A	1200	4	1450	4	No

differences in their cycles, as shown in the table, were in their "nucleation" temperatures and duration times.

The results of these tests show that the two heat treatment cycles did affect the second phase throughout the interior of the two rotors, although not to the same degree. The original #HT4 cycle, used on the test bars, resulted in some retained glass (see Table 60). Similarly, the modified #HT4 cycle (rotor #64) resulted in more glass than the modified #HT7s cycle (rotor #63).

The secondary phase composition of rotor #63 was identified as:

$$Y_{10}Si_6O_{24}N_2 \text{ ("H")} + Y_2Si_2O_7.$$

The secondary phase composition of rotor #64 was identified as:

$$Y_{10}Si_6O_{24}N_2 \text{ ("H")} + Y_2Si_2O_7$$

$$+ Y_2SiO_5 + \text{a small amount of glass.}$$

After the heat treatment, MOR test bars were cut from rotors #63 and #64 and from rotor #65 which did not undergo post-sintering heat treatment.

Room temperature four-point MOR bending tests were then carried out on five test bars from each rotor. The results are summarized in Table 61.

Table 61. Mean MOR Results for Heat-Treated Rotors.

Rotor #	Mean MOR (ksi)	Std Dev (ksi)	Heat Cycle (See Table 60)
63	79.5	3.4	HT4 (96 hrs)
65	87.6	3.4	None
64	79.5	4.8	HT4 (96 hrs)
63	74.6	7.2	HT7 (9 hrs)

These results show some deterioration of room-temperature strength with decreasing levels of glass in the secondary phases. It is expected, however, that high temperature strength will be greatest in the rotor with the least amount of the glassy secondary phase.

The overall strength level of these rotors is approximately 30-35 percent lower than the test bar strengths of 125 ksi previously reported. A chronic problem in any material/component development program is that of obtaining material properties similar to those of the test bar material in a large component, such as the AGT rotor. In this case, the difference in strength is attributed to porosity. Such porosity is believed to occur during the long sintering times required to achieve high density. An effort was made to eliminate porosity in the RM-20 rotors with hot isostatic pressing (HIP).

Sintering Equipment

The pressureless sintering process utilized a cold-walled vacuum furnace and a refractory metal hot zone. A major drawback of this system was reactivity of the $SiO_{(g)}$ with the shot refractory metal. The hot zone was limited to approximately 15 to 18 cycles before a complete rebuild was required. Significant in-house modifications increased the furnace life to approximately 25 cycles, but further improvement was necessary. Therefore, a furnace manufacturer was contracted to redesign the hot zone and other deficient areas to improve the sintering enviornment.

The new design provided for a smaller, more efficient hot zone faced with 0.005 inch thick tungsten sheet. After several cycles, deterioration was noted which rapidly accelerated with subsequent use. The hot zone became unusable after 23 cycles. An in-house redesign and rebuild effort resulted in an improved hot zone. Reconstruction included the replacement of the 0.005 inch tungsten face with 0.020 inch molybdenum sheet and molybdenum rods added to the ceiling structure for support. A sacrificial molybdenum sheet was placed over the floor in order to reduce the faster deterioration of the floor relative to the rest of the hot zone, caused by spilled packing powder reacting with the floor. To minimize the down-time needed for a hot zone rebuild, two additional hot zones were built, Table 62 shows the marked improvements achieved with in-house furnace modifications.

d) **Spin Testing RM-20 Rotors**
General Review

Extensive changes were made in the methods used to mount spin pit arbors to AGT rotors and the manner in which the rotors are balanced. Previously, the final spin pit arbor was mounted using "Loctite" and a 0.001 inch to 0.002 inch loose diametrical fit between the arbor and the rotor. This technique did not produce perfect concentricity between rotor shaft and the outer diameter (O.D.) of the steel arbor on which the assembly is mounted and spun during balancing. Tests revealed that this method introduced unbalanced forces which then had to be removed by grinding away rotor surfaces, usually the blades. Obviously, this was unacceptable for rotors which might be engine candidates. To overcome this problem, a press fit arbor was designed and the balancing process was split into two parts; an initial balance check and a final balance operation.

Initial Balance Check

To reduce the extensive grinding previously required to balance rotors, a method of relocating the geometric center of the rotor shaft through the mass center of the part was adopted. The mass center was located and the shaft portion of the rotor was ground as close to the center of the blades as possible. A steel sleeve, 3.50 inch long with 0.070 inch wall thickness, was press-fitted to the shaft. The press was 0.0015 inch on the diameter and the sleeve was fitted by heating before installation. The sleeve was installed while the rotor was still mounted on the grinding machine. When cooled, the O.D. of the sleeve was ground to fit the half-bearings of the balance machine. The initial check of unbalance was then made. Results revealed from

Table 62. Life Improvements Resulting from Furnace Redesign.

Category	Previous Design	Latest Design
Total number of cycles	23	23 (still usable)
Number of cycles with max temperature >1750C	8	12
Number of cycles with max temperature between 1510C and 1750C	0	20
Number of cycles with max temperature between 1300C and 1510C	15	0
Number of hours at temperature above 1750C	96	316

40 percent to 60 percent less unbalance than rotors mounted with Loctite. With the direction and size of the unbalance known, the offset of the rotor shaft could be calculated. The geometrical center of the shaft could be relocated in greater proximity to the mass center, further reducing the unbalance and allowing final balancing with minimal grinding.

Final Balancing

After the initial check, the sleeve was removed by heating it to 300F to 400F. The rotor was returned to the machine shop, mounted and adjusted until the shaft portion had zero runout. The machine check was then adjusted to reposition the mass center at the rotational center and the shaft was reground to run true to the mass center. The steel spin-pit arbor was installed with a 0.003 to 0.004 inch diametrical press fit and its O.D. ground to fit the balance machine half bearing. The quill shaft hole was also ground true to the mass center during this stage. These steps were all accomplished without dismounting the rotor from the original machine position used to regrind the shaft to the new location over the mass center. The rotor was then final balanced by grinding on the back and on the shaft just forward of the blade root on the exducer end. These steps reduced the unbalance from the 0.160 - 0.200 oz-in. previously encountered to 0.010 - 0.040 oz-in, an amount which can be corrected by grinding without destroying the rotor blades.

e) Spin Testing of RM-20 Rotors

Spin tests of RM-20 rotors were conducted in a vacuum pit using a Barber Stockwell 150,000 rpm air turbine. A summary of test results, along with failure analysis comments, is shown in Table 63.

This series of tests revealed an increasing uniformity in the speed and type of component failure. All rotors in this group were crack free, based on visual and Zyglo inspection, and fully bladed. All were cast with the same techniques, by the same people, from RM-20 SSN material. Although previously tested rotors (RM material) failed at higher speeds, they were not fully bladed and blade failures predominated. Most of the earlier rotors tested were made of SRBSN material.

In the RM-20 rotors, there was a general trend toward improved blade quality, as reflected by the number of hub failures in the early stages of RM-20 material development. This suggested that the large flaw size of the cast rotor material (as compared to test bars) was controlling the ultimate failure speed of

Table 63. AGT RM-20 Rotor Spin Test Results.

Rotor No.	HIP Y/N	Density g/cm^3	RPM at Hub Failure	Comments
065	N	3.289	95,620	No blade failure prior to hub failure
066	N	3.290	95,000	No blade failure prior to hub failure
069	N	3.289	88,480	One blade failed causing quill failure, followed by hub failure.
072	N	3.290	94,200	No blade failure prior to hub failure
076	N	3.298	84,800	No blade failure prior to hub failure
078	Y	3.303	85,000	No blade failure prior to hub failure
080	Y	3.293	101,600	No blade failure prior to hub failure
083	Y	3.294	98,500	Lost a blade at 96,470 rpm
094	Y	3.304	112,980*	Was partial sintered prior to HIPping; heat treated following HIP Lost 1st blade at 104,060 rpm Lost 3rd blade at 109,360 rpm Lost 3rd blade at 112,980
097	Y	3.307	100,780	No blade failure prior to hub failure
105	Y	3.304	103.780	Lost 1st blade at 93,000 rpm Lost 3rd blade at 96,600 rpm Lost 3rd blade at 103,780 rpm Followed by hub failure.

*Did not fail, reached max. rig rig speed.

**In several rotors (as noted), blade failure at lower speeds preceeded the final hub failure.

these rotors. All of these rotors were pressureless sintered with a 36-hour hold at temperature. This long hold time was believed to result in increased porosity and correspondingly lower strength, having a pronounced affect on the highly stressed hub during spin testing.

In an effort to reduce porosity, rotors No. 75 through No. 105 were HIPped after bisque firing by ASEA Cerama using their proprietary glass encapsulation process. HIPping conditions were a maximum temperature of 1700C and a soak time of two hours at a pressure of 160 MPa.

One noteworthy aspect of the failure of the HIPped rotors was the recurrence of blade failures at speeds below the utlimate hub burst speed. Rotor No. 94 failed in three blades but

reached the limiting speed of the spin pit air turbine without hub failure and was retired with the hub intact. This rotor was within 940 rpm of the 105,000 rpm qualification speed when a blade failed and it sustained a 112,980 rpm ultimate speed without hub failure; indicating that HIPping raised the hub strength to adequate levels, but blades again became the limiting factor. Blade quality and strength adequate for a 95,000 rpm hub capability were now the critical parameters determining rotor durability. This is also illustrated by rotor No. 105 which failed in three blades before hub failure occurred in excess of 103,700 rpm. The overall results confirmed that a measurable increase in hub strength resulted from HIPping.

Analysis of RM-20 Spin Pit Tested Rotors

A porosity analysis was conducted on both pressureless sintered and HIPped RM-20 rotors as a means of explaining the higher burst speeds of HIPped rotors.

The spin-to-failure tests resulted in the rotors bursting into many small fragments. These pieces were too small to be accurately traced to their original position in the pre-failed rotors. Consequently, nine fragments (3 x 20 mm), one from each rotor, were chosen randomly. The nine pieces were cut and polished to permit microscopic examination of the porosity. The porosity evaluation was performed using DIMA (Digital Imaging Analysis). Both the percent of overall porosity and the largest pore dimension and its area were measured on five consecutive 'fields' (0.62 x 0.96 mm each) per sample at 180X magnification.

Noticeable variations in porosity were seen when scanning across the rotor samples. In one sample, total porosity ranged from 0.5 percent to 9.6 percent. The smallest variation per sample was 0.2 to 0.7 percent. No correlation could be established between total porosity of the pressureless sintered versus the HIPped rotor material. There was, however, considerable range (1 to 200 microns) in the size of pores found in the nine rotor samples. It was observed that even when the percent of total porosity was small, large isolated pores existed throughout the sample. The largest pore of each sample was measured and recorded. The relationship between the rotor's burst speed and the largest pore size of its corresponding fragment was plotted and is shown in Figure 356. This plot shows the data falling into two groups: one group had smaller pores, corresponding to rotors with the higher burst speeds. The second group had larger pores, corresponding to the rotors with the lower burst speed. In addition, when the individual data points in Figure 356 were evaluated relative to sintering process, it was determined that the smaller pores (high burst speed group), corresponded to the HIPped rotors; whereas the larger pores (low burst speed group), were found in the pressureless sintered rotors.

The flexural strength data obtained from test bars cut from pressureless sintered and HIPped rotors further substantiate these results. As shown in Table 64, the average strength of the HIPped rotor material was 111 ksi versus 75 ksi for pressureless sintered RM-20 material. Clearly, the overall results of porosity size determination, fracture strength evaluation and spin testing demonstrate the need to reduce pore size in the RM-20 rotor material.

f) The Effect of Heat Treatment on the Flexural Strength of RM-20 Rotor Material

The effects of heat treatment on the HIPped RM-20 rotor material were studied in terms of flexural strength and secondary phases. Modulus of rupture was measured at room temperature and in some cases at 1200C. Speciman size was 1.25 x 0.25 x 0.125 inch, upper span 0.375 inch, lower span 0.75 inch and the loading rate was 0.02 in/min. Table 65 summarizes these results, indicating the type of heat treatment, specimen (rotor versus test bar), secondary phases present and strength results at room temperature and 1200C.

The flexural strength of the as-HIPped RM-20 material cut from a rotor was 111.3

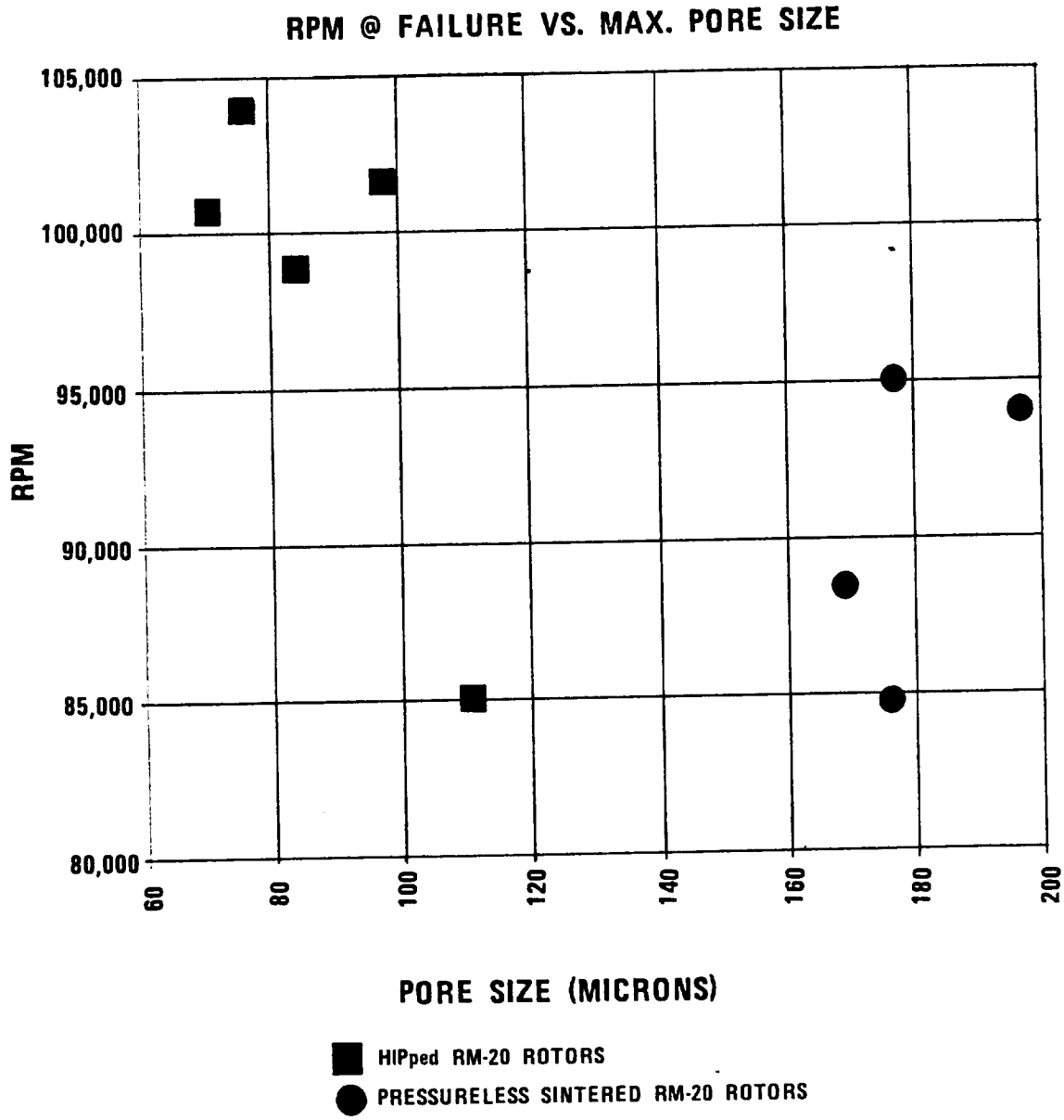

Figure 356. Rotor Pore Size Versus Spin Test Rotor Speed.

Table 64. Flexural Strength Of Pressureless Sintered and HIPped RM-20 Rotor Material.

Pressureless Sintered RM-20			HIPped RM-20		
Sample No.	MOR		Sample No.	MOR	
	(MPa)	(ksi)		(MPa)	(ksi)
63-1	508.4	73.8	79A-1	810.0	117.6
63-2	537.4	78.0	79A-2	767.6	111.4
63.3	502.8	73.0	79A-3	619.0	89.8
63.4	446.9	64.9	79A-4	838.0	121.6
63.5	581.0	84.3	79A-5	798.9	116.0
Average	515.3	74.8	Average	766.6	111.3

ksi. X-ray diffraction analysis indicated a β-silicon nitride crystalline primary phase with an amorphous secondary phase. When heat treated as a half-section rotor (Heat Schedule C), the RT strength was reduced by approximately 10 percent - not totally unexpected in view of the reduced secondary phase glass content and formation of H-phase ($Y_5Si_3O_{12}N$) and $Y_2Si_2O_7$. The 1200C MOR was 71.5 ksi for this heat treated rotor material.

Heat Treatment B, with a complete rotor and a shorter total heat treat time, resulted in very little difference in room temperature flexural strength when compared to non-heat treated material. X-ray diffraction of this material revealed the presence of H-phase but no glassy secondary phase. The 1200C MOR was 59 ksi. No significance was attached to this slightly diminished high temperature strength due to the small sample size.

An interesting phenomena associated with these heat treat studies was the pronounced affect of heat treatment on the smaller specimen (in this case, the MOR test bar) versus the previously discussed rotor subsequently cut into MOR bars. This can be seen in the last three tests reported in Table 65. In heat treat schedule B + D, MOR test bars were heat treated for 96 hours at 1450C. This treatment resulted in a severe room temperature strength reduction to 73 ksi. Secondary phases were H-phase and glass. Schedule B + F, using a shorter time but higher heat treat temperature of 1700C, resulted in a further strength reduction. As expected, this higher temperature produced more glassy secondary phase material. On the other hand, when small

Table 65. The Effect of Heat Treatment On Flexural Strength and Secondary Phases In RM-20 Rotor Material.*

Heat Treatments Performed	Secondary Phases Observed	4-Point MOR (ksi)	
		at RT	at 1200C
A	G	111.3(5)	
A + C	H _ Yi _ g	99.3(5)	71.5(1)
B	H	104.9(3)	58.7(2)
B + D	H + g	73.2(3)	
B + E	Yi + K	117.1(3)	69.1(1)
B + F	G	66.0(3)	

* Notations:

1. Heat Treatments
   - A = As HIPped rotor (No H.T.)
   - B = Complete rotor, 96 hours at 1450C
   - C = One half rotor, 16 hours at 1450C followed by 36 hours at 1450C, followed by 96 hours at 1450C
   - D = Test bar, 96 hours at 1450C
   - E = Test bar, 96 hours at 1450C with packing powder
   - F = Test bar, 36 hours at 1700C
2. Secondary Phases
   - G = Glass (major); g = glass (minor)
   - H = $Y_5Si_3O_{12}N$; K = $YSiO_2N$; Yi = $Y_2Si_2O_7$
3. Strength
   - Loading Rate: 0.5 mm/min
   - Sample size is shown in ( ) following the strength value (average)

specimens were packed in powder and heat treated using schedule B + E, reduction in strength did not occur. In fact, the highest strength of 117 ksi was obtained. Phases produced by this schedule were β -silicon nitride, K phase and $Y2Si_2O_7$.

g) **Stress Rupture of RM-20 Rotor Material**

The stress rupture characteristics of RM-20 rotor material are shown in Table 66. Stress rupture, as in previously described MOR tests, was measured in 4-point bending. Stress levels evaluated were 30, 40 and 50 ksi and temperature levels were 800, 1000 and 1200C. Measurements were made on RM-20 material prepared as follows:

Group 1 - Test specimens cut from "as-HIPped" rotor

Group 2 - Same as above but test specimens heat treated 96 hours at 1450C

Group 3 - Test specimens cut from a rotor that was previously heat treated 96 hours at 1450C

As shown in Table 66, the as-HIPped material sustained over 200 hours without failure at a stress of 50 ksi and test temperature of 800C. At 1000C under the same load, specimen failure occurred in 1.1 hours, however, at the lower load of 40 ksi, this RM-20 material again sustained over 200 hours of testing at 1000C without failure. At 1200C, the material failed in 1.3 hours at the 40 ksi load. Failure analysis of the specimens showed evidence of slow crack growth, as well as oxidation. At 1200C and 30 ksi, the material did not fail up to 140 hours of testing. However, visual inspection of the specimen during the test revealed bending. X-ray analysis of this as-HIPped material confirmed the presence of glass in the secondary phases, accounting for the deformation.

The Group 2 and 3 heat treatment experiments were designed to eliminate this secondary glass phase. X-ray analysis in both cases disclosed recrystallization of the glass. In the Group 2 heat treatment of the test specimen, $Y_2Si_2O_7$ was formed. In Group 3, the glass recrystallized as H-phase. With either heat treatment, however, stress rupture was not improved at the 1200C temperature and 20-30 ksi stress level. In all probability sufficient residual glass, although not detected by x-ray analysis, was present to cause sample deformation and oxidation.

In the previously described MOR experiments, heat treatment of the test specimens in packing powder resulted in conversion of the glassy phase to K-phase ($YSiO_2N$). Unfortunately, program timing did not permit these experiments to be extended to stress rupture evaluation. Future testing should address this form of heat treatment as a possible means of extending the capability of RM-20 silicon nitride.

h) **Development of Improved RM-20 Rotor Material**

Failure of the HIPped RM-20 material to adequately address the AGT rotor stress rupture requirements initiated a search for other possible compositions. The short time remaining on the contract, however, discouraged any drastic modifications of our present approach or material. Recent information cited in the literature (13, 14) pointed to ZrO_2 additions as sintering aids capable of improving the strength of silicon nitride. Zirconia seemed an ideal candidate for investigation--it has the potential for overcoming RM-20's limitations while being relatively easy to test and implement.

Hot pressing was chosen as the initial means of consolidating the powder mixtures of partially-stabilized zirconia (PSZ) and RM-20. It permitted more rapid assessment of the composition's potential properties and, to some extent, the sinterability of the material. Hot pressing time can be a measure of the amount of liquid phase present - the more liquid, the shorter the time required to hot press - and the amount present generally correlates well with sinterability. However, if a particular composition emerged as a likely candidate, a parallel study, undertaken to evaluate its slip-casting potential, would also be used to evaluate sinterability.

Table 66. Stress Rupture Test Results RM-20 Rotor Material.

Specimen No.	Stress (MPa)	Stress (ksi)	Temp. (C)	Results And Observations
GROUP 1. "AS-HIPped" Rotor * X-RAY DATA: B + G				
79A-7	344.7	50	800	214 Hrs. sustained
79A-6	344.7	50	1000	1.1 Hrs. failed
79A-8	275.8	40	1000	212 Hrs. sustained. Slight discoloration
79A-9	275.8	40	1200	1.3 Hrs. failed. Slow crack growth and oxidation
79A-10	206.8	30	1200	140 Hrs. sustained specimen shows bending and heavy discoloration
GROUP 2. After Test Bar Heat Treatment: 96 Hrs. at 1450C * X-RAY DATA: B + Yi				
79A-11	275.8	40	1200	12 Min. failed. Slow crack growth and oxidation.
79A-12	206.8	30	1200	44 Hrs. sustained. Specimen shows bending and discoloration
* B = Beta Si_3N_4; Yi = $Y_2Si_2O_7$ G = Glass (major); g = glass (minor)				
GROUP 3. After Rotor Heat Treatment: 96 Hrs. at 1450C * X-RAY DATA: B + H				
89A-11	137.9	20	1200	100 Hrs. sustained. Specimen shows bending and discoloration
89A-10	206.8	30	1200	22 Hrs. sustained. Specimen shows bending and discoloration
* B = Beta Si_3N_4; H = $Y_5Si_3O_{12}N$				

Various PSZ and RM-20 powder batches of 200 grams each were mixed for 2 hours in half-liter polyethylene bottles with absolute alcohol as a vehicle. A dozen hot pressed silicon nitride milling media (1/2 in long x 1/2 in diameter) were included to facilitate mixing. The powder mixtures were ready for hot pressing after removal of the milling media and evaporation of the alcohol.

The mixtures were hot pressed in a graphite die lined with molybedenum foil at 4000 psi. The cycle time required to hot press was defined to be from the time the die punches started to move until the motion was less than 0.001 in./15 min. The resulting hot pressed billets were 6.67 mm in diameter by approximately 1.75 mm in thickness.

The compositions and the initial results of these experiments are summarized in Table 67. Also included in this table are three samples of the same composition which were slip cast and sintered. All of the hot pressed samples achieved greater than 99 percent of their theoretical density. It should also be noted that the PSZ containing samples were hot pressed in much shorter time than the base RM-20 material. This suggested the likelihood of good sinterability. Indeed, the first slip casting and sintering attempt achieved densities as high as 98.5 percent of theoretical.

Both the hot pressed and sintered samples were sectioned for further study. Test specimens were cut from each of the billets for use in a static oxidation test and other evaluations, such as MOR, creep, thermal expansion, etc. The static oxidation results (Figure 357), discouraged any hopes that PSZ additions could overcome RM-20's limitations. All of the ZrO_2 containing samples exhibited poor oxidation resistance, as evidenced by the discoloration of their initial dark appearance. The dramatically different results obtained in samples of similar composition warrants further comment. The abbreviated hot pressing cycle used to achieve full density in compositions Ai, Bi and Ci (where unreacted raw materials were used in place of RM-20), was too short to complete the alpha-to-beta phase transformation. The presence of both silicon nitride phases in these samples may account for their total deterioration during oxidation. In the other samples, oxidation was directly proportional to the amount of PSZ present. The only exception occurred between samples IV and V, where the additional alumina in V appeared to alter the effects of the additional PSZ.

Although additions of PSZ to the RM-20 material might ultimately have improved room temperature rotor performance, the oxidation test clearly revealed its "Achilles heel" and further testing was discontinued.

TASK 2.7 - STATOR - FORD

Introduction

The stator configuration selected for the AGT101 engine was of a 19-vane, radial flow design. Nominal overall dimensions were:

Outside diameter	7.0 inches
Inside diameter	5.2 inches
Total thickness	0.6 inch

Design alternatives considered were (a) a stator assembled from individual vane segments and (b) a monolithic configuration having one solid and one segmented shroud. The latter configuration was designed to reduce thermal gradients which could result in excessive stresses during transients.

Several potential advantages were inherent in the monolithic construction:

- **Ease of Handling** - One large part versus 19 pieces would be processed through all stages of fabrication and assembly.
- **Reduced Machining Costs** - There would be a maximum of four surfaces and no critical circumferential stack-up tolerances requiring machining.
- **Reduced Leakage** - Leak paths through the shrouds would be reduced by one half.
- **Experience** - Ford had already demonstrated the capability of monolithic axial

Table 67. The Effect of PSZ Addition to RM-20 Si_3N_4 Material.

Hot Pressed									
Weight Percent									
Ident.	RM-20	PSZ	Si_3N_4	Al_2O_3	Temp. Deg. C	Time Min.	Density g/cm3	X-Ray Data (*)	
Base	100	0	0	0	1800	271	3.308	B,K	
I	99.5	0.5	0	0	1675	94	3.315	B,G	
II	99	1	0	0	1675	74	3.323	B,Y,g	
III	98	2	0	0	1675	70	3.336	B,H,g	
IV	96	4	0	0	1675	68	3.375	B,Z,G	
V	90	8	0	2	1675	17	3.438	B,Z,G	
A	60	10	30	0	1675	115	3.436	B,Z,g	
B	70.6	5.9	23.5	0	1675	145	3.388	B,Z,g	
C	83.3	2.8	13.9	0	1675	107	3.342	B,Z,g	
	Si_3N_4	Y_2O_3	Al_2O_3						
Ai	54	4.8	1.2	10	30	0	1675	44	3.420	A,B,Z,G
Bi	63.5	5.6	1.4	5.9	23.5	0	1675	29	3.353	A,B,Z,G
Ci	75	6.7	1.7	2.8	13.9	0	1675	32	3.322	A,B,Z,G
Slip Cast and Sintered									
As	60	10	30	0	1800	36hr	3.306	B,Z,G	
Bs	70.6	5.9	23.5	0	1800	36hr	3.311	B,Z,G	
Cs	83.3	2.8	13.9	0	1800	36hr	3.262	B,Z,G	

(*) (A) Alpha Si_3N_4, (B) Beta Si_3N_4, (Z) ZrO_2, (Y) $Y_2Si_2O_7$, (H) $Y_5Si_3O_{12}N$, (K) $YSiO_2N$, (G) Glass (major), (g) glass (minor)

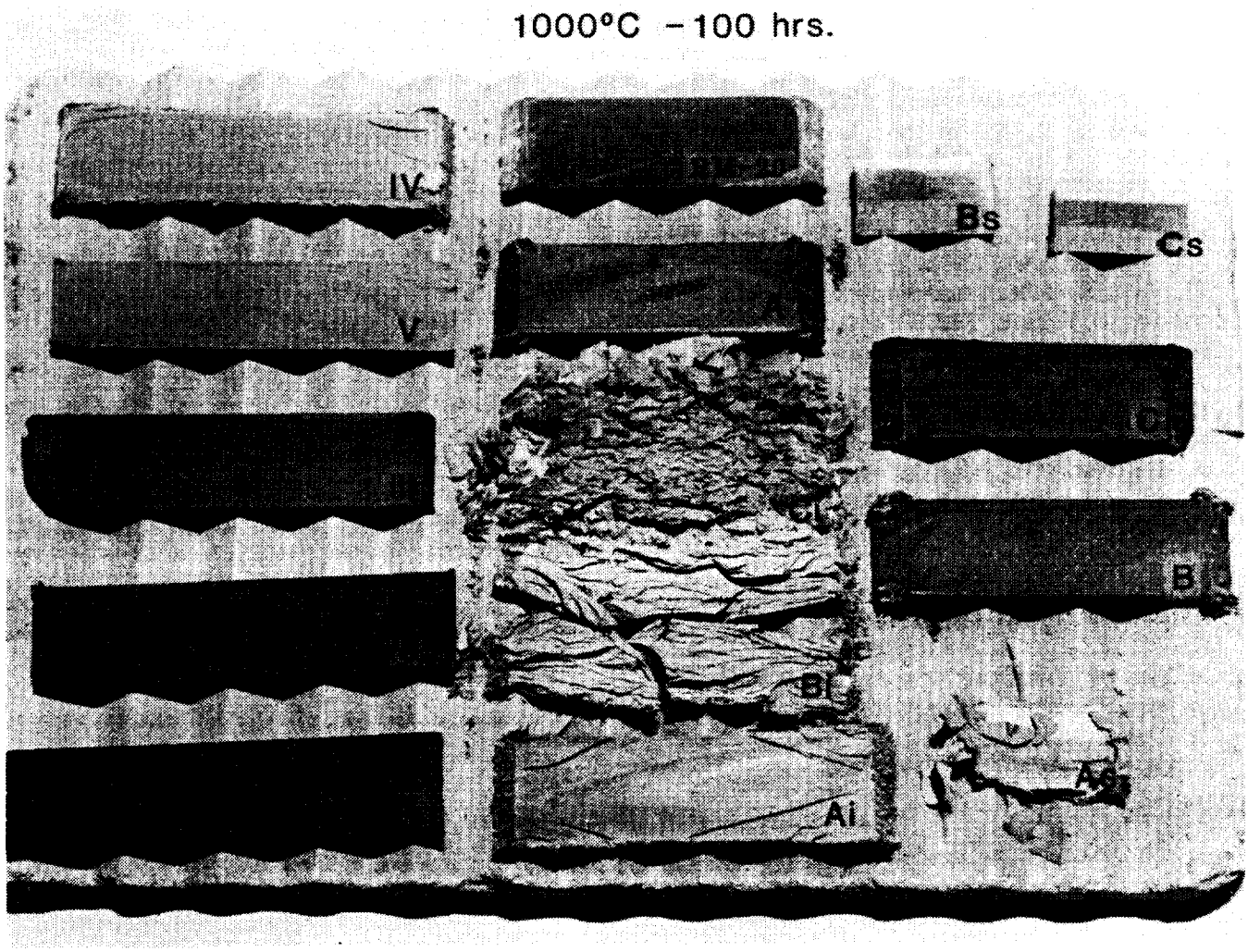

Figure 357. Static Oxidation Test.

stator molding for the 820 engine program. (1,15) Molding and forming this component of individual vane segments was readily supported by existing inhouse technology and that of other suppliers.

Based on these advantages and seeking to advance the technology of complex shape forming, Ford elected the challenge of a monolithic stator and worked on this design until February, 1984 when lack of funding caused elimination of this effort.

Flow Modeling

Among the many important parameters for injection molding tool design are gate type and location. Both can influence melt front weld lines and significantly affect component strength. For the AGT stator, a diaphragm gate along the inside diameter of the solid shroud would prevent weld lines in the shroud. However, the vanes and segmented shrouds would be filled in parallel, constricting the flow through each vane to 5 percent (1/19) of the machine maximum flow rate. Conversely, a single point gate (at any location) would produce a shroud weld line but permit a flow rate through each vane of 50 percent machine maximum by filling paired vanes sequentially.

Cornell University was contracted to conduct computer flow modeling studies to ex-

amine the influence of flow rate, material temperature and die temperature on the vane fill pattern (16). Of primary concern was the possibility of inadequate fill or the formation of weld lines in the thin trailing edge of the vane.

Their studies indicated that, for the idealized isothermal case and projecting flow rates <50 percent of those anticipated through a diaphragm gate, good vane fill would occur as shown in Figure 358. In this case, the melt front at the trailing edge advances to the segmented shroud before the shroud fills. However, projecting an unheated tool and the expected flow rates for a diaphragm gate, the model predicted complete freezing of the melt front along the trailing edge before reaching the shroud. Only back flow from the shroud would complete the vane trailing edge, resulting in a cold weld line. As the flow rate was increased to that predicted for a point gate, the melt front approached that of the isothermal case. Thus the study emphasized the need for precise die temperature control and flexibility in design of the gate region to facilitate changes in gate configuration.

Tooling Design

The stator tool design (Figure 359) incorporates three independent water temperature control circuits. Five cavity pressure transducers and four thermocouples are included to monitor and control molding parameters. Removable die inserts enable rapid changes in gating.

Previous experience in the injection molding of complex-shaped components related the occurrence of cracks in the molded part to the sequencing of insert removal and parting of the die. Consequently, considerable effort was spent in designing flexibility into the tool. This included independent sequencing of the two sets of 19 inserts forming the vane contour. In addition, the die was designed to independently sequence the gate parting line before opening the die and ejecting the stator.

Tool Development

Initial development work on molding the AGT stator was directed toward tool installation and operational check out. Several deficiencies were related to installation and construction. The platens of the vertical molding machine were bowing, transmitting the clamping forces at the tool perimeter, leaving the central section completely unsupported. The platen deflection pattern was measured and circular shims installed at the tool/platen interfaces to correct the problem. Dimensional measurements of molded stators, however, suggested that internal tool components were deflecting. Specific ares of deflection were measured during molding trials and locations which required internal stiffening were identified. Also, cold weld lines were occurring in the trailing edge of the vane. The tool was returned to the vendor for correction of the internal deflection problems and enlargement of the cavity to increase the vane trailing edge thickness from 0.030 to 0.040 inch.

Molding Development - Diaphragm Gate

Stator molding was initiated using the 0.010 inch thick gate; 12 full and six short shots were made. The fill pattern observed on the short shots was non-uniform as shown in Figure 360, Views (a) and (b). Complete cavity fill was achieved as indicated in Figure 360 View (c).

Measurements of the gate material at the inside diameter of the solid shroud revealed that the actual gate size varied from 0.006 to 0.014 inch. This variation was the result of eccentricity between the tool details which form the gate. The direction of eccentricity matched the fill pattern seen in the short shots. This is, the cavity area first to fill was at the larger gate dimension. Full shots had a weld line in the solid shroud opposite the larger gate area.

Seven of the full shots were visually inspected for defects in the vane trailing edges. In general, the trailing edges were sound with over half the vanes in each stator having no observable defect. Trailing edge knit lines, or signs of cold packing, were found in the remainder of the vanes. Three types of typical

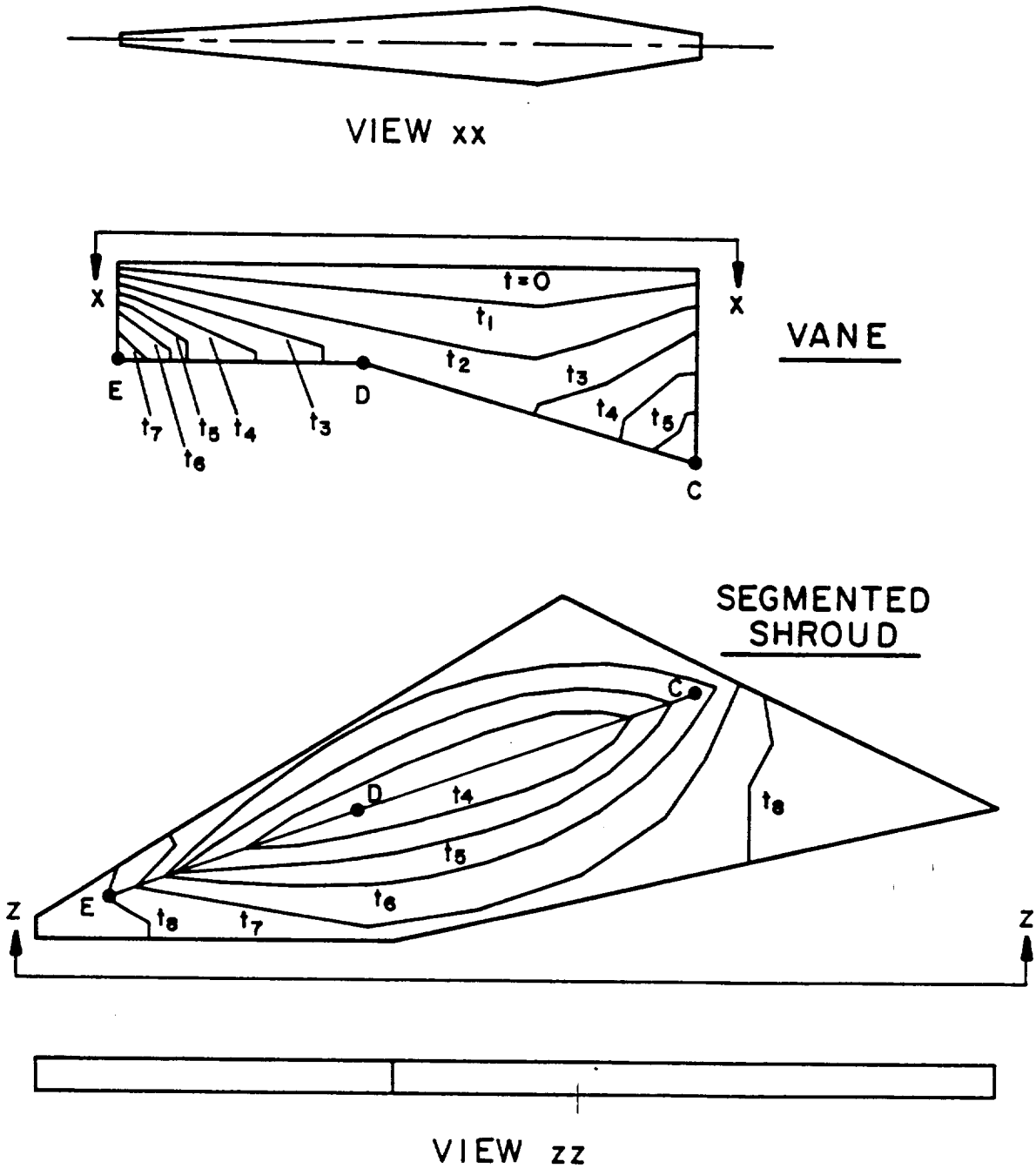

Figure 358. Cornell Melt Front Advance.

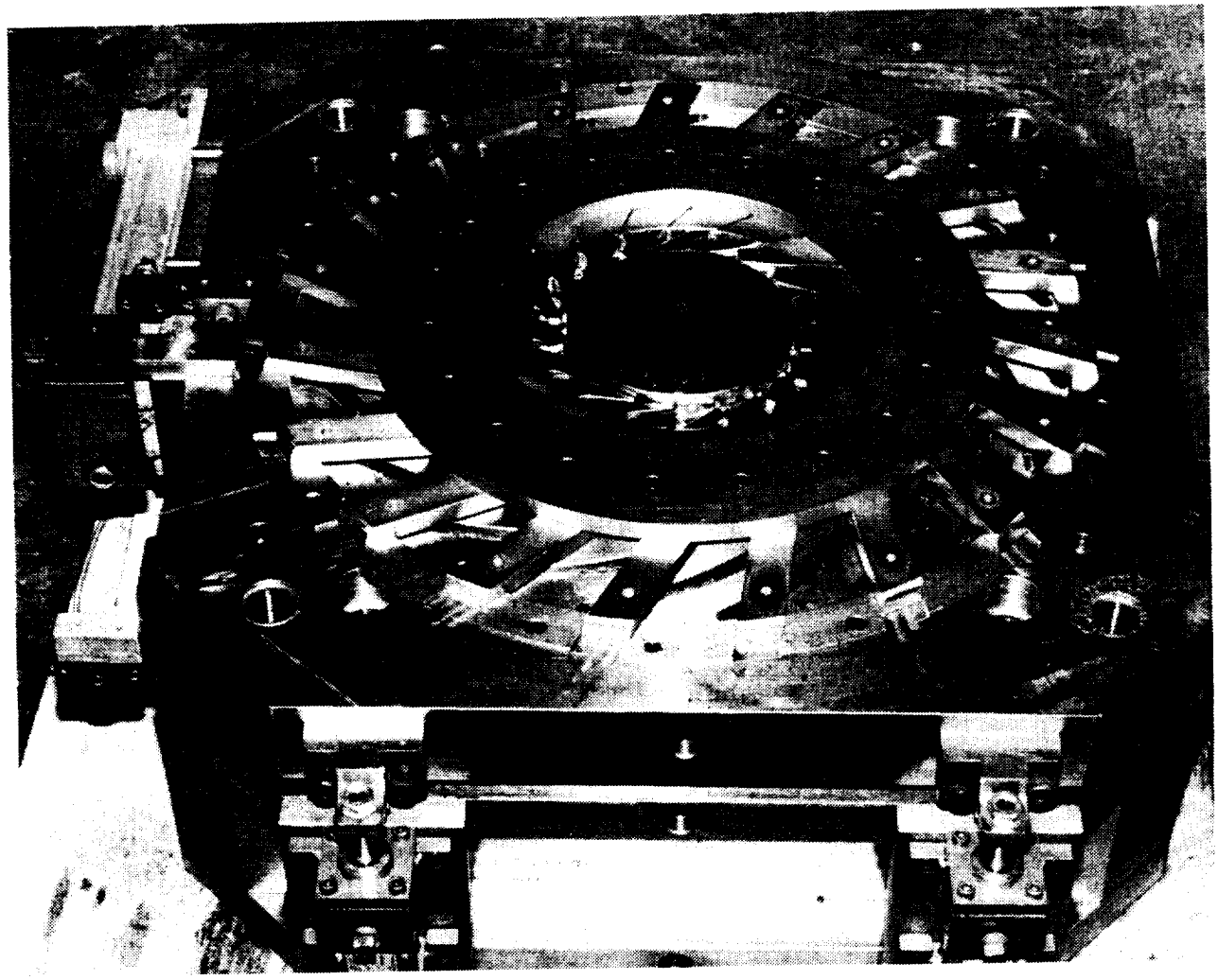

Figure 359. Stator Tool.

trailing edge conditions are shown in Figure 361. The relative frequency of each type of vane was:

Vane Appearance	Average Vanes per Stator
No defect	10.7
Knit lines	1.3
Cold packing	7.1

The tool insert forming the gate was reworked to make a concentric gate 0.015-inch thick and an extensive parametric study was conducted. Stators were molded at material temperatures of 200, 250 and 275F and tool temperatures of 90 and 110F. Several shots were also made at varied injection pressures.

The first series of shots was made at material and tool temperatures of 200 and 90F, respectively. These stators were visually inspected and compared with stators molded using the eccentric gate and identical temperatures. The data are summarized below:

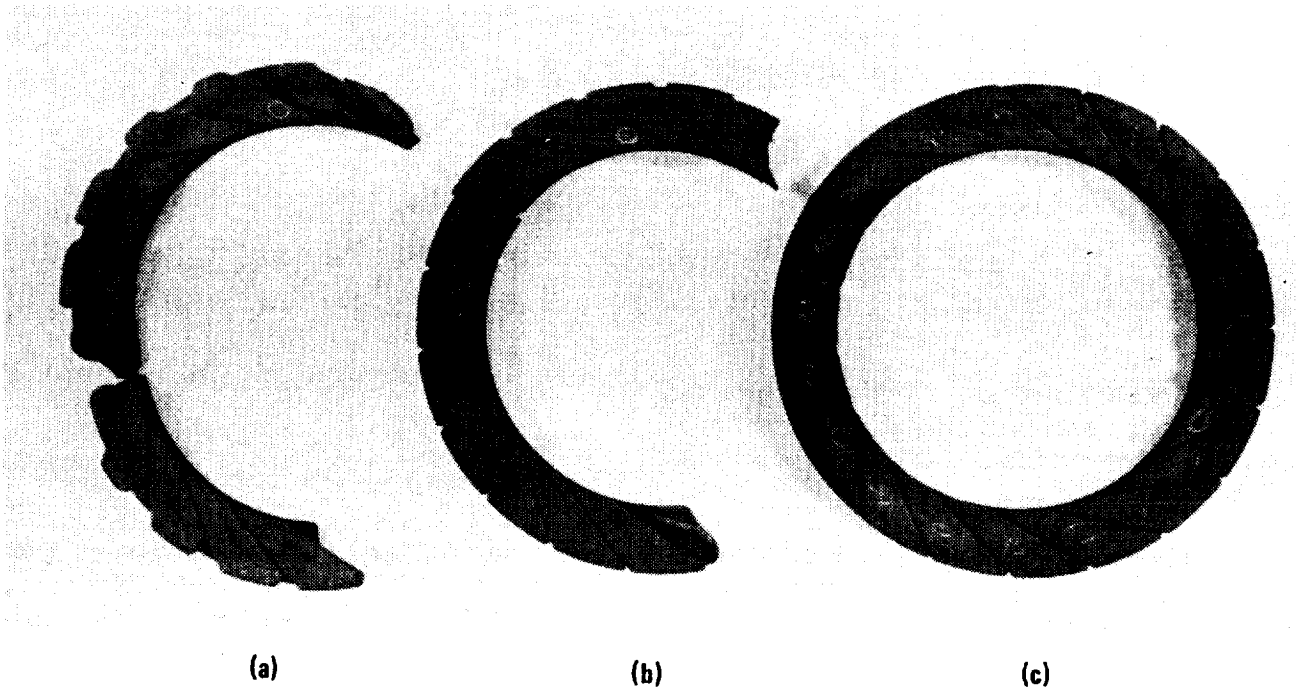

(a) (b) (c)

Figure 360. Fill Pattern With 0.010 Inch Eccentric, 0.006-0.014-inch Diaphragm Gate Short Shorts (a) and (b), and Full Shot (c).

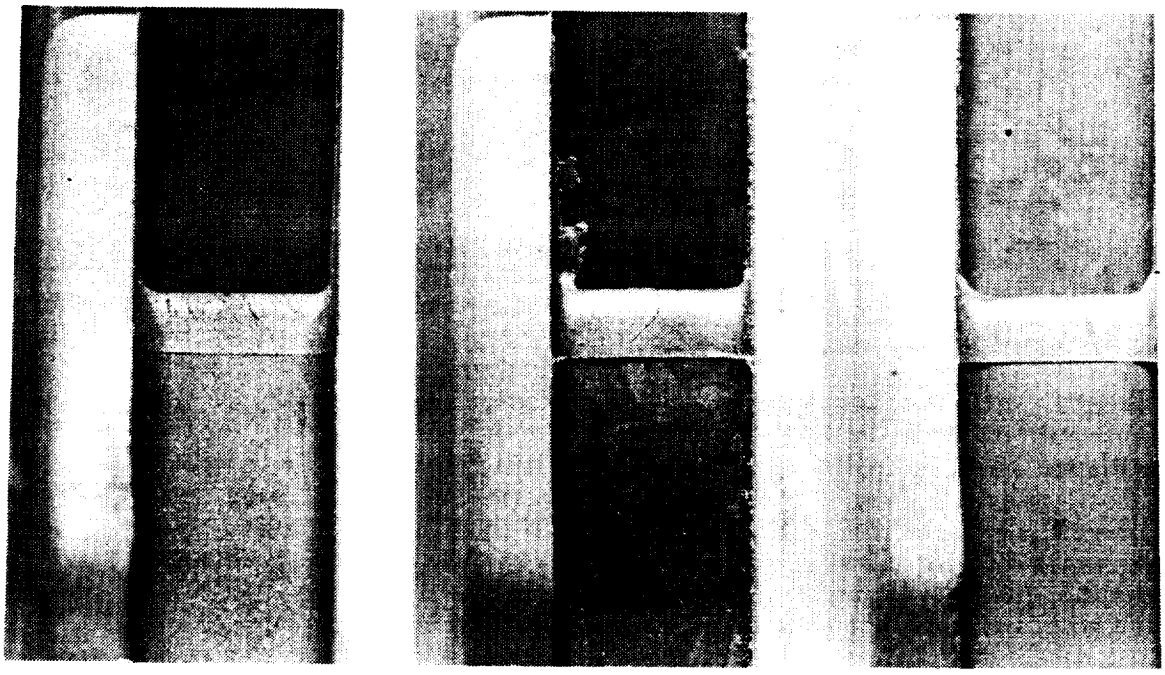

(a) (b) (c)

Figure 361. Vane Trailing Edges Typically Formed With Eccentric Gate Good Fill (a), Knot Line (b) and Cold Packing (c).

Gate Configuration	Knit Lines	Cold Packing	No Defect
Eccentric (0.006 - 0.014 inch)	1.3	7.0	10.7
Concentric (0.015 inch)	6.0	17.0	0.6

The overall condition of the stators had obviously degenerated significantly and vanes appeared which had both knit lines and cold packing flaws.

The effects of material and tool temperatures on vane trailing edge flaws are shown in Figures 362 and 363. The data for these

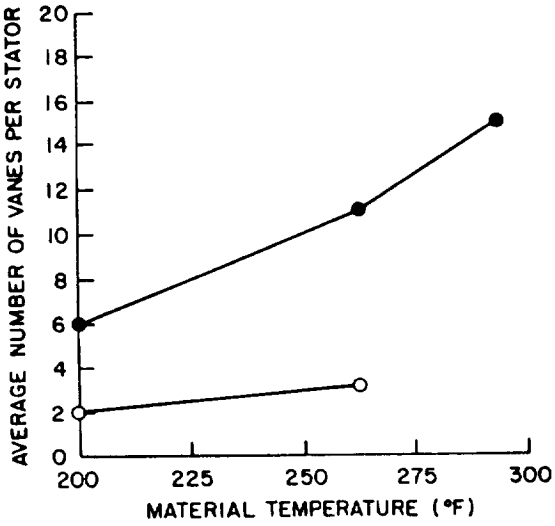

Figure 362. Effect of Material Temperature on Vane Trailing Edge Knit Line Flaws.

figures were generated from visual inspection of all the vanes on 20 stators fabricated during a parametric study. At least three stators were formed at each set of conditions.

Predictably, the curves show that cold packing diminished with higher tool and material temperatures. An increase in either temperature tended to keep the material softer

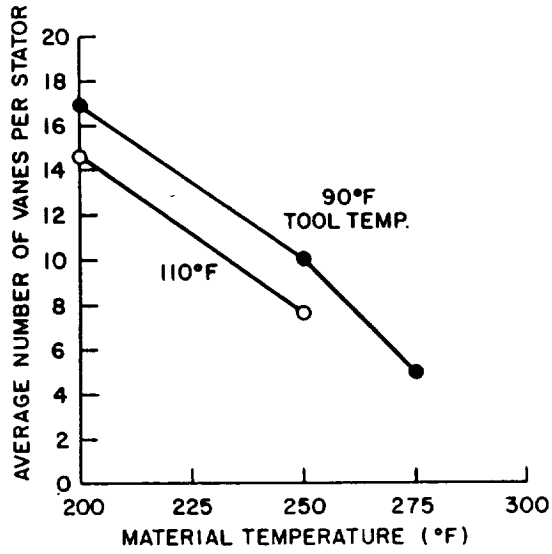

Figure 363. Effect of Tool Temperature on Vane Trailing Edge Cold Packing Flaws.

until the cavity packing pressure was reached. The same factors would be expected to produce fewer knit lines and, in fact, knit lines were observed to decrease with increasing tool temperature. However, at lower tool temperatures, knit lines increased with increasing material temperature. (Figure 362).

The "short shots" shown in Figure 364 demonstrate the effect of material temperature on the fill pattern for a constant tool temperature and flow rate. At low material temperatures, the fill pattern moves primarily in a circumferential direction similar to the eccentric gate condition which produced fewer knit lines. As the material temperature is increased, the fill pattern changes to more uniform radial filling, reducing the flow rate through each vane and producing weld lines as predicted in flow modeling.

During the parametric study, a more critical flaw type was observed under certain conditions. Vane cracks occurred either in the trailing edge or in the vane-to-shroud fillet. The relative frequency of cracks as a function of material and tool temperature is shown in

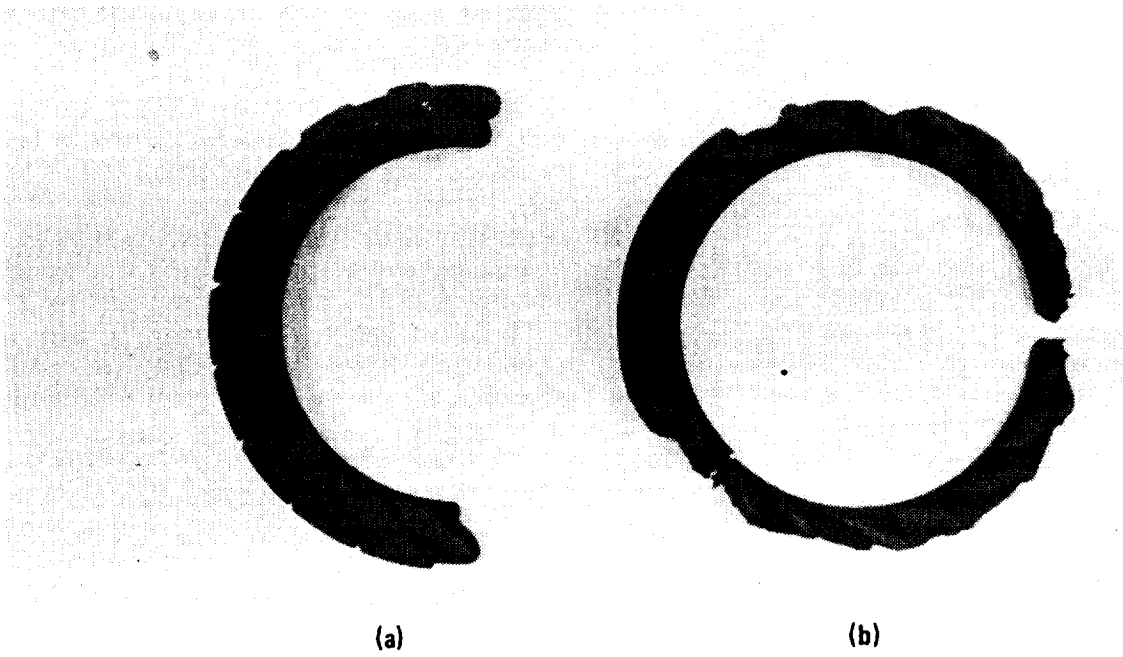

Figure 364. Changing Fill Pattern With Material Temperature Concentric Diaphragm Gate (0.015 in) Material Temperatures of 200F (a) and 275F (b).

Figure 365. Raising either temperature tended to produce cracks.

The effect of the diaphragm gate size was investigated by increasing the gate thickness from 0.015 to 0.065 inch. Ten shots were made (nine full and one short) with material temperatures ranging from 225 to 275F at a constant tool temperature of 80F. The results indicated that with the thick gate:

- o Uniform radial fill occurred at all temperatures.
- o Virtually no cold packing appeared in the vane trailing edges.
- o Knit lines were evident in all vanes.
- o Knit lines became "tighter" and less obvious with increasing material temperature.
- o Vane or vane/shroud fillet cracks were present at all temperatures.

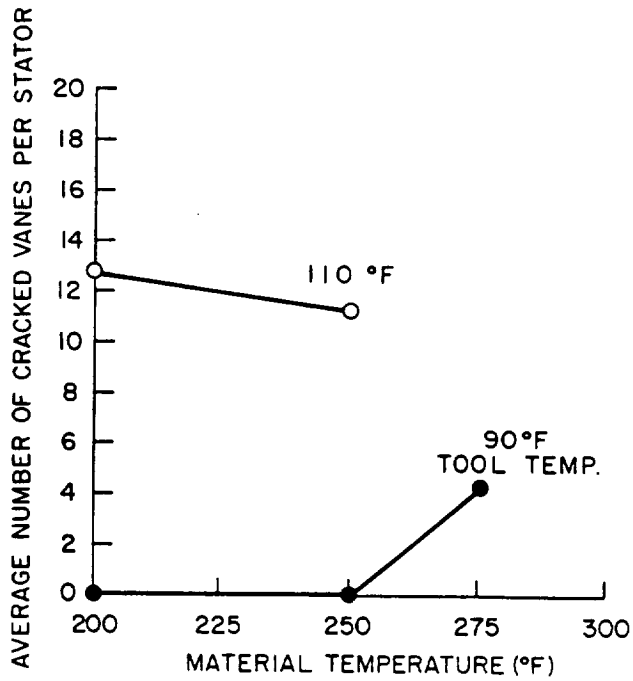

Figure 365. Relative Frequency of Vane Cracks as a Function of Material and Tool Temperature.

Parametric studies with the diaphragm gate configuration revealed that no combination of conditions was likely to produce flaw-free parts. However, it was clearly evident that all three defects (knit lines, cold packing and cracks) could be significantly altered.

Cracks in the vane trailing edge or the vane/shroud fillets were attributed primarily to tensile loads on the stator during die opening. The entire conical runner section usually adhered to the upper half of the tool, breaking off at the gate during opening. The most frequent cracks occurred when using the thicker gate which developed higher loads. The thin gate shots at lower tool and material temperatures were not cracked as shown earlier in Figure 361. At higher temperatures cracks appeared, believed to result from adherence of the part to the tool. Crack prevention appeared to be a function of the loads borne by the stator during tool opening.

Molding Development - Single Point Gate

Improvements in tool gating could resolve all three problem areas. Switching from the diaphragm gate to a single point gate had the advantage of:

- Sequentially filling vanes, effectively increasing the flow rate and eliminating trailing edge knit lines.
- Developing a thick melt front while filling the vanes and eliminating the cold packing.
- Reducing the gate cross-sectional area, minimizing the load required to break off the gate runner during tool opening.

One potential disadvantage was expected. The circumferential fill pattern would result in one solid shroud weld line 180 degrees from the gate.

A cone-shaped metal insert was fabricated to fill the original runner cavity. A one-half inch wide radial slot was then cut into the insert, running from the central sprue to the original gate at the solid shroud inside diameter.

Short shots disclosed that a circumferential fill pattern developed with a uniformly thick melt front (Figure 366). When full shots were made, there were no signs of trailing edge knit lines or cold packing. The full shots, however, revealed a localized "hot spot" in the shroud near the gate. Changing the injection hold times before tool opening and ejection resulted in stators with either "pull-out" of the shroud material or shroud cracks (Figure 367).

Fourteen full shots were made during a study of the effect of gate size, flow rate and tool temperature on the pull-out and cracking. The material temperature and injection pressure were held constant at 250F and 1800 psi (9000 psi equivalent cavity pressure). The gate size, flow rates and tool temperatures investigated were:

Gate size (inch)	**- 0.015 x 0.5**	**- 0.015 x 1.0**
Flow rate (in^3/sec)	**- 4.4**	**- 8.8**
Tool temp (F)	**- 70**	**- 90**

All 14 stators had either pull-out or cracks, but no strong correlation between any of the above parameters and flaw type was evident. Since the machine was being operated manually during the study, significant variations occurred in the injection molding sequence times (injection hold, tool open and ejection). The timing of these events was available from analog instrumentation recordings of cavity pressures for each shot.

The flaw types were quantified and plotted as a function of time as shown in Figures 368 and 369. Pull-out was quantified by measuring the length of chord of the affected area. Cracks were quantified as the number of optically detectable cracks in the stator shroud.

At a tool temperature of 70F, pull-out was reduced to zero when the tool opening time exceeded 14 seconds from the start of injection. Cracks appeared only when ejection

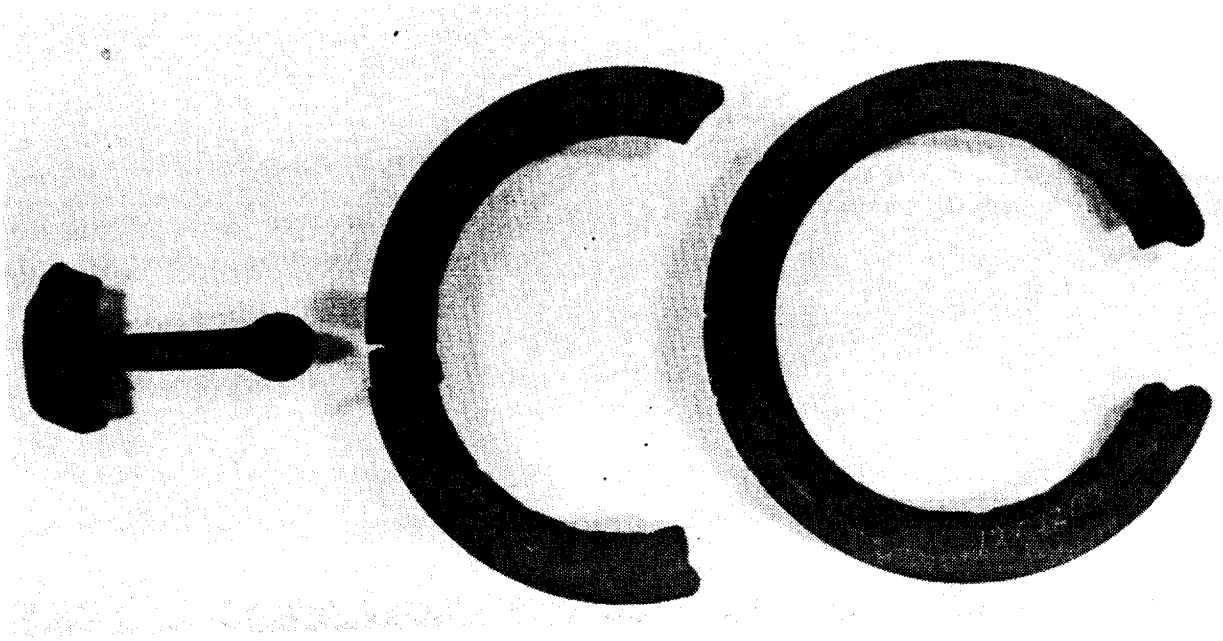

Figure 366. Short Hot Fill Pattern When Using Single Point Gate.

(Far Left Shot Includes Sprue and Runner)

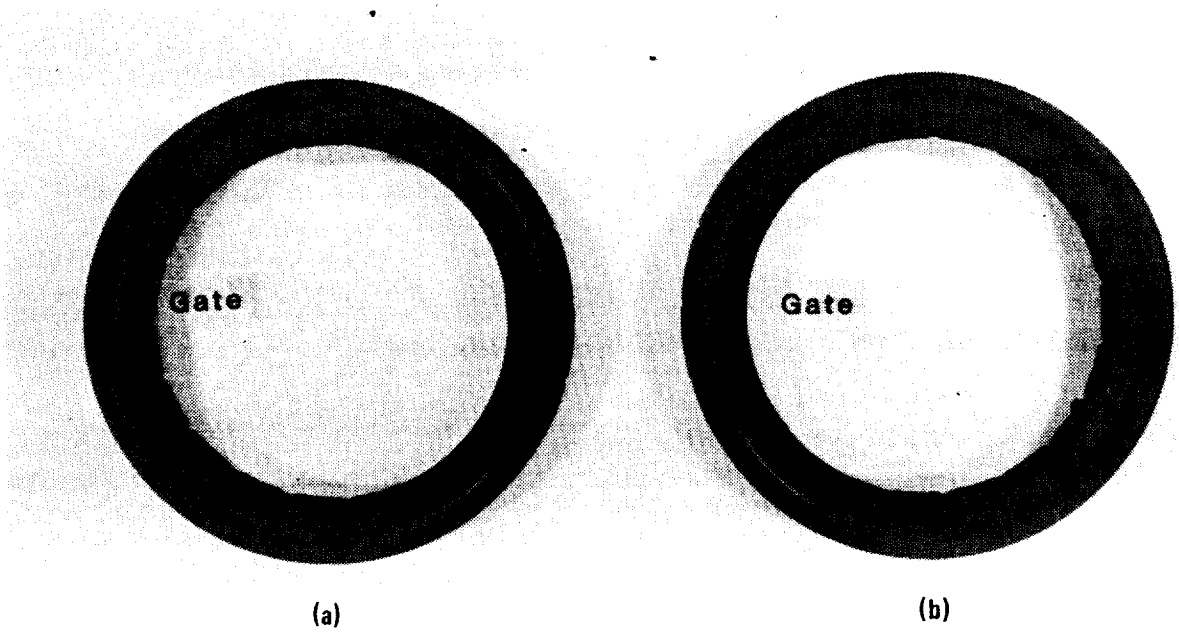

Figure 367. Full Shots Using Point Gate Material Pull-Out in Gate Area (a) and Solid Shroud Cracks (b).

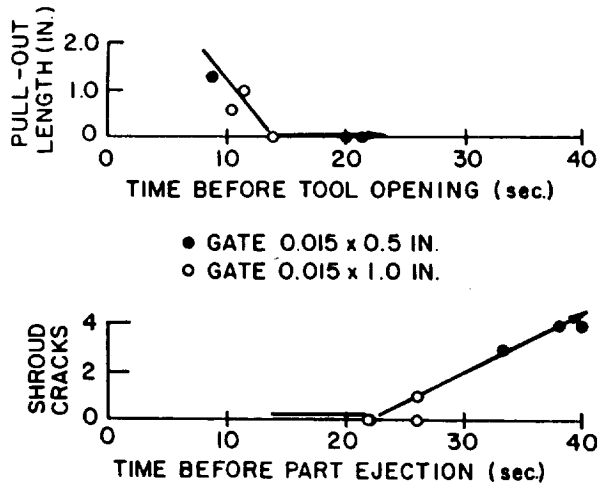

Figure 368. Effect of Injection Sequence Timing on Material Pull-Out and Shroud Cracks - Tool Temperature, 70F.

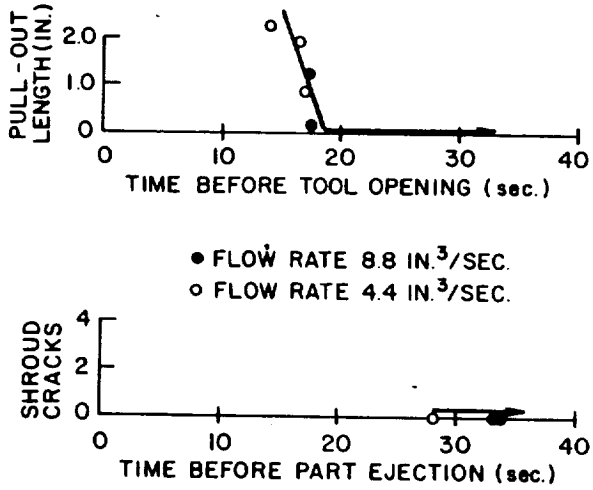

Figure 369. Effect of Injection Sequence Timing on Material Pull-Out and Shroud Cracks - Tool Temperature 90F.

times were greater than 22 seconds. At a tool temperature of 90F, the "no pull-out time" increased to 19 seconds and cracks did not appear at ejection times $\leq$34 seconds. Clearly, a time "window" existing in both cases where no pull-out or cracks would be expected.

Seventeen additional stators were modeled utilizing the point gate to further investigate the time window, lower material temperatures, higher injection pressures, larger gate size, an overflow at the solid shroud weld line and use of a hot sprue bushing. Precise control of hold times for tool opening and part ejection. Effectively prevented pull-out and solid shroud cracks. None of the other variables had a significant effect on molded part quality.

The best tooling configuration and molding conditions for overall good quality stators were:

- o Gate size - 0.015 x 3.0 inches
- o Use of a hot sprue bushing
- o Tool temperature - 90F (top and bottom)
- o Material temperature - 225F
- o Injection flow rate - 8.8 in^3/sec
- o Injection pressure - 1950 psi (9750 psi cavity)
- o Injection hold time - 5-7 seconds
- o Tool open time - 15-16 seconds
- o Ejection time - 18-20 seconds

A production run of 24 consecutive shots was made over a three-day period. These stators were intended for complete processing through machining, as candidates for possible engine testing. Of the 24 stators, four were rejected for molding flaws during the post molding visual inspection. All 24 passed x-ray inspection.

Subsequent inspections during processing disclosed fine fillet cracks at the vane-to-shroud junction on both leading and trailing edges. Re-inspection of "as molded" stators revealed that the cracks could be seen in the molded state.

Fillet Crack Investigation

The discovery of fillet cracks in the "shipper candidate" stators mandated a re-inspection of all available stators, with particular attention to the leading edge (LE) and trailing edge (TE) fillet areas. All available stators molded from the 2.7 density material

were re-inspected: 23 of the batch intended for further testing and 10 others molded during development studies. A summary of the inspection findings relative to leading and trailing edge cracks is presented in Table 68.

Leading edge cracks were found in all of the test candidate stators, averaging 7.5 vanes per stator and ranging from 1 to 13. Trailing edge cracks appeared in an average of 2.8 vanes per stator; and ranged from 0 to 12 in

Table 68. Fillet Crack Inspection Results.

	Stator Serial Number	LE Cracks	TE Cracks	Total Cracks
SHIPPER CANDIDATES	1206201	12	4	16
	02	7	1	8
	02	8	0	8
	04	3	0	3
	05	4	1	5
	06	6	16	18
	07	--	--	--
	08	4	8	12
	1208201	9	2	11
	02	11	0	11
	03	11	0	11
	04	5	0	5
	05	5	7	12
	06	6	0	6
	07	9	6	15
	08	1	0	1
	1209201	13	4	17
	02	4	8	12
	03	9	1	10
	04	8	0	8
	05	11	1	12
	06	7	3	10
	07	13	1	14
	08	7	5	12
DEVELOPMENT STUDIES	0113201	0	0	0
	027206	0	0	0
	1129203	18	0	18
	04	17	0	17
	1130203	4	0	4
	1202202	5	0	5
	1203201	5	0	5
	04	5	0	5
	05	3	0	5
	06	4	0	4

number. Six stators had no trailing edge cracks. The ten experimental stators had a significantly different crack distribution; two had fillet cracks and none had the typical trailing edge cracks. (These ten stators, however, had other defects).

Although 23 stators were molded under nominally identical conditions, some process variability occurred. Size parameters were identified which showed significant shot-to-shot variation:

- o Cracked vane number
- o Injection hold time (t_I)
- o Time to die open (t_O)
- o Time to part ejection (t_E)
- o Cavity pressure at t_O (Pcav)
- o Cavity pressure difference, (ΔPcav) front to rear, at t_O

Figures 370 and 371 show the frequency of cracks relative to vane numbers. Leading edge cracks occurred 100 percent of the time

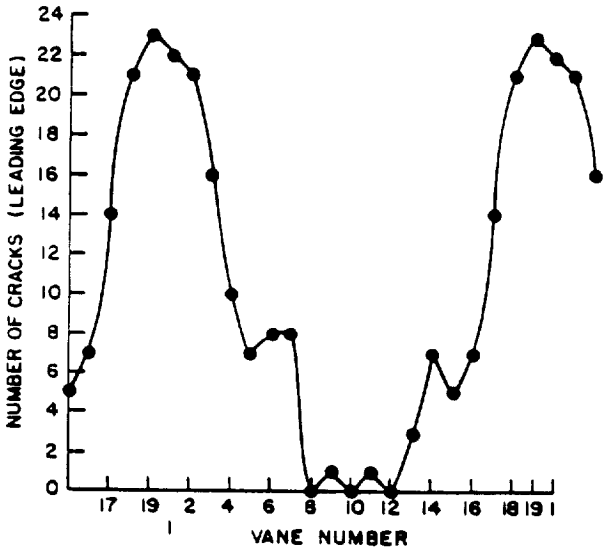

Figure 370. Frequency of Cracks Relative to Vane Numbers (Leading Edge).

at vane number 19 in the center of the gate region. Vanes 8, 10 and 12 - opposite the gate - had no cracks in any of these stators. Trailing edge cracks were more randomly distributed, but a four-vane segment existed

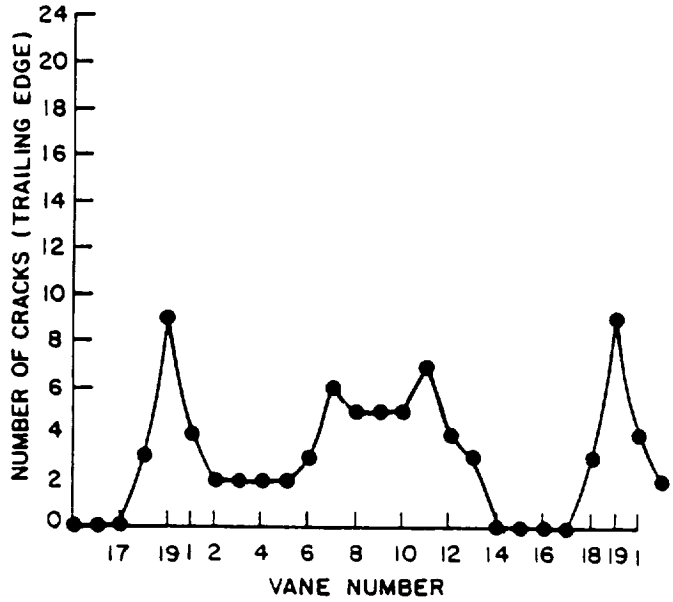

Figure 371. Frequency of Cracks Relative to Vane Number (Trailing Edge).

where no cracks occurred (vanes 14 through 17).

Plots of vane cracks versus injection times (t_I, t_O and t_E) are shown in Figures 372 and 373. No clear pattern or trend appears for leading edge cracks. For the trailing edge cracks, however, die open time (t_O) appears to influence crack frequency where increasing t_O reduces cracks. No cracks appear when this variable is greater than 16.1 seconds. Cavity pressure did not correlate with either type of crack.

Significant differences were found in the frequency of fillet cracks between 24-stator batch and the 10 experimental stators which were inspected (Table 68). Two of the latter were crack-free. All ten had no trailing edge cracks. In addition, the frequency of leading edge cracks in these stators could be summarized in three categories: no vanes cracked, all vanes cracked or approximately 25 percent of the vanes had cracks.

Ten variables were identified which could be used to compare the two batches of stators

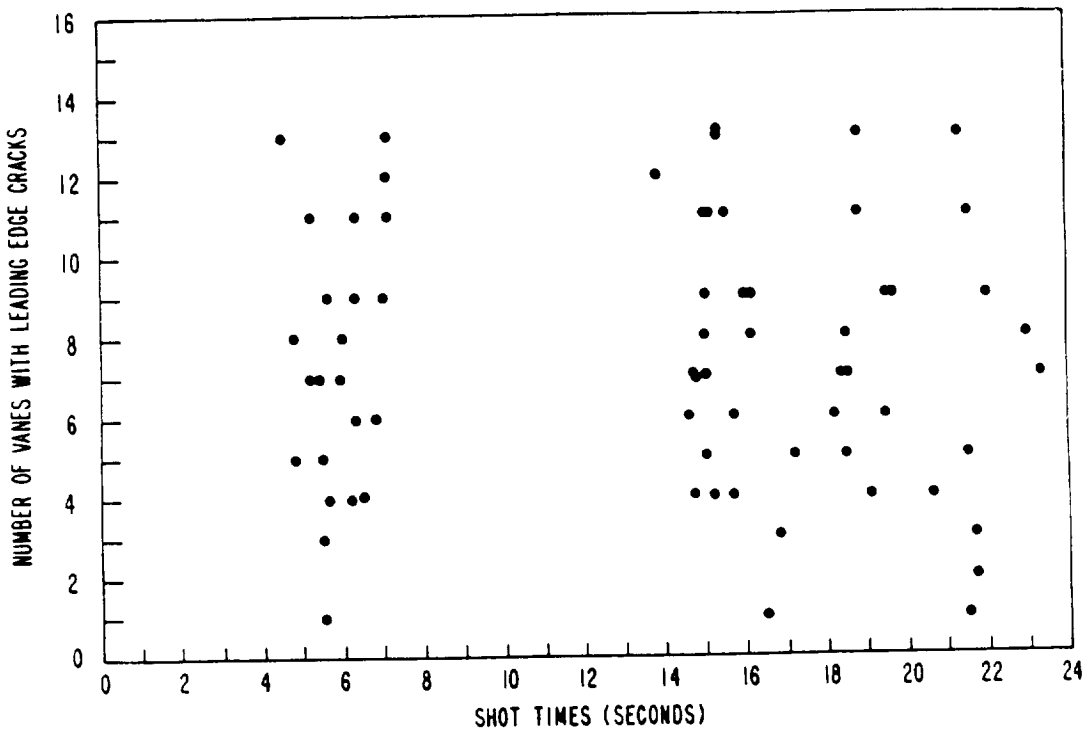

Figure 372. Plot of Leading Edge Cracks vs. Injection Time.

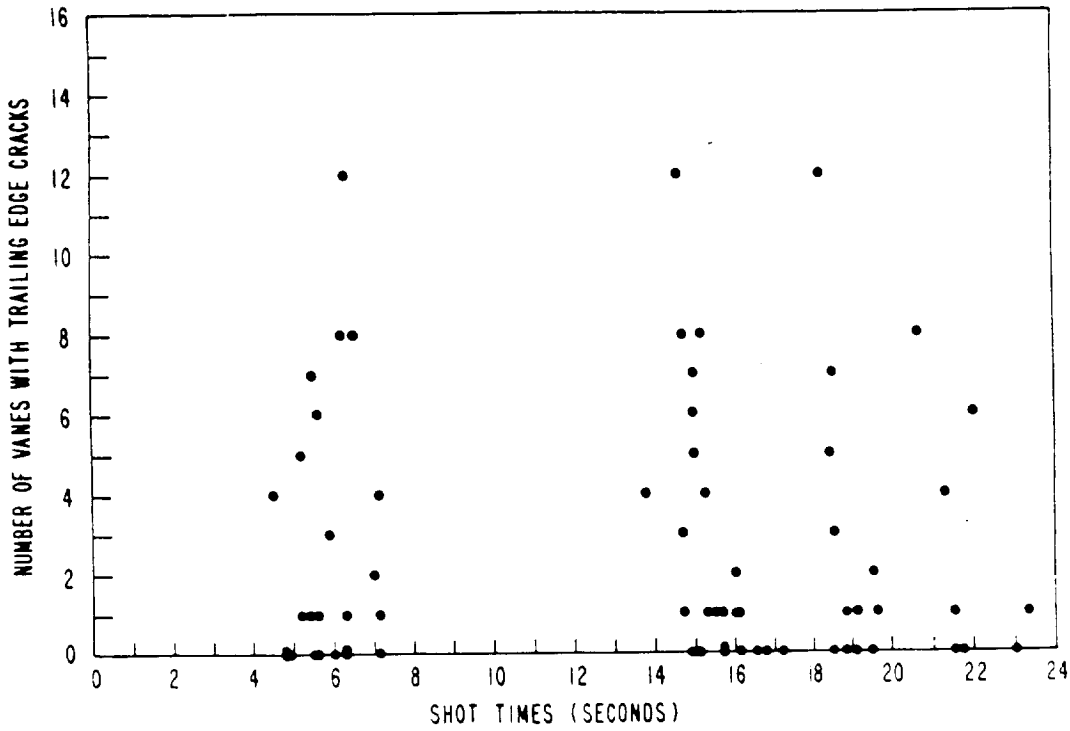

Figure 373. Plot of Trailing Edge Cracks Vs. Injection Time.

relative to leading edge cracks. The variables were:

- Gate type (full 360 degrees versus arc segment)
- Sprue type (standard tapered versus hot sprue)
- Injection pressure (hydraulic pressure setting)
- Melt temperature setting
- Mold temperature
  top half
  bottom half
- Injection times
  inject and hold
  time to die open
  time to ejection
- Cavity pressures (residual at t_o)

Table 69 shows the value or range for these variables for the best and worst shots of the 24-batch stators and the three groupings for the developmental shots. Three variables stand out as being unique to the best developmental shots: gate type, sprue type and injection pressure. The eccentric, full 360 degree gate had previously produced a fill pattern essentially the same as an arc-segment gate. Therefore this variable was considered insignificant in the development of leading edge cracks. However, sprue type and injection pressures were potentially important parameters influencing leading edge cracks.

In summary, a review of all available data regarding the leading and trailing edge cracks in the vane-to-segmented-shroud fillet suggested that four variables had influenced the cracks:

- **Gate location** - all point gate (arc segment) shots were made with the gate in the same location which may have masked another tool problem.

Table 69. Fillet Crack Inspection Results - Variables.

	No. of Leading Edge Cracks	Gate Type	Sprue Type	Inj. Press.	Melt Temp.	Variables Mold Temp. (Top)	Mold Temp. (Bot.)	Injection Times (Inj.)	Injection Times (Open)	Injection Times (Ejct.)	PCAV at t_{open}
Shipper Best (1)	1	0.015 X 3.6	Hot	1980	225	90	90	5.5	16.5	21.5	600 - 800
Shipper Worst (1)	13	0.015 X 3.0	Hot	1980	225	90	90	4.5	15.3	21.3	800 - 1600
Other Best (2)	0	Full Eccentric 0.015/ 0.025	Taper	900 - 1500	225 - 240	80 - 95	80 - 95	5.5 8.1	--	--	--
Other Fair (6)	3 - 5	0.015 X 3.0	Hot	1800 - 1980	200 - 250	70 - 90	70 - 90	5.2 8.1	12.4 20.8	15.6 30.6	500 - 2500
Other Worst (2)	17 - 18	0.015 X 3.0	Hot	1800	250	75	75	5.9 - 8.6	14.1 - 14.5	20.0 - 21.6	600 - 1000

- o **Sprue type** - the only stators without leading edge cracks were made with a standard tapered sprue.

- o **Injection pressure** - developmental shots made with reduced pressures had no leading edge cracks.

- o **Die open time** - trailing edge cracks were reduced with longer times and none appeared for t_o >16.1 seconds.

Molding Investigations and Development

Molding studies investigated each significant variable. Stators were molded repeating the same conditions as used for the 24-stator batch. Several shots were made, changing only one variable from the baseline conditions. Finally, shots were made combining all three variable changes. All of the stators were then inspected with particular attention given to the leading and trailing edge fillets at the segmented shrouds. The inspection results are summarized in Table 70, along with comparative data from the baseline.

The six shots replicating the 24-batch conditions generally repeated the baseline results. The variance in the number of leading edge cracks may reflect material batch inconsistency. When the gate was rotated during these shots, the crack pattern followed the gate, indicating a flow-related phenomenon rather than a localized tool problem.

Each of the three other variables showed an improvement over the repeat shots in terms of fillet cracks. However, at lower injection pressure, the parts experienced solid-shroud pull-out and cracking at the edges of the gate, due to localized overheating. This problem persisted when all three variables were combined. A similar pattern was observed to a lesser degree in the 24-batch stators. Again, the difference might have been a function of material batch inconsistency. This investigation indicated that the variables identified significantly influenced the development of leading and trailing edge fillet cracks.

In order to reduce localized overheating in the gate region, and to continue stator molding development, the gate size was increased. An insert was installed which increased the gate width to 0.065 inch, maintaining an arc length of 3.0 inches. Preliminary shots showed that the overheating problem was corrected.

A parametric study was initiated to examine the effects of material melt temperature. Ten shots were made over the temperature range of 225 to 270F. These stators were visually inspected for all types of flaws. The inspection results are summarized in Table 71. The total number of flaws should be compared to 10.3 flaws per stator observed in the batch of 24.

Further molding process improvements and tool temperature measurements indicated that

Table 70. Variable Investigation using 0.015 X 3.0 Gate.

	Shipper Base Line	Repeat Shipper Conditions	Variable Changed		Combined Sprue	
			Taper Sprue	T_o = 17 sec	IP = 1300	T_o = 17 IP = 1300
Number of Shots	24	6	4	4	4	3
Average Number LE Cracks	7.5	3.0	1.8	1.3	0.8	0.3
Average Number TE Cracks	2.8	2.7	0.3	0.0	0.3	0.0

Table 71. Material Temperature Investigation 0.065 X 3.0 Gate.

			225F	250F	270F
Number of Shots			2	6	2
LE Crack	SS	*	3.5	1.2	1.5
	S		0.0	0.0	0.0
	other		0.0	0.3	0.0
TE Crack	SS	*	1.5	0.3	0.0
	S		0.0	0.3	0.5
	other		1.5	1.0	2.0
Shroud Cracks			0.0	0.7	0.5
Total Flaws			6.5	3.8	4.5

Notes:

SS = Vane To Segmented Shroud Fillet
S = Vane to Solid Shroud Fillet
* = Location in Shipper Cracks

trailing edge cracks could be related to the temperature of the inner inserts which form the vane trailing edge. As no water temperature control circuits were available in that region of the tool, auxiliary electrical heaters were installed. However, because of budget cut-back, no funding was allocated to continue the investigation.

Lack of funding for stator molding development and the concurrent availability of single stator vanes, caused this effort on a monolithic, 19-vane stator to be dropped in February 1984. As of that time, twelve stators were delivered to Garrett for evaluation. Two of those delivered had only one crack each. Table 72 summarizes leading and trailing edge cracks of these stators.

Table 72. Stators Delivered to Garrett.

Stator S/N	Number of Cracks	
	LE	TE
1215202	1	0
1221306	0	2
1110308	1	4
1130306	1	0
0125408	0	3
0221406	1	2
1206203	9	0
1206206	8	13
1020307	1	4
1206308	2	1
1208205	5	7
1209206	7	3

TASK 2.7 - FLOW SEPARATOR HOUSING

Introduction

The flow separator housing is a ceramic component that channels the gas flow through the heat exchanger, acts as a support structure for hot flow path components and provides a sealing surface for the rotating heat exchanger.

The material selected for this component is a low thermal expansion lithium aluminum silicate (LAS) ceramic, made by Corning Glass

Works as their Code 9458 LAS. The process for making the flow separator housing consists of slip casting an aqueous suspension of crushed glass into the desired shape in Plaster of Paris molds. The component then is removed from the mold, dried, sintered, and diamond-machined, as required.

Physical Properties of 9458 LAS

Physical property data on Code 9458 material is shown in Table 73 and Figures 374, 375 and 376.

Table 73. Physical Properties of Corning 9458 LAS.

Bulk Density	2.3 g/cm^3
Apparent Porosity	Zero
Thermal Instability - Linear (500 hours at 2100F)	±100 ppm* max.
(500 hours at 2200F	±200 ppm* max.

*Particles per million

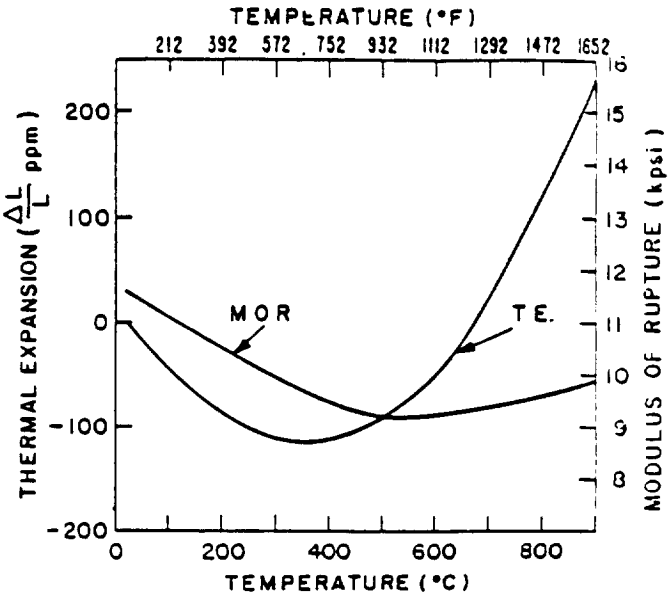

Figure 374. Strength and Thermal Expansion of Corning Code 9458 Lithium Aluminum Silicate.

The bulk density of 9458 LAS measured approximately 2.3 g/cm^3 or ~92 percent of theoretical density. The apparent or open porosity is nominally zero.

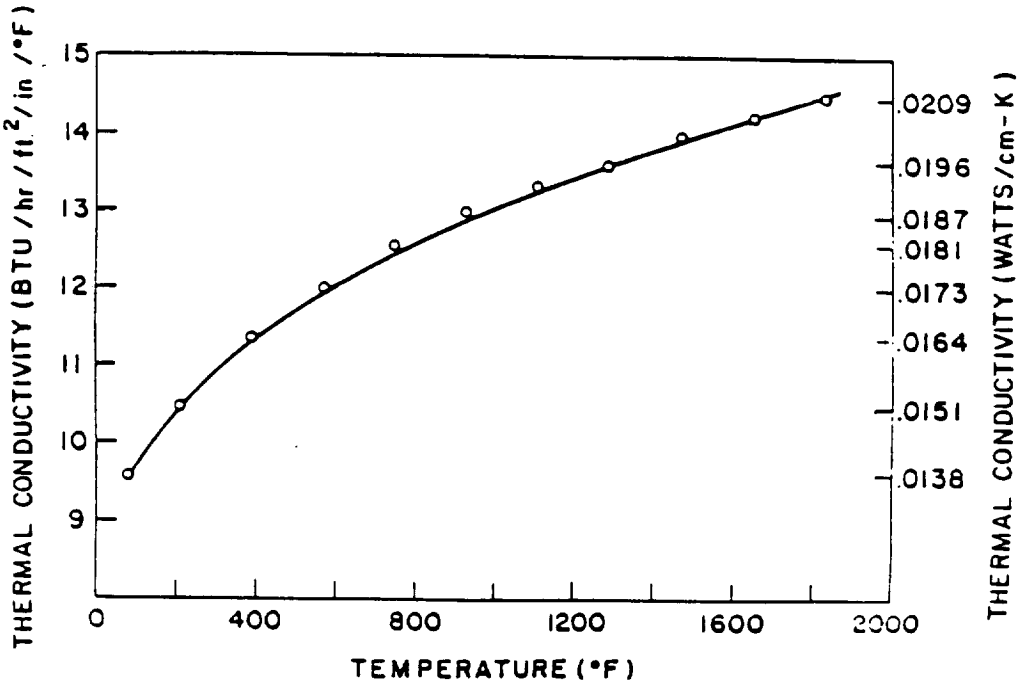

Figure 375. Thermal Conductivity ofCorning Code 9458 Lithium Aluminum Silicate.

The thermal expansion of 9458 shown in Figure 374 is characteristic of beta spodumene-type ceramics. The material undergoes negative expansion from room temperature to approximately 300C, followed by a much sharper positive expansion up to 900C.

The flexural strength data in Figure 374 shows a slight decrease in strength over the range from room temperature to 500C. Above 500C the strength increases, indicating the possibility of microcrack healing.

Thermal conductivity, based on measurements of specific heat and thermal diffusivity, was averaged using two different techniques (Figure 375). Unlike most ceramics, there is an increase in conductivity with temperature.

Figure 376 shows the modulus of elasticity of 9458 LAS. The MOE is approximately

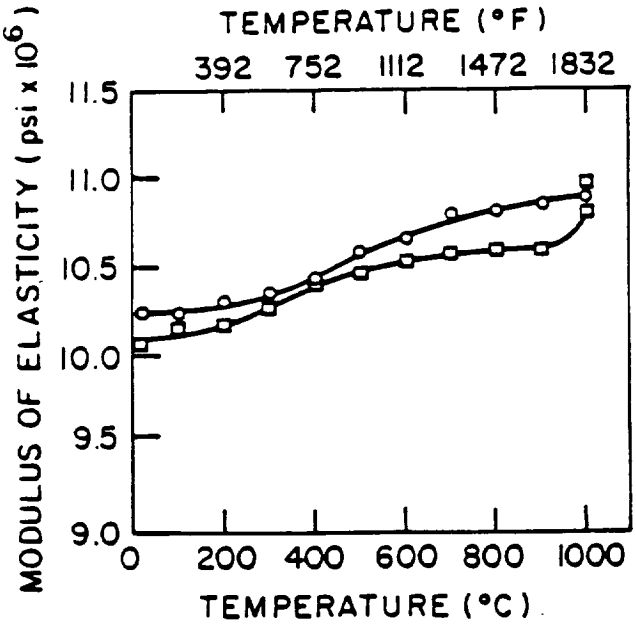

Figure 376. Modulus of Elasticity of Corning Code 9458 LAS.

10,000,000 psi at room temperature and approaching 11,000,000 psi at 1000C.

Dimensional stability of the LAS material was measured by machining one inch cubes and subjecting them to temperatures varying from 1800F to 2200F (in increments of 100F) for 500 hours at each temperature. Measurements were made on cube faces prior to the test and at 250-hour intervals during exposure, with an optical comparator and a series gage block to measure dimensional changes. This technique was accurate to ±10 ppm. Results of this test are shown in Figure 377. The Corning 9458 LAS material retained 100 ppm stability up to 2100F. Above 2100F, additional contraction occurred, and the material fell below the lower limit of - 100 ppm.

Mechanical Testing

The flow separator housing is subjected to thermal and mechanical loads in the engine. In order to provide some assurance that this component will sustain the mechanical loads and to eliminate defective housings early in processing, a test fixture was designed and fabricated to duplicate the engine static operating pressures on the housing.

The test fixture, assembled with a wooden model of the flow separator housing is shown in Figure 378. The fixture is designed to support the housing, simulating engine mounting conditions and sealing the housing to the fixture with rubber gaskets. Hydrostatic pressure loads could be applied within a containment vessel available at Corning. Lifting eyes assist in moving the assembly in and out of the vessel. The upper plate is provided with fittings for a pressure line and an air bleed valve.

The flow separator housing is mounted on a silicone rubber gasket which has the same configuration as the regenerator cold seal assembly. The gasket is molded to the base plate. On the underside of the clamp ring is another silicone rubber gasket which functions as the engine's flow divider regenerator seal. As the clamp ring is bolted to the base plate, the housing flanges are sandwiched between the two gaskets, and the gaskets are compressed to 80 percent of their free height. In the upper plate an "O" ring provides the sealing normally provided between the transition

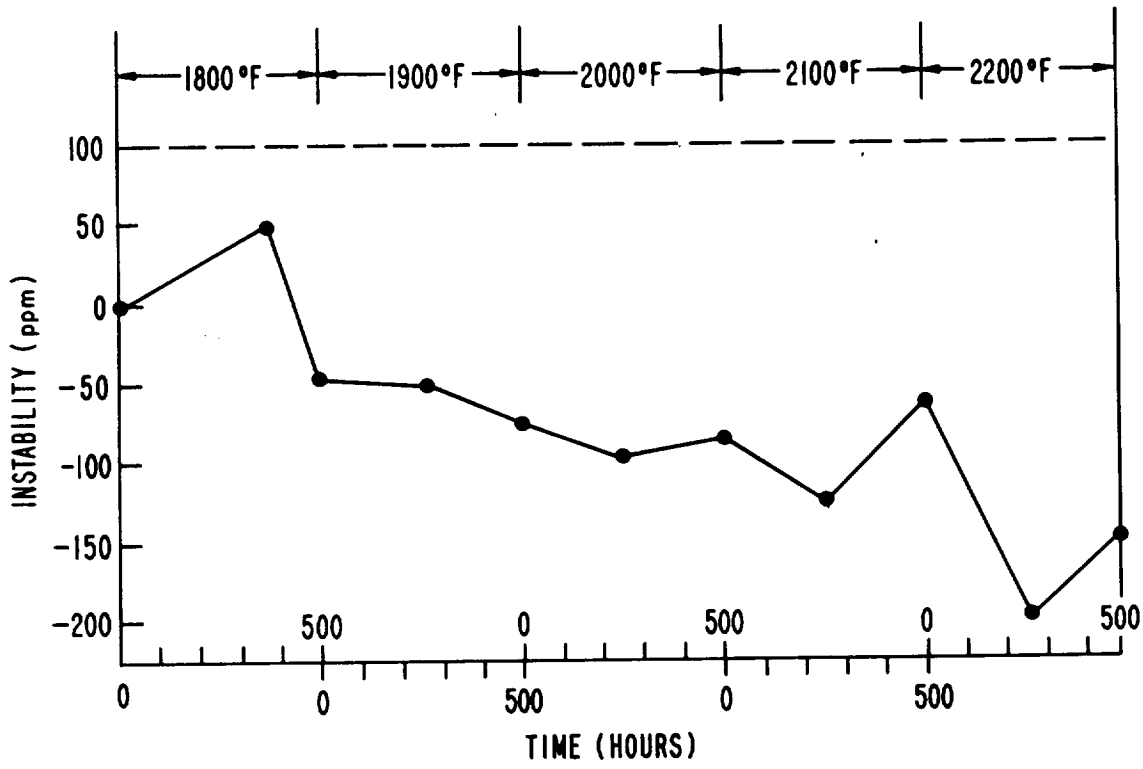

Figure 377. Dimensional Stability of Corning 9458 LAS Material at Various Times and Temperatures.

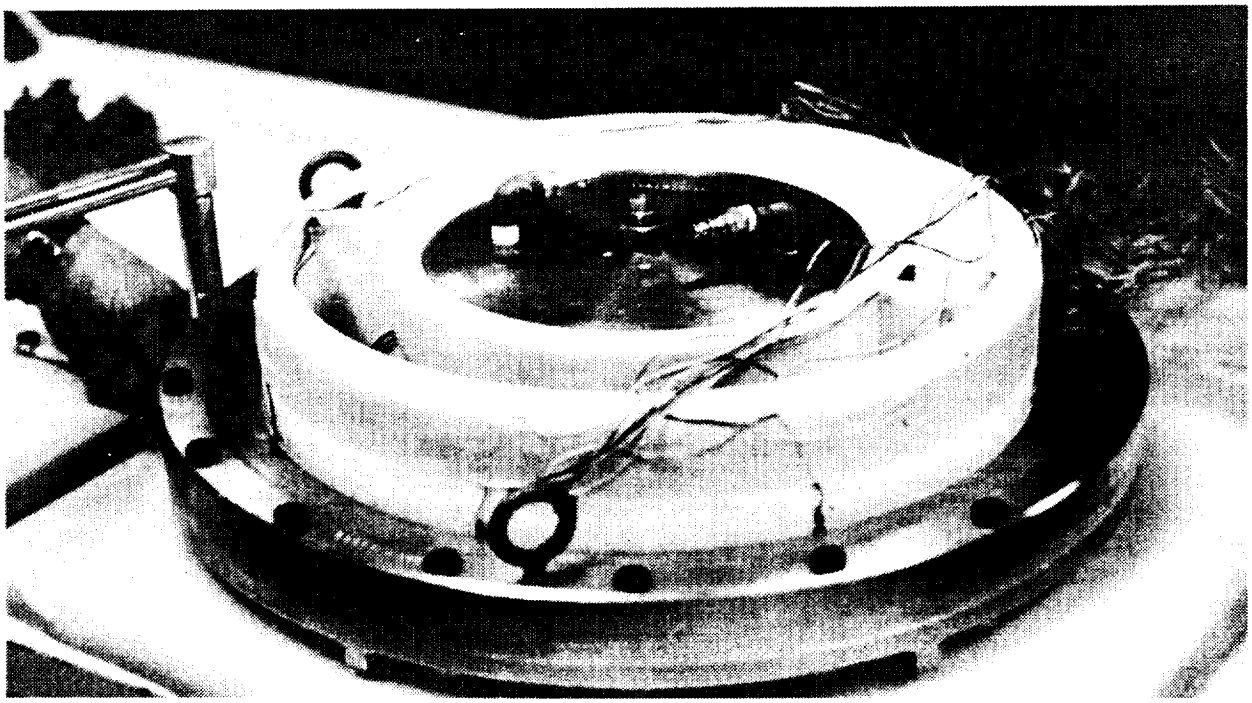

Figure 378. Flow Separator Housing Pressure Test Fixture Shown Assembled to Wooden Model of the Housing.

duct, the turbine shroud and the flow separator housing. Thus the high pressure cavity is sealed and loads can be applied to simulate engine operating pressures.

Each flow separator housing was tested at a pressure 25 percent greater than the maximum mechanical load exerted on the component at full engine speed. All components met the 65 psi mechanical load specification.

Strain Gage Measurements

The flow separator housing mechanical test ratus but also permitted the correlation of 3D stress analysis with mechanical stresses encountered in engine operation. Fourteen uniaxial and 17 triaxial strain gages were attached to SN-8 in critical areas, as shown in Figures 379 and 380. Strain gage data were recorded up to 60 psi in increments of 4 psi in both air and water environments.

Component Fabrication

The initial phase of component fabrication consisted of wooden model machining, pattern design, pattern fabrication and Plaster of Paris mold construction. A series of slip casting experiments was designed to test the feasibility of casting a relatively flaw-free flow separator housing. These experiments revealed the need for a number of design modifications, particularly a double bulkhead wall (Figure 381). With this double wall, casting could be achieved without the incidence of very large voids at the junction of the outer wall/bulkhead and bore/bulkhead.

Table 74 lists the flow separator housings delivered by Corning Glass, inspected by Ford and approved for shipment to Garrett for engine or test rig evaluation. At Ford these housings were visually inspected using dye penetrant and radiographic techniques.

Most of the early flow separator housings, although by no means flaw-free, were of reasonable quality. A period of poor quality followed, in which several components were rejected due to very large casting voids in areas where mechanical and thermal stresses were highest. During this period, a number of process modifications and mold changes were effected. These improvements, coupled with an acceptance specification that permitted casting voids in non-critical areas of the housing, resulted in additional acceptable components for delivery to Garrett. In summary, for a period of five years up to April 1985, the accept/reject ratio for flow separator housing was approximately 1:2. At this point in the AGT101 program, the decision was made that housing quality permitted housings to be shipped directly from Corning, and the Ford inspection technology was transferred to Garrett.

CONCLUSIONS AND RECOMMENDATIONS

This report covers material and process developments by the Ford Motor Company on three key components of the AGT101 gas turbine. These components are the 1) silicon nitride turbine rotor 2) reaction-bonded silicon nitride one-piece stator, and 3) lithium aluminum silicate flow separator housing. The following are conclusive remarks and recommendations for future work on each of these activities.

Rotor Development

- Two materials - sintered, reaction-bonded silicon nitride (SRBSN) and sintered silicon nitride (SSN) - were investigated using the fugitive wax slip casting process to form AGT rotors.

- Investigating experiments shows that the instability of silicon and water prevented the formation of stable slip systems using the SRBSN process.

- However, pre-reacting a compact of silicon and sintering additives produced a silicon nitride powder stable in the presence of water. This material, designated RM-20, was used in conjunction with the fugitive wax slip casting process to make prototype gas turbine rotors.

Figure 379. Ceramic Flow Separator Housing Showing Strain Gages In Place.

- Test bars cut from RM-20 rotors did not have the same material quallity as material cut from a billet. These findings emphasized the importance of developing and fabricating components of test bar quality.
- HIPping of RM-20 rotors versus pressureless sintering resulted in material closest to billet/test bar quality.
- Both pressureless sintered and HIPped silicon nitride rotors showed a glassy secondary phase which affected the stress rupture properties of RM-20.
- The glassy secondary phase was reduced, but not eliminated, through heat treatment. This heat treatment, when done in the absence of packing powder, also resulted in reduced flexural strength. It is recommended that future heat treatment by accomplished in packing powder.
- Crack-free rotors were produced and cold spin tested to failure speeds in excess of 100,000 rpm.

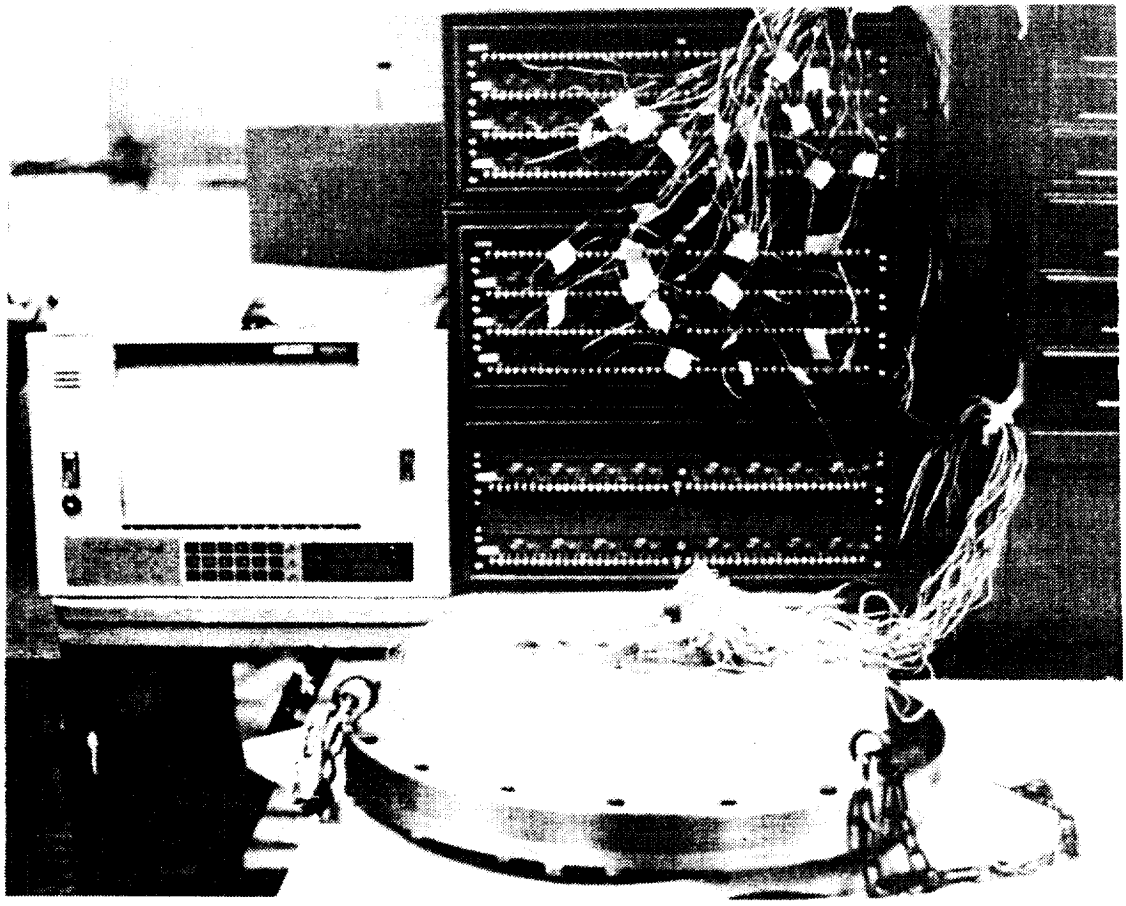

Figure 380. Ceramic Flow Separator Housing Mounted to Mechanical Test Fixture.

- Pore size in the rotor material was most important as related to ultimate failure speed. Future work should focus on reducing pore size as well as total porosity.

- Slip casting using the fugitive wax procedure is a viable process for making prototype rotor components. Future work using this process should address:

  1) Shorter casting time
  2) Increased slip suspension time
  3) Reduction of pore size in the finished rotor

- For the long range, and particularly for low cost, high volume production, the injection molding process and SRBSN is recommended as a rotor material and forming porcess over slip cast SSN and the fugitive wax process. Successes in this area will require improved injection molding binder systems permitting binder burnout of thick section ceramic components.

Reaction Bonded Silicon Nitride Stator

- Injection molding of the complex shaped, monolithic, radial stator was shown to be feasible.

- Lack of funding during th AGT program and concurrent availability of single stator vanes caused the effort on a monolithic, 19-vane stator to be dropped. At that time, twelve stators were delivered for evaluation.

- The molding development efforts revealed complex interaction of many molding

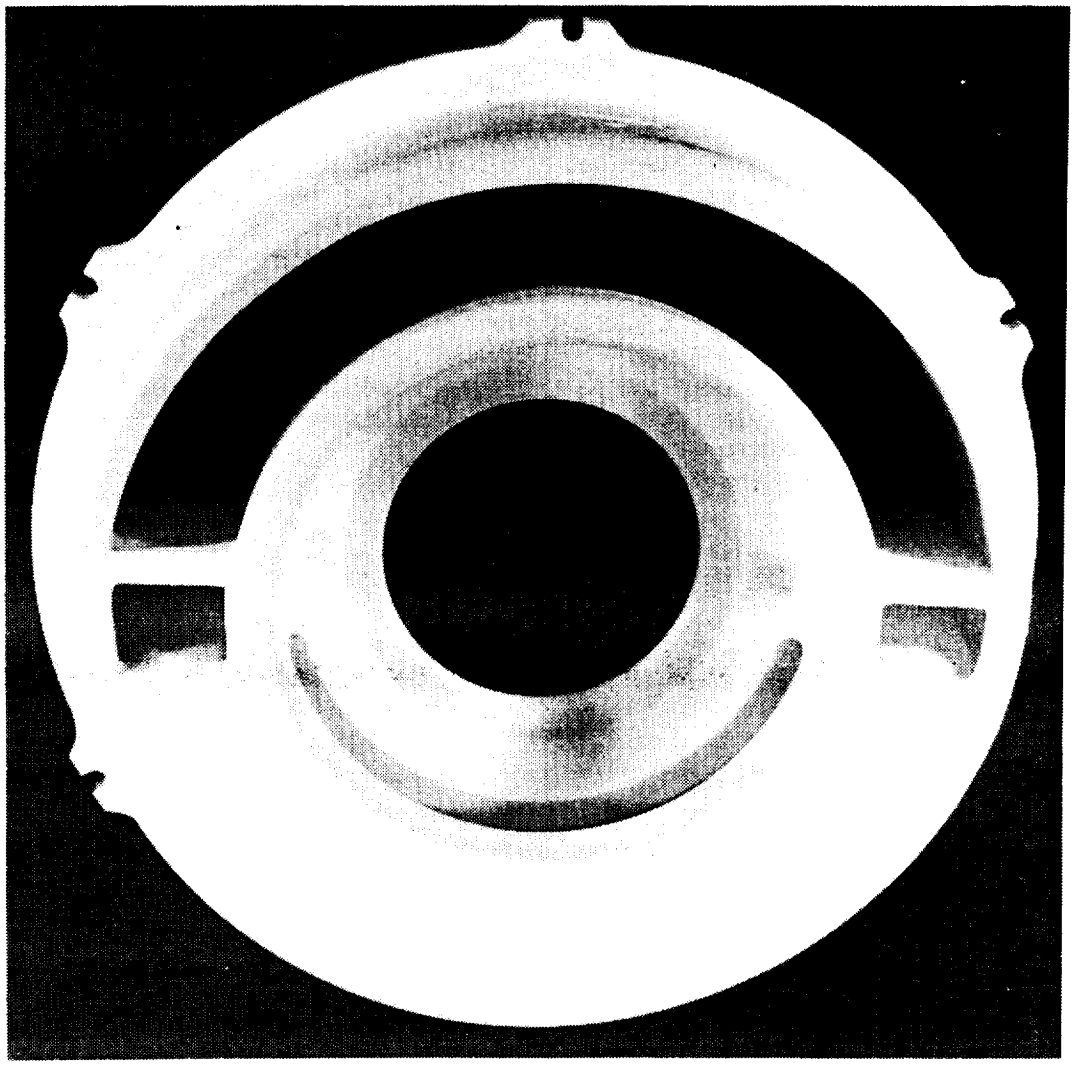

Figure 381. Ceramic Flow Separator Housing with Double Wall Bulkhead.

Table 74. AGT Flow Separator Housing Quality (Period 1980 - 1985).

FSH (No.)	Quality/Comments	FSH (No.)	Quality/Comments
SN-8	Accepted	SN-27	Rejected/Large Voids
SN-12	Accepted	SN-28	Accepted via Deviation (Large Voids)
SN-14	Accepted		
SN-15	Rejected/Large Voids	SN-30	Accepted
SN-17	Accepted	SN-33	Rejected/Machined Incorrectly
SN-21	Rejected/Large Voids		
SN-23	Rejected/Large Voids	SN-37	Rejected/Large Voids
SN-24	Rejected/Large Voids	SN-38	Rejected/Oversize Bore
SN-25	Rejected/Large Voids	SN-41	Rejected/Large Voids

variables influencing several different fabrication defects. As such, more extensive use of statistical experimental design should be applied to resolve the relationship to, and significance of each of the variables to specific flaw types.

- Computer flow modeling was shown to be a very useful tool for providing direction in injection molding tool design and in establishing material flow rate requirements. Efforts should be continued to explore modeling techniques with specific emphasis on the nonisothermal modeling of simple shapes and experimental verification.

- Tool deflection and temperature control were shown to be critical considerations in injection molding die design. These should be evaluated analytically during die design to reduce time consuming delays during tool tryout.

Lithium Aluminum Silicate Flow Separator Housing

- Lithium aluminum silicate is a suitable ceramic material for fabricating large complex components such as the flow separator housing used in the AGT101 gas turbine program.

- The double bulkhead configuration of the flow separator housing demonstrated the importance of component design, not only in meeting performance criteria, but critical fabrication criteria as well. This design modification eliminated the incidence of very large voids at the junction of the outer wall/bulkhead as well as the bore/bulkhead.

- Although the components produced were not totally flaw-free, nondestructive testing and proof test procedures that permitted casting voids in non-critical areas of the housing are feasible.

- This program demonstrated that slip casting is the correct process choice for fabricating large complex components such as the flow separator housing in prototype form. On a long range basis, however, it is felt that a glass ceramic process will be required to attain cost competitiveness in high volume production.

REFERENCES

1) McLean, A.F. and Fisher, E.A., "Brittle Materials Design, High Temperature Gas Turbine," Final Report AMMRC Contract No. DAAG 46-71-C-0162, (AMMRC TR 81-14), March, 1981.

2) Mangels, J.A., Tennenhouse, G.J., "Densification of Reaction Bonded Silicon Nitride," Bull. Amer. Ceram. Soc., Vol. 59, No. 12, (1980), p. 1216.

3) Gazza, G.E., "Hot-Pressed Si_3N_4," J. Amer. Ceram. Soc., Vol. 56, No. 12, 1973, p. 662.

4) Mangels, J.A., "Sintered Reaction Bonded Silicon Nitride for the AGT101 Turbine Rotor," DOE Automotive Technology Development Contractors' Coordination Meeting, Dearborn, MI, Nov. 11-13, 1980.

5) Mangels, J.A., "Sintered Reaction Bonded Silicon Nitride for the AGT101 Turbine Rotor - An Update," DOE Automotive Technology Development Contractors" Coordination Meeting, Dearborn, MI, Oct. 26-30, 1981.

6) Benn, K.W., Carruthers, W.D., "3500 Hour Durability Testing of Commercial Ceramic Materials," Third Quarterly Progress Report, DOE/NASA Contract DEN 3-27, 1978.

7) Hinsolt, G., Knoch, H., Huebner, H., Kleinlein, F.W., "Mechanical Properties of Hot Pressed Silicon Nitride with Different Grain Structures," J. Amer. Ceram. Soc., Vol. 62, No. 1-2, 1979, p. 29-32.

8) Johnson, C.F., Hartsock, D.L., "Thermal Response of Ceramic Turbine Stators," Ceramics for High Performance Applications, Burke, J.J., Gorum, A.E., Katz, R.N., editors, Brook Hill Pub. Company, 1974, p. 549-562.

9) Govila, R.K., Mangels, J.A., Baer, J.R., "Fracture of Yttria-Doped, Sintered Reaction Bonded Silicon Nitride," J. Am. Ceram. Soc., 68 (7), 413-41 (1985).

10) Govila, R.K., "Fracture of Flash Oxidized, Yttria-Doped Sintered Reaction-Bonded Silicon Nitride," accepted for publication in J. Mater. Sci. (1986).

11) Govila, R.K., "Strength Characterization of Yttria-Doped, Sintered, Reaction Bonded Silicon Nitride," Tech. Report SR-86-36, Ford Motor Co., 03-21-86.

12) Tenth Annual Report - AGT101 Program, (NASA CR-179485) June 1984-85.

13) Sanders, W.A. and Mieskowski, D.M., "Strength and Microstructure of Si_3N_4 Sintered with ZrO_2 Additions," Adv. Ceram. Matls., 1, [2], 66-173 (1986).

14) Dutta, S. and Buzek, B., "Microstructure, Strength and Oxidation of a 10 wt. Percent Zyttrite-Si_3N_4 Ceramic," 67 [2], 89-92 (1984).

15) Arnon, N. and Trela, W., "Evaluation of Ceramics for Stator Applications - Gas Turbine Engines," Final Report DOE/NASA Contract No. 0019-83/1 (NASA CR-168140), March, 1983.

16) Hieber, C.A., Isayev, A.I. and Socha, L.S., "An Explorator Investigation of Injection Molding a Highly Ceramic-Filled Material," Cornell University, Ithaca, N.Y., May, 1981.

This Page Intentionally Left Blank

APPENDIX C

PURE CARBON COMPANY
ADVANCED GAS TURBINE (AGT)
TECHNOLOGY DEVELOPMENT PROJECT
FINAL REPORT

Pure Carbon

Early in the AGT101 project, Pure Carbon Co., acting as British Nuclear Fuel Ltd (BNFL) U.S. distributor provided simulated rotors and test bars of Refel reaction-sintered SiC for evaluation. Reaction-sintered SiC products are fabricated by a process in which a porous SiC/carbon body is exposed to silicon at elevated temperatures and the carbon is converted to bonding SiC. No material shrinkage occurs during the conversion process. Green materials to be reaction sintered may be formed by a variety of routes, e.g., slip casting, injection molding, extrusion, isopressing and warm molding, and the green body may be machined before firing. Requirements of binder removal prior to firing and silicon penetration during firing, however, impose thick section limitations on component geometries. These limitations are determined experimentally, although penetration up to 2.54 cm (1 inch) has been demonstrated.

Based on these known limitations, BNFL performed a study to demonstrate binder bake-out and carbon conversion in the thick rotor sections prior to the initiation of a rotor fabrication development program. This study was performed using isopressed and green machined simulated rotors.

Four of these simulated rotors were received from Pure Carbon. Dimensional inspection and surface characteristics were favorable. Density of one rotor was measured as 3.07 g/cm^3. Room temperature strength of one cut-up sample was (49.1 ksi), with a Weibull modulus of 10.

Two Pure Carbon simulated rotors were spin tested to failure. The best result was a failure at 92,000 rpm.

Pure Carbon also provided several seal rings for the regenerator hot shield O.D. of reaction sintered SiC. Deliveries and test activities were curtailed in mid-1981.

This Page Intentionally Left Blank

APPENDIX D

LIST OF SYMBOLS, ABBREVIATIONS, AND ACRONYMS

Acronym	Definition
ACC	AiResearch Casting Company
AE	Acoustic emissions
AGT	Advanced gas turbine
AGT101	AGT model being developed by Garrett/Ford
Al_2O_3	Aluminum oxide, brand name Sol Gel
AS	Aluminum silicate composition, regenerator core
ASEA	ASEA Pressure Systems, Inc., Los Angeles
ATS	Air turbine starter
Astroloy	High temperature superalloy
CBO	Standard Oil, formerly Carborundum Company, Niagara Falls, NY
CFDC	Combined Federal Driving Cycle
cfm	cubic feet per minute, ft^3/min
Corning	Corning Glass Works
dB	Decibel
DES-1000	Chrome-oxide coating from Kaman Sciences
DF	Diffusion flame (relates to combustor/nozzle)
DF-2	Diesel fuel grade 2
DOE	Department of Energy
ECU	Electronic control unit
EDX	Energy dispersive x-ray analysis technique
EPA	Environmental Protection Agency
F	Fahrenheit (degrees of)
FPI	Fluorescent-penetrant inspection
FSH	Flow separator housing
Ford	Ford Motor Company
Fuller's earth	fine, dust-like material for detecting flow paths
g	Gravity, 1-g = force equal to one gravity
g/cm^3	Grams per cubic centimeter
GE-Cordierite	Coating material made by General Electric
Garrett	Garrett Turbine Engine Company, Division of The Garrett Corporation
He	Helium (used for leak path detection)
HIP	Hot isostatic pressing
HP	High pressure
HPSN	Hot pressed silicon nitride
Hz, CPS	Hertz, cycles per second
IBM	International Business Machine, Inc.
ID	Inner diameter
IDH	Inner diffuser housing
inch	U.S. customary linear unit
in.HgA	Inches of mercury, absolute
in-lb	Inch-pounds (work)
I-85	Copper base coating material (regenerator seals)
I-112	Zine-oxide coating material, regenerator seals

APPENDIX D

LIST OF SYMBOLS, ABBREVIATIONS, AND ACRONYMS (Contd)

Acronym	Definition
JP-4	Kerosene base aviation jet fuel
k	Thousands of a unit, e.g., rpm, X1000
ksi	One-thousand pounds per square inch
Kyocera	Kyocera International, Inc., Kyoto, Japan
LAS	Lithium-aluminum-silicate composition-regenerator core
lb-in	Pound-inch (torque)
lb/min	Pounds per minute (flow)
LP	Low pressure
MAS	Magnesium-aluminum-silicate composition, regenerator core
MAR-M 247	Nickel based alloy, dual alloy turbine rotor
mil	One-thousandth of one inch
MOR	Modulus of rupture
N	Speed, rpm
NASA	National Aeronautics and Space Administration
NDE	Nondestructive evaluation
NGK	NGK - Locke, Inc.
NO_x	Nitric oxides
OD	Outer diameter
ODH	Outer diffuser housing
pH	Relative acidity to alkalinity balance
psia	pounds per square inch, absolute
psid ΔP	Differential pressure, pounds per square inch
psig	pounds per square inch, gage
pound, lb	U.S. customary weight measure 0.373 kilograms
p-p	Peak-to-peak
P_{rig}	Rig pressure psi
PV	Pressure-velocity value
RBSN	Reaction bonded silicon nitride
rpm	revolutions per minute
RM-20	Sintered reaction bonded silicon nitride ceramic material
SASC	Sintered alpha silicon carbide ceramic material
SC201 (SiC)	Silicon carbide ceramic material
Si_3N_4	Silicon nitride
S/N	Serial Number
S-77	Zinc-oxide based coating, regenerator seals
SN-71	NGK ceramic materials, sintered silicon nitride
SN-73	NGK ceramic materials, sintered silicon nitride
SN-81	NGK ceramic materials, sintered silicon nitride
SN-82	NGK ceramic materials, sintered silicon nitride
SN 220M	Kyocera ceramic materials, sintered silicon nitride
SN 250M	Kyocera ceramic materials, sintered silicon nitride
SN 270M	Kyocera ceramic materials, sintered silicon nitride
SSN	Sintered silicon nitride ceramic material

APPENDIX D

LIST OF SYMBOLS, ABBREVIATIONS, AND ACRONYMS (Contd)

Acronym	Definition
shp	Shaft horsepower
T	Temperature
Ti	Titanium
TIT	Turbine inlet temperature
$T_{3.5}$	Rating point - combustor inlet temperature
$T_{4.1}$	Rating point - turbine inlet temperature
UT	Ultrasonic techniques, inspection processes
W	Flow, rate as specified
Wayne-Kerr	Rotor dynamic measuring devices
watt	Electrical power - one volt x one ampere
Waspaloy	Heat resistant, high temperature superalloy
Y_2O_3	Yttrium oxide
Zyglo	Surface defect inspection process, brand name
2-D	Two-dimensional
3-D	Three-dimensional
μ	Micro, one millionth
$\mu\epsilon$	Microstrain

This Page Intentionally Left Blank

APPENDIX E

REFERENCES

1) Garrett Turbine Engine Company, "Advanced Gas Turbine (AGT) Powertrain System Development for Automotive Applications," Semiannual Progress Report Number 1 (October 1979 through June 1980), NASA Report CR-165175, November 1980, Contract DEN3-167.

2) Garrett Turbine Engine Company, "Advanced Gas Turbine (AGT) Powertrain System Development for Automotive Applications," Semiannual Progress Report Number 2 (July 1980 through December 1980), NASA Report CR-165329, June 1981, Contract DEN3-167.

3) Garrett Turbine Engine Company, "Advanced Gas Turbine (AGT) Powertrain System Development for Automotive Applications," Semiannual Progress Report Number 3 (January 1981 through December 1981), NASA Report CR-167983, June 1982, Contract DEN3-167.

4) Garrett Turbine Engine Company, "Advanced Gas Turbine (AGT) Powertrain System Development for Automotive Applications," Semiannual Progress Report Number 4 (July 1981 through December 1981), NASA Report CR-167983, June 1982, Contract DEN3-167.

5) Garrett Turbine Engine Company, "Advanced Gas Turbine (AGT) Powertrain System Development for Automotive Applications," Semiannual Progress Report Number 5 (January through June 1982). Contract DEN3-167.

6) Garrett Turbine Engine Company, "Advanced Gas Turbine (AGT) Powertrain System Development for Automotive Applications," Semiannual Progress Report Number 6 (July 1982 through December 1982), NASA Report CR-168246, June 1983, Contract DEN3-167.

7) Garrett Turbine Engine Company, "Advanced Gas Turbine (AGT) Powertrain System Development for Automotive Applications," Semiannual Progress Report Number 7 (January 1983 through June 1983), NASA Report CR-174694, December 1983, Contract DEN3-167.

8) Garrett Turbine Engine Company, "Advanced Gas Turbine (AGT) Powertrain System for Automotive Applications," Semiannual Progress Report 8 (July 1983 through December 1983), NASA Report CR-174809, June 1984, Contract DEN3-167.

9) Garrett Turbine Engine Company, "Advanced Gas Turbine (AGT) Powertrain System for Automotive Applications," Semiannual Progress Report 9 (January 1984 through June 1984), NASA Report CR-174886 December 1984, Contract DEN3-167.

10) Garrett Turbine Engine Company "Advanced Gas Turbine (AGT) Technology Development Project" Technical Summary Report 10 (July 1984 through June 1985), NASA Report CR-179485 July 1986, Contract DEN3-167.

11) Garrett Turbine Engine Company "Brayton Cycle Solarized Advanced Gas Turbine" Final Report (February 1980 through March 1986) NASA Report CR-179559, December 1986, Contract DEN3-181.

12) Govila, R.K. "Strength Characterization of Yttria-Doped, Sintered, Reaction Bonded Silicon Nitride", Tech. Report SR-86-36, Ford Motor Co., 03-21-86.

1. Report No.	2. Government Accession No.	3. Recipient's Catalog No.
CR-180891		

4. Title and Subtitle	5. Report Date
Advanced Gas Turbine (AGT) Technology Development Project	December 1987
	6. Performing Organization Code
7. Author(s)	8. Performing Organization Report No.
Engineering Staff of Garrett Auxiliary Power Division A Unit of Allied-Signal Aerospace Company	31-3725(12)
	10. Work Unit No.
9. Performing Organization Name and Address	
Garrett Auxiliary Power Division 2739 E. Washington Street Phoenix, Arizona 85034	11. Contract or Grant No. DEN3-167
	13. Type of Report and Period Covered Final October 1979-June 1987
12. Sponsoring Agency Name and Address	14. Sponsoring Agency Code
U.S. Department of Energy Office of Transportation Systems, Heat Engine Propulsion Division, Washington, D.C., 20585	DOE/NASA/0167-12

15. Supplementary Notes

Final Report under Interagency Agreement
Project Manager T.N. Strom, Propulsion Systems Division
NASA-Lewis Research Center, Cleveland, Ohio, 44135

16. Abstract

This report is the final in a series of Technical Summary Reports for the Advanced Gas Turbine (AGT) Technology Development Project, authorized under NASA Contract DEN3-167 and sponsored by the DOE. The project was administered by Mr. Thomas N. Strom, Project Manager, NASA-Lewis Research Center, Cleveland, Ohio. This report summarizes plans and progress from October 1979 through June 1987.

Project effort conducted under this contract is part of the DOE Gas Turbine Highway Vehicle Systems Program. This program is directed at providing the United States automotive industry the high-risk, long range technology necessary to produce gas turbine engines for automobiles that will have reduced fuel consumption and reduced environmental impact. The intent is that this technology will be capable of reaching the marketplace by the 1990s.

The Garrett/Ford automotive Advanced Gas Turbine has been designated the AGT101. The AGT101 nominally is a 74.5 kw (100 shp) engine, capable of speeds to 100,000 rpm and operating at turbine inlet temperatures to 1370C(2500F) with a specific fuel consumption level of 0.18 kg/kw-hr(0.3 lbs/hp-hr) over most of the operating range.

This final report summarizes the powertrain design, power section development, and component/ceramic technology development. Appendices include summary reports of progress from Ford Motor Company, AiResearch Casting Company and Pure Carbon, acting as major subcontractors and suppliers of ceramic materials and components. Standard Oil Company's Unique and Common work accomplished under this program is published in topical report (TBD).

17. Key Words (Suggested by Author(s))	18. Distribution Statement
Advanced Gas Turbine Single Shaft Engine Ceramic Turbine Turbine Transmission	Unclassified - Unlimited Star Category 85 DOE Category UC-96

19. Security Classif. (of this report)	20. Security Classif. (of this page)	21. No. of Pages	22. Price*
Unclassified	Unclassified	384	A17

* For sale by the National Technical Information Service, Springfield, Virginia 22161